Cardiff University - School of Chemistry

# Solubility and Phase Behaviour of selected Pharmaceutical Excipients in 2H, 3H-Perfluoropentane

Thesis presented for the degree of *Doctor of Philosophy*

by

Marie Côte





ProQuest LLC
789 East Eisenhower Parkway
P.O. Box 1346
Ann Arbor, MI 48106-1346

**DECLARATION**

This work has not previously been accepted in substance for any degree and is not being concurrently submitted in candidature for any degree.

Signed .....Marie..... (candidate)
Date ..22 September 2008

**SATEMENT 1**

This thesis is the result of my own investigations, except where otherwise stated. Other sources are acknowledged by footnotes giving explicit references. A bibliography is appended.

Signed .....Marie..... (candidate)
Date ..22 September 2008

**STATEMENT 2**

I hereby consent for my thesis, if accepted, to be available for photocopying and for inter-library loan, and for the title and summary to be made available for outside organisations.

Signed .....Marie..... (candidate)
Date ..22 September 2008

# *Abstract*

The behaviour of pharmaceutical excipients was studied in 2H, 3H-perfluoropentane (HPFP), a partially fluorinated liquid considered as a highly suitable model propellant for medicinal pressurized metered-dose inhalers (pMDIs) used in drug delivery to the lungs. The additives chosen belonged to three main categories: ethylene oxide oligomers and derivatives, chosen for their wide range of applications in pharmaceutical formulations, their harmlessness and low cost; a hydrophobically modified cyclodextrin that shows potential for controlled release via host-guest interactions and some interesting solubility pattern in HPFP; a family of tetrahydroxy diesters that act as unprecedented organogelators for mixtures of HPFP and a partially fluorinated alcohol co-solvent.

By studying ethylene oxide oligomers and derivatives in HPFP and fully fluorinated analogue PFP, it was found that the solubility of the oligomers could be tuned by varying the nature of their end-group and the polarity of the fluorinated liquids employed. Methyl groups, either placed at the extremities, thus blocking the hydroxyl end-groups of dihydroxyl end-capped polyethylene glycols, or directly added on the polymer backbone, clearly enhanced their solubility. The Lower Critical Solution Temperature initially observed was either displaced or removed via the presence of the additional methyl groups. On the other hand, such phase separation could also be induced by the subsequent addition of PFP; it is shown that such behaviours are dominated by end-group/solvent interactions. This study was published in two papers, *Journal of Pharmacy and Pharmacology*, 2008, **60**: p. 593-599 and *International Journal of Pharmaceutics*, 2008, **362**: p. 147-152.

As an attractive formulation means, the hydrophobic triacetylated-β-cyclodextrin (TAβCD) was chosen amongst others for its partial solubility in model propellant HPFP. The observation that various batches of the same chemical entity lead to highly different solubility profiles in HPFP resulted in the full characterisation of two existing polymorphs for this compound. The monitored conversion of one form into the other was achieved, and the amorphous form could be fully recrystallysed into the higher energy form via a limited seeding process. HPFP acted as a discriminator of the two crystalline forms. More details may be found in *Journal of Physical Chemistry C*, 2008, **112**: p.14570-15578.

The monitoring of the solubility via solvent properties, as seen in the first part, was also used in the formation of self-assembled supramolecular organogels. The addition of non-solvent HPFP to an initially stable sol composed of a small tetrahydroxy diesters in the fluoroalcohol 1H, 1H-heptafluorobutanol initiated their coming out of solution. However, instead of simply precipitating, the tetrahydroxy diester molecules self-assemble into long cylindrical fibres that form a 3-dimensional network capable of entrapping the fluorinated liquids, leading to a system that is both solid-like macroscopically and liquid-like microscopically. Such gels are thermoreversible and can be obtained at gelator concentrations as low as 0.1 wt%, thus, surface tension and capillary action are thought to be the principal forces behind these structures, along with hydrogen-bonding between the gelators molecules, rather than a specific gelator-solvent interaction. This work is the reference for both *Chemical Communications*, 2005, **31**: p. 3998-4000 and a manuscript to be submitted.

# *Acknowledgements*

I would like to express my gratitude to a number of people who all contributed to this thesis, in a way or another.

I would first like to thank Cardiff University and my academic supervisor Dr. Peter C. Griffiths for his continuous support, for his trust and for giving me entire freedom regarding this project.

I wish to thank AstraZeneca for their sponsorship and my two successive industrial supervisors, Dr. Philippe G. A. Rogueda and Pr. Clive Washington, for their greatly appreciated help and enthusiasm, their welcoming in the Charnwood and Loughborough laboratories, and for contributing to my attendance to international conferences.

I thank Pr. David W. Knight and Dr. Ian Morgan for the (nearly 'on-demand') synthesis and supply of essential materials for this project, and wish them success in pursuing this work.

I wish to warmly thank Pr. Kenneth D. M. Harris and Dr. Colan E. Hughes for their time, their help, and the many fruitful discussions that made our collaboration such an enjoyable time and a great learning experience for me.

I wish to thank Sarah, Champa, Tuss, Zeena, who made the lab a nice and welcoming place in the 1st year, and Rob also, who handed his PhD project over to me, giving a nice basis to work on. I wish to thank Nilmini and Paola, for being such nice people to share the lab with in the 3rd year, and Alison, Abdul, Craig and Gemma (who is now carrying on and expanding the work in this thesis) for all making the lab a more enjoyable place to be. A special mention to the fishtank for providing living company during the 2nd year.

I wish to thank the people who made Cardiff a great place to be, in particular Heike, Richard, Pierre and Anna, Nico, Guillermo and Serena. I also thank the people in my new job back in France who kept asking to get the write-up finished so that I could join them hiking, rock-climbing, squashing, rafting... I wish to offer a special thank to astrophysicist T.F.C for his kindness and support all the way through this work, and for his tasty time-saving cuisine.

Finally, I wish to thank my family for their continuous encouragements and positivism, and in particular my grandparents to whom I wish to dedicate this thesis.

# *Table of Contents*

*(A compact disk is provided as part of this thesis and can be found on the inside front cover, that contains a footage of the recrystallisation process studied in Chapter 6)*

# *Project Overview*

**Chapter 1** sets the PhD project into context by providing a comprehensive review of the use of fluorinated systems in biomedical applications, with emphasis on the switch from environmentally damaging chlorofluorocarbons (CFCs) to hydrofluoroalkanes (HFAs) in pressurized metered-dose inhalers, and the need of a HFA model propellant.

**Chapter 2** presents the theoretical aspects of techniques or concepts that were considered for obtaining the results presented in Chapters 4, 5, 6 and 7.

**Chapter 3** covers the materials and methods used throughout the project. It is organised into sections referring to the specific result Chapters for which they are relevant.

**Chapter 4** details the solubility of a series of ethylene oxide oligomers in model propellant 2H, 3H-perfluoropentane (HPFP) and underlines the fundamental importance of the structure of the end-group of the oligomer and solvent polarity.

**Chapter 5** follows on the previous study and describes the behaviour in HPFP of derivatives bearing ethylene oxide moieties as a common structural feature, in the form of propylene glycol oligomers, poly(ethylene oxide) monododecyl ether surfactants and a poly(ethylene oxide)-poly(propylene oxide)-poly(ethylene oxide) triblock copolymer.

**Chapter 6** highlights the role of HPFP as a discriminator for various polymorphic forms of a hydrophobically modified cyclodextrin, having host-guest chemistry potentials for control release applications.

**Chapter 7** provides an insight into the gelation of fluorinated liquids using small and non-fluorinated molecules that act as organogelators at very low concentrations, forming thermoreversible self-assembled supramolecular structures.

# Chapter 1 Introduction

Fluorinated systems generate great interest in the chemical industry. They are being used as solvents in the electronic industry, as heat transfer medium in the refrigerant industry [1], as novel compounds with very low surface energy properties in the surfactant industry, or as drug delivery systems and also therapeutic molecules for pharmaceutics and medical applications, such as lung fluid replacement or blood substitutes [2]. However, due to the particular physical and chemical properties of fluorinated compounds, i.e. both lipo- and hydrophobic, such applications mostly rely on the fluorinated liquids being formulated with the addition of excipients, to turn them into useful products. So far, the performance of these products can be measured and assessed, but descriptives and predictive tools are still required to understand the behaviour of the additives. This project initially focused on the behaviour of common pharmaceutical excipients in a novel fluorinated liquid used as a model propellant for metered-dose inhalers (as used for drug delivery to the lungs), the aim being to initiate a comprehensive description of the behaviour of such formulations that are useful to the pharmaceutical industry [3]. Subsequent studies described in the later chapters broaden this to the study of unusual or unexpected systems and their characterization, still bearing in mind their relevance to pharmaceutical applications.

This chapter will introduce the metered-dose inhaler technology, along with the inherent challenges of switching from CFCs to non ozone-depleting propellants. Emphasis will be placed on the specific properties of fluorinated compounds and their implications for uses in biomedical fields.

## 1.1 Drug delivery via the lungs and metered-dose inhaler technology

### 1.1.1 Drug delivery via the lungs

Drugs can be administered to the body in a variety of ways, be it topical (e.g. creams and ointments), oral (e.g. tablets) or parenteral (e.g. injections). In most cases the active pharmaceutical ingredient (API) needs to first pass into the bloodstream to then reach the affected area needing treatment. The lungs, with their large surface area,

present an efficient and direct route to the bloodstream [4]. The activity of their degradatory enzymes is also much lower than that of the kidneys or liver [5]. Both these characteristics render the lungs an attractive and viable alternative to oral or parental routes for the delivery of APIs to the systemic circulation [6]. The lungs themselves can be the organs challenged, as in the case of asthma or chronic obstructive pulmonary disease. In all cases, the API needs to reach the lungs and the pressurized metered-dose inhaler (pMDI) technology allows such a targeted drug administration [7, 8].

### 1.1.2 Pressurized metered-dose inhalers (pMDIs)

The pMDI is a compact, sealed drug delivery device that is an inexpensive, reliable and patient compliant form of administering the drug to the lungs. Riker Laboratories were the first to launch such a device in 1956 with Medihaler-Iso™ and Medihaler-Epi™, for the treatment of pulmonary condition, and are considered as pioneers for targeted drug delivery. The key components of the pMDI are the propellant, the drug formulation, the metering valve and the actuator nozzle. By adjusting these parameters, the particle size characteristics of the emitted spray can be finely tuned [9], and as shown by Dalby *et al.*, a mass median aerodynamic diameter of *ca.* 3 μm is necessary for the aerosol to be deposited in the lower respiratory tract [10, 11]. The size of the drug particles is critical for an effective lung treatment, as particles larger than 10 μm will deposit in the oro-pharinx and will not reach the lungs, while very small particles will be exhaled before colliding with the endothelium, the thin layer of cells lining the interior surface of blood vessels [12]. A typical pMDI device is shown schematically in Figure 1-1.

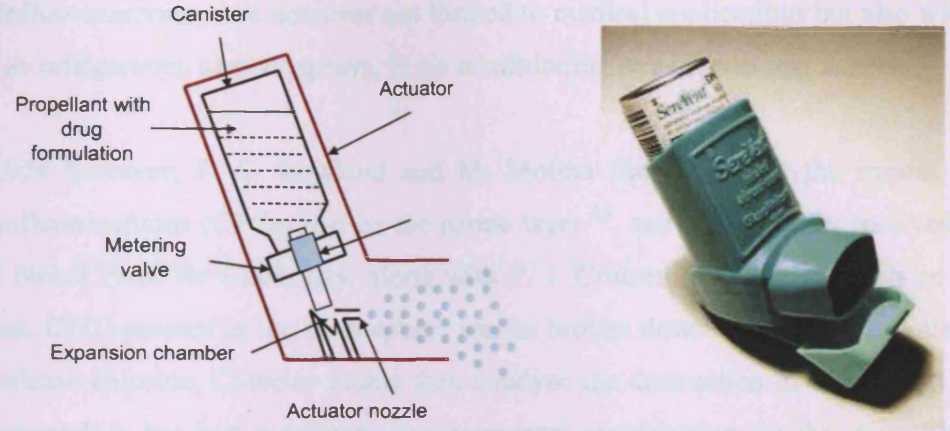


**Figure 1-1 (left panel) Scheme of a typical pMDI device highlighting the key components, and (right panel) picture of a marketed pMDI device, picture taken from Ref. [13].**

The propellants used are liquefied gases that provide the energy to aerosolize the drug formulation. They should be non-toxic, non-flammable and compatible with the drugs, either formulated as solutions or in suspension, and possess the appropriate volatility and density [14]. The vapour pressure should also be kept constant in order to ensure a consistent dose delivery throughout the product life. The drug in pMDIs is formulated with the help of surfactants and cosolvents, so as to increase drug solubilisation in solutions or to prevent aggregation in suspensions. The surfactants also lubricate the metering valve mechanism which ensures a reproducible volume for dose deliveries. Some taste-masking agents can also be added. The formulation is expelled through the actuator nozzle, whose size is critical in the spray formation and thus in the efficient lung deposition of the drug [9].

## 1.2 Chlorofluorocarbon (CFC) propellants, alternatives and formulations

### 1.2.1 CFCs properties and environmental issues

Chlorofluorocarbons met the demanding requirements for propellants in pMDI technology. Pressurized in the pMDI canister, CFCs form a system composed of the liquid and its saturated vapour, which dynamic equilibrium results in a constant vapour pressure, irrespective of whether the can is full or nearly empty [9]. Since the pMDIs' launch, CFCs used were Freon™ 12 (dichlorodifluoromethane, $CCl_2F_2$) as the major component, with Freon™ 11 (trichlorofluoromethane, $CCl_3F$) and Freon™ 114 (dichlorotetrafluoroethane, $CClF_2CClF_2$) as pressure modifiers. These

chlorofluorocarbons were however not limited to medical applications but also widely used as refrigerants, aerosol sprays, in air conditioning or as fire extinguishers.

In 1974 however, F. S. Rowland and M. Molina first presented the impact that chlorofluorocarbons (CFCs) had on the ozone layer [15], and subsequently received the 1995 Nobel Prize for Chemistry, along with P. J. Crutzen, for their research on this subject. CFCs present in the stratosphere can be broken down by ultraviolet radiation and release chlorine. Chlorine atoms then catalyse the destruction of ozone ($O_3$) and this ozone loss has had a dramatic environmental repercussion, as the stratospheric ozone layer protects the Earth's surface from harmful UV-B by absorbing most of the radiation [16]. In 1987, the Montreal protocol, aiming at progressively phasing out the use of CFCs in all applications, was signed [17], which effectively implied a new start for the inhalation industry, with a full reformulation process for existing products via the selection of new propellants, excipients and container systems. Facing such a challenge, some manufacturers preferred to invest efforts into the optimisation of Dry Powder Inhalers (DPIs), therefore removing the need for a propellant or solubilising media altogether. DPIs had already been introduced in 1973 but never reached the efficiency and popularity of pMDIs. Most developers however decided to keep to the pMDI technology and search for suitable alternative propellants [18].

### 1.2.2 CFCs alternatives and their formulation

Hydrofluoroalkanes (HFAs) were identified as suitable replacements to CFCs. HFA decomposition leads to hydrogen fluoride, which is inert in the stratosphere thanks to its bond strength, and further fluorine was not found to deplete the ozone layer [19]. HFAs are still minor 'green house' gases though [20], but the benefit to human health provided by pMDIs was found to outweigh the environmental concern [12]. The closest matching HFAs to CFC Freon™ 12 were found to be HFA-134a and HFA 227ea, whose structure is shown in Figure 1-2, and these were adopted as propellants in pMDIs.

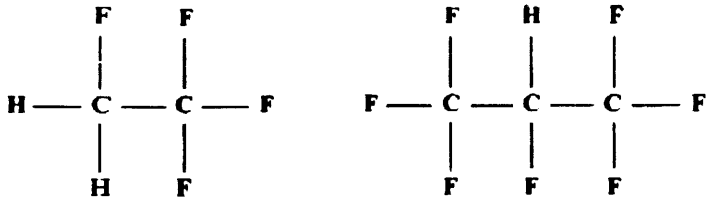

**Figure 1-2 Structure of propellants HFA-134a (left) and HFA 227ea (right).**

HFAs physicochemical properties do not however fully match those of the CFCs, and the shift to HFAs is not, in many ways, straightforward [21]. First, extensive toxicity studies (genetic and reproduction toxicology, cardiac sensitivity, maximum inhalation doses and excretion rates...) needed to be performed on the new HFAs prior to any medical application [22]. Then, the HFA may interact with the pMDI device differently than the CFC used to. Drug particles were found to adhere to the surface of the cans and to the valve, resulting in a variability of the dose delivered, and coatings were developed so as to prevent this adherence. It should also be ensured that HFAs do not act as solvents for the valve elastomers so that concentrations of extractable and leachables are kept to a minimum in the formulation [23]. Finally, the drug formulation itself had to be revisited, as many excipients were reported to have very low solubility in HFAs. This is the result of the rather different physical properties of CFCs and HFAs. While CFCs are fully halogenated, HFA-134a and HFA 227ea respectively posses one or two small hydrogen atoms. The presence of fluorine instead of chlorine atoms in both HFA propellants enhances the electronegativity of the halogen mantel and creates a dipole on the hydrogen-carbon bonds [24]. The Kauri-butanol values (the amount of solvent under consideration that must be added to a solution of kauri gum in n-butyl alcohol for precipitation of the gum to occur [25]) and Hildebrand solubility parameters (*cf.* Chapter 2, p. 2-10) do not differ greatly from CFCs to HFAs (with the exception of Kauri-butanol value for CFC 11) and cannot be used to predict the differences in solvency properties observed. However, the increased polarity is reflected by dipole moments and dielectric constants that are larger in HFAs than those observed in CFCs. HFAs' polarizability is also smaller and is reflected in the low intermolecular interactions and boiling points of the propellants. The solubility of water in HFAs was found much greater than in CFCs (e.g., 610 ppm and 2220 ppm respectively for HFA 227 ea and HFA 134a against 100 ppm and 91 ppm for CFC 11/12 and CFC 12/114 , at 25 °C) due to the availability of hydrogen-carbon dipoles [24].

The surfactants that were traditionally used in CFC pMDIs, such as hydrocarbon-based sorbitan trioleate, oleic acid and lecithin, are poorly soluble in HFAs, unless co-solvents, such as ethanol, are added [24, 26]. These surfactants are hydrophobic with low hydrophilic-lipophilic balance (HLB) values [27] (respectively 1.0, 1.8 and 7.3 for oleic acid, sorbitan trioleate and lecithin), and replacements for HFA's were investigated amongst the more hydrophilic surfactants, that showed to be more readily soluble in HFAs. For example, polyethylene glycol of molecular weight 300 g $mol^{-1}$ with a HLB value of 20 has an apparent solubility of ca. 4 w/w% in HFA 134a compared to less than 0.01 w/w% in CFC11 [24]. However, so far the inhalation approved surfactants require the use of co-solvents to be soluble in the propellant and this is not always appropriate for the pMDI formulation. At this point it is essential to emphasize the fact that two types of pMDIs formulations exist: solution based systems, in which the drug is dissolved in the propellant, and suspension-based systems, in which the drug is in the form of micronized particles distributed in the propellant [10].

Most of the HFA-pMDIs utilize the suspension formulation, mainly due to the general poor solubility of the drugs in HFAs [28]. In his review, Smyth listed a group of 17 common marketed pMDIs, out of which 14 are formulated as suspensions [26]. In a suspension system, the use of co-solvents for the solubilisation of the surfactants necessary to prevent particles aggregation [29] will also promote the solubility of the suspended drug, leading to crystal growth problems via Ostwald ripening, in which entropy favours the dissolution of smaller particles and their recrystallisation on larger ones, and thus is incompatible with suspension formulations [30]. As explained by Vervaet and Byron [24], suspension systems should ideally be formulated with drugs that are insoluble in the continuous phase. If crystal growth may appear to cause problems, the tools available to the formulator are the use of a different physical form of the drug substance, the engineering of the surface characteristics for the retardation of dissolution, or still the selection of the most stable polymorph. The effect of the crystalline structure of compounds with regards to their solubility is indeed a key parameter and will be highlighted in Chapter 6 of this thesis, with hydrophobically modified β-cyclodextrins that have different packing arrangements. Even though using a co-solvent, Steckel *et al.* obtained a stable micronized suspension. They established a two-step procedure in which the model drug budesonide was firstly dissolved in a cyclodextrin and poly(ethylene glycol)-containing solution of ethanol

that was then precipitated via the addition of the HFA propellant which acted as a non-solvent, giving a micronized suspension which remained stable for over three months [31]. The addition of a non-solvent to destabilize an initially stable solution will be applied in Chapter 7, however for a different end.

As further expressed by Ashayer *et al.*, pMDI suspensions are often unstable and phase separation, via flocculation or creaming, contributes to poor product performance [32]. Such instability can find its origins in strong attractives forces between the drug particles, or the particles and the inhaler device, although in the latter case, Vervaet and Byron propose that it may not be the attraction between the canister and the drug particles as much as the repulsion by the propellant itself that leads to suspended solids preferring to settle on HFA depleted surfaces [24]. Two main methods are used for the stabilisation of particles. One is based on electrostatic effects and the Dejarguin-Landau-Vervew-Overbeek (DLVO) theory, grounded in aqueous media where the suspension stabilisation is introduced by repulsive electrostatic interactions generated by the intrerpenatration of the ionic electrical double layer. Such an application of the DLVO theory for drug particles suspended in non-aqueous media is yet to be validated [28]. As reported by Ashayer *et al.* [32], work by Pugh *et al.* show that for electrostatic stabilization to be effective, the zeta-potential of carbon black suspension in non-aqueous media had to be greater than 100mV, which is much more than what reported for salbutamol sulphate, a model drug used in pMDIs. Thus, drug stabilisation via repulsive double layer interaction in non-aqueous media has been accepted to be of negligible influence [33]. The other means of stabilisation involves the introduction of steric effects via the presence of polymeric additives. Their role is to reduce the effective inter-particle attractive forces via the formation of a protective sheath that can impart repulsive forces, thus preventing aggregation. Ideally, the additive will be able to interact with the drug particles and with the surrounding medium, being both adsorbed to the particle surface via lipophobic blocks and remain freely in the surrounding media via lipophilic blocks. This lipophilic block, when extended, creates a layer surrounding the particles that will limit the van der Waals interactions between the drug particles [33]. To assess the efficacy of the polymeric additive, Ashayer *et al.* propose to directly measure the forces involved, via the use of atomic force microscopy (AFM). Initially developed as an imaging tool, AFM has been used since to measure a wide array of forces, in

aqueous or non- aqueous media, between a variety of surfaces or even in biological systems. Rogueda *et al.* have pioneered the study of adsorbed polymer layers interaction in pMDIs to quantify the efficacy of polymeric additives and can-coatings on the drug particle adhesion forces [32-36].

On the other hand, developments in solution pMDI are being made, and solution-based formulations have even shown an improved dose uniformity and a higher lung deposition than suspension ones [37]. However, solution-based formulation suffers from a poorer chemical stability of the drugs, an increased concentration of surfactants acting as stabilisers, and the toxicological profile of the surfactant itself. Lately much investigation has concentrated towards the generation of emulsion- and microemulsion-systems based on water/fluorocarbon/surfactant for the delivery of drugs to the lungs, many of the drugs intended for pulmonary delivery being indeed insoluble in propellants, but soluble in water [38]. Stable water in fluorocarbon emulsions were designed using F-alkyl dimorpholinophosphates, $C_nF_{2n+1}C_mH_{2m}OP(O)[N(CH_2CH_2)_2O]_2$, which are strongly fluorophilic and weakly hydrophilic amphiphiles [39]. Their cytotoxicity was measured and found to decrease with increasing fluorinated-chain length of the surfactant. The reverse emulsion consisting of perfluorooctyl bromide as the external phase, water as the internal phase and the aforementioned surfactant with n= 8 or 10 and m=11 was rated as non cytotoxic [40]. Further investigations were performed on this emulsion and both promising toxicological data and evidence of systemic delivery of insulin via intranasal route were reported in mice [41]. Using such a reverse emulsion, with amphiphile structure n=8 and m=11, Butz *et al.* developed a packaged pMDI aiming at targeting hydrophilic drugs into the lungs, propelled using hydrofluoroalkanes HFA 134a and HFA 227 [42]. The drugs solubilized or dispersed in water constituted the internal phase of the emulsion, and homogeneous and reproducible doses of cafeine could be delivered this way. Even though perfuorooctyl bromide and the reverse emulsion were soluble in all proportions in both HFA propellants HFA 134a and HFA 227, Butz *et al.* highlight the fact that no emulsion could be formed when using the fluorinated surfactant with a mixture of water and propellant on their own. The fluorinated propellant cannot be a substitute for the emulsion external fluorocarbon phase perfluorooctyl bromide, thus the preparation of a reverse water-in-fluorocarbon phase is required. The reverse water in fluorocarbon emulsion was composed of 95%

v/v perfluorooctyl bromide, 5% v/v NaCl solution (0.9% w/v) and 1.5% w/v of surfactant, and best results were obtained with ratios of emulsion/propellant going from 2/3 to 3/2, using HFA 227. Then, microemulsions are attractive systems, as their formation is spontaneous and results in a thermodynamically stable system within a well-defined temperature-composition domain. They can possess a wide variety of microstructures, such as oil or water droplets surrounded by monolayers of surfactant and co-surfactant that are dispersed in the aqueous or hydrophobe phase respectively. The structure can also be bicontinous and consist of channels of oil and water interpenetrating, also surrounded by monolayers of surfactant and co-surfactant. For a pMDI application, the microstructure chosen would be a water-in-oil (propellant) microemulsion so that the water soluble API can be dissolved in the aqueous core of the droplets [43]. Using the same compounds as Butz *et al.*[42], Courrier *et al.* formed microemulsions, but the surfactant concentration required was this time much higher and comprised between 8 and 30% w/v. Using such a composition, the initial droplet mean diameter was 11.5 ±0.5 nm and did not change for at least six months. At lower surfactant concentrations, they observed the formation of what they called a 'miniemulsion' where the droplet mean diameter was initially 40 nm but reached 200 nm after 200 days, such a degradation attributed to Oswald ripening [44]. Patel *et al.* synthesized partially fluorinated non-ionic surfactants of general formula $C_nF_{2n+1}C_mH_{2m}O[(CH_2CH_2O)_p]H$ and looked for formulations rich in propellant HFA 134a that would lead to reverse water in fluorocarbon microemulsions, using the HFA as the external fluorocarbon phase. Only the surfactant bearing n=4, m=2 and p=6 was found to form a microemulsion, however, this microemulsion could not be achieved with the sole use of the surfactant and it required the addition of an alcohol cosurfactant, namely short chain hydrocarbon alcohols such as ethanol, propanol or pentanol [37]. Fluorinated surfactants having a higher molecular weight than their hydrocarbon counterparts and larger amounts being needed, Patel *et al.* further stress the fact that such a high solid content in the pMDI formulation could reduce its volatility, therefore leading to sprays that are too large to penetrate far into the lungs where they are needed.

To summarize, the compulsory switch from CFCs to HFAs generated massive investments in what used to be a stagnant technology, leading to significant technological and medical improvements [45]. While only 5 to 25% of the CFC-

propelled drug dose would reach the lungs, the efficiency has now increased to 60 % of delivered drug with HFA-pMDIs [46]. HFA-pMDIs are also far less sensitive to temperature as far as the dose delivery is concerned, and now, an increasing number of medicines are to be administered using the pMDI technology, such as insulin, proteins, antibodies, anticancer drug [21]. Figure 1-3 provides a concise view of the pMDI development from its launch in the 1950s until the current time.

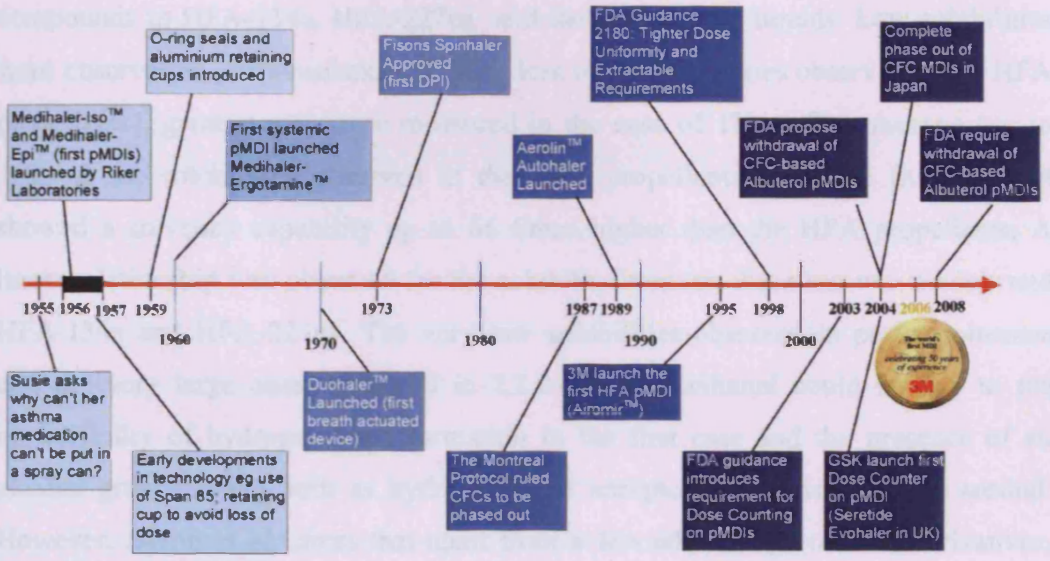


**Figure 1-3 History of the pMDI, taken from Ref. [18] (FDA :Food and Drug Administration).**

### 1.2.3 In need of a liquid model for gaseous HFA propellants

Using simple sealed equipment was usually sufficient to study CFC pMDI formulations, even though still volatile, at ambient temperature and pressure [29]. However, when the formulations could not be studied in situ, one made use of a model propellant. The two most used models were P113 (1,1,2-trichlorotrifluoroethane) and chloroform, which acted as standards for the description of pressurized systems, along with being cheap and well characterized [47]. In the case of HFA-134a and HFA-227ea which are gasses at room temperature and atmospheric pressure, with boiling points of -26.3 °C and -16.5 °C respectively, a simple seal does not suffice anymore and such low boiling points render any benchtop experiment unpractical. Although much research is generated towards the design of apparatus adapted to the pressurized regime, there is an evident need for a model propellant,

possessing comparable physico-chemical properties, except for a higher boiling point, and from which results could be extrapolated and transferred to the actual propellants HFA-134a and HFA-227ea.

### 1.2.3.1 Potential models

Dickinson *et al.* [48] proposed perfluorohexane, 1H-perfluorohexane and 2,2,2-trifluoromethanol as models for HFA-propellants, based on the solubility of a range of compounds in HFA-134a, HFA-227ea and the investigated liquids. Low solubilities were observed in perfluorohexane (1% or less of the solubilities observed in the HFA propellants), greater ones were measured in the case of 1H-perfluorohexane (up to 26% of the solubilities observed in the HFA propellants), and the fluoroalcohol showed a solvency capability up to 66 times higher than the HFA propellants. A linear relationship was observed for the solubility between these last two models and HFA-134a and HFA-227ea. The very low solubilities observed in perfluorohexane and the very large ones measured in 2,2,2-trifluoromethanol could be due to the impossibility of hydrogen-bond formation in the first case and the presence of an alcohol group, acting both as hydrogen-bond acceptor and donator in the second. However, Byron *et al.* stress that apart from a few ethylene glycol and derivatives, very few compounds are effectively soluble in hydrofluoroalkanes [24, 49] and Rogueda points out that a selection based on solubility might not be the most meaningful [47]. Rogueda further explains that a suitable model should possess structural similarities, such as a straight carbon backbone, a low degree of hydrogen substitution in the middle of the chain, a short enough chain to match the propellants but long enough to allow a workable boiling point (ideally above 50 °C), matching dielectric and optical properties and similar density to the propellants. It was found that the best commercially available model was 2H, 3H-perfluoropentane, abbreviated HPFP, presented in Figure 1-4. It possesses a boiling point of 53.6 °C and was further used by Young *et al.* [34] and Ashayer *et al.* [32] to investigate molecular interactions via atomic force microscopy.

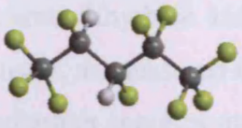

**Figure 1-4 Structure of model propellant 2H, 3H-perfluoropentane (HPFP).**

Such a molecule presents two stereogenic centers and therefore may exist in the forms of 4 different enantiomers, which are erythro diastereoisomer (a mixture of RS and SR enantiomers) and threo diastereoisomer (a mixture of RR and SS enantiomers). The diastereoisomers could be separated via distillation and *Kao et al.* found that their sample provided by DuPont consisted of a mixture of 90% threo and 10 % erythro [50]. For the materials used in this work, Fluorochem and AppolloScientific did not wish to comment on the relative amounts of the stereoisomers. The hydrogen atom position could impact on the likely interactions between a solute and the solvent, via hydrogen bonding possibilities for example.

### 1.2.3.2 Studies in model propellant 2H, 3H-perfluoropentane (HPFP)

At this stage, it is still necessary to develop a fundamental understanding of solvation and solubility in HFA propellants [51, 52], and thus too in model propellant HPFP whose use is relatively novel. To date, such studies on the behaviour of common pharmaceutical excipients in HPFP are still scarce.

A preliminary screening by James [53] showed that the compounds solubility in HPFP depends on the effective presence of oxygen and to a lesser extent, nitrogen moieties, although this should be balanced with the molecular weight of the compounds. Previous work by Paul *et al.*[54] focused on additives poly(ethylene glycol) (PEG) 600 and 1000 g $mol^{-1}$ and polymer containing recurring amide units, poly(vinyl pyrrolidone) (PVP), of molecular weight comprised between 25,000 and 54,000 g $mol^{-1}$, in HPFP. A concentration dependence of PEG size was found, showing that the polymer moderates the solvent quality, and a size reduction occurred via the addition of a fluorinated non-solvent. No specific interaction could be deciphered between PEG and PVP and the enhanced solubility of PVP in HPFP, when in presence of PEG, was attributed to the moderation of the solvent properties. A cloud-point phase separation of PEG in HPFP solution with temperature was also noted. The use of PEG and PVP in HPFP was found to greatly reduce the interaction force between the drug formoterol fumarate dihydrate and both a neat aluminium canister and a drug-coated aluminium canister, as measured by Ashayer *et al.* and Rogueda *et al.* using AFM [32, 36]. The lowest adhesion energies measured were still 2 to 3 orders of magnitude higher than "kT" therefore indicating that sole Brownian motion would

not overcome the particles' adhesion and aggregation phenomenon. Using AFM, it was further shown that the coating of the aluminium can was necessary to avoid adhesion of the drug particles to the interior surface and repulsion was obtained with both chloroprene and fluorinated polymer coatings [35]. Ridder *et al.*'s studies aimed at finding soluble surfactants in HFA-134a, HFA-227ea and HPFP. Soluble surfactants were found amongst polyoxyethylene-ethers and poly(ethylene oxide) - poly(propylene oxide) block copolymers, for which evidence of micelle formation was shown in HFAs [55]. Rogueda found HPFP to be a very good model for HFA-227ea, and slightly less so for HFA-134a, as far as the solubility of homopolymers PEGs and PVP were concerned [47], whereas Ridder *et al.* found HPFP to be closer to HFA-134a, with regards to the surfactants solubility studies [47, 55].

The key focus of this thesis was to understand what chemical moieties play a role in increasing or decreasing the polymers' solubility in HPFP, and characterise the latter solubility by their phase separation processes. This should be conducted on oligomers or polymers that show relevance for the pharmaceutical industry, that have been selected for their miscibility in model propellant HPFP and that are readily available commercially. These include compounds based on ethylene oxide, propylene oxide and their derivatives in the form of polymers, block co-polymers and surfactants. However, one should note that even though such additives are in use in aqueous pharmaceutical formulations, such as parenteral dosage forms [56, 57], ophthalmic [58], oral [59], rectal preparations [60, 61] or nasal administration [62], their toxicity profile with respects to pulmonary drug targeting is not yet established. Compounds belonging to the cyclodextrin family, which can act as carriers providing sustained release for the drugs due to their host-guest chemistry potential, have been cited as promising additives for HFA pMDIs [63]. The behaviour of a hydrophobically-modified cyclodextrin in HPFP is also presented.

## 1.3 Fluorinated materials: properties and biomedical perspectives

Major work in the fields of fluorinated systems applied to drug delivery and biomedical research has been advanced by Marie-Pierre Krafft and Jean G. Riess and

co-workers, whose excellent papers and reviews will be the basis of the following section.

### 1.3.1 Properties of fluorinated liquids

Fluorinated liquids possess unique physico-chemical properties that distinguish them from their hydrogenated counterparts, due to the specificities of the fluorine atom itself. The fluorine atom, yet small, is still substantially larger that hydrogen, with van der Waals radii of 1.47 Å and 1.20 Å respectively. This results in fluoroalkyl chains being bulkier than hydrogenated ones, with cross-section of around 30 and 20 $Å^2$ respectively. The mean volume for $CF_2$ and $CF_3$ are estimated to 38 and 92 $Å^3$ vs 27 and 54 $Å^3$ for $CH_2$ and $CH_3$ groups. Consequently, conformational freedom of the fluoroalkyl chains is strongly reduced, leading to higher rigidity compared to alkyl chains, with a gauche/trans energy difference of 4.6 kJ $mol^{-1}$ for fluoroalkyl chains and 2.0 kJ $mol^{-1}$ for alkyl chains. So as to minimize steric hindrance, fluoroalkyl chains adopt a helical conformation, as compared to alkyl chains' planar zig-zag. Fluorine has a high ionization potential and low polarisability. It is the most electronegative of all elements, which is reflected in the strength of the C-F bond, the strongest known in organic chemistry, equal to ~ 488 kJ $mol^{-1}$ in comparison to ~ 415 kJ $mol^{-1}$ for the C-H bond. The C-F bond strength also increases with fluorine substitution, reaching 531 kJ $mol^{-1}$ in a terminal $CF_3$. The C-C bond strength is also reinforced by the presence of fluorine substituents, and equals 413 kJ $mol^{-1}$ in perfluoroethane, compared to 376 kJ $mol^{-1}$ in ethane. This results in fluorocarbons being thermally and chemically very stable and also inert biologically. The dense electron cloud of the fluorine atom provides a repellent sheath that protects the molecule from the attack of reagents. Fluoroalkyl chains are not metabolized and therefore are resistant in enzyme rich environments. These properties render fluoroliquids ideal for biomedical applications [64].

Fluorocarbons can be considered as gas-like fluids [65]. They may possess very strong intramolecular bonds, but their intermolecular cohesiveness is very low. The low polarisability of fluorine results in weak van der Waals interactions among $CF_2$ groups, compared to $CH_2$ ones, and liquid fluoroalkanes behave as gas-like fluids. Many valuable properties, such as very low surface tension, excellent spreading

properties, high fluidity, high vapour pressure, high compressibilities, or high gas solubilities, arise from these low cohesion energies. The low polarizability combined with the larger surface area of the fluoroalkyl chains results in enhanced hydrophobicity. Fluoroalkane chains also present a pronounced lipophobic effect, estimated to a third of their hydrophobicity [66]. The presence of two such properties usually thought as antagonist, *i.e.* lipophobicity and hydrophobicity, results in the promotion of self-aggregation, molecular organization, phase separation and exclusion of solutes that are not highly fluorinated [65], with the exception of $CO_2$.

As stated by Riess, fluoroalkyl chains and fluorocarbons are $CO_2$-philic. They show an enhanced solubility in liquid and supercritical $CO_2$, the reverse being also true with a large solubility of $CO_2$ in fluorocarbons [65]. Chain fluorination was found to be an essential feature in the design of surfactants for use in stabilising dispersions in supercritical $CO_2$, although for cost reasons and environmental issues much imput is given to the design of $CO_2$-active hydrocarbon compounds [67]. $CO_2$-philic catalysts are obtained via the grafting of fluorinated chains onto ligands [68] and $CO_2$ was effectively gelled via the self-association into rods and three-dimensional networks of an organogelator bearing urea moieties (providing means of hydrogen-bonding) and $CO_2$-philic fluoroalkyl chains, at concentrations inferior to 5 % w/w. The structure was preserved upon solvent removal and aerogels could be obtained [69]. Yonker searched for a specific interaction between $CO_2$ and fluorine by looking for differences in the relaxation rates $T_1$, measured by NMR, of $C_6F_6$ and $C_6H_6$ in $CO_2$ at high densities. However no change in the spin-lattice relaxation time for both $^{19}F$ and $^{1}H$ compounds were noted and Yonker concludes on the lack of any specific $CO_2$-fluorine interaction [70]. Using *ab initio* molecular orbital calculations, Fried *et al.* identified a favourable interaction between $CO_2$ and the trifluoromethyl group of trifluoromethane and trifluoropropane, the quadrupole-dipole interaction between $CO_2$ and the fluoroalkane respectively contributing largely to the total energy. The largest quadrupole-dipole interaction was found for $CO_2\cdots CF_3CH_2CH_3$ and equal to 11.5 kJ $mol^{-1}$, although still less than most hydrogen-bond interaction energies [71]. The existence of a specific $CO_2$-fluorocarbon interaction has long been studied and controversial, and to try and clarify the point, Raveendran *et al.* carried out further *ab initio* calculations which showed that in partially fluorinated hydrocarbons, the electron deficient C-H bond could participate in C-H···O hydrogen bonds with the

$CO_2$ oxygen atom. The study also showed that the more polar fluoromethanes interacted more favourably with $CO_2$ than the less polar ones, regardless of the number of fluorine atoms. This highlights the fact that $CO_2$, despite its molecular symmetry leading to a nett zero dipole moment, should be considered as a polar solvent as a result of the static charges on its individual atoms [72].

### 1.3.2 Fluorinated amphiphiles

Many valuable properties can also be gained from the association of fluorocarbons to polar headgroups in the form of fluorinated amphiphiles. Fluorinated surfactants display a much higher surface activity than their hydrogenated analogues, being able to decrease water surface tension from 72 mN $m^{-1}$ to typically 15-20 mN $m^{-1}$ versus 25-40 mN $m^{-1}$ respectively. The fluorocarbon-water interfacial tension can also be reduced to values approaching 1 mN $m^{-1}$ or less when using fluorinated surfactants. The critical micelle concentrations (cmc) are usually one to two orders of magnitude lower with fluorinated surfactants, the cmc depending primarily on the hydrophobicity of the tail. This means that fluorinated surfactants can be used in much lower quantities [65]. Matsuoka and Moroi [73] studied the micellization of fluorinated amphiphiles. Aggregates from fluorinated amphiphiles tend to form structures with less curvature, due to the stiffness of the fluorinated chain and the bulkiness of the fluorine atoms, and have a tendency to be rod-shaped rather than micellar [64]. Bilayers and vesicles can also be formed using single-chain fluorinated amphiphiles, when this is unfavourable for single-chain hydrogenated ones. A large variety of novel fluorinated surfactants have been synthesised, that are neutral, anionic or cationic, that bear single or double tails of variable lengths, with a diversity of hydrophilic headgroups such as polyols, amino acids, amine oxides, phospholipids, etc [65]. It was also found that such a subtle variation as the replacement of only one terminal fluorine atom by a hydrogen, *i.e.* replacing terminal $CF_3$- by H-$CF_2$- in the hydrophobe chain of a perfluoroalkyl triethyleneoxide methyl ether surfactant, lead to a dramatic increase in the cmc (by a factor of 4) and surface tension (by 9 mN $m^{-1}$) in aqueous solutions [74]. Such a finding showed that a fully fluorinated chain is perhaps not necessary provided the end-group is carefully controlled.

Semifluorinated alkanes (SFA) were also synthesised, consisting of one fluorocarbon chain and one hydrocarbon chain that form diblock compounds, as for example $C_nF_{2n+1}C_mH_{2m+1}$, abbreviated $F_nH_m$. In a similar fashion, triblocks can also be generated. The mutually phobic blocks generate interesting phenomena in all state of matter and produce micro-phase separation, segregation and self-assembly [75]. The two segments, being covalently bound, cannot phase separate. The high incompatibility of fluorocarbons and hydrocarbons originates in the different conformation of their chains. While the flexible hydrocarbon chains are arranged in a zig-zag conformation, $-(CF_2)_n-$ fluorinated chains show a 15/7 helical conformation ($2\pi/N$ with N=15/7 being the non-integer screw axis) which is much more rigid, the zig-zag conformation for fluoroalkanes being highly unstable due to the bulkiness of the fluorine atoms [76]. With the use of SFAs, Lo Nostro *et al.* were the first to observe the mixing at low temperature of perfluorooctane and isooctane, upon addition of $F_8H_{16}$, however, no stable aggregates could be witnessed. Upon cooling, solid gels were formed, constituted of copolymer ribbons entrapping the two solvents and forming a three-dimensional network, birefringent elongated structures could be observed under polarizing microscope [76]. SFA diblock compounds are able to form micelles in hydrocarbons and reverse micelles in fluorocarbons, however with low aggregation numbers [65]. SFA $C_6F_{13}C_{10}H_{21}$, was also used to stabilise a perfluorooctyl bromide emulsion that was shown to improve the tissue oxygenation in a model rabbit after acute hemorrhagic shock [38].

A wide variety of partially fluorinated surfactants and copolymers are then designed and tailor-made with particular systems and applications in mind, thus promoting advances in colloidal fluorous phase chemistry. Table 1 from M. P. Krafft [64] gives a wide array of synthetic fluorinated compounds destined for medical use that include phosphatides, polyhydroxylated telomers, amine oxides, aminoacids, glycophospholipids, polyols and sugars. The following Figure 1-5 taken from Riess [65] presents schematically some fluorous nanophases that can be obtained using fluorinated amphiphiles.

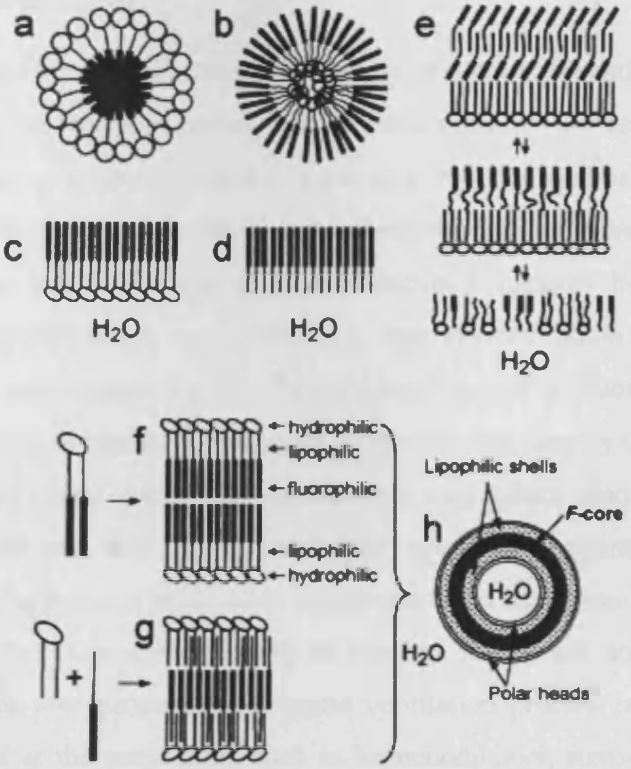


**Figure 1-5 Fluorous nanophases generated using fluorinated amphiphiles. Figure taken and legend adapted from Riess [65]. (a) micelle, (b) reverse micelle, (c) Langmuir film of a fluorinated surfactant, (d) Langmuir film of an fluoroalkyl/hydrogenoalkyl diblock, (e) reversible vertical segregation within a Langmuir film made of phospholipids and fluoroalkyl/hydrogenoalkyl diblocks, (f) bilayer membrane made from a double-tailed fluoroamphiphile, (g) bilayer membrane made from a complementary mixture of a standard phospholipid and an fluoroalkyl/hydrogenoalkyl diblock, (h) schematic representation of the fluorinated core that characterizes fluorinated-vesicles and fluorinated-tubules.**

### 1.3.3 Potential biomedical applications of fluorinated materials

On account of the properties previously introduced, fluorocarbons are being used as key compounds in drug delivery systems and biomedical research. While their uses in pulmonary drug delivery via pMDIs was explored previously, fluorocarbons are also considered for oxygen transport, in diagnosis as contrast agents, or as emulsions, microemulsions and gels for drug delivery [2, 64, 65, 77]. A critical factor in the use of fluorocarbons in biomedical applications is their excretion rate from the body, which should be rapid in the case of intravascular administration [64]. Fluorocarbons are dissolved by lipid carriers in the circulation and are eventually released via the lungs capillary. This rate depends on the fluorophilicity and lipophilicity balance of the selected fluorocarbon, and on its molecular weight [65].

### 1.3.3.1 Blood substitutes

The neat fluorocarbon perfluorooctyl bromide ($C_8F_{17}Br$) is investigated as a blood substitute, *i.e.* as an oxygen carrier, for the treatment of the respiratory distress syndrome. The use of a liquid instead of a gas promotes the lung oxygenation via the elimination of the gas-liquid interface and reduction of the alveolar surface tension. Liquid ventilation was also found to possess anti-inflammatory benefits and could heal acute lung injuries much more effectively than gas ventilation [78]. Perfluorooctyl bromide is also investigated as the fluorocarbon part of a fluorocarbon-in-water emulsion (60 %w/v), Oxygent™, that could be used during surgery to reduce the need for transfused blood from donors, and in the same way reduce blood shortages. Egg-yolk phospholipids are used as the emulsifier agent in Oxygent™ and a longer fluorocarbon, perfluorodecyl bromide, is also present as a few percents so as to reduce the solubility of the fluorocarbon phase in aqueous media and counteract Ostwald ripening [77]. It was also proposed that liquid ventilation process be used to deliver therapeutic agents at the same time, such as bronchodilators, steroids, anti-oxidants, instead of using the intra-venous route [64].

### 1.3.3.2 Contrast agents for ultrasound imaging

For the visualisation of the cardiovascular system, the blood flow, or for organ perfusion, a contrast agent is needed. Ultrasound imaging requires the presence of a good sound reflector, ideally in the form of a small gas bubble that is highly compressible, with a well controlled diameter that is stable enough in the blood stream so as to allow time for measurement. It should be able to reflect the sound waves orders of magnitude better than blood cells which are poor sound reflectors. Air-filled micro-bubbles collapse under the arterial blood pressure while perfluorocarbon-filled bubbles tend to expend until the perfluorocarbon is diluted to osmotic pressure via the introduction of air from the blood. Mathematical models have been designed that give the amount of perfluorocarbon vapour to inject so that a given stable bubble diameter is obtained, with diffusion rates of the soluble gases towards and outwards the bubbles equal at equilibrium [2]. Effective fluorocarbons for stabilising micro-bubbles are for example n-$C_6F_{14}$, $CF_3(OCF_2)OCF_3$ or $CF_3(OCF_2CF2)OCF_3$. Perfluorocarbons were preferred over their hydrocarbon analogues due to their much lower water solubility of an order of magnitude at least.

The developed contrast agents also make use of a shell around the micro-bubble. Optison® is a suspension of perfluoropropane microspheres with human albumin shell, Definity® uses perfluoropropane too but with a phospholipid coating, and SonoVue® chose poorly water soluble $SF_6$ and a polyethylene glycol membrane [65].

#### 1.3.3.3 Gels

One can see that the ability to form stable fluorocarbon gels having as relevant characteristics a controllable viscosity, permeation to oxygen, low friction and both hydro- and lipophobicity, is highly desirable. Such properties would render them ideal for topical applications, as for skin and wound protection, barrier creams, topical and ophthalmologic drug delivery, or uses in cosmetics [77]. Gelling fluorocarbons may however not be that straightforward, due to both their extreme fluidity and mobility and the fact that usual viscosity enhancers are not readily soluble in fluorocarbons. Still, fluorocarbon gels were formed with the aid of partially fluorinated species via an emulsion route, or using a fibrous matrix [64].

Using fluorinated polyethoxylated alcohols (especially $C_6F_{13}(CH_2)_2S(CH_2)_2(OCH_2CH_2)_2OH$ ), water-in-fluorocarbon gels were formed that are viscoelastic and quite transparent, and that can incorporate high water contents, from 50 up to 98%. The continuous phase is a water swollen micellar phase [79]. On the other hand, rigid and stable fluorocarbon-in-water gels were formed that contained as high as 99% v/v fluorocarbon (perfluorodiisopropyldecalin) and as little as 0.2% w/v of a fluorinated neutral amine oxide, such as $C_7F_{15}C(O)NH(CH_2)_3N(O)(CH_3)_2$, along to 1 % v/v water [80]. Many varied fluorocarbons (light, heavy, linear, cyclic) could be gelled: trichlorotrifluoroethane, perfluorooctyl bromide, perfluorooctyl ethane, perfluorodecalin, ... , that could resist heat-sterilization, that were shelf-stable and into which could be incorporated water soluble drugs, nutrient, etc, in the thin shell of hydrated surfactant. Gels were also formed via the incorporation of a thickener to the aqueous phase of a fluorocarbon-in-water emulsion. Fluorogel, which accelerated surgical wound healing by 20%, is made this way. It comprises a 55% v/v emulsion of perfluorodecalin, stabilized by a poloxamer and gelled by 1, 2-polypropylene glycol [64].

Gels were also formed using a fibrillar phase that entraps the liquid via surface tension and capillary action [66]. Fluorocarbon-hydrocarbon diblocks $F_nH_m$ can self-assemble into fibers, strands, tapes that lead to a 3-dimensional network immobilising the solvent. The microfibrils observed could come from a lamellar arrangement of the diblock structures. The gel structure can also be switched on and off as in the case of tubule-forming amphiphiles that convert upon heating from hollow cylindrical bilayer-based microstructures into giant vesicules and thus loose their gel consistency, which can then be regained upon cooling. The amphiphile involved is an anionic glucophospholipid in which a double-tailed hydrophobe is grafted through a phosphate linkage to the 0-6 position of a polar glucose head group. The double-tailed hydrophobe was either two hydrogenated chains or one fluorinated chain and one hydrogenated chain. The presence of the fluorinated hydrophobe chain led to increased temperatures for the tubule-vesicule interconversion [81].

Tae *et al.* [82] have designed hydrogels formed from the self-assembly of poly(ethylene glycol) of molecular weight 6000, 10,000 and 20,000 g $mol^{-1}$, capped at both ends with fluoroalkyl segments $-(CH_2)_2C_nF_{2n+1}$, with n=6, 8, 10. By varying the fluoroalkyl to PEG length, the associative phase behaviour of the polymers in water can be controlled. Once a sol-gel coexistence is achieved, the surface erosion rate of the gel, *i.e.* its dissolution rate, is controlled by the length of the fluoroalkyl chain. While the erosion of single-phase hydrogels is fast, it can be tailored for the sol-gel coexisting phase, which then offers possibilities in the controlled release of therapeutic proteins and in tissue engineering. Tae *et al.* further investigated this system and found that the hydrogel could be readily transformed into an injectable solution when in presence of N-methyl pyrrolidone, a toxicologically acceptable organic solvent. After injection, the water-soluble organic solvent diffused into the surrounding and the gel state was recovered. Human growth hormone was found to be stable in the hydrogel and slowly released for more than two weeks. Its release was predominantly due to its diffusion into the gel mesh and not to the gel surface erosion, as the lengthscale of the network mesh allowed it to pass through, but it is thought that when using a larger molecule such as DNA, the release profile will exclusively be controlled by the gel erosion [83].

Sawada *et al.* have synthesised novel fluoroalkylated end-capped 2-acrylamido-2-methylpropanesulfonic acid polymers with various fluoroalkyl end groups. These polymers not only formed hydrogels via their non-covalent self-assembly but also showed biological activity in vitro as inhibitors toward HIV-1. It was found that the anti HIV-1 activity became higher as the minimum concentration required to form a gel was decreased. The polymers self-assembly process is thought to be due to both the aggregation of the fluoroalkyl segments and to the electrostatic interaction between the amide cations and sulfonate anions present [84].

The topic of gelation is fully elaborated in Chapter 7, especially with regards to small organic molecules that act as gelators and the characteristics of the gels formed. To set into context, a study of fluorocarbon gels obtained using a novel chiral non-fluorinated small organic gelator based on a tetrahydroxy diester structure is performed.

## 1.4 Halogen bonding

Fluorocarbons and hydrocarbons were shown to be mutually incompatible. As seen previously, perfluorocarbon and hydrocarbon moieties can be coupled through covalent interactions as in the case of SFAs. However, a new type of non-covalent interaction, the halogen bond, has been found to allow the attractive interconnection of fluorocarbon and hydrocarbon moieties, leading to the generation of supramolecular assemblies. Major scientists in the field are Pierangelo Metrangolo, Tullio Pilati and Guiseppe Resnati, see references [85-91] for examples. As a general means, the halogen bond takes places via electron density donation from electron rich to electron poor sites, and occurs between X-Y compounds (X being the halogen, Y can be carbon, nitrogen, halogen, etc) and any lone pair possessing heteroatom D. The lone pair possessing heteroatoms work as electron donors while the halogens atoms work as the electron acceptors sites. The resulting bond is in the form of D···X-Y. All four halogens can act as halogen-bond donors, the strength of their interaction following the order I > Br > Cl > F. A peculiarity is observed with the fluorine atom, $F_2$ being a strong halogen-bond donor, whereas fluorocarbons are hardly ever involved in halogen bonds. The more electron withdrawing the moiety linked to the

halogen atom, the stronger the halogen bond, and in this sense iodoperfluoroalkanes are particularly suited for self-assembly engineering based on halogen-bonds [85].

The halogen bond is a directional interaction strong enough to overcome the phobicity of the fluoro- and hydrocarbon moeties when fluorinated halides are used [92]. In this aim, halogen bonds are formed between haloperfluorocarbons, noted $R_f$-X ($R_f$ being the aliphatic or aromatic perfluorinated residue), and heteroatom containing hydrocarbons, noted HC-D (HC being the hydrocarbon residue) that result in $R_f$-X···D-HC interactions. The halogen bond drives perfluorocarbon and hydrocarbon self-assembly in all solid, liquid and gas phases. Its strength and the resulting inter-atomic distances can be carefully monitored by the choice of the halide substituents. For example, in an infinite chain made of 4,4'-dipyridil and 1,4-diiodobenzene, the N···I interaction energy is 13.19kJ $mol^{-1}$ and the N···I-C interaction length 3.032 Å. When 1,4-diiodobenzene is replaced with diiodotetrafluorobenzene, the interaction energy becomes 24.32 kJ $mol^{-1}$ and the N···I-C interaction length 2.851 Å [85]. With regards to the lone pair possessing halogen-bond acceptor D, the strength of the halogen-bonds follows the order S < N < O when a hydrocarbon halide is employed, and S,O < N with a perfluorocarbon halide [87].

Highly structured self-assemblies can be formed through halogen bonding. This interaction can be considered as new "cement" for supramolecular architectures and can be applied for example in bottom-up approaches [85]. Supramolecular liquid crystalline polymers were constructed using halogen bonding as the complexes driving force [93], so were hybrid metallocene-perfluorocarbon materials [94]. Halogen bonds are also involved in chiral resolution in which formation of enantiopure co-crystals are observed [88, 89].

Halogen bonds have successfully been used to overcome the fluorocarbon-hydrocarbon phobicity and build infinite networks of co-crystals, or complexes when in the liquid phase [90, 91, 95-98]. X-Ray analysis is used to characterize the co-crystals formed in the solid-state [97] and $^{19}F$ NMR is highly sensitive to such complex formation in the liquid state [98]. Metrangolo *et al.* devised materials solely based on halogen bonds in which layers of perfluorocarbon and hydrocarbon alternated thanks to module segregation [90]. Corradi *et al.* investigated the strength of the hydrogen

bonds and halogen bonds in the building process of supramolecular architectures. They found that when a self-assembly process could be driven either by hydrogen or halogen bonds, the halogen bounds were stronger and displaced the hydrogen bonds, the halogen bonds being able to single out the molecules involved in the construction of the supramolecular assembly. This was shown in a competitive experiment in which equimolar amounts of (a) 1,2-bis(4-pyridyl)-ethane and (b) 1,4-diiodotetrafluorobenzene and (c) hydroquinone were all dissolved in excess acetone. Co-crystals of (a) and (b) separated in pure form while (c) remained in solution [86].

**References**


1. D.M. Lemal, *Perspective on Fluorocarbon Chemistry.* Journal of Organic Chemistry, 2004. **69**(1): p. 1-11.
2. J.G. Riess, *Blood substitutes and other potential biomedical applications of fluorinated colloids.* Journal of Fluorine Chemistry, 2002. **114**: p. 119-126.
3. Confidential outline of this PhD project provided by Astra Zeneca, 2004.
4. H.M. Courrier, *Pulmonary drug delivery systems: recent developments and prospects.* Critical Reviews™ in Therapeutic Drug Carrier Systems, 2002. **19**: p. 425-498.
5. M. Keller, *Innovations and perspectives of metered dose inhalers in pulmonary drug delivery.* International Journal of Pharmaceutics, 1999. **186**: p. 81-90.
6. B.L. Laube, D.E. Geller, T. Lin, R.N. Dalby, M. Diener-West, and P.L. Zeitlin, *Positive expiratory pressure changes aerosol distribution in patients with cystic fibrosis.* Respiratory Care, 2005. **50**: p. 1161-1176.
7. M.J. Wilby, *Increasing performance consistency of pMDIs.* Drug Delivery Technology, 2005. **5**: p. 56-58.
8. J. Pritchard, *The future of metered-dose inhalers.* Pharmaceutical Technology, 2005. **17**: p. 27-28.
9. S.P. Newman, *Principles of Metered-Dose Inhaler Design.* Respiratory Care, 2005. **50**(9): p. 1177-1190.
10. R.N. Dalby, E.M. Phillips, and P. Byron, *Determination of Drug Solubility in Aerosol Propellants.* Pharmaceutical Research, 1991. **8**(9): p. 1206-1209.
11. R. Dalby, M. Spallek, and T. Voshaar, *A review of the development of Respimat (P) Soft Mist TM Inhaler.* International Journal of Pharmaceutics, 2004. **283**(1-2): p. 1-9.
12. K.J. McDonald and G.P. Martin, *Transition to CFC-free metered dose inhalers - into the new millennium.* International Journal of Pharmaceutics, 2000. **201**: p. 89-107.
13. http://casesblog.blogspot.com/2007_11_01_casesblog_archive.html. Accessed on 14th September 2008.
14. T. Noakes, *Medical Aerosol Propellants.* Journal of Fluorine Chemistry, 2002. **118**(1-2): p. 35-45.
15. M.J. Molina and F.S. Rowland, *Stratospheric sink for chlorofluoromethanes: chlorine atomic-catalysed destruction of ozone.* Nature, 1974. **249**: p. 810-812.

16. M.A.A. Clyne, *Destruction of atmospheric ozone?* Nature, 1974. **249**: p. 796-797.
17. *The Montreal Protocol on Substances that Deplete the Ozone Layer.* http://www.unep.org/OZONE/pdfs/Montreal-Protocol2000.pdf , as accessed on May 6th 2008.
18. G. Fradley, *Fifty Years of the Pressurised Metered Dose Inhaler -Building on a Golden Heritage.* Future Drug Delivery, 2006(June): p. 1-4.
19. A.R. Ravishankara, A.A. Turnipseed, N.R. Jensen, S. Barone, M. Mills, C.J. Howard, and S. Solomon, *Do Hydrofluorocarbons Destroy Stratospheric Ozone?* Science, 1994. **263**(5143): p. 71-75.
20. F. Billiard and L. Lucas, *Fluorocarbons and global warming.* Revue Generale de Thermique, 1998. **37**: p. 417-423.
21. C.L. Leach, *The CFC to HFA Transition and Its Impact on Pulmonary Drug Development.* Respiratory Care, 2005. **50**(9): p. 1201-1208.
22. H.H. Emmen, E.M.G. Hoogendijk, W.A.A. Klopping-Ketelaars, H. Muijser, E. Duistermaat, J.C. Ravensberg, D.J. Alexander, D. Borkhataria, G.M. Rusch, and B. Schmit, *Human Safety and Pharmacokinetics of the CFC Alternative Propellants HFC 134a (1,1,1,2-Tetrafluoroethane) and HFC 227 (1,1,1,2,3,3,3-Heptafluoropropane) Following Whole-Body Exposure.* Regulatory Toxicology and Pharmacology, 1999. **32**: p. 22-35.
23. R.H. Cummings, *Pressurized metered dose inhalers : Chlorofluorocarbon to hydrofluoroalkane transition-Valve performance: pMDI in transition: CFC to HFA formulations.* Journal of allergy and clinical immunology, 1999. **104**(6): p. S230-S235.
24. C. Vervaet and P.R. Byron, *Drug-surfactant-propellant interactions in HFA-formulations.* International Journal of Pharmaceutics, 1999. **186**: p. 13-30.
25. E.L. Baldeschwieler, W.J. Troeller, and M.D. Morgan, *The Kauri Butanol Test for Solvent Power.* Industrial and Engineering Chemistry: Analytical Edition, 1935. **7**(6): p. 374-377.
26. H.D.C. Smyth, *The influence of formulation variables on the performance of alternative propellant-driven metered dose inhalers.* Advanced Drug Delivery Reviews, 2003. **55**(7): p. 807-828.
27. J.G. Clarke, S.R. Wicks, and S.J. Farr, *Surfactant mediated effects in pressurized metered dose inhalers formulated as suspensions. I. Drug/surfactant interactions in a model propellant system.* International Journal of Pharmaceutics, 1993. **93**: p. 221-231.
28. D. Traini, P. Rogueda, P. Young, and R. Price, *Surface Energy and Interparticle Force Correlation in Model pMDI Formulations.* Pharmaceutical Research, 2005. **22**(5): p. 816-825.
29. S.A. Jones, G.P. Martin, and M.B. Brown, *High-pressure aerosol suspensions - A novel laser diffraction particle sizing system for hydrofluoroalkanes pressurized metered dose inhalers.* International Journal of Pharmaceutics, 2005. **302**: p. 154-165.
30. A. Gupta, S.W. Stein, and P.B. Myrdal, *Balancing ethanol cosolvent concentration with product performance in 134a-based pressurized metered dose inhalers.* Journal of aerosol medicine 2003. **16**(2): p. 167-174.
31. H. Steckel and S. Wehle, *A novel formulation technique for metered does inhaler (MDI) suspensions.* International Journal of Pharmaceutics, 2004. **284**: p. 75-82.

32. R. Ashayer, P.F. Luckham, S. Manimaaran, and P. Rogueda, *Investigation of the molecular interactions in a pMDI formulation by atomic force microscopy.* European Journal of Pharmaceutical Science, 2004. **21**: p. 533-543.
33. D. Traini, P.M. Young, P. Rogueda, and R. Price, *Investigation into the influence of polymeric stabilizing excipients in inter-particulate forces in pressurised metered dose inhalers.* International Journal of Pharmaceutics, 2006. **320**: p. 58-63.
34. P.M. Young, R. Price, D. Lewis, S. Edge, and D. Traini, *Under pressure: predicting pressurized metered dose inhaler interactions using the atomic force microscope.* Journal of Colloid and Interface Science, 2003. **262**: p. 298-302.
35. P.G.A. Rogueda, M. Grosvenor, P. Luckham, and S. Manimaran, *Quantification of the interactions between a micronised drug and a selection of surfaces found in a pressure metered dose inhaler (pMDI).* Proceedings of the Annual Meeting and Exposition of the American Association of Pharmaceutical Scientists, 26-30 October 2003, Salt Lake city, USA, 2003.
36. P.G.A. Rogueda, M. Grosvenor, P. Luckham, and S. Manimaran, *Evaluation of the effectiveness of stabilisers in reducing cohesive forces between drug particles in pressure metered dose inhalers (pMDIs).* Proceedings of the Annual Meeting and Exposition of the American Association of Pharmaceutical Scientists, 26-30 October 2003, Salt Lake city, USA
2003.
37. N. Patel, M. Marlow, and M.J. Lawrence, *Formation of fluorinated nonionic surfactant microemulsions in hydrofluorocarbon 134a (HFC 134a).* Journal of Colloid and Interface Science, 2003. **258**: p. 345-353.
38. M.-P. Krafft, A. Chittofrati, and J.G. Riess, *Emulsions and microemulsions with a fluorocarbon phase* Current Opinion in Colloid and Interface Science, 2003. **8**: p. 251-258.
39. V.M. Sadtler, M.P. Krafft, and J.G. Riess, *Achieving Stable, Reverse Water-in-Fluorocarbon Emulsions.* Angewandte Chemie International Edition, 1996. **35**(17): p. 1976-1978.
40. H.M. Courrier, M.P. Krafft, N. Butz, C. Porté, N. Frossard, A. Rémy-Kristensen, Y. Mély, F. Pons, and T.F. Vandamme, *Evaluation of cytotoxicity of new semi-fluorinated amphiphiles derived from dimorpholinophosphate.* Biomaterials, 2003. **24**(4): p. 689-696.
41. H.M. Courrier, F. Pons, J.M. Lessinger, N. Frossard, M.-P. Krafft, and T.F. Vandamme, *In vivo evaluation of a reverse water-in-fluorocarbon emulsion stabilized with a semifluorinated amphiphile as a drug delivery system through the pulmonary route.* International Journal of Pharmaceutics, 2004. **282**: p. 131-140.
42. N. Butz, C. Porte, H. Courrier, M.P. Krafft, and T.F. Vandamme, *Reverse water-in-fluorocarbon emulsions for use in pressurized metered-dose inhalers containing hydrofluoroalkane propellants.* International Journal of Pharmaceutics, 2002. **238**: p. 257-269.
43. N. Patel, M. Marlow, and M.J. Lawrence, *Fluorinated ionic surfactant microemulsions in hydrofluorocarbon 134a (HFC 134a).* Journal of Colloid and Interface Science, 2003. **258**: p. 354-362.
44. H.M. Courrier, T.F. Vandamme, and M.-P. Krafft, *Reverse water-in-fluorocarbon emulsions and microemulsions obtained with a fluorinated*

*surfactant.* Colloids and Surfaces A: Physicochemicals and Engeneering Aspects, 2004. **244**: p. 141-148.

45. W.W. Busse, S. Brazinsky, K. Jacobson, W. Stricker, K. Schmitt, J.V. Burgt, D. Donnell, S. Hannon, and G.L. Colice, *Efficacy response of inhaled beclomethasone dipropionate in asthma is proportional to dose and is improved by formulation with a new propellant.* Journal of Allergy and Clinical Immunology, 1999. **104**(6): p. 1215-1222.
46. B.A.-S. Brown, *5 Myths About MDIs.* http://www.drugdeliverytech.com/ME2/dirmod.asp?sid=4306B1E9C3CC4E07A4D64E23FBDB232C&nm=Back+Issues&type=Publishing&mod=Publications%3A%3AArticle&mid=8F3A7027421841978F18BE895F87F791&tier=4&id=061FDE6119B3402B8D7F0D9B3B94767B [Accessed on 20/07/2008].
47. P.G.A. Rogueda, *HPFP, a Model Propellant for pMDI's.* Drug Development and Industrial Pharmacy, 2003. **29**(1): p. 39-49.
48. P.A. Dickinson, P.C. Seville, H. McHalle, N.C. Perkins, and G. Taylor, *An investigation of the Solubility of Various Compounds in the Hydrofluoroalkane Propellants and Possible Model Liquid Propellants.* Journal of Aerosol Medecine, 2000. **13**(3): p. 179-186.
49. F.E. Blondino and P.R. Byron, *Surfactant dissolution and water solubilization in chlorine-free liquefied gas propellants.* Drug Development and Industrial Pharmacy, 1998. **24**(10): p. 935-945.
50. C.-P.C. Kao, A.C. Sievert, M. Schiller, and J.F. Sturgis, *Double Azeotropy in Binary Mixtures 1,1,1,2,3,4,4,5,5-Decafluoropentane High-Boiling Diastereoisomer+Tetrahydrofuran.* Journal of Chemical & Engineering Data, 2004. **49**: p. 532-536.
51. L. Wu, R.P.S. Peguin, P. Selvam, U. Chokshi, and S.R.P.d. Rocha, *Molecular Scale Behavior in Alternative Propellant-Based Inhaler Formulations*, in *Inhalation Aerosols: Physical and Biological Basis for Therapy*, A.J. Hickey, Editor. 2007, Taylor and Francis. p. 373-397.
52. P. Selvam, R.P.S. Peguin, U. Chokshi, and S.R.P.d. Rocha, *Surfactant Design for the 1,1,1,2-Tetrafluoroethane-Water Interface: ab initio Calculations and in situ High-Pressure Tensiometry.* Langmuir, 2006. **22**(21): p. 8675-8683.
53. R. James, *Solubility of polymers in fluorinated liquids*, in *MSc Thesis*. 2006, Cardiff University.
54. A. Paul, P.C. Griffiths, R. James, D.J. Willock, and P.G. Rogueda, *Explaining the phase behaviour of the pharmaceutically relevant polymers poly(ethylene glycol) and poly(vinyl pyrrolidone) in semi-fluorinated liquids.* Journal of Pharmacy and Pharmacology, 2005. **57**: p. 973-980.
55. K.B. Ridder, C.J. DaviesCutting, and I. Kellaway, *Surfactant solubility and aggregate orientation in hydrofluoroalkanes.* International Journal of Pharmaceutics, 2005. **295**: p. 57-65.
56. C.-S. Yong, B.-J. Park, D.-H. Kim, B.-K. Yoo, J.S. Woo, K. Bhamdari, Y. Jahng, H.-G. Choi, and M.H. Lee, *In Vivo Evaluation of Microemulsion System for Oral and Parenteral Delivery of Rutaecarpine to Rats.* Drug Development and Industrial Pharmacy, 2007. **33**(5): p. 531-534.
57. J.D.J.d. Vries, M.J.A.d. Graaff-Teulen, R.E.C. Henrar, J.J.K.v.d. Bosch, A. Bult, and J.H. Beijnen, *Pharmaceutical development of a parenteral formulation of the novel anti-tumor agent carzelesin (U-80, 244).* Investigational New Drugs, 1994. **12**(4): p. 303-314.

58. E. Vega, M.A. Egea, O. Valls, M. Espina, and M.L. Garcia, *Flurbiprofen Loaded Biodegradable Nanoparticles for Ophtalmic Administration.* Journal of Pharmaceutical Sciences, 2006. **95**(11): p. 2393-2405.
59. J. Shokri, J. Hanaee, M. Barzegar-Jalali, R. Changizi, M. Rahbar, and A. Nokhodchi, *Improvement of the dissolution rate of indomethacin by a cogrinding technique using polyethylene glycols of various molecular weights.* Journal of Drug Delivery Science and Technology, 2006. **16**(3): p. 203-209.
60. M. Miyake, N. Kamada, Y. Oka, T. Mukai, T. Minami, H. Toguchi, M. Odomi, K.-I. Ogawara, K. Higaki, and T. Kimura, *Development of suppository formulation safely improving rectal adsorption of rebamipide, a poorly adsorbable drug, by utilizing sodium laurate and taurine.* Journal of Control Release, 2004. **99**: p. 63-71.
61. E.I. Taha, A.-A.A. Zaghloul, A.A. Kassem, and M.A. Khan, *Salbutamol Sulfate Suppositories: Influence of Formulation on Physical Parameters and Stability.* Pharmaceutical Development and Technology, 2003. **8**(1): p. 21-30.
62. E. Bechgaard, K. Lindhardt, and L. Martinsen, *Intranasal absorption of melatonin in vivo bioavailability study.* International Journal of Pharmaceutics, 1999. **182**: p. 1-5.
63. P. Rogueda, *Novel Compounds (WO 2005/053637 A2)*, in *Patent Cooperation Treaty (PCT/GB2004/004957)*, W.I.P. Organization, Editor. 2004: United Kingdom.
64. M.-P. Krafft, *Fluorocarbons and fluorinated amphiphiles in drug delivery and biomedical research.* Advanced Drug Delivery Reviews, 2001. **47**: p. 209-228.
65. J.G. Riess, *Fluorous micro- and nanophases with a biomedical perspective.* Tetrahedron, 2002. **58**: p. 4113-4131.
66. M.-P. Krafft, *Highly Fluorinated Compounds Induce Phase Separation in, and Nanostruturation of Liquid Media. Possible Impact on, and Use in Chemical Reactivity Control.* Journal of Polymer Science: Part A: Polymer Chemistry, 2006. **44**: p. 4251-4258.
67. J. Eastoe, A. Dupont, and D.C. Steyler, *Fluorinated surfactants in supercritical $CO_2$.* Current Opinion in Colloid & Interface Science, 2003. **8**: p. 267-273.
68. D. Koch and W. Leitner, *Rhodium-Catalyzed Hydroformylation in Supercritical Carbon Dioxide.* Journal of the American Chemical Society, 1998. **120**(51): p. 13398-13404.
69. C. Shi, Z. Huang, S. Kilic, J. Xu, R.M. Enick, E.J. Beckman, A.J. Carr, R.E. Melendez, and A.D. Hamilton, *The Gelation of $CO_2$: A Sustainable Route to the Creation of Microcellular Materials.* Science, 1999. **286**: p. 1540-1543.
70. C.R. Yonker, *Solution Dynamics of Perfluorobenzene, Benzene, and Perdeuteriobenzene in Carbon Dioxide as a Function of Pressure and Temperature.* Journal of Physical Chemistry A, 2000. **104**: p. 685-691.
71. J.R. Fried and N. Hu, *The molecular basis of $CO_2$ interaction with polymers containing fluorinated groups: computational chemistry of model compounds and molecular simulation of poly[bis(2,2,2-trifluoroethoxy)phosphazene].* Polymer, 2003. **44**: p. 4363-4372.
72. P. Raveendran, Y. Ikushima, and S.L. Wallen, *Polar Attributes of Supercritical Carbon Dioxide.* Accounts of Chemical Research, 2005. **38**: p. 478-485.
73. K. Matsuoka and Y. Moroi, *Micellization of fluorinated amphiphiles.* Current Opinion in Colloid and Interface Science, 2003. **8**: p. 227-235.

74. J. Eastoe, A. Paul, A. Rankin, R. Wat, J. Penfold, and J.R.P. Webster, *Fluorinated Nonionic Surfactants Bearing Either CF3- or H-CF2- Terminal Groups: Adsorption at the Surface of Aqueous Solutions.* Langmuir, 2001. **17**(25): p. 7873-7878.
75. P. LoNostro, *Aggregates from semifluorinated n-alkanes: how incompatibility determines self-assembly.* Current Opinion in Colloid and Interface Science, 2003. **8**: p. 223-226.
76. P. LoNostro, C.Y. Ku, S.-H. Chen, and J.-S. Lin, *Effect of Semifluorinated Copolymer on the Phase Separation of a Fluorocarbon/Hydrocarbon Mixture.* Journal of Physical Chemistry, 1995. **99**: p. 10858-10864.
77. J.G. Riess and M.P. Krafft, *Fluorinated materials for in vivo oxygen transport (blood substitutes), diagnosis and drug delivery.* Biomaterials, 1998. **19**: p. 1529-1539.
78. J.S. Greenspan, M.R. Wolfson, and T.H. Shaffer, *Liquid ventilation.* Seminars in Perinatology, 2000. **24**(6): p. 396-405.
79. J.C. Ravey, M.J. Stébé, and S. Sauvage, *Water in fluorocarbon gel emulsions: Structures and rheology.* Colloids and Surfaces A: Physicochemical and Engineering Aspects, 1994. **91**: p. 237-257.
80. M.P. Krafft and J.G. Riess, *Stable highly Concentrated Fluorocarbon Gels.* Angewandte Chemie International Edition, 1994. **33**(10): p. 1100-1101.
81. F. Giulieri, F. Guillod, J. Greiner, M.-P. Krafft, and J.G. Riess, *Anionic Glucophospholipids-A New Family of Tubule-Forming Amphiphiles.* Chemistry-A European Journal, 1996. **2**(10): p. 1335-1339.
82. G. Tae, J.A. Kornfield, J.A. Hubbell, D. Johannsmann, and T.E. Hogen-Esch, *Hydrogels with Controlled Surface Erosion Characteristics from Self-Assembly of Fluoroalkyl-Ended Poly(ethylene glycol).* Macromolecules, 2001. **34**: p. 6409-6419.
83. G. Tae, J.A. Kornfield, and J.A. Hubbell, *Sustained release of human growth hormone from in situ forming hydrogels using self-assembly of fluoroalkyl-ended poly(ethylene glycol).* Biomaterials, 2005. **26**(25): p. 5259-5266.
84. H. Sawada, S. Katayama, Y. Ariyoshi, T. Kawaze, Y. Hayakawa, T. Tomita, and M. Baba, *Fluorinated functional materials possessing biological activities:gel formation of novel fluoroalkylated end-capped 2-acrylamido-2-methylpropanesulfonic acid polymers under non-crosslinked conditions.* Journal of Materials Chemistry, 1998. **8**(7): p. 1517-1524.
85. P. Metrangolo, H. Neukirch, T. Pilati, and G. Resnati, *Halogen Bonding based recognition Processes: A World Parallel to Hydrogen Bonding.* Accounts of Chemical Research, 2005. **38**: p. 386-395.
86. E. Corradi, S.V. Meille, M.T. Messina, P. Metrangolo, and G. Resnati, *Halogen Bonding versus Hydrogen Bonding in Driving Self-Assembly Processes.* Angewandte Chemie International Edition, 2000. **39**(10): p. 1782-1786.
87. P. Metrangolo and G. Resnati, *Halogen Bonding: A Paradigm in Supramolecular Chemistry.* Chemistry-A European Journal, 2001. **7**(12): p. 2511-2519.
88. H. Neukirch, E. Guido, R. Liantonio, P. Metrangolo, T. Pilati, and G. Resnati, *Spontaneous resolution in a halogen bonded supramolecular architecture.* Chemical Communications, 2005: p. 1534-1536.
89. A. Farina, S.V. Meille, M.T. Messina, P. Metrangolo, G. Resnati, and G. Vecchio, *Resolution of Racemic 1,2-Dibromohexafluoropropane through*

*Halogen-Bonded Supramolecular Helices.* Angewandte Chemie International Edition, 1999. **38**(16): p. 2433-2436.

90. P. Metrangolo, T. Pilati, G. Resnati, and A. Stevenazzi, *Halogen bonding driven self-assembly of fluorocarbons and hydrocarbons.* Current Opinion in Colloid and Interface Science, 2003. **8**: p. 215-222.
91. D.B. Fox, R. Liantonio, P. Metrangolo, T. Pilati, and G. Resnati, *Perfluorocarbon-hydrocarbons self-assembly: halogen bonding mediated intermolecular recognition.* Journal of Fluorine Chemistry, 2004. **125**: p. 271-281.
92. M.-P. Krafft, *Fluorinated colloids and interfaces.* Current Opinion in Colloid & Interface Science, 2003. **8**: p. 213-214.
93. J. Xu, X. Liu, T. Lin, J. Huang, and C. He, *Synthesis and Self-Assembly of Difunctional Halogen-Bonding Molecules: A New Family of Supramolecular Liquid-Crystalline Polymers.* Macromolecules, 2005. **38**(9): p. 3554-3557.
94. M. Amati, F. Lelj, R. Liantonio, P. Metrangolo, S. Luzzati, T. Pilati, and G. Resnati, *Hybrid iodoperfluoroalkane-ferrocene supramolecular arrays: the shortes contacts iodine forms with nitrogen atoms and unsaturated moieties.* Journal of Fluorine Chemistry, 2004. **125**: p. 629-640.
95. P. Cardillo, E. Corradi, A. Lunghi, S.V. Meille, M.T. Messina, P. Metrangolo, and G. Resnati, *The N•••I Intermolecular Interaction as a General Protocol for the Formation of Perfluorocarbon-Hydrocarbon Supramolecular Architectures.* Tetrahedron 2000. **56**: p. 5535-5550.
96. M.T. Messina, P. Metrangolo, W. Panzeri, T. Pilati, and G. Resnati, *Intermolecular recognition between hydrocarbon oxygen-donors and perfluorocarbon iodine-acceptors: the shortest O•••I non-covalent bond.* Tetrahedron, 2001. **57**: p. 8543-8550.
97. D.D. Burton, F. Fontana, P. Metrangolo, T. Pilati, and G. Resnati, *Halogen bonding self-assembly of (E)-1,2-diiodo-1,2-difluoroethene with nitrogen substituted hydrocarbons.* Tetrahedron Letters, 2003. **44**: p. 645-648.
98. P. Metrangolo, W. Panzeri, F. Recupero, and G. Resnati, *Perfluorocarbon-hydrocarbon self-assembly Part 16. $^{19}F$ NMR study of the halogen bonding between halo-perfluorocarbons and heteroatom containing hydrocarbons.* Journal of Fluorine Chemistry, 2002. **114**: p. 27-33.

# Chapter 2 Theory and Techniques

**Foreword**

This chapter presents the theoretical background to some of the techniques used for the studies presented in this thesis. It does not intend to be an exhaustive review of all techniques tested during the PhD, but instead focuses on those that are not so common in a standard chemistry lab, such as small-angle neutron scattering (SANS) and pulsed field gradient spin-echo nuclear magnetic resonance (PGSE-NMR), even though the actual time spent using those remains quite small. The thermodynamics of polymers in solution is a pre-requisite for any polymer solubility study and is developed first. The last part focuses on some thermo-analytical methods used, thermogravimetric analysis (TGA) and differential scanning calorimetry (DSC), which are concisely presented.

## 2.1 Polymers in solution

### 2.1.1 Introduction

Polymers find uses in a very wide range of industries, from pharmaceuticals to heavy engineering [1], due to the range of properties that can be achieved: high performance polymers can be used as artificial joints and prosthetics (inertness) [2], as building materials, such as polyvinylchloride PVC (strength) [3], as conducting polymers (electrical properties) [4], as protective coatings [5] (impermeability), etc.

Many applications also rely on the polymers being either dispersed or dissolved in solution and used as additives, providing specific enhanced bulk properties to the overall multi-component formulation. Polymers in solutions are used as lubricants, viscosity modifiers, colloidal stabilisers, in detergency and cosmetic formulations, etc. Hence, the understanding of polymer solubility in various solvents is of utmost interest. As a general trend, it has been identified that "like" solvents dissolve "like" polymers. However, this is not always the case, as can be seen for example with poly(ethylene glycol) (PEG) which is not soluble in ethylene glycol, although both being composed of highly similar chemical entities [6]. As a general rule, the solubility

increases as the polymer molecular weight decreases. The notion of solvent quality, where solvents can be classified as "good" or "poor" for a particular polymeric solute, is often employed. A good solvent will be highly compatible with the polymer, via favourable solvent-polymer interactions, when on the contrary, in poor solvents, these interactions will be fewer. The Flory-Huggins interaction parameter $\chi$ is employed to express the solute-solvent compatibility, as will be presented in section 2.1.3.

To obtain a homogeneous polymer-solvent solution, the fundamental thermodynamic criterium is that the Gibbs free energy of mixing $\Delta G^{mix}$ should be negative. This happens when the Gibbs free energy of the solution is lower than the Gibbs functions of the separate components of the mixture [7]. Theories have been suggested to explain solubilisation and provided some constants specific to each component, these theories can be used as a predictive tool.

In the following sections, the various configurations of polymers in solution will firstly be examined, and the notion of radius of gyration described. Then, the thermodynamics of mixing polymers and solvents will be presented, in particular using the Flory-Huggins theory.

## 2.1.2 Configurations of polymer chains in solution

### 2.1.2.1 Various concentration regimes

Depending on the concentration regime of the polymer solution, polymer-polymer interactions will significantly vary, and polymer-polymer interactions can arise even at low polymer concentration, due to the potentially extended nature of the random coil conformation [8].

Three regimes can be distinguished: dilute, semi-dilute, and concentrated. The crossover between the dilute and semi-dilute regimes is characterised by C*, known as the overlap concentration. For concentrations $c<C^*$, every polymer chain present can be considered as a single non-interacting chain, with respects to the other polymer chains present. In the semi-dilute regime, even though the volume fraction of the polymer is still small, the chain of one polymer is likely to come in contact with

chains of other polymers, forming a non-connected network that possesses a mesh size smaller than the radius of gyration. As the concentration is increased, the mesh size decreases as the polymer coils are pushed even more into one another. Then, when c>>C*, in the concentrated regime, all chains are highly entangled and the systems has properties comparable to a polymer melt. Figure 2-1 summarises the three regimes described.

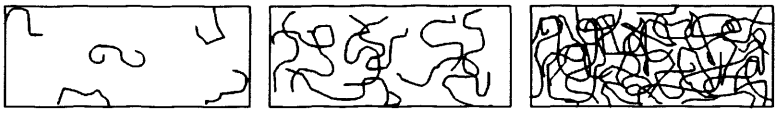


**Figure 2-1 Dilute, semi-dilute and concentrated regimes in a polymer solution.**

Typical concentrations for C* lie in the range of 0.1-10 % w/w. The overlap concentration C* can be estimated knowing the radius of gyration of the polymer chain ($R_g$), and its degree of polymerization ($N_p$), keeping in mind that the radius of gyration depends on the quality of the solvent for the given polymer. The overlap concentration may be expressed as:

$$C^* = \frac{3N_p}{4\pi N_{Av}} \frac{10^{-3}}{R_g^3} \qquad \textbf{Equation 2-1}$$

with $N_{Av}$ Avogadro's number, provided the coil volume is assumed to be a sphere of radius $R_g$.

### 2.1.2.2 Possible configuration of the polymer chain

The interactions occurring between polymer molecules can be neglected when the polymer solution is in the dilute regime. However, the polymer chain can still fold in various ways, which depend on its molecular weight, its linear or branched architecture, the quality of the solvent used or the temperature. The triangle of Haug [8, 9] illustrates the three "extreme" types of polymer configuration, and is reproduced in Figure 2-2.

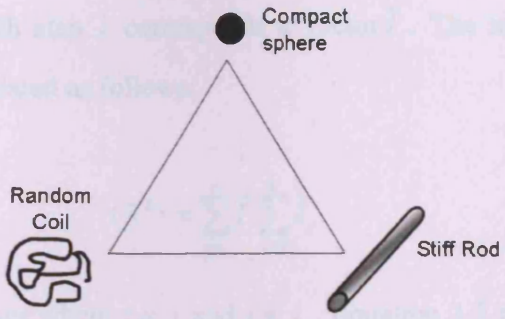


**Figure 2-2 Triangle of Haug representation of the three extreme types of polymer conformation.**

In a poor solvent, the polymer chain folds back on itself in order to minimize its contacts with the solvent, and a globular form is obtained. Other polymers adopt a stiff rod conformation. This can be driven by the presence of a helical structure, as is the case with a short DNA double helix. Most of the time, the polymers adopt a random coil conformation. This structure is much less well-defined and is usually described by its average characteristics [8].

### 2.1.2.3 Radius of gyration

#### *End-to end distance*

If pictured extended, in a stiff rod model, the polymer may present a rather large contour length. However, due to elasticity and bond rotation, polymers are often more or less compact and in a random coil state. The polymer chain may adopt many configurations that can only be characterised via average properties. As suggested by Flory [10], a polymer goes through a random walk in space, and Flory's model predicts that the end-to-end distance R is proportional to $\sqrt{n}$, n being the total number of bonds. Figure 2-3 illustrates this concept.

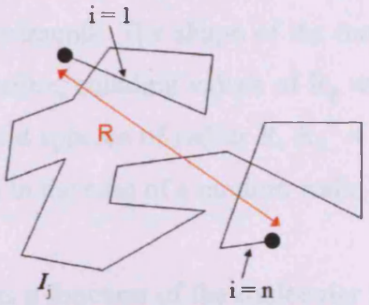


**Figure 2-3 Schematic random walk of a polymer.**

In this model, to each step $i$ corresponds a vector $\vec{l}_i$. The mean square end-to-end distance can be calculated as follows:

$$\langle R^2 \rangle = \sum_{i=1}^{n} \vec{l}_i \sum_{j=1}^{n} \vec{l}_j \qquad \textbf{Equation 2-2}$$

By differentiating cases where $i = j$ and $i \neq j$, Equation 2-2 becomes:

$$\langle R^2 \rangle = \sum_{i \neq j}^{n} \vec{l}_i \cdot \vec{l}_j + \sum_{i}^{n} \vec{l}^2{}_i \qquad \textbf{Equation 2-3}$$

Both $\vec{l}_i$ and $\vec{l}_j$ are at random orientation towards one another, the product of both being of equal positive or negative value, hence, the sum in the first term of Equation 2-3 is zero. This leads to $\langle R^2 \rangle = nl^2$, and can be applied to a random walk process obtained via diffusion. However, R is not easily accessible, but what can readily be measured is $R_g$, the radius of gyration.

### *Radius of gyration*

The radius of gyration $R_g$ of an homopolymer, i.e. a polymer consisting of identical repeating units, in a coil state, is defined as follows [8]:

$$\langle R_g^2 \rangle = \left( \sum_{i=1}^{Np} \left| \vec{r}_i - \vec{r}_{cM} \right|^2 \right) / Np \qquad \textbf{Equation 2-4}$$

with $r_i$, the position of segment i, $r_{cM}$ the location of the centre of mass and Np the degree of polymerization. Values for $R_g$ can be accessed via, among others, viscosity, diffusion or scattering experiments. The shape of the molecule greatly influences the radius of gyration and therefore, equating values of $R_g$ with the molecular size should be done cautiously. For solid spheres of radius R, $R_g^2 = (3/5)\ R^2$; for solid rigid rods of length l, $R_g^2 = l^2/12$, and in the case of a random walk, $R_g^2 = R^2/6$ [11].

$R_g$ can also be expressed as a function of the molecular weight M of the polymer, as presented in Table 2-1.

| | |
|---|---|
| Random coil | $R_g \propto M^{\alpha}$ |
| Compact sphere | $R_g \propto M^{0.33}$ |
| Ideal chain in ideal solution | $R_g \propto M^{0.5}$ |
| Stiff linear configuration | $R_g \propto M$ |

**Table 2-1 Proportionality of $R_g$ with regards to molecular weight M of the polymer, in various configurations.**

In the random walk model of the ideal chain, the polymer segments can overlap, but in order to exist, the chain must have a finite volume. Real chains are not completely free to rotate and their geometry is conditioned by fixed valence angles, rotation around bonds and by interactions between chain elements. Such interactions can take place both on a short range (steric repulsion between neighbouring atoms) and on a long range (both attractive and repulsive forces between segments, or between segments and the solvent). The terminology used for these interactions is excluded volume effects, which should be accounted for. In such a case, the chain could expand beyond its "ideal" dimension (expressed by $R_g \propto M^1$), and therefore have an exponent α greater than 1. Flory showed that the exponent would equal 6/(D+2), D being the spatial dimension, i.e. in a three-dimensional space, $R_g^2 \propto M^{6/5}$, or $R_g^2 \propto M^{1.2}$.

Nearly 30 years ago, Pierre-Gilles de Gennes showed that both the ideal chain and excluded volume models could be joined via the scaling theory, in which the polymer chain is divided into blobs: inside each blob, the polymer chain does not overlap, but the blobs themselves do not have to be self-avoiding. This is illustrated in Figure 2-4.

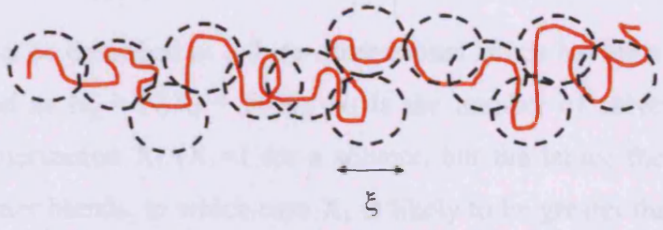


**Figure 2-4 Schematic diagram of a polymer chain in a semi-dilute solution, visualized as a succession of blobs of size ξ**

For **g** monomers per blob of size ξ, the end-to-end distance can be expressed as

$$R_g \propto n^{0.5} g^{0.1} \qquad \textbf{Equation 2-5}$$

In the case of an ideal chain, **g** equals 1 so that Equation 2-5 becomes $R_g \propto n^{0.5}$, and this corresponds to the expression presented earlier in the case of an ideal chain in ideal solution. In the fully excluded volume model, only one bond is present per blob, so that **n** equals **g** and Equation 2-5 becomes $R_g \propto n^{0.6}$, therefore $R_g^{\,2} \propto n^{1.2}$ which corresponds to Flory's excluded volume expression of $R_g$.

### 2.1.3 Thermodynamics of polymer solutions

#### 2.1.3.1 Free energy of mixing

A condition upon which a polymer will be soluble in a solvent is that the resulting Gibbs free energy of mixing, $\Delta G_{mix}$, is negative. Gibbs energy of mixing can be expressed as:

$$\Delta G_{mix} = \Delta H_{mix} - T\Delta S_{mix} \qquad \textbf{Equation 2-6}$$

with $\Delta H_{mix}$ the enthalpy of mixing, T the temperature and $\Delta S_{mix}$ the entropy of mixing. The contributions of the enthalpy and entropy of mixing towards the free energy of mixing can be accessed via statistical thermodynamics and in this aim the Flory-Huggins lattice model can be used. The Flory-Huggins theory was first developed separately by Paul Flory and Maurice Huggins [12, 13] and published in 1941, and after several improvements and adaptations. It is suited to describe the semi-dilute concentration regime of a polymer solution.

#### 2.1.3.2 The lattice model

The solution can be described as a three-dimensional lattice having a total number of sites $N_g$, defined as $N_g = N_1X_1 + N_2X_2$. $N_1$ is the number of solvent molecules of degree of polymerization $X_1$ ($X_1$=1 for a solvent, but the lattice theory can also be applied to polymer blends, in which case $X_1$ is likely to be greater than 1) and $N_2$ the number of polymer molecules with a degree of polymerization $X_2$ >1. No more than one solvent molecule or polymer segment can occupy a single site at a time. For ease of representation, the lattice is illustrated in Figure 2-5 in a two-dimensional model.

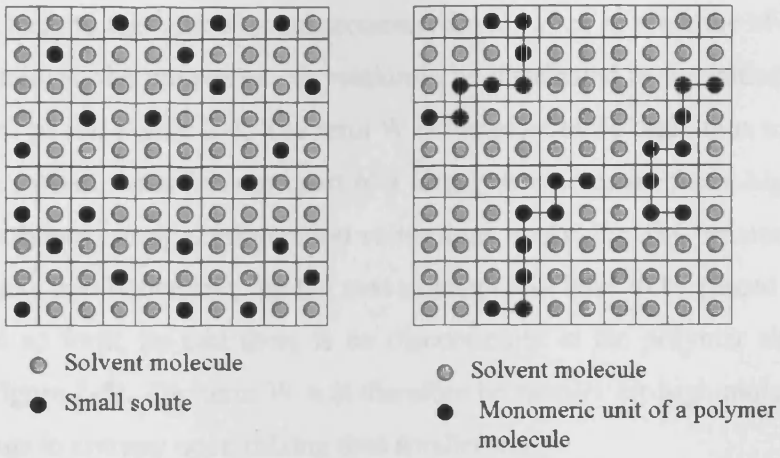


**Figure 2-5 Two-dimensional lattice model where (left panel) the solutes are distributed randomly and (right panel) the distribution is restricted, modelling the different segments constituting a polymer chain. The volume fraction of the solute is in both cases equal to 0.24.**

To use this model, several assumptions should be made: (a) the lattice is fully filled with either solvent molecules or polymer segments; (b) the molecules are all of equal size, be it polymer segments or solvent; (c) the system is homogeneous; (d) the Flory-Huggins parameter, described in the next sections, is purely enthalpic. In such a lattice, the distribution of solute molecules can either be random or constrained, as is explained in the following section.

### *Entropy of mixing*

When mixing a solvent and a polymer, the entropy increase comes from two effects [8]. First, mixing two different species creates an entropy increase, as is the case with any binary mixture, however the solute concentration here is low and few polymers are present, on a molar basis. This contribution is therefore small. The most important effect comes from the fact that in solution, the polymer molecules gain configuration entropy compared to when in the melt, prior to mixing. Many arrangements are indeed possible for solvent molecules and monomeric units in a polymer solution. According to thermodynamic statistics, the configuration entropy for a polymer solution can be expressed as:

$$S_{conf} = S_{mix} = k \cdot \ln W \qquad \textbf{Equation 2-7}$$

with k the Boltzmann constant and W the number of total possible arrangements in the lattice.

Coming back to the lattice model presented above, when in presence of low molecular weight solutes, the molecules can randomly be distributed in the lattice, as illustrated in the left panel, Figure 2-5. The term W is therefore quite high, thus too the entropy. However, when the solutes are part of a larger ensemble, such as a higher molecular weigh polymer, some configuration restrictions apply: the first monomeric unit can occupy any free lattice site, but the next segment will have to be placed in an adjacent site, and so forth, so that there is no discontinuity in the polymer chain (see right panel, Figure 2-5). The term W will therefore be smaller for high molecular weights, the change in entropy upon mixing thus smaller too.

The entropy change upon mixing polymer and solvent is equal to $\Delta S_{mix} = S_{mix} - S_1 - S_2$ , $S_1$ and $S_2$ being the entropy of the pure solvent and of the pure solute respectively, it is shown that it can be expressed as:

$$\Delta S_{mix} = -k(N_1 \ln \phi_1 + N_2 \ln \phi_2) \qquad \textbf{Equation 2-8}$$

with $\phi_i$ the volume fraction of component i (originally the site fraction of component i). By noting $N_1 = \phi_1 N_g / X_1$, $N_2 = \phi_2 N_g / X_2$, $N_g = n_g N_{Av}$ and $R = N_{Av} k$, the entropy of mixing per mole of lattice site can be written:

$$\Delta S_{mix,m} = \Delta S_{mix} / n_g = -R(\frac{\phi_1}{X_1} \ln \phi_1 + \frac{\phi_2}{X_2} \ln \phi_2) \qquad \textbf{Equation 2-9}$$

### *Flory-Huggins parameter χ*

The Flory-Huggins interaction parameter $\chi$ is a measure of the solvent power for a given solute. $\chi$ can be expressed as in Equation 2-10:

$$\chi = \frac{z\Delta\varepsilon_{12}}{kT} \qquad \textbf{Equation 2-10}$$

where z is the number of nearest neighbours for a lattice site (coordination number) and $\Delta\varepsilon_{12}$ the interchange energy per contact. On mixing, new solvent-polymer contacts arise (1-2), replacing some of the polymer-polymer (2-2) and solvent-solvent

(1-1) ones present in the pure compounds. The formation of the (1-2) contact implies breaking (1-1) and (2-2) contacts, and can be represented as follows:

$$\frac{1}{2}(1-1)+\frac{1}{2}(2-2)\rightarrow(1-2) \qquad \textbf{Equation 2-11}$$

The interchange energy per contact $\Delta\varepsilon_{12}$ is given by:

$$\Delta\varepsilon_{12}=\varepsilon_{12}-\frac{1}{2}(\varepsilon_{11}+\varepsilon_{22}) \qquad \textbf{Equation 2-12}$$

$\varepsilon_{11}$ and $\varepsilon_{22}$ being the contact energies for the solvent and the polymer respectively.

$\chi$ can also be expressed using the Hildebrand solubility parameter $\delta$, which is material-specific, so that:

$$\chi=\frac{V(\delta_1-\delta_2)^2}{RT} \qquad \textbf{Equation 2-13}$$

$$\delta=\sqrt{\frac{(\Delta H_v-RT)}{V_m}} \qquad \textbf{Equation 2-14}$$

with V the volume of a polymer segment, $\Delta H_v$ the heat of vaporisation and $V_m$ the molar volume. The Hildebrand solubility parameter $\delta$ (usually expressed in $cal^{1/2}\,cm^{3/2}$) is the square root of the cohesive energy density, which represents the separation energy required to remove the unit volume of molecules from their neighbours, to an ideal gas. Solutes and solvents that possess close values of solubility parameters will be likely to interact favourably.

### *Enthalpy of mixing*

Upon mixing, a change in energy can occur as new solvent-polymer interactions are formed, replacing some of the solvent-solvent and solute-solute ones. The change in enthalpy upon mixing can be expressed as:

$$\Delta H_{mix}=N_g\phi_1\phi_2kT\chi \qquad \textbf{Equation 2-15}$$

with $\chi$ the Flory-Huggins interaction parameter, as described above. $\chi$ determines the quality of a solvent for a given polymer and is inversely proportional to the temperature. In this sense, $\chi$ can be considered as an enthalpic quantity. In a similar

way as for the entropy of mixing, the enthalpy of mixing can be expressed per mole lattice site as:

$$\Delta H_{mix,m} = \Delta H_{mix} / n_g = RT\phi_1\phi_2\chi \qquad \textbf{Equation 2-16}$$

### *Gibbs energy of mixing*

Combining the entropy and enthalpy of mixing terms leads to the Gibbs free energy of mixing expression:

$$\Delta G_{mix,m} = RT\left[\left(\frac{\phi_1}{X_1}\ln\phi_1 + \frac{\phi_2}{X_2}\ln\phi_2\right) + \phi_1\phi_2\chi\right] \qquad \textbf{Equation 2-17}$$

The Flory-Huggins theory can unfortunately have limitations when it comes to quantitative predictions. For example, interaction parameters are often concentration dependant. Specific polymer-solvent interactions can also occur, such as hydrogen-bonding, or polymer-polymer associations may arise, which are not accounted for here. The Flory-Huggins parameter $\chi$ also comprises an entropy contribution arising from new solute-solvent contacts that change the vibrational frequencies of the components, which renders it not purely enthalpic.

## 2.1.3.3 Phase equilibria

Polymer solutions may display a rich variety of phase diagrams. These are dictated by the type of temperature dependence of the $\chi$ parameter, and Flory-Huggins theory can be used to predict the polymer solution equilibrium behaviour. Figure 2-6 presents typical phase behaviour of polymer solutions, along with the variation of the $\chi$ parameter with temperature.

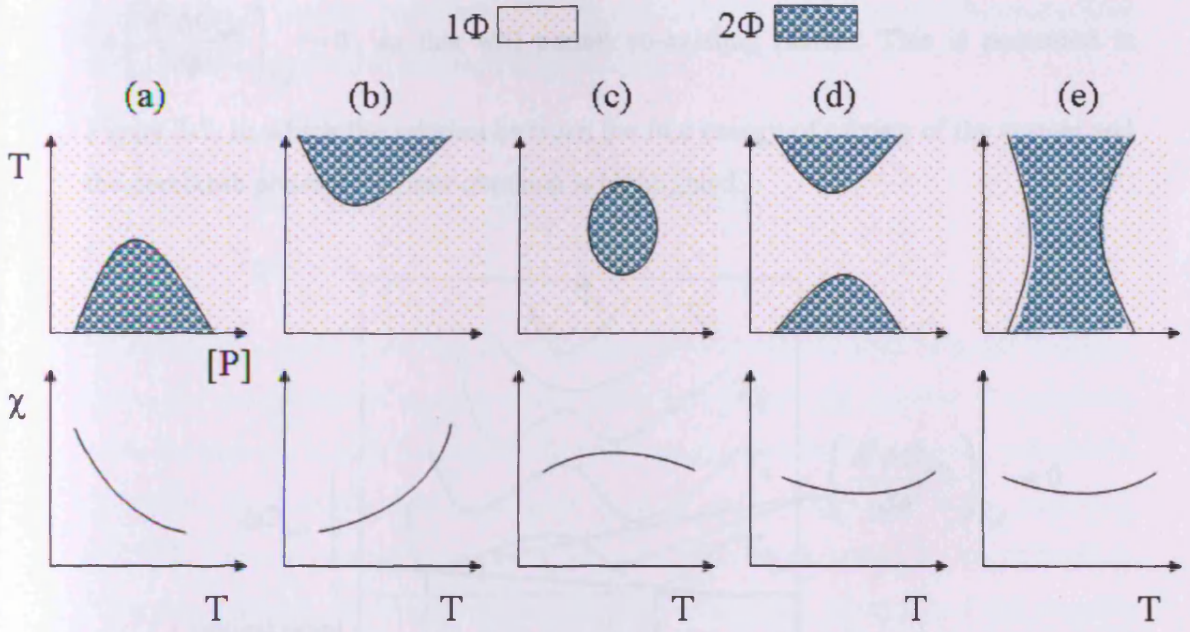


**Figure 2-6 Range of phase behaviours observed in polymer solutions (top row), along with the variation of the χ parameter with temperature (bottom row). On the schematic diagram, the biphasic region (2Φ) is in dark shading and the monophasic region (1Φ) in light shading. T is the temperature and [P] the polymer concentration. Adapted from Ref. [11].**

In the biphasic regions presented in Figure 2-6, the system consists of two separated layers of solution, one polymer rich, the other polymer depleted. Panel (a) presents a system with an upper critical solution temperature (UCST), characteristic of a system for which the heat of mixing is endothermic and phase separation enthalpically driven. Phase separation occurs when the temperature is taken below the binodal curve. In panel (b), a lower critical solution temperature (LCST) is observed. This behaviour is found in exothermic systems, which demix upon temperature increase, via an entropically driven process. Then panel (c) shows a closed loop phase behaviour, obtained when the function χ vs. temperature presents a maximum; panel (d) shows both UCST and LCST behaviours and panel (e) an hour-glass shape one, obtained when the function χ vs. temperature presents a minimum.

The phase separation curves are obtained via the free energy of mixing curves for the given system. Full miscibility can only be obtained when the Gibbs free energy of mixing of the system is smaller to the Gibbs free energy of the component themselves, and of any possible co-existing phases. For a monophasic system, the curve $\Delta G_{mix}$ vs. polymer concentration must not have points of inflexion,

i.e. $\left(\frac{\delta^2 \Delta G_{mix}}{\delta \phi^2}\right)_{T,P} = 0$, as this will permit co-existing phases. This is presented in Figure 2-7, in which the relation between the free energy of mixing of the system and the demixion phase behaviour obtained is highlighted.

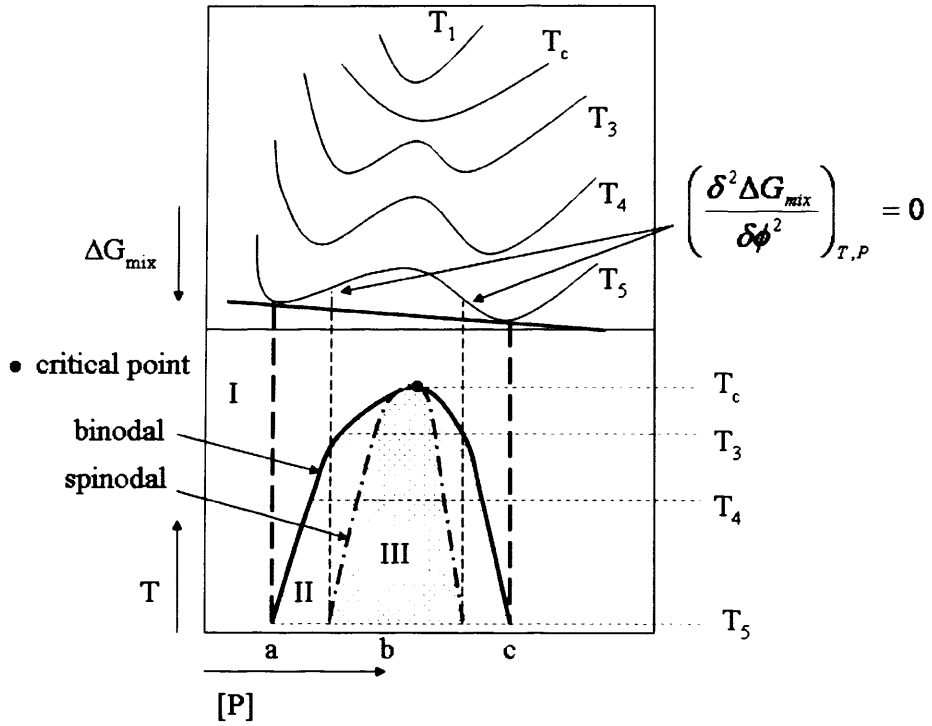


**Figure 2-7 Free energy of mixing curves at various temperatures and corresponding binodal and spinodal curves, for a polymer-solvent system presenting an upper critical solution temperature. Region I: stable, region II: metastable, and region III: unstable. Adapted from Ref. [7] and Ref. [14]**

In Figure 2-7, as the temperature decreases, the system phase separates (UCST type). If a system having a polymer concentration **b** comprised between **a** and **c**, is placed at a temperature $T_5$, its free energy of mixing is always higher than either of the two coexisting phases: the system cannot be thermodynamically stable and phase separation takes place. When the temperature is raised, from $T_5$ to $T_c$, the binodal curve contracts, up to a point where the limits of the two-phase coexistence coalesce and a homogeneous mixture is obtained. $T_c$ is referred to as the critical solution temperature. Above $T_c$, the mixture is a homogeneous solution.

The binodal curve is also known as the cloud-point curve and in the biphasic region, the composition of the two separated layers can be extrapolated by projection of the

corresponding binodal coordinates on the horizontal axis. At the critical point, both demixing phases possess the same composition.

## 2.2 Small angle neutron scattering (SANS)

### 2.2.1 Introduction

Small-angle neutron scattering is a very powerful technique used to probe the size, shape and orientation of components of colloidal systems, *i.e.* systems of nanometer scale dimensions. SANS belongs to the small angle scattering techniques, which also comprises small-angle light scattering (SALS) and small-angle X-ray scattering (SAXS). These are complementary techniques, all of them based on the interaction occurring between the incident radiations (neutrons, light, X-rays) and the particles present in the system under investigation. Typical colloidal systems (micelles, microgels, microemulsions for example) possess a size range of 10-10,000 Å. Probing the sample using comparable wavelengths enables the scientist to obtain information about the size, shape and interaction between the various components present [15].

The three small-angle scattering methods differ by the nature of the radiation produced, which in turn has an impact on the actual length scales that can be probed, and the type of sample environment that can be applied.

Light and X-rays are both electromagnetic radiation that interact with the electron cloud surrounding atomic nuclei. Light scattering, with wavelengths comprised between 4000-8000 Å, will preferably be used for larger colloidal particles, but cannot be used in the case of optically opaque samples. X-rays, with wavelengths of 0.5-2.3 Å, can probe smaller systems of the size order of 100 Å, but due to the high energy of the X-ray photon, the presence of radiative heating can damage more fragile systems such as biological ones and is difficult to circumvent. From an experimental point of view, SAXS samples must be very thin, a condition that is not always readily manageable when for example samples require complex containers. The wavelengths generated in the case of neutron radiation, typically comprised between 0.1-30 Å, can probe sizes in the range of ~10 to 1000 Å, and the energy of the neutron is far less than that of the X-ray photon, for a comparable wavelength. Neutron radiation

therefore provides both a non-invasive and non-destructive method to probe colloidal systems.

However, the most fundamental difference is that neutrons interact with the nuclei of the atoms, and not the electron cloud, which has important implications. Figure 2-8 presents in a schematic way what neutrons and X-rays 'see' when in the presence of various atoms.

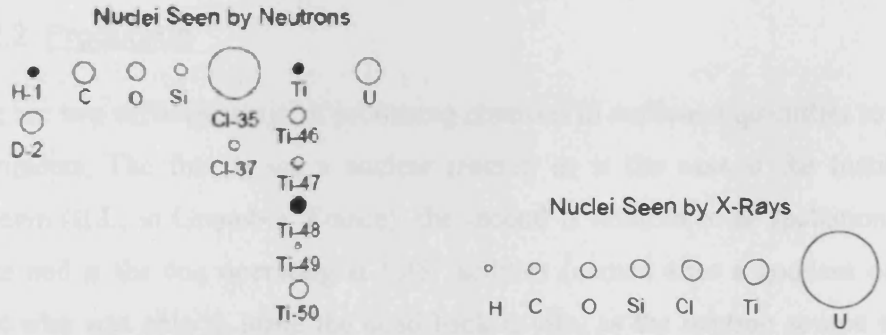


**Figure 2-8 Schematic diagram comparing the neutron interaction with various atoms (nuclei dependant), compared to the X-Ray interaction (electron cloud dependant). Courtesy of Boualem Hammouda, from www.ncnr.nist.gov/programs/sans/pdf/hammouda_part_i_neutron_scattering. pfd, corrected.**

SANS allows the distinction between isotopes of the same element, the most widely exploited example being the Hydrogen - Deuterium contrast. The scattering power of different isotopes leads to the contrast variation technique, in which some parts of the colloidal system can be highlighted or rendered invisible.

The following sections will concisely describe important elements relating to SANS, from neutrons and their production to the instrumentation required, a background to scattering theory and the first steps in the data analysis via estimation of the size and shapes of the colloidal structures present in the samples of interest.

## 2.2.2 Neutrons and their production

### 2.2.2.1 Neutrons

The neutron is an uncharged particle with a mass of $1.6749 \times 10^{-27}$ kg (slightly more than a proton, the proton mass being $1.6726 \times 10^{-27}$ kg, and 1839 times more than an electron, the electron mass being $9.1094 \times 10^{-31}$ kg). It has a spin of ½ and possesses a

magnetic moment. When taken away from the atomic nucleus, the neutron is an unstable particle with a mean lifetime of ~1000 seconds. It decays through the emission of both an electron and an antineutrino to become a proton.

The first correct description of neutrons dates back to 1932, when James Chadwick (Cavendish Laboratory, Cambridge), showed that a newly discovered radiation form was composed of uncharged particles bearing the approximate mass of a proton [16].

#### 2.2.2.2 Production

There are two different ways of producing neutrons in sufficient quantities to perform experiments. The first is via a nuclear reactor, as is the case at the Institut Laue Langevin (ILL, in Grenoble, France), the second is referred to as spallation neutron source and is the one operating at ISIS facilities (named after a goddess of ancient Egypt who was able to bring the dead back to life, as the neutron source was built using many components coming from previous dismantled accelerators), in Rutherford Appleton laboratories, Didcot, U.K.. ISIS and ILL are the world's two most powerful neutron sources at the time of writing.

##### *Nuclear reactor*

In a nuclear reactor, neutrons are produced continuously by the fission of Uranium-235. Each fission releases two to three neutrons, one of which is used to sustain the chain reaction. Wavelength selection of neutrons can be obtained through a crystal monochromator or by selecting the desired neutron velocity with a mechanical chopper. This results in high flux beams having a narrow wavelength distribution. Figure 2-9 shows the fission chain reaction producing neutrons in a nuclear reactor and Figure 2-10 shows the nuclear reactor and instruments layout scheme at ILL.

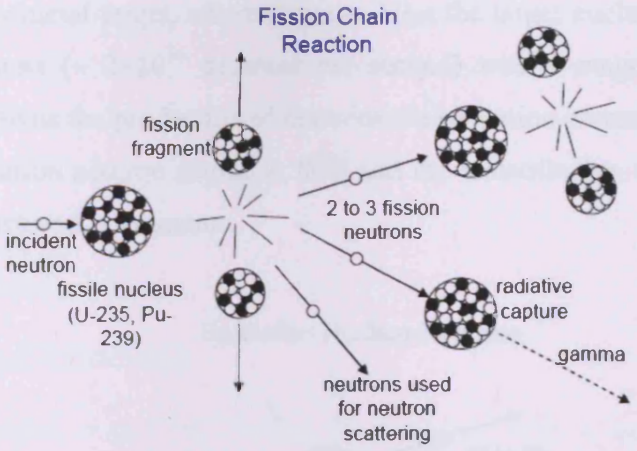


**Figure 2-9 Fission chain reaction producing neutrons in a nuclear reactor. Courtesy of Boualem Hammouda, from www.ncnr.nist.gov/programs/sans/pdf/hammouda_part_i_neutron_scattering.pfd.**

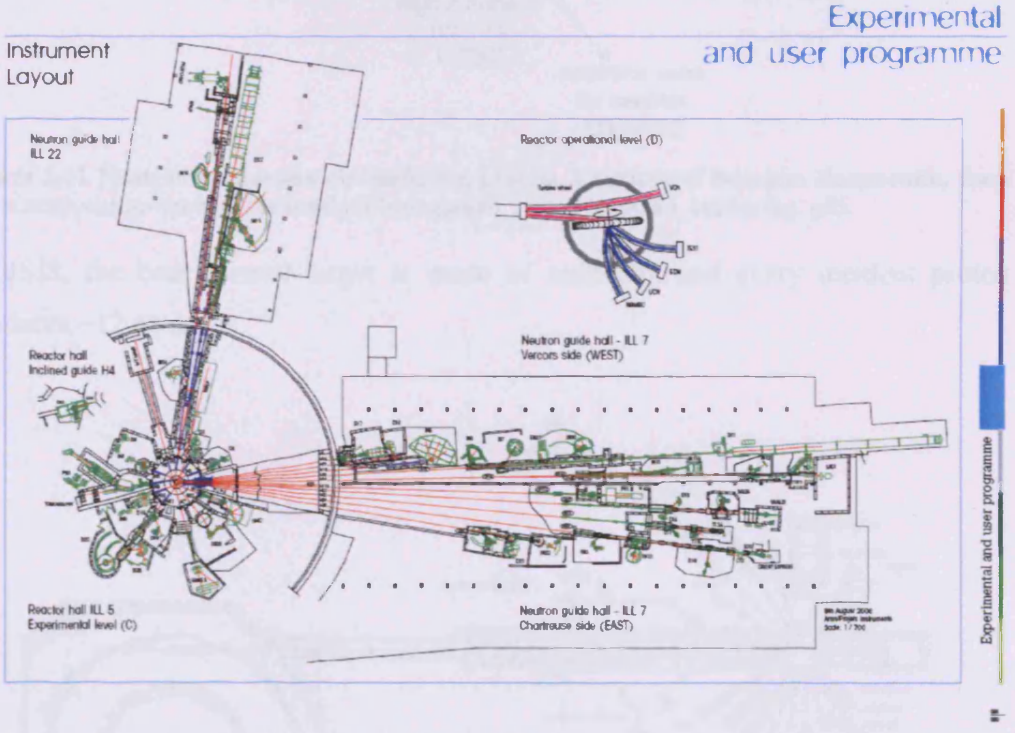


**Figure 2-10 Nuclear reactor source at ILL (Courtesy of the ILL webpage, http://www.ill.fr/fileadmin/users_files/documents/instruments_and_support/instruments_and_groups/instrument-list-2007.pdf).**

### *Spallation*

The other method of generating neutrons is by a process called spallation, in which no disintegration of the nuclei is involved [17]. High energy proton pulses (of a 50 Hz frequency) obtained via acceleration in a synchrotron (to 800 MeV) are directed

towards a heavy metal target, where they can blast the target nuclei apart, producing pulses of neutrons (~ $2\times10^{16}$ neutrons per second) with a range of wavelengths. Figure 2-11 presents the production of neutrons via spallation process and Figure 2-12 shows the spallation neutron source at ISIS and the redistribution of the neutrons to various beamlines and instruments.

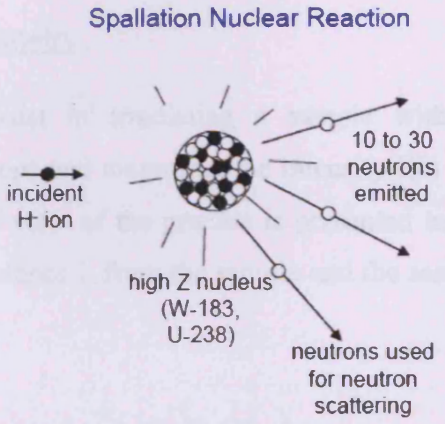


**Figure 2-11 Neutron production via spallation process. Courtesy of Boualem Hammouda, from www.ncnr.nist.gov/programs/sans/pdf/hammouda_part_i_neutron_scattering. pfd.**

At ISIS, the heavy metal target is made of tantalum, and every incident proton produces ~12 neutrons.

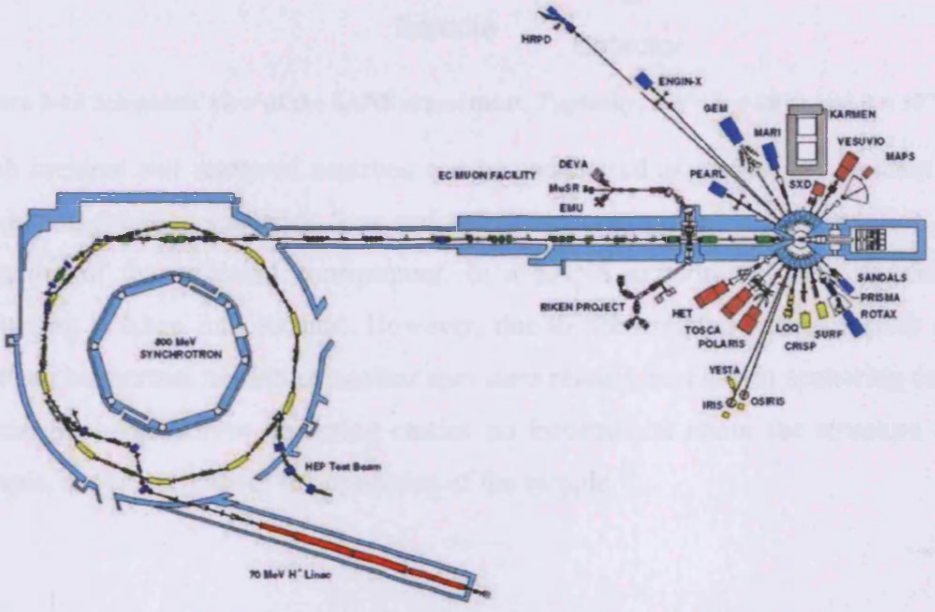


**Figure 2-12 Spallation neutron source at ISIS [18].**

The use of neutron radiation is therefore not a simple laboratory 'benchtop' technique. The large and costly facilities required are mostly financed and operated by several countries at governmental level, and the neutron beam time allocated through a competitive peer-reviewed proposal system.

### 2.2.3 SANS technique

#### 2.2.3.1 Scattering geometry

SANS experiments consist in irradiating a sample with a beam of white or monochromomatic neutrons and measuring the intensity I(θ) of the scattered beam at an angle θ. A schematic view of the process is presented in Figure 2-13, where the detector is placed at a distance L from the sample and the scattered beam measured at a radial distance Rd.

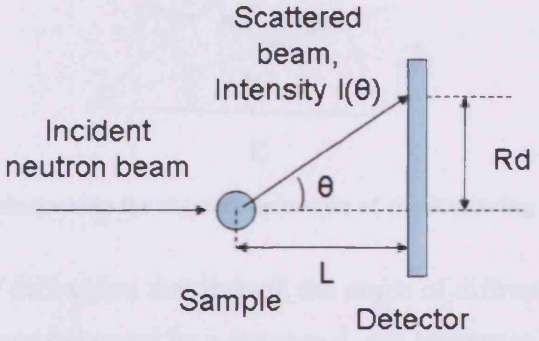


**Figure 2-13 Schematic view of the SANS experiment. Typically, 1m < L < 20 m and θ < 10°.**

Both incident and scattered neutrons can be considered as waves, the incident beam producing coherent scattering from ordered atom nuclei and giving information on the structure of the colloidal arrangement. In a SANS experiment, only the coherent scattering is taken into account. However, due to uncorrelated intramolecular events that can be thermal motion or nuclear spin state related, incoherent scattering can also occur. Such incoherent scattering carries no information about the structure of the sample, but can tell about the dynamics of the sample [17].

### 2.2.3.2 Scattering vector Q

When considering a SANS experiment, the use of the scattering vector **Q** is generally preferred to the angle θ. Q is the modulus of the resultant between the incident and scattered wavevectors $k_i$ and $k_s$, where in the case of elastic scattering

$$k_i = k_s = \frac{2\pi n}{\lambda} \qquad \textbf{Equation 2-18}$$

so that

$$Q = \left|\vec{Q}\right| = \left|\vec{k}_s - \vec{k}_i\right| = \frac{4\pi n}{\lambda}\sin\frac{\theta}{2} \qquad \textbf{Equation 2-19}$$

The refractive index of the medium, *n*, is equal to 1 for neutrons. Figure 2-14 shows the geometric relationship involved.

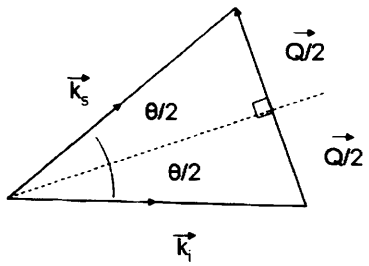


**Figure 2-14 Geometry relationship for the determination of the scattering vector Q.**

Then, Bragg's law of diffraction that links θ, the angle of diffraction of a radiation of wavelength λ, for planes separated by a distance d, can be written as follow:

$$\lambda = 2d \cdot \sin\frac{\theta}{2} \qquad \textbf{Equation 2-20}$$

Substituting Equation 2-19 into Bragg's law of diffraction leads to the following equation,

$$d = \frac{2\pi}{Q} \qquad \textbf{Equation 2-21}$$

which relates Q values to a distance d. A peak in the I(Q) vs. Q diffraction pattern at a given $Q_{peak}$ value will indicate a characteristic distance d present in the colloidal arrangement of the sample. Sharp Bragg peaks can be seen for samples made at higher concentrations, or investigated under external forces such as shear flow, and

that present a more ordered phase. The nearest neighbour distance, or plane separation can be calculated such as $d = 2\pi / Q_{peak}$.

The dimension of Q is that of a $(\text{length})^{-1}$, and usually expressed as $Å^{-1}$. Q therefore depends on both the angle θ and the neutron wavelength. This highlights the two different approaches to SANS: with a monochromatic neutron source (ILL), the useful Q-range can be spanned by measuring the scattering intensity at different angles, which is achieved by using a moveable detector so that the sample to detector distance can be varied. In the case of spallation sources (ISIS, LOQ), the detector is fixed, but neutrons wavelengths vary and are determined by the time-of-flight method.

The collected data can therefore be presented as plots showing I(Q) as a function of Q and need not take into account the wavelength of the neutron. Small scale structures are probed at high Q values, typically above 0.5 $Å^{-1}$, whereas larger scale structures, as encountered in the case of micellar aggregates for example, are probed at lower Q values, typically between 0.006 to 0.3 $Å^{-1}$.

### 2.2.3.3 SANS Instrumentation

Figure 2-15 shows the schematic diagram of the D11 fixed wavelength SANS diffractometer used at ILL, in which the position of the detector is adjustable in order to probe the scattering intensity at different angles.

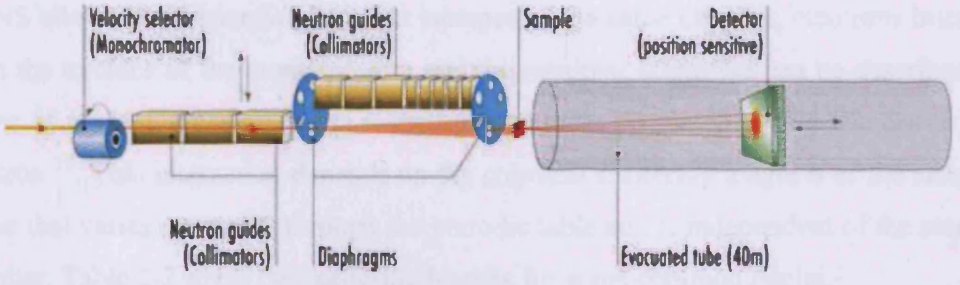


**Figure 2-15 Diagram for the fixed-wavelength SANS diffractometer D11 present at ILL (Courtesy of the ILL webpage, http://www.ill.fr/instruments/instrument-groups/instruments/d11/home/).**

Figure 2-16 shows the schematic diagram of the LOQ instrument used at ISIS, in which the detector is fixed but the neutron beam used is white.

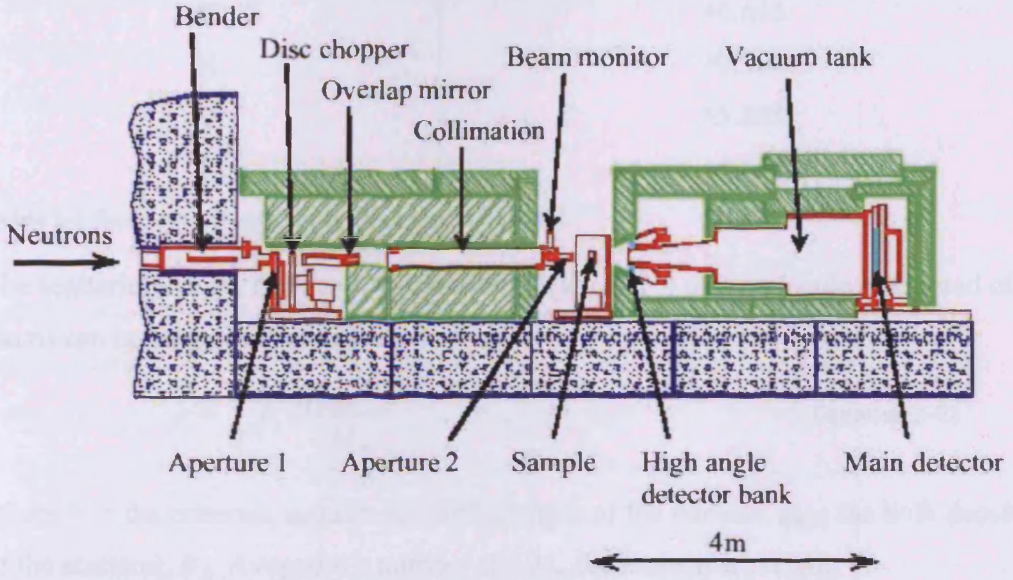


**Figure 2-16 Diagram for the fixed-geometry SANS diffractometer LOQ present at ISIS [18].**

Both fixed and moveable set-ups allow the spanning of the useful regions encountered in the case of colloidal assemblies, typically distances between 10 Å and 1000 Å, that can be measured using Q values comprised between ~ 0.006 $Å^{-1}$ and 0.6 $Å^{-1}$.

### 2.2.4 Scattering length density and Contrast variation

#### 2.2.4.1 Scattering Length Density

SANS allows the distinction between isotopes of the same element. Neutrons interact with the nucleus of the atoms present and the resultant scattering can be described in terms of nucleus cross section, i.e. the apparent area presented by the nucleus to the neutron [19]. This interaction depends on the coherent scattering length **b** of the atom, a value that varies randomly through the periodic table and is independent of the atomic number. Table 2-2 gives the scattering lengths for some common nuclei.

| Atomic Nucleus | Scattering Length (b) / femtometer ($10^{-15}$ m) |
|---|---|
| $^{1}H$ | –3.741 |
| $^{2}H$ (D) | +6.671 |
| C | +6.646 |
| N | +9.362 |
| O | +5.803 |
| F | +5.654 |

**Table 2-2 Scattering lengths of some common nuclei [20].**

The scattering length density **ρ** (dimension of (length)$^{-2}$) of a molecule composed of **i** atoms can be calculated as follow:

$$\rho = \sum_i b_i \cdot \frac{\rho_{bulk} N_A}{M_w} \qquad \textbf{Equation 2-22}$$

where $b_i$ is the coherent neutron scattering length of the nucleus, $\rho_{bulk}$ the bulk density of the scatterer, $N_A$ Avogadro's number and $M_w$ the molecular weight.

In the SANS experiment, the intensity I(Q) (dimension (length)$^{-1}$) is measured, which will provide the information on the structure of the sample, and can be expressed as follows:

$$I(Q) = N_p V_p^{\,2} (\Delta\rho)^2 P(Q) S(Q) + B_{inc} \qquad \textbf{Equation 2-23}$$

where $N_p$ is the number of scattering bodies, $V_p$ the volume of the scattering body, $(\Delta\rho)^2$ the contrast term, P(Q) the form factor, S(Q) the structure factor and $B_{inc}$ the incoherent backgroud.

The contrast term therefore plays an important role in the intensity measured, and corresponds to the square of the difference in the scattering length density of the solute, or particle $\rho_p$ and the solvent $\rho_s$. It is expressed as:

$$(\Delta\rho)^2 = (\rho_p - \rho_s)^2 \qquad \textbf{Equation 2-24}$$

### 2.2.4.2 Contrast variation

As seen in Equations 2-24, if both the solute and the solvent have identical scattering length densities, the contrast term equals zero, there will be no SANS and therefore no structural information will be obtained. In this case, solute and solvent are said to be contrast matched.

The scattering length densities of the colloidal domain under investigation and that of the surrounding medium should therefore be far apart. This can be achieved by suitably substituting hydrogen for deuterieum, either in the solvent or the solute, or in some specific part of the solute. This introduces some contrast and enables to selectively observe a chosen moiety of the system. Figure 2-17 summarizes this principle in a purely diagrammatic and hypothetic fashion. By successively matching the background to one of the element present in the investigated species, the red lobes can be probed (panel **b**), and then the blue ones (panel **c**), while in panel **a** no differentiation could be made. Figure 2-18 shows the contrast match illustration in the realistic case of a core shell particle, for which the core, the shell and the surrounding medium can selectively be hydrogenated or deuterated.

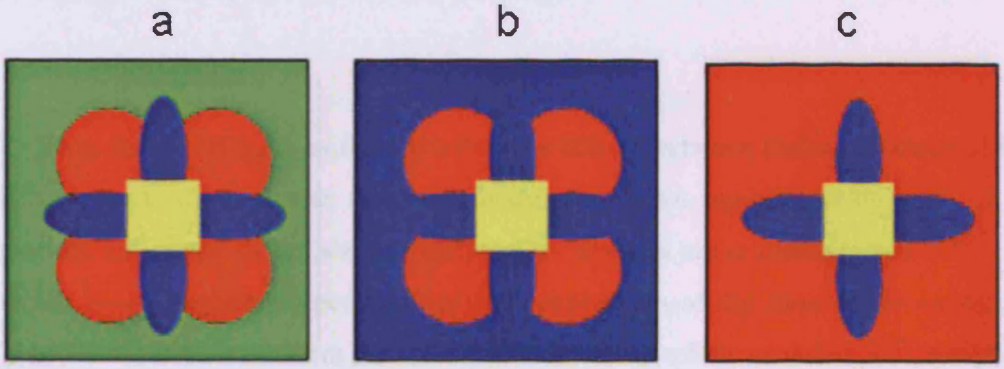


**Figure 2-17 Illustration of the contrast variation principle. Courtesy of Charles Glinka, adapted from www.ncnr.nist.gov/programs/sans/tutorials/index.html.**

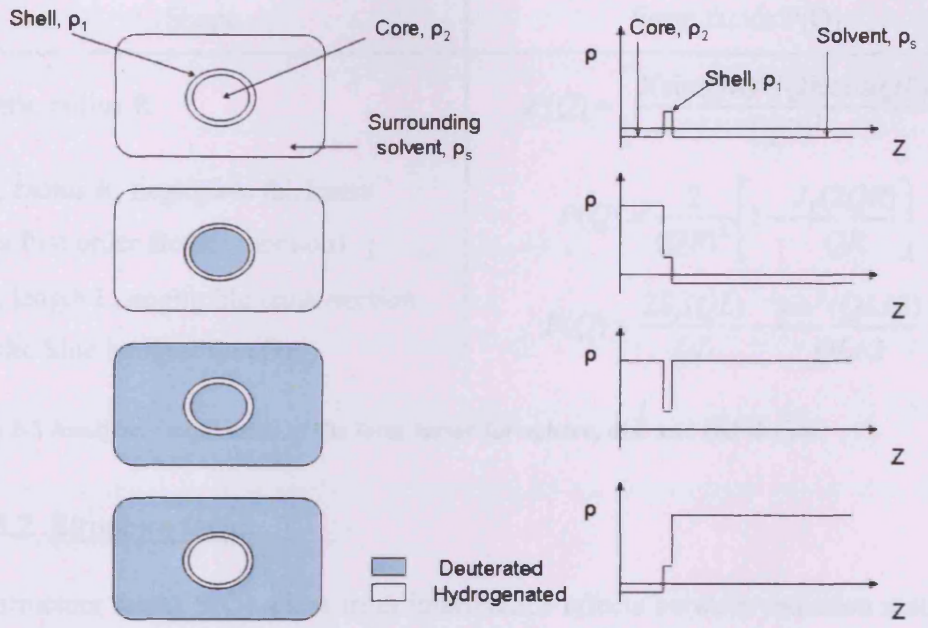


**Figure 2-18 Illustration of the Hydrogen/Deuterium contrast use in the case of a core-shell particle. Z is the distance from the centre of the scattering body [15].**

### 2.2.5 Form and structure factor

As seen in Equation 2-23, the collected signal I(Q) contains a form (or shape) factor and structure factor, respectively P(Q) and S(Q).

#### 2.2.5.1 Form factor

The form factor P(Q) arises from interference effects between radiation scattered by different parts of the same scattering body, *i.e.* on an intramolecular level. It is therefore influenced by the size and shape of the element under investigation [17, 20].

For the most common shapes, an analytical expression of the form factor exists. In Table 2-3 are shown the form factors expressions for a sphere of radius R [21], a disc of radius R and negligible thickness and a rod of length L and negligible cross-section [20].

| Shape | Form factor P(Q) |
|---|---|
| **Sphere**, radius R | $P(Q)=\left[\frac{3(\sin(QR)-QR\cos(QR))}{(QR)^3}\right]^2$ |
| **Disc**, radius R, negligible thickness ($J_1$: a first order Bessel function) | $P(Q)=\frac{2}{(QR)^2}\left[1-\frac{J_1(2QR)}{QR}\right]$ |
| **Rod**, length L, negligible cross-section ($S_i$ : the Sine integral function) | $P(Q)=\frac{2S_i(QL)}{QL}-\frac{\sin^2(QL/2)}{QL/2}$ |

**Table 2-3 Analytical expression of the form factor for sphere, disc and rod shapes.**

### 2.2.5.2 Structure factor

The structure factor S(Q) arises from interference effects between radiation scattered by different scattering bodies, *i.e.* on an intermolecular level. It depends on the spatial correlation of the particles and can arise in systems where interparticle interactions occur (charged particles, highly concentrated systems). The interparticle structure factor is expressed as:

$$S(Q)=1+\frac{4\pi N_p}{QV}\int_0^\infty[g(r)-1]r\cdot\sin(Qr)dr \qquad \textbf{Equation 2-25}$$

where r is the radial distance from the centre of any scattering body, and g(r) is determined by the radial distribution function which indicates the distance of each nearest neighbour. Information about the relative position of the scattering bodies can be obtained through the structure factor. However, for dilute systems, S(Q) is weak and lies outside the Q range investigated. Such interparticle information via S(Q) can only be obtained in strongly interacting and/or concentrated systems [20].

## 2.2.6 Measurements required

Accessing the scattering intensity arising from the sample under investigation necessitates several measurements. Both the scattering and transmittance need to be measured for these cases: the empty beam, the cell, the background solvent present in the investigated sample, a calibration sample and the investigated sample; then, the data is normalised to account for the type of instrument used.

During a SANS experiment, a small volume of the sample is illuminated by the collimated neutron beam. The incident radiation can then be scattered, transmitted, and/or absorbed. A detector records the flux of radiation scattered into a solid angle element, this flux can be expressed as follows:

$$I(\lambda,\theta) = I_0(\lambda)\Delta\Omega\eta(\lambda)T(\lambda)V_s\frac{d\Sigma}{d\Omega}(Q) \qquad \textbf{Equation 2-26}$$

with $I_0(\lambda)$ the incident flux, $\Delta\Omega$ the solid angle element, $\eta$ the detector efficiency, $T(\lambda)$ the sample transmission, $V_s$ the illuminated sample volume and $\frac{d\Sigma}{d\Omega}(Q)$ the differential scattering cross-section, which contains the information on the size, shape and interactions of the scatterers [20].

### 2.2.7 SANS approximations

Once the scattering pattern I(Q) vs. Q has been recorded for a given sample, it can be useful to have a first estimation of the size and shape of the scattering particles present. This can also serve as a starting point for the data fitting using more refined and complex models. These approximations are known as the Guinier and Porod approximation and are valid only in dilute systems having negligible interaction.

In the low Q regime the Guinier approximation can be used to probe disc, spheres and cylindrical shapes and is expressed as follows:

$$I(Q) \propto Q^{-D}\exp\left(-\frac{Q^2R^2}{K}\right) \qquad \textbf{Equation 2-27}$$

where D is equal to 1, 0 and 2 and K to 4, 5 and 12 for cylinders, spheres and discs respectively.

By plotting various quantities against $Q^2$, the characteristic dimension (noted R) of the particle can be obtained, i.e. the disc thickness, the sphere radius or the cylinder radius. Table 2-4 shows the different Guinier representations for these shapes.

| Shape | Guinier Plot | Characteristic dimension R |
|---|---|---|
| Disc | $\ln[I(Q)\cdot Q^2]$ vs. $Q^2$ | $Thickness=\sqrt{slope\times 12}$ |
| Sphere | $\ln[I(Q)]$ vs. $Q^2$ | $Radius=\sqrt{slope\times 5}$ |
| Cylinder | $\ln[I(Q)\cdot Q]$ vs. $Q^2$ | $Radius=\sqrt{slope\times 4}$ |

**Table 2-4 Guinier plots and extracted characteristic dimensions for a disc, a sphere and a cylinder shape.**

One restriction applies to the spherical shape Guinier representation, for which the product Q·R must be smaller than 1. The curve giving a linear decay over the low Q values will give the most probable particle shape.

In the high Q regime, the Porod approximation can be used. In this region, I(Q) is more sensitive to the scattering arising from local surfaces and can be related to the total interfacial area, so that:

$$I(Q) = 2\pi(\Delta\rho)^2\left(\frac{S}{V}\right)Q^{-4} \qquad \textbf{Equation 2-28}$$

with S/V the total interfacial area per unit volume of sample, in $cm^{-1}$. The Porod approximation is limited to smooth interfaces, in a Q range much greater than the reciprocal characteristic dimension, *i.e.* for $Q >> 1/R$.

### 2.2.8 Typical scattering data for spheres, discs and rods

Figure 2-19 shows the typical data obtained when $P(Q)^2$ is plotted as a function of (a) QR for monodisperse spheres, R being the radius of the sphere; (b) Qd for long rods of length L and diameter d; (c) Qt for thin discs of diameter D and thickness t.

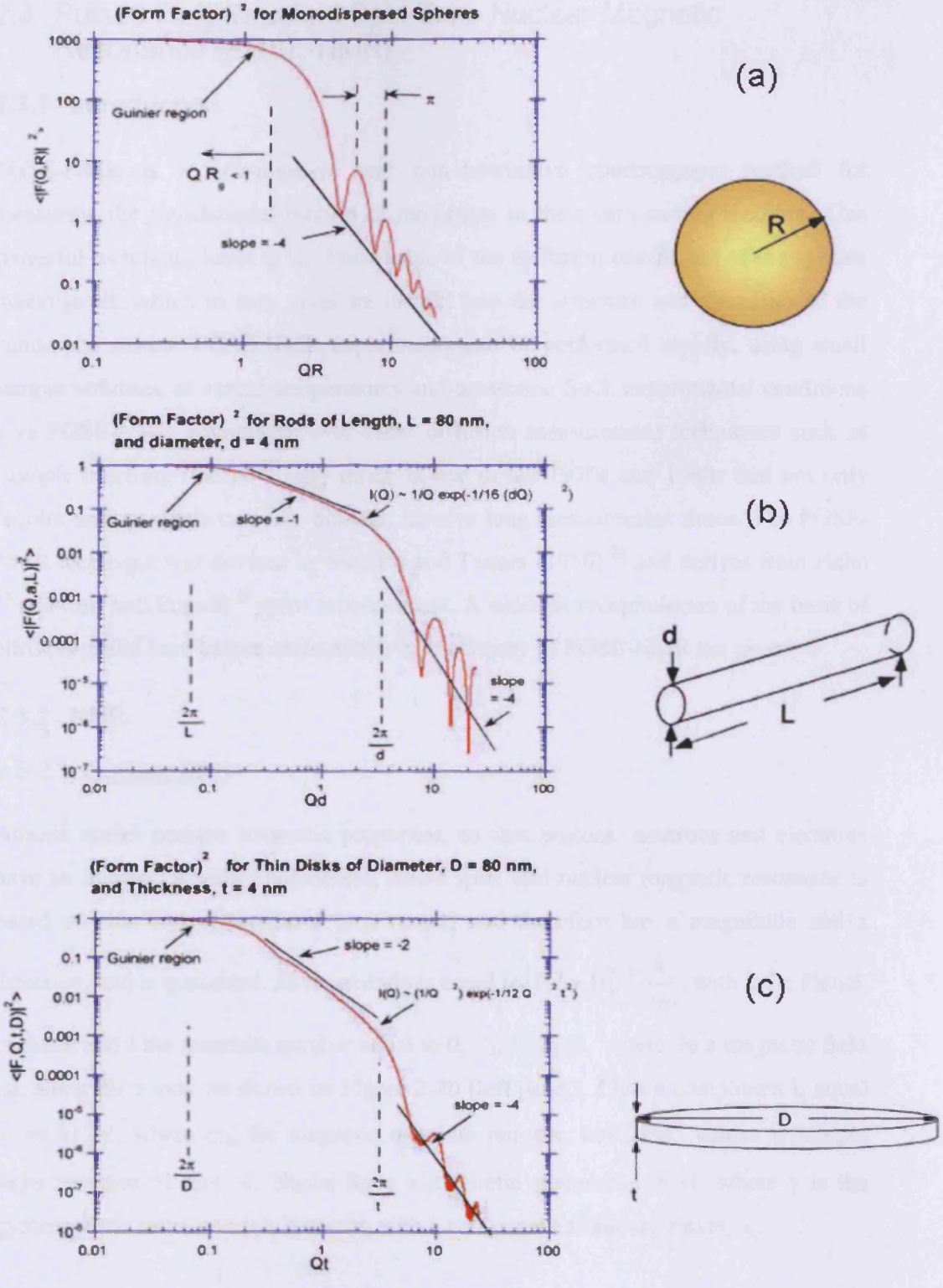


**Figure 2-19. Form factors squared as a function of (Q × characteristic dimension of the shape), for a sphere, a rod and a disc. Courtesy of Charles Glinka, taken from www.ncnr.nist.gov/programs/sans/pdf/SANS_dilute_particles.pdf.**

## 2.3 Pulsed Field Gradient Spin-Echo Nuclear Magnetic Resonance (PGSE-NMR)

### 2.3.1 Introduction

PGSE-NMR is a non-invasive and non-destructive spectroscopic method for measuring the translational motion of molecules in their surrounding medium. This powerful technique leads to the knowledge of the diffusion coefficient of the species investigated, which in turn gives an insight into the structure and dynamics of the condensed matter. PGSE-NMR experiments can be performed rapidly, using small sample volumes, at varied temperatures and pressures. Such experimental conditions give PGSE-NMR advantages over other diffusion measurement techniques such as isotopic labelling tracers [22] very much in use in the 1970s and 1980s that not only require uneasy synthetic work but also involve long measurement times. The PGSE-NMR technique was devised by Stejskal and Tanner (1950) [23] and derives from Hahn [24] and Carr and Purcell [25] spin- echo concept. A succinct recapitulation of the basis of NMR is useful here before more details of the theory of PGSE-NMR are given.

### 2.3.2 NMR

#### 2.3.2.1 Nuclear Spin

Atomic nuclei possess magnetic properties, so that protons, neutrons and electrons have an intrinsic angular momentum, called spin, and nuclear magnetic resonance is based on this fact. The spin $\boldsymbol{I}$ is a vector, and therefore has a magnitude and a direction, and is quantized. Its magnitude is equal to $[I(I+1)]^{1/2}\frac{h}{2\pi}$, with h the Planck constant and I the quantum number equal to 0, $^1/_2$, 1, $^3/_2$, 5, $^5/_2$, etc. In a magnetic field $B_0$, along the z axis, as shown on Figure 2-20 (left panel), $\boldsymbol{I}$ has a component $I_z$ equal to $m_I h/2\pi$, where $m_I$, the magnetic quantum number, has 2I+1 values in integer steps between +I and –I. Nuclei have a magnetic moment $\boldsymbol{\mu} = \gamma\mathbf{I}$, where $\gamma$ is the gyromagnetic ratio, and $\boldsymbol{\mu}$ is a vector, with a component along the z axis, $\mu_z$.

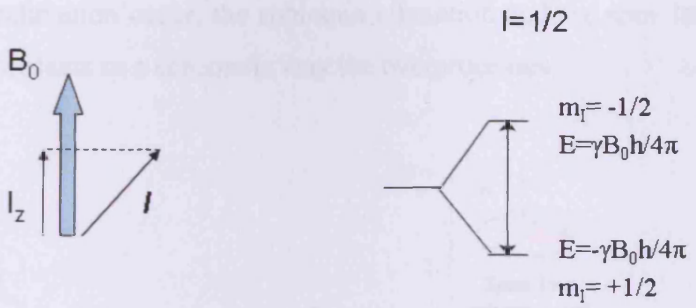


**Figure 2-20 z-axis component of the spin vector (left panel), energy levels allowed for a nucleus of spin I=1/2, as in the case of the proton (right panel).**

In the absence of an external magnetic field, all 2I+1 orientations have the same energy and the spins of magnetic nuclei are oriented randomly. However, when placed between the poles of strong magnets, the spins take well-defined states. In a field $B_0$, all the possible 2I+1 orientations each have an energy E so that $E = -\mu_z \cdot B_0$ , i.e. $E = -m_I \gamma B_0 h / 2\pi$ . In the case of the hydrogen nuclei, the energy levels can be represented as in Figure 2-20 (right panel).

When irradiated with an electromagnetic radiation of the appropriate frequency, a magnetic nucleus absorbs energy and its spin goes from a low energy state to a high one: it is said to be in resonance. The nuclei precess with Larmor frequency $\nu = -\gamma B_0 / 2\pi$ , equal to the resonance frequency. The exact value required for resonance is determined by the nature of the nucleus itself and the external field. The resonance frequency also depends, for a given nucleus, on the environment the nucleus experiences in the molecule, an effect known as the chemical shift [26]. Each chemical shift corresponds to a slightly different frequency.

### 2.3.2.2 Pulse and relaxation process

A short strong pulse of radiofrequency radiation applied along the x-axis rotates the net magnetization towards the y-axis (cf. Figure 2-21), a 90° pulse ($\pi/2$) rotates the magnetization of 90° and so forth.

Following disturbance by a pulse, the spins return to their equilibrium state via relaxation, by an energy exchange between themselves and their surroundings. Two

processes of relaxation occur, the spin-spin relaxation and the spin–lattice relaxation. Figure 2-21 presents in a schematic way the two processes.

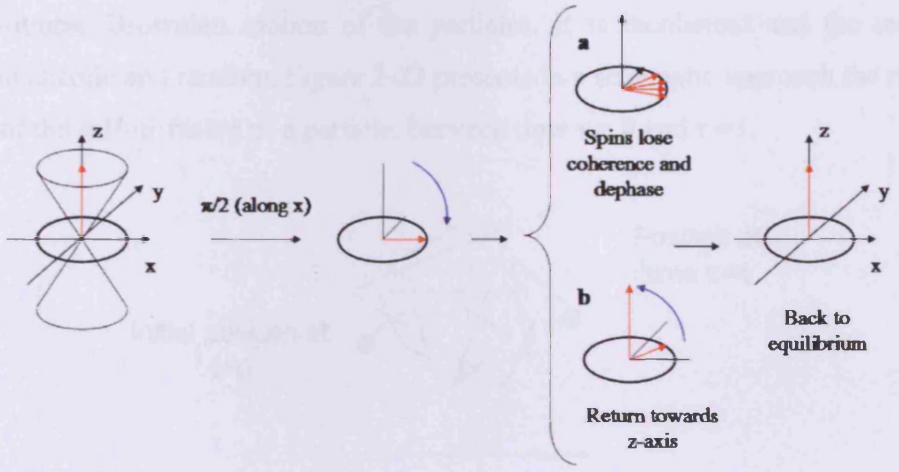


**Figure 2-21 Relaxation processes of the spins following a 90° pulse along the x axis: (a) Spin-spin relaxation and (b) Spin-lattice relaxation.**

The spin-spin relaxation is transversal, in the (xy) plane, and the relaxation time is called $T_2$. The spin-lattice relaxation time is $T_1$ and this relaxation process is longitudinal, taking place along the z-axis. Both relaxation processes occur concomitantly. The knowledge of $T_1$ gives access to information about the molecular environment of the nucleus. Both relaxation times can be measured using NMR, and determine in essence the various parameters used in the diffusion experiment.

### 2.3.3 Concepts and theory in PGSE-NMR

#### 2.3.3.1 Diffusive process and self-diffusion coefficient

Translational diffusive mass transfer affects a multitude of processes; physical (permeation of fluids through porous adsorbents such as oil reservoir rocks), chemical (properties of ordered fluids such as liquid crystals) or biological (circulation of body fluids, functioning of living cells), on time scales ranging from picoseconds to very long time (years, centuries) [27].

Diffusive mass transfer can be driven by external forces such as electric fields and other gradients, such as concentration, temperature, or pressure. In these cases, the

diffusion process is said to be directed. However, diffusive mass-transfers are also present even when no such forces occur. In this later case, internal thermal agitation drives the motion of particles. The process is known as self-diffusion and is caused by the isotropic Brownian motion of the particles. It is incoherent and the resulting motion chaotic and random. Figure 2-22 presents in a schematic approach the random walk of the self-diffusion of a particle, between time $\tau = 0$ and $\tau = t$.

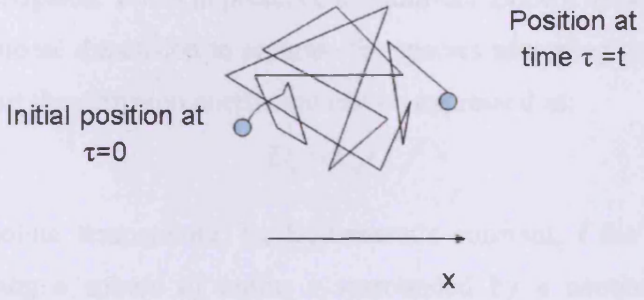


**Figure 2-22 Schematic view of the random walk of a particle due to thermal motion, i.e. its self-diffusion.**

This is the process which is quantified using PGSE-NMR, and the quantity of interest is the self-diffusion coefficient noted $D_s$. In an isotropic system, the mean square displacement is given by the Einstein relation [28]. This relation links $D_s$ to the mean square displacement of the particle of interest after a time t, in a three-dimensional space, as follows:

$$D_s = \lim_{t \longrightarrow \infty} \frac{1}{6t} \langle |r(t) - r(0)|^2 \rangle \qquad \textbf{Equation 2-29}$$

with r(0) and r(t) the locations of the particle at times $\tau = 0$ and $\tau = t$, the angular brackets signifying an average. Every component of a multi-component system can be assigned a self-diffusion coefficient. Equation 2-29 is valid when the observation time is much greater than the actual time scale of the elementary translational motion process. This timescale can be greatly affected by the viscosity of the sample under investigation, and hence its solid, liquid or gaseous state.

In low viscosity liquids, diffusion is associated with displacements of $10^{-4}$ to $10^{-5}$ m per second. This leads to diffusion coefficients $D_s$ of the order of $10^{-9}$ to $10^{-12}$ $m^2$ $s^{-1}$. Such a diffusion coefficient of $10^{-9}$ $m^2$ $s^{-1}$ corresponds to a displacement, during a 1 second time frame in the three-dimensional space, of $7.7 \times 10^{-5}$ m, i.e. a little less than

0.1 mm. For highly viscous liquids, or those that are supercooled, the displacement is significantly reduced by several orders of magnitude and can be equal to $10^{-7}$ m per second, or less, which is equivalent to the slow diffusion regime observed in solids with $D_s$ of the order of $10^{-15}$ $m^2$ $s^{-1}$ or lower. For gases, fast diffusion is observed, with diffusion coefficients reaching up to 1 $m^2$ $s^{-1}$ [29].

The self-diffusion coefficient leads directly to information about the size and shape of the species investigated. When in presence of multi-component systems, it can also be used as an additional dimension to separate the species according to their mobility [30]. The magnitude of the diffusion coefficient can be expressed as:

$$D_s = k_B T / f \qquad \textbf{Equation 2-30}$$

with T the absolute temperature, $k_B$ Boltzmann's constant, f the frictional factor. When considering a sphere of radius r surrounded by a continuous medium of viscosity $\eta$, f can be expressed by the Stokes relation, Equation 2-31.

$$f = 6\pi\eta r \qquad \textbf{Equation 2-31}$$

Substituting Equation 2-31 into Equation 2-30 leads to the Stokes-Einstein relation:

$$D_s = k_B T / 6\pi\eta r \qquad \textbf{Equation 2-32}$$

which in turns leads to the hydrodynamic radius r of the species under investigation, once the diffusion coefficient $D_s$ is known.

### 2.3.3.2 Principle of diffusion-NMR

The basic principle behind NMR experiments probing the translational motion of spin-bearing molecules is that the spatial coordinates of spins can be distinguished and labelled by the application of magnetic field gradients, which produce a spatially dependant magnetic field. The NMR frequency of the spins becomes a function of their coordinates and by their motion in this frequency-labelled space, the spins acquire phase shifts in their precession. Such phase shifts reflect their frequency and the history of their spatial coordinates, so the translational motions experienced by the spins are directly linked to the statistics of the phase shifts. Measuring these phase shifts gives access to their translational displacement, hence to their diffusion coefficient.

If the magnetic field inhomogeneity results from a constant field gradient g, produced and controlled externally by suitable gradient coils, it can be written in three dimensions as:

$$g = \frac{\partial B_z}{\partial x} i + \frac{\partial B_z}{\partial y} j + \frac{\partial B_z}{\partial z} k \qquad \textbf{Equation 2-33}$$

where i, j and k are the unit vector in the x, y and z directions of the magnetic field of strength $B_0$. The total field B present at position r is equal to:

$$B = B_0 + g \cdot r \qquad \textbf{Equation 2-34}$$

Due to this gradient, the magnetic field varies as $B(r) = B_0(r) + \Delta B(r)$, and so does the Larmor frequency ($\omega$) of the nuclei with a gyromagnetic ratio $\gamma$, as:

$$\omega = \gamma(B_0(r) + \Delta B(r)) \qquad \textbf{Equation 2-35}$$

This means that any nucleus changing its location will have its Larmor frequency varied. Such a frequency change can be observed in a spin-echo experiment [29].

#### 2.3.3.3 Spin Echo concept

The effect of radiofrequency (rf) pulses was explored by Hahn [24] and led to the spin-echo concept: an initial 90° ($\pi/2$) rf pulse is applied along the x axis, creates phase coherence and turns the magnetization of the $B_0$ field into the (xy) plane. Then, spins 'fan out' and dephase during a time $\tau$. A 180° ($\pi$) pulse then inverts the dephasing effect, and spins start clustering again and refocus. After a time lapse of $2\tau$, the fast spins have been able to catch up the slow ones, refocusing on the x axis and the Hahn spin-echo is observed and recorded. This process is illustrated in Figure 2-23.

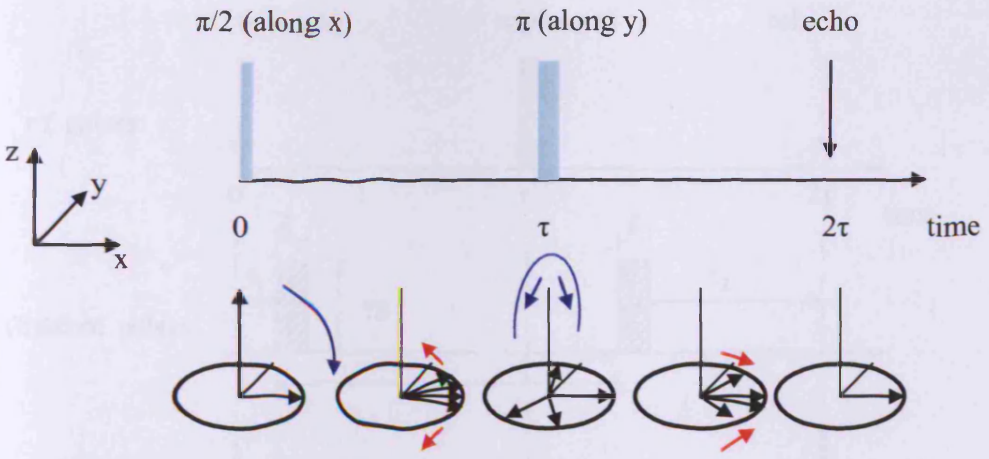


**Figure 2-23 Illustration of the basic Spin-Echo pulse sequence.**

The echo observed at 2τ can only be formed fully if the precession frequency of every spin is constant in the time lapse considered. However, if the nuclei move from their initial coordinates in this inhomogeneous magnetic field, their frequency will vary and the spin-echo signal will be attenuated. Therefore, for incoherent motion occurring as is the case in self-diffusion displacement, the refocusing of the spin vectors will be incomplete at the time of the echo. A typical time for the interval 2τ lies in the range of 1-1000 ms [28].

### 2.3.3.4 PGSE methods

#### *Stejskal-Tanner sequence*

The basic spin-echo experiment was revisited and greatly improved by Stejskal and Tanner [23], by the introduction of pulsed-gradients, leading to the PGSE-NMR technique. In a PGSE-NMR experiment, field gradient pulses are applied in the spin-echo sequence. These field gradient pulses have an amplitude g, a duration δ and are separated by a time Δ. The diagram for the first Stejskal and Tanner pulsed field-gradient experiment is showed in Figure 2-24.

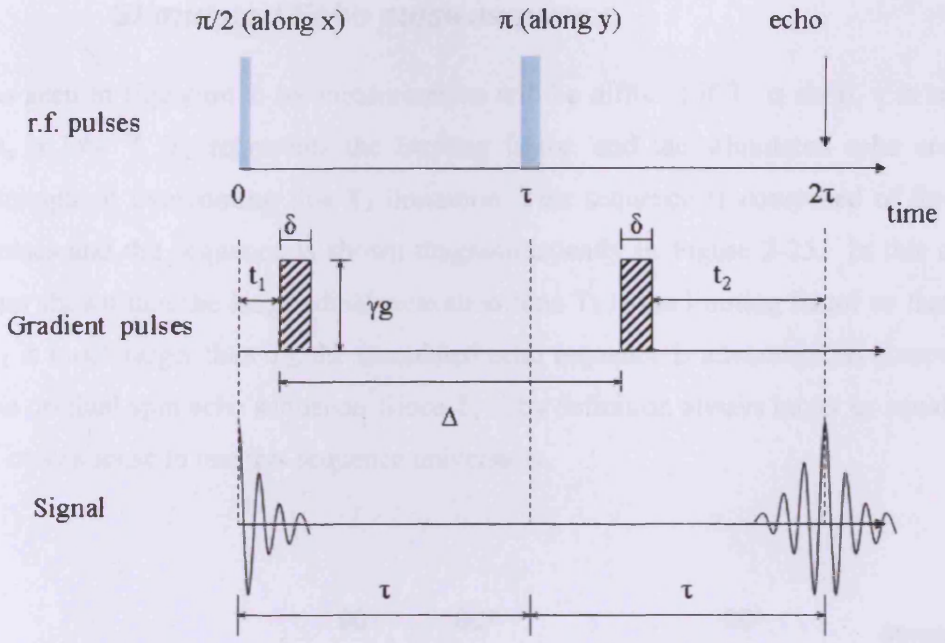


**Figure 2-24 The Stejskal-Tanner PGSE experiment, comprising a 90° - τ -180° spin echo sequence with two field gradients superimposed.**

The first field-gradient pulse encodes the spin positions in the gradient direction, through phase shifts. The second, in conjunction with the π r.f. pulse, has the effect of refocusing the phase shifts to regenerate an echo signal that will reflect the spins motion in the gradient direction during the time Δ. The echo attenuation in the experiment described in Figure 2-24 is given by Equation 2-36:

$$A = A_0 \exp\left[-\frac{2\tau}{T_2} - \gamma^2 D_s g^2 \delta^2 (\Delta - \delta/3)\right] \qquad \textbf{Equation 2-36}$$

with $A_0$ the initial amplitude at $\tau = 0$. In Equation 2-36, the first exponential term, $\exp\left(-\frac{2\tau}{T_2}\right)$, relates to the attenuation due to transversal relaxation, while the second term, $\exp\left(-\gamma^2 D_s g^2 \delta^2 (\Delta - \delta/3)\right)$ relates to the attenuation due to diffusion.

Depending on the pulse sequence designed and applied, several PGSE methods exist. They can be used in specific context, such as in the case of heterogeneous samples where random field gradients are present in the material itself, or to probe very high or low diffusion coefficient values. The one that is used in the study presented in Chapter 7 is the stimulated echo method and is described in the following section.

### *Stimulated Echo pulse sequence*

As seen in Equation 2-36, measurements will be difficult if $T_2$ is short, $\gamma$ is small or $D_s$ is low [29]. $T_2$ represents the limiting factor, and the stimulated echo sequence attempts at overcoming this $T_2$ limitation. This sequence is composed of three 90° pulses and the sequence is shown diagrammatically in Figure 2-25. In this case, it was shown that the longitudinal relaxation time $T_1$ is the limiting factor so that when $T_1$ is much larger than $T_2$, the stimulated echo sequence is advantageous compared to the original spin echo sequence. Since $T_1$ is by definition always larger or equal to $T_2$, it makes sense to use this sequence universally.

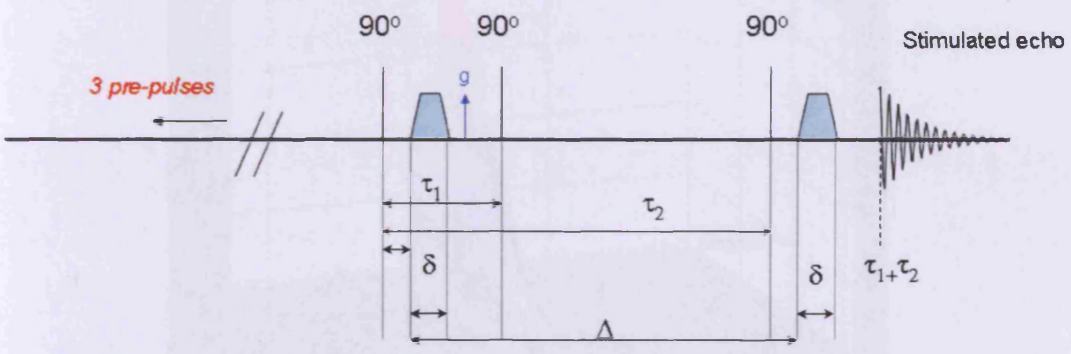


**Figure 2-25 Stimulated Echo sequence used in the study presented in Chapter 7.**

The first 90° pulse turns the magnetisation into the (xy) plane. The spins then start losing phase coherence as a result of the different precession rates and acquire phase shifts in the plane of rotation. After a time $\tau_1$, the second 90° pulse is applied and collects the phase shifts in the z-direction, where they are not affected by the field gradient and relax in the longitudinal direction. After a time $\tau_2$, the phase shifts are restored with a reversed sign by a third 90° pulse. The spins then form an echo recorded at time $\tau_1 + \tau_2$.

Three pre-pulses are applied before each sequence. Indeed, the pulsed gradient experiments depend on current pulses that produce heat, mechanical forces and eddy currents. As the pulses need to be extremely reproducible, applying pre-pulses allows the system to come to a state close to the one experienced during the PGSE sequence.

By suitably choosing the values of the diffusion time Δ and that of the gradient pulse applied, a wide range of self-diffusion coefficient can be probed.

### 2.3.3.5 FT-PGSE NMR

The echo attenuation can be Fourier transformed. This leads to a high resolution spectrum where each peak, assignable to the components present in the system, attenuates. Therefore, the self-diffusion coefficient can simultaneously be measured for various species present in a multi-component system, as illustrated in Figure 2-26.

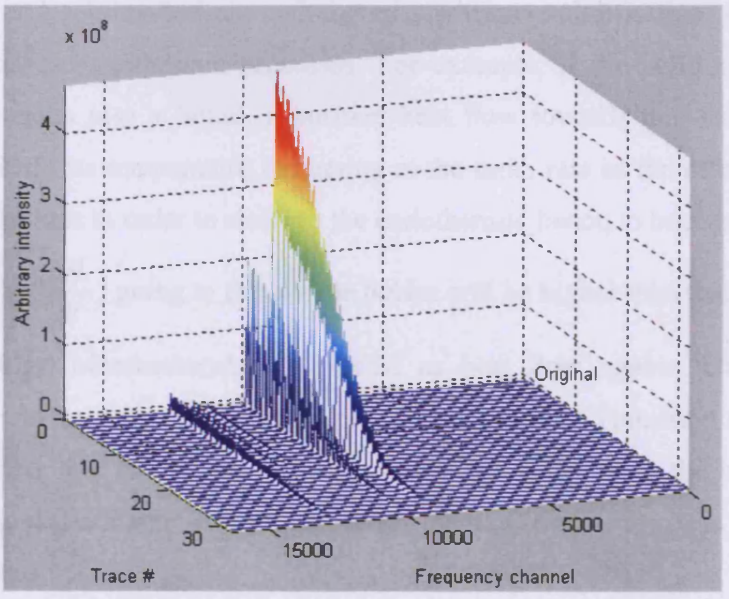


**Figure 2-26 Fourier Transform of the echo attenuation. The attenuation rate of various components of the system can be probed simultaneously.**

The spin-echo decay can then directly be linked to the diffusion coefficient via the following Equation 2-37, where the signal decay is noted A(δ), δ being the field gradient pulse duration, g its intensity, σ the ramp time and Δ the diffusion time:

$$A_{(G,\delta)} = A_0 \exp\left(-kD_s\right) \qquad \textbf{Equation 2-37}$$

where $k = -\gamma^2 g^2 \left( \frac{30\Delta(\delta+\sigma)^2 - (10\delta^3 + 30\sigma\delta^2 + 35\sigma^2\delta + 14\sigma^3)}{30} \right)$, γ is the gyromagnetic ratio of the nucleus under investigation, here proton and the $A_0$ term is related to the total number of protons in the sample.

## 2.4 Differential Scanning Calorimetry (DSC)

### 2.4.1 Principle

DSC is a thermo-analytical technique that measures the amount of heat, or energy, required to establish a nearly zero temperature difference between the sample under investigation and an inert sample reference, when an identical temperature regime (heating or cooling) is applied to both, at a controlled rate. A change in the state of the sample, even though isothermal, either dissipates or necessitates energy, i.e. it is an exothermic or endothermic process. Physical transformation such as fusion, vaporization and sublimation are endothermic, whereas solidification, condensation and deposition are exothermic processes. For example, if the solid sample under investigation melts into a liquid, a positive heat flow towards this sample will be necessary to keep its temperature increasing at the same rate as the reference, as the sample absorbs heat in order to undergo the endothermic fusion to become liquid. The heat flow $\frac{dq}{dt}(=\frac{dH}{dt})$ going to the sample holder will be higher than that going to the reference holder. Measurements are plotted as heat flow against either time or temperature, and exo- or endo-thermic peaks are observed. Transition temperatures can be accessed, and so can the enthalpy values associated with the phase-change processes, by calculating the area present under the transition peaks, as is illustrated in the next sections.

### 2.4.2 Apparatus

The calorimeter used in DSC consists of a sample holder and a reference holder. A resistance heater and a temperature sensor are connected to both holders. So as to increase the temperature of both holders at the chosen rate, currents are applied to the two heaters. It is the difference in power provided to the two heaters in order to maintain them at the same temperature which leads to $\frac{dq}{dt}$. The sample under investigation is placed in a sealed aluminium pan. Quantities used range from 1 to 10 mg. An empty sealed aluminium pan is placed on the reference holder. A schematic view of a DSC is presented in Figure 2-27.

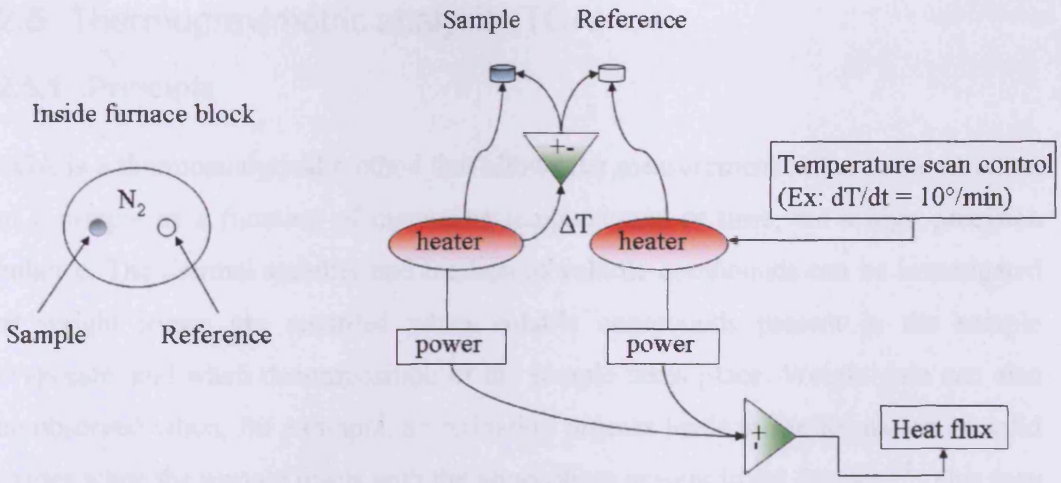


**Figure 2-27 Schematic diagram of a DSC, (left panel) inside the furnace, the atmosphere is saturated with azote; (right panel) triangles represent amplifiers that calculate the difference between the incoming signals.**

### 2.4.3 Typical data

A typical thermograph that may be obtained using DSC is presented in Figure 2-28, which shows an endothermic step which could be a glass transition, two endothermic transitions that could be melting ones and an exothermic peak that could be crystallisation. Such a sample could consist of a mix of some amorphous polymer that shows glass transition upon heating ($T_g$), and a crystalline compound that melts at a well-defined temperature ($T_{m1}$), then recrystallizes ($T_{recrys}$) into a higher melting-form crystal which in turns then melts ($T_{m2}$).

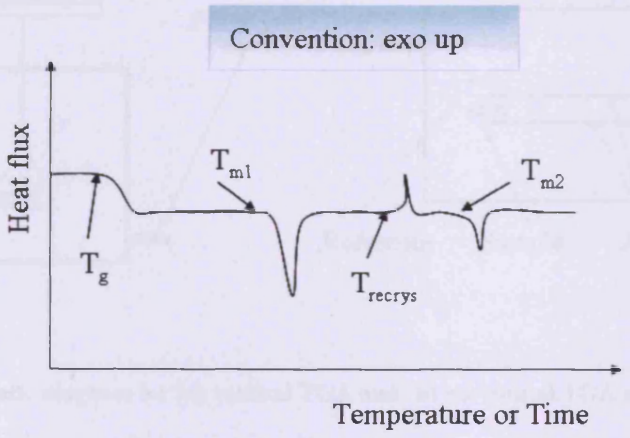


**Figure 2-28 Typical DSC diagram showing the onset temperatures of a glass transition, a recrystallization and two fusion. The convention adopted is that exothermic processes show a peak going up.**

## 2.5 Thermogravimetric analysis (TGA)

### 2.5.1 Principle

TGA is a thermoanalytical method that allows the measurement of the mass variation of a sample as a function of increasing temperatures, or time, via a high precision balance. The thermal stability and fraction of volatile compounds can be investigated as weight losses are recorded when volatile compounds present in the sample evaporate, and when decomposition of the sample takes place. Weight gain can also be observed when, for example, an oxidation process leads to the formation of solid oxides when the sample reacts with the atmosphere present in the furnace [31]. This may be desired, in the case of oxidation studies, but can also be prevented by carrying out measurements in an inert atmosphere, such as Argon. TGA can further be coupled with other analytical equipments such as FTIR or MS, which analyse the volatile compounds produced from the TGA.

### 2.5.2 Apparatus

TGA equipment relies on the presence of a balance whose design can either be vertical or horizontal [32]. The sample of typical mass comprised between 2 and 10 mg is deposited in a non-covered aluminium pan. Figure 2-29 presents the schematic diagram for the two types of TGA equipment.

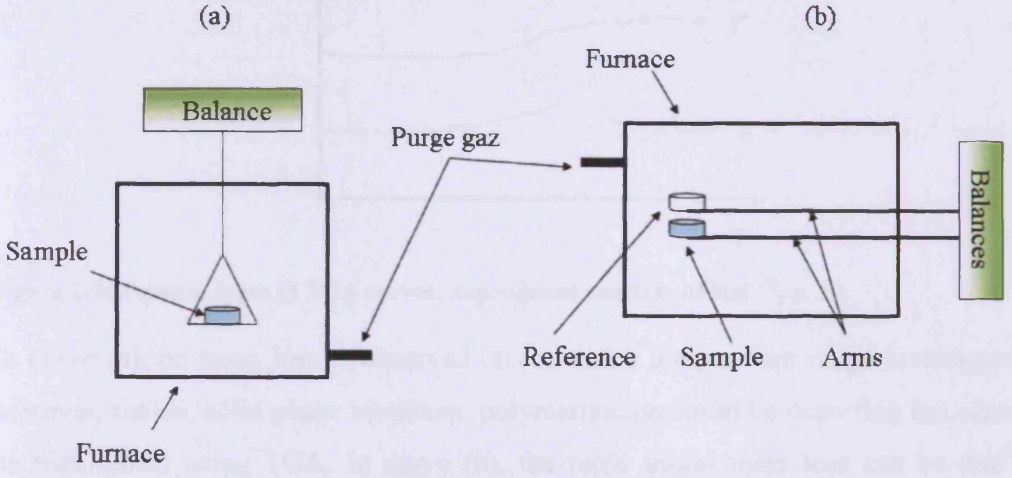


**Figure 2-29 Schematic diagram for (a) vertical TGA and (b) horizontal TGA apparatus.**

In the case of a vertical system, the sample pan hangs from the balance and the instrument does not generally possess a reference pan. Such instruments should be calibrated according to the purge gas used, as buoyancy effects arise due to density

variation of the gas with temperature. In the case of a horizontal disposition, two horizontal arms are present, that are each linked to a balance. At the end of one arm is placed the sample in an aluminium pan, at the end of the second arm is an empty pan that is used for reference. In this case, the balance arms undergo thermal expansion and this should be compensated for via prior calibration.

### 2.5.3 Typical data

Data is usually recorded as mass (m) as a function of temperature (T), or time (t), but can also be plotted as the differential $\frac{dm}{dT}$ or $\frac{dm}{dt}$. Figure 2-30 presents typical types of TGA curves obtained in various cases described below.

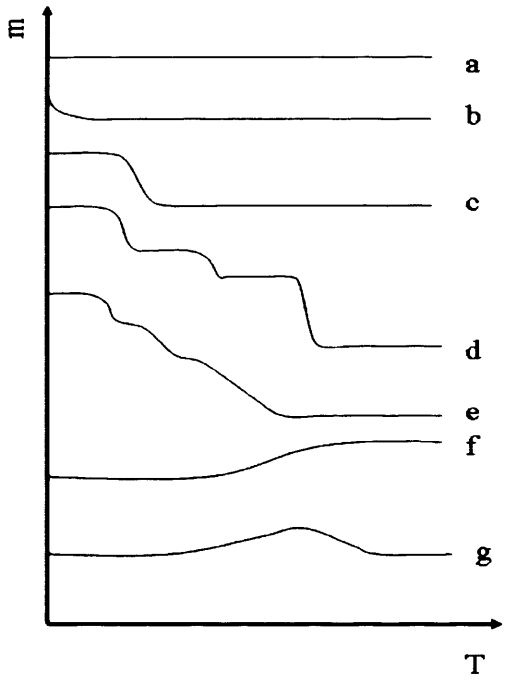


**Figure 2-30 Possible types of TGA curves. Reproduced courtesy of Ref. [32], p. 18.**

In curve (a), no mass loss is observed on the entire temperature range investigated, however, fusion, solid phase transition, polymerization could be occurring but cannot be highlighted using TGA. In curve (b), the rapid initial mass loss can be due to desorption or drying of surface moisture. In curve (c), a well-defined single step mass loss is observed, perhaps due to the presence of one volatile species in the sample. Sample shown in curve (d) possesses several various volatile compounds that may have different boiling point temperatures, and decomposes into intermediates that are

relatively stable. Curve (e) is a multi-stage decomposition as well as curve (d) but intermediates are less stable. A mass gain is observed in curve (f) that would be typical of the oxidation process of a metal (ex. $2Ag + ½ O_2 \rightarrow Ag_2O$), and in curve (g), the oxidised metal would decompose, hence the mass-loss, when taken to higher temperature.

**References**


1. *Colloid Science - Principles, methods and applications*, ed. T. Cosgrove. 2005, Oxford: Blackwell Publishing.
2. H.A. McKellop, *The lexicon of polyethylene wear in artificial joints.* Biomaterials, 2007. **28**: p. 5049-5057.
3. M.P. Stevens, *Polymer Chemistry - An introduction.* 2nd Edition ed. 1990, New York: Oxford University Press. p. 31.
4. M. Schrodner, R.-I. Stohn, K. Schultheis, S. Sensfuss, and H.-K. Roth, *Polymer field effect transitors made by laser patterning.* Organic Electronics, 2005. **6**: p. 161-167.
5. P. Manoudis, S. Papadopoulou, I. Karapanagiotis, A. Tsakalof, I. Zuburtikudis, and C. Panayiotou, *Polymer-Silica nanoparticles composite films as protective coatings for stone-based monuments.* Journal of Physics: Conference Series, 2007. **61**: p. 1361-1365.
6. *Poly(ethylene Glycol) Chemistry - Biotechnical and Biomedical Applications.* Topics in Applied Chemistry, ed. J.M. Harris. 1992, New York: Springer. p. 3.
7. J.M.G. Cowie, *Polymers: Chemistry & Physics of Modern Materials.* 2nd Edition ed. 1991, London: Blackie Academic & Professional.
8. D.F. Evans and H. Wennerström, *The Colloidal Domain.* Advances in Interfacial Engineering Series. 1994, New York: VCH.
9. S. Hokputsa, K. Jumel, C. Alexander, and S.E. Harding, *Hydrodynamic characterisation of chemically degraded hydraulic acid.* Carbohydrate Polymers, 2003. **52**: p. 111-117.
10. P.J. Flory, *Principles of Polymer Chemistry.* 1953, Ithaca, New York: Cornell University Press.
11. H.-G. Elias, *An Introduction to Polymer Science.* 1st Edition ed. 1997, Weinheim and New York: VCH Publishers.
12. M.L. Huggins, *Solutions of Long Chain Compounds.* Journal of Chemical Physics, 1941. **9**: p. 440.
13. P.J. Flory, *Thermodynamics of High Polymer Solutions.* Journal of Chemical Physics, 1941. **9**: p. 660-661.
14. U. Eisele, *Introduction to Polymer Physics.* 1990, Berlin Heildelberg: Springer-Verlag.
15. J. Eastoe, *Surfactant Chemistry.* 2003, (Book arising from a series of advanced lectures given in October 2002 at the China Research Institute for Daily Chemical Industry (RIDCI) TaiYuan)
16. J. Chadwick, *Possible Existence of a Neutron.* Nature, 1932. **129**: p. 312.
17. J.S. Higgins and H.C. Benoit, *Polymers and Neutron Scattering.* Oxford series on neutron scattering in condensed matter, ed. S.W. Lovesey and E.W.J. Mitchell. 1996: Oxford University Press.

18. *Lecture given by R. K Heenan at Cardiff University, November 2004.*
19. P.C. Griffiths and S.M. King, *Small-Angle Neutron Scattering Studies of Polymer Adsorption*, in *Encyclopedia of Surface and Colloid Science*. 2002, Marcel Dekker: New York.
20. S.M. King, *Small Angle Neutron Scattering.* www.isis.rl.ac.uk/largescale/loq/documents/sans.htm, 2000.
21. V. Castelletto and I.W. Hamley, *Modelling small-angle scattering data from micelles* Current Opinion in Colloid & Interface Science 2002. **7**(3-4): p. 167-172.
22. R.R. Edwards, *Isotopic Tracers in Chemical Systems.* Annual Review of Nuclear Science, 1952. **1**: p. 301-342.
23. E.O. Stejskal and J.E. Tanner, *Spin Diffusion Measurements: Spin Echoes in the Presence of a Time-Dependent Field Gradient.* Journal of Chemical Physics 1965. **42**(1): p. 288-292.
24. E.L. Hahn, *Nuclear induction due to free Larmor precession.* Physical Reviews, 1950. **77**: p. 297-298.
25. H.Y. Carr and E.M. Purcell, *Effects of diffusion on free precession in nuclear magnetic resonance experiments.* Physical Reviews, 1954. **94**: p. 630-638.
26. P.J. Horne, *Nuclear Magnetic Resonance*. Oxford Chemistry primers. Vol. 32. 1995, New York: Oxford University Press.
27. K.J. Parker, *Diffusion & Flow in Fluids*, in *Encyclopedia of Nuclear Magnetic Resonance*, D.M. Grant and R.K. Harris, Editors. 1996, Wiley: Chichester. p. 1615.
28. P. Stilbs, *Fourier Transform Pulsed-Gradient Spin Echo Studies of Molecular Diffusion.* Progress in Nuclear Magnetic Resonance Spectroscopy 1987. **19**(1): p. 1-45.
29. H. Weingartner and M. Holz, *NMR studies of self-diffusion in liquids.* Annual Reports on the Progress of Chemistry Section C, 2002. **98**: p. 121-155.
30. W.S. Price, F. Elwinger, C. Vigouroux, and P. Stilbs, *PGSE-WATERGATE, a new tool for NMR diffusion-based studies of ligand-macromolecule binding.* Magnetic Resonance in Chemistry, 2002. **40**: p. 391-395.
31. Y. Cadoret, D. Monceau, M.-P.Bacos, P. Josso, V. Maurice, and P. Marcus, *Effect of platinum on the growth rate of the oxide scale formed on cast nickel aluminide intermetallic alloys.* Oxydation of Metals, 2005. **64**(3/4): p. 185-205.
32. M.E. Brown, *Introduction to Thermal Analysis - Techniques and Applications*. 1988, London: Chapman and Hall

# Chapter 3 Materials and Methods

This thesis is articulated around three main studies, each involving different materials and sometimes experimental approaches. For clarity, all materials and methods used in these studies have been collected in Chapter 3 herein, in appropriate sections.

## 3.1 Fluorinated liquids

2H,3H-perfluoropentane (HPFP), perfluoropentane (PFP), and 1H,1H-heptafluorobutanol (HFB) were purchased from Apollo Scientific; perfluorodecalin (PFD) was purchased from Fluorochem. HPFP was washed first with acidic and then basic alumina (Aldrich), filtered (Whatman filter paper, Cat No 1001 125), and stored over molecular sieves; PFP and PFD were dried and stored over molecular sieves and HFB was used as received.

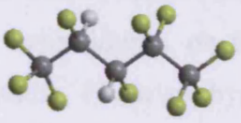

2H, 3H-perfluoropentane (HPFP)

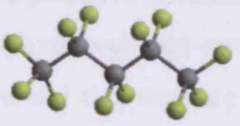

perfluoropentane (PFP)

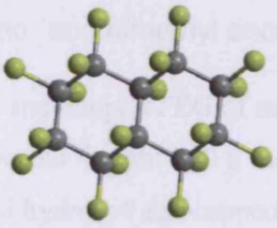

perfluorodecalin (PFD)

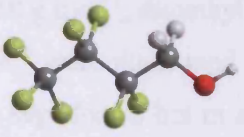

1H, 1H-heptafluorobutanol (HFB)

**Figure 3-1 Structure of the fluorinated solvents used.**

Some selected properties (suppliers'data) of the fluorinated solvents are listed in Table 3-1.

| | Density / g.cm$^{-3}$ | Boiling Point / °C | Purity / % |
|---|---|---|---|
| HPFP | 1.58 | 53.6 | 98 |
| PFP | 1.664 | 29 | 97 |
| HFB | 1.6 | 95-97 | 98 |
| PFD | 1.908 | 142 | 97 |

**Table 3-1 Density, boiling point and purity of the fluorinated solvents used (suppliers' data).**

HPFP has 2 chiral centres which are the carbons bearing the hydrogen atoms. Supplier's information indicates it is a mixture of the different stereoisomers. PFD, presented in the trans conformation in Figure 3-1 is in fact a mixture of the cis and trans conformations. cis-PFD and trans-PFD are also commercially available separately.

## 3.2 EO-polymers and derivatives (Chapter 4 & Chapter 5)

### 3.2.1 Materials

#### 3.2.1.1 Dihydroxyl end-capped Poly (ethylene glycol) (PEG)

Dihydroxyl end-capped PEGs of molecular weight 100 g $mol^{-1}$, 200 g $mol^{-1}$, 300 g $mol^{-1}$, 400 g $mol^{-1}$, 600 g $mol^{-1}$, 1000 g $mol^{-1}$, 1,500 g $mol^{-1}$ were either purchased from Sigma-Aldrich, Fluka or were a generous gift from AstraZeneca. Unless otherwise stated, they were stored for 72 hrs in a 60 °C oven prior to sample preparation. As will be seen in the results section, the presence of minimum amounts of water has major impact on the behaviour of dihydroxyl end-capped PEGs in fluorinated liquids. PEGs are hygroscopic in nature and this measure was taken in order to ensure minimum moisture was present.

#### 3.2.1.2 Mono- and dimethyl end-capped Poly (ethylene glycol)

Monomethyl end-capped PEG of molecular weight 350 g $mol^{-1}$, dimethyl end-capped PEG of molecular weight 250 g $mol^{-1}$ and 500 g $mol^{-1}$ were purchased from Fluka. Similarly to dihydroxyl end-capped PEGs, they were kept for 72 hrs in a 60 °C oven prior to sample preparation. They were otherwise used as received.

#### 3.2.1.3 Poly (ethylene oxide) mono dodecyl ethers

Three ethylene oxide based surfactants were employed. Tetra (ethylene glycol) monododecyl ether ($C_{12}EO_4$, Brij30™), deca (ethylene glycol) monododecyl ether ($C_{12}EO_{10}$) and poly (ethylene glycol)-23-monododecyl ether ($C_{12}EO_{23}$, Brij35™) were purchased from Sigma-Aldrich. They were kept for 72 hrs in a 60 °C oven prior to sample preparation. These poly(ethylene oxide) monododecyl ethers were chosen

so that the molecular weights of the ethylene oxide headgroups would match the previously describe PEGs.

#### 3.2.1.4 Dodecane

Dodecane was purchased from Acros Organics and stored over molecular sieves. It was chosen so as to match the poly (ethylene glycol) monododecyl ether surfactants hydrophobic tail group.

#### 3.2.1.5 Water

For experiments investigating the impact of moisture on the systems, Millipore grade water obtained from the laboratory equipment was used.

#### 3.2.1.6 Poly (propylene glycol) (PPO)

Poly (propylene glycol) of molecular weights 425 g $mol^{-1}$, 725 g $mol^{-1}$, 1,000 g $mol^{-1}$, 2,000 g $mol^{-1}$, 4,000 g $mol^{-1}$ were purchased from Sigma-Aldrich and used as received.

#### 3.2.1.7 Poloxamer

Poloxamer of molecular weight 1,100 g $mol^{-1}$ ($EO_2PO_{16}EO_2$) was purchased from Aldrich and used as received.

### 3.2.2 Methods

#### 3.2.2.1 Preparation of single solvent systems

Samples were prepared by mass in glass screw top vials sealed with polytetrafluoroethylene (PTFE) tape to prevent solvent evaporation, then wrapped into parafilm to protect against water penetration. In all cases, the solute was weighed first and the solvent successively added, this to ease sample preparation, the fluorinated liquids used here being highly volatile.

#### 3.2.2.2 Phase transition measurements

After 48 hours equilibration at room temperature, samples were immersed in a temperature-controlled water bath and the temperature gradually raised from -15 °C at a rate of 1 °C every 30 min with constant agitation until the temperature reached

60 °C. Hysterisis effects were negated by invoking much slower rates on both heating and cooling temperature ramps once an approximate phase transition temperature had been estimated. Visual phase transition temperatures were recorded.

#### 3.2.2.3 Phase composition assessment

A dry-weight method was employed to characterize the polymer concentration in each separating layer. This study was conducted on dihydroxyl end-capped PEG 200 in HPFP systems, for which several 20 wt% polymer samples were prepared. They were let to equilibrate for 24 hrs in a water bath at set temperatures of 15 °C, 20 °C, 25 °C, 30 °C, 35 °C, 40 °C and 45 °C. For each temperature, the upper and lower layers were removed separately using a plastic syringe with a flat-ended needle and transferred to pre-weighed vials. These were placed in a 60 °C oven until constant mass. Measurements were performed in triplicate at each temperature.

#### 3.2.2.4 Influence of the presence of water

Set amounts of millipore water were added to aliquots of dihydroxyl end-capped PEG 200 that had been kept in a 60 °C oven for 72 hrs prior to the samples preparation. The amounts of added water were calculated so that the final sample composition would consist of a constant polymer concentration equal to 3 wt% with added water present in quantities ranging from 0 to 3000 ppm, the remaining being HPFP. The pre-mixing of water to PEG 200 was chosen for practical purposes. At such concentrations, PEG 200 and water are fully miscible, which is not the case for water and HPFP, a system where the maximum solubility of water in HPFP is (390±40) ppm [1]. The cloud point was then visually recorded in the same fashion as previously described. The polymer concentration of 3 wt% was chosen so as to obtain the largest temperature decrease of the cloud-point in an accessible and workable temperature range, as will be seen in the result section of Chapter 4.

#### 3.2.2.5 Preparation of binary solvent system and elaboration of the ternary phase diagrams

For the ternary phase diagrams, HPFP and PFP, being fully miscible, were mixed in different ratios and added to set amounts of polymer. Samples were placed in a temperature controlled water-bath set at 20 °C and persistent turbidity witnessed visually indicated the phase separation of the system. The cloud-point temperatures

for these ternary systems were also recorded, for a constant polymer concentration of 3 wt%, in a range of HPFP/PFP ratios. The phase separation temperatures were visually assessed, as previously described.

### 3.2.2.6 Samples for SANS

SANS measurements were performed on the fixed-geometry, time-of-flight, LOQ diffractometer at the ISIS spallation source in Oxford. Neutron wavelengths between 2.2 Å and 10 Å (LOQ) were employed, spanning Q ranges of approximately 0.009 $Å^{-1}$ to 0.3 $Å^{-1}$. All samples were placed in 2mm pathlength, UV-spectrophotometer quartz cells (Hellma Ltd, UK). These were placed in a computer-controlled sample changer, an aluminium rack contained within an aluminium coated box. All readings were taken at room temperature, or at higher set temperatures. Due to the minimal scattering seen with small polymers and fluorinated molecules, exposure times of typically of 60 min were necessary. All scattering data was normalised for sample transmission and incident wavelength distribution, corrected for backgrounds using an empty cell and corrected for the efficiency of the detector using the instrument-specific software package.

### 3.2.2.7 Samples for PGSE-NMR

PGSE-NMR was used to probe the aggregation of the surfactant molecules via the measure of their diffusion coefficient as a function of concentration. Three Brij30™ surfactant solutions were prepared in HPFP, at concentrations equal to 0.3 wt%, 1 wt% and 3 wt%. Similar concentrations were prepared in deuterated methanol and these samples were used as control experiments. The diffusion coefficient ($D_s$) of the surfactant was measured for each solution at 298.3 K, and the corresponding hydrodynamic radii ($R_h$) calculated via the Stokes-Einstein relation presented below.

$$R_h = \frac{kT}{6\pi D_s \eta} \qquad \textbf{Equation 3-1}$$

where k is Boltzmann's constant, T the temperature and η the solvent viscosity. The solvent viscosity was measured using a U-tube viscosimeter and compared to literature value. Values of $R_h$ were compared for samples in d-methanol, where no

aggregation behaviour is supposed to occur, and in HPFP, the system under investigation. The instrument and sequence used for the PGSE-NMR experiments is the same as the one used for the fluorogel study and described in further details in the following section 3.4.2.5.

#### 3.2.2.8 Observation of surfactant-HPFP mixtures under crossed polarizing filters mounted on a microscope

In order to seek the presence of a liquid crystalline phase in the surfactant-HPFP mixtures, a microscope bearing two light polarizer filters placed on either side of the sample stage was used. The light polarizer filters were orientated to a 90° angle, so that no light can passes through provided no birefringent sample is placed in between the two filters. Then, a drop of surfactant was deposited between a glass plate and a coverslip, and placed on the microscope stage, thus in between the two filters. HPFP was added with a Pasteur pipette at the side of the coverslip, and via capillarity came in contact with the surfactant, the solvent front advancing and creating a gradient in concentration. The sample was examined for light polarizing properties that would demonstrate the presence of a preferred alignment or arrangement of the solute molecules in the presence of the fluorinated solvent. This experiment was compared to another experiment where the solvent used was water. All experiments were performed at room temperature.

## 3.3 Triacetyl-β-cyclodextrin (Chapter 6)

### 3.3.1 Materials

Four commercial samples of triacetyl-β-cyclodextrin (TAβCD) were purchased from three different suppliers: Aldrich (**A1**: Lot S05254-263 and **A2**: Lot S35068), Cyclolab (**C**: batch number CYL-2116) and Molekula (**M**: batch number 21619) and are referred to as TAβCD-A1, TAβCD-A2, TAβCD-C and TAβCD-M respectively. A series of triacetyl-β-cyclodextrin samples was prepared by melting then cooling amounts of TAβCD-A1, TAβCD-A2, TAβCD-C or TAβCD-M (denoted TAβCD-Melt) and by dissolving TAβCD of all origins in HPFP, then evaporating the solvent at room temperature (denoted TAβCD-HPFP).

### 3.3.2 Methods

#### 3.3.2.1 Sample preparation

All samples were prepared by weight. The desired amount of TAβCD was first weighed in a screw-top glass vial and solvent added. Teflon tape was wrapped around the neck of the vials to prevent solvent evaporation.

#### 3.3.2.2 Solubility study

The solubility of TAβCD was assessed using two different methods, simple dry-weight experiments and solution $^1$H NMR. Both methods gave identical results within statistical error bars. A solubilisation kinetics study was also conducted on TAβCD-A1, TAβCD-A2, TAβCD-C and TAβCD-M, with equilibration times ranging from 3 seconds (minimum time elapsed between making the solution and filtering it) to 30 days, in a 20 °C temperature-controlled cupboard.

##### 3.3.2.2.1 Dry weight method

For the preliminary study, a simple dry-weight method was employed to assess the solubility of the various TAβCD's in HPFP. Known amounts of TAβCD were left to equilibrate in HPFP for 24 hours, either on an end-over-end rotator or with magnetic stirrers (no differences were observed regarding the stirring method) at set temperatures. Samples were then passed through a 0.2 μm filter into pre-weighed vials. HPFP was left to evaporate (HPFP boiling point = 54 °C) until constant mass and the dry samples weighed. The concentration $C_{TA\beta CD}$ in the filtered sample was calculated as follow:

$$C_{TA\beta CD}(wt\%) = \frac{M_{dry} - M_{empty}}{M_{full} - M_{empty}} * 100$$

where $M_{empty}$ is the mass of the empty vial, $M_{full}$ the mass of the vial containing the filtered liquid and $M_{dry}$ the mass of the vial after heating to constant weight. Each sample was measured in triplicate at least.

### 3.3.2.2.2 $^1$H NMR method

As a complementary approach, quantification of the solution concentration was also determined by solution $^1$H NMR. This technique was found to be much more time efficient, and was chosen for the solubilisation kinetics experiments. In the first instance, samples were made according to the procedure described above. After a chosen equilibration period, the samples were filtered using 0.2 µm Whatman disposable filters mounted at the tip of a plastic syringe. An aliquot of the filtered solution was promptly added in an NMR tube containing $CDCl_3$, and the spectrum recorded. The ratio of the height of characteristic peaks belonging to TAβCD and HPFP was then calculated, and converted to a concentration in wt% using a calibration curve, determined according to the procedure described below.

Choice of the characteristic peaks and ratio of their heights

Figure 3-2 shows the characteristic solution $^1$H NMR spectra of TAβCD/$CDCl_3$, and of TAβCD/ HPFP/ $CDCl_3$.

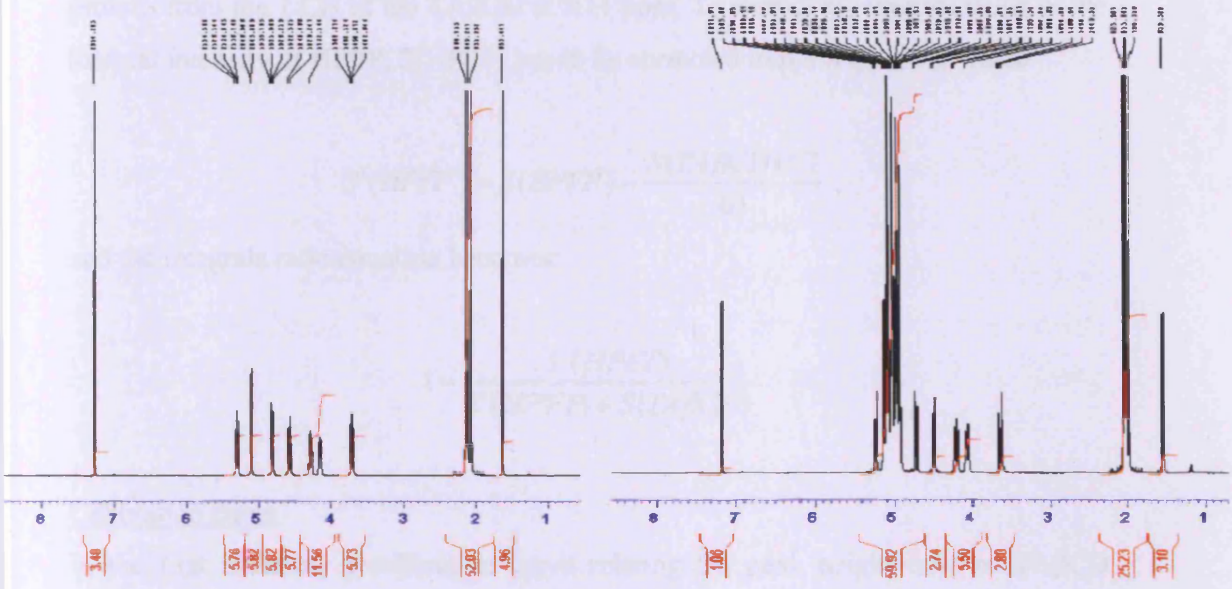


**Figure 3-2 $^1$H NMR spectra of TAβCD$_C$ (left) and a solution of TAβCD$_C$ in HPFP (right).**

For TAβCD, seven groups of peaks of equal integrals are observed at $\delta_H$ of 5.31, 5.11, 4.82, 4.58, 4.29, 4.16, and 3.73 ppm corresponding to the seven protons. The acetyl proton signal is found at $\delta_H$ of 2.12 ppm and its intensity is the strongest as it accounts for 63 protons (three protons on each of the three acetyl groups, present on the seven units of the cyclic compound). For HPFP, a multiplet is observed at $\delta_H$ 5.13 ppm (2 H, m, 2 x CH).

To characterise TAβCD, it was decided to use the integral of the strongest signal, at 2.12 ppm. The ratio of HPFP to TAβCD signals was therefore defined as:

$$1-\frac{S(HPFP)}{S(HPFP)+S(TA\beta CD)},$$

where S(HPFP) is the integral value at 5.13 ppm and S(TAβCD) the integral value at 2.12 ppm.

However, as seen in Figure 3-2, HPFP is masking the 5.11 ppm signal from TAβCD. The integral value for HPFP therefore contains an additional term coming from the 7 protons from the 7 CH of the TAβCD at 5.11 ppm. To extract the original value of the integral intensity of HPFP, S(HPFP) has to be corrected into a S'(HPFP), where

$$S'(HPFP)=S(HPFP)-\frac{S(TA\beta CD)*7}{63},$$

and the integrals ratio equation becomes:

$$1-\frac{S'(HPFP)}{S'(HPFP)+S(TA\beta CD)}$$

Calibration curve

In the first instance, a calibration curve relating the peak height ratio to TAβCD concentration was measured. This was done using the highly soluble TAβCD-C. Samples with known concentrations ranging from 0.5 wt% to 13 wt% were prepared. In all cases, all TAβCD-C had fully dissolved, resulting in a clear solution. Each

sample was made in triplicate and two aliquots were taken from each sample, then all six solutions were measured once. The calibration curve obtained is shown in Figure 3-3 and the error bars represent the standard deviations obtained.

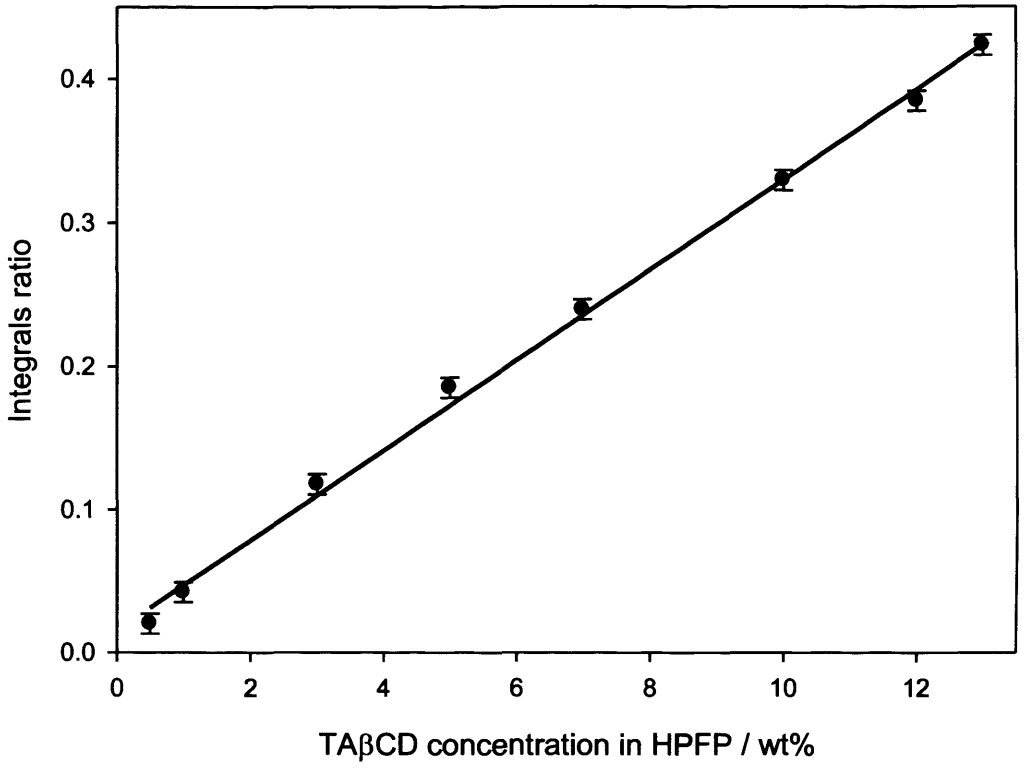


**Figure 3-3 Calibration curve for solutions of known concentrations of TAβCD in HPFP, the straight line is a linear fit to the data.**

A linear fit to the data points of equation $y = 0.031x + 0.016$ was calculated, with a correlation coefficient $R^2$ equal to 0.9972. This calibration was then used for the kinetics experiment in order to work back to the concentration of TAβCD-A1, TAβCD-A2, TAβCD-C and TAβCD-M as a function of time. Again, each sample was made in triplicate and two aliquots were taken from each sample, then all six solutions were measured once.

### 3.3.2.3 Solution-state NMR spectroscopy

Solution state NMR experiments were performed on a Bruker 400MHz spectrometer at 300 K in $CDCl_3$. $^1H$ spectra were acquired with 16 scans and a spectral width of 6.4 kHz. $^{13}C$ Spectra were acquired with 256 scans and a spectral width of 17 kHz.

### 3.3.2.4 Melting point measurements

The melting point of the various materials was firstly evaluated using a Reichert melting point apparatus, pictured in Figure 3-4.

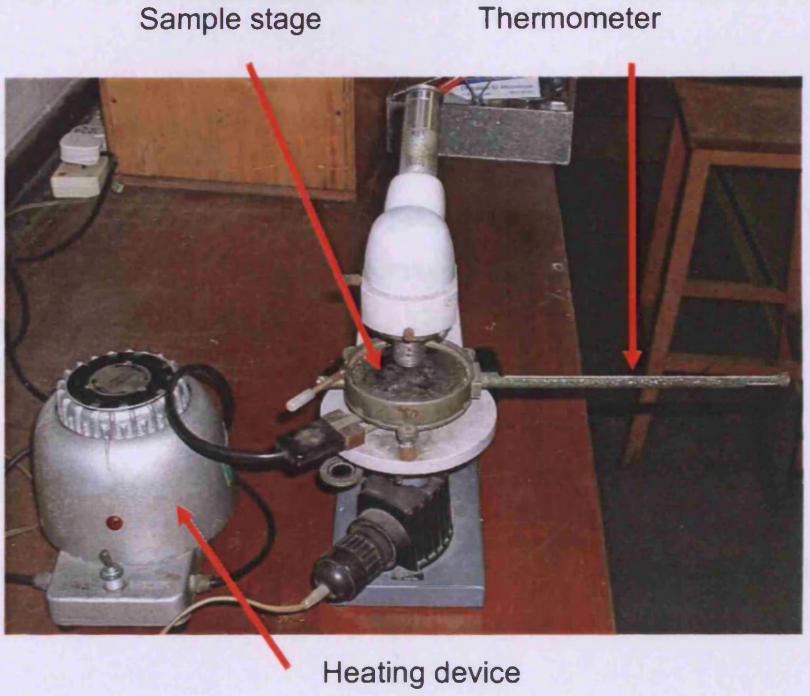


**Figure 3-4 Reichert melting point apparatus.**

TAβCD was placed between two glass cover slips, on the heating stage. Three measurements were taken for each sample.

Melting temperatures were further assessed via differential scanning calorimetry and optical microscopy.

### 3.3.2.5 Differential scanning calorimetry

DSC experiments were performed on a Q100 from TA Instruments. Unless otherwise stated, all temperature ramps were performed at 10 °C $min^{-1}$. A typical run consisted of three steps: a decrease in temperature from 25 °C to –50 °C, followed by an increase in temperature to 250 °C and a cooling ramp back to 35 °C (rate 30 °C $min^{-1}$). Two-cycle runs were also performed in which the temperature was taken twice from 25 °C to 250 °C and back to the initial value at a constant rate of 10 °C $min^{-1}$. For the experiments observing the conversion of form β to form α, the temperature was increased from ambient to 150 °C, where it was maintained for two hours, then

increased to the temperature of 250 °C before cooling back to room temperature. For experiments observing the recrystallization of the melt into form α, the temperature was decreased from 25 °C to –50 °C, then increased and held for one hour at 210 °C. Each melting point was taken at the onset temperature of the endothermic peak.

### 3.3.2.6 Thermogravimetric analysis

Thermogravimetric measurements were performed on a Mettler Toledo TGA/STD A851e on 4 - 6 mg samples. The temperature range investigated was 25 - 250 °C, with a ramp at a rate of 10 °C $min^{-1}$. These measurements were carried out at AstraZeneca Laboratories, on their Macclesfield site, UK.

### 3.3.2.7 Optical Microscopy

The recrystallisation of the TAβCD melt into form α was witnessed and recorded using the experimental set up shown in Figure 3-5.

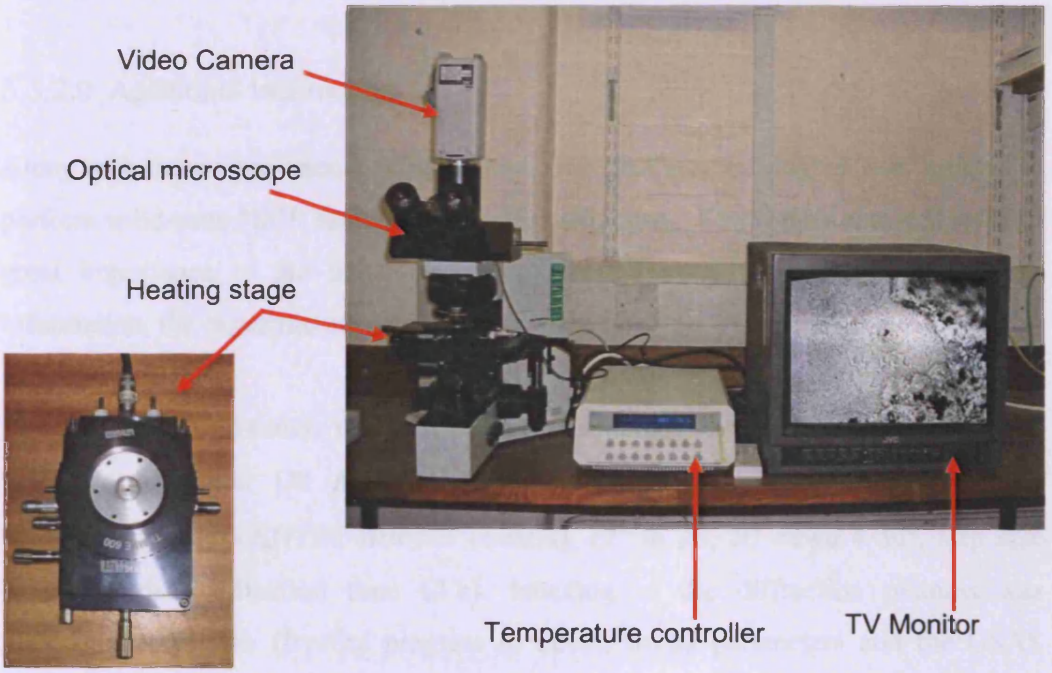


**Figure 3-5 Experimental set-up for the visualisation and recording of the recrystallisation.**

A heating stage (Linkam THMSE 600) linked to its temperature controller (Linkam TMS 93) was positioned on the Olympus BX 50 microscope stage. A colour video

camera (JVC, model TK-C1380) was mounted on the microscope, and linked to either a TV monitor or a PC. A piece of solid amorphous melt (TAβCD-Melt) was placed on the heating stage. A very small amount TAβCD-A1 was deposited on the amorphous solid. The video recording was started and the heating stage temperature was raised to 180 °C where it was held for 12 hours, after which the recording was stopped. The temperature was then raised to 250 °C at a rate of 10 °C $min^{-1}$ and the melting point of the newly formed material recorded. A similar experiment in which no TAβCD-A1 was used was also performed as a control.

#### 3.3.2.8 Scanning Electron Microscopy (SEM)

SEM was performed on a high resolution Veeco FEI XL30 ESEM (Environmental Scanning Electron Microscope) FEG (Field Emission Gun) in high vacuum mode. Small amounts of the various TAβCDs were deposited on double-sided carbon tabs sticking to aluminium stubs and were gently brushed with a soft paper to remove excess material. Samples were then covered with a thin coating made of 90% gold and 10% palladium. The magnifications investigated ranged from 65 to 100 000 and the digital images presented here were captured at magnifications of 500 and 5000.

#### 3.3.2.9 Additional techniques

Along with these experiments, collaboration with Dr Colan E. Hughes was initiated to perform solid-state NMR and X-ray powder diffraction. The results obtained were of great importance to the understanding of the presently studied system and for information, the experimental details can be found below.

Powder X-ray diffraction was carried out at ambient temperature in transmission mode on a Bruker D8 Advance diffractometer (tape mounted, Cu $K\alpha_1$ (Ge-monochromated), VANTEC detector covering 12° in 2θ, 2θ range 4-50°, step size 0.01672°, data collection time 12 h). Indexing of the diffraction patterns was performed using the Crysfire program to obtain initial parameters and the GSAS program [2] to refine the parameters by performing a Le Bail fit [3].

Solid-state NMR was carried out on a Chemagnetics Infinity Plus spectrometer with a $^{1}H$ frequency of 300 MHz. Samples were held in a 4 mm diameter rotor. All experiments were performed using cross polarization from $^{1}H$ to $^{13}C$ at an MAS frequency of 12 kHz. $^{1}H$ decoupling was applied during acquisition with a nutation frequency of 80 kHz. The duration of the FID measured was 51.2 ms with a spectral width of 20 kHz.

## 3.4 Low molecular-mass organogelators LMOGs (Chapter 7)

### 3.4.1 Materials

All materials presented in this section were a gift from Professor. D. W. Knight (Cardiff University) and used as received. Various families of tetrahydroxy diesters were studied as a function of the inner carbon chain length and the nature of the end-groups.

The isopropyl end-group series was found to form gels and such molecules were considered as Low molecular mass organogelators. Their structure is shown in Figure 3-6, and their molecular weight is presented in Table 3-2.

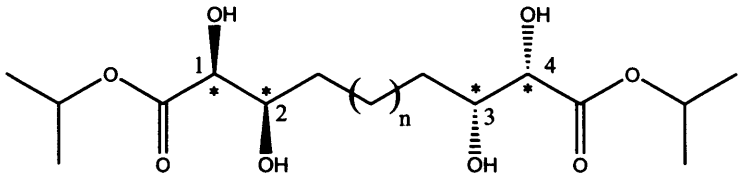


**Figure 3-6 Structure of the tetrahydroxy diester LMOGs, n=3, 4, 5, 6, 8 and 10.**

| $G_n$ | $G_3$ | $G_4$ | $G_5$ | $G_6$ | $G_8$ | $G_{10}$ |
|---|---|---|---|---|---|---|
| Mw / g mol$^{-1}$ | 364.4 | 378.4 | 392.4 | 406.5 | 434.5 | 462.5 |

**Table 3-2 Molecular weights of the isopropyl end-group gelator family, $G_3$, $G_4$, $G_5$, $G_6$, $G_8$ and $G_{10}$.**

These gelators are referred to as $G_n$, with n = 3, 4, 5, 6, 8 and 10 according to their inner carbon chain length. As seen in Figure 3-6, the gelators are chiral, bearing four

asymmetric carbons denoted 1, 2, 3 and 4. Enantiomeric purity was determined by Professor. D. W. Knight's group using gas chromatography on a Chiraldex GTA column and was found to be >99%.

A 50/50 racemic mixture of +/– gelator $G_6$ was also provided, which consisted of an equimolar mixture of the two molecules presented in Figure 3-7 . The stereochemistry for (+)$G_6$ is S, R, R, S and for (–)$G_6$ is R, S, S, R.

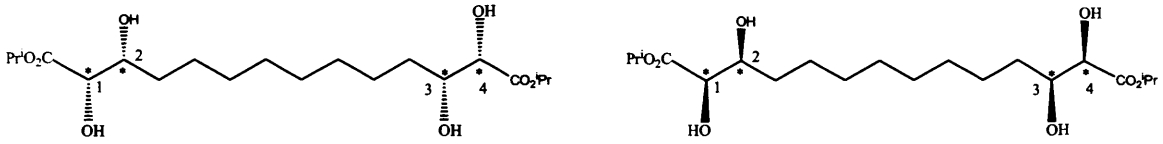


**Figure 3-7 (+)$G_6$ structure (left) and (–)$G_6$ structure (right).**

Variations around the previous gelator structure, only differing by the nature of the end-groups, were tested but were not found to form gelling structures in similar conditions to those applied to the isopropyl LMOGs series seen above. They are listed in Table 3-3.

| End group | Backbone chain length (n) |
|---|---|
| Iso butyl | n = 4, 6 |
| Tertio butyl | n = 8 |
| Iso amyl | n = 4 |

**Table 3-3 Available non-gelling molecules tested.**

## 3.4.2 Methods

### 3.4.2.1 Sample preparation and notation

The tetrahydroxy diesters are soluble in the fluorinated alcohol HFB but not in HPFP, PFP or PFD. With the isopropyl end-group gelators, gelation is induced by either first dissolving the gelator in HFB and subsequently adding the non solvent that promotes gelation, or by adding the gelator directly to the solvent blend, in a known solvent ratio. However gels prepared by adding the gelator directly to the solvent blends were found to be less reproducible. In this work, we chose to use HPFP as the non-solvent

and all gels were obtained by first dissolving the gelator in HFB and subsequently adding HPFP, at room temperature. All samples were prepared by weight. The composition is referred to as the final gelator concentration in wt%, and the solvent ratio expressed as a weight ratio. As an example, a composition referred to as 0.2 wt% $G_n$ in a 10/90 HFB/HPFP solvent ratio is composed of 0.2 wt% gelator $G_n$, 9.98wt% HFB and 89.82 wt% HPFP.

Provided a high enough gelator concentration, gelation of pure HFB can also be achieved, without the use of the non-solvent HPFP. Often gelation requires a heating-cooling cycle [4, 5], but these present fluorinated gels form spontaneously at room temperature.

### 3.4.2.2 Phase behaviour assessment

The time-scale for gel formation was found to differ according to the composition of the sample. Some would form in a matter of seconds while others would require one day or two. However, after a period of seven days no noticeable changes could be observed. The sample assessment was therefore conducted after a settling period of seven days, at room temperature. A simple measure of gelation has been used to quantify the phase behaviour of the investigated systems: the sample must be stable to tube inversion: a gel shows no flow [4].

### 3.4.2.3 Gel-to-sol transition temperature: $T_{gel\text{-}sol}$

The gels were found to be thermoreversible. Upon a temperature increase, gels would melt and become liquid. They would then recover their gel state when cooled. The gel-to-sol transition temperature ($T_{gel\text{-}sol}$) of the samples was measured using the well-established tube inversion method [6-8]. The glass vials containing the samples are immersed in a temperature-controlled water bath and the temperature at which the gel falls from the vial and becomes liquid when inverted is noted. The temperature was incremented by steps of 5, 2 or 1 °C, dependent on the phase boundary being recorded. Close to $T_{gel\text{-}sol}$, smaller increments were employed. 30 min equilibration

time was allowed at each set temperature before the assessment of the sample was made.

### 3.4.2.4 SANS

SANS measurements were performed on both the fixed-geometry, time-of-flight, LOQ diffractometer at the ISIS spallation source in Oxford, and on the steady state reactor source D11 diffractometer at ILL in Grenoble. Neutron wavelengths between 2.2 Å and 10 Å (LOQ) and 6 Å (D11) were employed, spanning Q ranges of approximately 0.009 $Å^{-1}$ to 0.3 $Å^{-1}$. All samples were placed in 2mm pathlength, UV-spectrophotometer quartz cells (Hellma Ltd, UK). These were placed in a computer-controlled sample changer, an aluminium rack contained within an aluminium coated box. All readings were either taken at room temperature, or at higher set temperatures. At higher temperatures, the temperature control was achieved via the use of a thermostated circulating waterbath through the base of the sample changer, ensuring a stability of 0.5 °C. Exposure times were typically of 60 min.

Gels were either formed in the cell, by adding the gelator, dissolving it in the fluorinated alcohol and then adding the non-solvent in the correct proportion, or prepared in a separate vial, melted, and transferred to the SANS cell when liquid, allowing then the gel to reform upon cooling. Dependant on which instrument was used, all scattering data were:

-normalised for sample transmission and incident wavelength distribution,
-corrected for background using a solvent (or mixture of solvents) filled cell, which is also used to remove the background coming from the cell itself, and inherent instrumental background arising from vacuum windows,
- corrected for the efficiency of the detector using the instrument-specific software package.

In order to obtain a first estimation of the size and shape of the particles, a Guinier approached was applied to our data. The Guinier approximation links the scattering

obtained at low Q to a characteristic dimension of the scatterers. It is valid for non interacting particles over a restricted Q range, and can be expressed as:

$$I(Q) \propto Q^{-D} \exp\left(-\frac{Q^2 R^2}{K}\right) \qquad \textbf{Equation 3-2}$$

The exponent D is equal to 1 for cylinders, 0 for spheres and 2 for discs, and K is equal to 4, 5 and 12 for cylinders, spheres and discs respectively. R represents the characteristic dimension of the particles, which are the cross-sectional radius in the case of cylinders, the radius for spheres and the thickness for discs. Using a simple fitting routine with the Sigmaplot software, where the library of fitting functions can be manually implemented, the agreement between the fit and the data was compared for the three particles shapes and the characteristic dimension of the particle extracted. The Guinier approximation for a cylindrical shape was found to result in the best agreements. A more elaborate model based on a worm-like assembly of cylindrical shapes was then chosen. The fittings were realised with the FISH program [9], using a Gaussian coil for wormlike chains, named the Kholodenko worm-like chain model. Best fit values of the parameters describing the size and shape of particles present in the samples were determined via non-linear least squares iterative processes.

The worm-like chain model was derived by Kholodenko [10] from a Gaussian coil model, and is presented below. For long thin rods,

$$I(Q) \propto P_{Worm}(Q) * P_{Axial}(Q) \qquad \textbf{Equation 3-3}$$

$$P_{Worm}(Q) = \frac{2}{3n}\int_0^{3n}\left(1-\frac{y}{3n}\right)f(y)dy \qquad \textbf{Equation 3-4}$$

For $Q \le \frac{3}{l}$, $f(y) = \frac{\sinh(Ey)}{E\sinh(y)}$ with $E = \left[1-\left(\frac{Ql}{3}\right)^2\right]^{1/2}$

For $Q > \frac{3}{l}$, $f(y) = \frac{\sin(Fy)}{F\sinh(y)}$ with $F = \left[\left(\frac{Ql}{3}\right)^2 - 1\right]^{1/2}$

with $n$ the number of chain elements, $l$ the statistical chain element length (giving the total chain length L=$nl$)

Within this model, LTYP=71 was chosen, in which $P_{Axial}(Q)$ has a radial Guinier form, such as:

$$P_{Axial}(Q) = N(\rho_1 - \rho_3)^2 (AL)^2 \exp\left(-\frac{1}{2}Q^2 R_{Ax}^2\right) \qquad \textbf{Equation 3-5}$$

with $\rho_1$ and $\rho_3$ the scattering length densities for the worm and solvent, $N$ worms per unit volume, A the cross sectional area and $R_{Ax}$ the cross sectional radius of the chain, assuming a Gaussian scattering density.

### 3.4.2.5 PGSE-NMR

PGSE-NMR experiments were performed on a Bruker AMX360 spectrometer, using a stimulated echo sequence in conjunction with current-regulated field gradient drivers and ramped gradient pulses. Three field gradient pre-pulses were applied before every scan. Experiments were performed at set temperatures, ranging from 296.3 K to 323.3 K. The temperature stability was maintained to 0.5 °C. However, heating was achieved by passing an air flux generated from the bottom of the sample, which could result in an inhomogeneous temperature throughout the sample. This is a feature difficult to circumvent that can result in the generation of convection movements, on top of the Brownian motion that is under investigation. The well-established procedure for extracting the self-diffusion coefficient ($D_s$) quantifying the isotropic Brownian motion of a species in a complex NMR dataset is to isolate a peak assignable in an unambiguous manner to one of the components, extract the peak height or integral and fit the signal decay to Equation 3-6 below [11, 12]. The signal decay is noted $A(\delta)$, $\delta$ is the field gradient pulse duration, G is its intensity, $\sigma$ the ramp time and $\Delta$ the diffusion time.

$$A_{(G,\delta)} = A_0 \exp-(kD_s)^{\beta} \qquad \textbf{Equation 3-6}$$

where $k = -\gamma^2 G^2 \left( \frac{30\Delta(\delta+\sigma)^2 - (10\delta^3 + 30\sigma\delta^2 + 35\sigma^2\delta + 14\sigma^3)}{30} \right)$, $\gamma$ is the gyromagnetic ratio of the nucleus under investigation, in our case a proton, the $A_0$ term is related to the total number of protons in the sample and $\beta$ is an empirical parameter relating to the polydispersity. In the present case heterogeneity in diffusion

behaviour was not an issue and β was kept to 1, as for a monodisperse sample. A typical dataset obtained is shown in Figure 3-8 for a sample free of convection and in Figure 3-9, with the presence of convection movements.

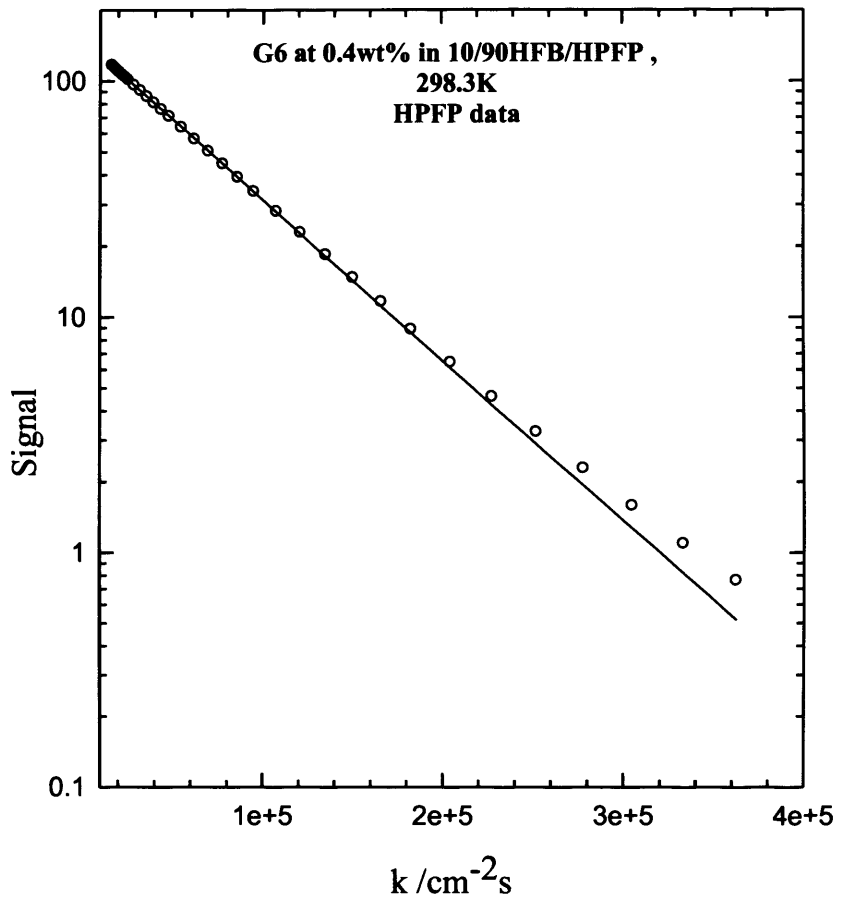


**Figure 3-8 Typical PGSE-NMR data with the exponential signal decay fit, no convection present.**

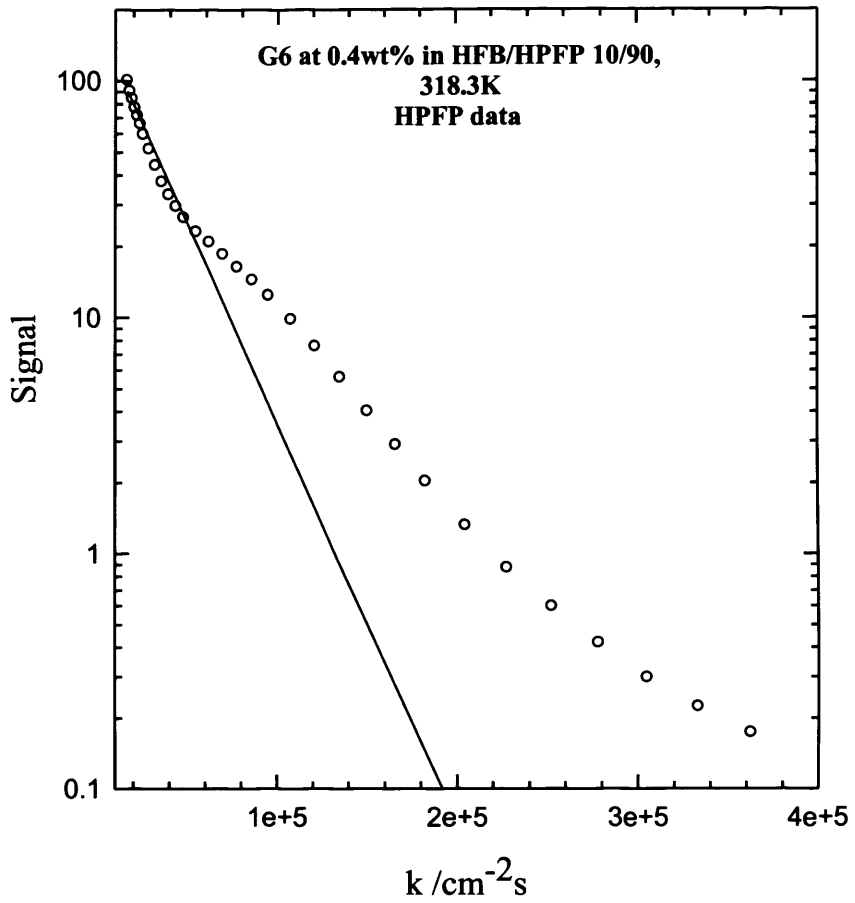


**Figure 3-9 Typical PGSE-NMR data with the exponential signal decay fit, convection present.**

Samples were either made directly in the NMR tubes, or prepared in separate vials and then pipetted to the NMR tubes when liquid. In order to lock the magnetic field with a deuterium signal, a filament containing $D_2O$ was prepared and inserted in the NMR tube, before the gelation process had been induced. Samples were then sealed with Teflon tape in order to avoid evaporation of the highly volatile fluorinated solvents. When the set temperature was different from room temperature, a 60 min equilibration time was allowed to the sample in the NMR spectrometer before starting an experiment. An experimental error of 5 % is considered for all data, representing the sample to sample reproducibility achieved, as determined by P. C. Griffiths on previous measurements when setting up the equipment.

### 3.4.2.6 Scanning Electron Microscopy (SEM)

SEM was performed on a high resolution Veeco FEI XL30 ESEM in high vacuum mode. Small amounts of gelator $G_8$ raw powder was deposited on double-sided carbon tabs sticking to aluminium stubs. A gel of composition 1 wt% $G_8$ in 10/90

HFB/HPFP was prepared according to the previously described procedure, and a fraction of it was deposited on the carbon coated aluminium stub. It was left at ambient air overnight until all solvent had evaporated. Samples were then covered with a thin coating made of 90% gold and 10% palladium. The magnifications investigated ranged from 74 to 120000 and the digital images presented here were captured at magnifications ranging between 500 and 80000.

**References**


1. P.G.A. Rogueda, *HPFP, a Model Propellant for pMDI's.* Drug Development and Industrial Pharmacy, 2003. **29**(1): p. 39-49.
2. A.C. Larson and R.B. Von Dreele, *General Structure Analysis System (GSAS).* Los Alamos National Laboratory Report, 2004: p. LAUR 86-748.
3. A. Le Bail, H. Duroy, and J.L. Fourquet, *Ab Initio Structure Determination of Lisbwo6 by X-Ray-Powder Diffraction.* Materials Research Bulletin, 1988. **23**: p. 447-452.
4. P. Terech and R.G. Weiss, *Low Molecular Mass Gelators of Organic Liquids and the Properties of Their Gels.* Chemical Reviews, 1997. **97**: p. 3133-3159.
5. D.J. Abdallah and R.G. Weiss, *n-Alkanes Gel n-Alkanes (And Many Other Organic Liquids).* Langmuir, 2000. **16**: p. 352-355.
6. J.E. Eldridge and H.D. Ferry, *Studies of the cross-linking process in gelatin gels. III. Dependance of the melting point on concentration and molecular weight.* Journal of Physical Chemistry, 1954. **58**: p. 992-995.
7. P. Terech, G. Clavier, H. Bouas-Laurent, J.-P. Desvergne, B. Deme, and J.-L. Pozzo, *Structural variations in a family of orthodialkoxyarenes organogelators.* Journal of Colloid and Interface Science, 2006. **302**(2): p. 633-645.
8. M. George, S.L. Snyder, P. Terech, and R.G. Weiss, *Gelation of Perfluorinated Liquids by N-Alkyl Perfluoroalkanamides.* Langmuir, 2005. **21**: p. 9970-9977.
9. R.K. Heenan, *RAL Report 89-129.* RAL Report 89-129, 2005.
10. A.L. Kholodenko, *Analytical Calculation of the Scattering Function for Polymers of Arbitrary Flexibility Using the Dirac Propagator.* Macromolecules, 1993. **26**: p. 4179-4183.
11. P.C. Griffiths, P. Stilbs, K. Paulsen, A.M. Howe, and A.R. Pitt, *FT-PGSE NMR Study of Mixed Micellization of an Anionic and a Sugar-Based Nonionic Surfactant.* Journal of Physical Chemistry B, 1997. **101**: p. 915-918.
12. A. Paul, P.C. Griffiths, R. James, D.J. Willock, and P.G. Rogueda, *Explaining the phase behaviour of the pharmaceutically relevant polymers poly(ethylene glycol) and poly(vinyl pyrrolidone) in semi-fluorinated liquids.* Journal of Pharmacy and Pharmacology, 2005. **57**: p. 973-980.

# Chapter 4 Ethylene Oxide oligomers in model propellant HPFP and in dual solvent systems combined with PFP or PFD

**Foreword**

As presented in Chapter 1, fluorinated liquids possess high chemical and physical stabilities, are tolerated by the human body and therefore show great promises in the biomedical fields, but require extensive formulation. The results from a preliminary polymer screening study suggested that a condition upon which polymers would be soluble in model propellant 2H, 3H-decafluoropentane (HPFP) was that they contained oxide moieties [1]. PEGs, PEO and poloxamers (copolymers made of ethylene oxide and propylene oxide blocks) are already used as excipients in aqueous pharmaceutical formulations, such as parenteral dosage forms [2, 3], ophthalmic [4], oral [5], rectal preparations [6, 7] and nasal administration [8]. Their solubility in water at physiological temperatures [9], along with their relatively low prices, make them ideal additives. However, the literature on the behaviour of ethylene oxide polymers in fluorinated liquids is still scarce. In this regard, the phase diagrams are studied for a series of ethylene oxide oligomeric additives in HPFP. The influence of the end-group nature is investigated by blocking the hydroxyl end-groups via a methyl moiety, either on one end of the polymer chain only, or on both. The effect of the hydrogen bonding capabilities of the solvents on the polymers solubility is also studied by systematically substituting HPFP for the fully fluorinated analogue perfluoropentane (PFP).

## 4.1 Introduction

Poly(ethylene glycols) (PEGs) and poly(ethylene oxides) (PEOs) are linear macromolecules of general formula HO–($CH_2$–$CH_2$–O–)$_n$–H. Both names PEG and PEO refer to the same chemical entities, but depending on their molar mass the oligomers / polymers are referred to as PEGs for the lower molecular weights, or PEO for the higher ones. The name poly (ethylene glycol) refers to the glycolic nature displayed by the oligomers due to significant contributions from their hydroxyl end-groups, whereas poly (ethylene oxide) refers to a polymer that does not feel any end-

group contributions anymore. The name transition is found between 3350 and 10 000 g $mol^{-1}$ in usual chemical companies catalogues [10].

PEGs and PEOs are some of the most commonly used macromolecules in pharmaceutical and industrial applications, mostly because of their high water solubility. Their phase behaviour in water has received much interest and is found to exhibit a lower consolute solution temperature (LCST) [11-14]. The solubility of PEO in water is an anathema in itself since the next homologues polybutylene and polymethylene are insoluble in water [9, 15]. Short EO chains (having a degree of polymerisation $m \leq 48$) are completely miscible in water even at high temperatures; for slightly longer chains, a closed loop solubility gap is observed, and for $m>180$, only a LCST is observable. PEO solution properties in water critically depend on its molecular weight, and the clouding temperature decreases with an increase in the chain length [11, 12]. Various models have been proposed to account for the solubility of PEO in water and the occurrence of LCST-type phase separation [16]. In the structured water model proposed by Kjellander and Florin [12], the similarity of the distance between two nearest oxygen atoms (2.85 Å), and the distance between two closest oxygen atoms in the helical conformation of PEO (2.88 Å), suggests a good fit of the PEO molecules within the water lattice. Phase separation results due to the breakdown of the highly structured water at higher temperatures leading to the aggregation of the polymer molecules. Goldstein proposed that intermolecular hydrogen bonds between PEO and water is responsible for PEO solubility, and their destruction, modifying the solvent-solvent and solute-solvent interactions, would account for their phase separation at higher temperatures [17, 18]. Karlström *et al.* [19, 20] discussed the solubility and phase separation in terms of the large dipole moment residing on the preferred gauche conformation of PEO at lower temperatures, a contribution that is removed at higher temperatures since the non-polar isomers have higher statistical weight.

The phase behaviour of PEO polymers in solvents other than water has received less attention. However, clouding phenomena of PEO has been reported in solvents such as formamide, tert-butyl acetate [11], carbon dioxide [21-23] and some organic solvents [10, 24-26]. In this work, the focus is on the behaviour of low molecular weight poly(ethylene glycols) (PEGs) both in the model propellant HPFP and in mixtures

with perfluoropentane (PFP) or perfluorodecalin (PFD). The effect of the end-group nature on the solubility of the PEGs is investigated using mono- and di-methyl end-capped PEG derivatives.

## 4.2 Behaviour of dihydroxyl end-capped PEGs in HPFP

### 4.2.1 Effect of temperature on the phase equilibrium

On heating, originally clear monophasic samples of dihydroxyl end-capped PEG in HPFP start to scatter light strongly at well-defined temperatures and become turbid. Such samples then separate over time to give two distinctive clear layers once the equilibrium state is reached. Figure 4-1 illustrates this behaviour. The separating layers are a less dense polymer enriched upper phase and a more dense polymer-depleted lower phase ($\rho_{HPFP} = 1.58$ g cm$^3$, $\rho_{PEGs} = 1.12$ g cm$^3$).

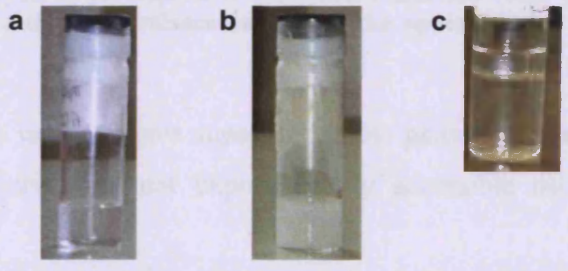


**Figure 4-1 Appearance of PEG/HPFP samples, (a) below the cloud point, (b) at the cloud point and (c) at a temperature above the cloud-point, once equilibration is reached.**

Using non-ionic polymers, this behaviour is typical of a cloud-point type system [27]. Figure 4-2 presents the temperature-concentration profile of dihydroxyl end-capped PEG 200 in HPFP, determined both by visual assessment and by polymer concentration quantification. Indeed, at equilibrium, the upper and lower phases may be separated and the polymer concentration quantified by mass after evaporation of the solvent. By projecting these concentrations onto the solute concentration axis, the solubility phase diagram may be constructed. This system is found to demonstrate lower consolute solution temperature (LCST) type behaviour, the critical LCST being the temperature at the minimum of the phase boundary curve. Immiscibility occurs when the temperature of the polymer solution is raised above the LCST curve [27].

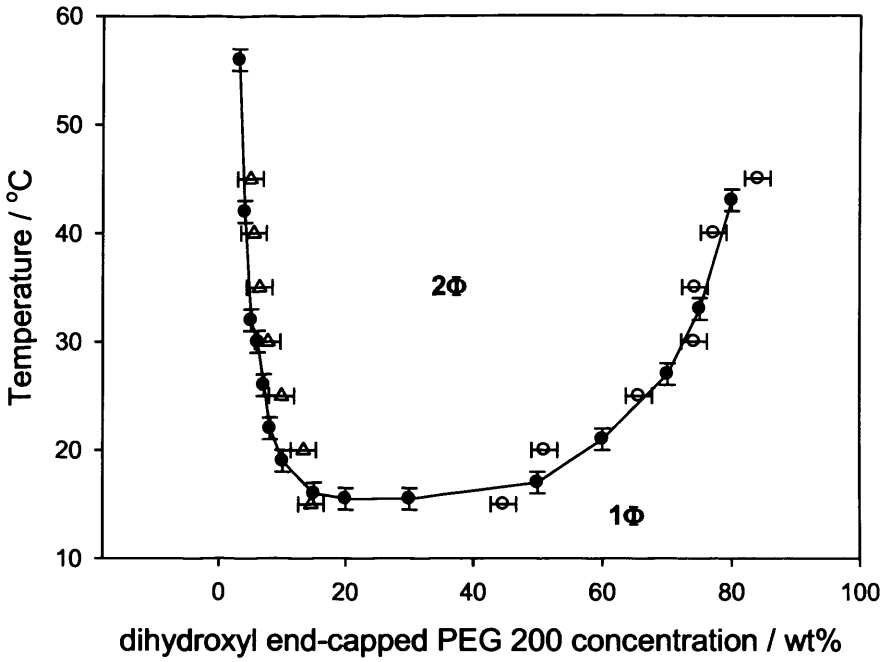


**Figure 4-2 Temperature-polymer concentration phase diagram of dihydroxyl end-capped PEG 200 in HPFP; filled symbols correspond to the visually assessed cloud point whilst the open symbols correspond to the mass balance analysis of the upper (circles) and lower (triangle) phases.**

As is clear, the two methods give super-imposable phase boundaries. However, the minimum of the curve was not experimentally accessible using the dry-weight method.

### 4.2.2 Effect of moisture on phase equilibrium

The phase behaviour of PEG in HPFP was found to be very sensitive to moisture. The cloud-point was measured for systems comprising a constant 3 wt% dihydroxyl end-capped PEG 200 concentration in HPFP and various amounts of added water, ranging from 0 to 3,000 ppm. Table 4-1 presents the results obtained.

| Added water / ppm | Clouding temperature / °C |
|---|---|
| 0 | 47 ± 1 |
| 125 | 47 ± 1 |
| 250 | 46 ± 1 |
| 500 | 44 ± 1 |
| 1000 | 34 ± 1 |
| 2000 | 12 ± 1 |
| 3000 | 0 ± 1 |

**Table 4-1 Clouding temperatures for samples composed of 3 wt% dihydroxyl end-capped PEG 200 in HPFP with added water contents ranging from 0 to 3000 ppm.**

A polymer concentration of 3 wt% was chosen so as to have the largest scope of measurable cloud-point temperatures. As seen in Table 4-1, minimum amounts of water have a significant impact on the clouding temperature, driving it down. A cloud-point temperature decrease of nearly 50 °C was observed when 3,000 ppm water was present, underlining the necessity of keeping the polymers as dry as possible. As described in *Chapter 3 - Materials and Methods*, all polymers were stored in a 60 °C oven for 72 hrs prior to usage. The cloud-point temperatures were however measured in parallel for both dihydroxyl end-capped PEG 200 used as received and dihydroxyl end-capped PEG 200 stored in a 60 °C oven for 72 hrs prior to usage, over the entire concentration range and no difference in the cloud-point were observed within experimental error. This does not mean that the polymer samples are free of water, but that the difference in the water content, if present, is very small (250 ppm or below). It should be remembered that for an industrial application, drying a large volume of polymers can only realistically be achieved via gentle or moderate heating.

### 4.2.3 Effect of Molecular weight on the phase equilibrium

Phase boundaries were visually investigated for various molecular weights of dihydroxyl end-capped poly(ethylene glycols), ranging from 100 g $mol^{-1}$ to 1,500 g $mol^{-1}$ and the results are presented in Figure 4-3 and Figure 4-4.

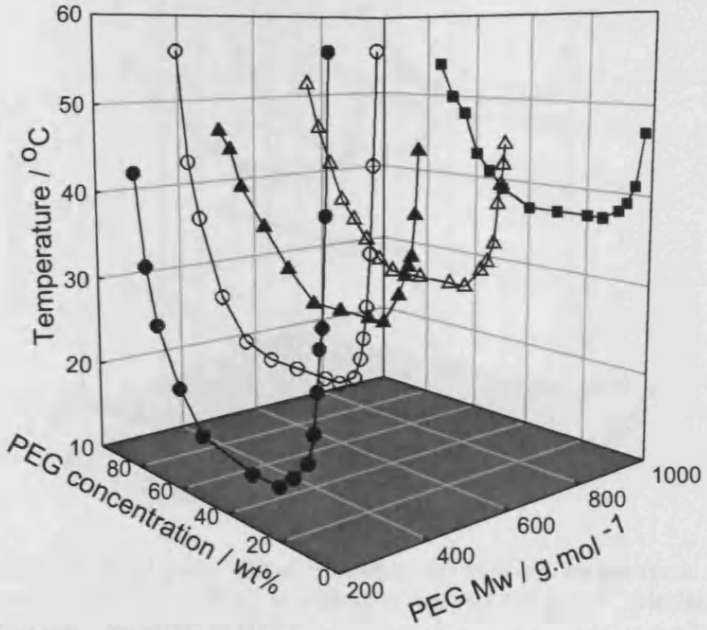


**Figure 4-3 Temperature-polymer concentration phase diagram of dihydroxyl end-capped PEGs of molecular weights 200 g mol$^{-1}$ (filled circles), 300 g mol$^{-1}$ (open circles), 400 g mol$^{-1}$ (filled triangles), 600 g mol$^{-1}$ (open triangles) and 1000 g mol$^{-1}$ (filled squares) in HPFP.**

As seen in Figure 4-3, LCST-type phase boundaries were observed for hydroxyl end-capped PEGs of 100 < molecular weight < 1,500 g mol$^{-1}$. The cloud-point temperature was strongly concentration and molecular weight dependant for all molecular weights, displaying a sharp increase towards both very low and very high polymer concentrations. As shown on Figure 4-4, PEGs with molecular weights 400, 600 and 1,000 g mol$^{-1}$ were also found to exhibit a two-phase region at lower temperatures, coinciding with their melting behaviour. At low temperatures, such systems were biphasic consisting of a coexisting waxy solid and liquid. As the temperature increases through the melting point of the polymer (5-8 °C for Mw 400 g mol$^{-1}$, 17-22 °C for Mw 600 g mol$^{-1}$ and 35-40 °C for Mw 1,000 g mol$^{-1}$) samples first become monophasic before reaching the higher cloud-point boundary presented in Figure 4-3.

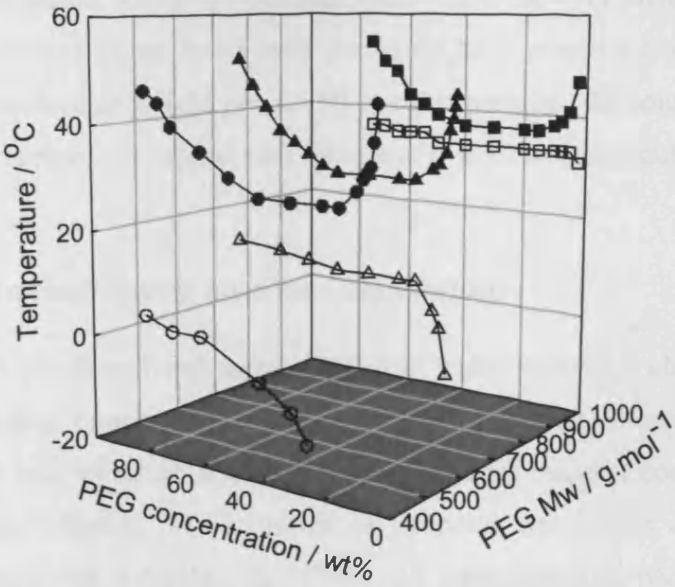


**Figure 4-4 Superimposed cloud point (filled symbols) and melting temperature curves (open symbols) for dihydroxyl end-capped PEGs of molecular weights 400 g mol$^{-1}$ (circles), 600 g mol$^{-1}$ (triangles) and 1000 g mol$^{-1}$ (squares) in HPFP.**

An increase in molecular weight drove the LCST higher, the critical temperature being 15 °C, 25 °C, 30 °C, 32 °C and 37 °C for molecular weights of 200, 300, 400, 600 and 1,000 g mol$^{-1}$ respectively, implying a greater solubility window. However, the melting curve was also strongly molecular weight dependant and as the molecular weight was increased, these two curves coincided. For dihydroxyl end-capped PEG of Mw 1,500 g mol$^{-1}$, the two behaviours collapsed and the temperature required to melt the polymer appeared higher than its cloud-point phase boundary; samples were therefore always biphasic, either solid/liquid or liquid/liquid. For the lowest dihydroxyl end-capped PEG molecular weight investigated, 100 g mol$^{-1}$, samples were always liquid/liquid biphasic and it can be theorised, based on molecular weight scaling, that a monophasic liquid state exists but its temperature range was inaccessibly too low for the experimental set-up. A sample of 10 wt% PEG 100 mol$^{-1}$ in HPFP was placed in a freezer compartment having a temperature of –20 °C and the monophasic domain could be reached. The LCST for such a sample must therefore lie between –20 °C and –15 °C, the latter being the minimum temperature achieved in the temperature controlled cooling bath, for which the refrigerant was a water / ethylene glycol mixture.

Considering the low molecular weights and narrow molecular weight range of the polymers investigated, ~2 to ~23 ethylene oxide units, the very different solubilities and widely different phase behaviours are likely be a manifestation of end-group effects rather molecular weight *per se*. To test this premise, the solubility of mono-methyl and di-methyl end-capped PEG species of comparable molecular weights were investigated.

### 4.2.4 Effect of end-group on phase equilibrium

As opposed to dihydroxyl end-capped PEG 200 which showed a cloud-point phase separation profile, monomethyl end-capped PEG 350 and dimethyl end-capped PEG 250 were fully miscible with HPFP over the entire range of concentrations and temperatures investigated. The presence of hydroxyl end-groups on the polymer therefore reduced its solubility in HPFP and methylation prevented the phase separation. Phase separation of the mono- and dimethlyl end-capped systems could only be witnessed upon addition of a fully fluorinated solvent, as is be presented in the coming sections.

## 4.3 Behaviour of PEGs in binary solvents

### 4.3.1 Addition of PFP and PFD to PEGs

Addition of the fully fluorinated solvent perfluoropentane (PFP, the fully fluorinated analogue to HPFP) to solutions of dihydroxyl end-capped PEG in HPFP resulted in a lowering of the phase separation temperature, thus reducing the solubility domain. This was also found to be the case upon addition of fully fluorinated solvent perfluorodecalin (PFD). The three fluorinated liquids are fully miscible with one another, but PEGs are insoluble in both the fully fluorinated solvents PFP and PFD, that can thus be considered as non-solvents in this system. The insolubility of PEG in PFP and PFD was verified via $^{1}$H-solution NMR. Figure 4-5 presents the cloud-point temperature as a function of the proportion of added non-solvent for dihydroxyl end-capped PEG 600 concentrations ranging from 3 to 15 wt% and for proportions of added PFD comprised between 0 and 15 wt%.

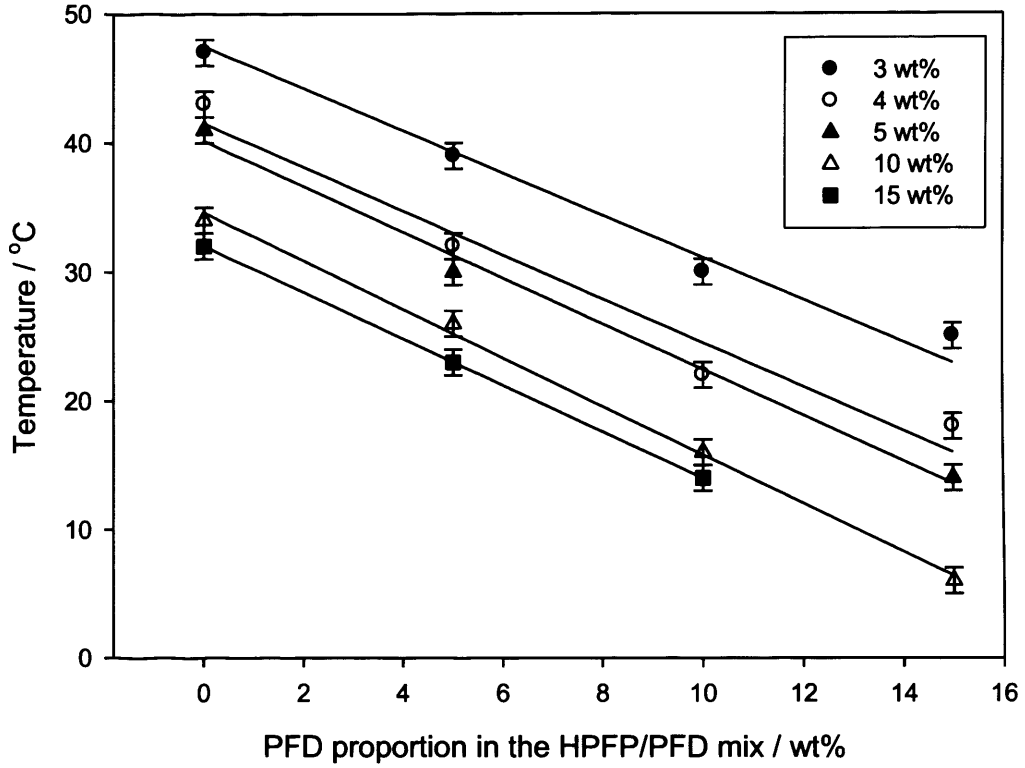


**Figure 4-5 Cloud-point temperature for various polymer concentrations of dihydroxyl end-capped PEG 600, as a function of the proportion of PFD in the HPFP/PFD fluorinated liquids mix. The full lines are linear regressions.**

As seen in Figure 4-5, the cloud-point decreases upon addition of the fully fluorinated liquid PFD. For each polymer concentration, the cloud-point temperature as a function of PFD proportion series can be fitted using a linear regression and all lie in a parallel fashion. This shows that although the polymer concentration affects the cloud-point of the system, as seen in Figure 4-3, the rate at which the cloud-point decreases upon addition of PFD is independent of the polymer concentration, at least within the concentration range studied here. An average drop of (25.5 ± 2.6) °C in the cloud-point is observed upon the addition of 15 wt% PFD in the HPFP/PFD solvent mix.

A similar study was conducted on 3 wt% dihydroxyl end-capped PEG 300, gradually replacing HPFP by PFD or PFP. The cloud-point temperatures obtained are presented in Figure 4-6.

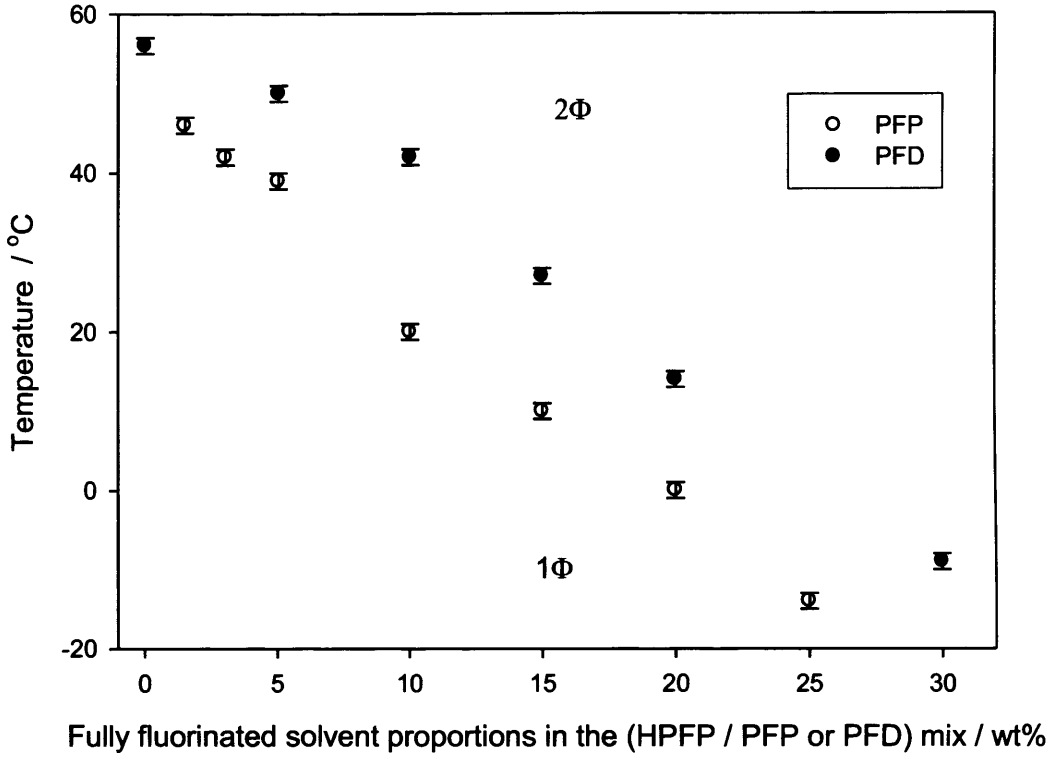


**Figure 4-6 Cloud-point temperature for various proportion of PFP and PFD in the solvent mixture, expressed as wt%, at a constant 3 wt% dihydroxyl end-capped PEG 300 concentration.**

For identical proportions of the two fully fluorinated liquids in the (HPFP/ PFP or PFD) solvent mix, the cloud-point temperature of the system is lower when using PFP rather than PFD. At this stage, it is worth remembering that HPFP and PFP only differ by the presence of two hydrogen atoms on carbons 2 and 3, PFP being the fully fluorinated analogue to HPFP. However, if the lowering in the cloud-point temperatures is due to the disruption of solvent-solute interactions, then a more meaningful way of plotting these data would be to use the molar ratios. An identical weight ratio of PFP and PFD will indeed consist of more PFP molecules than PFD ones, their respective molecular weight being 288 g $mol^{-1}$ and 462 g $mol^{-1}$. On Figure 4-7 are re-plotted the cloud-point temperatures presented previously, as a function of the mol% proportions of PFP and PFD in the fluorinated solvents mix.

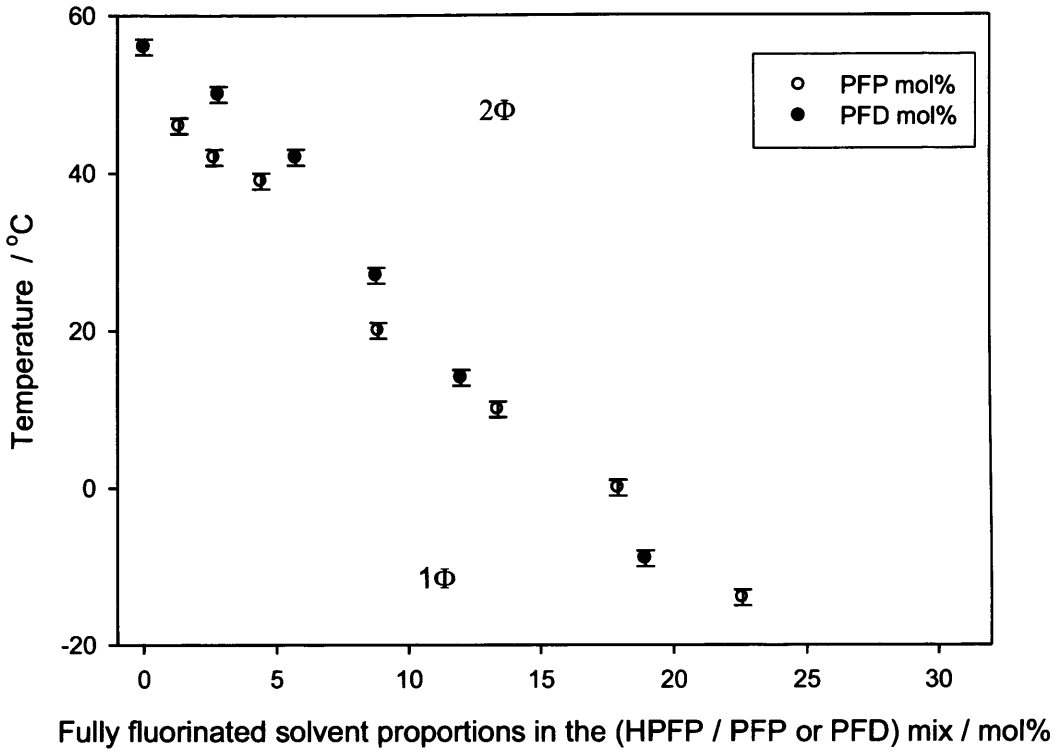


**Figure 4-7 Cloud-point temperature for various proportion of PFP and PFD in the solvent mixture, expressed as mol%, at a constant 3 wt% dihydroxyl end-capped PEG 300 concentration.**

Plotted as mol%, the two curves come much closer together and virtually fall onto the same line. This could suggest that the solubility is directly linked to the number of HPFP molecules present, and thus to the number of hydrogen atoms available on the fluorinated liquid; hydrogen atoms that could participate in the formation of hydrogen bonds between the solute and the solvent. However, all cannot be explained by the reduced hydrogen bonding possibilities upon addition of fully fluorinated solvent. Let us consider a system composed of 3 wt% dihydroxyl end-capped PEG 300 in 70/30 HPFP/PFD solvents weight ratio. Such a system has a cloud-point temperature of $(-9 \pm 1)$ °C and is consequently biphasic at room temperature. The weight composition of this system is 3 % polymer, 29.1 % PFD and 67.9 % HPFP. The effective concentration of the polymer in HPFP only can be calculated, and equals to 3/(67.9+3)*100 = 4.23 %. At such a concentration, full miscibility in HPFP is still observed. This means that even though HPFP would still act as a solvent at such a polymer concentration, the presence of the fully fluorinated liquid provokes the phase separation of the system. HPFP and PFD can therefore not be considered separately,

and contribute to forming a new solvent phase bearing intrinsic characteristics very different to each of them taken separately.

### 4.3.2 Effect of end-group in binary solvents

As seen previously, the addition of the fully fluorinated solvent PFP to solutions of dihydroxyl end-capped PEG in HPFP results in a lowering of the already present phase separation temperature. Varying the polymer end-groups and taking the cases of monomethyl and dimethyl poly(ethylene glycols) solutions in HPFP, the addition of PFP now provokes the phase separation. Figure 4-8 presents the ternary diagrams for solutions of dihydroxyl end-capped PEG 200, monomethyl end-capped PEG 350 and dimethyl end-capped PEG 250 in binary HPFP/PFP solvents whilst Figure 4-9 shows the cloud-point temperature as a function of the solvent content, at a constant polymer concentration of 3 wt%. This polymer concentration was chosen arbitrarily such that a significant change in the cloud point would be experimentally accessible.

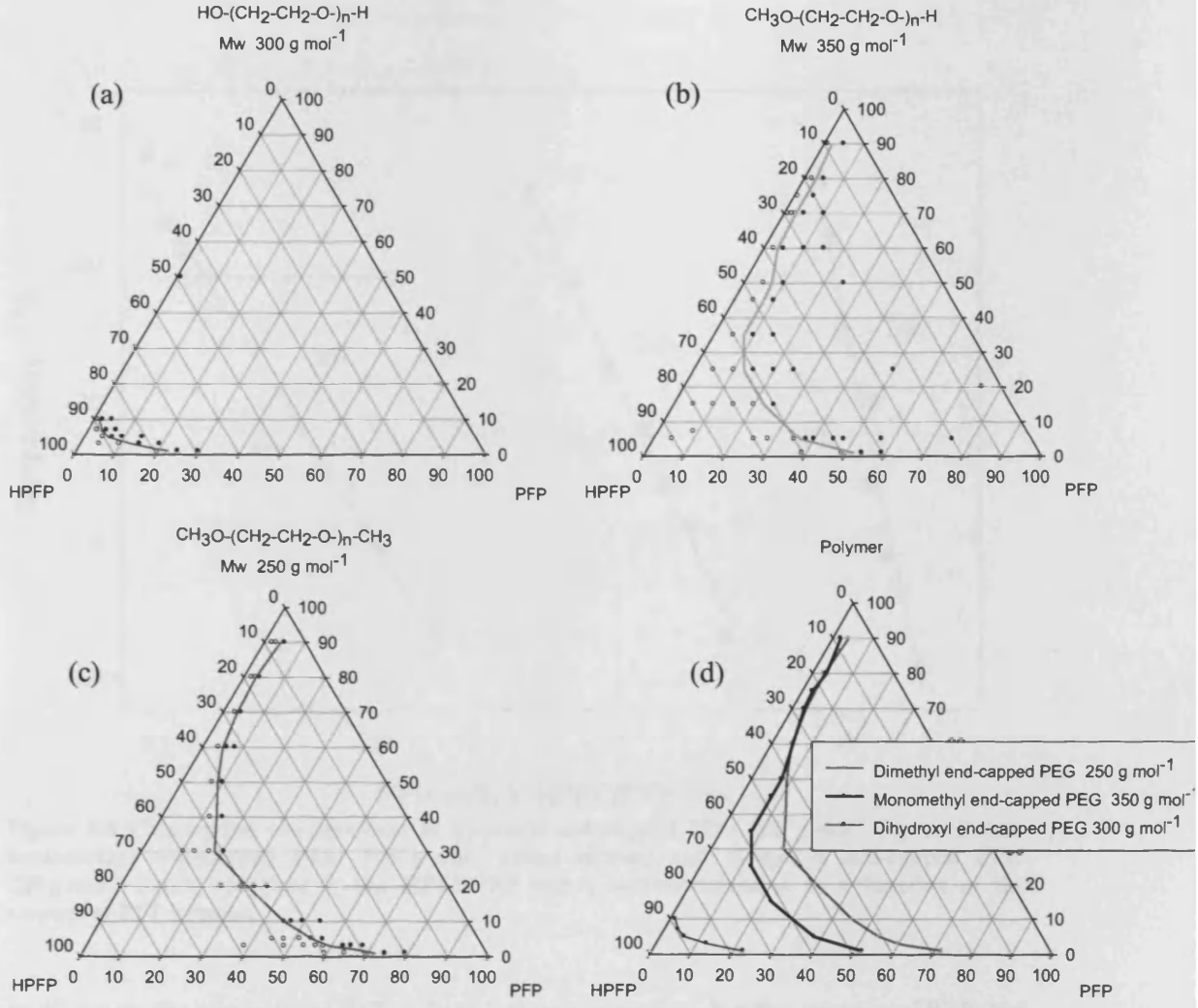


**Figure 4-8 Ternary phase diagrams recorded at 20 °C for (a) dihydroxyl end-capped PEG 300 g mol$^{-1}$, (b) monomethyl end-capped PEG 350 g mol$^{-1}$, (c) dimethyl end-capped PEG 250 g mol$^{-1}$ and (d) all three polymers on the same diagram. In (a), (b) and (c), monophasic systems are represented by open symbols and biphasic systems by filled ones.**

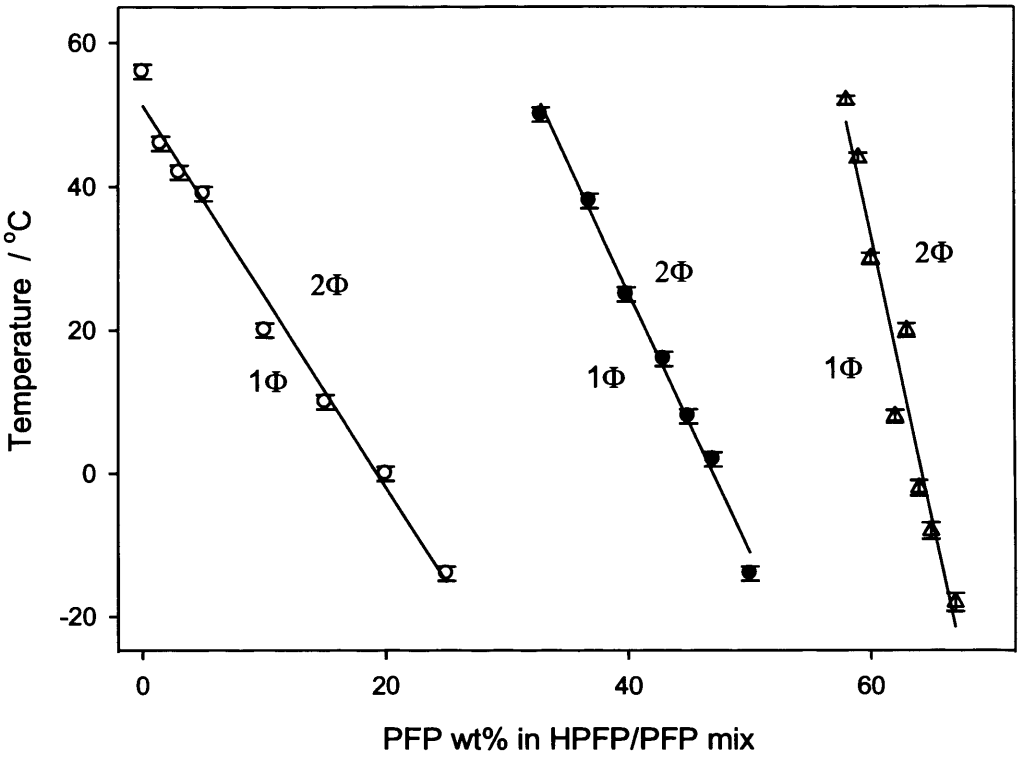


**Figure 4-9 Cloud-point temperatures of hydroxyl end-capped PEG 300 g mol$^{-1}$ (open circles), monomethyl end-capped PEG 350 g mol$^{-1}$ (filled circles) and di-methyl end-capped PEG 250 g mol$^{-1}$ (open triangles) in the HPFP/PFP binary solvent mixtures as a function of the amount of PFP present.**

In all cases, the presence of PFP induced phase separation, but the amount of PFP that the system could tolerate before separating clearly depended on the nature of the polymer end-group. For a constant polymer concentration, the order in which higher amounts of PFP can be incorporated into a polymer/HPFP system before phase separation occurs was di-methyl > mono- methyl > dihydroxy end-capped PEG. For the mono- methyl and di-methyl end-capped PEG, this effect was more prominent in the region diluted in polymer, and from 50 wt% polymer onwards, the two curves overlap. This clearly demonstrates the importance of the end-group nature on the behaviour of such small polymers. As seen previously, further fully fluorinated solvent can be incorporated while keeping a monophasic sample as the methylation of the end-group is increased. However, as seen in Figure 4-9, the slopes of the cloud point curves become steeper as the level of methylation of the end-group is increased. Although the amount of PFP that can be incorporated before phase separation

occurred increased with the end-group methylation, the PFP range within which the cloud-point drop was observed is much narrower.

The three polymers investigated here were not commercially available in an identical molecular weight and it must therefore be questioned whether the slight variation in molecular weight could be responsible for the observed PFP uptake. To differentiate end-group and molecular weight effects, the same measurements were performed using dimethyl end-capped PEG of molecular weight 500 g $mol^{-1}$, and its phase boundary was found to lie between monomethyl end-capped PEG 350 and dimethyl end-capped PEG 250. Therefore, dimethyl end-capped PEG of molecular weight 500 g $mol^{-1}$ would tolerate the presence of smaller amounts of PFP than its lower molecular weight equivalent, but still higher than the monomethyl end-capped PEG of lower molecular weight. The results observed were therefore not a molecular weight artefact but could be confidently attributed to an end-group effect.

## 4.4 Discussion

Regions of high solubility were found to exist for dihydroxyl end-capped PEG polymers with molecular weight between 200 and 1000 g $mol^{-1}$ in HPFP, albeit under limiting temperatures. Strictly speaking, given the low degrees of polymerization (~ 4 to ~ 23), these polymers should be referred to as oligomers. Polymers are generally regarded as having very limited solubility in hydrofluoroalkanes. Indeed, it was found in this study that once the molecular weight exceeded 1,000 g $mol^{-1}$, EO-polymers were insoluble in HPFP. However, in the lower extreme, the dimer of ethylene glycol was also found to be insoluble in HPFP. There was therefore a narrow molecular weight window for which these oligomers exhibit regions of high solubility. A lower critical solution temperature (LCST) was observed for these systems and phase separation occurred as the temperature was increased, with LCST increasing with molecular weight. LCST-type behaviour and closed loop phase diagrams for ethylene oxide polymers in water were reported by Saeki *et al.* [11], but for higher molecular weights than studied here, typically from 2,180 to 1,020,000 g $mol^{-1}$. The LCST was found to decrease with increasing degree of polymerization of the polymer and laid mostly at temperatures above the boiling point of water. They also observed the occurrence of both UCST and LCST in the organic solvent t-butyl acetate for

molecular weights ranging from 8,000 g $mol^{-1}$ to 21,200 g $mol^{-1}$. LCST behaviour is usually observed for systems whose mixing is exothermic, implying strong and enthalpically favoured solute-solvent interactions. Such interactions could arise from strong hydrogen bonds between the hydrogen atoms in the solvent and lone electron pairs on PEG oxygen atoms.

The LCST was found to be highly molar-mass dependant for hydroxyl end-capped PEGs in HPFP systems. Contrary to data reported in water and organic solvents, the LCST increased with increasing molecular weight, an effect that has been shown to be due to the hydroxyl end-groups, whose presence reduced the solubility. As the molecular weight is increased, the end-group effect becomes 'diluted' and therefore less important. The temperature required to destabilize the system was increased, but at the same time, the melting point was also increased, narrowing the width of the solubility temperature window. This was especially pertinent for PEG 1,500, for which the melting and cloud point curves overlap, leading to immiscibility over the entire range of concentration and temperature investigated. The presence of minimum amounts of water was found to dramatically decrease the cloud-point of the systems. Dihydroxyl end-capped PEG 200 was driven out of the HPFP solution by small quantities of water. The PEG-water interaction is stronger than the PEG-HPFP one, and once in presence of moisture, PEG tends to partition out of the fluorinated liquid to form an upper polymer-rich aqueous solution. It is not excluded that some HPFP molecules may be driven by PEG into this new phase, but most HPFP was found to remain free of polymer in the lower phase.

Evidence for the end-group effect may be seen with the mono- and dimethylation of the hydroxyl end-groups with which full miscibility was observed in HPFP, for oligomers of very similar molecular weights. The solute-solute attractions via the terminal hydroxyl groups are reduced or fully blocked, and the hydrogen bond driven solute-solvent attraction between the ether oxygen and the partially fluorinated solvent hydrogen remains, favouring the dissolution of mono- and dimethyl end capped PEGs in HPFP. The presence of oxygen in the polymer was found to be a prerequisite to achieve solubility [1] but the presence of alcohol groups at the end of the chain does not enhance this character whereas their methylation favours it. One may envisage a situation where moderate polarity along the polymer backbone

($CH_2CH_2$–O–) will promote a favourable interaction with the polar solvent –CHFCHF– yet a terminal polar group on the polymer may offer a route to a stronger inter-polymer interaction. The molecular weight dependence of solubility, and thus the end-group effect has already been reported by Spitzer *et al.* for the partition of dihydroxyl end-capped PEGs between water and organic solvents [10, 26]. A critical molecular weight above which the end-group contribution is removed occurred around 2000 g $mol^{-1}$. However, for molecular weights as low as 300 g $mol^{-1}$ – 400 g $mol^{-1}$, PEG was found to start favouring its partition into the organic phase. LCST for PEGs was also observed in super-critical $CO_2$ by Drohmann *et al.* [21] who report that PEG solubility can be increased by decreasing its molecular weight or blocking the terminal hydroxyls by non-polar headgroups. The ether oxygens were found to enhance PEO solubility when compared to simple hydrocarbons, provided the oxygen was in a readily accessible position to $CO_2$. As a general finding, carbonyl groups enhance the solubility of the polymer in $CO_2$ by favourable cross-interactions, either by quadrupole ($CO_2$)-dipole (solute) interaction or Lewis acid/base, $CO_2$ being the Lewis acid [22, 28, 29].

Mono- and dimethyl end capped PEGs were found to present a cloud-point behaviour only when the partially fluorinated fluoroalkane HPFP was gradually replaced by the fully fluorinated analogue PFP. PFP is fully miscible with HPFP, but has no solvation capability towards the ethylene oxide oligomers considered here. Indeed, the lack of any hydrogen bond donating capability of PFP was found to be crucial, so as to have sufficiently strong interactions with the EO segments. Moreover, the addition of increasing amounts of PFP resulted in a sharp decrease of the cloud point. This was also seen with another fully fluorinated solvent, PFD. Although the amount of PFP that can be incorporated before phase separation occurred increased with the end-group methylation, the range of PFP amounts within which the cloud-point drop was observed is much narrower as methlylation was increased. Such early precipitation of the polymer observed upon the addition a non co-solvent is a method already used in polymer fractionation [10, 24]. This mixed solvents study clearly shows that hydrogen bonding between the solvent and the solute, in competition with the end-group interactions, are the driving force behind PEG oligomers solubility in these fluorinated liquids of interest.

## 4.5 Conclusion

The dihydroxyl end-capped polyethylene glycols investigated in this study all behaved as typical cloud-point systems in model propellant HPFP, showing a lower critical solution temperature. Regions of very high solubility were found to exist, contrary to the "myth" that such polymeric materials are largely insoluble in partially fluorinated media. It is hypothesised that a specific, temperature dependent interaction between the ether group of the EO moiety and the –CHF group of the HPFP dominates the observed phase behaviour, along with a competing end-group effect that becomes less important as the molecular weight is increased. By suitably modifying the ethylene oxide end-groups (by blocking them via methylation) and by tuning the hydrogen bonding capabilities of the solvents (gradually replacing partially fluorinated solvent by fully fluorinated ones), some control of the phase behaviour could be achieved.

Over a wide range of temperatures and concentrations, dihydroxyl end-capped PEGs exhibited a lower critical solution temperature (LCST) that was strongly molecular weight dependent. In stark contrast, mono-methyl and di-methyl end-capped PEOs were fully miscible with HPFP over the same temperature and concentration ranges, suggesting that the phase behaviour was dominated by end-group/solvent interactions. By systematically substituting HPFP for the fully fluorinated analogue perfluoropentane (PFP), the ability of these end-groups to interact with the solvent was perturbed and LCST type behaviour was induced in the previously fully miscible mono- and di-methyl end-capped PEGs. Concomitantly, with increasing PFP content the LCST of the di-hydroxyl end-capped PEGs was driven to lower temperatures. The phase behaviour of these systems could be controlled by "tuning" the end-group structure of the ethylene oxide oligomers, and varying the hydrogen bonding capabilities of the fluorinated solvents.

## 4.6 Further work

To further continue this work, quite a few pathways can be seen worth investigating. As shown in this study, blocking the PEGs hydroxyl end-groups via methylation dramatically increased their solubility in HPFP and their tolerance towards the presence of fully fluorinated liquids. Therefore, it could be interesting to take this

reasoning a step further and study the behaviour in such solvents of crown ethers of the ethylene oxide oligomer type, which being macrocyclic oligomers, have no end-groups. Similar molecular weights as those studied for linear PEGs here would be obtained with 12-crown-4 to 27-crown-9 or larger (respectively 176 and 396 g $mol^{-1}$). Such molecules display a hydrophobic exterior, which could be useful for their solubilisation process in fluorinated liquids. However, crown ethers are labelled as irritants, and their oral and skin toxicity were found to be much greater than that of ordinary ethers [30]. Such compounds would perhaps not be chosen as suitable excipients in the case of HFA pMDIs.

Then, it would also be of interest to investigate the thermodynamic properties of such systems and in particular to characterise the phase transfer of the polymer solute from one fluorinated solvent to another, following a method described by Spitzer *et al.* and applied to binary mixtures of aqueous and organic solvents (water / dichloromethane, chloroform, chlorobenzene) [10, 26]. Access to the partition coefficients would enable the calculation of the Gibbs energy of transfer of the solute. Performing solution calorimetry would also allow the measurement of solution enthalpies and enthalpy changes associated with the phase transfer. In this regard, work by M. Spitzer and W. Loh are a constant source of inspiration.

**References**


1. R. James, *Solubility of polymers in fluorinated liquids*, in *MSc Thesis*. 2006, Cardiff University.
2. C.-S. Yong, B.-J. Park, D.-H. Kim, B.-K. Yoo, J.S. Woo, K. Bhamdari, Y. Jahng, H.-G. Choi, and M.H. Lee, *In Vivo Evaluation of Microemulsion System for Oral and Parenteral Delivery of Rutaecarpine to Rats.* Drug Development and Industrial Pharmacy, 2007. **33**(5): p. 531-534.
3. J.D.J.d. Vries, M.J.A.d. Graaff-Teulen, R.E.C. Henrar, J.J.K.v.d. Bosch, A. Bult, and J.H. Beijnen, *Pharmaceutical development of a parenteral formulation of the novel anti-tumor agent carzelesin (U-80, 244).* Investigational New Drugs, 1994. **12**(4): p. 303-314.
4. E. Vega, M.A. Egea, O. Valls, M. Espina, and M.L. Garcia, *Flurbiprofen Loaded Biodegradable Nanoparticles for Ophtalmic Administration.* Journal of Pharmaceutical Sciences, 2006. **95**(11): p. 2393-2405.
5. J. Shokri, J. Hanaee, M. Barzegar-Jalali, R. Changizi, M. Rahbar, and A. Nokhodchi, *Improvement of the dissolution rate of indomethacin by a cogrinding technique using polyethylene glycols of various molecular weights.* Journal of Drug Delivery Science and Technology, 2006. **16**(3): p. 203-209.

6. M. Miyake, N. Kamada, Y. Oka, T. Mukai, T. Minami, H. Toguchi, M. Odomi, K.-I. Ogawara, K. Higaki, and T. Kimura, *Development of suppository formulation safely improving rectal adsorption of rebamipide, a poorly adsorbable drug, by utilizing sodium laurate and taurine.* Journal of Control Release, 2004. **99**: p. 63-71.
7. E.I. Taha, A.-A.A. Zaghloul, A.A. Kassem, and M.A. Khan, *Salbutamol Sulfate Suppositories: Influence of Formulation on Physical Parameters and Stability.* Pharmaceutical Development and Technology, 2003. **8**(1): p. 21-30.
8. E. Bechgaard, K. Lindhardt, and L. Martinsen, *Intranasal absorption of melatonin in vivo bioavailability study.* International Journal of Pharmaceutics, 1999. **182**: p. 1-5.
9. H.S. Ashbaugh and M.E. Paulaitis, *Monomer Hydrophoicity as a Mechanism for the LCST Behavior of Poly(ethylene oxide) in Water.* Industrial and Engineering Chemical Research, 2006. **45**: p. 5531-5537.
10. M. Spitzer, E. Sabadini, and W. Loh, *Poly(ethylene glycol) or Poly(ethylene oxide)? Magnitude of end-group Contribution to the Partitioning of Ethylene Oxide Oligomers and Polymers between Water and Organic Phases.* Journal of Brazilian Chemical Society, 2002. **13**(1): p. 7-9.
11. S. Saeki, N. Kuwahara, M. Nakata, and M. Kaneko, *Upper and lower critical solution temperatures in poly(ethylene glycol) solutions.* Polymer, 1976. **17**: p. 685-689.
12. R. Kjellander and E. Florin, *Water Structure and Changes in Thermal Stability of the system Poly(ethylene oxide)-water.* Journal of the Chemical Society, Faraday Transactions 1, 1981. **77**: p. 2053-2077.
13. D.Q.M. Craig, *A review of Thermal methods used for the analysis of the crystal form, solution thermodynamics and glass transition behaviour of polyethylene glycols.* Thermochimica Acta, 1995. **248**: p. 189-203.
14. B. Hammouda, D.L. Ho, and S. Kline, *Insight into Clustering in Poly(ethylene oxide) Solutions.* Macromolecules, 2004. **37**: p. 6932-6937.
15. J. Israelachvili, *The different faces of poly(ethylene glycol).* Proceedings of the National Academy of Sciences, 1997. **94**: p. 8378-8379.
16. A.A. Samii, G. Karlstrom, and B. Lindman, *Phase Behavior of Poly(ethylene oxide)-Poly(propylene oxide) Block Copolymers in Nonaqueous Solutions.* Langmuir, 1991. **7**: p. 1067-1071.
17. R.E. Goldstein, *On the theory of lower critical solution points in hydrogen-bonded mixtures.* Journal of Chemical Physics, 1984. **80**(10): p. 5340-5341.
18. J. Hirschfelder, D. Stevenson, and H. Eyring, *A Theory of Liquid Structure.* Journal of Chemical Physics, 1937. **5**: p. 896-912.
19. G. Karlström, *A new Model for Upper and Lower Critical Solution Temperature in Poly(ethylene oxide) Solutions.* Journal of Physical Chemistry, 1985. **89**: p. 4962-4964.
20. B. Lindman and G. Karlström, *Aqueous Solutions of Nonionic Surfactants and Polymers - Intermolecular Interactions and the Mechanism of Clouding.* Zeitschrift Für Physikalische Chemie, 1987. **155**(1-2): p. 199-209.
21. C. Drohmann and E.J. Beckman, *Phase behaviour of polymers containing ether groups in carbon dioxide.* Journal of Supercritical Fluids, 2002. **22**: p. 103-110.
22. S.G. Kazarian, M.F. Vincent, F.V. Bright, C.L. Liotta, and C.A. Eckert, *Specific Intermolecular Interaction of Carbon Dioxide with Polymers.* Journal of the American Chemical Society, 1996. **118**: p. 1729-1736.

23. M.L. O'Neill, Q. Cao, M. Fang, K.P. Johnston, S.P. Wilkinson, C.D. Smith, J.L. Kersshner, and S.H. Jureller, *Solubility of Homopolymers and Coppolymers in Carbon Dioxide.* Industrial and Engineering Chemical Research, 1998. **37**: p. 3067-3079.
24. L.H.M.d. Silva and W. Loh, *Polymer induced multiphase generation in water/organic solvent mixtures. Strategies towards the design of triphasic and tetraphasic liquid systems.* Chemical Communications 1998: p. 787-788.
25. M. Spitzer, L.H.M.d. Silva, and W. Loh, *Liquid Biphase Systems Formed in Ternary Mixtures of Two Organic Solvents and Ethylene Oxide Oligomers or Polymers.* Journal of Brazilian Chemical Society, 2000. **11**(4): p. 375-380.
26. M. Spitzer, E. Sabadini, and W. Loh, *Entropically Driven Partitioning of Ethylene Oxide Oligomers and Polymers in Aqueous/Organic Biphasic Systems.* Journal of Physical Chemistry B, 2002. **106**: p. 12448-12452.
27. B. Jonsson, B. Lindman, K. Holmberg, and B. Kronberg, *Surfactants and Polymers in Aqueous Solution.* Wiley, 1998.
28. F. Rindfleisch, T.P. DiNoia, and M.A. McHugh, *Solubility of polymers in supercritical $CO_2$.* Journal of Physical Chemistry 1996. **100**(38): p. 15581-15587.
29. J.C. Meredith, K.P. Johnston, J.M. Seminario, S.G. Kazarian, and C.A. Eckert, *Quantitative Equilibrium Constants between $CO_2$ and Lewis Bases from FTIR Spectroscopy.* Journal of Physical Chemistry, 1996. **100**: p. 10837-10848.
30. E. Weber, *Crown Ethers.* Ullmann's Encyclopedia of Industrial Chemistry, 2007. 2007 Edition, John Wiley and Sons.

# Chapter 5 Ethylene Oxide derivatives in HPFP

**Foreword**

The previous chapter focused on describing the behaviour of poly(ethylene glycol) oligomers (PEGs) in model propellant HPFP. Building on the insight obtained for such systems, the behaviour of ethylene oxide derivatives (EO-derivatives) in model propellant HPFP is now explored. First, the behaviour of polypropylene glycols (PPG) of various molecular weights is investigated, and compared to that of poly(ethylene glycol) oligomers. Then, the EO-derivatives chosen are a poloxamer and three polyethylene oxide monododecyl ethers ($C_{12}EO_4$, $C_{12}EO_{10}$ and $C_{12}EO_{23}$), which bear ethylene oxide moieties and $C_{12}$ chains as common features, in conjunction with either propylene oxide moieties (for the poloxamer) or a hydrophobic tail group (for polyethylene oxide monododecyl ethers). The poloxamer, a block copolymer consisting of EO and PO moieties, is compared to individual PPG and PEGs behaviour. Polyethylene oxide monododecyl ethers are compared to combinations of PEG and dodecane. Finally, the self-assembly potential of $C_{12}EO_4$ in HPFP is investigated using neutron scattering, PGSE-NMR and cross-polarised light microscopy.

## 5.1 Summary of PEGs behaviour in HPFP

Dihydroxyl end-capped poly(ethylene glycol) oligomers present a LCST-type phase boundary in HPFP. Their behaviour was previously described in Chapter 4 and can be seen in Figures 4-2 and 4-3. An increase in molecular weight drives the LCST towards higher temperatures, implying a greater solubility window, but the melting curve is also a strong function of molecular weight. Low molecular weight PEGs are very soluble in HPFP, but over a temperature range that is not easily accessible during manufacture of formulations or storage/use of the resultant products. Higher molecular weight hydroxyl ended PEGs are largely -and for most practical purposes- insoluble in HPFP. Indeed, for molecular weights equal to or greater than 1,500 g $mol^{-1}$, the temperature required to melt the polymer is higher than the LCST and therefore samples are always biphasic, either solid/liquid or liquid/liquid.

## 5.2 Behaviour of poly(propylene glycol) in HPFP

Two names are given to this chemical entity, poly(propylene glycol) (PPG) and poly(propylene oxide) (PPO), for identical reasons to those explained in the case of poly (ethyle oxide), *cf.* Chapter 4. The structure of poly(propylene oxide) is presented in Figure 5-1 below. The polymers used in this study are linear and atactic.

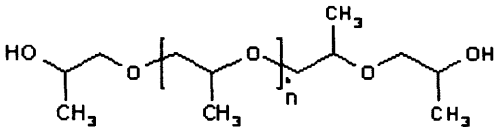


**Figure 5-1 Structure of linear poly(propylene oxide).**

PPGs were found to exhibit much higher solubilities in HPFP, for higher molecular weights, over workable temperature windows compared to PEGs in HPFP. The phase behaviour of PPG in HPFP, for PPG molecular weights of 1,000, 2,000 and 4,000 g $mol^{-1}$ is presented in Figure 5-2.

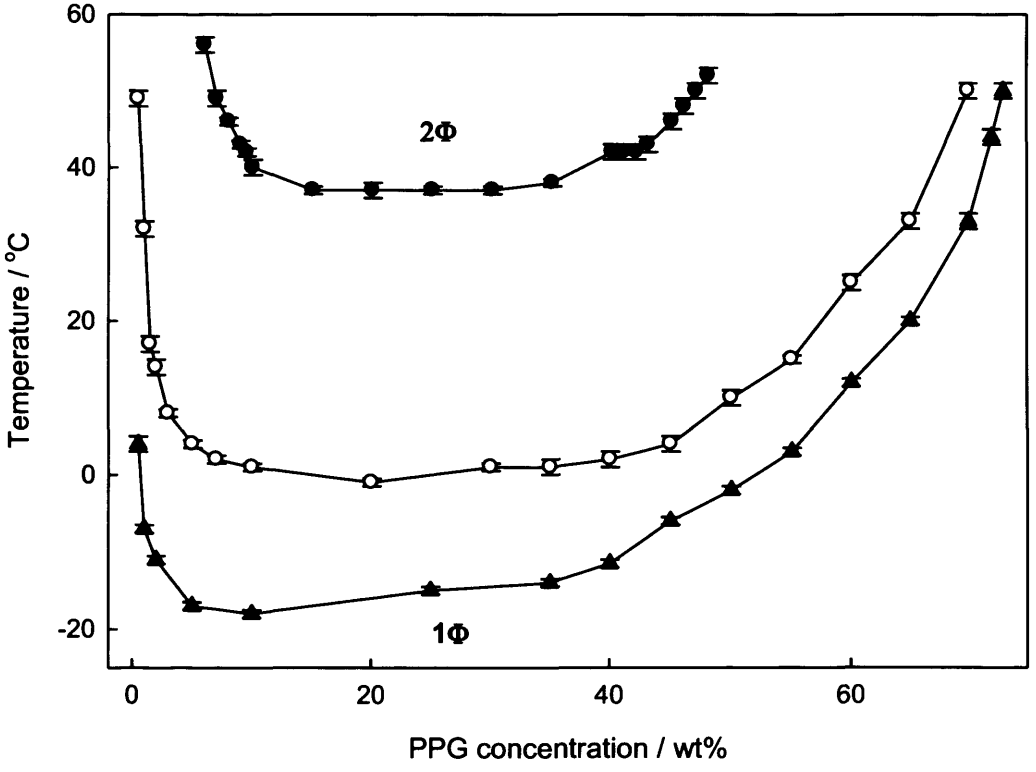


**Figure 5-2 Temperature-polymer concentration phase diagram for PPGs of molecular weights 1,000 g $mol^{-1}$ (filled circles), 2,000 g $mol^{-1}$ (empty circles) and 4,000 g $mol^{-1}$ (filled triangles) in HPFP.**

As seen in the case of PEGs, PPG also present a LCST-type behaviour. It exhibits the pronounced concentration dependence at the extremes of concentration as in the PEG case, but with two striking differences. First, the LCST now decreases with increasing molecular weight, the opposite to that observed for PEG. The solubility window for PPG in HPFP extends to higher molecular weights compared with the EO analogues. Large solubility windows were found for PPG of molecular weights 2,000 and 4,000 g $mol^{-1}$. PPGs of molecular weights 425 g $mol^{-1}$ and 700 g $mol^{-1}$ were found to be fully miscible over the entire range of concentrations and temperatures investigated above, and no LCST curve could be witnessed.

In the case of PEGs, it was seen that the presence of hydroxyl end-groups reduced the solubility. As the molecular weight was increased, the end-group effect became 'diluted' and therefore less important. The temperature required to destabilise the system was therefore increased, but at the same time, the melting point was also increased, narrowing the width of the solubility temperature window.

In the case of PPGs, polymers become less soluble as the molecular weight is increased, thus as the number of hydroxyl end-groups are reduced. The phase separation observed could in this case be due to polymer entanglements becoming more important as the molecular weight of the polymer increases. The presence of the methyl groups on the ethylene oxide backbone can also induce steric hindrance and render the hydroxyl end-groups less approachable, thus minimizing intermolecular hydrogen bonding. It was seen in the PEG series that the presence of methyl groups positioned at chain ends increased PEG solubility in HPFP. Even though not blocking terminal hydroxyl groups in PPGs, the presence of methyl groups along the ethylene oxide backbone could on its own act as a solubility enhancer. This is clearly shown with PPG 400 g $mol^{-1}$ and 725 g $mol^{-1}$ which are miscible with HPFP in all proportions and on the entire temperature range investigated, despite of their hydroxyl end-groups. In such cases, the solubility increase arising from the methyl groups presence competes with the destabilising hydroxyl end-groups interaction and seems to overcome it; meanwhile, increasing the polymer molecular weight introduces entanglements leading to earlier phase separation for higher and increasing molecular weights.

## 5.3 Poloxamer $EO_2PO_{16}EO_2$

A poloxamer is a non-ionic amphiphilic block copolymer composed of ethylene oxide and propylene oxide moieties, the ethylene oxide blocks being at the polymer end-groups, on each side of the propylene oxide blocks. The general formula can be expressed as $H(\text{-}OCH_2CH_2)_x[OCH(CH_3)\text{-}CH_2\text{-}]_y(\text{-}OCH_2CH_2\text{-})_zOH$. The behaviour of a low molecular weight copolymer $EO_2PO_{16}EO_2$ (1,100 g $mol^{-1}$) was recorded in HPFP.

Poloxamer $EO_2PO_{16}EO_2$ solutions in HPFP phase separate upon temperature increase, similarly to PEGs and PPGs series previously described. In order to try and decipher the respective role played in $EO_2PO_{16}EO_2$ by the EO end-blocks on the one hand and by the PO middle blocks on the other hand, the phase behaviour of the poloxamer is represented along the ones of PEG and PPG polymers of comparable molecular weights, respectively PEG 1,000 g $mol^{-1}$ and PPG 1,000 g $mol^{-1}$ (the closest available molecular weight matches), in Figure 5-3.

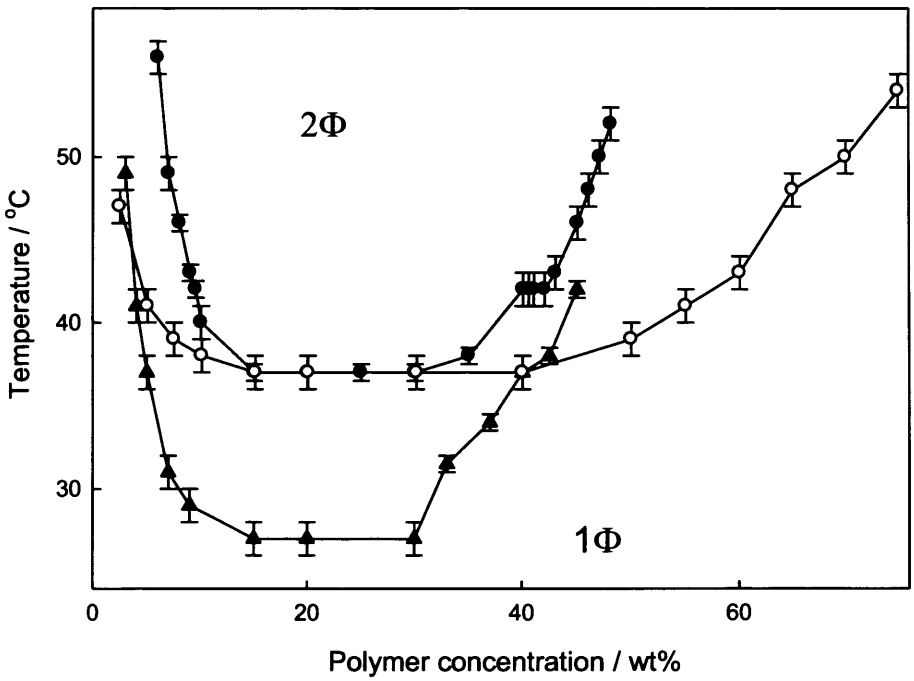


**Figure 5-3 Temperature-polymer concentration phase diagram for poloxamer $EO_2PO_{16}EO_2$ (filled triangles), PEG 1,000 g $mol^{-1}$ (empty circles), and PPG 1,000 g $mol^{-1}$ (filled circles) in HPFP.**

$EO_2PO_{16}EO_2$ shows a LCST phase separation profile with a critical temperature of 27 °C. This is lower than the critical temperatures observed for PEG 1,000 g $mol^{-1}$ and PPG 1,000 g $mol^{-1}$, both equal to 37 °C. Although PEG 1,000 g $mol^{-1}$ and PPG 1,000 g $mol^{-1}$ have the same critical temperature, their profile is different, as the concentration range upon which PEG 1,000 g $mol^{-1}$ phase separates is wider than that of PPG 1,000 g $mol^{-1}$. Over a workable temperature range, the monophasic domain is observed for concentrations below 2.5 wt% and above 75 wt% for PEG 1,000 g $mol^{-1}$, and below 6 wt% and above 48 wt% for PPG 1,000 g $mol^{-1}$. In this respect, the concentration range within which the poloxamer solutions in HPFP are monophasic (below 3 wt% and above 45 wt%) bears more similarities with the one obtained with PPG 1,000 g $mol^{-1}$. Although the polymer molecular weights are not strictly identical, the presence of EO end blocks on the poloxamer seems to shift the LCST towards lower temperatures, without affecting the workable concentration range. The presence of methyl groups on the polymer backbone could enhance its solubility, therefore achieving the dissolution of higher polymer concentrations. At the same time, the ease of accessibility of the terminal hydroxyl groups present on the EO end-blocks could favour H-bonding between the polymer molecules and lead to an earlier dephasing of the system, as witnessed by a lowering of the critical temperature. It is difficult, investigating one poloxamer only, to decipher the exact role and weight of the EO and PO blocks, and a more systematic study would be required, using a whole range of poloxamers available.

## 5.4 $C_{12}EO_n$ surfactants in model propellant

Poly(ethylene oxide) monododecyl ether surfactants ($C_{12}EO_n$) consist of a hydrophobic hydrocarbon tail group and an ethylene oxide hydrophilic head group. The three compounds selected for this study are tetra(ethylene glycol) monododecyl ether, deca(ethylene glycol) monododecyl ether and poly(ethylene oxide)-23-monododecyl ether. They are referred to as $C_{12}EO_4$ or Brij30™, $C_{12}EO_{10}$, and $C_{12}EO_{23}$ or Brij35™, respectively. It should be remembered that these surfactants are polydisperse both in head-group and tail-group and the notations $C_{12}EO_4$, $C_{12}EO_{10}$ and $C_{12}EO_{23}$ only represent an average. For instance, as stated by Poulsen *et al.* [1], Brij30™ is a mixture of components $H(CH_2)_nO\text{-}(CH_2\text{-}CH_2O)_m\text{-}H$ with significant

amounts for n = 10,12,14,16 and m = 0,1,...,9. The manufacturer states an average of $C_{12}EO_4$.

Their behaviour in model propellant HPFP was studied as a function of the headgroup molecular weight, and systematically compared to the behaviour of the separated surfactant forming moieties, *i.e.* dodecane and PEG.

### 5.4.1 $C_{12}EO_4$, $C_{12}EO_{10}$ and $C_{12}EO_{23}$

Figures 5-4 and 5-5 present the behaviour of $C_{12}EO_3$, $C_{12}EO_{10}$, and $C_{12}EO_{23}$ in HPFP.

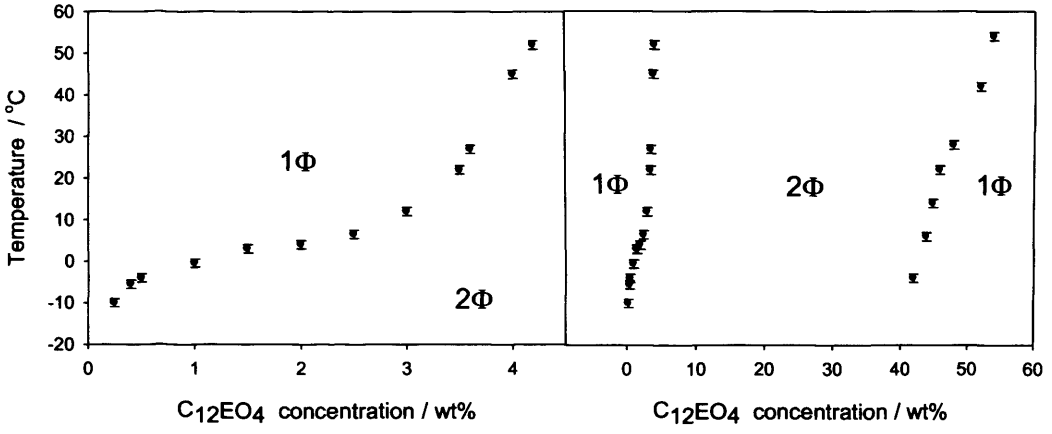


**Figure 5-4 Temperature- concentration phase diagram for surfactant $C_{12}EO_4$ in HPFP, (left) at low concentrations and (right) at both low and high concentrations.**

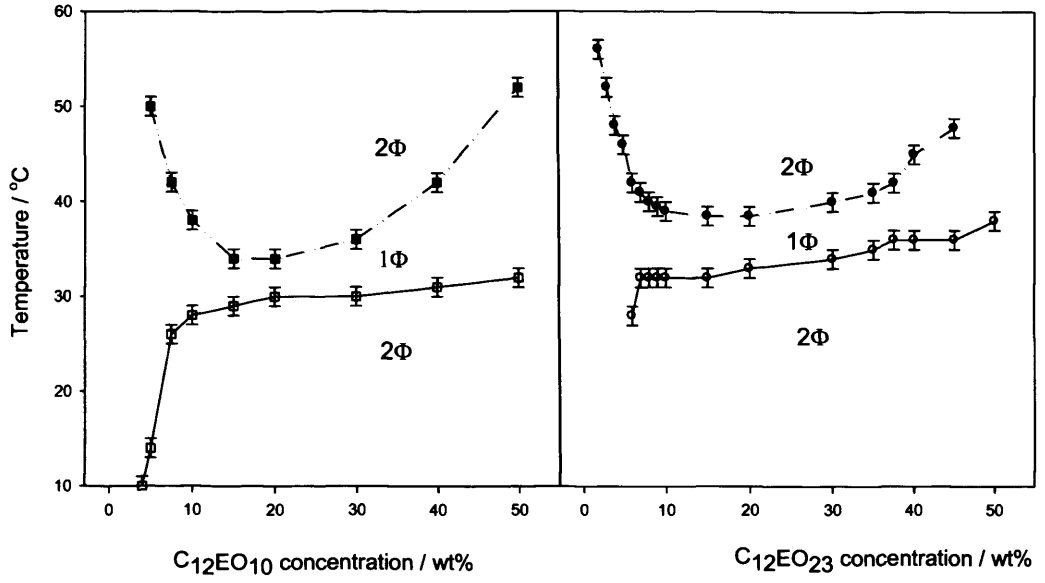


**Figure 5-5 Temperature-concentration phase diagram in HPFP for (left) $C_{12}EO_{10}$ and (right) $C_{12}EO_{23}$, showing the LCST (filled symbols) and the melting transition (open symbols).**

The behaviour of the surfactant bearing the shortest ethylene oxide head group, $C_{12}EO_4$, differs radically from the ones of $C_{12}EO_{10}$ and $C_{12}EO_{23}$. As seen in Figure 5-4, at the lower concentrations (0.1 to 4.2 wt% in HPFP), an upper consolute solution temperature (UCST) phase transition is observed, *i.e.* the surfactant solubility increases with an increase in temperature. Then, the system is always found to be biphasic over the entire range of temperatures investigated, until a LCST phase separation behaviour is observed at higher surfactant concentrations, typically between 42 and 54 w%. This behaviour is reminiscent of hour-glass shape phase separation curves, as described by Saeki *et al.* in the case of poly(ethylene glycol) 719,000 g $mol^{-1}$ in t-butyl acetate [2], or by Siow *et al.* for polystyrene 19,800 g $mol^{-1}$ in acetone [3], that could be caused by the proximity of the UCST and LCST that merge, leading to a shape that can be compared to an hour-glass.

$C_{12}EO_{10}$ and $C_{12}EO_{23}$ present a very similar behaviour in HPFP, as seen in Figure 5-5. They both show a LCST behaviour, but also exhibit a two-phase region at lower temperatures, coinciding with their melting behaviour. At low temperatures, these systems are biphasic, consisting of a coexisting waxy solid and liquid. As the temperature increases through the melting point of the surfactants, samples first

become monophasic before reaching the higher cloud-point boundary and separate into two distinctive liquid layers.

### 5.4.2 Comparison of the surfactant profiles with dodecane and PEG

In order to try and factor out individual contributions from the tail and head moieties of the surfactants, their phase behaviour profiles previously determined in section 5.4.1 were checked against those of dodecane, PEG 400 g $mol^{-1}$ and PEG 1,000 g $mol^{-1}$. Dodecane was used to model the hydrophobic tail moiety, and dihydroxy end-capped PEGs of molecular weights 400 and 1,000 g $mol^{-1}$ were chosen as the closest match available to model the $EO_{10}$ (~ 440 g $mol^{-1}$) and $EO_{23}$ (~ 1,010 g $mol^{-1}$) headgroups, respectively.

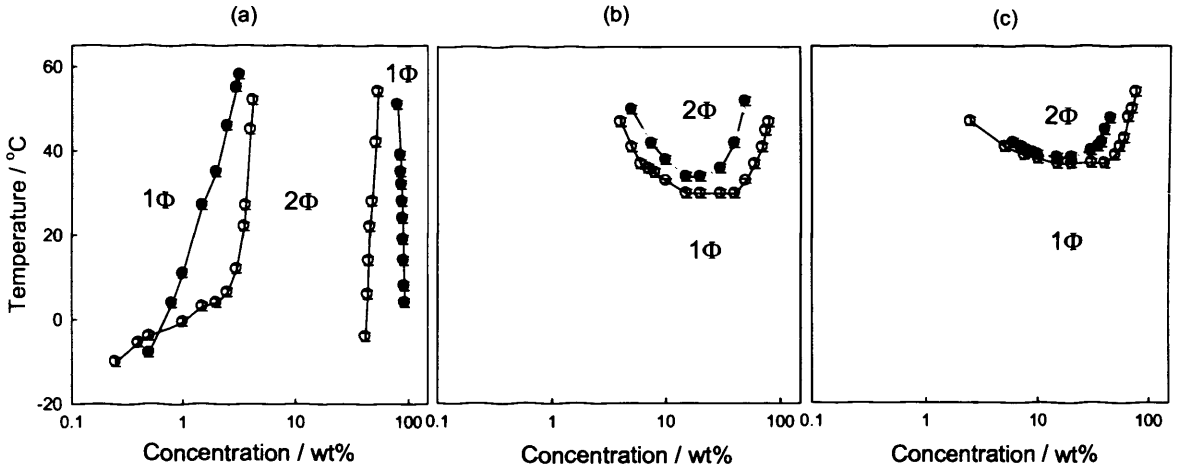


**Figure 5-6 Phase behaviour of polyethylene glycol based surfactants in HPFP and representative comparitors in HPFP (a) dodecane (filed symbols) and $C_{12}EO_4$ (open symbols), (b) PEG 400 g $mol^{-1}$ (open symbols) and $C_{12}EO_{10}$ (filled symbols) and (c) PEG 1,000 g $mol^{-1}$ (open symbols) and $C_{12}EO_{23}$ (filled symbols). Melting curves in (b) and (c) are not shown.**

As shown in Figure 5-6, the profiles obtained for dodecane are not that dissimilar to that observed for $C_{12}EO_4$, and those obtained for $C_{12}EO_{10}$ and $C_{12}EO_{23}$ match closely those of dihydroxy end-capped PEGs of molecular weights 400 and 1,000 g $mol^{-1}$ respectively. Clearly, the dodecane fragment dominates the behaviour of the excipient bearing the short EO chain, whilst the ethylene glycol fragment dominates the behaviour of the excipients bearing the longer EO chains. Besides, the critical temperatures of $C_{12}EO_{10}$ (34 °C) and $C_{12}EO_{23}$ (38.5 °C) are only slightly higher, respectively, than those of PEG 400 (30 °C) and PEG 1000 g $mol^{-1}$ (37 °C). As was

previously done in Chapter 4, in which the hydroxyl end-groups of the PEGs were replaced by methyl groups, one can here consider the dodecyl group as a replacement for one of the hydroxyl end-groups. In this case, a LCST phase separation is still observed for both $C_{12}EO_{10}$ and $C_{12}EO_{23}$ : the solubility enhancement is nowhere near as efficient as the one induced by the smaller methyl group(s), the dodecyl moety does not interact as favourably with the solvent.

### 5.4.3 Mixtures of dodecane and dihydroxy end-capped PEGs

An attempt was made at re-creating the surfactant $C_{12}EO_4$ composition by mixing dodecane and dihydroxy end-capped PEG 200 g $mol^{-1}$. Then, several mixtures of dodecane and dihydroxy end-capped PEG were investigated, in which the ratio of the two components, and the molecular weight of the ethylene oxide oligomer, were varied. The aim was not so much to try and mimic the surfactant behaviour, but to see whether dodecane and PEGs were interacting, or showing signs of associative behaviour.

#### 5.4.3.1 50/50 mix of dodecane and PEG200

The molecular weight of $C_{12}EO_4$ head-group is ~ 190 g $mol^{-1}$ and that of dodecane is ~170 g $mol^{-1}$, both components are therefore present in an approximately 50/50 ratio by weight in the surfactant molecule. Figure 5-7 presents the behaviour of a mixture composed of a 50/50 ratio by weight of dodecane and dihydroxy end-capped PEG 200 g $mol^{-1}$, along with that of surfactant $C_{12}EO_4$.

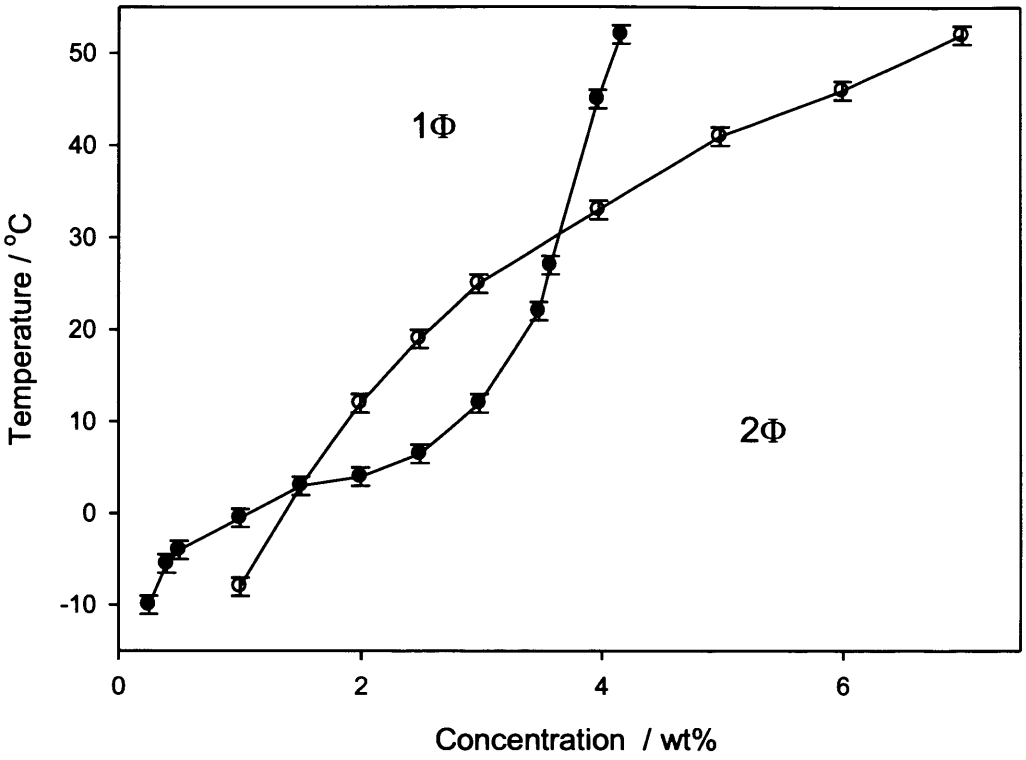


**Figure 5-7 Phase behaviour of a 50/50 mixture of dodecane and dihydroxy end-capped PEG 200 g mol$^{-1}$(open symbols) and surfactant $C_{12}EO_4$ (filled symbols), at low concentrations.**

The 50/50 dodecane - dihydroxy end-capped PEG 200 g mol$^{-1}$ mixture is biphasic at the lower temperatures, and fully solubilises upon temperature increase, similar to dodecane itself and $C_{12}EO_4$. As can be seen in Figure 5-7, the ranges of both concentrations and temperatures upon which the phase transition was detectable for the head and tail moieties mixture are very comparable to that of the surfactant, however, their profiles are rather different. Higher concentrations ranging from 40 to 55 wt%, so as to match the LCST window observed for the surfactant, were investigated as well. However, no monophasic domain was present. For such compositions, the concentration of dodecane is comprised between 20 and 27.5 w% and as seen on Figure 5-4, such samples are always biphasic. In a similar way, in the (20-27.5) wt% concentration range window, PEG 200 g mol$^{-1}$ in HPFP is always biphasic once the temperature goes beyond 15 °C. Provided no interaction occurs in mixtures of dodecane and PEG 200 g mol$^{-1}$ at such concentration, samples can therefore only be biphasic.

### 5.4.3.2 Varying dodecane to PEG 200 g $mol^{-1}$ ratio

The influence of the ratio between dodecane and PEG 200 g $mol^{-1}$ on the cloud point of the system at the lower concentrations was investigated. Ratios chosen, expressed as dodecane / PEG 200 g $mol^{-1}$ wt%, were 100/0, 75/25 and 50/50 and results obtained are presented in Figure 5-8.

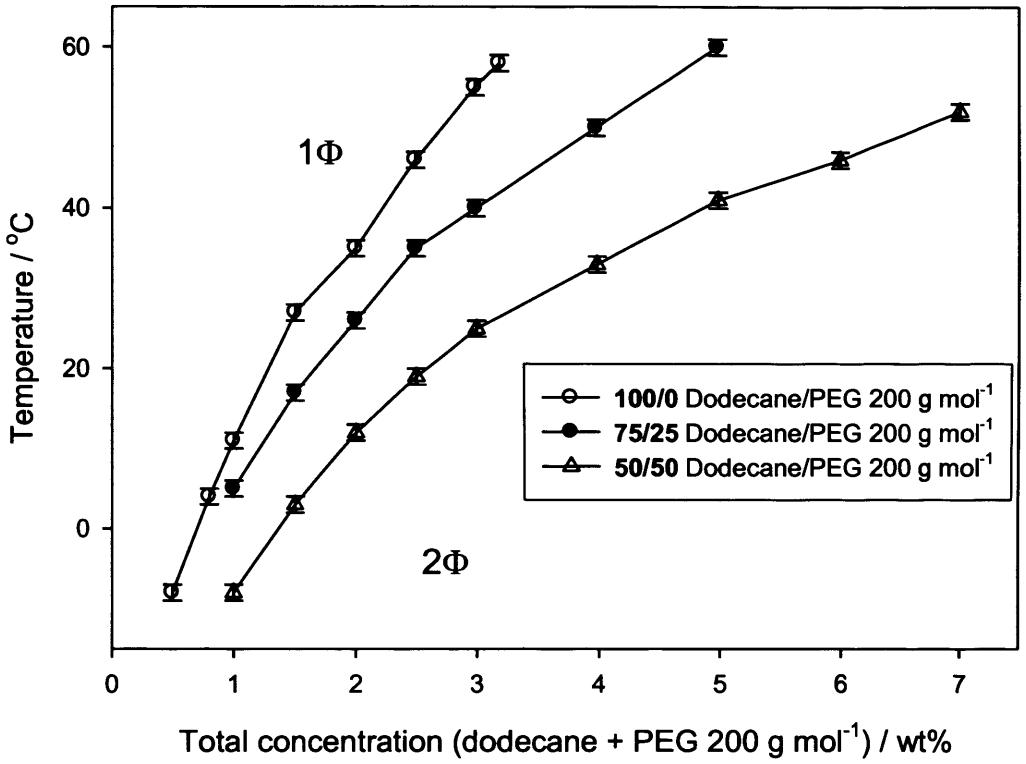


**Figure 5-8. Influence of dodecane/PEG 200 g $mol^{-1}$ mixing ratio on the phase behaviour - (empty circles) 100/0, (filled circles) 75/25, (empty triangles) 50/50.**

At such concentrations, the system is biphasic at the lower temperatures and fully solubilises upon temperature increase. This UCST behaviour was observed for all ratios investigated, and the temperature at which the system became monophasic was shifted towards lower temperatures as the proportions of PEG 200 g $mol^{-1}$ was increased. However, it has been seen previously that at such PEG 200 g $mol^{-1}$ concentrations, i.e. 3.5 wt% and below, clouding of the systems occurs only at temperatures above 50 °C, *cf.* Figure 4-2. PEG may therefore not be taking part in the cloud-point observed and it would be worth plotting the data in an alternative manner, using the dodecane concentration as the abscise, instead of the total (dodecane + PEG 200 g $mol^{-1}$) concentration. Figure 5-9 shows such a re-plot.

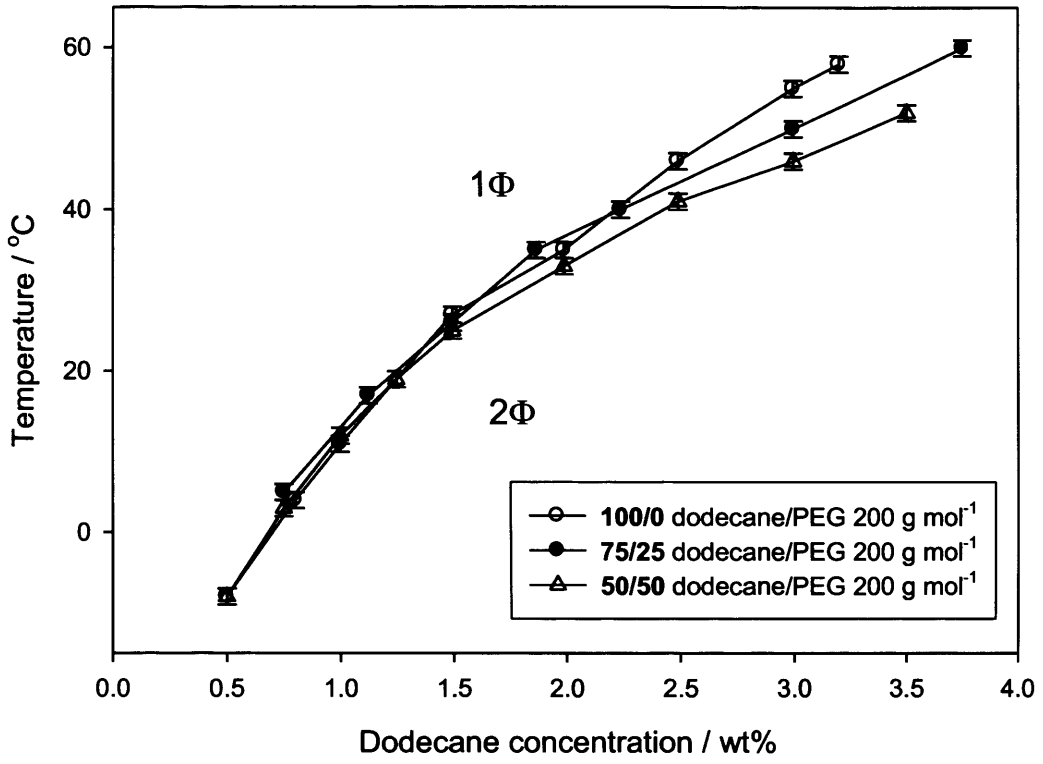


**Figure 5-9. Cloud-point temperature as a function of dodecane concentration, for various dodecane/PEG 200 g mol$^{-1}$ ratios. (empty circles) 100/0, (filled circles) 75/25, (empty triangles) 50/50.**

The three curves now overlap, implying that PEG 200 g mol$^{-1}$ has a very limited influence on the solubility behaviour of these solutions. At such concentrations, dodecane is the component driving the behaviour of the systems.

### 5.4.3.3 Varying PEG molecular weight

Finally, similar experiments were performed in which the effect of the diydroxyl end-capped PEG molecular weight was investigated, in 50/50 dodecane/PEG in HPFP samples. The molecular weights investigated were 200 g mol$^{-1}$ 300 g mol$^{-1}$ and 600 g mol$^{-1}$, and the results are presented in Figure 5-10.

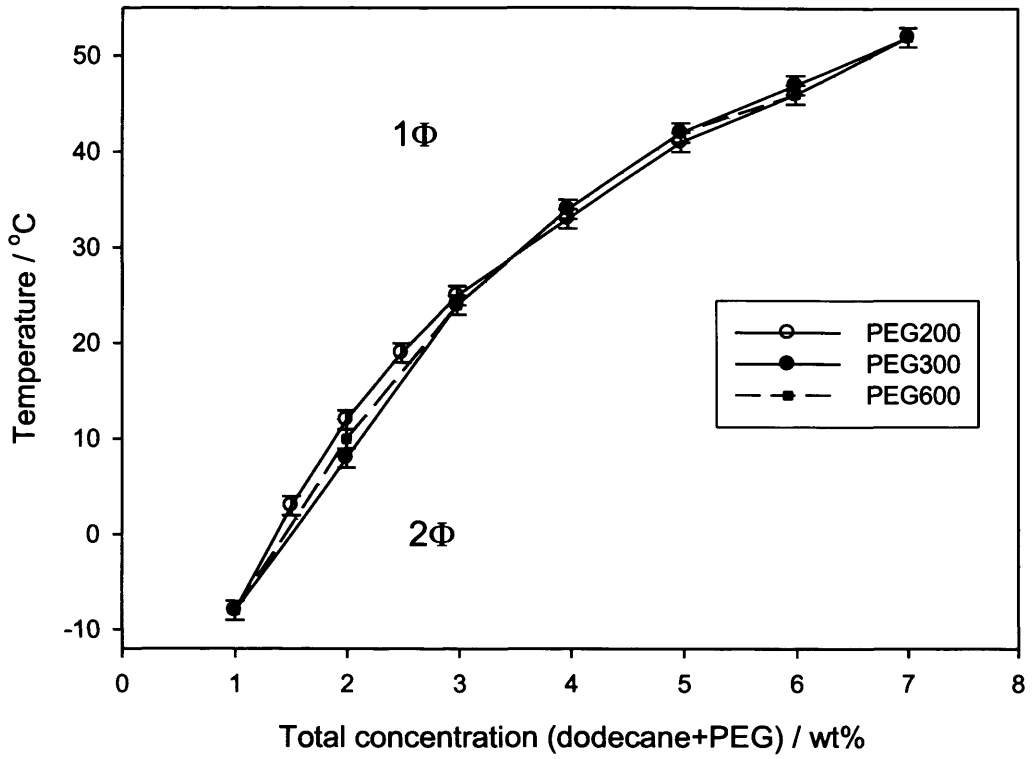


**Figure 5-10. Effect of PEG Mw on the phase behaviour for 50/50 wt% dodecane/PEG samples in HPFP. (empty circles) PEG 200 g mol$^{-1}$, (filled circles) PEG 300 g mol$^{-1}$, (filled squares) PEG 600 g mol$^{-1}$.**

The data obtained for the three different molecular weights overlap. PEG 200 g mol$^{-1}$ was previously found to have no influence on the phase separation curves obtained (Figure 5-9), and it is the case for these higher molecular weights as well. The overlapping curves suggest that at such a ratio, PEG molecular weight has no influence on the phase behaviour of the samples, once again confirming dodecane is controlling the solubility behaviour and is not affected by the presence of PEG.

## 5.5 Does aggregation occur for $C_{12}EO_n$ surfactants in HPFP?

When in water, the surfactants used in this study are able to form aggregates [4]. Depending on their concentration, several various structures can be obtained, such as micellar, lamellar phases, liquid crystalline phases. In water, the critical micellar concentrations (cmc) have been reported for these surfactants and values in millimol per litre for Brij30™ and Brij35™ are as follows:

| Surfactant | cmc (mM) |
|---|---|
| Brij 30™ (average $C_{12}EO_4$) | 0.023 -0.05 [5,6] |
| Brij 35™ (average $C_{12}EO_{23}$) | 0.048-0.17 [7] and ref. herein |

**Table 5-1. Values of the cmc in mM for Brij 30™ and Brij 35™ in water.**

In this study, the interest lies in determining whether the surfactant molecules form aggregates in model propellant HPFP. This is probed via small-angle neutron scattering, PGSE-NMR experiments and direct visualisation under cross-polarised light.

Ridder et al. [8] report the micellization of Brij 30™ in HPFP, identifying a cmc, in a type II association behaviour, i.e. an association characterised by (a) a moderately defined cmc; (b) large aggregation numbers that become constant for higher surfactant concentrations; (c) monomer-n-mer aggregation model. The cmc of Brij30™ was measured via iodine solubilisation experiments and the iodine absorbance maximum recorded as a function of the surfactant concentration. Cmc was found equal to 0.0062 wt% (i.e. ~ 10 times that of an aqueous solution). The orientation of the aggregates was probed via fluorescence spectroscopy using the microviscosity sensitive fluorescence probe 1,3 dipyrenylpropane, for a surfactant concentration in model propellant equal to 1 wt%. $L_1$- aggregate orientation was detected, i.e. micelles in which the hydrophobic tails are orientated towards the centre of the aggregate and the hydrophilic moiety lies at the exterior, towards the bulk solvent.

### 5.5.1 Assessing aggregation via SANS

The presence of aggregates in samples consisting of Brij30™, $C_{12}EO_{10}$ or Brij35™ in HPFP was investigated via small-angle neutron scattering (SANS). Table 5-2 gives the scattering length density (sld) values for the various surfactants and the solvent used.

| Material | Sld / $10^{-6}$ Å$^{-2}$ |
|---|---|
| HPFP | 3.108 |
| Brij30™ ($C_{12}EO_4$) | 0.098 |
| $C_{12}EO_{10}$ | 0.341 |
| Brij35™ ($C_{12}EO_{23}$) | 0.480 |

**Table 5-2. Scattering length densities (Sld) for the surfactants Brij30™, $C_{12}EO_{10}$ or Brij35™ and model propellant HPFP.**

All SANS measurement were performed on samples that were homogeneous, i.e. in their respective monophasic domain, previously visually determined. The concentrations investigated were 3.25 wt% for Brij30™, 3.25 wt%, 6 wt% and 40 wt% for $C_{12}EO_{10}$ and 3.25 wt%, 6 wt% and 35 wt% for Brij35™. Measurements were performed either at 25 °C for surfactant concentrations of 3.25 wt% and 6 wt% or 35 °C for surfactant concentrations of 35 and 40 wt%. Figure 5-11 presents the scattering data obtained for all surfactants at a constant concentration of 3.25 wt% in HPFP, Figure 5-12 the scattering data for $C_{12}EO_{10}$ in HPFP at concentrations of 3.25 wt%, 6 wt% and 40 wt%, and Figure 5-13 the scattering data for Brij35™ in HPFP at concentrations of 3.25 wt%, 6 wt% and 35 wt%.

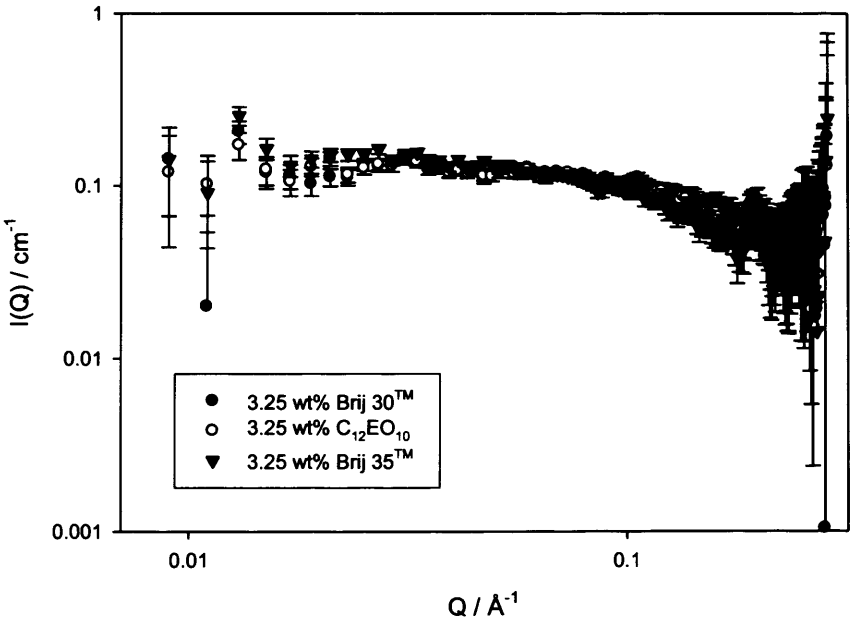


**Figure 5-11. Scattering data for surfactant (filled circles) Brij30™, (empty circles) $C_{12}EO_{10}$ and (filled triangles) Brij35™ at 3.25 wt% in HPFP.**

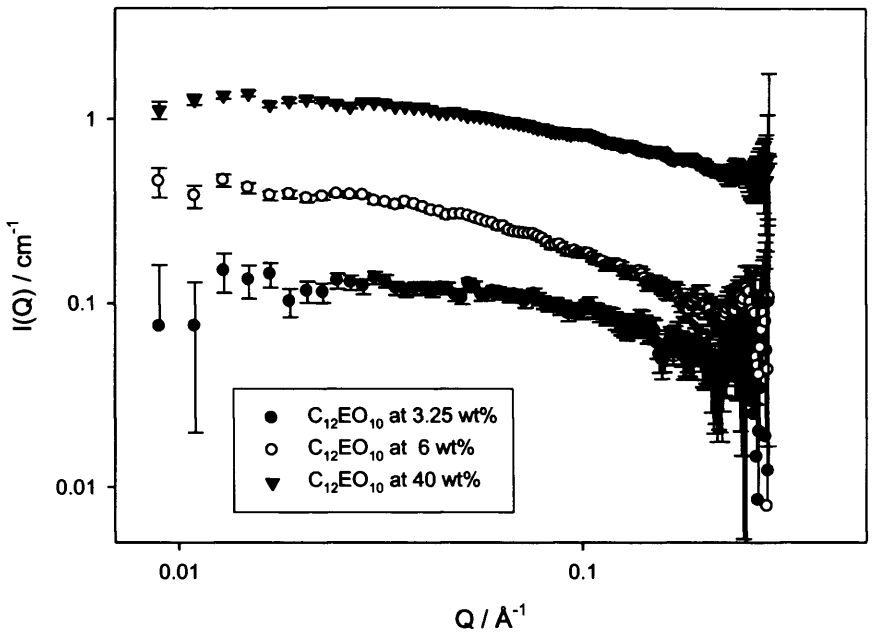


**Figure 5-12. Scattering data for $C_{12}EO_{10}$ at (filled circles) 3.25 wt%, (empty circles) 6 wt% and (filled triangles) 40 wt% in HPFP.**

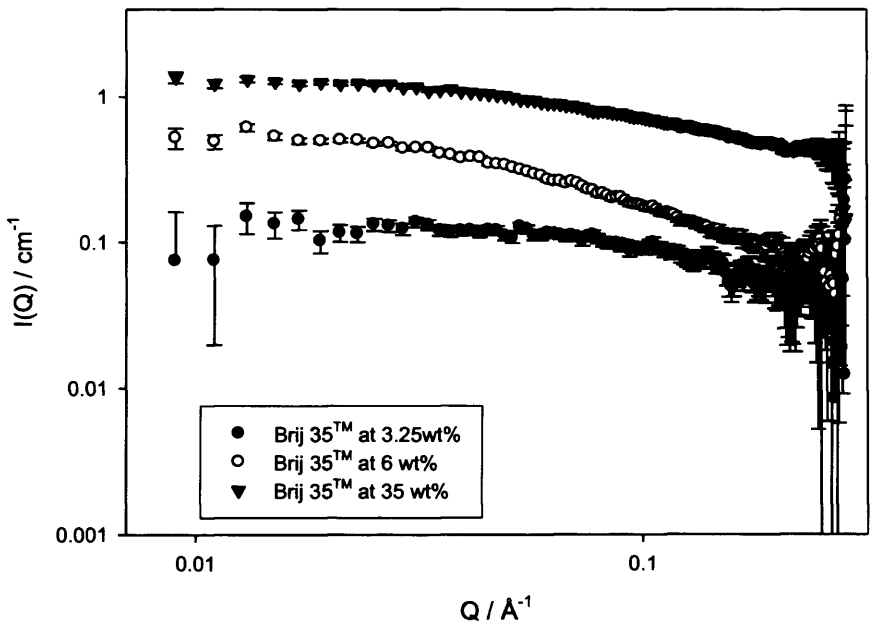


**Figure 5-13. Scattering data for Brij 35™ at (filled circles) 3.25 wt%, (empty circles) 6 wt% and (filled triangles) 35 wt% in HPFP.**

In Figure 5-11, no differences in the scattering pattern can be observed between the solutions of the various surfactants, at a constant concentration of 3.25 wt%. The scattering appears featureless and rather flat, indicating that no large aggregates or

molecular arrangements bearing a characteristic distance seem to be present in the samples. In a similar fashion, no feature appears in the scattering pattern as the concentration of the surfactant is raised, as seen in Figure 5-12 and Figure 5-13.

The theoretical neutron scattering pattern for a solution comprising spherical micellar arrangements of the surfactants used in this study can be modelled for various aggregation numbers, and compared to the scattering data obtained here. In this end, a simple monodispere solid sphere model is chosen to represent the spherical micellar arrangements. The scattering intensity I(Q) can be expressed as:

$$I(Q) = A\left[3\left(\frac{\sin(Qr) - Qr\cos(Qr)}{(Qr)^3}\right)\right]^2 + B_{inc} \qquad \textbf{Equation 5-1}$$

with r the sphere radius, $B_{inc}$ the scattering arising from the incoherent background and A the scale, obtained for I(Q=0), so that:

$$A = 10^{-16} N V_{tot}^{\ 2} (\Delta\rho)^2 \qquad \textbf{Equation 5-2}$$

where N particles per $cm^3$ have a total volume $V_{tot}$ ($Å^3$), which is the volume of the surfactant molecule times its aggregation number, and $\Delta\rho$ is the scattering length density difference between the particles and the surrounding medium in $Å^{-2}$.

The volume of the surfactant molecule can be estimated via Equation 5-3. For a saturated hydrocarbon chain, the volume (v) of the hydrocarbon core is, in $nm^3$:

$$v = 0.027(n_c + n_{Me}) \qquad \textbf{Equation 5-3}$$

With $n_c$ the total number of carbon atoms per chain and $n_{Me}$ the number of methyl groups [9], giving a tail-group molecular volume of 351 $Å^3$. No such formula exists for the ethylene oxide moieties but the molecular volume of the head-group can be approached simply using the molecular weight and density of the moiety, via the following equation:

$$V = \frac{Ms}{\rho \cdot N_A} \qquad \textbf{Equation 5-4}$$

with $M_s$ the molecular weight of the head-group, $\rho$ its density and $N_A$ Avogadro's number, giving a molecular volume of ~ 300 Å$^3$ for the hydrophilic headgroup. An estimate of the total volume V of a Brij30™ surfactant molecule is therefore V = $V_{hydrocarbon\ core} + V_{ethylene\ oxide\ moiety}$ so that V~ 650 Å$^3$.

Figure 5-14 presents the experimental scattering data obtained for 3.25 wt% Brij30™ in HPFP, along with the corresponding theoretical scattering calculated for aggregation numbers of 3, 10 and 20.

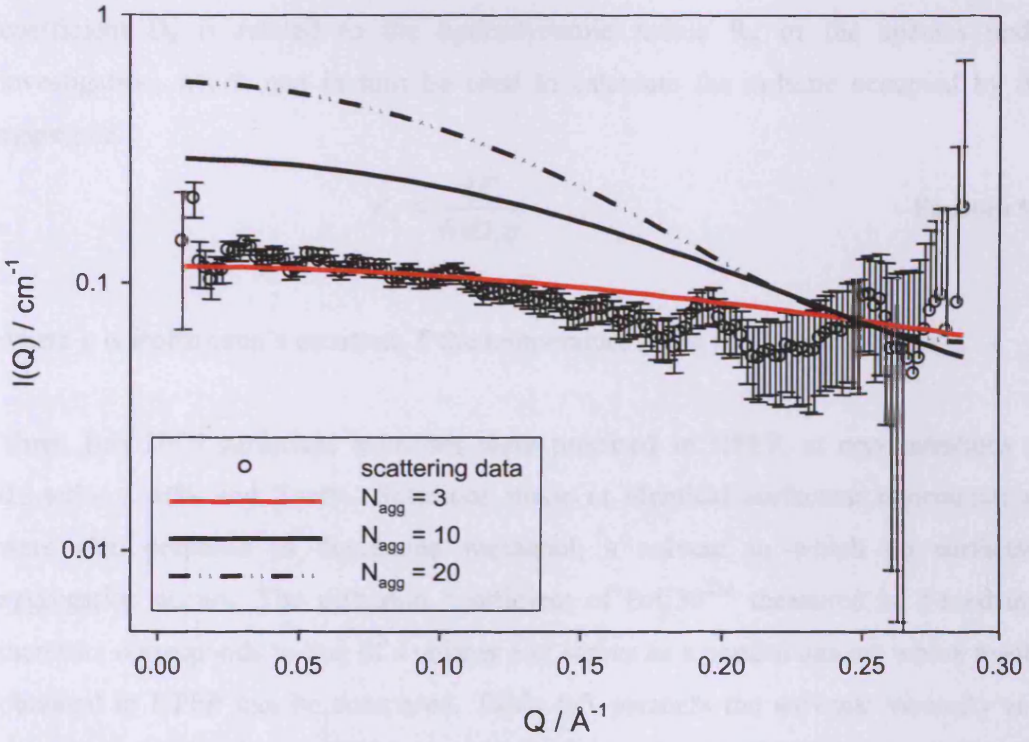


**Figure 5-14. Scattering data for 3.25 wt% Brij ™ in HPFP along with theoretical scattering for spherical micellar structures of aggregation number 3, 10 and 20.**

As seen on Figure 5-14, the theoretical scattering obtained with an aggregation number of 3 does not quite follow the shape of the experimental data, but its absolute intensity does. The closest matching profile, when considering the overall shape and curvature of the scattering data, is obtained with an aggregation number of 10. However, its absolute intensity is twice that of the experimental dataset, and in order to obtain equal absolute intensities, the scattering length density of the surfactant

would have to be $5 \times 10^{-6}$ Å$^{-2}$, which is not physical for this surfactant. The aggregates, if present, may of course not be spherical. However, regardless of their potential shape, if aggregates are present, they are bound to be of very limited aggregation number, which in turn questions the presence of micellar arrangements as per Ridder *et al.* [8].

### 5.5.2 Assessing aggregation via PGSE-NMR

Aggregation was further probed via PGSE-NMR. The diffusion coefficient of a species measured in the PGSE-NMR experiment can give useful insight into its aggregation state. Using the Stokes-Einstein equation presented below, the diffusion coefficient $D_s$ is related to the hydrodynamic radius $R_h$ of the species under investigation, which can in turn be used to calculate the volume occupied by the aggregate.

$$R_h = \frac{kT}{6\pi D_s \eta} \qquad \textbf{Equation 5-5}$$

where k is Boltzmann's constant, T the temperature and η the solvent viscosity.

Three Brij 30™ surfactant solutions were prepared in HPFP, at concentrations of 0.3 wt%, 1 wt% and 3 wt%. Solutions made at identical surfactant concentrations were also prepared in deuterated methanol, a solvent in which no surfactant aggregation occurs. The diffusion coefficient of Brij30™ measured in d-methanol therefore corresponds to that of a unimer and serves as a control against which results obtained in HPFP can be compared. Table 5-3 presents the solvents viscosity at a temperature of 298.3 K and Table 5-4 presents the values of the diffusion coefficients measured and the corresponding hydrodynamic radii.

| Solvent | d-methanol | HPFP |
|---|---|---|
| Viscosity / mPa·s | 0.55 | 0.50 |

**Table 5-3. Solvent viscosity for d-methanol and HPFP, at 298K**

| Solvent | d-methanol | | | HPFP | | |
|---|---|---|---|---|---|---|
| Brij30™ / wt% | 0.3 | 1 | 3 | 0.3 | 1 | 3 |
| $D_s$ / $m^2 \cdot s^{-1}$ ($\times 10^{10}$) | 6.3 | 6.7 | 7.3 | 5.7 | 6.8 | 5.7 |
| $R_h$ / Å | 6.4 | 5.9 | 5.5 | 7.7 | 6.4 | 7.7 |

**Table 5-4. Diffusion coefficients and corresponding hydrodynamic radii for Brij30™ in d-methanol and HPFP at concentrations comprised between 0.3 and 3 wt%.**

As seen in Table 5-4, the hydrodynamic radius is not found to vary greatly with the surfactant concentration, for concentrations comprised between 0.3 and 3wt%, both in d-methanol and HPFP. In order to investigate the physical meaning of such diffusion coefficient and hydrodynamic radius values, the volume V of the Brij 30™ molecule or aggregate can be calculated, using a spherical model, so that:

$$V = \frac{4}{3}\pi \cdot R_h^3 \qquad \textbf{Equation 5-6}$$

In d-methanol, this leads to an average volume of ~ 860 $Å^3$, which is of comparable range with the previously estimated value of 650 $Å^3$ for the Brij 30™ unimer (see section 5.5.1). This confirms the hypothesis that no aggregation takes place in d-methanol. Hydrodynamic radii values in HPFP are only slightly larger than in d-methanol, and the average volume calculated is ~ 1610 $Å^3$, which could indicate the presence of dimers. However, no large aggregates are present, as would be expected in the case of micellar arrangements.

### 5.5.3 Seeking aggregation via visualisation under cross-polarised light

Brij30™, $C_{12}EO_{10}$ and Brij35™ were all tested on their own, in the presence of HPFP and in the presence of water, for light polarisation effects. The surfactants on their own all appeared dark, meaning that there is no directional dependence of the refractive index of the sample and all light is fully stopped by the cross-polariser filters. Identical results were observed when the surfactants were in presence of HPFP for which all samples appeared dark. Birefringent behaviour was however observed for the surfactant in the presence of water (no HPFP) as the water diffused through the surfactant, as shown in Figure 5-15, characteristic of the presence of a mesophase.

**Figure 5-15 Selected shot from a Brij30™/water sample under cross-polarised light.**

## 5.6 Conclusion

Building on the results obtained with mono-methylated, di-methylated and di-hydroxylated PEGs, the behaviour of ethylene oxide derivatives was investigated in model propellant HPFP. The presence of extra methyl groups on an ethylene glycol backbone was found to enhance the polymer solubility, as witnessed with PPG polymers. The most striking effect with the PPG polymers was the fact that the critical temperature decreased when increasing the polymers molecular weight, opposite to what was observed in the case of PEGs, implying that the effect of the hydroxyl end-groups is weaker and that the greater solubility is a reflection of the presence of the methyl groups. The behaviour of the poloxamer was found to follow the same principle, the presence of the inner PPG block enhancing the polymer solubility on a wider range of concentration, while the PEG end-blocks induced earlier phase separation, resulting in a reduction of the critical temperature. The replacement of a hydroxyl terminal group by a dodecyl moiety did not result in improving the EO polymer solubility as greatly as did the smaller methyl moiety, as seen with the surfactants $C_{12}EO_{10}$ and $C_{12}EO_{23}$ that showed highly similar phase behaviour to their di-hydroxylated PEG 600 g mol$^{-1}$ and PEG 1000 g mol$^{-1}$ comparitors. For the polyethylene oxide monododecyl ether surfactants $C_{12}EO_4$, $C_{12}EO_{10}$, and $C_{12}EO_{23}$, the dodecane fragment was found to dominate the behaviour of the excipient bearing the short EO chain, whilst the ethylene glycol fragment

dominated the behaviour of the excipients bearing the longer EO chains. The potential aggregation of Brij30™ surfactant was also investigated and as opposed to what can be observed in aqueous systems, the presence of micellar aggregates or any type of structured arrangements was on this occasion not found to occur in partially fluorinated liquid HPFP.

## 5.7 Further work

As explained in the result and discussion section, the $C_{12}EO_n$ surfactants are only averages of more polydisperse components. The Japan-based company Nikko Chemicals provides a selection of polyoxyethylene dodecyl ethers that are pure and monodisperse. Provided sufficient funds are available, it could be of interest to carry out a systematic study on these surfactants, and find the number of ethylene oxide units threshold at which the phase behaviour dependency shifts from being tail-group driven to head-group driven. Then, the phase behaviour of one poloxamer was investigated, however, there exist a wide range available, with various EO blocks/PO blocks ratios that could be studied in order to obtain a clearer picture of each block's role. The extra methyl groups present on the EO backbone of the PPG polymers seems to favour their solubility, although the hydroxyl end-groups are still free. One could take this a step further and investigate the effect of end-group methylation on PPGs, as was conducted on PEGs. The paths explored and presented in Chapters 4 and 5 have now lead to the continuation of this work in the form of a new PhD project, starting at the time of writing these lines and that aims at pursuing the characterisation of a selection of the systems presented here.

**References**

1. A. K. Poulsen, 'Unusually large acrylamide induced effect on the droplet size in AOT/Brij30 water-in oil microemulsions', *Journal of Colloid and Interface Science, 306* (2007), 143-53.
2. S. Saeki, N. Kuwahara, M. Nakata and M. Kaneko, 'Upper and lower critical solution temperatures in poly(ethylene glycol) solutions', *Polymer, 17* (1976), 685-9.
3. K. S. Siow, G. Delmas and D. Patterson, 'Cloud-Point Curves in Polymer Solutions with Adjacent Upper and Lower Critical Solution Tempertures', *Journal of Physical Chemistry, 5* (1972), 29-34.
4. J. W. Goodwin, *Colloids and Interfaces with Surfactants and Polymers: an Introduction*, (Chichester, 2004).

5. Z. Liu, A. M. Jacobson and R. G. Luthy, 'Biodegradation of Naphtalene in Aqueous Nonionic Surfactant Systems', *Applied and Environmental Microbiology, 61* (1995), 145-51.
6. H. Akbas, T. Sidim and M. Iscan, 'Effect of Polyoxyethylene Chain Length and Electrolyte on the Viscosity of Mixed Micelles ', *Turkish Journal of Chemistry, 27* (2003), 357-63.
7. S. H. Brooks, A. Berthod, B. A. Kirsch and J. G. Dorsey, 'Flow-injection system for determintaion of critical micelle concentrations of ionic and nonionic surfactants', *Analytica Chimica Acta, 209* (1988), 111-21.
8. K. B. Ridder, C. J. DaviesCutting and I. Kellaway, 'Surfactant solubility and aggregate orientation in hydrofluoroalkanes', *International Journal of Pharmaceutics, 295* (2005), 57-65.
9. D. F. Evans and H. Wennerström, *The Colloidal Domain*, (New York, 1994).

# Chapter 6 Triacetyl-β-cyclodextrin in HPFP

**Foreword**

When screening common polymers and excipients for their solubility in the model propellant 2H,3H-decafluoropentane, unexpected results were found with the compound triacetyl-β-cyclodextrin (TAβCD), a hydrophobically modified cyclodextrin. TAβCD from various suppliers exhibited drastically different solubilities in HPFP and melting points, although having identical chemical composition. Since such behaviour is highly reminiscent of polymorphism, a collaboration was initiated with K.D.M. Harris' group at Cardiff University, specifically with the help of Dr Colan E. Hughes who performed the relevant X-ray powder diffraction and solid-state NMR experiments, offered an open access to the thermoanalytical equipments and his experience and availability for many fruitful discussions. Different polymorphs of TAβCD were identified and polymorphism was found to be the key parameter ruling the solubility of TAβCD in HPFP.

## 6.1 Introduction

### 6.1.1 Solid form diversity: the importance of polymorphism in the pharmaceutical industry

The ability of a solid to exist in more than one crystal structure is known as polymorphism. Although identical in chemical composition, the various polymorphs of the same molecule can have drastically different physical properties, such as melting point, density, chemical and physical stabilities, solubility, flow properties [1]. The cases of solubility and dissolution rate are of particular relevance to pharmaceutical formulations, as oral drugs are often administered as crystalline solids. The rate at which they dissolve, hence impacting on their bioavailability, is highly dependant on their crystal structure. The ability to synthesise one or another polymorph with high reproducibility is key to the process of a drug manufacture [2]. Also, polymorphs have the tendency to spontaneously transform from a less stable form to a more stable one. As a consequence, it is better to find and fully characterize the most stable form at the early stages of drug development [3, 4]. On an intellectual property point of view, one active ingredient can be patented several times if different

polymorphs are isolated. Hence, polymorphism of both drugs and excipients has been the focus of much attention for over 40 years now and will continue to be a key investigation area in all pharmaceutical formulations [5].

### 6.1.2 Natural cyclodextrins

Cyclodextrins (CDs) are cyclic oligosaccharides which are produced by the degradation of starch via the action of an enzyme, called cyclodextrin glycosyltransferase (CGT-ase) [6]. This enzyme can be produced by several bacteria, one of them being Bacillus macerans. Chemically, CDs are made of repeating units of at least 6 D-(+) glucopyranose units linked by α –(1,4) glucosidic bonds. The three naturally occurring cyclodextrins are the α-, β-, and γ-CDs, comprising of 6, 7 or 8 glucose units respectively. Their chemical structure is presented in Figure 6-1. Their favoured configuration is in the form of a toroid, as shown in Figure 6-2, with a hydrophobic inner cavity. The hydrophobicity of the cavity is a result of the electron rich environment, mainly due to the presence of the glycosidic oxygen atoms.

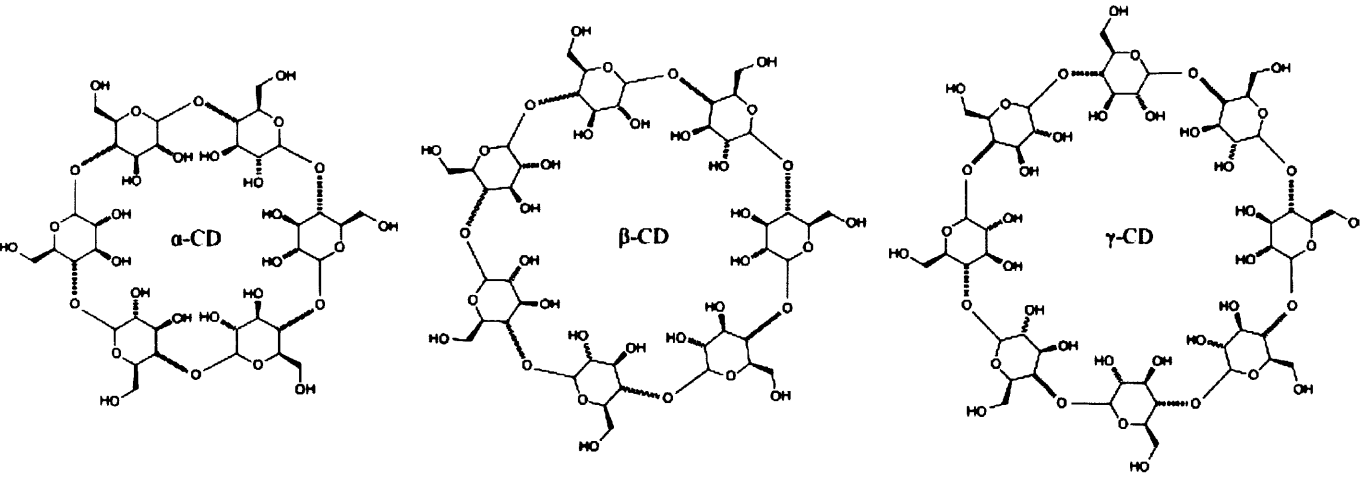


**Figure 6-1. Chemical structure of α, β, and γ-cyclodextrins [7].**

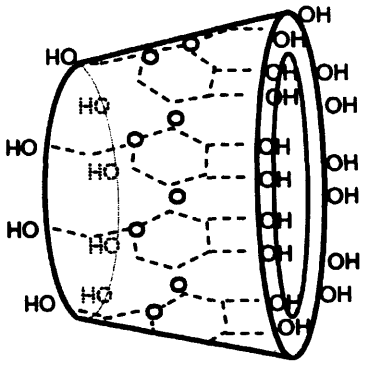

**Figure 6-2. Toroid configuration of γ-cyclodextrin [7].**

Due to the presence of the cavity, CDs are able to form non-covalent host-guest inclusion complexes, the size of the cavity determining possible guests. They are of particular interest in pharmaceutical applications, as they can act as drug carriers providing sustained release for the drugs. Table 6-1 summarises the cavity dimensions of α-, β-, and γ-CD.

| Cyclodextrin | Mw /g.mol$^{-1}$ | Cavity diameter /Å | Cavity volume / Å$^3$ |
|---|---|---|---|
| α | 972 | 4.7~5.3 | ~174 |
| β | 1135 | 6.0~6.5 | ~262 |
| γ | 1297 | 7.5~8.3 | ~427 |

**Table 6-1. Molecular weight and characteristic cavity dimensions for the 3 natural CDs [8].**

### 6.1.3 Chemically modified cyclodextrins

In order to tailor the physical and chemical properties of the cyclodextrins for particular applications, it is possible to introduce many different chemical moieties in place of the OH- groups present on the upper and lower parts of the toroid. CDs can be rendered hydrophilic (methylated, hydroxyalkylated, branched), hydrophobic (alkylated, acylated) or ionisable (anionic CDs). Hydrophilic CDs may be used to improve the low dissolution of poorly water-soluble drugs, enhancing bioavailability, while hydrophobic CDs act as sustained release carriers for water soluble drugs, or those showing short biological half-lives [9, 10].

### 6.1.4 Triacetylated-β-cyclodextrin (TAβCD)

The structure of TAβCD along with the detail of its repeating unit are shown in Figure 6-3.

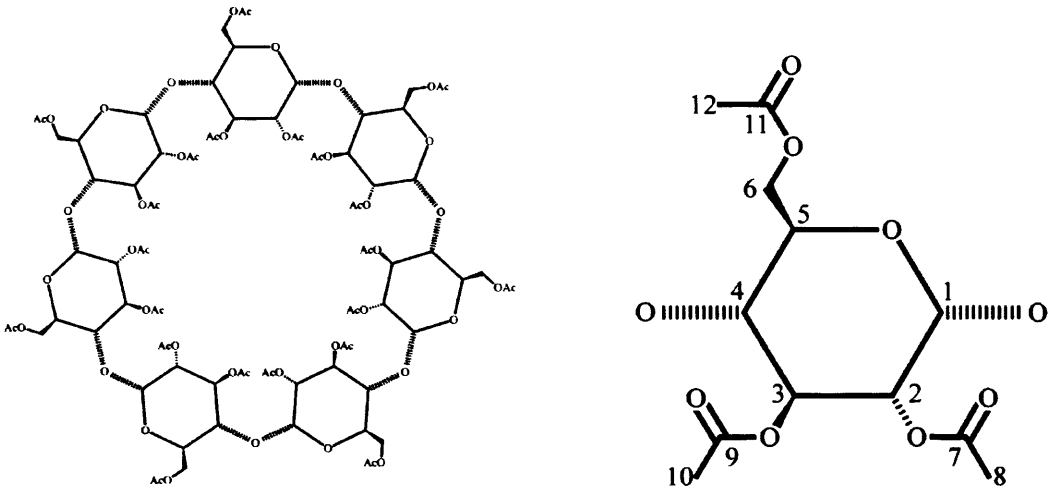


**Figure 6-3 TAβCD structure (left) and close up on its repeating unit (right).**

Previous studies have already highlighted TAβCD as a sustained release carrier for various drugs such as azydothymidine (potent anti-AIDS active) [11], or nicardipine hydrochloride (a calcium channel blocker) [12, 13]. It can also be of use for homogeneous catalysis, where organometallic catalysts such as diphenyl(4-phenylpheny)phosphine form inclusion complexes with TAβCD in order to increase their solubility in the medium of interest [14, 15]. Thus in this case, the combination of TAβCD as the excipient and HPFP as the propellant is a promising line of investigation [16].

In this study, TAβCDs from various suppliers showed very different behaviours in HPFP, despite being chemically identical. Polymorphism for this compound was first reported in 2006 by Bettinetti *et al.* [17], and whilst Añibarro *et al.* [18] solved the crystal structure of the methanolate solvate, no implications of polymorphism on their behaviour in liquid or solid formulations have been published to date.

The four commercial samples of triacetyl-β-cyclodextrin (TAβCD) used in the following study were purchased from three different suppliers: Aldrich (**A1**: Lot S05254-263 and **A2**: Lot S35068), Cyclolab (**C**: batch number CYL-2116) and

Molekula (**M**: batch number 21619) and are referred to as TAβCD-A1, TAβCD-A2, TAβCD-C and TAβCD-M respectively. A series of triacetyl-β-cyclodextrin samples was prepared by melting then cooling amounts of TAβCD-A1, TAβCD-A2, TAβCD-C or TAβCD-M (denoted TAβCD-Melt) and by dissolving TAβCD of all origins in HPFP, then evaporating the solvent at room temperature (denoted TAβCD-HPFP).

## 6.2 Results

### 6.2.1 Preliminary solubility study

Figure 6-4 presents the physical appearance of samples made of 10 wt% TAβCD-A1 and TAβCD-C in HPFP, at room temperature after 24 hours equilibration time, shaken (a) or left still (b). In the two pictures, TAβCD-A1 is in the left-hand vial and TAβCD-C in the right-hand one.

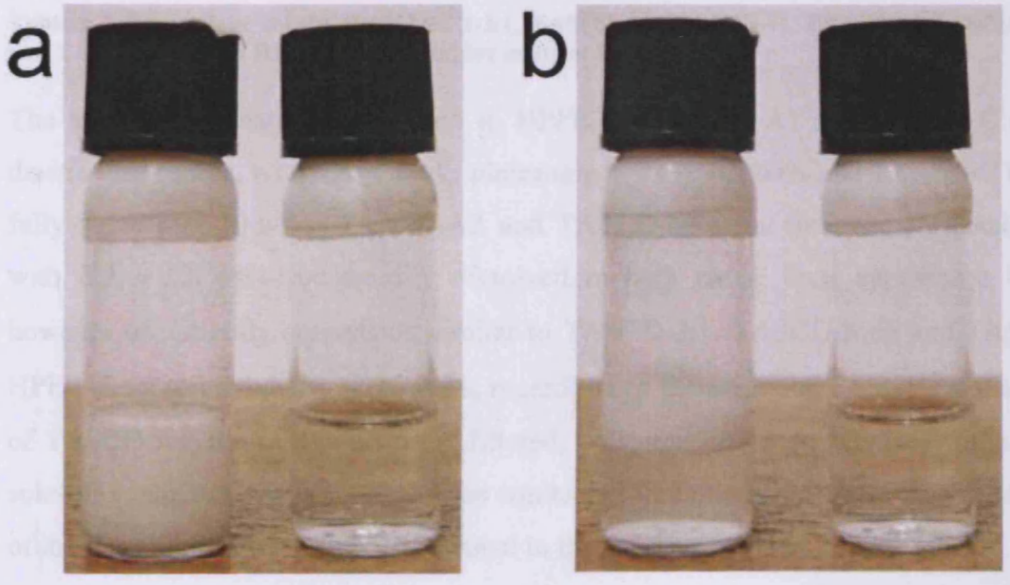


**Figure 6-4 Physical appearance of 10wt% TAβCD-A1 (left-hand vial) and TAβCD-C (right-hand vial) in HPFP at room temperature, shaken (a) or left still (b).**

While all TAβCD-C was successfully dissolved, most TAβCD-A1 remained as a suspension in HPFP, rendering the sample an opaque white. With time, the turbid sample eventually underwent creaming, leading to a lower layer of mostly dense HPFP ($\rho$ = 1.595 g cm$^{-3}$) and a white upper layer of insoluble TAβCD-A1, as seen in Figure 6-4(b). Samples were kept over 5-month periods with no changes in

appearance. Dry weight results from initial 10 wt% samples of TAβCD-A1, TAβCD-A2, TAβCD-C TAβCD-M, TAβCD-Melt and TAβCD-HPFP after a 24-hour equilibration time are shown in Table 6-2.

| Sample | Amount dissolved after 24 hrs / wt% |
|---|---|
| TAβCD-A1 | 1.5 ± 0.2 |
| TAβCD-A2 | 6.7 ± 0.2 |
| TAβCD-M | 6.7 ± 0.2 |
| TAβCD-C | 10.0 ± 0.1 |
| TAβCD-Melt | 10.0 ± 0.1 |
| TAβCD-HPFP | 10.0 ± 0.1 |

**Table 6-2 Dry-weight results for TAβCD-A1, TAβCD-A2, TAβCD-C, TAβCD-M TAβCD-Melt and TAβCD-HPFP in HPFP. Initial samples made at 10 wt%.**

The amounts of material dissolved in HPFP for TAβCD-A1 and TAβCD-C show drastic differences, with TAβCD-A1 plateauing at 1.5 ± 0.2 wt% and TAβCD-C being fully soluble at 10 wt%. TAβCD-A2 and TAβCD-M show intermediate solubility, with 6.9 ± 0.2 wt% successfully dissolved in both cases, their appearance being however of a cloudy suspension similar to TAβCD-A1. TAβCD-Melt and TAβCD-HPFP show full solubility at 10 wt%, regardless of the origin of TAβCD. In the case of TAβCD-A1, the insolubles were filtered, collected, dried and re-used for further solubility experiments. This cycle was conducted three times in a row. The solubility of the "insolubles" was found to be equal to that of the raw powder TAβCD-A1.

The maximum solubility of raw TAβCD-C was assessed and it was found that 20 wt% could be successfully solubilized. Higher concentrations were not investigated due to an increase in the viscosity, rendering it impossible for the solution to pass through the 0.2 μm filter. However, such high concentration samples remained clear and homogeneous. Similar concentrations were obtained using TAβCD-HPFP (collected from the dry-weight assays), and TAβCD-Melt obtaining clear, homogeneous samples.

### 6.2.2 Kinetics of solubilisation

The dissolution of TAβCD was measured as a function of time on samples made at initially 10 wt% TAβCD-A1, TAβCD-A2, TAβCD-C and TAβCD-M in HPFP, for time intervals ranging from 3 seconds (immediately after the addition of the fluorinated solvent to TAβCD) to one month. Results are presented in Figure 6-5 below. The lines do not represent fits but are a guide to the eye.

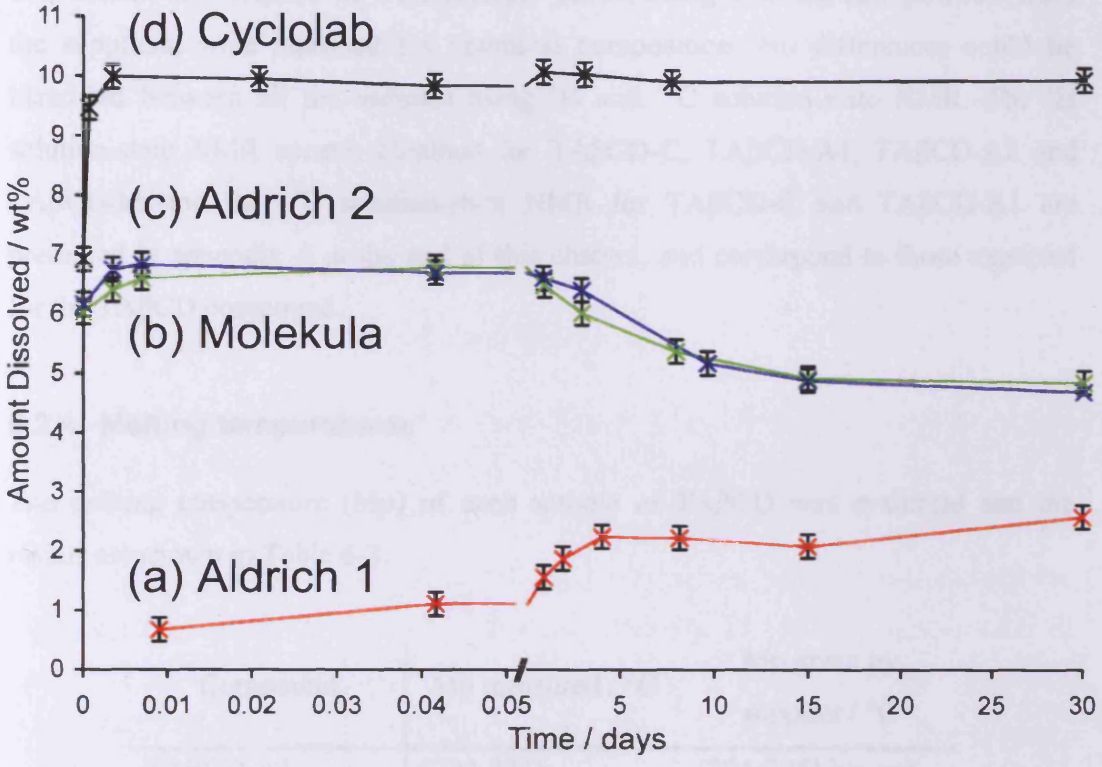


**Figure 6-5 Amount of TAβCD dissolved in HPFP measured via $^1$H-NMR as a function of time for TAβCD-A1(a), TAβCD-M (b), TAβCD-A2 (c) and TAβCD-C (d). Initial samples made at 10 wt%.**

Immediately after the addition of HPFP ($t_0$), the TAβCD-C concentration already equals 6.9 ± 0.2 wt% and further increases to plateau at 10.0 ± 0.2 wt% after 5 min. The concentration then does not vary until the end of the experiment after 30 days. All TAβCD-C is fully solubilised in HPFP. TAβCD-A1 solubility is much lower, as expected from the preliminary solubility study, and equals 0.7 ± 0.2 wt% after 13 min. It then increases to reach a plateau region of 2.2 ± 0.2 wt% after four days. Both TAβCD-A2 and TAβCD-M show very similar solubility profiles as a function of time. After 10 min, a maximum solubility of 6.8 ± 0.2 wt% is measured for both samples, which from then decreases to 4.7 ± 0.2 wt% after 30 days. The kinetics

experiments were not continued further than this one month period but the present results give a good indication of the different processes taking place, and will be discussed later.

### 6.2.3 Chemical composition

TAβCD from dry-weight experiments was collected and insolubles from TAβCD-A1, TAβCD-A2 and TAβCD-M were filtered. These, along with the raw powders from the suppliers, were analysed for chemical composition. No differences could be identified between all the samples using $^{1}H$ and $^{13}C$ solution-state NMR. The $^{1}H$ solution-state NMR spectra obtained for TAβCD-C, TAβCD-A1, TAβCD-A2 and TAβCD-M and the $^{13}C$ solution-state NMR for TAβCD-C and TAβCD-A1 are presented in appendix A at the end of this chapter, and correspond to those expected for the TAβCD compound.

### 6.2.4 Melting temperatures

The melting temperature (Mp) of each sample of TAβCD was evaluated and the results are shown in Table 6-3.

| Compound | Mp measured / °C | Mp given by supplier / °C |
|---|---|---|
| TAβCD-A1 | (220-224) | (204-206) litt. val. |
| TAβCD-A2 | (191-194)<br>(220-223) | (204-206) litt. val. |
| TAβCD-C | (201-203) | Not given |
| TAβCD-M | (190-194)<br>(218-220) | Not given |
| TAβCD-Melt | (140-224) | n/a |
| TAβCD-HPFP | (140-224) | n/a |

**Table 6-3 Melting points measured for the various TAβCDs - Comparison to the supplier's data.**

Two melting points were found for TAβCD-A2 and TAβCD-M. Some of the raw material melted at the lowest temperature-range indicated, the melting process then stopped until the 2nd temperature range was reached where all remaining material melted. The two temperature ranges were sharp and well resolved. TAβCD-HPFP and TAβCD-Melt both showed a very broad melting temperature range, that was more reminiscent of a glass transition with a decreasing viscosity upon temperature increase, than a sharp melting transition. Finally, values given by Aldrich on their datasheet were not found to correspond to the measured temperatures. This was further investigated by contacting Aldrich, whose explanation was that if their compound showed a higher melting point, then it was purer than the one used for the literature data. This melting behaviour was further investigated via differential scanning calorimetry.

### 6.2.5 Differential Scanning Calorimetry (DSC)

Figure 6-6 presents the DSC curves for the raw material TAβCD-C, TAβCD-A1 and TAβCD-A2 in standard runs. When the temperature increase is performed at 10 °C $min^{-1}$(Figure 6-6 b), TAβCD-C presents two melting points, at 194 ± 1 °C and at 219 ± 1 °C. When the ramp is carried out at 30 °C $min^{-1}$ (Figure 6-7 a), only the lower melting point is observed. TAβCD-A1 melts at a single temperature of 219 ± 1 °C. TAβCD-A2 shows two melting points at 185 ± 1 °C and 215 ± 1 C. TAβCD-M shows a very similar thermograph to TAβCD-A2: the melting temperatures are identical but the ratio of the endotherms appears to be very slightly different. On the cooling ramp, no recrystallization peak appears, but an endothermic step is observed for all samples at 120-134 °C, similar to a glass transition.

Figure 6-7 presents the DSC curves for (a) TAβCD-C using a temperature ramp of 30 °C $min^{-1}$, (b) TAβCD-C with a 2 hour temperature hold at 150 °C, (c) TAβCD-C with a 1 hour temperature hold at 210 °C (d) a two-cycle run on TAβCD-A1. By exposing the TAβCD-C sample for timed periods at 150 °C (below its melting point) in the DSC apparatus, it was possible to witness the melting peak at 219 ± 1 °C become enhanced and that at 194 ± 1 °C diminish. In a similar manner, by exposing the TAβCD-C sample for timed period at 210 °C (above its lower melting point) in the DSC apparatus, with a temperature ramp from –50 °C to 210 °C of 10 °C $min^{-1}$ ,

the higher melting peak was enhanced. For the two-cycle run on TAβCD-A1, on the first heating ramp a sharp melting peak is observed at 219 ± 1 °C while it is absent from the second heating ramp in which only a shallow endothermic step at 123-137 °C is detected.

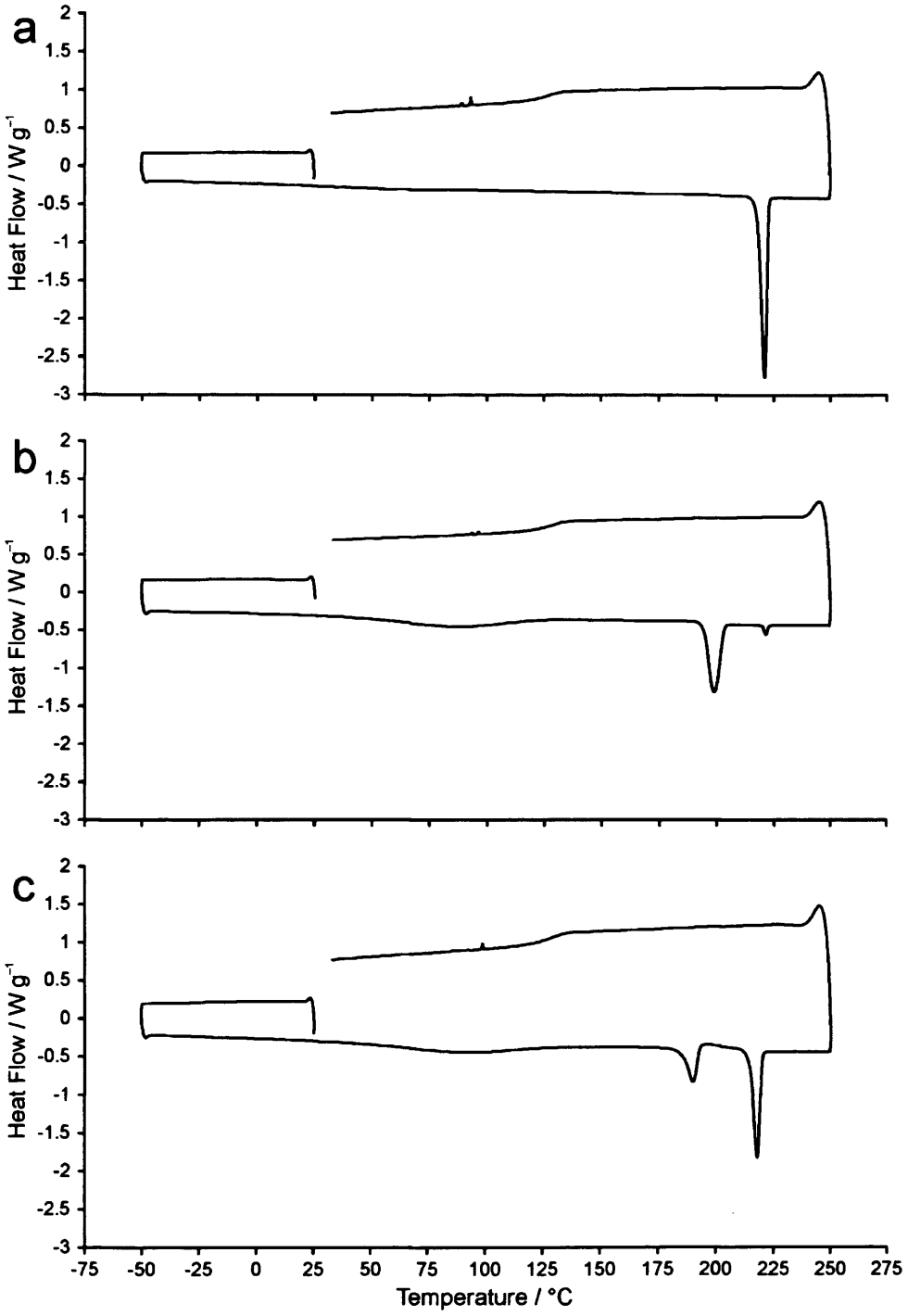


**Figure 6-6 DSC curves for (a) TAβCD-A1, (b) TAβCD-C, (c) TAβCD-A2.**

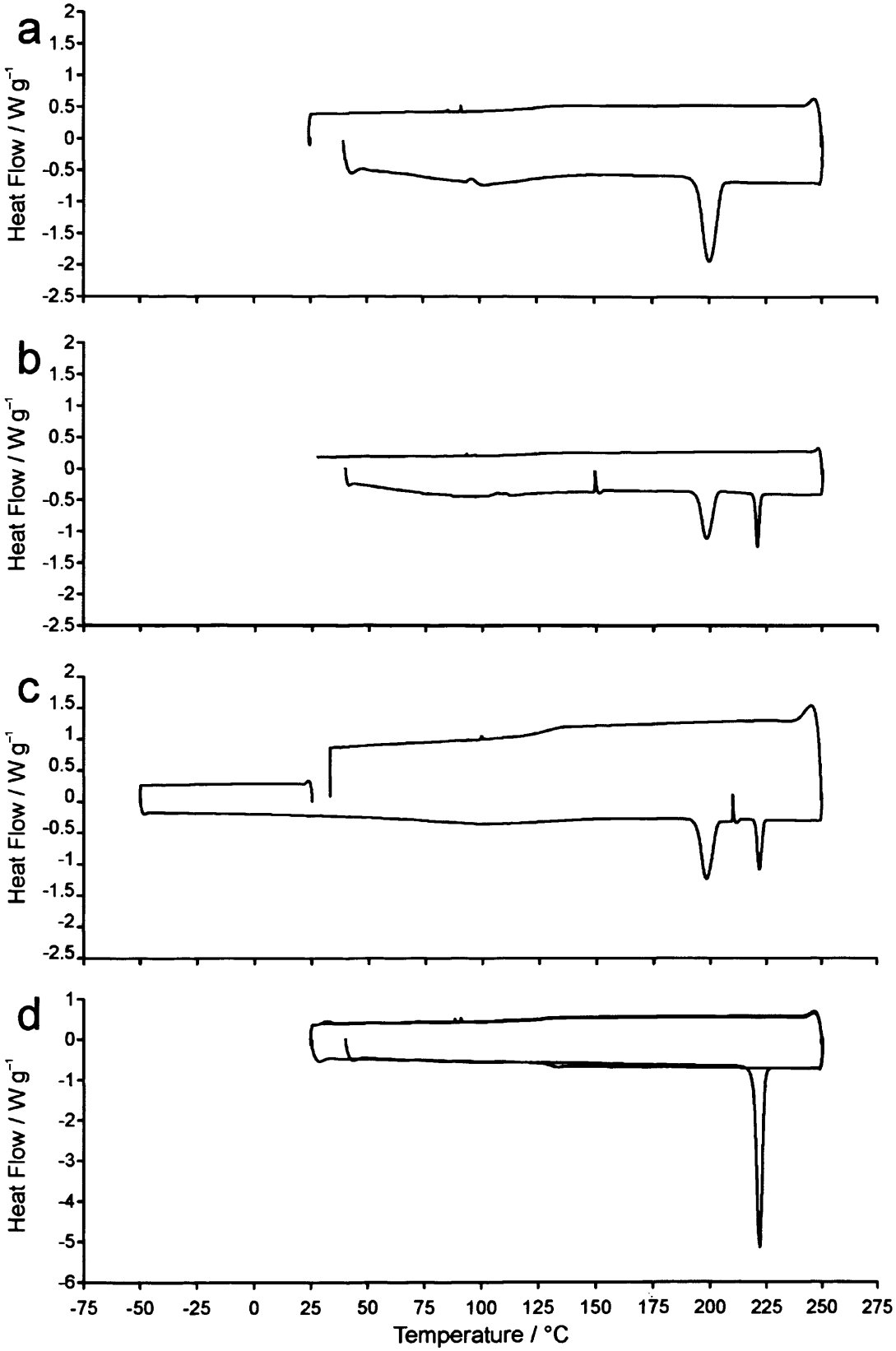


**Figure 6-7 DSC curves for (a) TAβCD-C using a temperature ramp of 30 °C min$^{-1}$, (b) TAβCD-C with a 2 hour temperature hold at 150 °C, (c) TAβCD-C with a 1 hour temperature hold at 210 °C (d) a two-cycle run on TAβCD-A1.**

### 6.2.6 Thermogravimetric analysis

The raw materials were investigated for mass loss via TGA measurements. A maximum initial loss of 0.7 wt% occurring between 25 °C and 45 °C was observed for all samples, as seen in Figure 6-8.

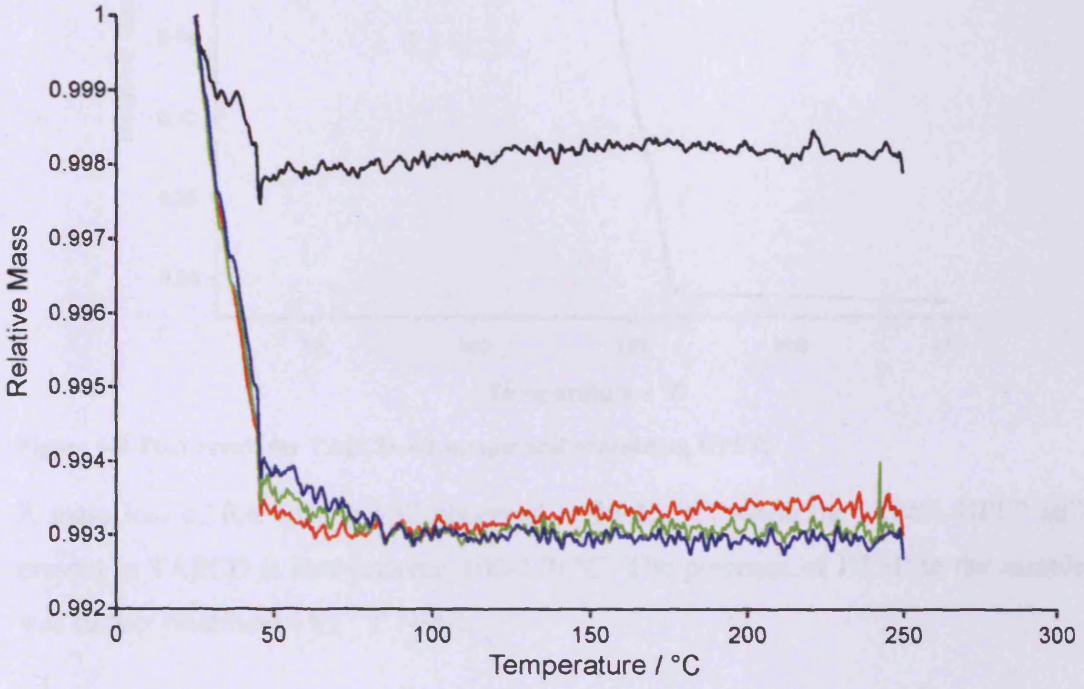


**Figure 6-8 TGA results for TAβCD-A1 (black), TAβCD-C (red), TAβCD-A2 (green) and TAβCD-M (blue).**

No further losses were observed on the entire temperature range (up to 250 °C). As a comparison, a sample from dry-weight experiments that still held HPFP solvent was run. The thermograph is presented in Figure 6-9.

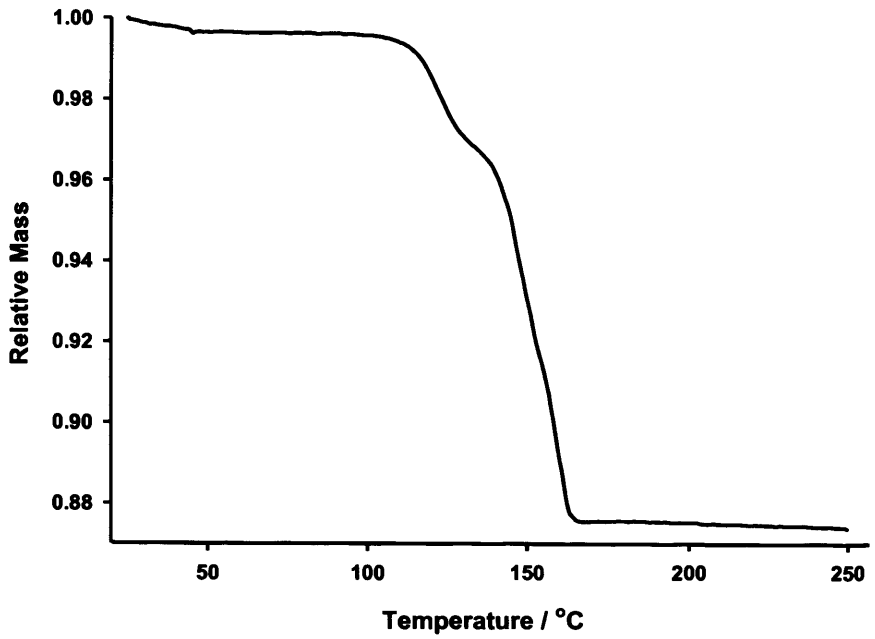


**Figure 6-9 TGA result for TAβCD-A2 sample still containing HPFP.**

A mass loss of 0.4 wt% is still observed at 25-45 °C, while the 12wt% HPFP still present in TAβCD is lost between 100-170 °C. The presence of HPFP in the sample was further established by $^{19}F$ NMR.

### 6.2.7 Scanning Electron Microscopy (SEM)

The digital images taken for TAβCD-A1, TAβCD-C and TAβCD-M raw powders at a magnification of 5000 are shown in Figure 6-10, along with pictures of TAβCD-A1 and TAβCD-C at a magnification of 500. TAβCD-A1 raw powder appears as a relatively narrow distribution in size of regular parallelepipedic blocks, of typical dimension 20×10×5 $\mu m^3$. Fine powder of no specific shape is present on the blocks and confers an impression of roughness. TAβCD-C appears as smooth-surfaced flat plates with sharp and regular angles, reminiscent of truncated hexagonal shapes, but with a wider distribution in size, ranging from 9 μm to 60 μm wide. Some smaller pieces that seem to come from broken plates lie on the surface. TAβCD-C also appeared to be much softer, as it was very easily deformed and cracked by repeated exposure to the electron beam. TAβCD-M appears as a heterogeneous mixture of very small particles and big blocks of no particular shape, with dimensions ranging from 0.4 μm to 11 μm.

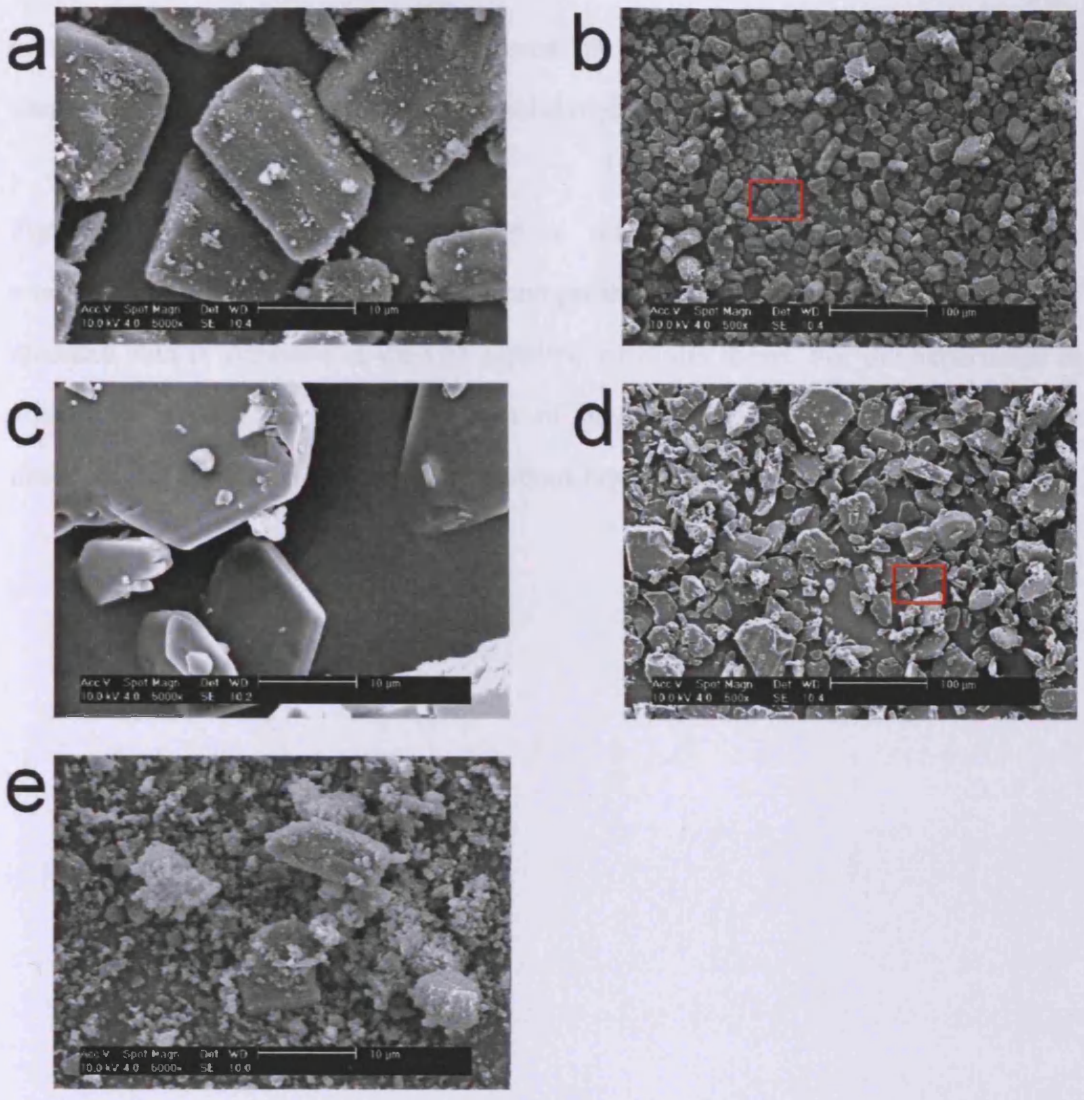


**Figure 6-10. SEM digital images captured at a magnification of 5000 for (a) TAβCD-A1, (c) TAβCD-C and (e) TAβCD-M and at a magnification of 500 for (b) TAβCD-A1 and (d) TAβCD-C. The red boxes in (b) and (d) indicate where the close-ups were taken for (a) and (c) respectively.**

### 6.2.8 Optical microscopy

As the temperature of the heating stage is raised to 180 °C, TAβCD-Melt becomes a viscous liquid and the small amount of TAβCD-A1 that was sprinkled on top remains solid. The liquid is isotropic, as investigated under a cross-polarizer. With time, the liquid TAβCD-Melt starts crystallizing and after five hours, almost the entire surface appears crystalline. To be fully certain the entire volume of the melt has successfully

crystallised, the experiment was continued for a further six hours at 180 °C. The temperature at which the newly formed solid melts is found to be 220 °C.

Figure 6-11 presents snapshots taken at different timed intervals during the recrystallization process. A 1000-time compressed video version of the 12 hours of recorded data is available in the CD supplied with this thesis. For the experiment in which the TAβCD-Melt piece is free of any TAβCD-A1, no crystallization is observed and the sample remains as a viscous liquid when held at 180 °C.

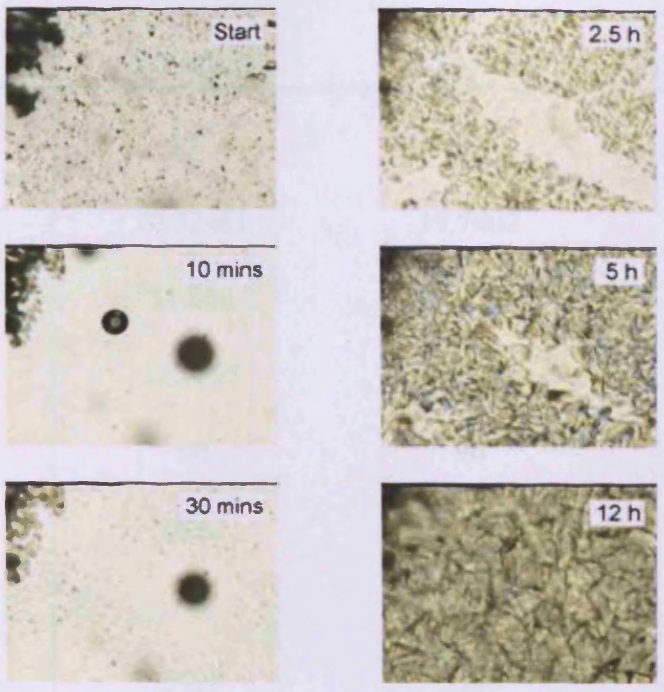


**Figure 6-11. Selected images from the recrystallization process of TAβCD-Melt at 180 °C, taken via an optical microscope linked to a personal computer.**

### 6.2.9 Additional results

The following data are the result of measurements performed and analysed by Dr. Colan E. Hughes and are needed to understand to full picture of this polymorphic system.

#### 6.2.9.1 Powder X-Ray Diffraction

Powder X-ray diffraction patterns were obtained on all four commercial samples of triacetyl-β-cyclodextrin. The patterns are shown in Figure 6-12. For TAβCD-C and TAβCD-A1, Le Bail fits were carried out and the space groups and cell parameters obtained are presented in Table 6-4, along with those obtained by Añibarro *et al.*[18] for the crystal structure of the methanolate.

| | α-TAβCD | β-TAβCD | TAβCD ·MeOH |
|---|---|---|---|
| Space Group | $P2_1$ | $P2_1$ | $P2_1$ |
| a/Å | 20.22461 | 19.7402 | 11.576 |
| b/ Å | 21.308 | 23.1595 | 21.105 |
| c/ Å | 11.6895 | 14.2492 | 20.3 |
| α | 90 | 90 | 90 |
| β | 86.61 | 124.79 | 93.58 |
| γ | 90 | 90 | 90 |
| Volume/ $Å^3$ | 5029 | 5350 | 4950 |

**Table 6-4. Space groups and cell parameters for α-TAβCD, β-TAβCD (at 20 °C) and the methanolate as reported by Añibarro *et al.*[18] (at –133 °C).**

The result of the Le Bail fit is shown in Figure 6-13. X-ray diffraction patterns for TAβCD-A2 and TAβCD-M were a combination of those of TAβCD-C and TAβCD-A1, clearly indicating that such sample contained mixtures of the two polymorphs. Both TAβCD-Melt and TAβCD-HPFP gave patterns with no diffraction peaks.

The volumes of the unit cells are 5029 and 5350 $Å^3$, compared to 4946 $Å^3$ for the published methanolate crystal structure [18], which also has space group $P2_1$ but which was acquired at –133 °C. It therefore seems likely that, as for the methanolate, this structure has a single molecule in the asymmetric unit, with two molecules of TAβCD in the unit cell. For such unit cell volumes, it was possible to calculate the densities of TAβCD-A1 and TAβCD-C, which were found to be equal to 1.333 and 1.256 g $cm^{-3}$, respectively.

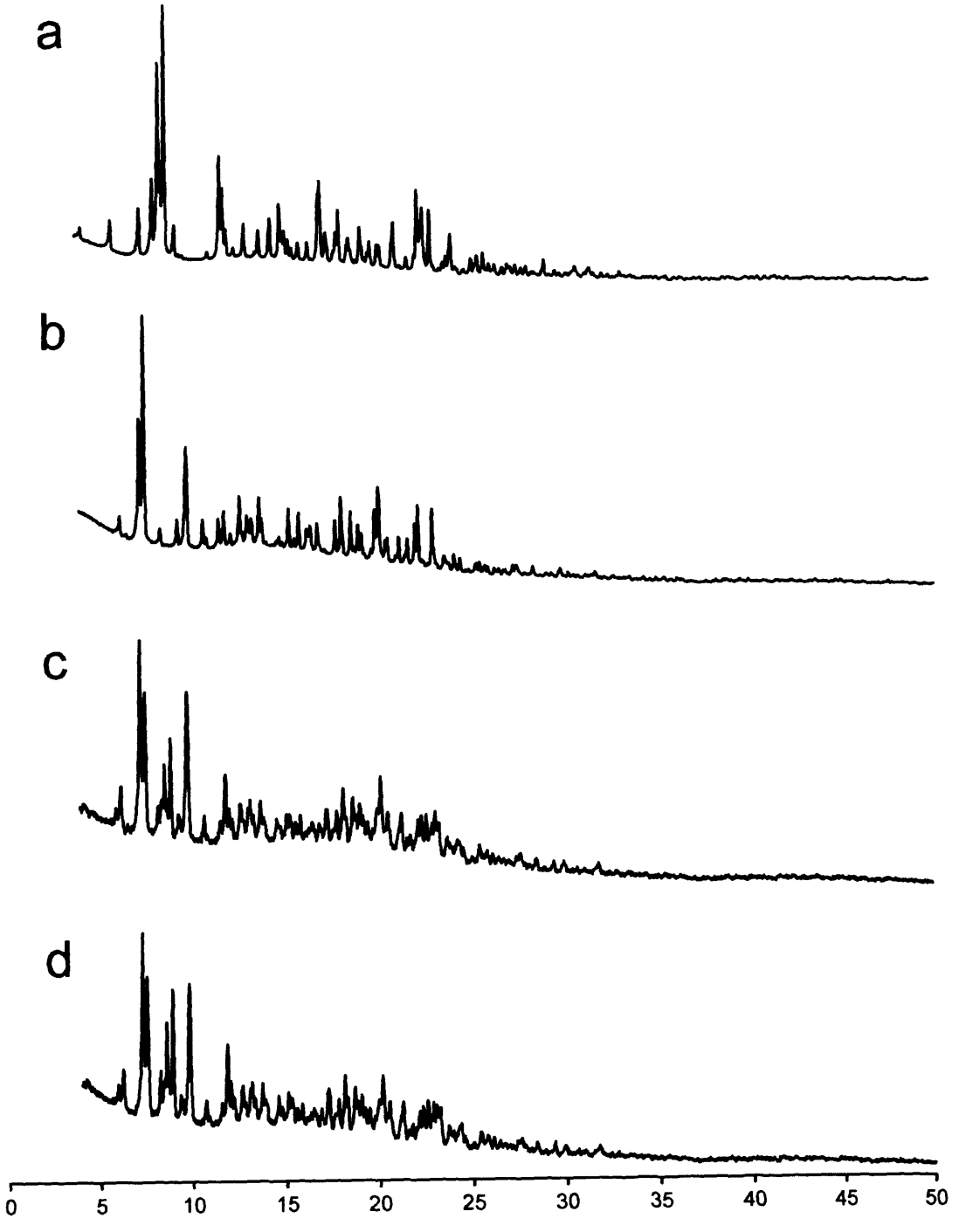


**Figure 6-12. Powder X-ray diffraction patterns for (a) TAβCD-A1, (b) TAβCD-C, (c) TAβCD-A2, (d) TAβCD-M, recorded with thanks by Dr. C. E. Hughes.**

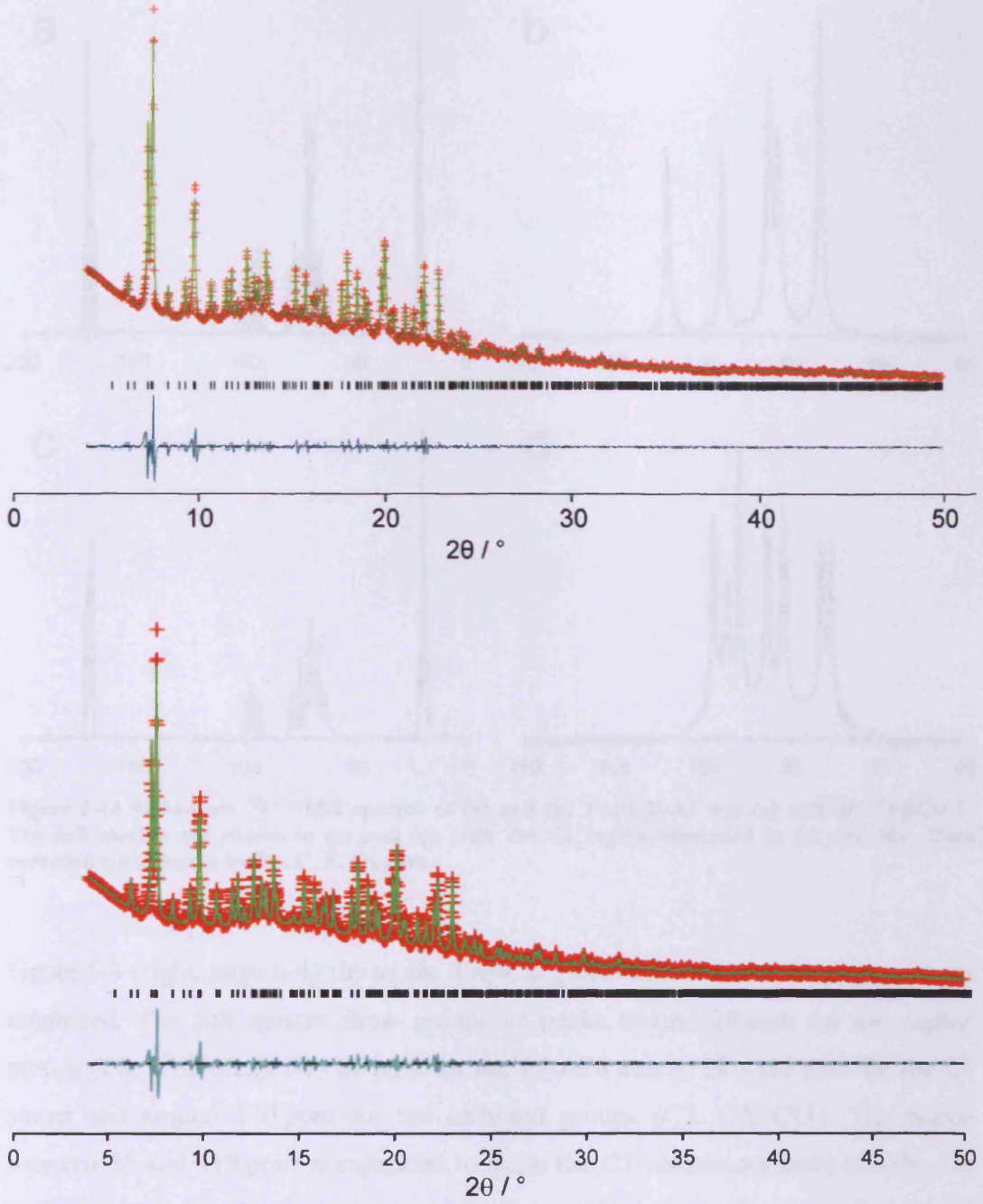


**Figure 6-13 Le Bail fits for the powder X-ray diffraction pattern of (top) TAβCD-A1 and (bottom) TAβCD-C. The red crosses are the experimental data, the green line is the fit and the blue line is the error. Analysis performed with thanks by Dr. C. E. Hughes.**

### 6.2.9.2 Solid-state NMR

Solid-state NMR spectra were obtained for the TAβCD-A1 and TAβCD-C samples and are show in Figure 6-14.

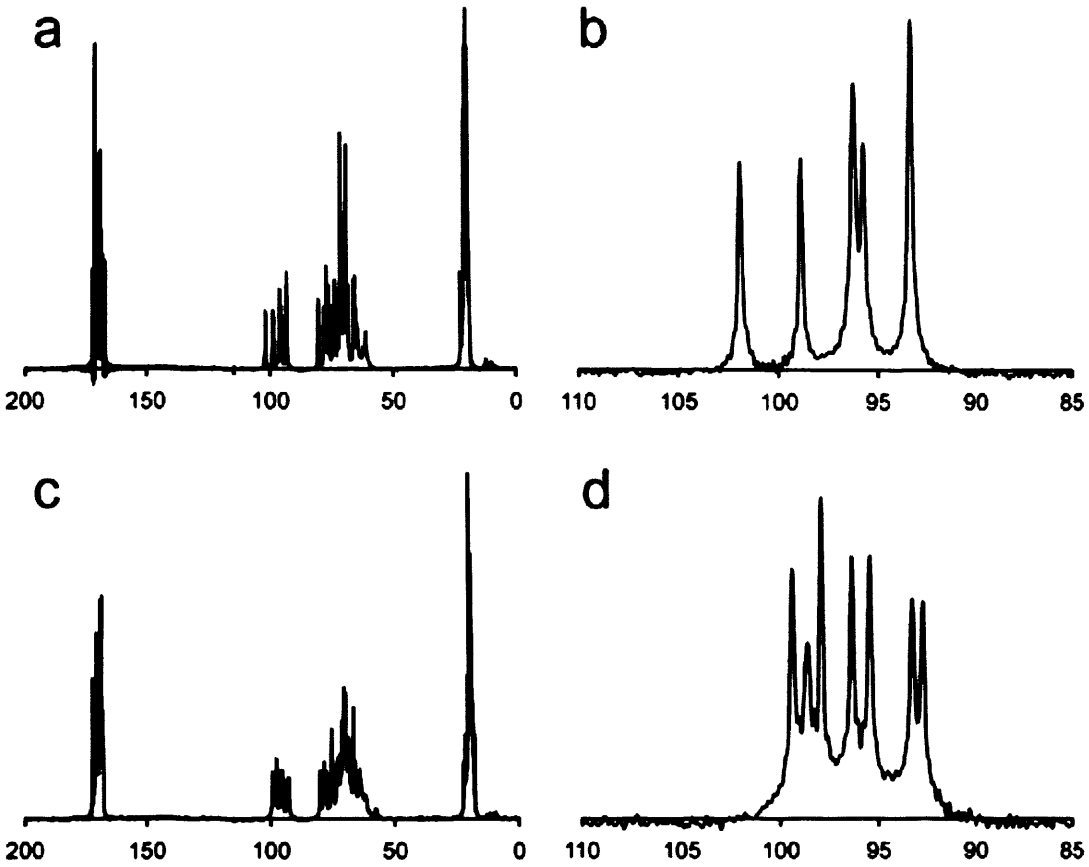


**Figure 6-14 Solid-state $^{13}C$ NMR spectra of (a) and (b) TAβCD-A1 and (c) and (d) TAβCD-C. The full spectra are shown in (a) and (c), with the C1 region expanded in (b) and (d). Data recorded with thanks by Dr. C. E. Hughes.**

Figure 6-3 (right, page 6-4) shows the TAβCD glucosidic unit with the carbon atoms numbered. The full spectra show groups of peaks around 20 ppm for the methyl groups (C8, C10, C12), 60 - 80 ppm for the C2 - C6 atoms, 90 - 105 ppm for the C1 atoms and around 170 ppm for the carbonyl groups (C7, C9, C11). The region between 85 and 110 ppm is expanded to show the C1 resonances more clearly. For each molecule in the asymmetric unit, there will be up to seven distinct C1 resonances, one for each of the seven sugars in the β-cyclodextrin ring. Five resonances were observed for the TAβCD-A1 sample and seven for the TAβCD-C sample. In Tables 6-5 and 6-6 are given the intensities of the peaks, obtained by fitting to Lorentzian linehapes.

| Frequency | Intensity |
|---|---|
| 93.37 | 27.54% |
| 95.73 | 15.77% |
| 96.26 | 25.76% |
| 98.89 | 14.45% |
| 101.91 | 14.53% |

**Table 6-5 Intensities of the fitted C1 peaks for TAβCD-A1, scaled as a percentage of the total intensity.**

| Frequency | Intensity |
|---|---|
| 92.75 | 9.17% |
| 93.31 | 14.52% |
| 95.45 | 15.78% |
| 96.39 | 16.02% |
| 97.93 | 13.53% |
| 98.64 | 13.74% |
| 99.40 | 12.45% |

**Table 6-6 Intensities of the fitted C1 peaks for TAβCD-C, scaled as a percentage of the total intensity.**

For TAβCD-A1, it was found that the five peaks are in the approximate ratio 2:1:2:1:1, indicating that the peaks at 93.37 and 96.26 ppm represent two C1 resonances, whilst the others each represent a single resonance. For TAβCD-C, only the peak at 92.75 ppm stands out as being less intense than the others. This may be due to a distortion of the fitting from the overlap of the adjacent peak. Otherwise, it appears that, for TAβCD-C, all seven expected C1 resonances have distinct chemical shifts. TAβCD-Melt gave a $^{13}C$ spectrum in which broad signals were seen in all four spectral regions identified. No sharp peaks were observed.

## 6.3 Discussion

The molecular structure of the different suppliers' TAβCDs are found to be identical but their behaviour in model propellant HPFP shows striking variations, going from a maximum solubility of 2.2 ± 0.2 wt% for TAβCD-A1 to over 20 wt% for TAβCD-C,

with intermediate solubilities for TAβCD-A2 and TAβCD-M. Such behaviour is very reminiscent of polymorphism.

X-ray powder diffraction indeed shows two distinctive patterns for TAβCD-A1 and TAβCD-C, with no overlap between the peaks present, indicating the presence of distinct crystalline phases in these two samples. By contrast, the patterns for TAβCD-A2 and TAβCD-M are a combination of the patterns for TAβCD-A1 and TAβCD-C, indicating the presence of a mixture of the two crystalline forms. The indexing of the patterns for TAβCD-A1 and TAβCD-C was attempted in order to obtain the crystallographic unit cells, assuming a single phase to be present in both cases. For TAβCD-C and TAβCD-A1, Le Bail fittings were carried out and a unit cells obtained, with volumes of 5350 $Å^3$ and 5029 $Å^3$ , compared to a value of 4946 $Å^3$ for the published methanolate crystal structure [18], which also has space group $P2_1$. As for the methanolate, TAβCD-C and TAβCD-A1 structures have a single molecule in the asymmetric unit, with two molecules of TAβCD in the unit cell. In the case of TAβCD-C, this was confirmed by solid-state $^{13}C$ NMR, which showed seven distinct resonances for the C1 nuclei, one for each of the seven C1 carbon atoms in one molecule. For TAβCD-A1, only five resonances were observed which therefore did not indicate the presence of more than one molecule in the asymmetric unit or more than one crystalline phase.

TGA measurements showed a maximum mass loss of 0.7 wt% at relatively low temperatures (25 - 45 °C). No further losses were observed over the entire temperature range (up to 250 °C). 0.7 wt% is below the theoretical value for TAβCD·$H_2O$, which would show a mass loss of 0.9 wt%. As it is not possible to have a fraction of a water molecule per molecule of TAβCD in a $P2_1$ unit cell, it could be concluded that this mass loss is not due to the loss of crystalline water, i.e. a stoichiometric hydrate. This and the relatively low temperature range in which the mass loss occurs suggest that the mass loss is due to either instrumental instability at the beginning of the measurements or ambient moisture and not to an inclusion complex or water present in the crystal structure. As a means of comparison, TGA was performed on a sample of TAβCD taken from a solution in HPFP which is known from $^{19}F$ NMR to contain some HPFP. This also showed a small mass loss at

the lower temperatures, along with a 12 wt% mass loss due to HPFP between 100 - 170 °C.

These results may be compared to those of Bettinetti *et al.* [17], where mass losses of 1.58 ± 0.003 wt% ($T_{onset} \approx 126°C$) are observed for the methanolate and 2.8 wt% at 18 - 103 °C and 1.05 wt% at 109 - 136 °C are observed for the isopropanolate-hydrate.

At this point, it is possible to make the following assignment. Since TAβCD-A1 and TAβCD-C are distinct, solvent-free, crystalline phases, they can be identified as two polymorphs of TAβCD. They are assigned as the α polymorph (TAβCD-A1) and β polymorph (TAβCD-C). TAβCD-A2 and TAβCD-M are mixtures of these two polymorphs, in very similar ratios as their respective solubilities are identical within the error bars.

The two polymorphs differ in their melting point, with 194 ± 1 °C and 219 ± 1 °C for forms β and α respectively. For TAβCD-C, a small amount of the α polymorph can be observed in the DSC when the temperature is increased at a rate of 10 °C $min^{-1}$. However, if the temperature is increased at a rate of 30 °C $min^{-1}$, this polymorph cannot be seen, implying that there is a degree of conversion from the β to the α polymorph at high temperatures. By exposing the TAβCD-C sample for timed periods at 150°C (below its melting point) in the DSC apparatus, it was possible to witness the α polymorph melting peak appearing and β polymorph peak diminishing, in full agreement with the high temperature X-ray powder diffraction results. It is thus possible to obtain the higher melting-point and more stable polymorph form α from form β by exposing it to a temperature that is lower than its melting point, i.e., the transformation from β to α is not due to recrystallization from the melt.

During the cooling ramp, no recrystallization peak appears but a step is observed for all samples at 120 - 134 °C, corresponding to a glass transition. When recovering the material at the end of the run, its appearance is indeed that of a glassy state. This was confirmed by a two-cycle run on TAβCD-A1. On the first heating ramp, a sharp melting peak at 219 ± 1 °C is observed while it is absent from the second heating

ramp in which only a shallow endothermic step at 123 - 137 °C, the glass transition, is detected.

It is also possible to obtain polymorph α on its own by recrystallizing a melt. As witnessed via optical microscopy, a sample of TAβCD-Melt held above its glass transition temperature in the presence of a very limited amount of TAβCD-A1 fully crystallizes. The sharp melting of the newly formed solid is observed at 220 °C, which corresponds to TAβCD-A1 melting temperature. It is thus possible to ascertain the presence of polymorph α, obtained via deliberate seeding. When TAβCD-A1 is not present, no recrystallization occurs, the sample remains liquid. This suggests that in order to recrystallize into form α, the presence of some polymorph α, even in very small quantities, is required. Polymorph α acts as a seed for the recrystallization process and allows it to be initiated. This phenomenon is also witnessed in the DSC experiments. The form α melting peak is enhanced when a TAβCD-C sample is held at 210 °C, thus past form β melting point but below form α one. As seen previously, the heating ramp allowed for some conversion of form β to form α, that in turn was able to seed and initiate the recrystallization of the melt. When increasing the speed of the temperature ramp to 60 °C $min^{-1}$ in order to avoid, or try to minimize as much as possible the formation of form α, and holding the melt at 210 °C similarly to the previous experiment, form α melting peak was still observed. This experiment was therefore not fully conclusive but showed that even at high speeds of temperature increase, it is difficult to prevent any β to α conversion from taking place. It also showed that very limited amounts of form α are sufficient to seed the crystallisation process.

The solubility could also be influenced by the size and shape of the raw powder. However, although particles from highly soluble TAβCD-C appear flatter and of smoother surface, they remain only slightly larger than poorly soluble TAβCD-A1 ones. TAβCD-M, of intermediate solubility, shows a wide range of particle sizes. No correlation could be found between the size and shape of the powder particles and the observed solubility in HPFP.

The solubility results can now be reassessed based on the knowledge of the polymorphic content of the different commercial samples. TAβCD-C is a single phase crystalline material solely composed of the lower melting point β polymorph. At least 20 wt% can be solubilized in HPFP. Both TAβCD-HPFP and TAβCD-Melt showed no diffraction pattern and are amorphous, regardless of their initial source (TAβCD-A1, TAβCD-A2, TAβCD-C or TAβCD-M), and solubilization of 20 wt% in HPFP could be achieved. TAβCD-A1 showed a distinct crystalline phase to TAβCD-C. This higher melting point α polymorph exhibited a very limited solubility in HPFP, inferior to 3 wt%. TAβCD-A1 contained no amorphous material as the solubility of the filtered insolubles was equal to that of the batch powder. As can be expected, form α being the most stable (having the higher melting temperature) and most dense polymorph, it showed the least solubility [4]. TAβCD-A2 and TAβCD-M are mixtures of the two previously described polymorphs in very similar ratios, showing intermediate solubility.

The kinetics of solubility showed some interesting features over a course of 30 days. Solubility of both TAβCD-A1 and TAβCD-C increase with time, TAβCD-A1 reaching a plateau value of 2.2 ± 0.2 wt% after 4 days and TAβCD-C being fully solubilised after only 5 mins. However, the solubility of TAβCD-A2 and TAβCD-M decreased with time, its maximum at 6.8 ± 0.2 wt% after 10 min and decreasing to 4.7 ± 0.2 wt% after 30 days. The hypothesis is that the successfully dissolved TAβCD, present in the liquid in an amorphous state, is in contact with the remaining insolubles of form α that sit on the fluorinated liquid surface (ρ HPFP = 1.595 g $cm^{-3}$, ρ TAβCD-A1 = 1.333 g $cm^{-3}$). Form α could therefore seed the crystallisation of the dissolved TAβCD into form α, which crystals would in turn come out of solution due to the much limited solubility of polymorph α, thus provoking a decrease in the amount of TAβCD present in solution.

## 6.4 Conclusion

Polymorphism was brought to light in commercial samples of TAβCD by their very different behaviours in CFC-free liquid model propellant 2H, 3H-decafluoropentane. X-ray powder diffraction showed that two polymorphs were present either on their own (form α in TAβCD-A1 and form β in TAβCD-C), or as mixtures of polymorphs

α and β (in TAβCD-A2 and TAβCD-M). Polymorphism was found to be the key parameter ruling the behaviour of TAβCD in this fluorinated model propellant. While 20 wt% TAβCD of the β form could be readily solubilized in the model propellant, this was reduced to 2.2 ± 0.2 wt% for α. Samples of amorphous TAβCD were produced (TAβCD-Melt and TAβCD-HPFP) and showed high solubility comparable to that of polymorph β, regardless of their commercial origin. It was possible to convert the less stable polymorph β to more stable α by exposing it in the DSC to a temperature of 150°C (below the melting point of β). Polymorph α could also be obtained by a successful recrystallization of an amorphous sample, in the presence of a minimum amount of form α that seeded the crystallization process. It was found that TAβCD-C and TAβCD-A1 diffraction patterns could successfully be indexed to a $P2_1$ unit cell space group with a unit cell volume of 5350 $Å^3$ and 5029 $Å^3$ respectively. Knowing and controlling the crystallinity of this hydrophobically modified cyclodextrin proves to be of major importance for its use in formulations, especially pharmaceutical ones as demonstrated here, where it could be used in the formation of stable suspensions and solutions in pMDIs [16].

## 6.5 Further work

As stated by M. Pudipeddi *et al.*[5], the ratio of the solubility of two polymorphs in various solvents is independent of the solvent itself. When performing $^1H$ and $^{13}C$ solution-state NMR, both α and β forms of TAβCD were found to be highly soluble in $CDCl_3$. It can however be theorised that for high enough concentrations, the α polymorph will show a lower solubility than the β polymorph, in the same ratio as the one observed here using HPFP. HPFP was in the present case a perfect solvent to record the solubility difference occurring between the two polymorphs, and hence guide this study. Indeed, it was a good enough solvent so that both α and β forms would show some solubility, but also poor enough so that the solubility limit of the α form would be reached within workable concentration, taking into account the limited supply of material that was available. It would now be of interest to set up a systematic screening of potential solvents and relate the observed solubility of the α and β forms to the solvents intrinsic properties, such as polarity, H-bonding

capabilities, dielectric constant and so forth, in order to build a predictive tool that will allow access to the behaviour of such an excipient in a variety of solvents.

Then, accessing the full crystalline arrangement of the TAβCD molecules in form α and β would be a plus. Time on the high flux powder diffraction spectrometer at Daresbury laboratories (Station 9.1) was obtained by Kenneth Harris' group and the elucidation of the crystal structures is ongoing.

The behaviour of this system has generated great interest and is now part of a proposal for further studies.

**References**


1. A. Llinas, K.J. Box, J.C. Burley, R.C. Glen, and J.M. Goodman, *A new method for the reproducible generation of polymorphs: two forms of sulindac with very different solubilities.* Journal of Applied Crystallography, 2007. **40**(2): p. 379-381.
2. M. Mueller, U. Meier, D. Wieckhusen, R. Beck, S. Pfeffer-Hennig, and R. Schneeberger, *Process Development Strategy to Ascertain Reproducible API Polymorph Manufacture.* Crystal Growth and Design, 2006. **6**(4): p. 946-954.
3. J.M. Miller, B.M. Collman, L.R. Greene, D.J.W. Grant, and A.C. Blackburn, *Identifying the stable polymorph early in the drug discovery-development process.* Pharmaceutical Development and Technology, 2005. **10**(2): p. 291-297.
4. D. Singhal and W. Curatolo, *Drug polymorphism and dosage form design: a practical perspective.* Advanced Drug Delivery Reviews, 2004. **56**: p. 335-347.
5. M. Pudipeddi and A.T.M. Serajuddin, *Trends in Solubility of Polymorphs.* Journal of Pharmaceutical Sciences, 2004. **94**(5): p. 929-939.
6. E.M.M.D. Valle, *Cyclodextrins and their uses: a review.* Process Biochemistry, 2004. **39**: p. 1033-1046.
7. *http://en.wikipedia.org/wiki/Image:Cyclodextrin.svg, accessed on October 5th 2007.*
8. K. Uekama, *Design and Evaluation of Cyclodextrin-Based Drug Formulation.* Chemical & Pharmaceutical Bulletin, 2004. **52**(8): p. 900-915.
9. V. Lemesle-Lamache, D. Wouessidjewe, M. Cheron, and D. Duchene, *Study of β-cyclodextrin and ethylated β-cyclodextryn salbutamol complexes, in vitro evaluation of sustained-release behavior of salbutamol.* International Journal of Pharmaceutics, 1996. **141**: p. 117-124.
10. K. Uekama, F. Hirayama, and H. Arima, *Recent Aspect of Cyclodextrin-Based Drug Delivery System.* Journal of Inclusion Phenomena and Macrocyclic Chemistry, 2006. **56**: p. 3-8.

11. B.-Y. Seo, G.-B. Park, and K.-P. Lee, *Hydrophobic cyclodextrin derivatives as sustained release carrier of azidothymidine.* Korean Society of Pharmaceutics, 1996. **26**(2): p. 71-82.
12. I. Bratu, F. Veiga, C. Fernandes, A. Hernanz, and J.M. Gavira, *Infrared spectroscopic study of triacetyl-b-cyclodextrin and its inclusion complex with nicardipine.* Spectroscopy, 2004. **18**: p. 459-467.
13. C.M. Fernandes, R.A. Carvalho, S.P.d. Costa, and F.J.B. Veiga, *Multimodal molecular encapsulation of nicardipine hydrochloride by β-cyclodextrin, hydroxypropyl-β-cyclodextrin and triacetyl-b-cyclodextrin in solution. Structural studies by 1H NMR and ROESY experiments.* European Journal of Pharmaceutical Sciences, 2003. **18**: p. 285-596.
14. G. Filardo, M.d. Blasi, A. Galia, A. Ponchel, H. Bricout, A.D. Sayede, and E. Monflier, *Peracetylated β-cyclodextrin as solubilizer of arylphosphines in supercritical carbon dioxide.* Journal of Supercritical Fluids, 2006. **36**: p. 173-181.
15. A.D. Sayede, A. Ponchel, G. Filardo, A. Galia, and E. Monflier, *Host-guest inclusion complexes between peracetylated β-cyclodextrin and diphenil(4-phenylphenyl) phosphine: Computational studies.* Journal of Molecular Structure: THEOCHEM, 2006. **777**: p. 99-106.
16. P. Rogueda, *Novel Compounds (WO 2005/053637 A2)*, in *Patent Cooperation Treaty (PCT/GB2004/004957)*, W.I.P. Organization, Editor. 2004: United Kingdom.
17. G. Bettinetti, M. Sorrenti, L. Catenacci, F. Ferrari, and S. Rossi, *Polymorphism, pseudopolymorphism, and amorphism of peracetylated α–, β–, and γ–cyclodextrins.* Journal of Pharmaceutical and Biomedical Analysis, 2006. **41**: p. 1205-1211.
18. M. Añibarro, K. Gessler, I. Uson, G.M. Sheldrick, K. Harata, K. Uekama, F. Hirayama, Y. Abe, and W. Saenger, *Effect of Peracylation of β-Cyclodextrin on the Molecular Structure and on the Formation of Inclusion Complexes: An X-ray Study.* Journal of the American Chemical Society, 2001. **123**: p. 11854-11862.

# APPENDIX A

**$^1$H solution-state NMR for TAβCD-C, TAβCD-A1, TAβCD-A2, TAβCD-M**

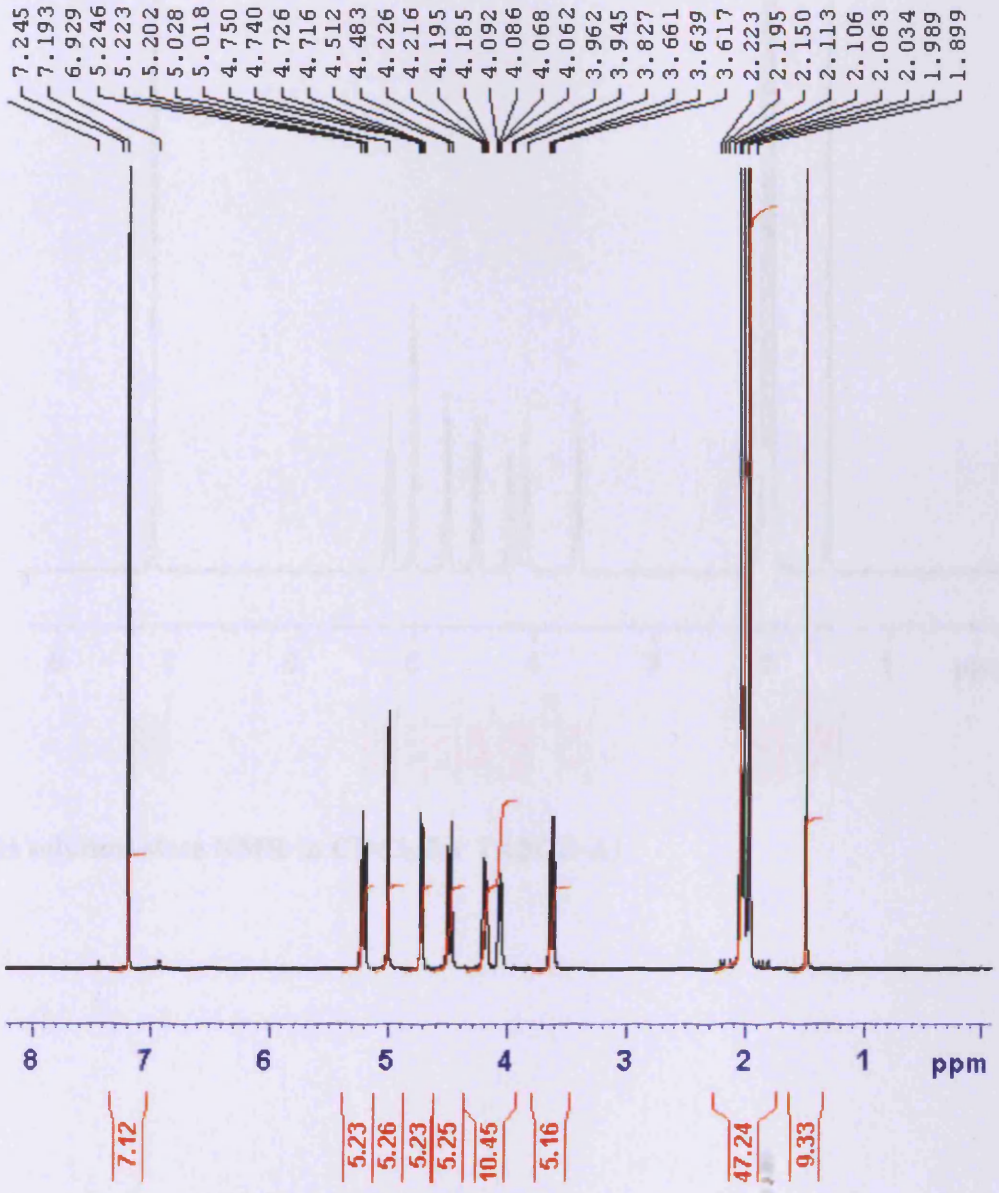


**$^1$H solution-state NMR in $CDCl_3$ for TAβCD-C**

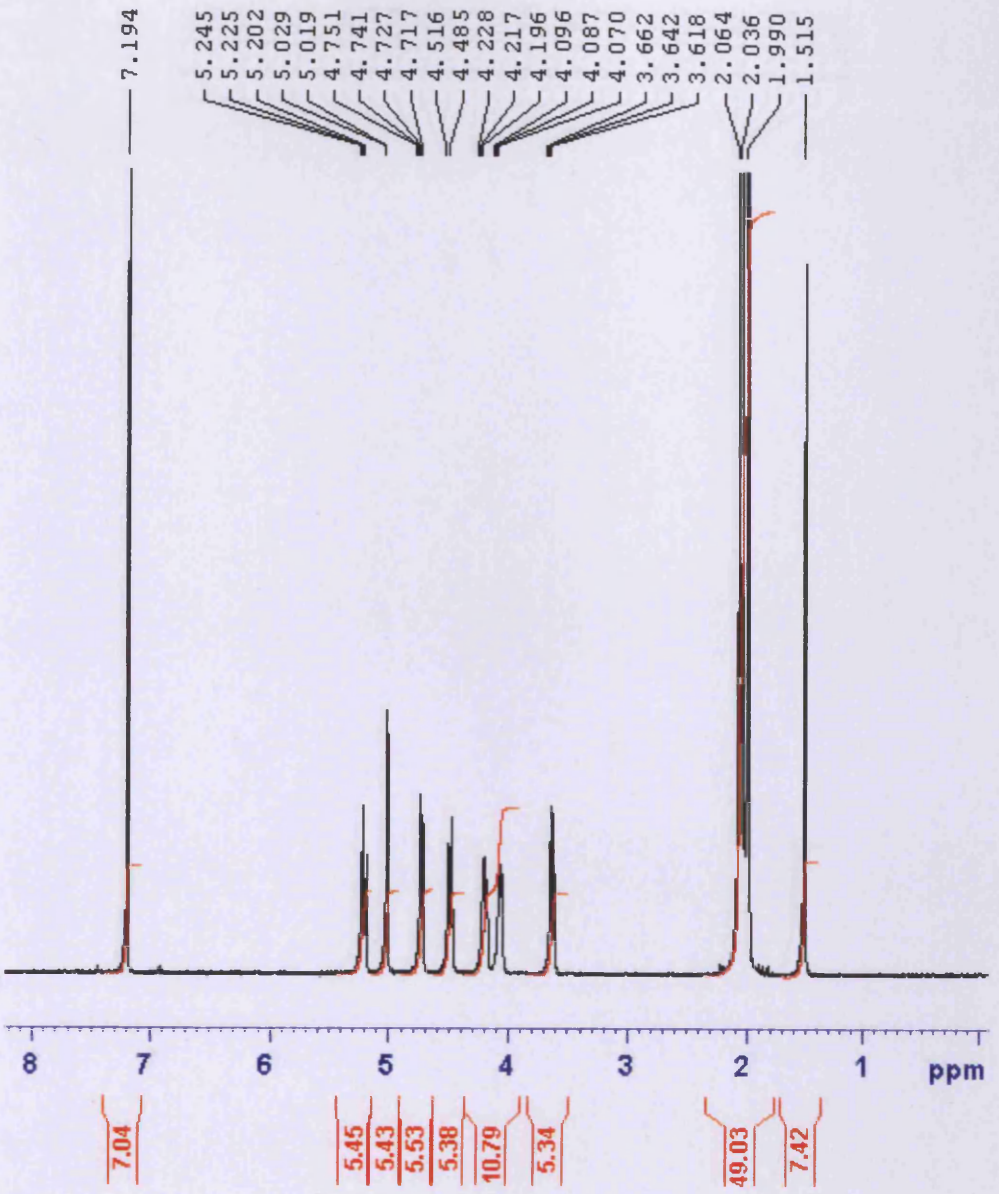


**$^{1}$H solution-state NMR in $CDCl_3$ for TAβCD-A1**

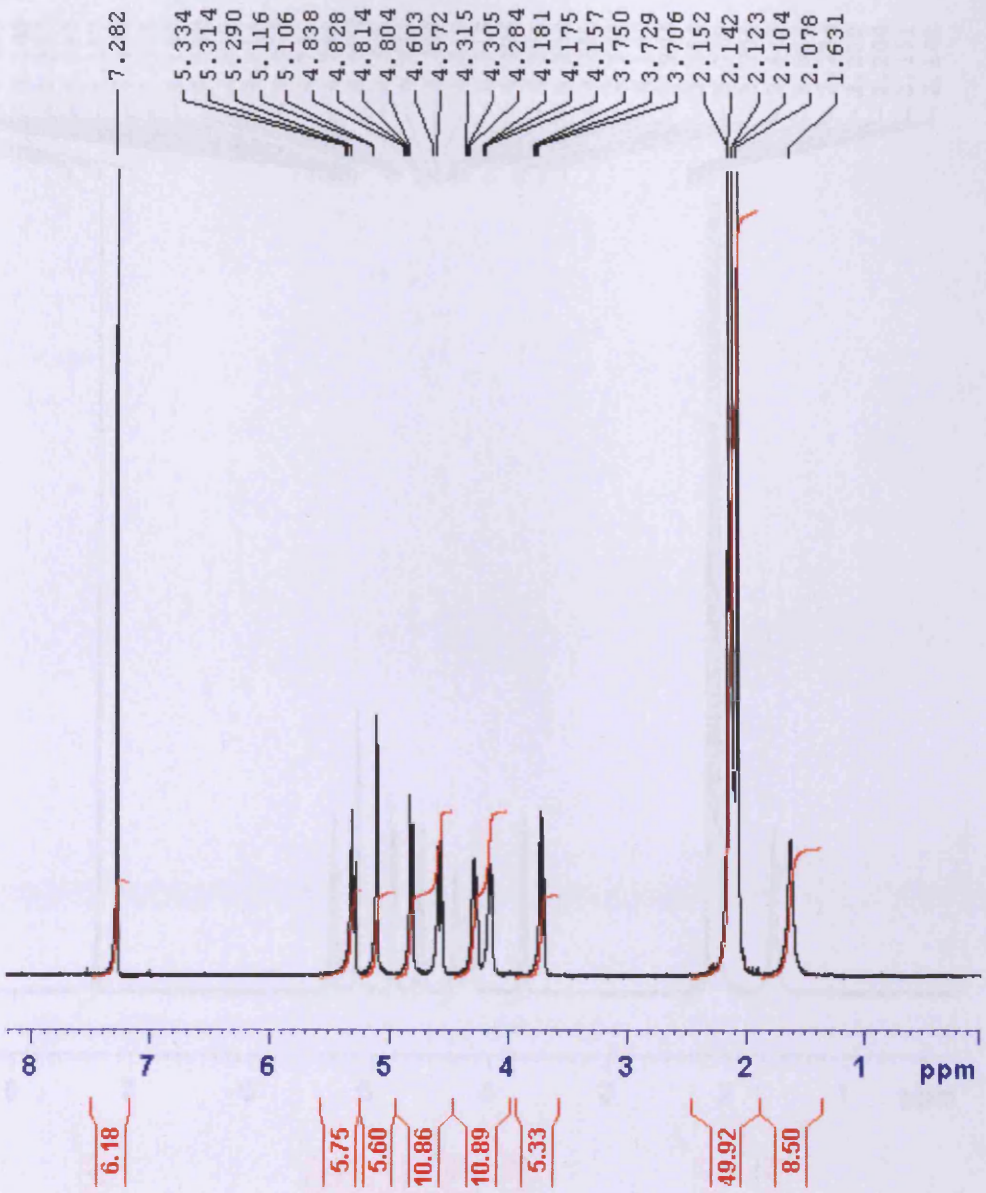


**$^{1}$H solution-state NMR in $CDCl_3$ for TAβCD-A2**

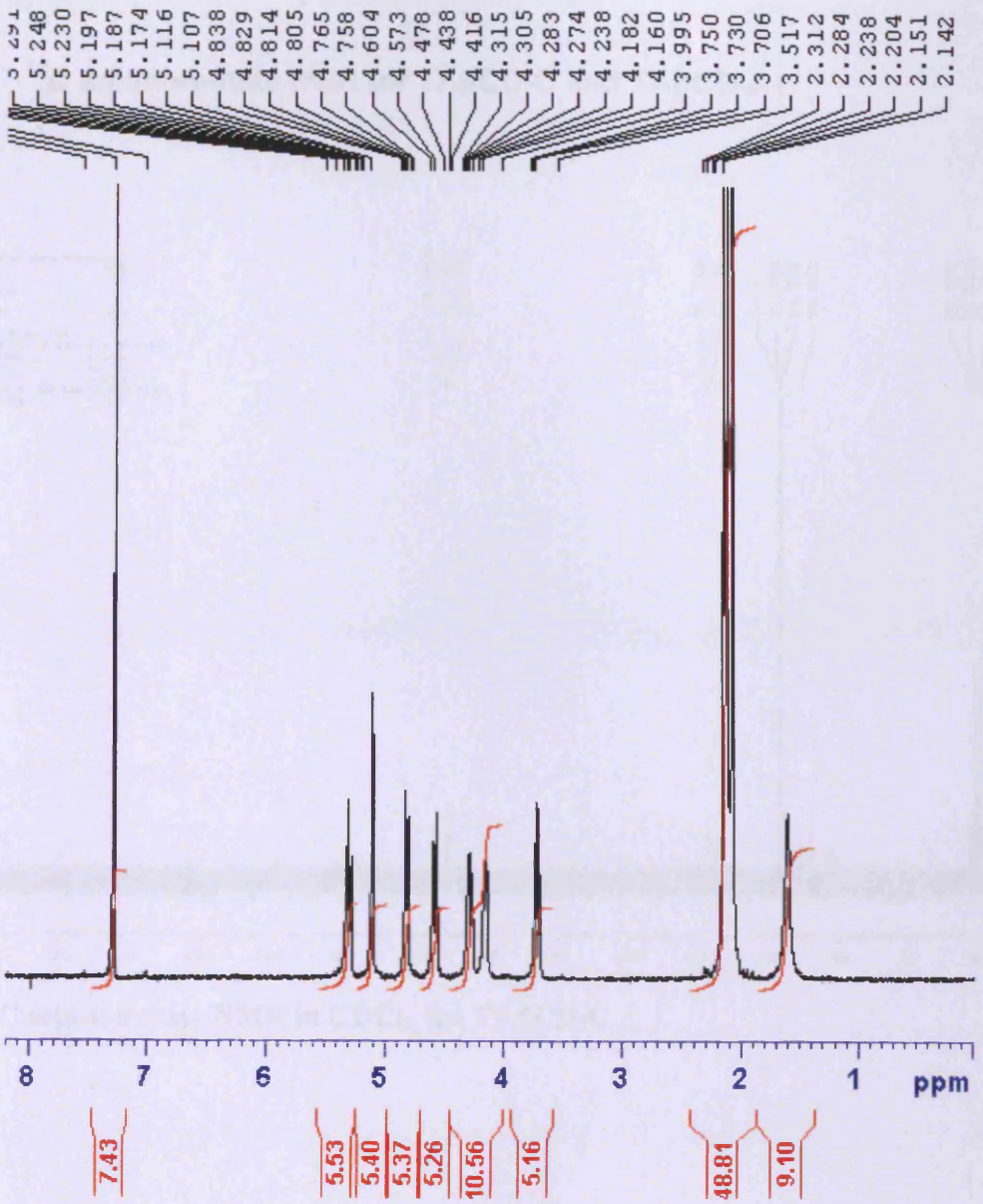


**$^1$H solution-state NMR in $CDCl_3$ for TAβCD-M**

## $^{13}C$ solution-state NMR for TAβCD-C and TAβCD-A1

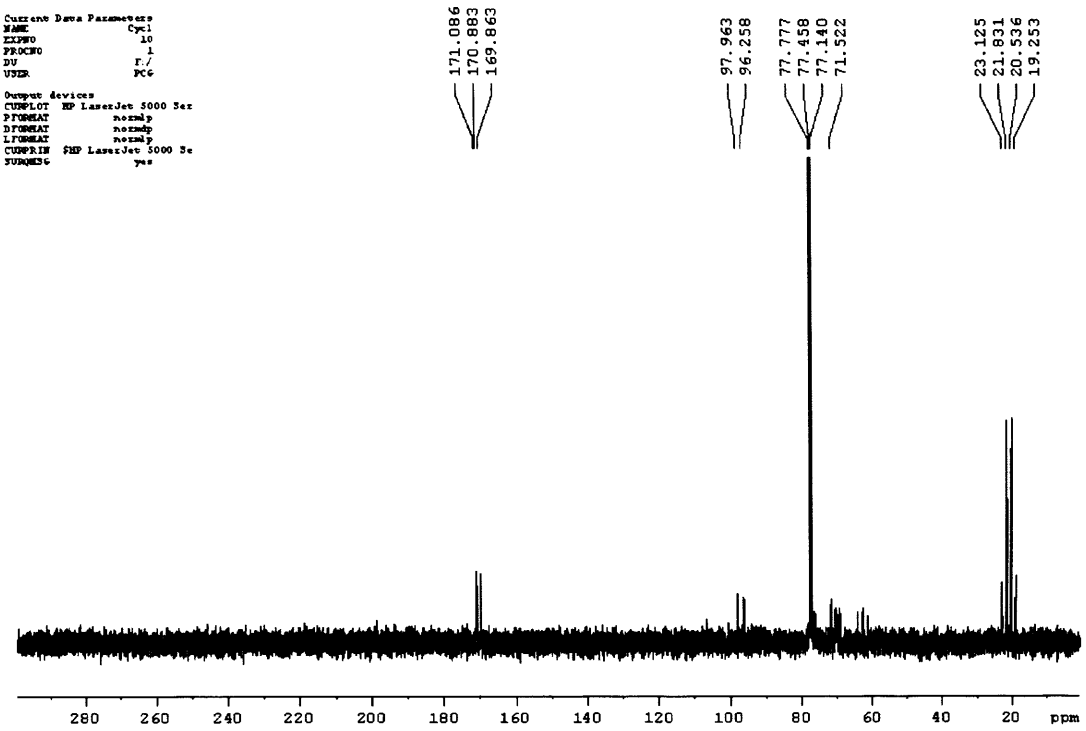


**$^{13}C$ solution-state NMR in $CDCl_3$ for TAβCD-C**

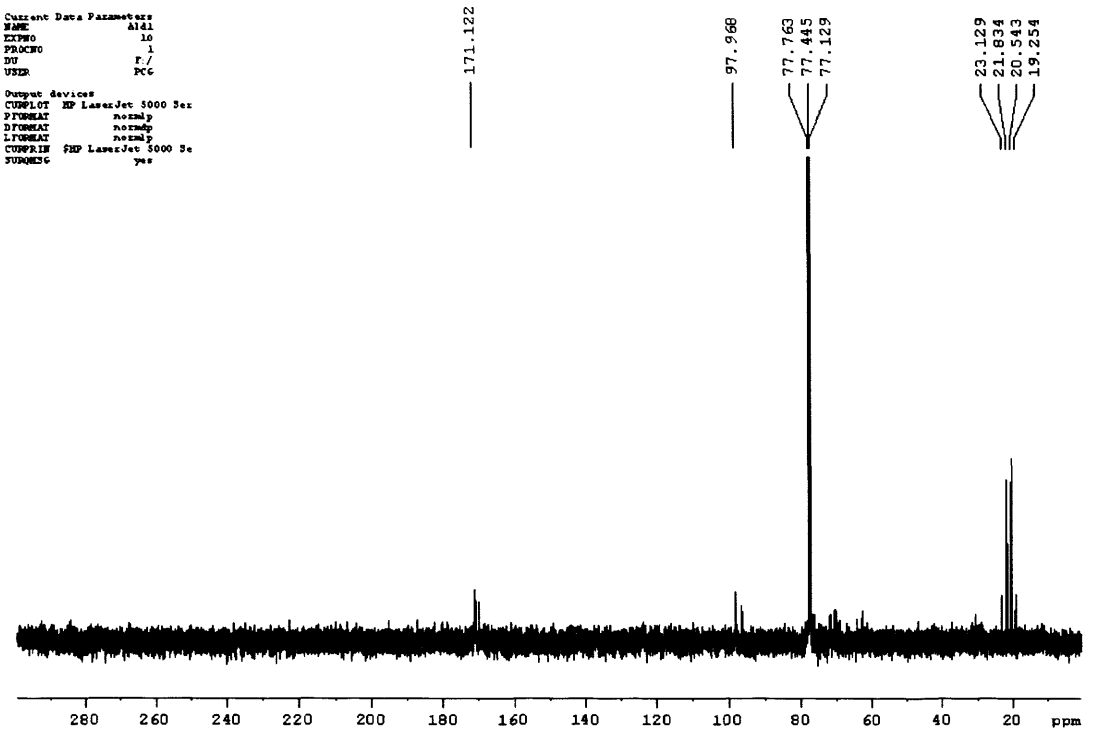


**$^{13}C$ solution-state NMR in $CDCl_3$ for TAβCD-A1**

# Chapter 7 Gelation of fluorinated liquids using non-fluorinated low molecular-mass organogelators

**Foreword**

This chapter presents the discovery of a new family of small organic molecules capable of gelling fluorinated liquids at very low concentrations. The past 15-20 years or so have seen a burst of interest in gelled systems obtained from the self-assembly through non-covalent interactions of small molecules that form macroscopically solid-like structures. The range of liquids that can be gelled is extremely broad (water, alcohols, alkanes, alkenes, acetone, toluene, DMSO, mineral oils, etc) [1]. Whilst fluorinated liquids have also successfully been gelled previously, the gelator molecules themselves were fluorinated to some extent [2, 3]. In the present case, the fluorinated liquids of interest form gelling architectures via the aggregation of non-fluorinated small organic molecules, which to our knowledge is the first occurrence of its kind [4]. Here, a concise introduction to supramolecular gels is given and the system of interest presented. Characterisation of the organogel systems both on macroscopic and microscopic levels is then provided and discussed.

## 7.1 Low molecular-mass organogelators (LMOGs)

### 7.1.1 Introduction

"Gels are a spectacular form of soft matter [...] they swell or contract under minute changes of certain control parameters [...]", as de Gennes puts it [5]. The gel state, neither liquid nor solid, or both liquid and solid, is however much easier to describe than to define. A little over thirty years ago, Flory defined a substance to be a gel if it had a macroscopic, continuous structure with macroscopic dimensions that were permanent on the time scale of the analytical experiment and was solid-like in its rheological behaviour [6, 7]. This definition clearly attests to their complexity. A simpler dictum that can be used for screening purposes is that of Dorothy Lloyd, as cited by Terech *et al.* [1]: if it looks like "Jell-O", it must be a gel.

The gel state of matter can be obtained using polymers, which form cross-linked networks swollen with a liquid [5]. The network structure can be the result of chemical or physical cross-linking. Chemical covalent cross-linking produces irreversible gels, in which the microscopic network is present at all times (unless above decomposition temperature). These can be obtained via chemical cross-linking e.g. via the random cross-linking of polymer chains under, for example, UV-light [8, 9]. Physical cross-linking may be driven by electrostatic or H-bonding interactions for example, such as in polyelectrolyte gels [10] or with poly-N- alkylacrylamides. In such cases, the network, and thus the gel stability depends on external parameters such as pH, liquid characteristics, temperature, etc.

Gel structures can also be obtained via the supramolecular assembly of much smaller molecules, of typical molecular weight below 2000 g $mol^{-1}$, that are known as low molecular-weight organogelators (**LMOGs**). In contrast to their polymeric counterparts, the immobilisation of the solvent is solely mediated by physical interactions that drive the self-assembly of the small molecules into the network [11]. The gelling structures obtained are known as molecular gels, or organogels, in which the LMOGs aggregate and lead to the formation of self-assembled fibrillar networks (**SAFINs**). This is the focus of the present work described in this chapter. Since its inception around 15 to 20 years ago, the field of molecular gels has shown an ever increasing interest. Very detailed accounts and reviews focused on supramolecular gels made from low molecular weight organogelators are published [1, 11-14]. However, no books dedicated to the subject could be found until 2006, when Richard G. Weiss and Pierre Terech edited the excellent "Molecular Gels – Materials with Self-Assembled Fibrillar Networks" [15]. Weiss and Terech commissioned leading experts to produce this well-rounded perspective of supramolecular assemblies of fibrillar networks.

## 7.1.2 LMOGs and SAFINs

### 7.1.2.1 Self-aggregation

LMOGs aggregate to form entangled self-assembled fibrillar networks SAFINs, via non-covalent interactions. These interactions can be H-bonding, aromatic $\pi$-$\pi$

stacking, electrostatic attractions, van der Waals interactions, donor-acceptor interactions, ..., or a combination of these [12]. London dispersion forces alone have also been found sufficient to form gels, for systems in which long n-alkanes (typically 24 to 36 carbon atoms) gel shorter n-alkanes (heptane to hexadecane) [16]; systems in which no heteroatom is present.

The concentrations at which gelling structures are obtained are generally low, typically < 2wt%, and gelators capable of forming a gel at concentrations lower than 1wt% are often classified as a "supergelator" [7]. The growth pattern of LMOG self-assembly is usually mono-dimensional, and nanoscale fibres, strands or tapes are obtained. However, some cases of two-dimensional aggregation modes have also been reported [13, 17]. The nanoscale objects, regardless of their shape, join in three-dimensional networks that entrap the liquid and prevent its flow. Fibres interact with one another via "junction zones" [18] and this gives rigidity to the three-dimensional porous network. Considering the very low gelator concentrations involved, the immobilization of the liquid component relies mainly on surface tension and capillary forces [11, 13]. The gel appears solid-like macroscopically, but the liquid molecules are able to diffuse rather freely microscopically [14, 19].

Molecular gels are usually obtained by first warming a gelator in the selected liquid until it is fully dissolved and then cooling the sol obtained below a characteristic sol-gel transition temperature ($T_{gel\text{-}sol}$) [1, 20]. Empirically, $T_{gel\text{-}sol}$ is the temperature below which the system shows no discernable flow, i.e. the temperature under which the liquid is successfully entrapped by the three-dimensional SAFIN. However, Suzuki et al. have reported the formation of organogels at room temperature, without the need of a heating-dissolution process which can in some cases be a disadvantage to industrial applications [21].

The lowest concentration of gelator molecules with which the gelling of a liquid can be obtained at room temperature is defined as the critical gelator concentration. Prior to the three-dimensional entanglement of fibres, LMOG molecules first need to form aggregates in the sol, and only then can they network through junction zones to form

the gel. The concentration at which LMOG molecules aggregate in the sol is the critical aggregation concentration [13].

LMOG organogels are thermoreversible, i.e. they can undergo numerous heating-cooling cycles in which they reversibly switch from a gelled state to a liquid sol. In both states, gelled and sol, the chemical composition of the system is unchanged, and the interconversion from gel to sol phases is only a function of the assembly and disassembly of the constituent molecules [15].

### 7.1.2.2 LMOGs: a broad range of molecules

LMOGs come in many forms and varieties, and despite a great deal of effort, it is not yet possible to *a priori* design a molecule that will be for sure an efficient gelator for a selected liquid [15]. Most LMOGs discoveries were so far fortuitous, usually observed during a recrystallization process [12]. LMOGs are classified according to their molecular structures, and can go from very simple molecules to ones having high complexity. The simplest gelators bear no heteroatom and are long alkane chains [16, 22] that can immobilise smaller alkanes, amongst other liquids, and for which the gelation efficiency[i] is found to increase with increasing their chain length [16, 23].

LMOGs with one heteroatom (usually oxygen O, nitrogen N, sulfur S or fluorine F) are more common, for which the intermolecular interactions depend on the type of heteroatom and on its location on the carbon chain. These can be ethers and thioethers, calixarene derivatives, alkoxylaryls, sorbitol derivatives, phenyl esters, aliphatic amines, perfluoroalkanes and related molecules [15].

Gelators can also possess two heteroatoms, such as n-alkanamides, aminoacid derivatives, peptides, urea derivatives, urethanes. The organogelator having the lowest known molecular weight (to date) possesses two heteroatoms. With a molecular weight of 88 g $mol^{-1}$, N,N'-dimethylurea, is able to form long fibrils via strong hydrogen bonds and forms gels both in silicon oil and in $CCl_4$ [24]. Three heteroatoms

[i] The term efficiency employed here covers the minimum concentration required to achieve gelation at room temperature, the diversity of liquids gelled and the thermal and temporal stabilities of the gels.

can also be present, usually with gelators that possess the two heteroatom functionalities from the ones listed above and somewhere else a fluorine or sulfur moiety.

Organogelator systems are therefore very diverse and even fullerene derivatives were found to act as organogelators [25]. However, despite the wide diversity of existing organogelators, minute changes on the structure of a given gelator, such as its stereochemistry for example, may significantly alter its gelling abilities [26, 27].

The role of the liquid in the gelation process is not fully elucidated, and no general liquid-gelator interaction could be identified during the sol-gel state transition. However, some interactions between the gelator and the solvent must occur. The formation of a gel is a competitive process between phase separation (nucleation, aggregation and precipitation) and solubilisation of the LMOG molecules [15]. As far as the liquids are concerned, the three main factors influencing both gelation and the self-assembly were found to be the polarity of the liquid, its molecular structure, and it solubilisation power for the gelator considered [18, 28, 29].

Increasing efforts are now focused towards the rational design and engineering of molecules that would show organogelation properties, in order to move away from the current fortuitous or trial and error approach [12, 30-33]. Predictive tools are needed, so that LMOGs structures can be tailored for specific applications and form gels that have pre-determined thermodynamic and rheological properties [15]. Incorporating structural features that are now known to promote mono-dimensional aggregation to form SAFINs (such as H-bonding or $\pi$-stacking motifs) is a start, but can be deceiving as even molecules possessing all attributes of a promising organogelator can be unsuccessful [34, 35].

### 7.1.2.3 Investigating the organogel physical properties (Ref. [1, 15])

Mechanical parameters are usually investigated via rheological measurements, in which the flow properties of the organogels can be quantified. Most organogels exhibit thermoreversibility and the transition-temperature $T_{gel\text{-}sol}$ can be measured.

The inverted test tube method, a simple tabletop method, is often sufficient. The gelled samples are held inverted in a temperature controlled waterbath and the temperature at which the gel falls down the tube is recorded. Plots of $T_{gel\text{-}sol}$ as a function of concentration can be used to obtain thermodynamic data, and so can thermal characterization methods such as differential scanning calorimetry. Different spectroscopies (fluorescence, IR, NMR, CD, ...) can also be used to determine $T_{gel\text{-}sol}$, the aggregation phenomena during which gelation occurs is followed via the amplitude variation with temperature of a selected spectral feature.

The precise structures of the aggregates responsible for providing a scaffold to the entrapped liquid can be investigated via a combination of direct imaging (in direct space, such as electron microscopy) and scattering techniques (in reciprocal space). Scanning and transmission electron microscopy are straightforward choices to determine the building blocks of complex systems. However observations may be subject to artefacts if confinement of the SAFINs distorts colloidal sizes or topology of entanglements. For typical distances present in colloidal systems, small-angle X-ray scattering (SAXS) and small-angle neutron scattering (SANS) probe the bulk of the system and provide a statistical average of the entire sample, but rely on a mathematical model to extract structural information.

#### 7.1.2.4 Applications

Organogels have extremely wide potential applications, only some of them are mentioned here. Organogels can be tailored to be sensitive to external stimuli, such as chemical entities [33], light [36] or sound [37] and are thus suitable as "smart gels" for sensing and actuating. LMOGs organogels also find more and more applications in the biomedical field, as drug delivery implants [38], are used for oil recovery and also in art conservation [39]. Gelation in supercritical fluids can also show great industrial perspectives, in the production of porous materials and aerogels. Most of the times LMOGs are insoluble in supercritical $CO_2$ and they require the presence of small amounts of a co-solvent (alcohol or halogenated liquid) in which the gelator is soluble. However, provided the LMOG is soluble in sc-$CO_2$ and insoluble when the $CO_2$ pressure is lowered, low density aerogels can be produced, therefore via "green

chemistry". C. Shi *et al.* reported examples of organogelators suitable for $CO_2$ gelation [40], which contain one or two urea groups to induce aggregation through H-bonds and a fluorinated group to promote solubility in $CO_2$.

## 7.2 System of interest

A family of tetrahydroxy diesters of molecular weight comprised between 364.4 g $mol^{-1}$ and 462.5 g $mol^{-1}$ was found to form gels in mixtures of the fluorinated liquids 1H, 1H heptafluorobutanol (HFB) and 2H, 3H- decafluoropentane (HPFP). With molecular weights below 1000 g $mol^{-1}$, these can be classified as LMOG's [7]. Such gelator molecules bear isopropyl end-groups, are chiral, and enantiomerically pure. Their structure is recalled here in Figure 7-1 but details can be found in Chapter 3-Materials and Methods.

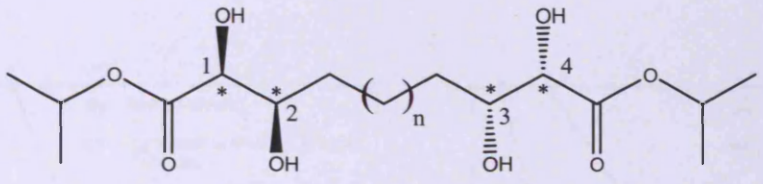


**Figure 7-1 Structure of the tetrahydroxy diester LMOGs, n= 3, 4, 5, 6, 8 and 10.**

A typical view of the gels obtained is shown in Picture 7-1 below.

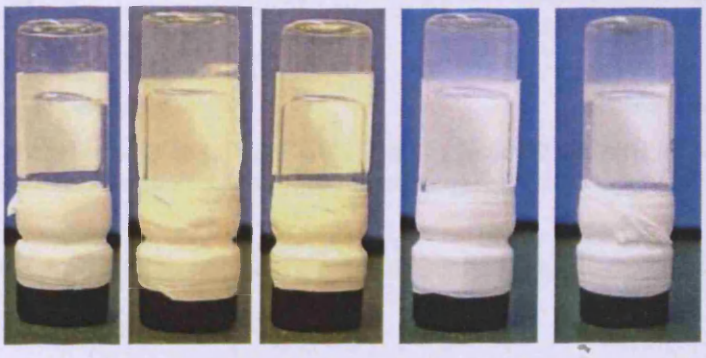

**Picture 7-1 Gels formed with, from left to right, gelators $G_4$, $G_5$, $G_6$, $G_8$ and $G_{10}$.**

To the best of our knowledge, gelation of fluorinated liquids could so far only be achieved when using fluorinated or semi-fluorinated LMOGs, where the segregation

between the carbon and the fluorinated segments would cause the system to aggregate and in some cases form supramolecular gelling architectures [2, 3].

## 7.3 Macroscopic studies of the gelling systems

All samples were prepared and assessed according to the procedures described in Chapter 3, section 3.4.

### 7.3.1 Phase behaviour assessment of the enantiomerically pure LMOGs

Gels were found to form at very low gelator concentration when an excess of non-solvent HPFP was used in comparison to HFB. As a first step, it was chosen to assess the phase behaviour of the series of gelators in two solvent mixtures of 10/90 and 20/80 HFB/HPFP. Figure 7-2 below presents the phase behaviour of $G_3$, $G_4$, $G_5$, $G_6$, $G_8$ and $G_{10}$ in a 10/90 HPFP/HFB solvent ratio and in a 20/80 HPFP/HFB solvent ratio, at room temperature.

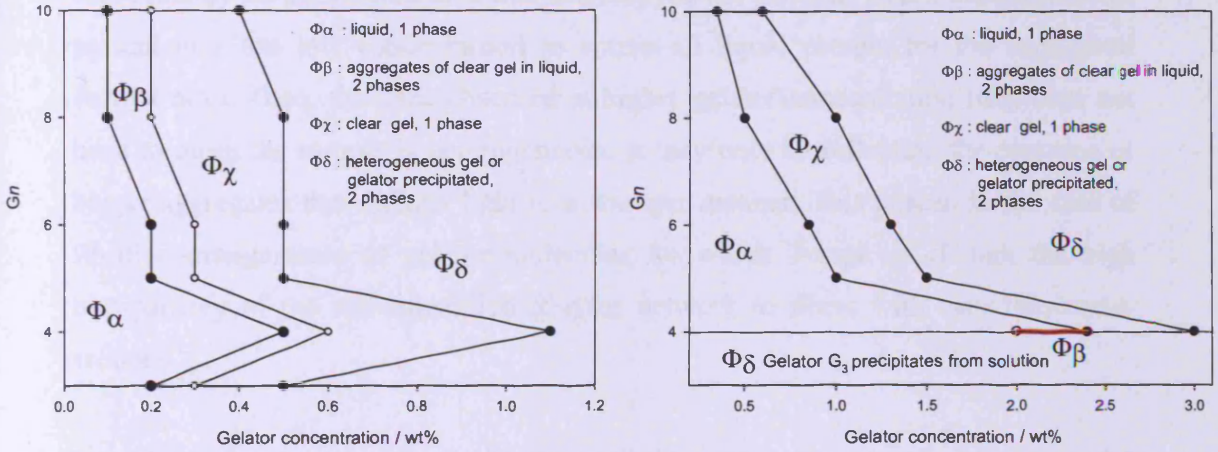


**Figure 7-2 Phase diagram of $G_3$, $G_4$, $G_5$, $G_6$, $G_8$ and $G_{10}$ in 10/90 HFB/HPFP solvent ratio (left) and in 20/80 HFB/HPFP solvent ratio (right), at room temperature.**

The two phase diagrams presented herein are described and discussed in the following sections.

#### 7.3.1.1 10/90 HFB/HPFP solvent ratio

In the 10/90 HFB/HPFP solvent ratio, four different macroscopic states are observed, indicated as $\Phi_\alpha$, $\Phi_\beta$, $\Phi_\chi$ and $\Phi_\delta$. At the lower concentration of gelator, a clear liquid

behaviour. However, samples made with $G_3$ were not stable over three weeks: the gelator slowly precipitates within the gel.

#### 7.3.1.2 20/80 HFB/HPFP solvent ratio

A rather similar phase diagram is obtained in the case of solvent ratio 20/80. However, some significant differences are to be highlighted. Firstly, no gels could be formed using gelator $G_3$, as precipitation of the gelator was always obtained at all concentrations investigated. This shows that there is a delicate balance as far as the chain length ($n$) is concerned: it seems that decreasing $n$ renders the self-assembly less susceptible for this family of gelators. Secondly, it appears clearly in this solvent mix that the concentration above which gelation occurs is a decreasing function of increasing $n$: less gelator is required to achieve gelation when longer gelators are used, going from 2.4wt% for $G_4$ to 0.5wt% for $G_{10}$. Then, the gelator concentrations required to achieve gelation are higher in solvent ratio 20/80 than in 10/90, the phase behaviour is in fact shifted to the right. When 0.2 wt% $G_8$ could gel a 10/90 HFB/HPFP solvent mix, 0.5 wt% are now required for the 20/80 ratio. In solvent mix 20/80 HFB/HPFP, state $\Phi_\beta$ in which gel aggregates coexist with free liquid was only observed for gelator $G_4$ (region highlighted on the graph in the form of a red line).
Table 7-1 summarises the minimum concentrations required from each gelator to obtain a solid-like structure in both solvents ratio.

| HFB/HPFP | $G_3$ | $G_4$ | $G_5$ | $G_6$ | $G_8$ | $G_{10}$ |
|---|---|---|---|---|---|---|
| 10/90 | 0.3 | 0.6 | 0.3 | 0.3 | 0.2 | 0.2 |
| 20/80 | n/a | 2.4 | 1 | 0.85 | 0.5 | 0.35 |

**Table 7-1 Minimum gelling concentration (/ wt%) for gelators $G_3$, $G_4$, $G_5$, $G_6$, $G_8$, and$G_{10}$ in 10/90 and 20/80 HFB/HPFP solvents ratio. The typical error is ± 0.05 wt% in all cases, representing the steps taken for the concentration screening.**

When increasing the proportions of HFB towards 30/70, 50/50 and pure HFB, ever increasing concentrations of gelator were required to achieve full gelation. Due to the very high consumption of gelator, the systematic study using $G_3$, $G_4$, $G_5$, $G_6$, $G_8$ and $G_{10}$ was performed only in the 10/90 and 20/80 solvent ratios. However, gelation of pure HFB was found possible using a minimum of 10 wt% $G_6$ and 10wt% $G_8$.

The fluoro-alcohol HFB acts as a solubilising media for the gelators. HFB and HPFP are fully miscible, but the tetra hydroxy diesters are insoluble in the model propellant HPFP. Upon addition of the non-solvent HPFP to an initially stable sol of gelator in HFB, gelator molecules aggregate and form a three-dimensional network that is able to entrap both solvents. When the proportion of HFB is increased, more gelator is required in order to form a gel. Indeed, with a higher content of HFB, more gelator molecules will stay dissolved in the fluoro-alcohol, and less will participate to the formation of the gelling architecture. There is a critical concentration below which no aggregation can be witnessed. This means that some of the gelator does not take part in the gelled network but remains free in solution, as observed by Willemen *et al.* [41].

### 7.3.1.3 Behaviour of racemic $G_6$

Racemic $G_6$ consists of an equal molar mixture of the two diastereoisomers, (+)$G_6$ and (–)$G_6$. The aim of this experiment was to test whether these would be able to self-assemble and form gels, or if the gelling ability was a feature of the (+)$G_6$ form only, in which case the gel formation would be stereo specific.

Such cases have indeed already been reported, by Terech *et al.* [27] with 4-tert-butyl-1-phenyl-cyclohexanol as low molecular-mass organogelator, for which only the diastereoisomer with the aryl group in the axial configuration shows gelling properties. When the aryl group is in the equatorial position, no gels are formed and the isomer precipitates out of solution. Picture 7-2 presents the cis and trans isomers involved.

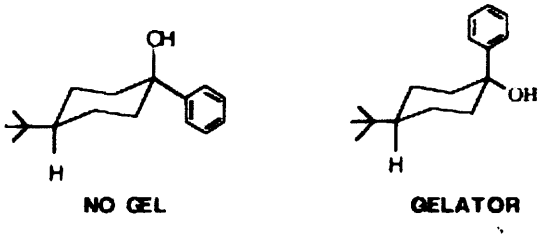


**Picture 7-2 Cis (aryl group in equatorial position) and trans (aryl group in axial position) isomers, respectively acting as non gelator and gelator, taken from Ref. [27].**

Racemic $G_6$ was therefore used to prepare samples, in 10/90 HFB/HPFP solvent ratio at concentrations of 0.3 wt%, 0.6 wt% and 0.9 wt%, and in 20/80 HFB/HPFP solvent

ratio at concentrations of 0.9 wt%, 1.5 wt%, and 2 wt% (i.e. encompassing twice the previous minimum gelling concentration). Full solubility was achieved in HFB, however, upon addition of HPFP, all samples showed flocculation of the gelator, as whitish aggregates. Only one sample was found to be stable to tube inversion. However, the structure formed was found to be very weak and easily broken upon shaking, and would reform on standing. Picture 7-3 shows the appearance of the sample where flocs have aggregated, before and after gentle shaking.

**Picture 7-3 +/– $G_6$ samples appearance, where flocs have aggregated (left) and broken after gentle shaking (right)**

Using the racemic mixture of $G_6$, it was not possible to obtain similar clear homogeneous gels as in the case of enantiomerically pure gelators. Racemic mixture concentrations encompassing twice the minimum gelling concentration as measured in the case of optically pure gelators were investigated, to account for the presence of a hypothetically non gelling stereoisomer. However, no gels could be formed. The self-assembly mechanism therefore seems to be highly stereo specific, and dependant on interactions based on the four hydroxyl groups present.

### 7.3.1.4 Varying gelator end-group

As described in Chapter 3 - Materials and Methods, variations around the gelator structure were made available, in which the molecules had similar inner chain length but were bearing isobutyl, tertiobutyl and isoamyl end-groups, instead of isopropyl as in the case of the gelators. Figure 7-3 summarises the systems investigated.

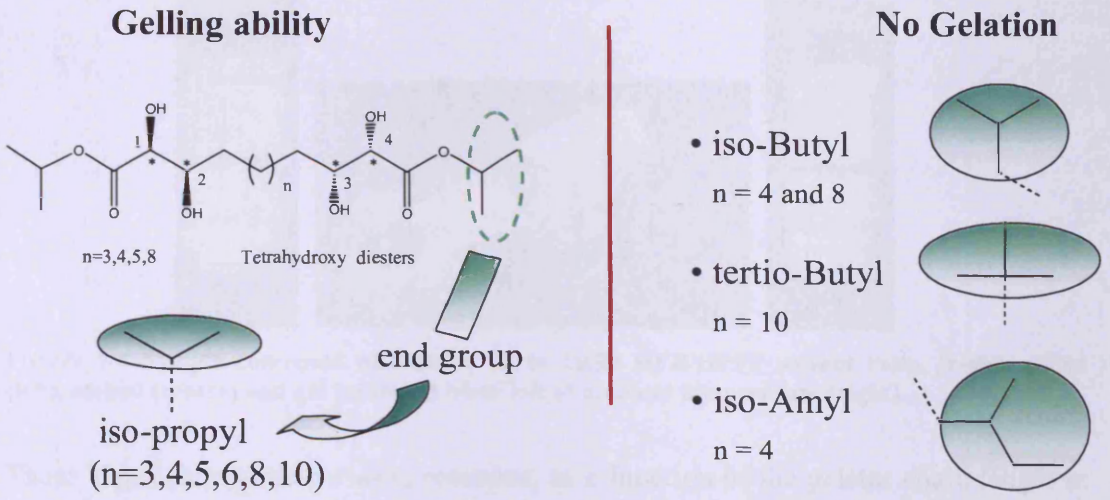


**Figure 7-3. End-groups and spacers available, and their ability as gelators of the fluorinated liquids investigated.**

Samples prepared in identical conditions led to precipitation and no gelling structure was obtained. This suggest that the nature of the end group, in addition to chirality and inner chain length as seen previously, is critical in the supramolecular self-assembly process. However, one cannot say for sure in what way the isopropyl end-groups are more favourable to the self assembly of the gelator molecules. The smaller size of isopropyl, compared to isobutyl, tertiobutyl and isoamyl could limit steric hindrance. Such bulkiness of the end-group could prevent approach of the hydrogen bonding groups, if hydrogen bonds are responsible for their self-assembly. However, less bulky end groups, such as ethyl or methyl ones were not available to test this hypothesis. From now on, all studies presented are carried out using the enantiomerically pure, isopropyl terminated low molecular weight gelator family.

### 7.3.2 Melting transition temperatures: $T_{gel\text{-}sol}$

Once a gel was formed, the supramolecular structures were found to be thermoreversible. On heating, they pass through a gel to sol phase transition ($T_{gel\text{-}sol}$) at well-defined temperatures and become liquid, with a viscosity comparable to that of the pure solvents. On cooling, they become solid-like again. Picture 7-4 shows a gel freshly formed (left), than melted (centre), and gelled again (right).

**Picture 7-4 Sample composed of 0.4wt% $G_6$ in 10/90 HFB/HPFP solvent ratio, freshly gelled (left), melted (centre) and gel reformed when left at ambient temperature (right).**

These $T_{gel\text{-}sol}$ temperatures were recorded, as a function of the gelator chain length in a given solvents ratio, and as a function of the solvent ratio for one particular gelator. The temperature at which the gel falls under the force of gravity when the sample vial is inverted was taken as $T_{gel\text{-}sol}$. Figure 7-4 shows the results obtained for $G_3$, $G_4$, $G_5$, $G_6$ and $G_8$ in a 10/90 HFB/HPFP solvents ratio. Figure 7-5 presents transition temperatures measured using gelator $G_6$ in 5/95, 10/90, 15/85, 20/80 and 30/70 HFB/HPFP solvents ratio.

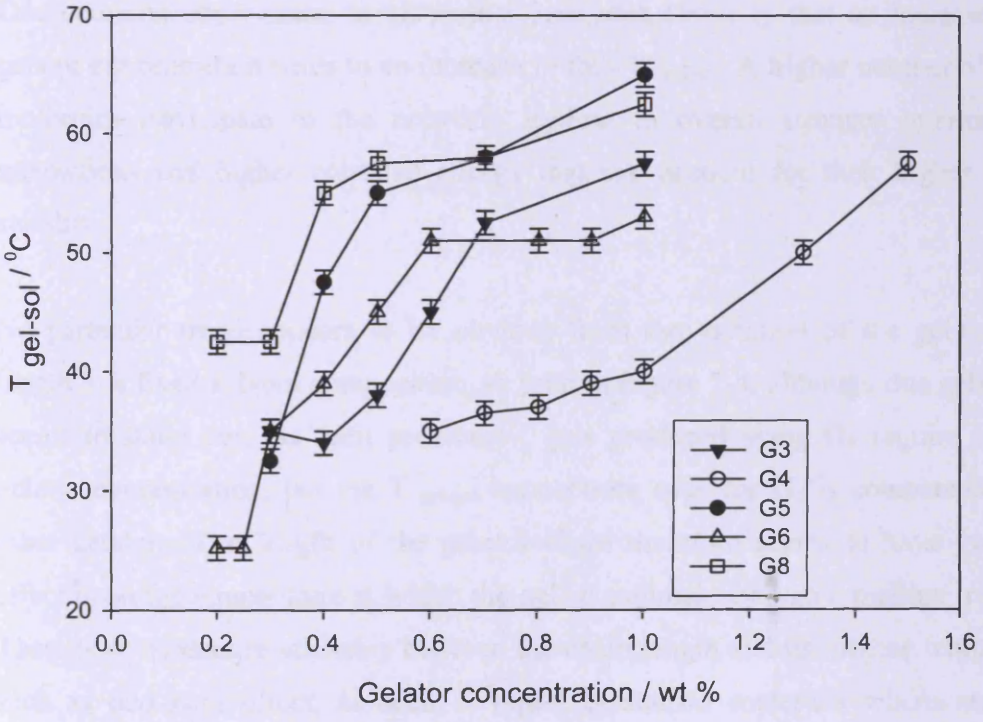


**Figure 7-4 $T_{gel\text{-}sol}$ for $G_3$, $G_4$, $G_5$, $G_6$ and $G_8$ in a 10/90 HFB/HPFP solvent environment.**

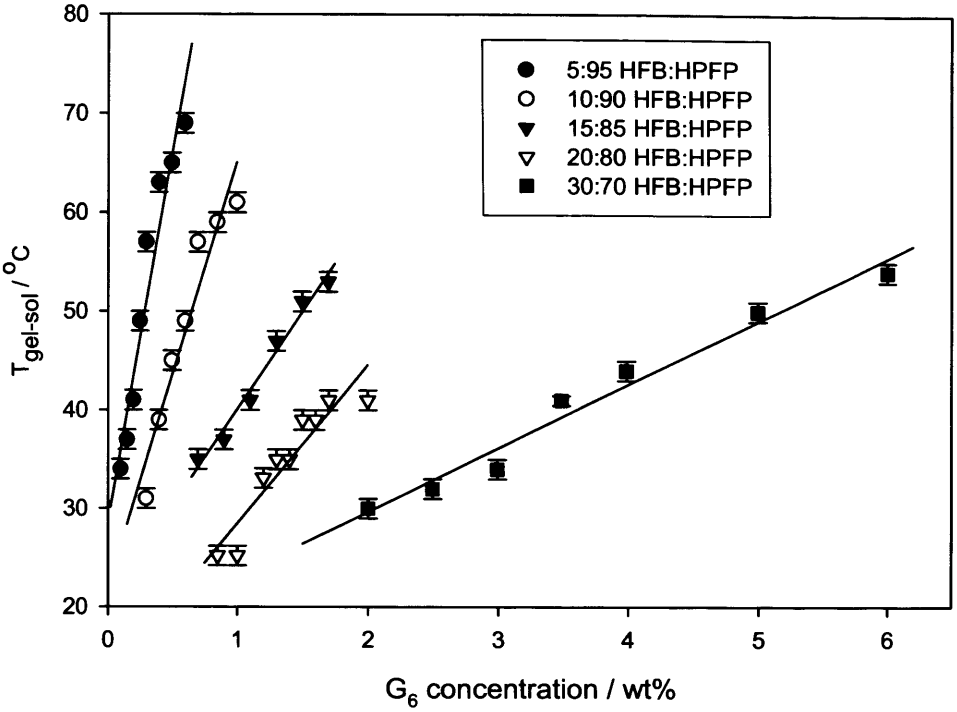


**Figure 7-5 T gel-sol for $G_6$ as a function of its concentration and the HFB/HPFP solvents ratios, with linear regressions.**

One common observation to all results presented above is that an increase in the gelator concentration leads to an increase in their $T_{gel-sol}$. A higher number of gelator molecules participate in the network, leading to overall stronger intermolecular interactions and higher cohesive energy that can account for their higher thermal stability.

No particular trend appears to be obvious from the variation of the gelator chain length in a fixed solvent composition, as seen in Figure 7-4, although one gelator, $G_4$, seems to stand out. As seen previously, gels produced using $G_4$ require a higher gelator concentration, but the $T_{gel-sol}$ temperature span for $G_4$ is comparable to the other gelators. The length of the gelator chain therefore seems to have very little effect upon the temperature at which the gelled samples undergo a melting transition. There is no evident relationship between the chain length and its melting temperature, such as odd-even effect, as seen in liquid crystalline materials where molecules bearing spacers of different parity (an odd or an even chain length) form dissimilar

molecular arrangements [42]. However, this does not seem to be the case here, as no pattern linked to the parity of the inner backbone chain can be drawn.

Then, as the proportion of HFB is increased more gelator is required to achieve a gelled state, but the $T_{gel\text{-}sol}$ temperatures still lay in the same range. As it is shown next, the melting temperatures measured herein can be used to extract thermodynamic information on the gelled systems.

### 7.3.3 Thermodynamic approach of the Melting transition temperatures

As described by Murata *et al.* [43] and Terech *et al.* [44], the energy associated with the melting transition of the gelled networks can be evaluated using the $T_{gel\text{-}sol}$ measured. Both papers refer to Eldridge and Ferry [45], who showed in 1954 that in the case of polymeric gels, the concentration (C) and $T_{gel\text{-}sol}$ ($T_m$) may be related by the following Equation 7-1,

$$\ln(C) = -\frac{\Delta H_{fc}}{RT_m} + Cnst \qquad \textbf{Equation 7-1}$$

The assumption here is that polymer chains associate in a binary manner to form crosslink points. $\Delta H_{fc}$ represents the heat of reaction of the association process, R the gas constant. It will be shown in the next section, using neutron scattering results, that in the gel phase, the organogelators form fibrillar aggregates, and in the sol phase, these aggregates dissociate into discrete molecules. Murata *et al.* [43] state that this transition can therefore be seen as the dissolution process of crystals, for which a very similar equation exists, shown below as Equation 7-2, and known as the Shröder-van Laar relation [16, 46].

$$\ln \chi = -\frac{\Delta H_f}{R}\left(\frac{1}{T} - \frac{1}{T_f}\right) \qquad \textbf{Equation 7-2}$$

This equation expresses the solubility $\chi$ at a given temperature T, for an ideal solution, with $\Delta H_f$ the melting energy and $T_f$ the melting point. Assuming the gelled systems form ideal solutions on melting, it is possible to plot Ln ($G_n$), where $G_n$ is explicitly the concentration of gelator with spacer *n,* as a function of the inverse absolute $T_{gel\text{-}sol}$

temperature. This yields to Figure 7-6 which presents results obtained for $G_3$, $G_4$, $G_5$, $G_6$ and $G_8$ in a 10/90 HFB/HPFP solvents ratio, and Figure 7-7 for those measured with $G_6$ in 5/95, 10/90, 15/85, 20/80 and 30/70 HFB/HPFP solvents ratio.

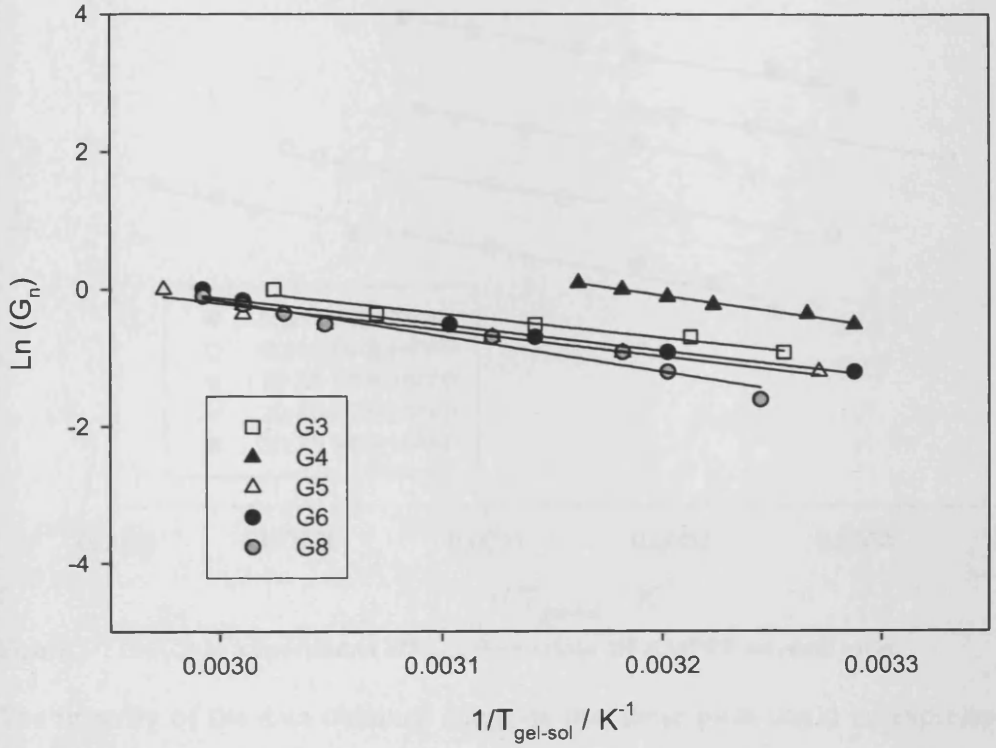


**Figure 7-6 $Ln(G_n)$ as a function of $1/T_{gel-sol}$ for $G_3$, $G_4$, $G_5$, $G_6$ and $G_8$ in a 10/90 HFB/HPFP solvent environment.**

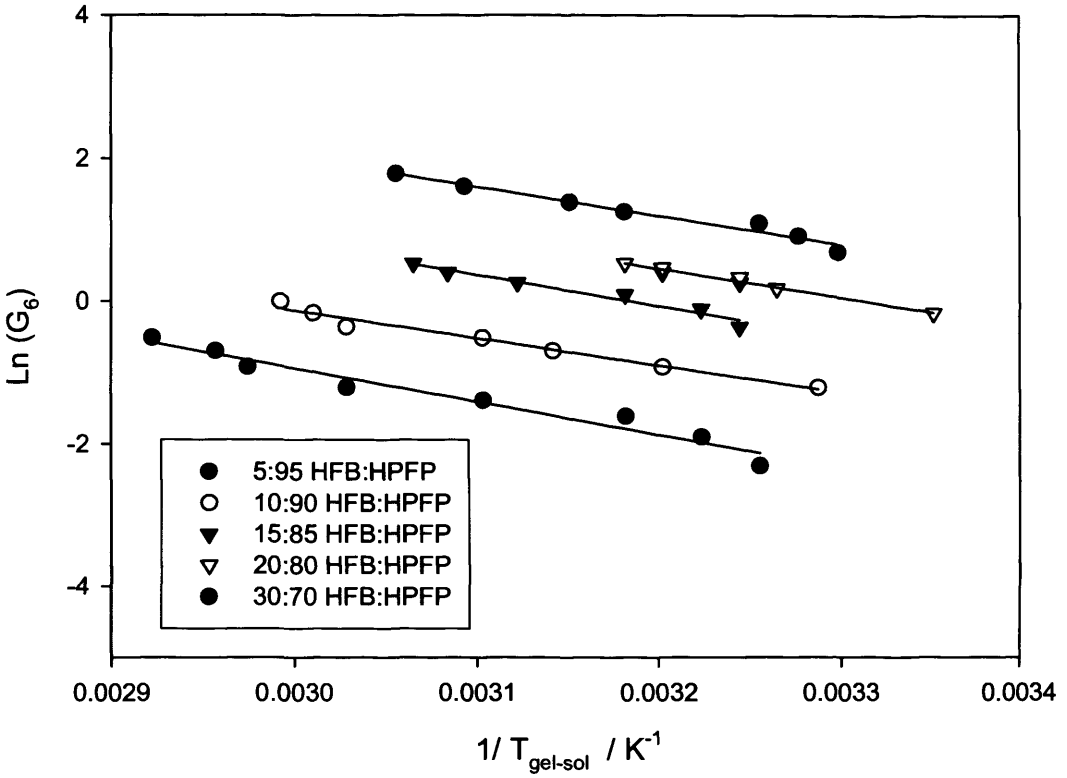


**Figure 7-7 Ln($G_6$) as a function of $1/T_{gel-sol}$ for various HFB/HPFP solvents ratio.**

The linearity of the data obtained suggests that these plots could be expressed using Equation 7-3 presented below, which is in spirit similar to Equation 7-2.

$$\ln(G_n) = -\frac{\Delta H_m}{R}\frac{1}{T_{gel-sol}} + Cnst \qquad \textbf{Equation 7-3}$$

With $\Delta H_m$ the phase transition enthalpy, $T_{gel-sol}$ the gel-to-sol transition temperature for a gelator concentration ($G_n$) and R the gas constant. In fact, the two processes, i.e the dissolution of solids in solution and the melting of a fibrillar network are very similar, as both relate to the disruption of intermolecular interactions that is then followed by the dispersion into homogeneous solutions [43]. Table 7-2 and Table 7-3 show $\Delta H_m$ values determined from the slopes previously obtained, for $G_3$, $G_4$, $G_5$, $G_6$ and $G_8$ in a 10/90 HFB/HPFP solvents ratio and for $G_6$ in 5/95, 10/90, 15/85, 20/80 and 30/70 HFB/HPFP solvents ratio respectively.

| $G_n$ | $G_3$ | $G_4$ | $G_5$ | $G_6$ | $G_8$ |
|---|---|---|---|---|---|
| $\Delta H_m$ / kJ mol$^{-1}$ | 28 ± 2 | 38 ± 2 | 32 ± 2 | 32 ± 2 | 39 ± 2 |

**Table 7-2 Phase transition enthalpies for $G_3$, $G_4$, $G_5$, $G_6$ and $G_8$ in a 10/90 HFB/HPFP solvent ratio**

| HFB/HPFP | 5/95 | 10/90 | 15/85 | 20/80 | 30/70 |
|---|---|---|---|---|---|
| $\Delta H_m$ / kJ mol$^{-1}$ | 38 ± 2 | 32 ± 2 | 36 ± 2 | 34 ± 2 | 34 ± 2 |

**Table 7-3 Phase transition enthalpies for $G_6$ in various HFB/HPFP solvents ratios**

Firstly, $\Delta H_m$ values extracted are all positive, showing that the melting process of the gel to sol transition is endothermic, therefore absorbs energy leading to a system of higher entropy, which is generally the case for a melting process. (Systems with opposite occurrences are reported, with, counter intuitively, the liquid's endothermic freezing on heating and the crystal's exothermic melting on cooling at ambient pressures [47, 48]). $\Delta H_m$ values are on the whole scarcely affected by the solvent composition or by the gelator chain length. However, $G_4$ seems to once again stand out from its closer neighbours, as seen in Table 7-2, with $\Delta H_m$ value of 38 ± 2 kJ mol$^{-1}$ compared to 28 ± 2 kJ mol$^{-1}$ and 32 ± 2 kJ mol$^{-1}$ for $G_3$ and $G_4$ respectively. As seen previously, higher concentrations of $G_4$ are required to form gels, at the same temperature as the other gelators. This means that $G_4$ is more soluble in these solvents, and this higher affinity with the solvents could be reflected by a higher $\Delta H_m$ [43]. Unfortunately, this reasoning is not universal. $G_8$ presents a higher $\Delta H_m$, but does not require higher gelator concentration to form gelling structures, *cf.* the phase behaviour diagrams, and the 5/95 HFB/HPFP solvent mixture is all but expected to enhance $G_6$ solubility. A study by Furman and Weiss [28] in which they investigate gels made of cholesteryl 4-(2-anthryloxy) butanoate (CBA) in hexadecane, 1-octanol and their mixtures, indicates that the stability of the gelator supramolecular assembly depends much more upon the bulk properties of the liquid(s) themselves than on discrete CBA-solvent intermolecular interactions and that the packing of the gelators in the self-assembled network is rather similar to the bulk crystal packing. This would suggest that solvent molecules do not take part in the self-assembly of gelator molecules, which could in turn explain $\Delta H_m$ insensitivity to the solvent composition.

The enthalpy values for our systems are nevertheless in full agreement with those reported in the literature for different LMOGs systems [43, 44]. However, the physical meaning of such values has not been explored yet. If it is supposed that the self-assembly of the gelator molecules is based on their ability to form intermolecular hydrogen-bonds, the donor being the alcohol group and the acceptor an oxygen atom from the ester functionality, the gelling structure would rely upon O–H···O bonds. The strength of such a hydrogen bond is approximately 5 kcal $mol^{-1}$, i.e. 20 kJ $mol^{-1}$. In this respect, according to the values listed in Table 7-2 and Table 7-3, a single cross-link in the gel network would statistically consist of one to two hydrogen bonds. This would seem sensible if the gelator functionalities are considered: as seen previously, both a maximum of four oxygen atoms per molecule can act as hydrogen-bonds acceptor (ester functionalities), and hydrogen-bonds donor (alcohol groups). This reasoning was directly transferred from Ferry *et al.*, who applied it to the cross linking of gelatin solutions of molecular weights comprised between 33,000 to 72,000 g $mol^{-1}$ and based on their melting temperatures, found that a single cross-link consisted of fewer than ten to up to 45 hydrogen bonds depending on the speed of the gelation process [45].

Considering a gel formed using 0.2 wt% $G_8$ in a 10/90 HFB/HPFP solvent mix, more than 800 solvent molecules can be immobilized by one single gelator molecule. With such a high ratio, direct intermolecular gelator-solvent interactions are unlikely to be responsible for holding the gelled structure in place. One hypothesis is that the gelator molecules self-assemble into a supramolecular structure that is able to hold the fluorinated liquids mainly by surface tension and capillary action, such as three dimensional networks of strands, as proposed by Furman and Weiss [28]. The microscopic properties of these gelling architectures were therefore investigated using small-angle neutron scattering and pulsed-gradient spin-echo NMR, and the resulting data are shown in the next sections.

## 7.4 SANS study

Small-angle neutron scattering was used to probe the gel structure on a microscopic level, and to gather information about the shape and size of the aggregated gelator

molecules. The gelator concentration, its chain length, the HFB/HPFP solvents ratio and the temperature were the parameters under investigation. All data were first analysed using the Guinier approximation, to decipher the gross morphology of the gel constituents, and then using the more complex Kholodenko worm-like chain model. The results obtained via the Guinier approach will firstly be presented for a selection of data, representative of the systems' diversity.

### 7.4.1 Scoping study: deciphering the gel gross morphology

Prior to any elaborate model search for the fitting of the gels scattering data, a scoping study is undertaken on a selection of samples, and the Guinier approximation for geometries corresponding to discs, spheres, and cylinders, applied.

Four samples were chosen in order to span varied solvent conditions, gelator concentrations, and gelator chain length and cover the range of experiments performed. They are as follow:

- 1 wt% $G_8$ in 10/90 HFB/HPFP at 25 °C , (denoted **a**)
- 10 wt% $G_6$ in 100/0 HFB/HPFP at 25 °C (denoted **b**)
- 0.5 wt% $G_6$ in 10/90 HFB/HPFP at 25 °C (denoted **c**) and 45 °C (denoted **d**)

The raw scattering data for samples **a** to **d** are presented in Figure 7-8.

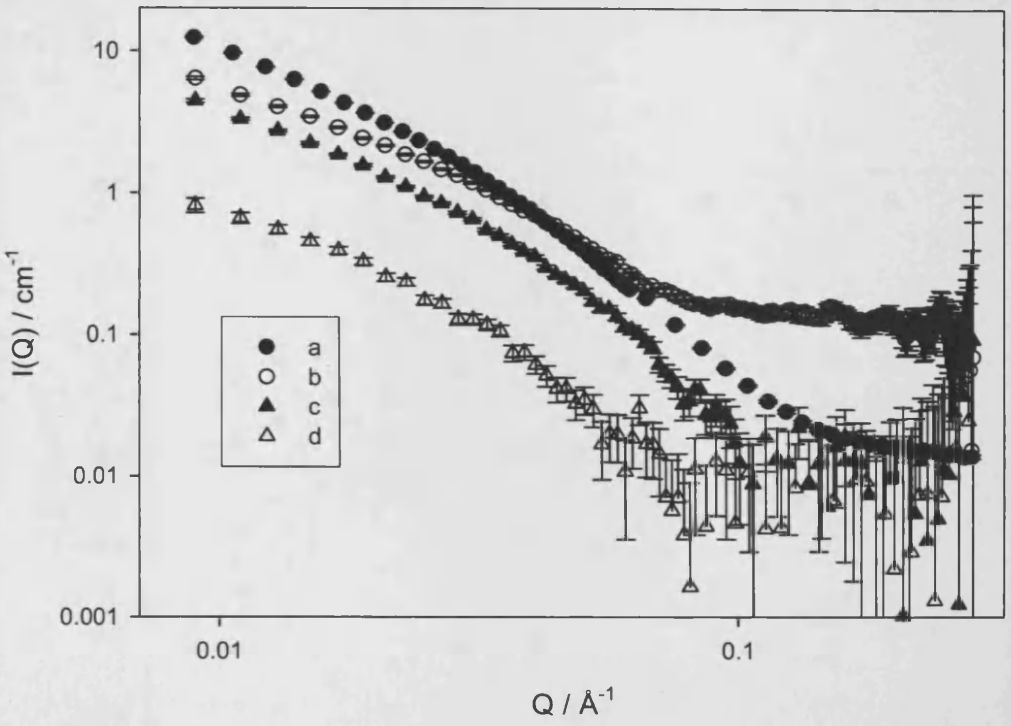


**Figure 7-8 Raw scattering data for samples a (filled circles), b (empty circles), c (filled triangles) and d (empty triangles).**

The Guinier approximation can be expressed as follows:

$$I(Q) \propto Q^{-D} \exp\left(-\frac{Q^2 R^2}{K}\right) \qquad \textbf{Equation 7-4}$$

where D is equal to 1, 0 and 2 and K to 4, 5 and 12 for cylinders, spheres and discs respectively. The characteristic dimension R, i.e. the sphere radius, the disc thickness, or the cylinder radius, can be obtained by plotting various quantities versus $Q^2$, as follows:

- Cylinders: $\text{Ln}[I(Q)\cdot Q]$ vs. $Q^2$ $\quad R = (\text{slope} \times 4)^{1/2}$
- Spheres: $\text{Ln}[I(Q)]$ vs. $Q^2$ $(Q\cdot R<1)$ $\quad R = (\text{slope} \times 5)^{1/2}$
- Discs: $\text{Ln}[I(Q)\cdot Q^2]$ vs. $Q^2$ $\quad R = (\text{slope} \times 2)^{1/2}$

Therefore, it is possible to predict the most probable particle shape by plotting the three curves described herein and select the one giving a linear decay over the low Q values. These three models are now applied to the four gelled samples described above.

Figure 7-9, 7-10 and 7-11 present the various Ln[I(Q) $\cdot Q^D$] vs. $Q^2$ curves for disc, sphere and cylinder shapes respectively, at low Q values ranging from 0.009 $Å^{-1}$ to 0.025 $Å^{-1}$.

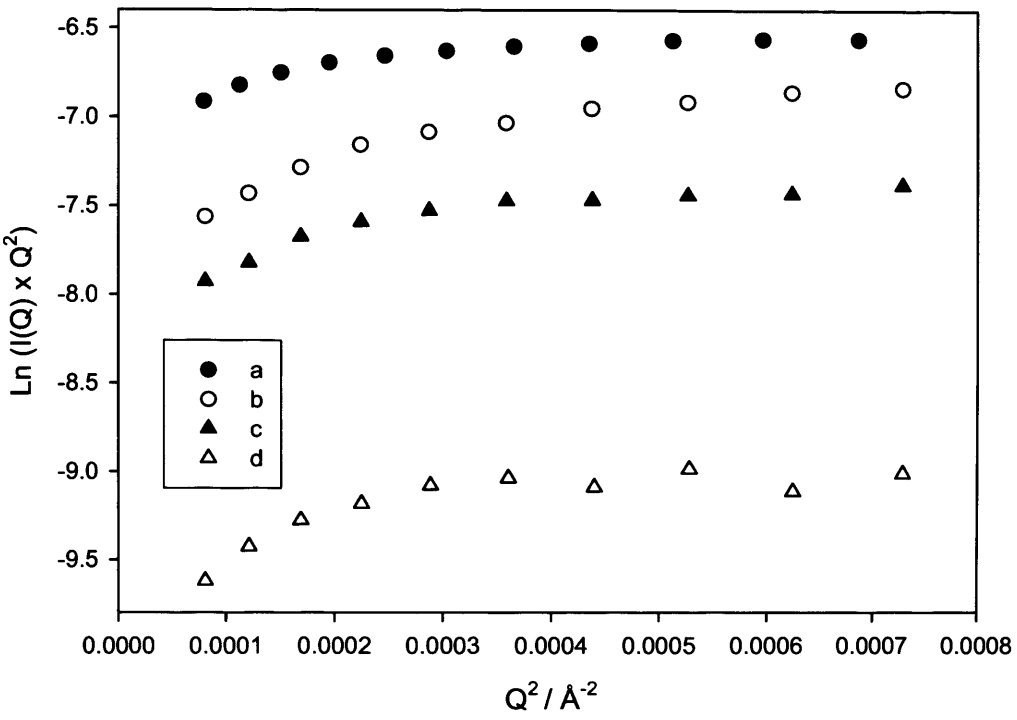


**Figure 7-9 Guinier approximation for a disc shape. Sample a (filled circles), b (empty circles), c (filled triangles) and d (empty triangles) at Q values comprised between 0.009 $Å^{-1}$ and 0.025 $Å^{-1}$.**

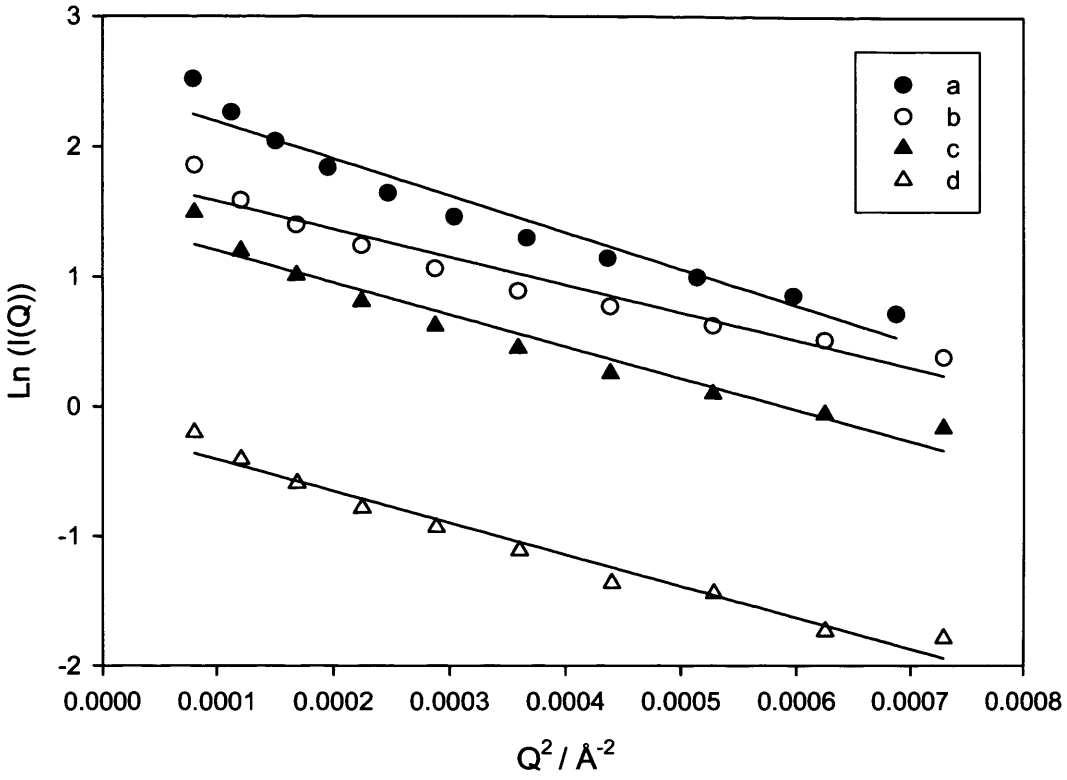


**Figure 7-10 Guinier approximation for a spherical shape for sample a (filled circles), b (empty circles), c (filled triangles) and d (empty triangles) at Q values comprised between 0.009 $Å^{-1}$ and 0.025 $Å^{-1}$, with linear fits to the data (full lines).**

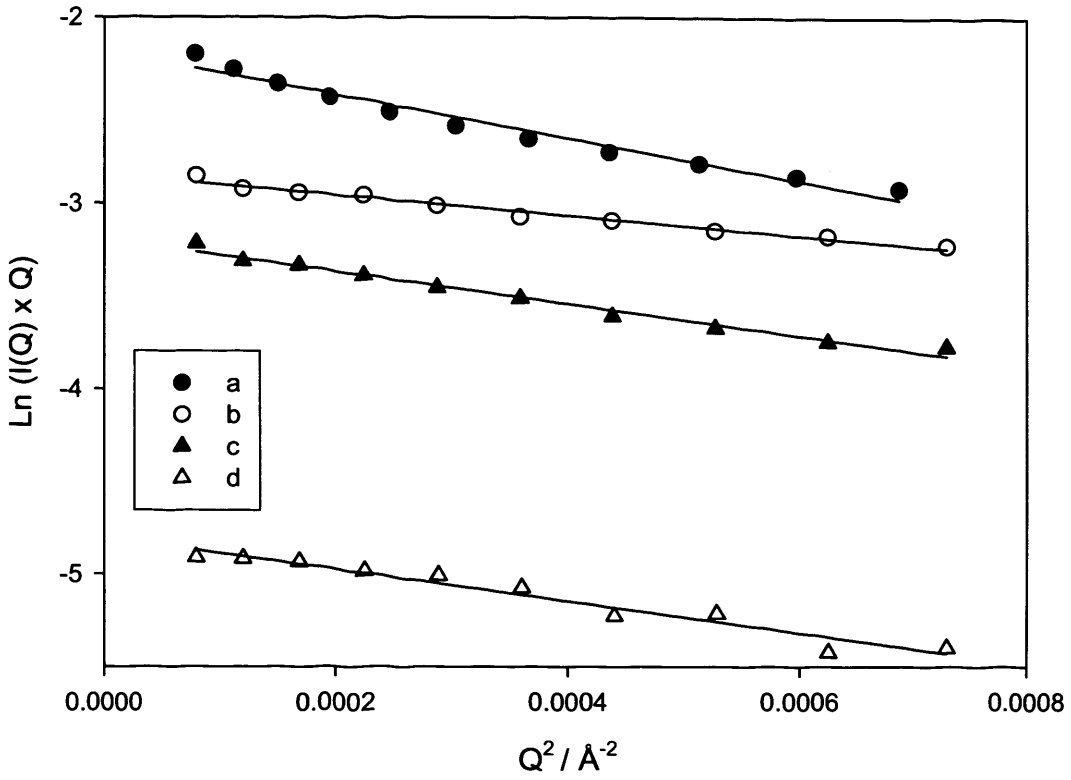


**Figure 7-11 Guinier approximation for a cylindrical shape for sample a (filled circles), b (empty circles), c (filled triangles) and d (empty triangles) at Q values comprised between 0.009 $Å^{-1}$ and 0.025 $Å^{-1}$, with linear fits to the data (full lines).**

Guinier approximation for disc shapes does not lead to a decay, but rather an upturn at low Q values. This geometry should be discarded. Both spherical and cylindrical shapes approximations lead to linear behaviour, but an analysis of the $\chi^2$ values suggests that the cylinder is more appropriate on a wider Q range. The calculated characteristic dimensions obtained for both the cylindrical and spherical approximations are presented in Table 7-4 below, along with the respective $\chi^2$ values of the linear fits.

| | Sphere Radius / Å | χ2 | Cylinder Radius / Å | χ2 |
|---|---|---|---|---|
| a | 124 | 0.9489 | 70 | 0.9722 |
| b | 103 | 0.9394 | 47 | 0.9767 |
| c | 111 | 0.9483 | 59 | 0.9807 |
| d | 111 | 0.9692 | 59 | 0.9492 |

**Table 7-4 Characteristic dimensions for spheres and cylinders along with the corresponding $\chi^2$ for linear fits, obtained from a Guinier analysis over the low Q data in samples a, b, c and d.**

For sample **d**, the $\chi^2$ value obtained using the spherical approximation is higher than the one obtained when using the cylindrical approximation. However, the spherical shape characteristic dimension is only valid under the condition that Q·R<1. The Q·R product values for the sphere radius of sample **d**, 111 Å, at the lowest and highest Q values used are presented in Table 7-5. To the exception of Q = 0.009, Q·R is always greater than 1, and it was concluded that the spherical shape should be discarded as well for this sample.

| | Q·R | |
|---|---|---|
| Sphere radius / Å | Q = 0.009 $Å^{-1}$ | Q = 0.025 $Å^{-1}$ |
| 111 | 0.999 | 2.775 |

**Table 7-5 Q·R values for the sphere radius of sample d, at Q values of 0.009 $Å^{-1}$ and 0.027$Å^{-1}$.**

Best results are found with the Guinier approximation for cylinders, leading to radii comprised between 59 Å and 70 Å. Even though the samples were chosen so as to explore the scatterers shape in varied ranges of solvents ratio, concentrations, temperatures, and chain lengths, they all fit best to cylindrical shapes, with radii of comparable values. The structure of the scatterers present in the gelled samples could therefore be compared to rods or fibrils. A model that allows one to fit over the entire Q range a morphology that both possesses a relatively curved dimension and an elongated one is the Kholodenko worm-like chain model. Therefore, this model was tested against the bulk of the scattering data using the FISH program [49].

The Kholodenko worm-like chain model was derived from a Gaussian coil model, where long thin rods are made of a succession of $n$ cylindrical elements of statistical length $\ell$ and radius $R_{ax}$ which could be represented as in Figure 7-12, in which $n$ = 10. The contour length of the chain, **L**, is equal to the product $n \cdot \ell$.

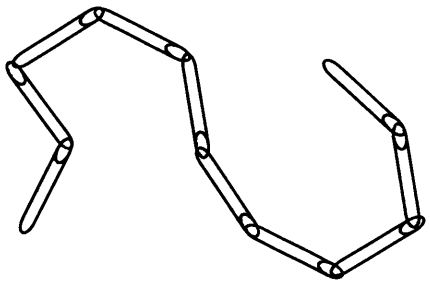

**Figure 7-12 Schematic view of a Kholodenko worm-like chain.**

The scattering intensity generated from Kholodenko worm like chains is proportional to two terms, as seen in Equation 7-5.

$$I(Q) \propto P_{Worm}(Q) * P_{Axial}(Q) \qquad \textbf{Equation 7-5}$$

The Kholodenko model smoothly interpolates between the Gaussian coil and rigid rod predictions and the number of segments (***n***) forming the chain gives an indication regarding the flexibility of the chain. The smaller the values for n, the stiffer the chain. When ***n*** tends towards infinity, the scatterer adopts a flexible Gaussian random coil whereas tendings toward 1, a rigid rod is obtained. The details of this model can be found in Chapter 3-Materials and Methods, section 3.4.2.4. Here, the focus will be drawn to the insight given by the fitted parameters regarding the size, shape and physical arrangement of the scatterers responsible for the gelled structure.

The characteristics of these long and thin rods will be investigated under various circumstances. They will be presented first as a function as the gelator concentration, then as a function of the gelator chain length, of the solvents ratio, and finally as a function of the temperature.

### 7.4.2 Sensitivity of the Kholodenko worm-like chain model to the radius and the length of the scatterers

Parameters extracted via the fits to the Kholodenko worm-like chains model led to the knowledge of the radius of the scatterers ($\mathbf{R_{ax}}$), the number of segments that compose them (***n***), and their statistical length ($\boldsymbol{\ell}$). The total contour length of the chain, **L**, is calculated, and equal to $\boldsymbol{n \cdot \ell}$. Prior to discussing the values of the parameters obtained, it was decided to first test the sensitivity of this model to $\mathbf{R_{ax}}$, ***n*** and $\boldsymbol{\ell}$, as follows. A

best fit giving physically sensible parameters was determined. Then, all parameters were kept to their optimal values, except for $\mathbf{R_{ax}}$, ***n*** and **l** that were varied, each one at a time. This study was conducted on a typical dataset, belonging to a sample composed of 0.8 wt% $G_6$ in 10/90 HFB/HPFP measured at 25 °C. Figure 7-13 presents the best fit obtained while all parameters were allowed to float, and Table 7-6 the corresponding parameter values.

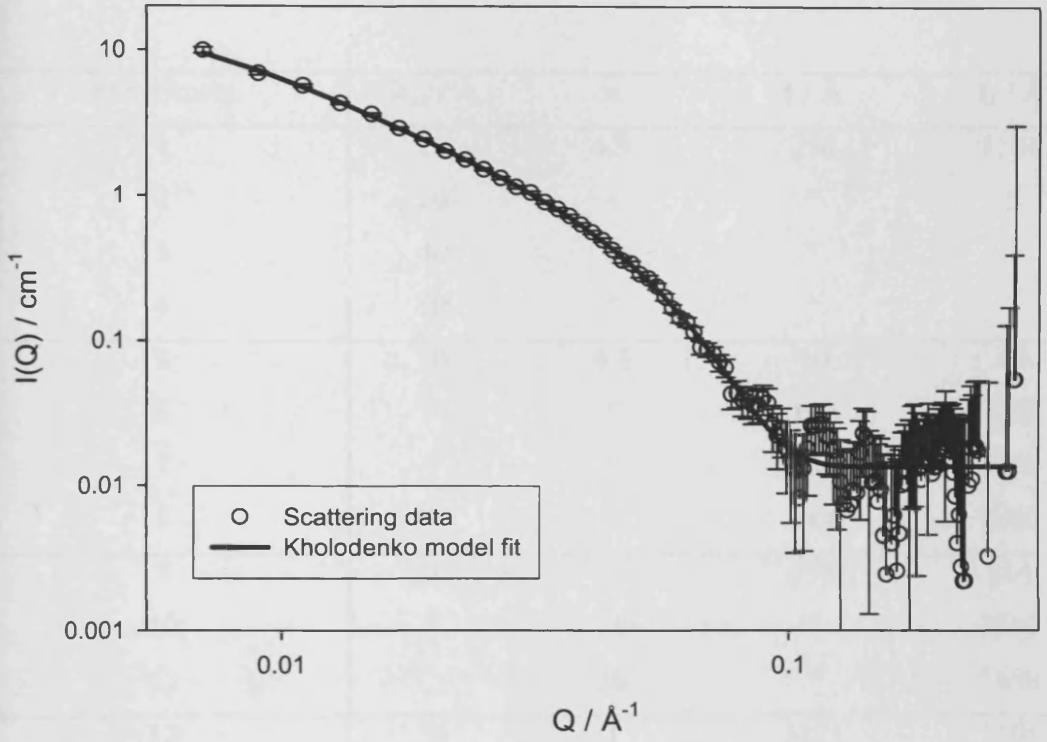


**Figure 7-13 Scattering data (empty circles) and optimal fit (full line) using the Kholodenko worm-like chain model.**

| n | ℓ / Å | L = n* ℓ / Å | Rax / Å |
|---|---|---|---|
| 4.3 | 256 | 1101 | 30 |

**Table 7-6 Corresponding parameter values for sample 0.8 wt% $G_6$ in 10/90 HFB/HPFP, 25 °C, fitted with of Kholodenko worm-like chain model.**

### 7.4.2.1 Experimental Design

The input values chosen to test the sensitivity of the radius $\mathbf{R_{ax}}$ were 10 Å, 20 Å, 40 Å and 50 Å. The total length **L** of the chain could be kept constant by varying both ***n***

and $\ell$ at the same time, as $\mathbf{L} = n \cdot \ell$, and the binary systems ($n$; $\ell$) chosen to test the sensitivity of n and l were (1; 1101), (10; 110.1), (100; 11.01) and (1000; 1.101). The total length of the chain can be varied by either changing the number of segments ($n$), or their respective length ($\ell$). To test the sensitivity of the chain length by an alteration of the length of the segments, $\ell$ values were chosen as 10, 100, 500, 2000, and to test the sensitivity of the chain length by an alteration of the number of segments, values were chosen as 1, 10 and 30, leading to the following experimental design described in Table 7-7.

| Experiment | $R_{ax}$ / Å | $n$ | $\ell$ / Å | L / Å |
|---|---|---|---|---|
| 1 | 10 | 4.3 | 256 | 1101 |
| 2 | 20 | " | " | " |
| 3 | 40 | " | " | " |
| 4 | 50 | " | " | " |
| 5 | 30 | 4.3 | 10 | 43 |
| 6 | " | " | 100 | 430 |
| 7 | " | " | 500 | 2150 |
| 8 | " | " | 2000 | 8600 |
| 9 | 30 | 1 | 256 | 256 |
| 10 | " | 10 | " | 2560 |
| 11 | " | 30 | " | 7680 |
| 12 | 30 | 1 | 1101 | 1101 |
| 13 | " | 10 | 110.1 | " |
| 14 | " | 100 | 11.01 | " |
| 15 | " | 1000 | 1.101 | " |

**Table 7-7 Experimental design aimed at testing the sensitivity of the Kholodenko worm-like chain model to $R_{ax}$, n, $\ell$ and L.**

### 7.4.2.2 Sensitivity to $R_{ax}$ (experiments 1-4)

Figure 7-14 presents the Kholodenko model data points for experiments 1 to 4, along with the raw scattering data and the best fit.

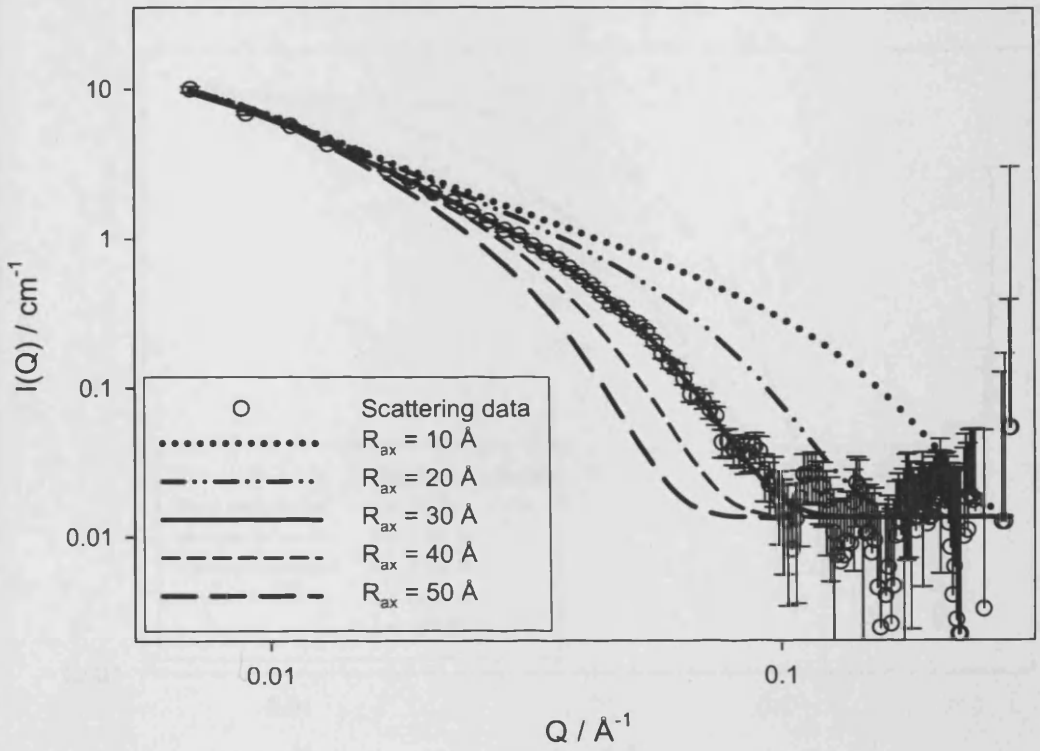


**Figure 7-14 Kholodenko model data points for experiments 1 to 4, along with the raw scattering data and the best fit.**

Although the entire range of radii tested (10 to 50 Å) resulted in adequate fits to low Q values up to 0.0150 Å, the radius of 30 Å was found to be the only fit over the entire Q range. The fits are very sensitive to $R_{ax}$ values in the mid Q range, and it is easily conceivable that a clear distinction could be made between radii values of $30 \pm 5$ Å.

### 7.4.2.3 Sensitivity to ℓ (experiments 5-8)

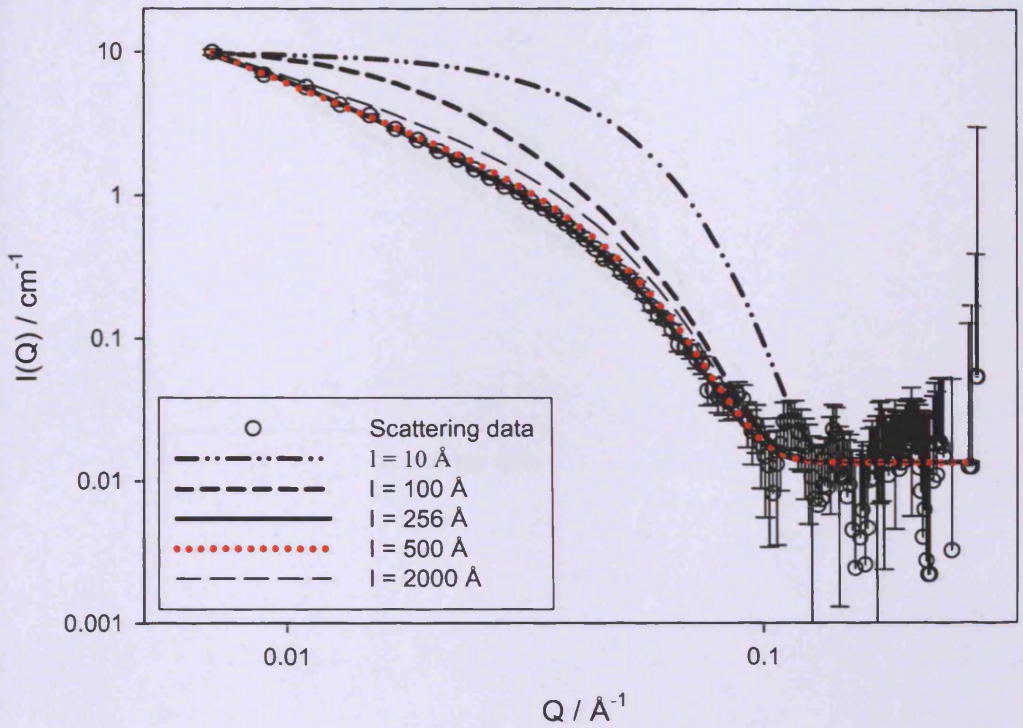


**Figure 7-15 Kholodenko model data points for experiments 5 to 8, along with the raw scattering data and the best fit.**

Decreasing the length of the statistical segments below their optimal value results in a poor fit to the data (ℓ = 10, 100 Å). However, for larger ℓ values (ℓ = 500, 2000 Å) and therefore longer chains, no prominent deviation from the optimal fit can be witnessed. It should be noted that for ℓ > 2000, the fit routine became very unstable and could not converge anymore. The model therefore seems to loose its sensitivity towards longer chain elements, although within a maximum length, above which no fitting convergence can be obtained.

### 7.4.2.4 Sensitivity to *n* (experiments 9-11)

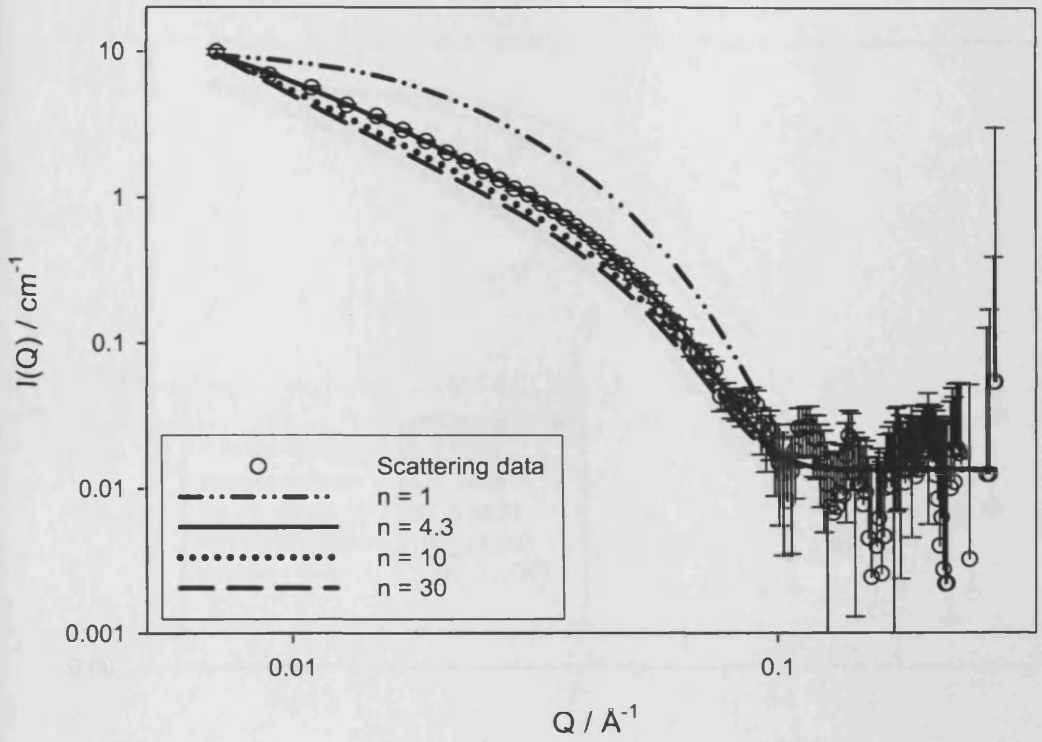


**Figure 7-16 Kholodenko model data points for experiments 9 to 11, along with the raw scattering data and the best fit.**

The strongest deviation from the ideal fit is witnessed for n = 1, *i.e.* for small chains consisting of only one rigid rod. The curvature of the fits is hardly affected by higher n values, and thus longer chains. For n values greater than 35 no convergence of the fitting routine was obtained. The model therefore seems to loose its sensitivity towards numerous chain elements and chain lengths, although within a maximum limit, above which no fitting convergence is found.

### 7.4.2.5 Sensitivity to (n; ℓ) couples for constant contour length L (experiments 12-15)

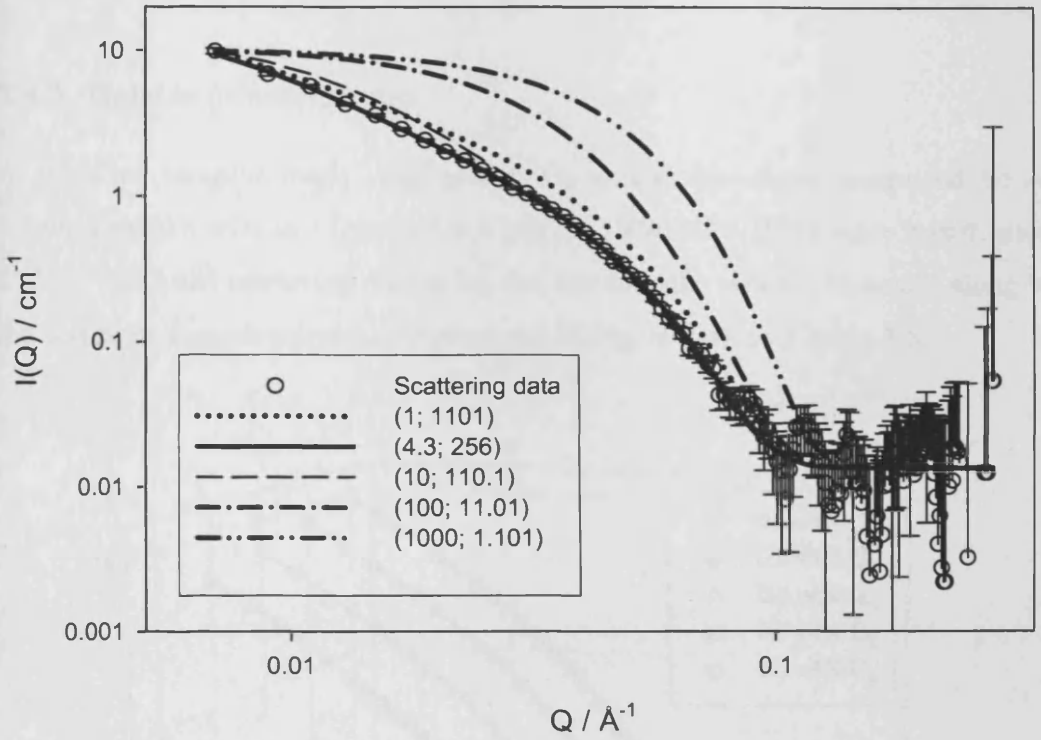


**Figure 7-17 Kholodenko model data points for experiments 12 to 15, along with the raw scattering data and the best fit.**

It was shown above that for longer chain lengths, the fittings were hardly sensitive to both the length of the statistical chain elements and their number. The impact of n and ℓ is now questioned for a fixed contour length L, fixed at its optimal value as determined in the first instance. For (n, ℓ) values of (1; 1100) and (10; 110.1), the curvature of the fittings is scarcely affected. However, as seen previously when n only is fixed to 1 (Exp. 9), or ℓ only fixed to 100 (Exp. 6), a strong deviation is observed. This suggests that, within a reasonable proximity to the optimum value, it is not so much the ratio of n and ℓ values that is important, but the total contour length of the chain. For highly different ratios of n and ℓ, *i.e.* (100; 11.01) and (1000; 1.101), a strong deviation is observed. For such cases, the extremes of the physical meaning of the parameters are attained, as a dimension of 11.01 Å is less than the length of one gelator molecule, and 1.101 Å would represent a dimension of the order of a bond length.

The most sensitive parameter seems to be the radius $R_{ax}$, and for long chains, the fittings are much less sensitive to the number of statistical elements and their statistical length.

### 7.4.3 Gelator concentration

A series of samples made with gelator $G_6$ at concentrations comprised between 0.4 wt% and 0.8 wt% in a fixed solvent ratio of 10/90 HFB/HPFP were investigated at 25 °C. The fitted scattering data using the Kholodenko worm-like chain, along with the corresponding parameters, are presented in Figure 7-18 and Table 7-8.

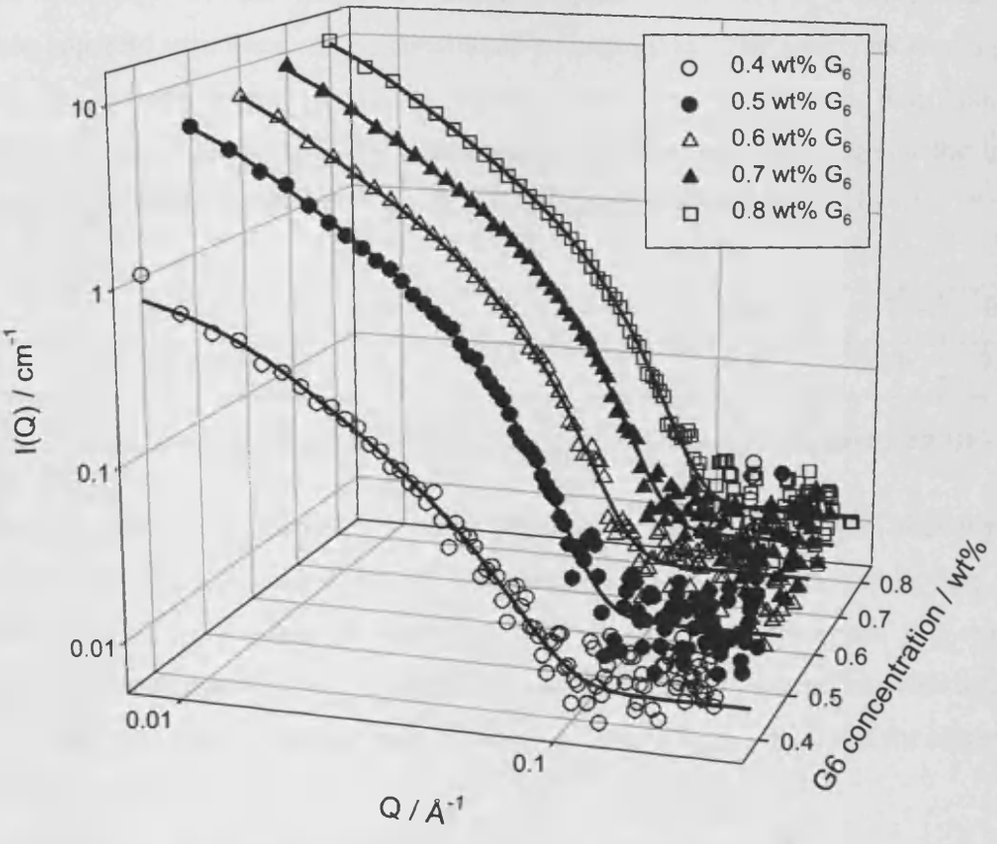


**Figure 7-18 $G_6$ in 10/90 HFB/HPFP solvent ratio, at concentrations of 0.4wt% (empty circles), 0.5 wt% (filled circles), 0.6 % (empty triangles), 0.7 wt% (filled triangles) and 0.8wt% (empty squares). The full lines are the Kholodenko fits.**

| | $R_{ax}$ / Å | $n$ | $\ell$ / Å | $L=n*\ell$ / Å |
|---|---|---|---|---|
| 0.4 wt% | 25 | 3.8 | 168 | 638 |
| 0.5 wt% | 31 | 3.3 | 293 | 967 |
| 0.6 wt% | 32 | 3.0 | 350 | 1050 |
| 0.7 wt% | 31 | 3.2 | 306 | 979 |
| 0.8wt% | 30 | 4.3 | 256 | 1100 |

**Table 7-8 Summary of the extracted parameters for $G_6$ in 10/90 HFB/HPFP, for concentrations comprised between 0.4 and 0.8 wt%.**

All concentrations present very similar fit parameters. The radius does not seem to be affected by the gelator concentration, nor does the number of statistical segments. It was shown that for such length, the model is rather insensitive to $\ell$ and L, therefore these apparent variations can be considered as negligible. The scatterers forming the gels can be seen as rather stiff, as made of very few segments n, thin fibre-like structures. The only concentration-dependant variation observed regards the initial scattering intensity (at Q=0.007 $cm^{-1}$), and values are presented in Table 7-9.

| $G_6$ / wt% | 0.4 | 0.5 | 0.6 | 0.7 | 0.8 |
|---|---|---|---|---|---|
| Initial intensity / $cm^{-1}$ | 1.04 | 5.57 | 6.65 | 8.28 | 9.96 |

**Table 7-9 Initial scattering intensity as a function of concentration for $G_6$ in 10/90 HFB/HPFP.**

The initial scattering intensity increases with the gelator concentration, showing that even though the size and shape of the scatterers were found to merely vary with concentration, the number of scatterers does increase. Scatterers do not vary in geometry but there are more entities as the concentration is increased. This leads to stiffer gels, and can be directly linked to the increase in $T_{gel\text{-}sol}$ observed for increasing gelator concentrations.

A similar experiment was conducted on samples made with gelator $G_4$ in an identical solvent ratio, 10/90 HFB/HPFP, at concentrations of 0.8 wt% and 1 wt%. The resulting fitted parameters are presented in Table 7-10 and the fitted scattering data in Figure 7-19.

| | $R_{ax}$ / Å | $n$ | $l$ / Å | L=$n$*$l$ / Å |
|---|---|---|---|---|
| 0.8 wt% | 25 | 2.7 | 347 | 937 |
| 1 wt% | 26 | 2.4 | 240 | 576 |

**Table 7-10 Summary of the extracted parameters for $G_4$ in 10/90 HFB/HPFP, for concentrations comprised of 0.8 and 1 wt%.**

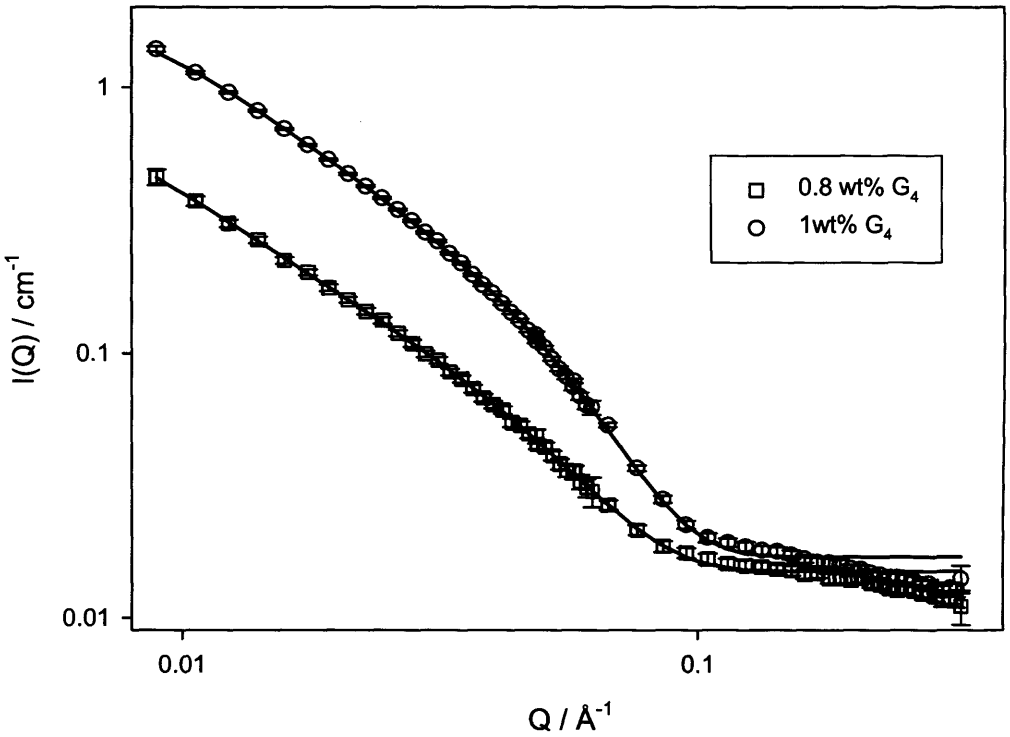


**Figure 7-19 $G_4$ in 10/90 HFB/HPFP solvent ratio, at concentrations of 0.8wt% (empty squares) and 1 wt% (empty circles). The full lines are the Kholodenko fits.**

The fit parameters are hardly concentration dependent. The worm-like chain geometries are very similar to the ones obtained in the previous case, suggesting the presence of stiff and thin rod-like scatterers. The initial intensity was also found to increase with concentration, demonstrating the presence of a higher number of these structures as the concentration increases. However, the initial intensity values were found to be smaller for gelator $G_4$ than $G_6$, suggesting that such $G_4$ samples, although prepared at comparable concentrations to those of $G_6$, contained a much more limited number of scatterers, hence fibrils. This is in full agreement with the observed phase behaviour completed in the macroscopic assessment of these gels (Section 7.3.1.). Indeed, $G_4$ was found to require a minimum concentration of 0.6 wt% to form a gel,

whereas this was as low as 0.3 wt% for $G_6$, in otherwise identical conditions. Fewer fibrils participate in the gel network, and hence can act as scatterers.

### 7.4.4 Gelator chain length

As shown previously, the geometry of the scatterers forming the gelled structure is hardly concentration-dependent, once a gel is formed. If not ideal, it is still possible to compare the fit parameter values obtained for gels made at different concentrations using $G_4$, $G_5$, $G_6$ and $G_8$, and thus investigate the effect of the gelator chain length on scatterer geometry. The samples used here are 0.8 wt% $G_4$, 0.6 wt% $G_5$, 0.8 wt% $G_6$ and 1 wt% $G_8$, in solvent ratio 10/90 HFB/HPFP, at 25 °C. Figure 7-20 presents the scattering data along with the Kholodenko worm-like chain fits, and Table 7-11 presents the parameters obtained from these fits.

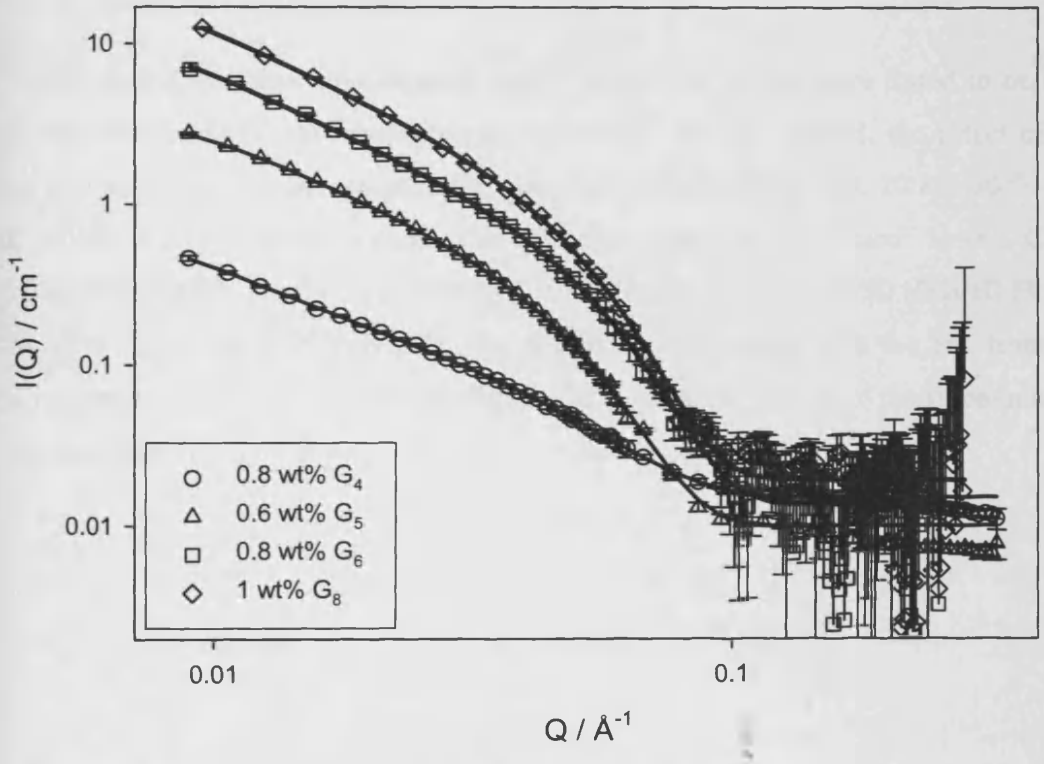


**Figure 7-20 Testing the influence of the gelator chain length. The full lines represent the Kholodenko fits.**

| | $R_{ax}$ / Å | $n$ | $l$ / Å | $L=n*l$ / Å |
|---|---|---|---|---|
| 0.8 wt% $G_4$ | 25 | 2.7 | 347 | 937 |
| 0.6 wt% $G_5$ | 33 | 2.0 | 322 | 644 |
| 0.8 wt% $G_6$ | 30 | 4.3 | 256 | 1101 |
| 1 wt% $G_8$ | 33 | 4.3 | 263 | 1131 |

**Table 7-11 Parameters for 0.8 wt% $G_4$, 0.6 wt% $G_5$, 0.5 wt% $G_6$, 0.35 wt% $G_8$, using a Kholodenko worm-like fit.**

No clear trend can be observed between the length of the gelator backbone and the various parameters obtained from the fits. As will be described later in section 7.4.7, one could suggest that the lengthier the gelator molecule, the larger the worm-like chain $R_{ax}$ values. However, gels made using $G_6$ and $G_4$ led to the smaller values of $R_{ax}$, whilst the larger ones were obtained with $G_5$ and $G_8$.

### 7.4.5 Solvent composition

Once a gelled structure was formed, the fit parameter values were found to be both hardly concentration and chain-length dependent. In this respect, the effect of the solvent ratio on scatterer geometry is now investigated, in 10/90, 20/80, 50/50 and 100/0 HFB/HPFP solvent ratios. The following samples were used: 1 wt% $G_8$ in 10/90 HFB/HPFP, 1 wt% $G_8$ in 20/80 HFB/HPFP, 5 wt% $G_8$ in 50/50 HFB/HPFP and 10 wt% $G_6$ in 100/0 HFB/HPFP. The scattering data along with the fits from the Kholodenko model are presented in Figure 7-21, while the values of the fit parameters are shown in Table 7-12.

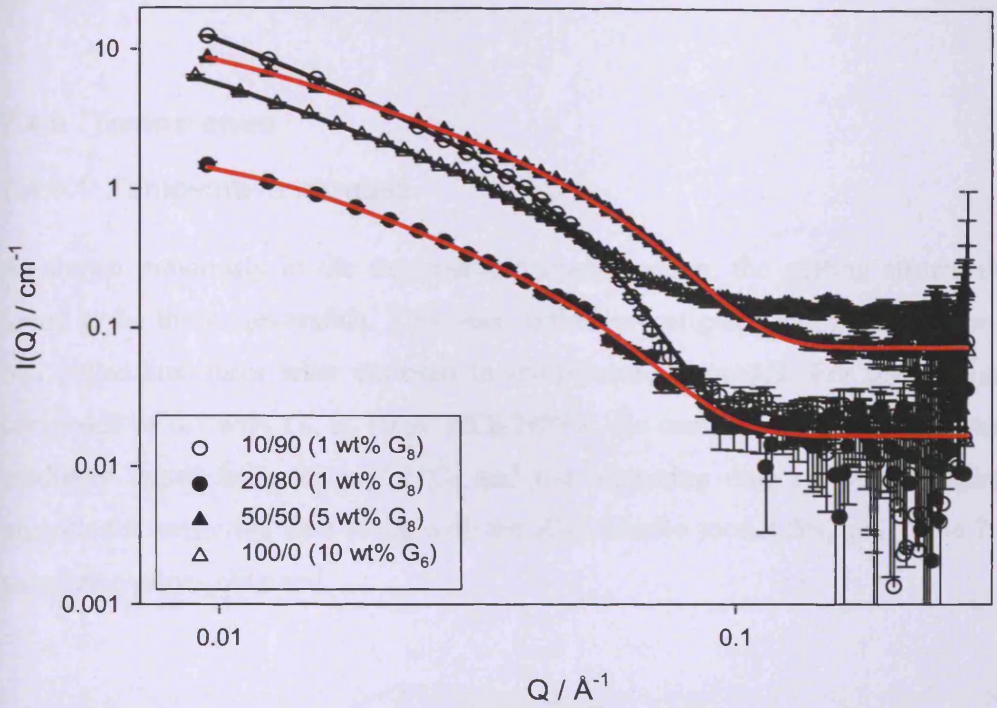


**Figure 7-21 Scattering data for gels formed in various HFB/HPFP solvent ratios, along with the Kholodenko model fits (black and red solid lines).**

| HFB/HPFP | $R_{ax}$ / Å | *n* | *l* / Å | L=*n***l* / Å |
|---|---|---|---|---|
| **10/90** 1 wt% $G_8$ | 33 | 4.3 | 263 | 1130 |
| **20/80** 1 wt% $G_8$ | 26 | 2 | 234 | 468 |
| **50/50** 5 wt% $G_8$ | 23 | 1.2 | 389 | 467 |
| **100/0** 10 wt% $G_6$ | 30 | 2.3 | 323 | 743 |

**Table 7-12 Fit parameter values for various HFB/HPFP solvent ratios.**

When considering solvent ratios of 10/90, 20/80 and 50/50 only, $R_{ax}$ is found to decrease with increases in the HFB proportion of the solvent mixture, thus suggesting a different packing of the gelator molecules. However, gels formed in a 100 % HFB present a larger $R_{ax}$ than those formed in 20/80 and 50/50 HFB/HPFP, and all $R_{ax}$ values still lay in a very similar range. The other parameters also offer very little variation. The geometry of the scatterers building up the gelled structure appears to be independent of the solvent ratios. As the HFB proportion is increased, higher gelator

concentrations are required to achieve gelation, but the apparent packing of the gelator molecules is unaffected.

### 7.4.6 Temperature

#### 7.4.6.1 Temperature increase

As shown previously in the macroscopic study section, the gelling structures were found to be thermoreversible. This was further investigated using SANS, for which two gelled structures were exposed to temperature increases. For the first sample, composed of 0.7 wt% $G_6$ in 10/90 HFB/HPFP, the sample changer temperature was gradually raised from 25 to 50 °C, and the scattering data recorded. Figure 7-22 presents the scattering data along with the Kholodenko model fits, and Table 7-13 the parameter values obtained.

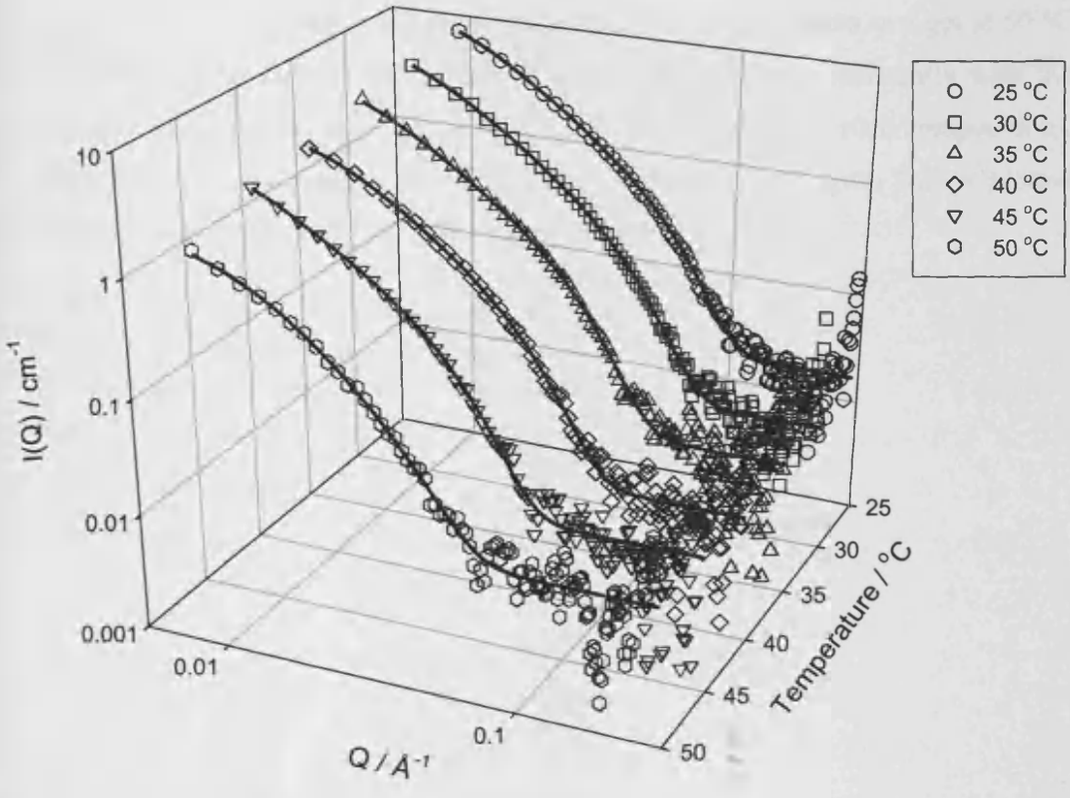


**Figure 7-22 Scattering data as a function of the temperature for 0.7 wt% $G_6$ in 10/90 HFB/HPFP- the full lines represent the Kholodenko model fits.**

| | $R_{ax}$ / Å | *n* | *l* / Å | L=*n***l* / Å |
|---|---|---|---|---|
| 25 °C | 27 | 7.3 | 151 | 1102 |
| 30 °C | 28 | 6.7 | 155 | 1039 |
| 35 °C | 30 | 4.8 | 190 | 912 |
| 40 °C | 30 | 5.1 | 156 | 796 |
| 45 °C | 36 | 2.9 | 294 | 853 |
| 50 °C | 34 | 12.6 | 85 | 1071 |

**Table 7-13 Parameter values for sample 0.7 wt% $G_6$ in 10/90 HFB/HPFP as a function of temperature.**

No clear trend can be observed regarding the evolution of the fit parameters with temperature, the variations obtained cannot be considered as significant, as shown by the sensitivity study of the model. The geometry of the scatterers therefore appears to remain constant throughout the temperature increase. However, the initial intensity does vary with concentration. Although the structure mostly remains as a gel at 50 °C (as witnessed as the sample was removed from the rack, and consistently with the macroscopic study which gave $T_{gel\text{-}sol} = 57 \pm 2$ °C for a sample of such composition), the initial intensity decreases as the temperature increases. On Figure 7-23 is plotted the initial intensity I(Q=0.009 $Å^{-1}$) as a function of the temperature.

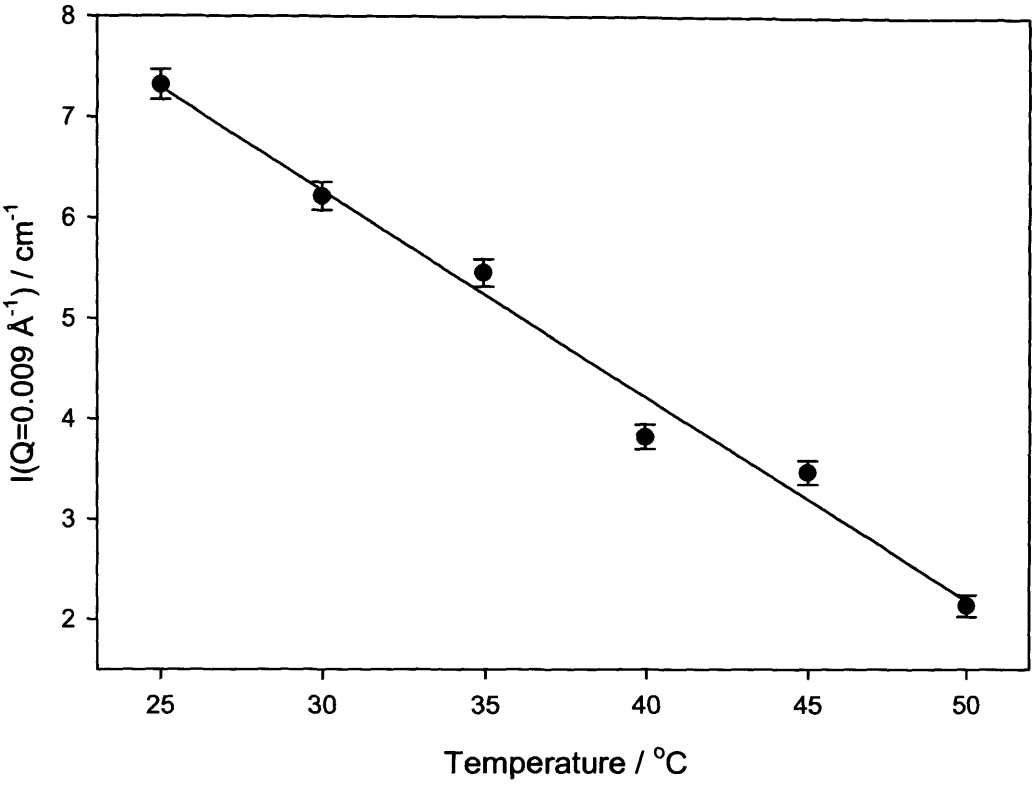


**Figure 7-23 I(Q=0.009Å$^{-1}$) for sample 0.7 wt% $G_6$ in 10/90 HFB/HPFP as a function of temperature**

The initial intensity is found to decrease in a rather linear fashion over the temperature range (25-50 °C). This demonstrates that even though the geometry of the scatterers was found to be invariant, there are less present in the sample as the temperature is increased. Fewer long and thin rods participate in the formation of the gelled network, which will eventually lead to a fully liquid state, when all gelator molecules are free in solution. This can be seen as a progressive desaggregation of the formerly aggregated gelator molecules, but it also shows that the melting process, over this temperature range, is continuous. This phenomenon could be witnessed thanks to the rather high $T_{gel\text{-}sol}$ for this sample. Provided a sample bearing a low enough $T_{gel\text{-}sol}$ is chosen, it was questioned whether a more abrupt decrease of the scattering could be witnessed. For this experiment, a sample of composition 10 wt% $G_6$ in 100/0 HFB/HPFP was chosen and its scattering measured at 25, 30 and 35 °C. The data obtained are presented in Figure 7-24.

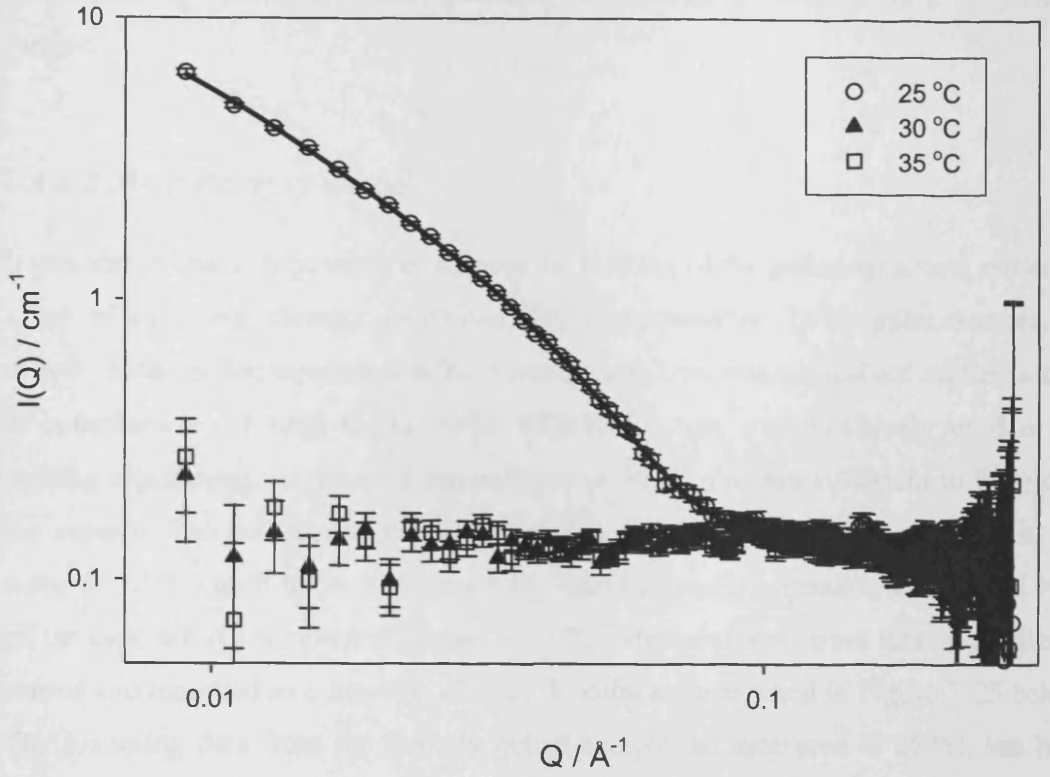


**Figure 7-24 10 wt% $G_6$ in 100/0 HFB/HPFP at 25 °C, 30 °C and 35 °C. The full line represents the Kholodenko model fit.**

At 25 °C, the sample is fully gelled and the scattering data is best fitted to a Kholodenko worm-like chain. The parameter values are listed in Table 7-14. When the temperature is increased to 30 °C, the former signal is totally collapsed. The structures that were present at 25 °C no longer exist at 30 °C and nor, *a fortiori*, at 35 °C. The sample removed from the rack is indeed fully liquid.

| $R_{ax}$ / Å | *n* | ℓ / Å | L / Å |
|---|---|---|---|
| 30 | 2.3 | 323 | 743 |

**Table 7-14 Fitted parameters for 10 wt% $G_6$ in 100/0 HFB/HPFP at 25 °C**

In such a case, the transition from a gelled state to a fully liquid one is clearly observed. However, no gradual decrease in the intensity could be witnessed (as in the former case) as the temperature increments applied encompassed the $T_{gel\text{-}sol}$ temperature of the sample.

These two experiments complement each other well, showing both the gradual nature of the melting transition, and the resulting flat scattering obtained for a fully liquid sample.

#### 7.4.6.2 Re-building of the gel

It was shown that it is possible to witness the melting of the gelled structure, either via a loss of scattering intensity, or its complete disappearance. In a similar manner, the re-built of the gelled structure can be investigated. This was carried out on the sample of composition 0.7 wt% $G_6$ in 10/90 HFB/HPFP that was previously used in the melting experiment, for which a temperature of 50 °C was not sufficient to fully melt the sample. The sealed cell containing the sample was therefore immersed in hot water (≈ 70 °C) until the sample was fully liquid (visually assessed), and placed back on the rack, set at a temperature equal to 25 °C. Measurements were then immediately started and recorded as a function of time. Results are presented in Figure 7-25 below. The scattering data from the initially gelled sample, as measured at 25 °C, has been added at t = 150 min as a calibrant against which the presented samples can be compared.

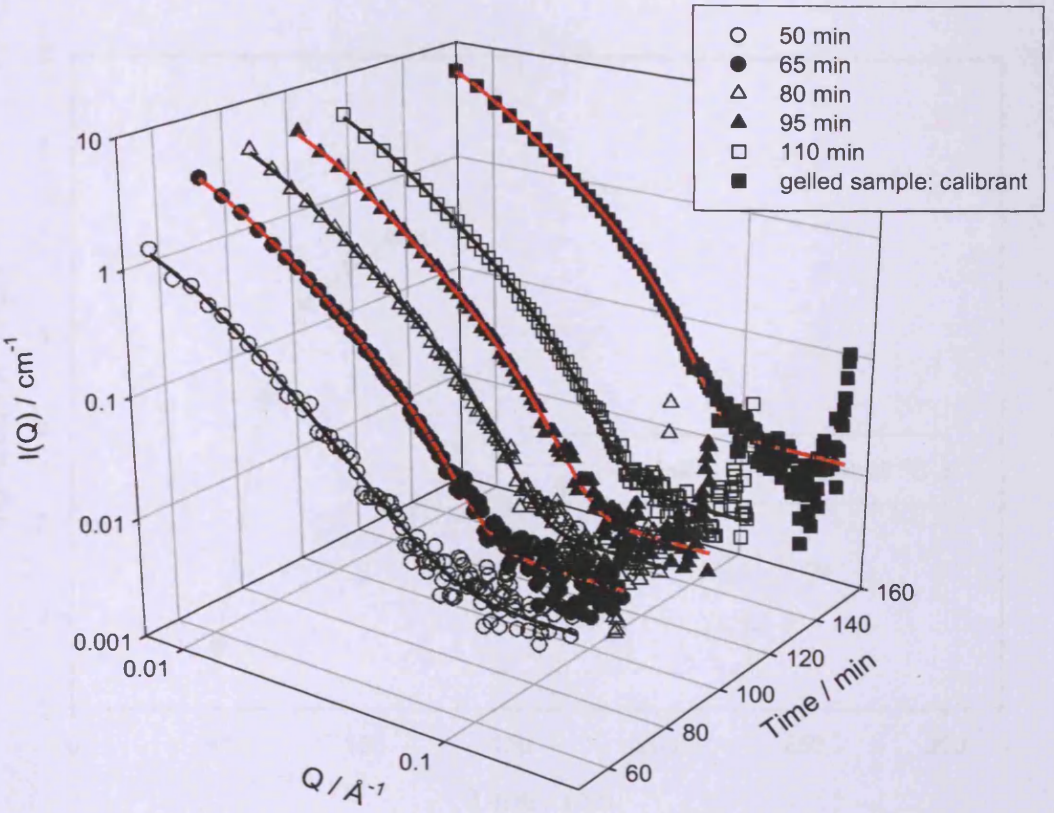


**Figure 7-25 Re-building of 0.7 wt% $G_6$ in 10/90 HFB/HPFP as a function of time, at 25 °C. The solid (red and black) lines present the Kholodenko model fits.**

Even though the measurements were started as soon as possible, a flat scattering, corresponding to a liquid state of the sample, could not be obtained. The re-building of the gel of such composition takes place to rapidly. Therefore, an easier way to witness the changes occurring with time is to plot the initial intensity I(Q = 0.009 $Å^{-1}$) as a function of time. These data are presented in Figure 7-26. The red data point placed at 300 min represents the value previously obtained at 25 °C, measured before any temperature increase was applied to the system. The time of 300 min was chosen arbitrarily.

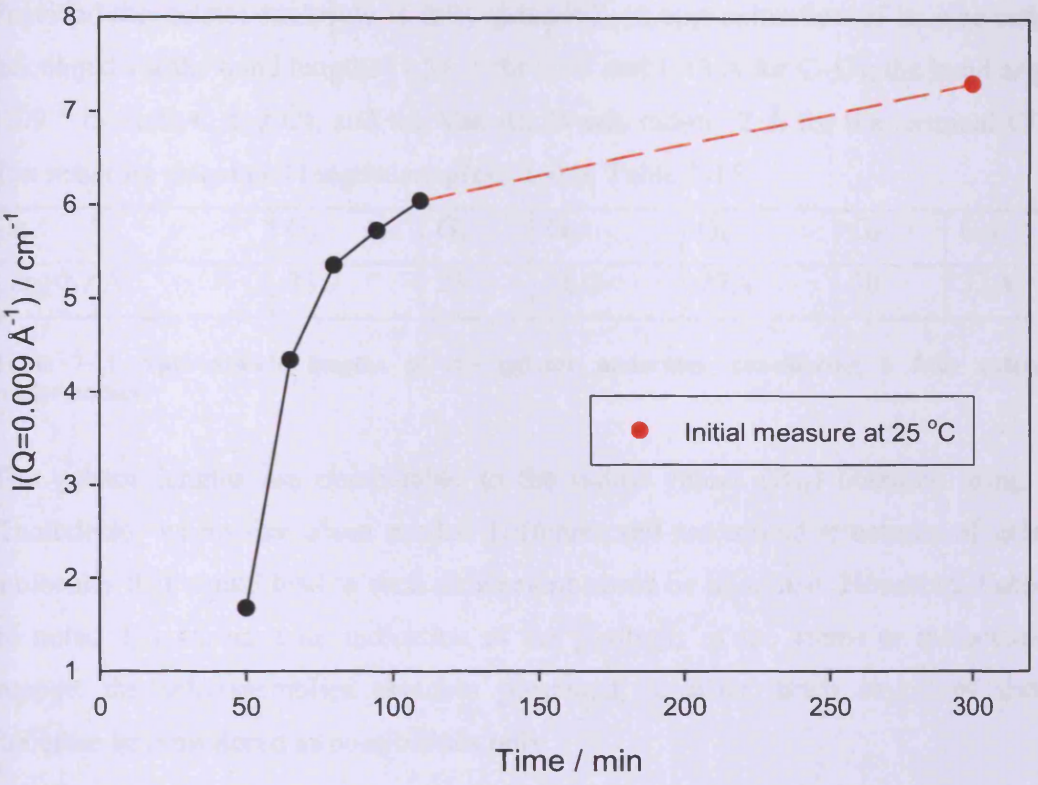


**Figure 7-26 I(Q = 0.009 Å$^{-1}$) as a function of time for the gel re-building, at 25 °C. The red data point represents the values obtained prior to any melting experiment, at 25 °C.**

The initial intensity I(Q = 0.009 Å$^{-1}$) increased with time, giving clear indication of the re-building process of the gel. However, the experiment could not be conducted over a long enough period to witness I(Q = 0.009 Å$^{-1}$) recover its original value, hence the gel its original structure. The gel re-building appears to take place very rapidly to start with, but the recovery of a fully gelled state is obtained for much longer times.

SANS allowed us to probe in the gelled structures the presence of aggregates bearing a cylindrical shape, which appeared to be worm-like chains that are able to form a fibrillar network entrapping the solvent. When a gelling structure develops, the radius of the worm-like chain was found to be invariant with concentration. Up to a certain point, the shape of the scatterers did not change upon an increase in temperature and only its intensity decreased. However, as seen in the case of the sample composed of 10 wt% $G_6$ in HFB solely, once fully liquid, the scattering pattern becomes flat.

### 7.4.7 Hypotheses on the self-assembly

Provided the gelator molecule is fully extended, an approximation of its size can be calculated via the bond lengths (1.54 Å for C–C and 1.42 Å for C–O), the bond angles (109 ° for both $\hat{C}$ and $\hat{O}$), and the Van der Waals radius (2 Å for the terminal $CH_3$). The resulting calculated lengths are presented in Table 7-15.

| Gn | $G_3$ | $G_4$ | $G_5$ | $G_6$ | $G_8$ | $G_{10}$ |
|---|---|---|---|---|---|---|
| Length / Å | 23.7 | 25 | 26.2 | 27.4 | 30 | 32.4 |

**Table 7-15 Approximate lengths of the gelator molecules, considering a fully extended conformation.**

The gelator lengths are comparable to the radius values ($R_{ax}$) obtained using the Kholodenko worm-like chain model. Different self-assembled structures of gelator molecules that would lead to such dimensions could be imagined. However, it should be noted that we have no indication of the positions of the atoms or molecules to support the self-assemblies sketches presented hereafter. Such structures should therefore be considered as possibilities only.

The gelator molecules can stack upon one another, or next to one another, via hydrogen bonding between their hydroxyl and ester groups, as sketched in Figure 7-27. Two hypotheses were envisaged regarding their aggregation behaviour, the first being a case where the gelator molecule would be paired and simply stack upon one another vertically, either in a straight fashion or with a twist angle, the second being the initial formation of coronas that would then stack upon one another, thus crating long fibrils.

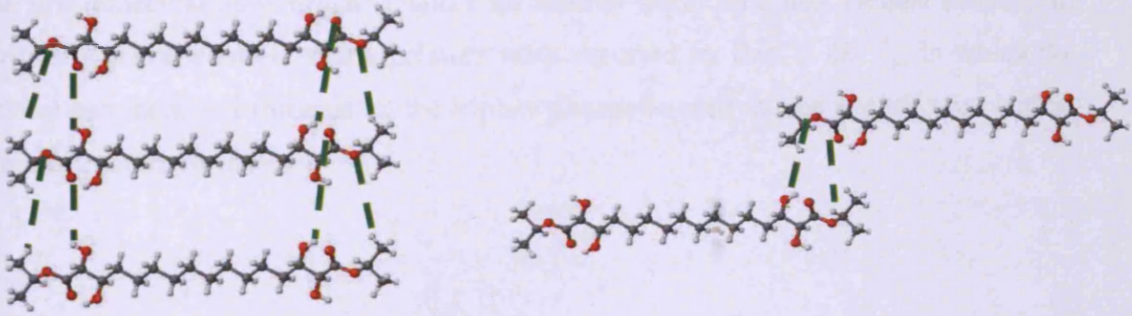

**Figure 7-27 Sketch of gelator molecules stacking via non-covalent H-bond interactions, one on top of another (left) or side by side (right).**

### 7.4.7.1 Pair stacking

In order to obtain radii such as those extracted via the fitting procedure, *i.e.* ≈ 30 Å, an average of two gelator molecules would have to be linked side by side, and then stack upon one an other. A straight stacking and a helicoidal one could be envisaged and are sketched in a naïve and schematic manner in Figure 7-28, where each segment represents a gelator molecule. However, the geometry resulting from a straight stacking (Figure 7-28, left) is closer to a flat ribbon than a cylinder. A twist of this structure (Figure 7-28, right), resulting in the helicoidal shape, could account for the cylindrical component 'seen' by the fitting model.

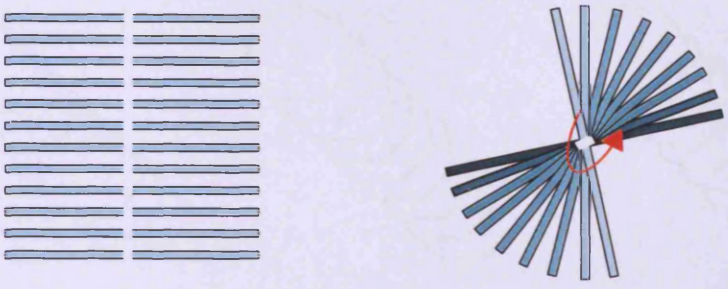

**Figure 7-28 Vertical stacking of pairs of gelator molecules, straight (left) and helicoidal (right)**

Occurrences of spontaneous assembly of molecules into helical spirals have been reported in the literature. Pantos *et al.* [50] created hydrogen-bonded helical organic nanotubes using amino-acid derived naphtalenediimide molecules, for which the helix direction was determined by the chirality of the amino acid employed. Zhan and co-workers [51] report on self-assembled helical spherical nanotubes, obtained using an L-glutamic acid based bolaamphiphile (molecules in which two or more hydrophilic groups are connected by hydrophobic functionalities), which also happened to act as an low molecular mass organogelators for alcohol-water mixtures. Helical stacking of triphenylbenzene-based organogelators were reported by Bao *et al.* [52], in which the chiral peripheral substituents on the triphenylbenzene core induce a clockwise helical microstructure formation.

### 7.4.7.2 Formation of coronas

To obtain long fibrils of similar radii, the gelator molecules could also associate as coronas, which would then stack upon one another to form long fibrils. Bearing in mind the average $R_{ax}$ of 30 Å, the circumference for the cylindrical section would be ≈ 189 Å, which would correspond to 6, 7 or 8 gelator molecules, depending on their estimated fully extended chain length. These coronas could be represented as hexa- hepta- or octogons in which each side stands for a gelator molecule, linked to its neighbour through non covalent interactions. The resulting long fibrils could be sketched as in Figure 7-29.

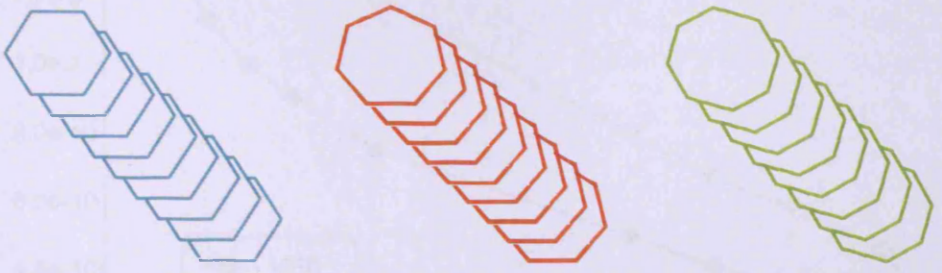

**Figure 7-29 Sketches for the 3 corona assemblies: (left) hexa-, (centre) hepta- and (right) octagonal.**

Finally, all gels investigated using small-angle neutron scattering were formed in the quartz cell itself. It is therefore possible that the cell dimensions could impose a constraint on the growth of the colloidal domain, when compared to the macroscopic study for which the gels were formed in larger glass vials.

## 7.5 PGSE-NMR study

PGSE-NMR was used to access the diffusion coefficients of the fluorinated solvents HFB and HPFP, firstly on their own, in the absence of LMOGs, and then within the gelled structures. Upon a temperature increase previously characterized, the gels undergo a gel to sol phase transition. The experiments proposed here address the question of the matrix state upon the diffusion coefficients of both solvents, as a direct measure of their mobility within the gel and in solution.

### 7.5.1 Diffusion of the solvents in the absence of gelator

Figure 7-30 shows the diffusion coefficient (Ds) of HFB and HPFP as a function of the fluoroalcohol weight fraction ($x_{HFB}$) in the solvent mix, at a fixed temperature of 296K. The diffusion coefficients of pure HPFP ($\mathbf{Ds}_{HPFP}$) and pure HFB ($\mathbf{Ds}_{HFB}$) are read at $x_{HFB}$ =0 and $x_{HFB}$=1 respectively.

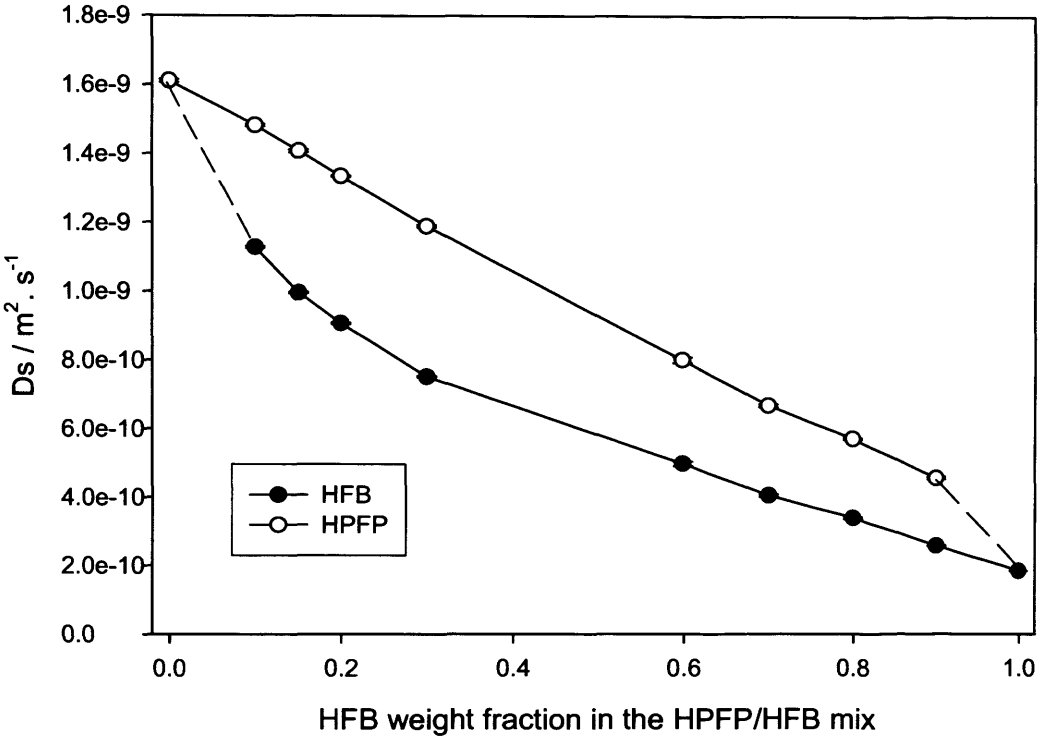


**Figure 7-30 Diffusion coefficient of HPFP and HFB as a function of HFB weight fraction in solutions of mixed solvents, at 296K.**

At 296.3K, the diffusion coefficient of HPFP is nearly an order of magnitude higher than that of HFB, respectively 1.61 x $10^{-9}$ $m^2$ $s^{-1}$ for HPFP and 1.85 x $10^{-10}$ $m^2$ $s^{-1}$ for HFB. Upon incremental additions of HFB, $\mathbf{Ds}_{HPFP}$ decreases linearly. HPFP molecules will indeed feel the slower HFB environment and their mobility is hindered, resulting in a decrease in HPFP diffusion coefficient. This difference in the diffusion coefficient is due to the different viscosities of HFB and HPFP, respectively equal to 3.47 mPas and 0.4186 mPas at 25 °C.

### 7.5.2 Diffusion of the solvents in a gelled network: effect of the temperature

Gels were formed using gelator $G_6$, at concentrations ranging from 0.3 wt% to 1wt%, in a 10/90 HFB/HPFP solvent ratio. In such conditions, all samples were gel-like at 296.3K. A sample free of gelator was re-made and kept for reference. Such gelator concentrations and solvent ratio conditions were chosen so that gels could form easily without requiring too high quantities of the gelator (of limited availability), and that they would have $T_{gel\text{-}sol}$ reachable with the PGSE-NMR heating device. Figure 7-31 shows the diffusion coefficient for HPFP as a function of the inverse temperature, for gelator $G_6$ concentrations comprised between 0 and 1wt%. A very similar graph is obtained for the measured diffusion coefficients of HFB and results are presented in Figure 7-32. An experimental error of 5 % is considered for all data, representing the reproducibility achieved by the PGSE-NMR spectrometer, as determined by P. C. Griffiths on previous measurements when setting up the equipment.

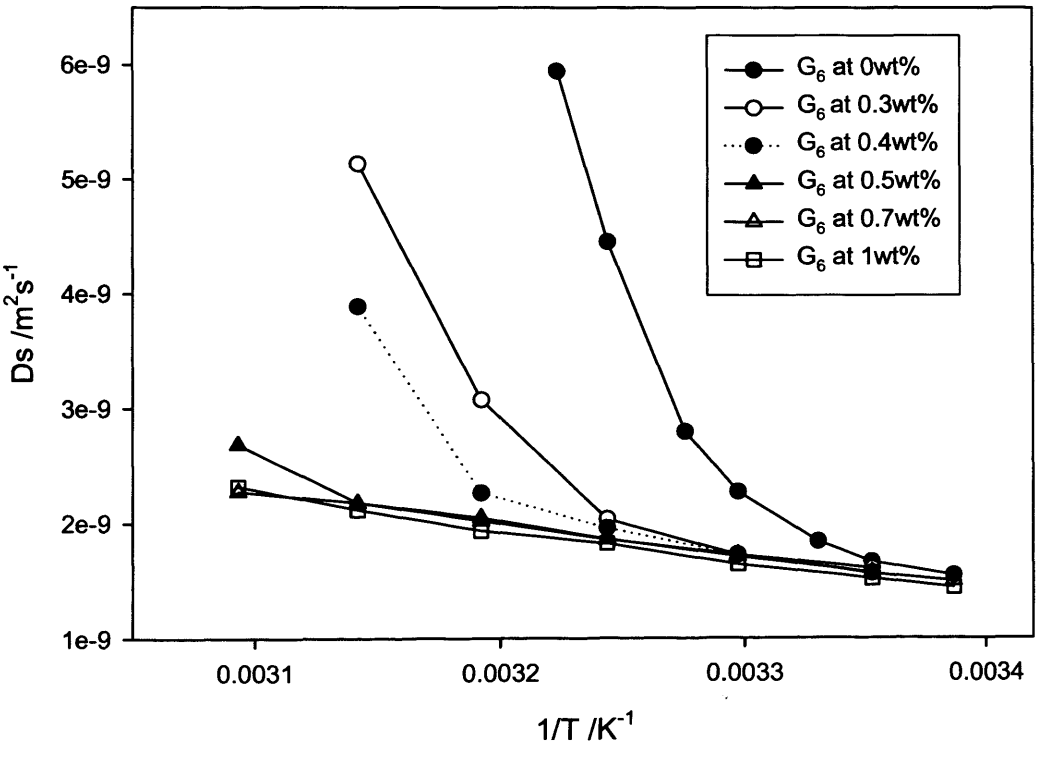


**Figure 7-31 HPFP diffusion coefficient as a function of inverse temperature, for gelator $G_6$ concentrations ranging from 0 to 1wt%.**

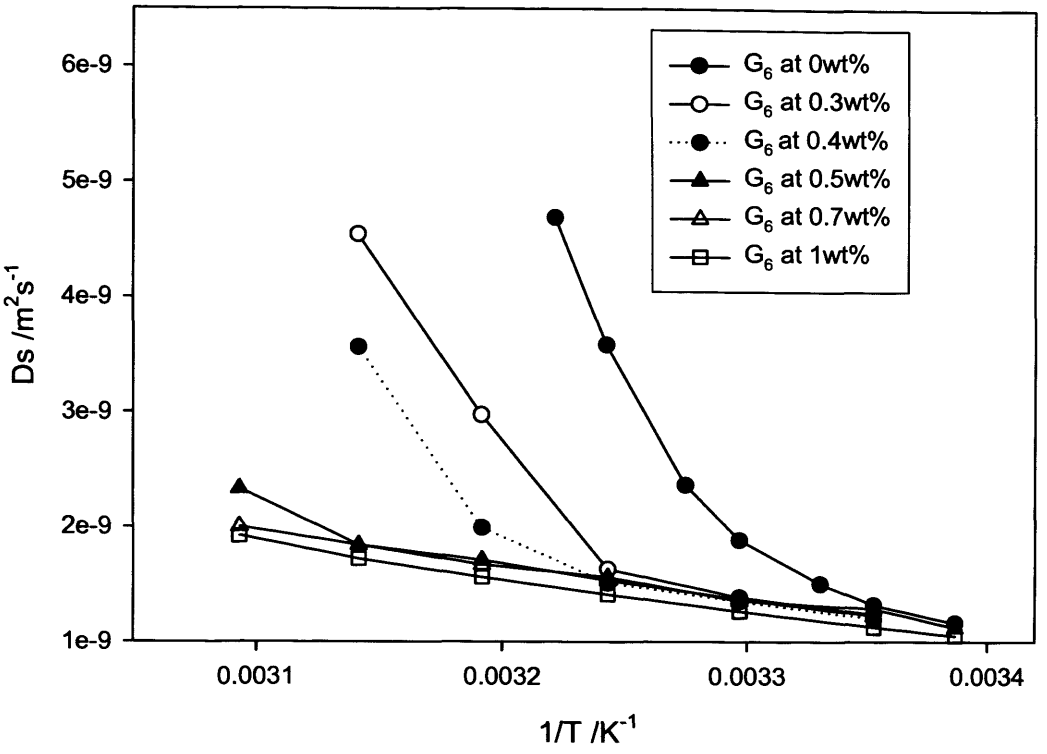


**Figure 7-32 HFB diffusion coefficient as a function of inverse temperature, for gelator $G_6$ concentrations ranging from 0 to 1wt%.**

As can be seen from Figure 7-31 and Figure 7-32, both $\mathbf{Ds}_{HFB}$ and $\mathbf{Ds}_{HPFP}$ respond in a very similar fashion to an increase in temperature, although HFB diffusion coefficient results are shifted to lower values compared to HPFP, for viscosity reasons explained previously.

Three key points should be noted from these results: the increase of the diffusion coefficient with temperature, the linearity or non-linearity of this increase, and the value of the diffusion coefficient at room temperature for all gelator concentrations.

### 7.5.2.1 Increase of Ds with temperature

Firstly, the diffusion coefficients of both HPFP and HFB for all samples increase with temperature. Several factors contribute to this effect. With temperature, the solvent molecules acquire higher thermal energy, and are able to move more vigorously.

Then, the intermolecular forces between the molecules of the liquids also become weaker, compared to the kinetic energy, as the temperature is raised. The viscosity of a liquid decreases with temperature and so does the density.

### 7.5.2.2 Linearity and non-linearity of the Ds increase

Samples made with 1wt% and 0.7wt% $G_6$ present a linear Ds-(temperature)$^{-1}$ relationship on the entire range of temperature. This is not the case for the lower concentrations of gelator, which show linearity up to a certain temperature, above which the diffusion coefficients increase dramatically. For the solvents free of gelator, no linear region is obtained, only an exponential increase is observed. This behaviour can be explained by the presence of convection movements taking place in the sample.

In an NMR probe, it is difficult to heat the sample homogeneously. Heating is usually performed by passing an air flux that is generated at the bottom of the sample. Temperature gradients therefore occur within the liquid sample, generally in a vertical fashion, inducing convection movements, as shown in Picture 7-5.

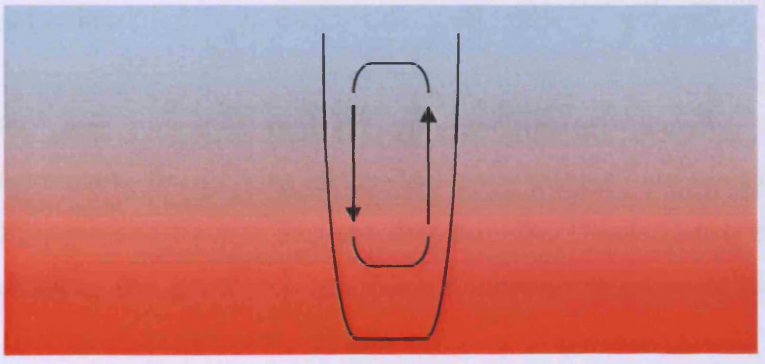


**Picture 7-5 Schematic view of convection movements in an NMR tube heated at its bottom.**

The temperature gradient leads to a density gradient, where a less dense material is created at the bottom of the sample (the "hot spot"), which then goes up, cools down, consequently increasing in density and therefore going back down. Convection movements occur along the vertical axis of the NMR tube [53].

In the diffusion experiments, the translational motion of the molecules is measured. Convection, being also a form of translational motion, will greatly alter the measured values. If convection is not taken into account, the measured diffusion coefficients will be larger then their convection-free value [54]. The effect is all the more pronounced with low viscosity liquids, as in our case. Two different approaches have been developed to account for or to prevent this phenomenon, either involving the design of a pulse sequence that suppresses the signal attenuation coming from convection [55], or by the specific tailoring of the NMR tubes geometry. For the convection suppression sequence, a 180 ° pulse is needed, but the equipment available here cannot produce such a pulse. Then, even though elaborate convection compensating pulse sequences have been written [56, 57] and can minimize the effect of convection, by no means do they prevent the phenomenon to happen. In the case of cylindrical samples, which are the ones used in NMR experiments, the temperature gradient is inversely proportional to the radius of the NMR tube to the power of four [55]. One way to diminish the effect of convection is therefore to design very narrow NMR tubes. It is also possible to use very small sample height, so that the temperature gradient will be reduced. This was tried by Hayamizu and Price [54] in an experiment where they set the sample height to 2mm, but this measure was effective only for highly viscous liquids.

In the present case, it seems that the gelling structure actually prevents such convection movements from taking place. But once the gels are melted, linearity is lost and the diffusion coefficients increase dramatically. This is clearly seen in Figure 7-33, by overlaying the gel-to-sol transition temperatures of each samples to the diffusion coefficient of, in this case, HPFP.

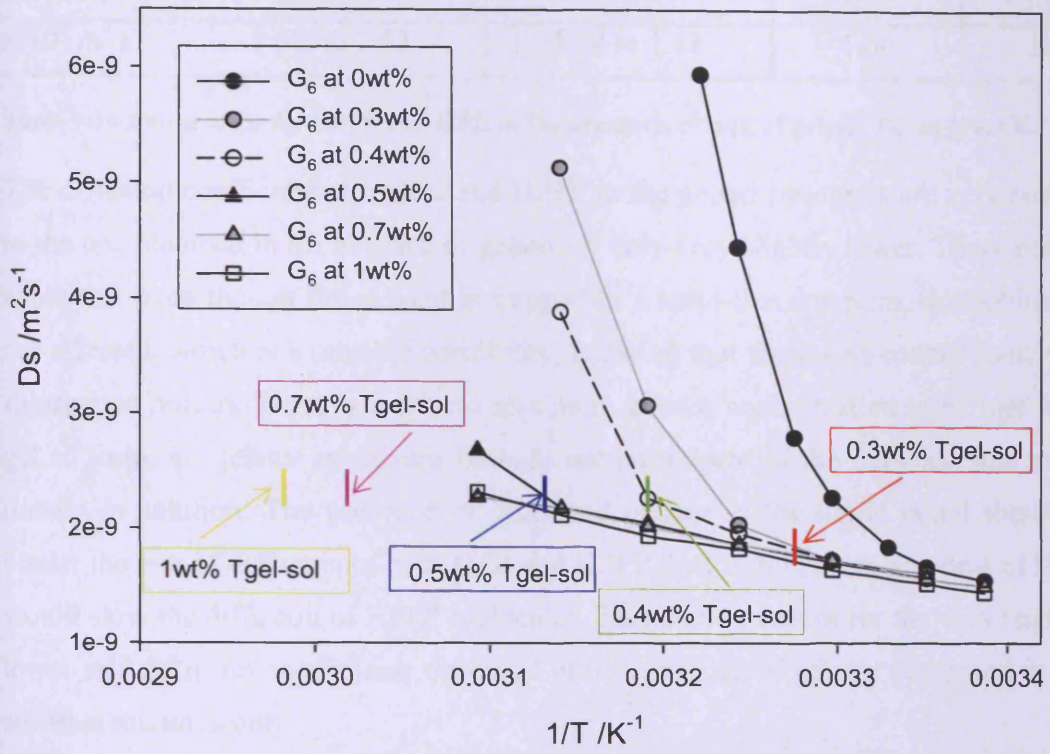


**Figure 7-33 Corresponding temperatures of the gel-to-sol transitions for gelator $G_6$ concentrations equal to 0.3wt% (red), 0.4 wt% (green), 0.5 wt% (blue), 0.7wt% (pink) and 1wt% (yellow).**

The temperatures at which the gel-to-sol phase transitions occur corresponds to the onset of the loss of linearity region for samples containing 0.3, 0.4 and 0.5 wt% $G_6$. In order not to damage the equipment, the higher transition temperatures corresponding to 0.7wt% and 1wt% $G_6$ were not investigated.

### 7.5.2.3 Ds at 296.3K as a function of gelator concentration

At 296.3 K, HPFP diffusion coefficient remains virtually unchanged over the entire range of gelator concentration, from 0wt% to 1wt%. This is also found to be the case for HFB. Table 7-16 summarises the range of self-diffusion coefficients obtained at 298.3 K for HPFP and HFB when gelled with gelator $G_6$ at concentrations ranging from 0.3 wt% to 1 wt%, and compares them to the self-diffusion coefficient for HPFP and HFB in a 10/90 HFB/HPFP mixture free of gelator at the same temperature.

| Temperature 298.3 K | 0.3 wt%-1 wt% $G_6$ HPFP | 0.3 wt%-1 wt% $G_6$ HFB | 0 wt% $G_6$ HPFP | 0 wt% $G_6$ HFB |
|---|---|---|---|---|
| Ds /$10^9$ $m^2$ $s^{-1}$ | 1.60 to 1.52 | 1.24 to 1.13 | 1.66 | 1.32 |

**Table 7-16 Range of Ds for HPFP and HFB in the presence, or not, of gelator $G_6$, at 298.3 K.**

The diffusion coefficients for HFB and HPFP in the gelled structures are very similar to the one obtained in the absence of gelator, if only very slightly lower. These results show that even though the solvent is trapped in a solid-like structure, its mobility is not affected, which is a sensible possibility, knowing that these gels consist mostly of fluorinated liquids. There is a critical minimum gelator concentration to be met for a gel to form, all gelator molecules thus do not participate in the network, and some remain in solution. The presence of dissolved gelator in the liquid could therefore hinder the rate of diffusion of both HFB and HPFP, just as minimum amounts of HFB would slow the diffusion of HPFP molecules. This could account for the very slightly lower self-diffusion coefficients observed in the presence of gelator compared to the solvents mixtures only.

## 7.6 Scanning Electron Microscopy (SEM)

SEM was performed on both the gelator raw powder and on dried gels that were left to ambient air until all solvent had evaporated. Ideally, to observe the gelled network *in situ*, it would have been preferable to either turn to environmental SEM, allowing to work under 'wet' conditions or to freeze dry a gelled sample in order to form a xerogel and keep the original structure intact. The liquid would have been slowly drawn off without causing the solid matrix in the gel to collapse from capillary action, as did happen with conventional evaporation. However, the environmental SEM and freeze-drying equipment were restricted to aqueous systems. Figure 7-34 presents digital images of the conventionally dried gel (of initial composition 1 wt% $G_8$ in 10/90 HFB/HPFP) and Figure 7-35 shows ones captured from gelator $G_8$ raw powder.

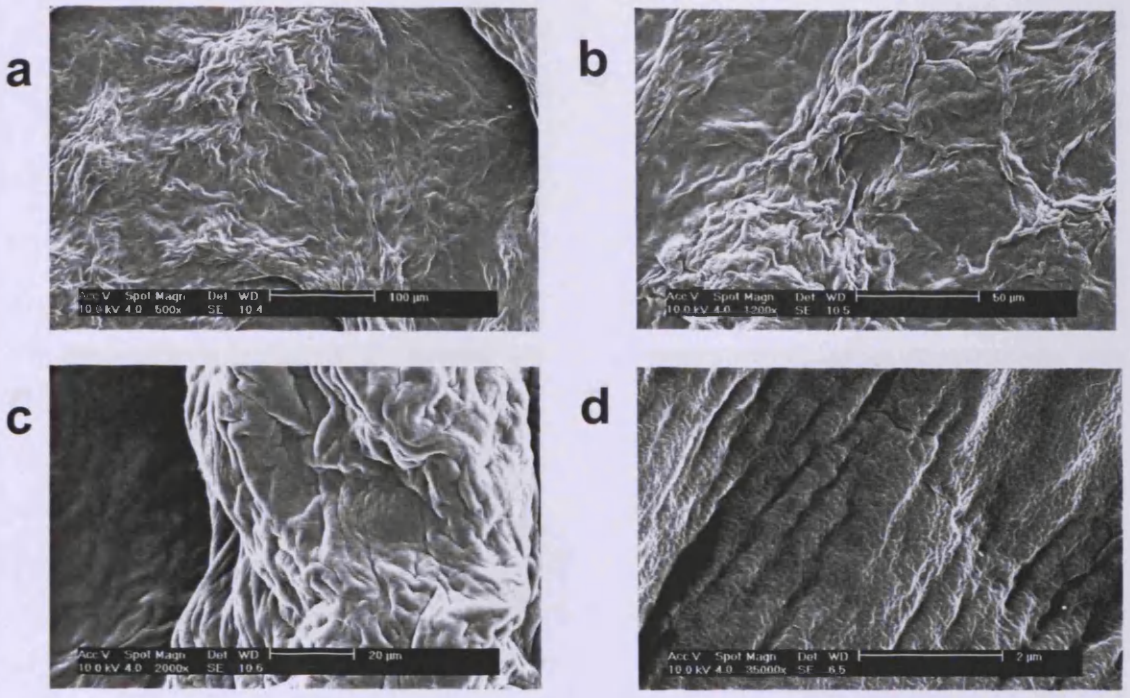


**Figure 7-34 SEM digital images of a conventionally dried-gel of original composition 1 wt% $G_8$ in 10/90 HFB/HPFP captured at magnifications of (a) 500, (b) 1 200, (c) 2 000 and (d) 35 000.**

The conventionally dried gels present a surface that shows some 3D contours, but no fibrillar network can be observed. It seems that the open structure present in the gels has totally collapsed upon solvent evaporation. This was also noted during the SEM sample preparation stage, where the sample volume was much smaller after than prior to the solvents evaporation. Some finer structures reminiscent of very thin fibrils trapped within the surface could be discerned at the higher magnification (picture d), however, they could also be small cracks from repeated exposure to the electron beam.

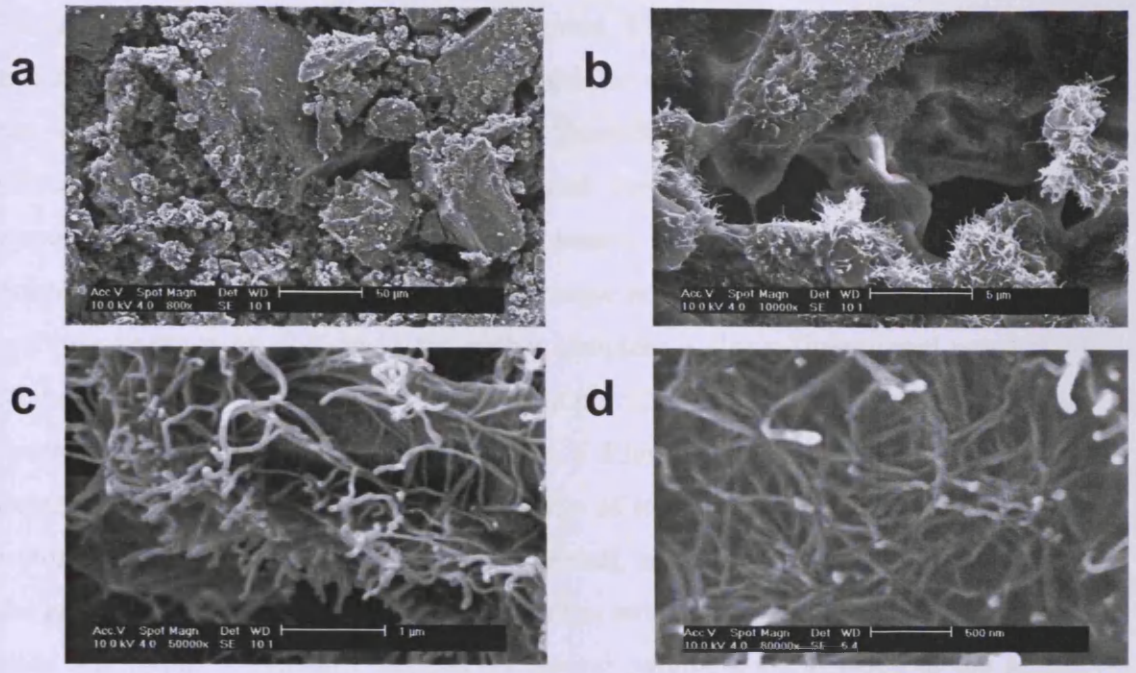


**Figure 7-35 SEM digital images of gelator $G_8$ raw powder captured at magnifications of (a) 800, (b) 10 000, (c) 50 000 and (d) 80 000.**

At low magnification (picture **a**), the raw powder appears as a heterogeneous mixture of small particles, medium aggregates and big blocks bearing no particular shape, with dimensions ranging from 3 μm to 120 μm. At higher magnification (picture **b**), the presence of fibril-like proturberences can be detected sticking out from the surface of the powder blocks. Further magnification (pictures **c** and **d**) shows they are homogeneous long thin flexible worm-like entities, of approximate length 2500 nm and cross section 50 nm. The cross sections of the worm-like entities detected in the raw powder differ by an order of magnitude from the ones observed in wet gels using small angle neutron scattering. However, the fact that such geometries are present even on the raw powder may indicate that the gelator is likely to develop such a structure when in solution.

## 7.7 Conclusion

A family of small tetrahydroxy diester molecules was found to gel fluorinated liquids, even at very low concentrations, and thus were considered as low molecular weight organogelators (LMOGs). To current knowledge, this is the first occurrence of

fluorinated liquids gelled by non-fluorinated LMOGs. The gels obtained were thermoreversible, and could be formed at gelator concentrations as low as 0.1 wt%, the remaining 99.9 wt% being entrapped fluoroliquids. Considering the very high solvent to gelator ratio, surface tension and capillary forces were thought to be responsible for the successful liquid entrapment, rather than systematic and direct gelator-solvent interactions. Indeed, small angle neutron scattering showed that long and thin fibrils were present in the gelled samples. A three dimensional network of strands could hold the fluorinated solvents in place, thus forming gelled structures. All neutron scattering data could be fitted to a Kholodenko worm-like chain model, described as a suite of n cylindrical segments of length $\ell$ and axial radius $R_{ax}$. Upon heating, the scattering intensity would decrease, and eventually fully collapse when the gel was taken above its gel-to sol transition temperature. Macroscopically, the gel state was found to critically depend on several parameters consisting in the gelator backbone chain-length, its concentration, the fluorinated solvents ratio and the temperature. However, once a gelled state was obtained, the dimensions characterizing these long fibrils ($R_{ax}$, n, and $\ell$), obtained by the fitting of the neutron scattering data, were hardly affected by such parameters. They presented an average axial radius of 30 Å, which led to hypotheses concerning the stacking of the gelator molecules, either as side by side pairs that would then vertically stack up onto one another, or to coronas made of 6 to 8 gelator molecules that would then vertically stack up in the same way, leading to long fibril-like assemblies. However, no molecular modelling and X-ray data are available to support these hypotheses. The gelator molecules can self-assemble through non-covalent interactions such as weak van der Waals attraction and strong hydrogen bonding. PGSE-NMR showed that even when the fluorinated solvents are trapped in the gelled structure, their diffusion coefficients, hence their mobility, is scarcely affected, further supporting the view of surface tension and capillary action as the main driving forces behind the retention of the liquid. The combination of LMOGs and pharmaceutically investigated fluorinated liquids could show great potential for uses in topical applications such as lubrication agents, wound treatments, or healing ointments.

**References**


1. P. Terech and R.G. Weiss, *Low Molecular Mass Gelators of Organic Liquids and the Properties of Their Gels.* Chemical Reviews, 1997. **97**: p. 3133-3159.
2. M. George, S.L. Snyder, P. Terech, and R.G. Weiss, *Gelation of Perfluorinated Liquids by N-Alkyl Perfluoroalkanamides.* Langmuir, 2005. **21**: p. 9970-9977.
3. M. George, S.L. Snyder, P. Terech, C.G. Glinka, and R.G. Weiss, *N-Alkyl Perfluoroalkanamides as Low Molecular-Mass Organogelators.* Journal of the American Chemical Society, 2003. **125**(34): p. 10275-10283.
4. P.C. Griffiths, M. Cote, R. James, P.G.A. Rogueda, I.R. Morgan, and D.W. Knight, *Gelation of fluorinated liquids by non-fluorinated low-molecular-mass molecules.* Chemical Communications, 2005. **31**: p. 3998-4000.
5. *Physical Properties of Polymeric Gels*, ed. J.P.C. Addad. 1996, Chichester: Wiley.
6. P.J. Flory, *Gels and gelling process.* Faraday Discussions of the Chemical Society, 1974. **57**: p. 7-18.
7. A. Valkonen, M. Lahtinen, E. Virtanen, S. Kaikkonen, and E. Kolehmainen, *Bile acid amidoalcohols: simple organogelators.* Biosensors and Bioelectronics, 2004. **20**: p. 1233-1241.
8. F. Ikkai and E. Adachi, *Novel Method of Producing Polymer Gels in Aqueous Solution Using UV Irradiation.* Macromolecular Rapid Communications, 2004. **25**: p. 1514-1517.
9. W. Li, L. Xu, D. Luo, H. Wu, J. Tu, and M. Yang, *A composite microporous gel polymer electrolyte prepared by ultra-violet cross-linking.* European Polymer Journal, 2007. **43**: p. 522-528.
10. H.J. Kwon, Y. Osada, and J.P. Gong, *Polyelectrolyte Gels-Fundamentals and Applications.* Polymer Journal, 2005. **38**(12): p. 1211-1219.
11. O. Gronwald, E. Snip, and S. Shinkai, *Gelators for organic liquids based on self-assembly: a new facet of supramolecular and combinatorial chemistry.* Current Opinion in Colloid & Interface Science, 2002. **7**: p. 148-156.
12. N.M. Sangeetha and U. Maitra, *Supramolecular gels: Functions and uses.* Chemical Society Reviews, 2005. **34**: p. 821-836.
13. D.J. Abdallah and R.G. Weiss, *The Quest for the Simplest Possible Organogelators and Some Properties of their Organogels.* Journal of the Brazilian Chemical Society, 2000. **11**(3): p. 209-218.
14. M. George and R.G. Weiss, *Molecular Organogels. Soft Matter Comprised of Low-Molecular-Mass Organic Gelators and Organic Liquids.* Accounts of Chemical Research, 2006. **39**(8): p. 489-497.
15. *Molecular Gels - Materials with Self-Assembled Fibrillar Networks*, ed. R.G. Weiss and P. Terech. 2006, Dordrecht: Springer.
16. D.J. Abdallah and R.G. Weiss, *n-Alkanes Gel n-Alkanes (And Many Other Organic Liquids).* Langmuir, 2000. **16**: p. 352-355.
17. Y. Zhou, T. Yi, T. Li, Z. Zhou, F. Li, W. Huang, and C. Huang, *Morphology and Wettability Tunable Two-Dimensional Superstructures Assembled by Hydrogen Bonds and Hydrophobic Interactions.* Chemistry of Materials, 2006. **18**(13): p. 2974-2981.
18. P. Terech, I. Furman, and R.G. Weiss, *Structures of Organogels Based upon Cholesteryl 4-(2-Anthryloxy)butanoate, a Highly Efficient Luminescing*

*Gelator: Neutron and X-ray Small-Angle Scattering Investigations.* Journal of Physical Chemistry, 1995. **99**: p. 9558-9566.
19. M. Hermansson, *The fluidity of hydrocarbon regions in organo-gels, studied by NMR.* Colloids and Surfaces A: Physicochemical and Engineering Aspects, 1999. **154**(3): p. 303-309.
20. G. Clavier, M. Mistry, F. Fages, and J.-L. Pozzo, *Remarkably simple small organogelators: di-n-alkoxy-benzene derivatives.* Tetrahedron Letters, 1999. **40**: p. 9021-9024.
21. M. Suzuki, Y. Nakajima, M. Yumoto, M. Kimura, H. Shirai, and K. Hanabusa, *Effects of Hydrogen Bonding and van der Waals Interactions on Organogelation Using Designed Low-Molecular-Weight Gelators and Gel Formation at Room Temperature.* Langmuir, 2003. **19**: p. 8622-8624.
22. S.P. Srivastava, A.K. Saxena, R.S. Tandon, and V. Shekher, *Measurement and prediction of solubility of petroleum waxes in organic solvents.* Fuel, 1997. **76**(7): p. 625-630.
23. D.J. Abdallah, S.A. Sirchio, and R.G. Weiss, *Hexatriacontane Organogels. The First Determination of the Conformation and Molecular Packing of a Low-Molecular-Mass Organogelator in Its Gelled State.* Langmuir, 2000. **16**: p. 7558-7561.
24. M. George, G. Tan, V.T. John, and R.G. Weiss, *Urea and Thioureo Derivatives as Low Molecular-Mass Organogelators.* Chemistry-A European Journal, 2005. **11**: p. 3243-3254.
25. K. Oishi, T. Ishi, M. Sano, and S. Shinkai, *Unexpected Discovery of a Novel Organic Gel System Comprised of [60]Fullerene-containing Amphiphiles.* Chemistry Letters, 1999: p. 1089-1090.
26. C.M. Garner, P. Terech, J.-J. Allegraud, B. Mistrot, and P. Nguyen, *Thermoreversible gelation of organic liquids by arylcyclohexanol derivatives.* Journal of the Chemical Society, Faraday Transactions, 1998. **94**(15): p. 2173-2179.
27. P. Terech, J.J. Allegraud, and C.M. Garner, *Thermoreversible Gelation of Organic Liquids by Arylcyclohexanol Derivatives: a Structural Study.* Langmuir, 1998. **14**: p. 3991-3998.
28. I. Furman and R.G. Weiss, *Factors Influencing the Formation of Thermally Reversible Gels Comprised of Cholesteryl 4-(2-Anthryloxy)butanoate in Hexadecane, 1-Octanol, or Their Mixtures.* Langmuir, 1993. **9**: p. 2084-2088.
29. R. Mukkamala and R.G. Weiss, *Physical Gelation of Organic Fluids by Anthraquinone-Steroid-Based Molecules. Structural Features Influencing the Properties of Gels.* Langmuir, 1996. **12**(6): p. 1474-1482.
30. R. Luboradzki, O. Gronwald, M. Ikeda, S. Shinkai, and D.N. Reinhoudt, *An Attempt to Predict the Gelation Ability of Hydrogen-bond-based Gelators Utilizing a Glycoside Library.* Tetrahedron, 2000. **56**: p. 9595-9599.
31. B. Escuder and J.F. Miravet, *Silk-Inspired Low-Molecular-Weight Organogelator.* Langmuir, 2006. **22**: p. 7793-7797.
32. G. Mieden-Gundert, L. Klein, M. Fischer, F. Vögtle, K. Heuzé, J.-L. Pozzo, M. Vallier, and F. Fages, *Rational Design of Low Molecular Mass Organogelators: Towards a Library of Functional N-Acyl-1,ω-Amino Acid Derivatives.* Angewandte Chemie International Edition, 2001. **40**(17): p. 3165-3166.

33. J.-L. Pozzo, G.M. Clavier, and J.-P. Desvergne, *Rational Design of new acid-sensitive organogelators.* Journal of Materials Chemistry, 1998. **8**: p. 2575-2577.
34. K. Yoza, Y. Ono, K. Yoshihara, T. Akao, H. Shinmori, M. Takeuchi, S. Shinkai, and D.N. Reinhoudt, *Sugar-integrated gelators of organic fluids: on their versatility as building-blocks and diversity in superstructures.* Chemical Communications, 1998. **8**: p. 907-908.
35. N. Amanokura, Y. Kanekiyo, S. Shinkai, and D.N. Reinhoudt, *New sugar-based gelators with an amino group, the gelation ability of which is remarkably reinforced by the hydrogen bond and the metal coordination.* Journal of the Chemical Society, Perkin Transactions 2: Physical Organic Chemistry, 1999. **10**: p. 1995-2000.
36. K. Murata, M. Aoki, T. Nishi, A. Ikeda, and S. Shinkai, *New cholesterol-based gelators with light- and metal-responsive functions.* Journal of the Chemical Society, Chemical Communications, 1991. **24**: p. 1715-1718.
37. T. Naota and H. Koori, *Molecules That Assemble by Sound: An Application to the Instant Gelation of Stable Organic Fluids.* Journal of the American Chemical Society, 2005. **127**: p. 9324-9325.
38. F. Plourde, A. Motulsky, A.-C. Couffin-Hoarau, D. Hoarau, H. Ong, and J.-C. Leroux, *First report on the efficacy of L-alanine-based in situ-forming implants for the long-term parenteral delivery of drugs.* Journal of Controlled Release, 2005. **108**: p. 433-441.
39. E. Carretti, L. Dei, and R.G. Weiss, *Soft matter and art conservation. Rheoreversible gels and beyond.* Soft Matter, 2005. **1**: p. 17-22.
40. C. Shi, Z. Huang, S. Kilic, J. Xu, R.M. Enik, E.J. Beckman, A.J. Carr, R.E. Melendez, and A.D. Hamilton, *The Gelation of $CO_2$: A Sustainable Route to the Creation of Microcellular Materials.* Science, 1999. **286**: p. 1540-1543.
41. H.H. Willemen, A.T.M. Marcelis, E.J.R. Sudhölter, W.G. Bouwman, B. Demé, and P. Terech, *A Small-Angle Neutron Scattering Study of Cholic Acid-Based Organogel Systems.* Langmuir, 2004. **20**: p. 2075-2080.
42. S. Umadevi, A. Jákli, and B.K. Sadashiva, *Odd-even effects in bent-core compounds containing terminal n-alkyl carboxylate groups.* Soft Matter, 2006. **2**: p. 875-885.
43. K. Murata, M. Aoki, T. Suzuki, T. Harada, H. Kawabata, T. Komori, F. Ohseto, K. Ueda, and S. Shinkai, *Thermal and Light Control of the Sol-Gel Phase Transition in Cholesterol-Based Organic Gels. Novel Helical Aggregation Modes As Detected by Circular Dichroism and Electron Microscopic Observation.* Journal of the American Chemical Society, 1994. **116**: p. 6664-6676.
44. P. Terech, D. Meerschaut, J.-P. Desvergne, M. Colomes, and H. Bouas-Laurent, *2,3-di-n-decyloxy-6,7-dichloroanthracene (Cl2DDOA), a new low-molecular-mass fluorescent organogelator: physical properties and structures.* Journal of Colloid and Interface Science, 2003. **261**: p. 441-450.
45. J.E. Eldridge and H.D. Ferry, *Studies of the cross-linking process in gelatin gels. III. Dependance of the melting point on concentration and molecular weight.* Journal of Physical Chemistry, 1954. **58**: p. 992-995.
46. P.W. Atkins, *Physical Chemistry, 5th Ed.* Physical Chemistry, 5th ed.Oxford University Press, 1994: p. 227.

47. E. Tombari, C. Ferrari, and G. Salvetti, *Endothermic freezing on heating and exothermic melting on cooling.* The Journal of Chemical Physics, 2005. **123**: p. 051104.
48. C. Ferrari, E. Tombari, and G. Salvetti, *Composition dependance and the nature of endothermic freezing and exothermic melting.* The Journal of Chemical Physics, 2007. **126**.
49. R.K. Heenan, *RAL Report 89-129.* RAL Report 89-129, 2005.
50. G.D. Pantos, P. Pengo, and J.K.M. Sanders, *Hydrogen-Bonded Helical Organic Nanotubes.* Angewandte Chemie International Edition, 2007. **46**: p. 194-197.
51. C. Zhan, P. Gao, and M. Liu, *Self-assembled helical spherical-nanotubes from an L-glutamic acid based bolaamphiphilic low molecular mass organogelator.* Chemical Communication, 2005: p. 462-464.
52. C. Bao, M. Jin, R. Lu, Z.S.X. Yang, D. Song, T. Xu, G. Liu, and Y. Zhao, *Clockwise helical stacking of triphenylbenzene-based organogelator induce by peripheral chirality.* Tetrahedron, 2007. **63**: p. 7443-7448.
53. N.M. Loening and J. Keeler, *Measurement of Convection and Temperature Profiles in Liquid Samples.* Journal of Magnetic Resonance, 1999. **139**: p. 334-341.
54. K. Hayamizu and W.S. Price, *A new type of sample tube for reducing convection effects in PGSE-NMR measurements of self-diffusion coefficients of liquid samples.* Journal of Magnetic Resonance, 2004. **167**: p. 328-333.
55. N. Hedin, T.Y. Yu, and I. Furo, *Growth of C12E8 Micelles with Increasing Temperature. A Convection-Compensated PGSE NMR Study.* Langmuir, 2000. **16**: p. 7548-7550.
56. G.H. Sørland, J.G. Seland, J. Krane, and H.W. Anthonsen, *Improved Convection Compensating Pulsed Field Gradient Spin-Echo and Stimulated-Echo Methods.* Journal of Magnetic Resonance, 1999. **142**: p. 323.
57. K.I. Momot and P.W. Kuchel, *Convection-compensating PGSE experiment incorporating excitation-sculpting water suppression (CONVEX).* Journal of Magnetic Resonance, 2004. **169**: p. 92-101.

# Chapter 8 Conclusion

Fluorinated systems are widely used in numerous industries involving chemistry (solvents for the electronics, heat transfer medium for refrigerants, novel compounds with very low surface properties for surfactants, drug delivery systems for pharmaceutics or therapeutic molecules for the medical world). The purpose of this work was directed towards pharmaceutical and biomedical applications, fields in which fluorinated systems are developed into a great variety of forms, be it as fluorinated surfactants, as part of direct or reverse emulsions with water, neat as in the case of liquid ventilation systems, or as fluorocarbon gels (gel emulsions or gels with a fibrous matrix), or propellant for pulmonary drug delivery.

The focus of this work was on the hydrofluoroalkane **2H, 3H-perfluoropentane** (HPFP), a partially fluorinated liquid used as a model propellant in medicinal pressurized metered dose inhalers, for drug delivery to the lungs purposes. Previous studies showed that the physical characteristics of HPFP suitably matched those of marketed propellants HFA 134a and HFA 227. With its boiling point of 53.6 °C, HPFP is liquid at ambient temperatures and pressures, which renders easier any benchtop study that does not require adaptation for the pressurized regime as in the case of HFA 134a and HFA 227. However, fluorinated liquids present both strong lipophobic and hydrophobic characters and require excipients to turn them into useful products. HPFP is no exception, and studies in this novel fluoroliquid are still scarce. The aim was therefore to initiate a comprehensive description of the equilibrium and dynamic properties of pharmaceutical excipients in HPFP and related fluoroliquids, and to design systems that could have potential applications for the pharmaceutical industry. For this, three main routes were explored.

First, common pharmaceutical excipients based on ethylene oxide oligomers and derivatives were investigated in HPFP and its fully fluorinated analogue PFP. Ethylene oxide polymers and derivatives were selected as they are mainly iniquitous, their cost is low, and they are indeed widely used in pharmaceutical formulations. Systems where the solubility could be switched on or off were devised, based on the nature of the ethylene oxide polymers end-group and the polarity of the fluorinated

liquids employed. While the dihydroxyl end-capped polyethylene glycol series all behaved as typical cloud-point systems in model propellant HPFP, showing a lower critical solution temperature that increased with molecular weight, the addition of methyl groups around the hydroxyl end-groups rendered the polymers fully soluble in HPFP, suggesting that the phase behaviour was dominated by end-group/solvent interactions. By gradually replacing HPFP by its fully fluorinated analogue perfluoropentane (PFP), a LCST-type behaviour was induced in the previously fully miscible mono- and di-methyl end-capped PEGs. The phase behaviour of these systems could be controlled by "tuning" the end-group structure of the ethylene oxide oligomers, and varying the hydrogen bonding capabilities of the fluorinated solvents. These results are published in *Journal of Pharmacy and Pharmacology*, 2008, **60**: p. 593-599. This study was then expanded to derivatives of ethylene oxide polymers such as propylene oxide polymers, a poloxamer and polyethylene oxide monododecyl ether surfactants. The presence of extra methyl groups was always found to favour the polymer solubility. However, replacement of a hydroxyl terminal group by a dodecyl moiety was not as successful and did not result in improving the EO polymer solubility as did the smaller methyl moiety. Whilst the ethylene glycol fragment still dominated the behaviour of the surfactants bearing the longer EO chains, the dodecane part was found to drive the solubility of the excipient bearing the shortest EO chain. This study can be found in *International Journal of Pharmaceutics*, 2008, **362**: p. 147-152. As further work, a possible next step would be the investigation of the thermodynamic properties of such systems, and in particular the characterisation of the phase transfer of the polymer solute from one fluorinated solvent to another. Access to the partition coefficients would enable the calculation of the Gibbs energy of transfer of the solute, and coupled with solution calorimetry measurements, a full thermodynamic description of the systems could be obtained. The influence of the excipients end- and pendant-groups could also be extended to the study of crown-ethers of the ethylene oxide oligomer type (being macrocycles, they bear no end-groups) and to the large family of poloxamers, by systematically investigating ranges of ethylene oxide / propylene oxide ratios, positions (regular or reverse poloxamers), and the effect of end-group methylation, as was conducted on poly (ethylene glycols). Such studies are currently being undertaken in the PhD project that has been initiated following up from this one.

The second path explored was the study in HPFP of the hydrophobically modified β-cyclodextrin TAβCD that can be used, thanks to its toroidal configuration, in the formation of host-guest complexes that are attractive systems for controlled-release drug delivery. The hydrophobic TAβCD was chosen amongst others for its partial solubility in model propellant HPFP. Various batches of TAβCD showed very different solubility profiles in HPFP and polymorphism was found to be the key factor ruling the solubility of this modified cyclodextrin in HPFP. Two polymorphs α and β were characterised. The controlled conversion of the less stable polymorph β to more stable form α could be achieved, and polymorph α could be obtained by a successful recrystallization of an amorphous sample in the presence of a minimum amount of form α that seeded the crystallization process. HPFP was found to act as a discriminator to separate the two existing polymorphs. Whilst the solubility ratio of polymorphs is accepted to be constant in all solvents, the fluoroliquid HPFP had the particularity to highlight the two polymorphs solubility difference over a workable concentration range. The solubility limit for the α form was indeed easily detectable at 2.2 ± 0.2 wt%, and fully contrasted with a solubility of over 20 wt% for the β form. These results form the bulk of the publication in *Journal of Physical Chemistry C*, 2008, **112**: p. 14570-14578. Having performed the studies in HPFP, it would now be of interest to set up a systematic screening of potential solvents and relate the observed solubility of the α and β forms to the solvents intrinsic properties, such as polarity, H-bonding capabilities, dielectric constant and so forth, in order to build a predictive tool that will allow access to the behaviour of such an excipient in a variety of solvents.

Finally, supramolecular assemblies were formed using small tetrahydroxy diester molecules as the self-assembling agent and a mixture of model propellant HPFP and co-solvent 1H, 1H-heptafluorobutanol as the entrapped liquid phase. The resulting gels can potentially be useful for topical applications such as lubrication agents, wound treatments, or healing ointments. These thermoreversible gels were formed at very low gelator concentrations. Neutron scattering revealed the presence of cylindrical arrangements of average axial radius of 30 Å and it is hypothized that the gelator molecules self-assembled into 3-dimensionnal fibrilar networks in which the solvents could be immobilized at a macroscopic level, due to surface tension and capillary action. PGSE-NMR showed that on a microscopic level, the diffusion rate of

the solvents entrapped in the gel scaffold was equal to the diffusion of the free liquids in the absence of gelator. The gelator backbone chain-length, its concentration, the fluorinated solvents ratio and the temperature were found to be the key parameters upon which the gel state achievement depends. This phenomenon can be directly linked to observations made in the preceding Chapter 4. In Chapter 4, it is seen that the introduction of fully fluorinated non-solvent PFP to fully miscible ethylene oxide / HPFP systems provokes the phase separation of the system. Here, the gel formation can be envisaged as a microscopic phase separation of the organogelator molecules upon addition of the non-solvent HPFP to previously liquid HFB sol. However, in the present case, the phase separation is somewhat ordered and the gelator molecules present in the sample self-aggregate to lead to this macroscopically solid-like although biphasic structure. Such gel formation using non-fluorinated organogelators and fluorinated liquids was unprecedented as so far the use of gelators that were themselves partially fluorinated was required to gel fluorinated liquids. The first results of this work can be read in *Chemical Communication*, 2005, **31**: p. 3998-4000 and a following manuscript is to be submitted shortly. Further work will follow so as to decipher the precise nature of the interactions and arrangement between the gelator molecules involved in the formation of the fibrilar network leading to the gel structures. A path involving their study on the theoretical side, using molecular modelling, is undergoing, and so is the use of infra-red and circular dichroism spectroscopies. X-ray diffraction could also be a valuable technique to elucidate the structural arrangement of the gelator molecules, both in the raw powder starting material and in the gel state.

# *Manuscripts*

- "Effect of molecular weight and end-group nature on the solubility of ethylene oxideoligomers in 2H, 3H-decafluoropentane and its fully fluorinated analogue, perfluoropentane" by Marie Côte, Philippe G. A. Rogueda and Peter C. Griffiths, ***Journal of Pharmacy and Pharmacology***, 2008, **60**: p. 593-599

- "Elaborating the phase behaviour of ethylene oxide oligomers and analogues in 2H, 3H-perfluoropentane" by Peter C. Griffiths, Marie Côte, Philippe G. A. Rogueda, ***International Journal of Pharmaceutics***, 2008, **362**: p. 147-152

- "Characterization of a Polymorphic System Exhibiting Substantial Variation of Solubility in a Fluorinated Solvent" by Marie Côte, Colan E. Hughes, Talbir K. Austin, Philippe G. A. Rogueda, Zhigang Pan, Kenneth D. M. Harris and Peter C. Griffiths, ***Journal of Physical Chemistry C***, 2008, **112**: p. 14570-14578

- "Gelation of fluorinated liquids by non-fluorinated low-molecular-mass molecules", by P. C. Griffiths, M. Côte, R. James, Ph. G. Rogueda, I. R. Morgan and D. W. Knight, ***Chemical Communications***, 2005, **31**:p. 3998-4000

- "Self-Assembling Chiral Gelators for Fluorinated Media" by Marie Cote, Tim Nicholls, David W. Knight, Ian R. Morgan, Philippe G.A. Rogueda, Steve M. King, Richard K. Heenan and Peter C. Griffiths, ***to be submitted to the Journal of the American Chemical Society***

JPP Journal of Pharmacy and Pharmacology

PP 2008, 60: 593–599
) 2008 The Authors
eceived September 25, 2007
ccepted February 1, 2008
OI 10.1211/jpp.60.5.0004
SN 0022-3573

# Effect of molecular weight and end-group nature on the solubility of ethylene oxide oligomers in 2H, 3H-decafluoropentane and its fully fluorinated analogue, perfluoropentane

Marie Cote, Philippe G. A. Rogueda and Peter C. Griffiths

## Abstract

Fluorinated liquids possess high chemical and physical stability, are tolerated by the human body and, therefore, show great promise in biomedical fields; however, they require extensive formulation. Phase diagrams are reported here for a series of ethylene oxide oligomeric additives in 2H,3H-perfluoropentane (HPFP), a non-chlorofluorocarbon fluorinated liquid regarded as a model propellant for pressurized metered-dose inhalers. Over a wide range of temperatures and concentrations, dihydroxyl end-capped poly(ethylene glycols) (PEGs) exhibited a lower critical solution temperature (LCST) that was strongly molecular weight dependent. In contrast, monomethyl (and thus monohydroxy) and dimethyl end-capped poly(ethylene oxides) were fully miscible with HPFP over the same temperature and concentration ranges, suggesting that the phase behaviour was dominated by end-group/solvent interactions. By systematically substituting HPFP for the fully fluorinated analogue perfluoropentane, the ability of these end-groups to interact with the solvent was perturbed and LCST-type behaviour was induced in the previously fully miscible monomethyl and dimethyl end-capped PEGs. Concomitantly, with increasing perfluoropentane content, the LCST of the dihydroxyl end-capped PEGs was driven to lower temperatures. Therefore, the phase behaviour of these systems may be controlled by 'tuning' the end-group structure of the ethylene oxide oligomers, and varying the hydrogen bonding capabilities of the fluorinated solvents.

chool of Chemistry, Cardiff niversity, Main Building, Park lace, Cardiff CF10 3AT, UK

larie Cote, Peter C. Griffiths

straZeneca Research and evelopment, Charnwood, akewell Road, Loughborough, 11 5RH, UK

hilippe G. A. Rogueda

**orrespondence:** P. C. Griffiths, chool of Chemistry, Cardiff niversity, Main Building, Park lace, Cardiff CF10 3AT, UK. mail: griffithspc@cardiff.ac.uk

**cknowledgement and nding:** Robert Jenkins and emma Talbot are cknowledged for performing, spectively, the APCI analysis of e polymers and determining to higher precision one of the ase boundaries in the ternary stem. Cardiff University and straZeneca are acknowledged r funding Marie Cote's udentship.

## Introduction

Fluorinated systems are remarkably versatile, finding applications as, for example, cleaning solvents for circuitry in the electronic industry or heat-transfer medium in the refrigerant industry (Lemal 2004). Recently, they have been the focus of much attention for pharmaceutical applications, being developed as blood substitutes (Riess 2002), contrast agents for ultrasound imaging (Sanchez et al 1995; Riess 2003), liquid ventilation (Greenspan et al 2000), or pressurized metered-dose inhalers (Rogueda 2003). Indeed, fluorocarbons possess unique physical and chemical properties that make them good candidates for use in biological systems and pharmaceutics. Chemical inertness is ensured by the enhanced strength of the C-C bond in fluorocarbons, and their helical conformation shields the chain from attacks by reagents (Rigby & Bunn 1949). Their acute toxicity was found to be no greater, and was sometimes even lower, than their hydrogenated equivalents (Riess & Krafft 1998). They exhibit low surface tension, low cohesive energy density, high compressibility and high gas-solubilizing capabilities (Krafft & Riess 1998; Riess & Krafft 1999). Hydrofluorocarbons are also environmentally much less damaging than chlorofluorocarbons, but there continues to be a great need to reformulate many materials using hydrofluorocarbons (Emmen et al 1999; McCulloch 1999; Ellis 2000).

In the case of pressurized metered-dose inhaler formulations, 2H,3H-perfluoropentane (HPFP) is found to be a suitable model propellant to replace chlorofluorocarbons (Rogueda 2003). Being both hydrophobic and lipophobic, hydrofluorocarbons are generally regarded as poor solvents and the addition of additives (excipients) is often required to turn them into useful products. However, studies investigating the solution properties of even common excipients in such solvents are scarce.

The phase behaviour of ethylene oxide polymers in water as, however, received much interest because it exhibits a ower critical solution temperature (LCST) (Saeki et al 1976; jellander & Florin 1981; Craig 1995; Hammouda et al 2004). he solubility of poly(ethylene oxide) (PEO) in water is an nathema in itself since the next homologues polybutylene and olymethylene are insoluble in water (Israelachvili 1997; Ashaugh & Paulaitis 2006). Short ethylene oxide chains (degree of olymerization $m \leq 48$) are completely miscible in water even at igh temperatures; for slightly longer chains, a closed loop solubility gap is observed, and for $m > 180$, only a LCST is observable. PEO solution properties in water critically depend on its olecular weight, and the clouding temperature decreases with a increase of the chain length (Saeki et al 1976; Kjellander & lorin 1981). Various arguments have been proposed to account or the solubility of PEO in water and the occurrence of LCST-ype phase separation (Samii et al 1991): the structured water odel was proposed by Kjellander & Florin (1981); Goldstein's pproach proposed the existence of intermolecular hydrogen onds between PEO and water, and their destruction modifies he solvent–solvent and solute–solvent interactions (Hirschfelder al 1937; Goldstein 1984); Karlström (1985) discussed solubily and phase separation in terms of the large dipole moment siding on the preferred gauche conformation of PEO at lower mperatures, a contribution that is removed at higher temperaes since the non-polar isomers have higher statistical weight.

The phase behaviour of PEO polymers in solvents other an water has received less attention. However, the clouding henomena of PEO has been reported in solvents such as rmamide, *tert*-butyl acetate (Saeki et al 1976), carbon dioxe (Kazarian et al 1996; O'Neill et al 1998; Drohmann & eckman 2002) and some organic solvents (da Silva & Loh 98; Spitzer et al 2000, 2002a, b).

In this work, we focus on the behaviour of low molecular eight poly(ethylene glycols) (PEGs) in the model propellant PFP and in mixtures with perfluoropentane (PFP). The fect of the end-group nature on the solubility of the PEGs as investigated using monomethyl and dimethyl end-capped EG derivatives.

## aterials and Methods

### aterials

hydroxy-poly(ethylene glycol), PEG of nominal molecular eights $M_n = 200$, 300, 400, 600, 1000 and 1500 g mol$^{-1}$, ly(ethylene glycol) monomethyl ether 350 g mol$^{-1}$ and 500 g l$^{-1}$ and poly(ethylene glycol) dimethyl ether 250 g mol$^{-1}$, re purchased from Acros Chemicals, Loughborough, UK, lka and Sigma-Aldrich, Gillingham, UK. All polymers were ed in a 60°C oven for 72 h before sample preparation, but othrise used without further purification. This drying procedure l a minimal effect on the molecular weight distribution. lecular weights were confirmed by Atmospheric Pressure emical Ionization (APCI) on a Waters LCT premier XE system; molecular weight characteristics are presented in Table 1.

The nature of the end-groups for monomethyl and dimethyl l-capped PEGs were confirmed by solution $^1$H nuclear gnetic resonance. HPFP (Apollo Scientific, Stockport, UK) was washed first with acidic and then basic alumina, filtered, dried and stored over molecular sieves; PFP was dried and stored over molecular sieves. For experiments investigating the impact of moisture on the systems, Millipore grade water was used.

**Table 1** Molecular weight characteristics of the poly(ethylene glycol) (PEG) polymers used in this study

| Polymer | MN (g mol$^{-1}$) | MW (g mol$^{-1}$) | Polydispersity |
|---|---|---|---|
| PEG200 | 280 | 325 | 1.16 |
| PEG300 | 407 | 430 | 1.05 |
| PEG400 | 468 | 490 | 1.05 |
| PEG600 | 630 | 660 | 1.05 |
| PEG1000 | 950 | 985 | 1.04 |
| Dimethyl end-capped PEG250 | 385 | 415 | 1.07 |
| Monomethyl end-capped PEG350 | 430 | 460 | 1.06 |

### Onset of phase separation

Samples were prepared by mass on a 3-g scale in glass screw-top vials, sealed with polytetrafluoroethylene tape to prevent solvent evaporation, then wrapped in parafilm to protect against water penetration. For the ternary phase diagrams, the fully miscible HPFP and PFP were first mixed in the appropriate ratio and added to polymer to yield a constant polymer concentration of 3wt% and a range of HPFP/PFP ratios. After 48 h equilibration at room temperature, these samples were immersed in a temperature-controlled water bath and the temperature gradually raised from –20°C with constant agitation until the temperature reached 60°C.

For temperatures above room temperature, an approximate LCST was determined by stepping the temperature in 5°C intervals, and equilibrating the sample at each temperature for 20 min. Subsequently, the sample was allowed to cool below this temperature and a more accurate LCST was recorded, equilibrating each sample for >1 h at 1°C intervals. For temperatures below room temperature, a similar protocol was employed but the LCST was determined principally from a controlled cooling cycle.

An iterative protocol was adopted to map out the concentration profile to span the polymer concentration range ($0.1\ \text{wt\%} < C_{\text{polymer}} < 90\ \text{wt\%}$), with the actual concentrations selected being determined by the shape of the phase transition profile, that is a lower frequency of data points where the curve was shallowest and higher where the profile exhibited a more pronounced concentration dependence.

### Statistical analysis

The LCST measurements were performed on a minimum of two samples at each concentration, and the LCST recorded from a minimum of two heating–cooling cycles per sample. The LCST quoted is, therefore, a sample of at least six measurements. The precise composition of every sample was known, having been prepared by weight to an accuracy of ~0.5 mg polymer per 3 g solvent.

### Quantification of polymer concentration in the PEG200/HPFP system

A dry-weight method was employed to quantify the polymer concentration in the two separate layers. A series of 20 wt% PEG200/HPFP samples (in triplicate) were prepared and equilibrated for 24 h in a water bath at the following temperatures: 15°C, 20°C, 25°C, 30°C, 35°C, 40°C and 45°C. All systems phase separated into two layers as expected; the upper and lower layers were separated using a plastic syringe with a flat-ended needle and transferred to pre-weighed vials. These were placed in a 60°C oven until constant mass.

### Statistical analysis

These measurements were performed in triplicate at each temperature, and the determined polymer concentrations recorded to an accuracy of ~0.5 mg. Differences between individual treatments were statistically identified using the Kruskal–Wallis test (in conjunction with Dunn's post-hoc test). A probability level that was less than 0.05 denoted significance.

### Preparation of PEG 200 in the HPFP/water system

Millipore water was added to aliquots of previously dried PEG200 before the sample preparation. The amounts of added water were such that: $C_{polymer}=3$ wt% and K[water]<3000 ppm. The pre-mixing of water with PEG200 was chosen for practical purposes because PEG200 and water are fully miscible, which is not the case for water and HPFP the maximum solubility of water in HPFP is 390±40 ppm; (Dogueda 2003). The cloud point was recorded visually as previously described.

## Results

### Behaviour of dihydroxy-poly(ethylene glycol) 200 (PEG200) in HPFP and impact of the presence of moisture

Figure 1 presents the temperature–concentration profile of dihydroxyl end-capped PEG200 in HPFP, determined both by visual assessment and by polymer concentration quantification. On heating, clear monophasic solutions of dihydroxyl end-capped PEG200 in HPFP became cloudy and then separated over time into a less dense polymer-enriched upper phase and more dense polymer-depleted lower phase ($\rho_{HPFP}=1.58$ g cm$^3$, $\rho_{PEGs}=1.12$ g cm$^3$), that is they demonstrated LCST-type behaviour, the critical LCST being the temperature at the minimum of the phase boundary curve (Jonsson et al 1998). These two phases may be separated and the polymer concentration quantified by mass after evaporation of the solvent. By projecting these concentrations onto the solute concentration axis, the solubility phase diagram may be constructed (Figure 1). The two methods give superimposable phase boundaries. However, the minimum of the curve was not experimentally accessible using the dry-weight method.

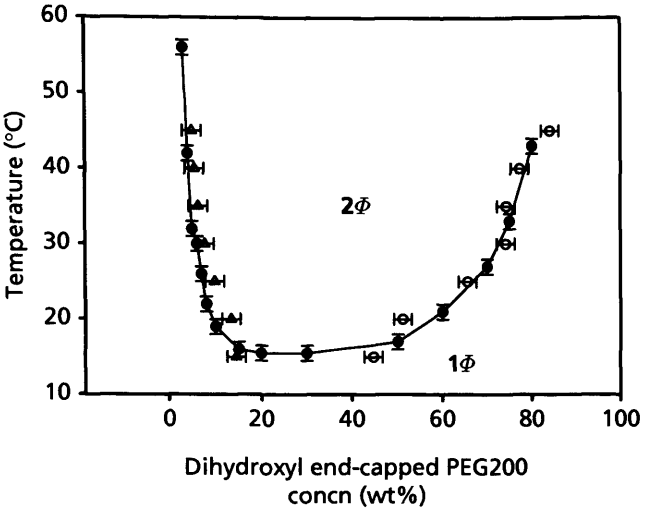


**Figure 1** Temperature–polymer concentration phase diagram of dihydroxyl end-capped PEG200 in HPFP; closed symbols correspond to the visually assessed cloud point; open symbols correspond to the mass balance analysis of the upper (circles) and lower (triangle) phases.

**Table 2** Clouding temperature for 3 wt% (dihydroxyl end-capped) poly(ethylene glycol)200 in 2H, 3H-perfluoropentane with water content ranging from 0 to 3000 ppm

| Water (ppm) | Clouding temperature (°C) |
|---|---|
| 0 | 47±1 |
| 125 | 47±1 |
| 250 | 46±1 |
| 500 | 44±1 |
| 1000 | 34±1 |
| 2000 | 12±1 |
| 3000 | 0±1 |

The phase behaviour of PEG in HPFP was very sensitive to moisture. Table 2 presents sample data for the clouding temperature for a system comprising 3wt% dihydroxyl end-capped PEG200 and various amounts of water. As seen in Table 2, minimum amounts of water had a significant impact on the clouding temperature, driving it to lower temperatures. A shift of nearly 50°C was observed when 3000 ppm water was present, underlining the necessity of drying the polymers.

### Molar mass dependence of dihydroxy-poly(ethylene glycols) solubility

Phase boundaries were visually investigated for various molecular weights of dihydroxyl end-capped poly(ethylene glycols), ranging from 300 to 1500 g mol$^{-1}$, and the results are presented in Figures 2 and 3.

As seen in Figure 2, LCST-type phase boundaries were observed for dihydroxyl end-capped PEGs of 300 < molecular weight < 1500 g mol$^{-1}$. The cloud-point temperature was strongly concentration and molecular weight dependent for all molecular weights, displaying a sharp increase towards

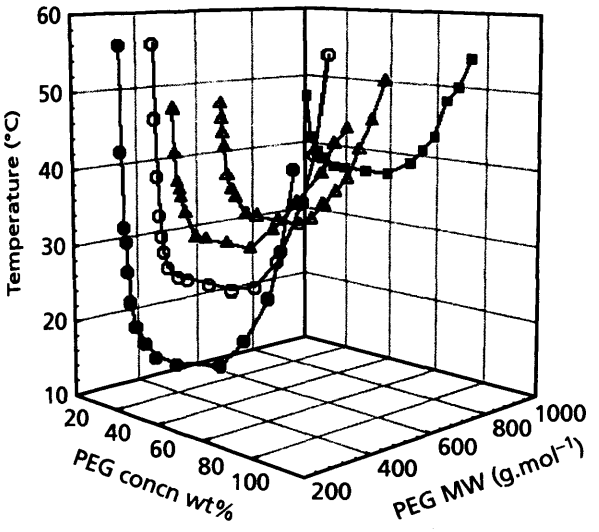


jure 2 Temperature–polymer concentration phase diagram of dihy-
xyl end-capped PEG200 (closed circles), PEG300 (open circles),
G400 (closed triangles), PEG600 (open triangles) and PEG1000
osed squares) in HPFP. Errors bars in the temperature axis have not
n included for clarity, these estimates being slightly greater than the
e of the symbol. For a more precise representation, see Figure 1.

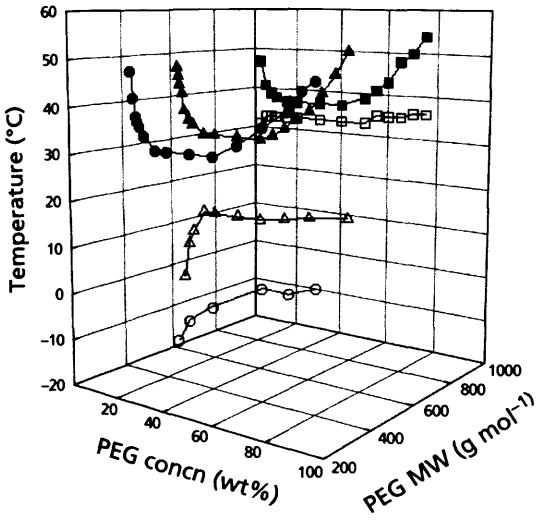


ure 3 Superimposed cloud point (closed symbols) and melting
perature curves (open symbols) for PEG400 (circles), PEG600
ngles) and PEG1000 (squares) in HPFP.

h very low and very high polymer concentrations. As
wn on Figure 3, PEG400, PEG600 and PEG1000 were
) found to exhibit a two-phase region at lower tempera-
s, coinciding with their melting behaviour. At low tem-
atures, such systems were biphasic, consisting of a
xisting waxy solid and a liquid. As the temperature
eases through the melting point of the polymer (5–8°C for
3400, 17–22°C for PEG600 and 35–40°C for PEG1000),
ples first become monophasic before reaching the higher
id-point boundary presented in Figure 2. As seen in
ire 2, an increase in molecular weight drove the LCST
ier, the critical temperature being 15°C, 25°C, 30°C, 32°C
37°C for PEG200, PEG300, PEG400, PEG600 and
31000, respectively, implying a greater solubility window.

However, the melting curve was also strongly molecular weight dependent and as the molecular weight was increased, these two curves coincided. For dihydroxyl end-capped PEG of MW 1500 g $mol^{-1}$, the two behaviours collapsed and the temperature required to melt the polymer was higher than its cloud-point phase boundary; therefore samples were always biphasic, either solid/liquid or liquid/liquid. For the lowest dihydroxyl end-capped PEG100, samples were always liquid/liquid biphasic and we hypothesize, based on molecular weight scaling, that a monophasic liquid state exists but at an experimentally inaccessible temperature range.

Considering the low molecular weights and narrow molecular weight range of the polymers investigated (~2 to ~23 ethylene oxide units), the very different solubilities and widely different phase behaviours are likely a manifestation of end-group effects rather molecular weight per se. To test this premise, the solubility of monomethyl and dimethyl end-capped PEG species of comparable molecular weights were investigated.

## Effect of end-group nature on PEG solubility

In contrast to dihydroxyl end-capped PEG200, which showed a cloud-point phase separation profile, monomethyl end-capped PEG350 and dimethyl end-capped PEG250 were fully miscible with HPFP over the entire range of concentrations and temperatures investigated. The presence of hydroxyl end-groups on the polymer therefore reduced its solubility in HPFP and methylation prevented the phase separation.

## Dihydroxyl, monomethyl and dimethyl end-capped PEGs in HPFP/PFP mixtures

Addition of the fully fluorinated solvent PFP to solutions of dihydroxyl end-capped PEG in HPFP resulted in a lowering of the phase separation temperature, thus reducing the solubility domain. Addition of PFP to solutions of monomethyl and dimethyl poly(ethylene glycols) in HPFP induced phase separation. Figure 4 presents the ternary diagrams for solutions of dihydroxyl end-capped PEG200, monomethyl end-capped

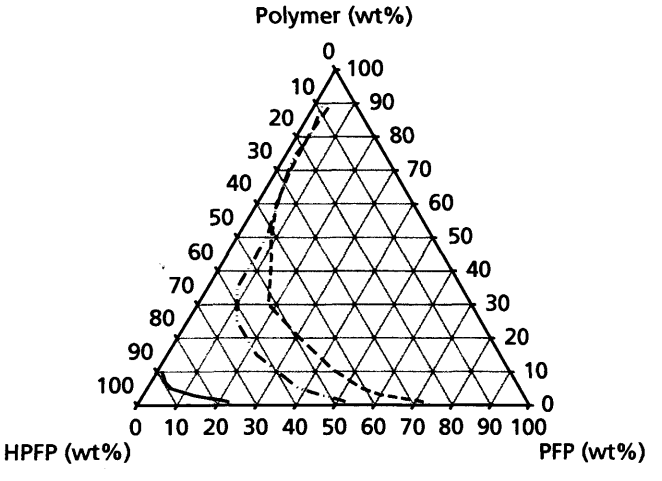


**Figure 4** Ternary phase diagrams recorded at 20°C for PEG300 (solid line), monomethyl end-capped PEG350 (dashed-dotted line) and dimethyl end-capped PEG250 (dashed line).

PEG350 and dimethyl end-capped PEG250 in binary HPFP/PFP solvents at 20°C, although temperature (20–45°C) had a negligible impact on the location of the phase boundaries. Figure 5 shows the cloud-point temperature as a function of the solvent content, at a constant polymer concentration of 3 wt%. This polymer concentration was chosen arbitrarily such that a significant change in the cloud point would be experimentally accessible.

In all cases, the presence of PFP induced phase separation, but the amount of PFP that the system could tolerate before dephasing depended on the nature of the polymer end-group. For a constant polymer concentration, the order in which higher amounts of PFP can be incorporated into a polymer/HPFP system before phase separation occurs was dimethyl > monomethyl > hydroxy end-capped PEG. For the monomethyl and dimethyl end-capped PEG, this effect was more prominent in the region diluted in polymer, and from 30 wt% polymer onwards, the two curves overlapped. This clearly demonstrates the importance of the end-group nature in the behaviour of such small polymers. As seen previously, further fully fluorinated solvent can be incorporated while keeping a monophasic sample as the methylation of the end-group was increased. However, as seen in Figure 5, the slopes of the cloud-point curves became steeper as the level of methylation of the end-group was increased. Although the amount of PFP that can be incorporated before phase separation occurred increased with the end-group methylation, the PFP range within which the cloud-point drop was observed is much narrower.

The three polymers investigated here were not commercially available in an identical molecular weight and it must therefore be questioned whether the slight variation in molecular weight could be responsible for the observed PFP uptake. To differentiate end-group and molecular weight effects, the same measurements were performed using dimethyl end-capped PEG 500, and its phase boundary was found to lie between monomethyl end-capped PEG350 and dimethyl end-capped PEG250. Therefore, dimethyl end-capped PEG500 would tolerate the presence of smaller amounts of PFP than its lower molecular weight equivalent, but still higher than the monomethyl end-capped PEG of lower molecular weight. The results observed were therefore not a molecular weight artefact but could be confidently attributed to an end-group effect.

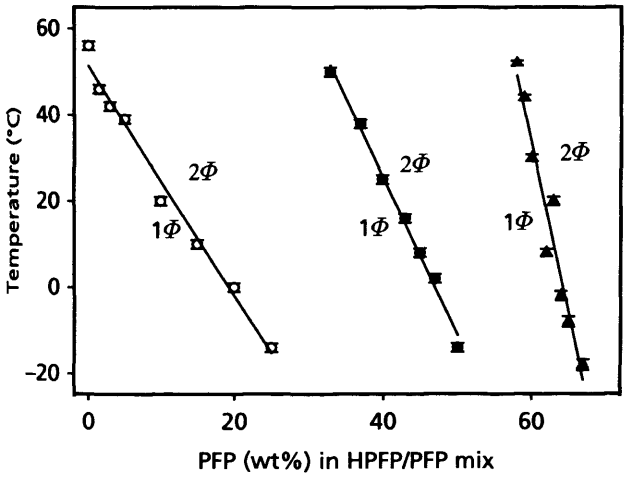


Figure 5 Cloud-point temperatures of PEG300 (open circles), monomethyl end-capped PEG350 (closed circles) and dimethyl end-capped PEG250 (open triangles) in the HPFP/PFP binary solvent mixtures as a function of the amount of PFP present.

## Discussion

Regions of high solubility were found to exist for dihydroxyl end-capped PEG polymers with molecular weight of between 300 and 1000 g $mol^{-1}$ in HPFP, albeit under limiting temperatures. Strictly speaking, given the low degrees of polymerization (~4 to ~23), these polymers should be referred to as oligomers. Polymers are generally regarded as having very limited solubility in hydrofluoroalkanes. Indeed, it was found in this study that once the molecular weight exceeded 1000 g $mol^{-1}$, ethylene oxide polymers were insoluble in HPFP. However, in the lower extreme, the dimer of ethylene glycol was also found to be insoluble in HPFP. There was therefore a narrow molecular weight window for which these oligomers exhibit regions of high solubility. A LCST was observed for these systems and phase separation occurred as the temperature was increased, with LCST increasing with molecular weight. LCST-type behaviour and closed-loop phase diagrams for ethylene oxide polymers in water were reported by Saeki et al (1976), but for higher molecular weights than studied here, typically from 2180 to 1020000 g $mol^{-1}$. The LCST was found to decrease with increasing degree of polymerization of the polymer and lay mostly at temperatures above the boiling point of water. They also observed the occurrence of both upper critical solution temperature and LCST in the organic solvent *tert*-butyl acetate for molecular weights ranging from 8000 to 21200 g $mol^{-1}$. LCST behaviour is usually observed for systems whose mixing is exothermic, implying strong and enthalpically favoured solute–solvent interactions. Such interactions could arise from strong hydrogen bonds between the hydrogen atoms in the solvent and lone electron pairs on PEG oxygen atoms.

The LCST was found to be highly molar mass dependent for hydroxyl end-capped PEGs in the HPFP system. Contrary to data reported in water and organic solvents, the LCST increased with increasing molecular weight, an effect that is proposed to be due to the hydroxyl end-groups, whose presence reduced the solubility. As the molecular weight was increased, the end-group effect becomes 'diluted' and therefore less important. The temperature required to destabilize the system was increased, but at the same time the melting point was also increased, narrowing the width of the solubility temperature window. This was especially pertinent for PEG1500, for which the melting and cloud-point curves overlap, leading to immiscibility over the entire range of concentration and temperature investigated. The presence of minimum amounts of water was found to dramatically decrease the cloud point of the systems. Dihydroxyl end-capped PEG200 was driven out of the HPFP solution by small quantities of water. The PEG–water interaction is stronger than the PEG–HPFP one, and once in the presence of moisture PEG tends to partition out of the fluorinated liquid to form an upper polymer-rich aqueous solution. It is not excluded that

me HPFP molecules may be driven by PEG into this new
ase, but most HPFP was found to remain free of polymer in
e lower phase.

Evidence for the end-group effect may be seen with the
nomethylation and dimethylation of the hydroxyl end-
ups with which full miscibility was observed in HPFP, for
igomers of very similar molecular weights. It is proposed
t the solute–solute attractions via the terminal hydroxyl
ups are reduced or fully blocked, and the hydrogen bond
ven solute–solvent attraction between the ether oxygen and
partially fluorinated solvent hydrogen remains, favouring
e dissolution of monomethyl and dimethyl end-capped
Gs in HPFP. The presence of oxygen in the polymer was
nd to be a prerequisite to achieve solubility (James 2006),
the presence of alcohol groups at the end of the chain does
t enhance this characteristic, whereas their methylation
vours it. One may envisage a situation where moderate
arity along the polymer backbone ($CH_2CH_2$-O-) will
mote a favourable interaction with the polar solvent,
HFCHF, yet a terminal polar group on the polymer may
er a route to a stronger inter-polymer interaction. The
lecular weight dependence of solubility, and thus the
d-group effect, has already been reported by Spitzer et al
002a, b) for the partition of dihydroxyl end-capped PEGs
tween water and organic solvents. A critical molecular
ight above which the end-group contribution is removed
rred around 2000 g mol$^{-1}$. However, for molecular
ights as low as 300–400 g mol$^{-1}$, PEG was found to start
vouring its partition into the organic phase. LCST for PEGs
s also observed in super-critical $CO_2$ by Drohmann &
kman (2002), who report that PEG solubility can be
reased by decreasing its molecular weight or blocking the
minal hydroxyls by non-polar headgroups. The ether
ygens were found to enhance PEO solubility when com-
ed with simple hydrocarbons, provided the oxygen was in
adily accessible position to $CO_2$. As a general finding,
bonyl groups enhance the solubility of the polymer in $CO_2$
favourable cross-interactions, either by quadrupole ($CO_2$)–
ole (solute) interaction or Lewis acid/base, $CO_2$ being the
wis acid (Kazarian et al 1996; Meredith et al 1996; Rind-
isch et al 1996), a conclusion that resonates with those
de here.

Monomethyl and dimethyl end-capped PEGs were
nd to present a cloud-point behaviour only when the
tially fluorinated fluoroalkane HPFP is gradually
laced by the fully fluorinated PFP. PFP is fully miscible
h HPFP, but has no solvation capability towards the
ylene oxide oligomers considered here. Indeed, the lack
any hydrogen-bond-donating capability of PFP was
nd to be crucial, so as to have sufficiently strong inter-
ions with the ethylene oxide segments. Moreover, the
lition of increasing amounts of PFP resulted in a sharp
rease of the cloud point. Although the amount of PFP
t can be incorporated before phase separation occurred
reased with the end-group methylation, the range of
P amount within which the cloud-point drop was
erved is much narrower as methlylation was increased.
h early precipitation of the polymer observed upon the
lition a non-co-solvent is a method already used in pol-
er fractionation (da Silva & Loh 1998; Spitzer et al 2002b). This mixed solvents study clearly shows that hydrogen bonding between the solvent and the solute, in competition with the end-group interactions, is the driving force behind the solubility of PEG oligomers in these fluorinated liquids of interest.

## Conclusion

The solubility of ethylene oxide materials in model propellant HPFP is complex. Regions of very high solubility exist, contrary to the myth that such polymeric materials are largely insoluble in partially fluorinated media. It is hypothesized that a specific, temperature-dependent interaction between the ether group of the ethylene oxide moiety and the -CHF group of the HPFP dominates the observed phase behaviour, along with a competing end-group effect that becomes less important as the molecular weight is increased. By suitably modifying the ethylene oxide end-groups and by tuning the hydrogen bonding capabilities of the solvents, some control of the phase behaviour may be achieved. It is hoped that this study will encourage theoretical activity on these fascinating and important systems to drive future developments in pharmaceutical applications.

## References


Ashbaugh, H. S., Paulaitis, M. E. (2006) Monomer hydrophobicity as a mechanism for the LCST behavior of poly(ethylene oxide) in water. *Ind. Eng. Chem. Res.* **45**: 5531–5537

Craig, D. Q. M. (1995) A review of thermal methods used for the analysis of the crystal form, solution thermodynamics and glass transition behaviour of polyethylene glycols. *Thermochim. Acta* **248**: 189–203

da Silva, L. H. M., Loh, W. (1998) Polymer induced multiphase generation in water/organic solvent mixtures. Strategies towards the design of triphasic and tetraphasic liquid systems. *Chem. Commun.*: 787–788

Drohmann, C., Beckman, E. J. (2002) Phase behaviour of polymers containing ether groups in carbon dioxide. *J. Supercrit. Fluids* **22**: 103–110

Ellis, B. (2000) Environmental issues in electronics manufacturing: a review. *Circuit World* **26**: 17–21

Emmen, H. H., Hoogendijk, E. M. G., Klopping-Ketelaars, W. A. A., Muijser, H., Duistermaat, E., Ravensberg, J. C., Alexander, D. J., Borkhataria, D., Rusch, G. M., Schmit, B. (1999) Human safety and pharmacokinetics of the CFC alternative propellants HFC 134a (1,1,1,2-tetrafluoroethane) and HFC 227 (1,1,1,2,3,3,3-heptafluoropropane) following whole-body exposure. *Regul. Toxicol. Pharmacol.* **32**: 22–35

Goldstein, R. E. (1984) On the theory of lower critical solution points in hydrogen-bonded mixtures. *J. Chem. Phys.* **80**: 5340–5341

Greenspan, J. S., Wolfson, M. R., Shaffer, T. H. (2000) Liquid ventilation. *Semin. Perinatol.* **24**: 396–405

Hammouda, B., Ho, D. L., Kline, S. (2004) Insight into clustering in poly(ethylene oxide) solutions. *Macromolecules* **37**: 6932–6937

Hirschfelder, J., Stevenson, D., Eyring, H. (1937) A theory of liquid structure. *J. Chem. Phys.* **5**: 896–912

Israelachvili, J. (1997) The different faces of poly(ethylene glycol). *Proc. Natl. Acad. Sci.* USA **94**: 8378–8379

James, R. (2006) *Phase behaviour of polymers in fluorinated media.* MSc Thesis, Cardiff University, UK

sson, B., Lindman, B., Holmberg, K., Kronberg, B. (1998) *urfactants and polymers in aqueous solution.* Wiley, Chichester, UK
lström, G. (1985) A new model for upper and lower critical olution temperature in poly(ethylene oxide) solutions. *J. Phys. hem.* **89**: 4962–4964
arian, S. G., Vincent, M. F., Bright, F. V., Liotta, C. L., Eckert, A. (1996) Specific intermolecular interaction of carbon dioxide ith polymers. *J. Am. Chem. Soc.* **118**: 1729–1736
lander, R., Florin, E. (1981) Water structure and changes in ermal stability of the system poly(ethylene oxide)-water. *J. hem. Soc., Faraday Trans. 1*, **77**: 2053–2077
ft, M. P., Riess, J. G. (1998) Highly fluorinated amphiphiles and ioidal systems, and their applications in the biomedical field. A ntribution. *Biochimie* **80**: 489–514
al, D. M. (2004) Perspective on fluorocarbon chemistry. *J. Org. hem.* **69**: 1–11
alloch, A. (1999) CFC and halon replacements in the environment. *Fluorine Chem.* **100**: 163–173
dith, J. C., Johnston, K. P., Seminario, J. M., Kazarian, S. G., ckert, C. A. (1996) Quantitative equilibrium constants between $O_2$ and Lewis bases from FTIR spectroscopy. *J. Phys. Chem.* **0**: 10 837–10 848
ell, M. L., Cao, Q., Fang, M., Johnston, K. P., Wilkinson, S. P., mith, C. D., Kersshner, J. L., Jureller, S. H. (1998) Solubility of mopolymers and copolymers in carbon dioxide. *Ind. Eng. hem. Res.* **37**: 3067–3079
s, J. G. (2002) Blood substitutes and other potential biomedical plications of fluorinated colloids. *J. Fluorine Chem.* **114**: 9–126
s, J. G. (2003) Fluorocarbon-based injectable gaseous microbub- es for diagnosis and therapy. *Curr. Opin. Colloid Interface Sci.* 259–266
Riess, J. G., Krafft, M. P. (1998) Fluorinated materials for in vivo oxygen transport (blood substitutes), diagnosis and drug delivery. *Biomaterials* **19**: 1529–1539
Riess, J. G., Krafft, M. P. (1999) Fluorocarbons and fluorosurfactants for in vivo oxygen transport (blood substitutes), imaging and drug delivery. *Mater. Res. Soc. Bull.* **24**: 42–48
Rigby, A. H., Bunn, C. W. (1949) A room-temperature transition in polytetrafluoroethylene. *Nature* **164**: 583–585
Rindfleisch, F., DiNoia, T. P., McHugh, M. A. (1996) Solubility of polymersin supercritical $CO_2$. *J. Phys. Chem.* **100**: 15 581–15 587
Rogueda, P. G. A. (2003) HPFP, a model propellant for pMDI's. *Drug Dev. Ind. Pharm.* **29**: 39–49
Saeki, S., Kuwahara, N., Nakata, M., Kaneko, M. (1976) Upper and lower critical solution temperatures in poly(ethylene glycol) solutions. *Polymer* **17**: 685–689
Samii, A. A., Karlstrom, G., Lindman, B. (1991) Phase behavior of poly(ethylene oxide)-poly(propylene oxide) block copolymers in nonaqueous solutions. *Langmuir* **7**: 1067–1071
Sanchez, V., Greiner, J., Riess, J. G. (1995) Highly concentrated 1,2-bis(perfluoroalkyl)iodoethene emulsions for use as contrast agents for diagnosis. *J. Fluorine Chem.* **73**: 259–264
Spitzer, M., da Silva, L. H. M., Loh, W. (2000) Liquid biphase systems formed in ternary mixtures of two organic solvents and ethylene oxide oligomers or polymers. *J. Braz. Chem. Soc.* **11**: 375–380
Spitzer, M., Sabadini, E., Loh, W. (2002a) Entropically driven partitioning of ethylene oxide oligomers and polymers in aqueous/organic biphasic systems. *J. Phys. Chem. B* **106**: 12448–12452
Spitzer, M., Sabadini, E., Loh, W. (2002b) Poly(ethylene glycol) or poly(ethylene oxide)? Magnitude of end-group contribution to the partitioning of ethylene oxide oligomers and polymers between water and organic phases. *J. Braz. Chem. Soc.* **13**: 7–9

International Journal of Pharmaceutics 362 (2008) 147–152

Contents lists available at ScienceDirect

International Journal of Pharmaceutics

Journal homepage: www.elsevier.com/locate/ijpharm

Pharmaceutical Nanotechnology

# Elaborating the phase behaviour of ethylene oxide oligomers and analogues in 2H, 3H-perfluoropentane

Peter C. Griffiths[a,*], Marie Côte[a], Philippe G.A. Rogueda[b]

[a] School of Chemistry, Cardiff University, Main Building, Park Place, Cardiff CF10 3TB, United Kingdom
[b] AstraZeneca Research and Development Charnwood, Bakewell Road, Loughborough LH11 5RH, United Kingdom

ARTICLE INFO

*Article history:*
Received 20 December 2007
Accepted 7 June 2008
Available online 13 June 2008

*Keywords:*
Phase behaviour
Fluorinated media
Excipients
Polymers
Surfactants

ABSTRACT

Pressure metered dose inhalers (pMDIs) are seen as an attractive option for the delivery of active molecules to the bloodstream *via* the lungs. Formulation issues are important as it is necessary to disperse the active substance into a volatile propellant. The phase behaviour of a range of common formulation agents – excipients – in 2H, 3H-perfluoropentane is reported here, focussing on the effects of simple elaboration of a central ethylene-oxide (EO) moiety. The base series of hydroxyl terminated EO fragments exhibited lower consolute solution temperature (LCST) behaviour that was strongly molecular weight-dependent. Substitution of methyl groups in place of the hydroxyl groups at the terminus of the EO fragment had a pronounced effect on the solubility of the oligomeric or polymeric material, the material becoming fully miscible with the HPFP. Substitution of methyl groups along the backbone of the hydroxyl terminated EO greatly enhanced the solubility of the materials, but the exhibited phase behaviour was still that of LCST. Longer alkyl groups at the terminus of the EO were found to promote the solubility compared to the hydroxyl terminated material, but to a relatively smaller degree compared with the methyl group. It is hoped that these simple "design rules" should facilitate the development of designer excipients tailored for a particular application.



## 1. Introduction

Drug delivery *via* the lungs has long been used to treat asthma and chronic obstructive pulmonary disease. However, the large surface area of the lungs presents an efficient route to the bloodstream (Courrier, 2002), and when coupled with the much lower activity of degradatory enzymes (at least compared to the kidneys and liver) (Keller, 1999) the lungs are increasingly being seen as an attractive and viable alternative to oral or parental routes for the delivery of actives to the systemic circulation (Laube et al., 2005). This is in no small part due to the well-understood technology of pressure metered dose inhalers (pMDI) (Wilby, 2005; Pritchard, 2005).

The pMDI which contains a drug either dissolved or dispersed into a compressed propellant is an inexpensive, reliable and patient compliant form for administering the drug to the lungs. However, the switch from ozone-depleting chlorofluorocarbon (CFC) propellants to hydrofluoroalkane (HFA) propellants presents a challenge as many formulation components are reported to have a very low solubility in these media (Byron, 1990), and accordingly, it is necessary to develop a fundamental understanding of solvation and solubility in HFA propellants (Peguin et al., 2006). HFA media find use as drug delivery systems (Riess, 2002), but this latter use is dependent on extensive formulation, usually incorporating co-solvents such as ethanol (Gupta et al., 2003).

The phase behaviour of a polymer in a solvent can exhibit a rich detail. Common characteristics include upper and lower consolute temperatures (UCST, LCST), in which the polymer undergoes a soluble/insoluble transition on passing through a well-defined temperature reflecting the balance of the enthalpic interaction term quantified by the $\chi$ parameter and the entropic interaction that favours miscibility. UCST and LCST behaviours are a result of monotonic dependencies of the $\chi$ parameter (decreasing and increasing, respectively) with temperature. "Hour glass" shaped phase diagrams arise due to an overlap of UCST and LCST behaviours (Siow et al., 1972), defined by a minimum in the $\chi$-temperature behaviour whereas a "closed miscibility loop" (Chang and Bae, 1998; Bae et al., 1991) phase diagram is observed where the $\chi$-temperature behaviour exhibits a maximum, often when the free energy of mixing also contains a further term relating to a specific, orientation-dependent interaction, *e.g.* hydrogen bond.

The phase behaviour has been measured for an extensive range of polymer/solvent systems and can be predicted, in the case of

* Corresponding author. Tel.: +44 29 20875858; fax: +44 2920 874030.
*E-mail address:* griffithspc@cardiff.ac.uk (P.C. Griffiths).
*URL:* http://www.cardiff.ac.uk/chemy/contactsandpeople/academicstaff/griffiths.html (P.C. Griffiths).

0378-5173/$ – see front matter © 2008 Elsevier B.V. All rights reserved.
doi:10.1016/j.ijpharm.2008.06.006

non-polar systems, by the Patterson–Flory theories of polymer solutions. However, in the case of polar polymer solutions, the phase separation phenomenon cannot be described by van der Waals forces alone (Saeki et al., 1976).

Arguably the most studied polar polymer/solvent system is poly(ethylene oxide) (PEO) in water (Saeki et al., 1976; Kjellander and Florin, 1981; Craig and Johnson, 1995; Hammouda et al., 2004); indeed, the solubility of PEO is an anathema itself since the next homologues polybutylene and polymethylene are insoluble in water (Israelachvili, 1997; Ashbaugh and Paulaitis, 2006). Short PEO chains (degree of polymerisation, $m \leq 48$) are completely miscible with water even at high temperatures; for slightly longer chains, a closed loop solubility gap is observed, yet for $m > 180$, only a LCST is found. This phase behaviour is very sensitive to molecular weight, and generally the cloud point decreases with an increase in chain length (Saeki et al., 1976; Kjellander and Florin, 1981). Various models have been proposed to account for the phase behaviour of PEO in water (Samii et al., 1991); water molecules experiencing weak van der Waals interactions with the EO groups possess higher structure compared to those in the bulk, which undergo an entropically driven disruption with increasing temperature resulting in aggregation and ultimately phase separation (Kjellander and Florin, 1981); the destruction of solubility enhancing hydrogen bonds between PEO and water (Goldstein, 1984; Hirschfelder et al., 1937) such that the solubility is then determined by the subtle balance of solvent–solvent and solute–solvent interactions; at lower temperatures the preferred gauche conformation of PEO exhibits a large dipole moment leading to a favourable interaction with the water (Karlström and Andersson, 1985), whereas at higher temperatures, non-polar isomers have higher statistical weight leading to a significant reduction in solubility.

The phase behaviour of PEO polymers in solvents other than water has received less attention. However, clouding phenomena of PEO has been reported in solvents such as formamide, *tert*-butyl acetate, super-critical carbon dioxide (sc-$CO_2$) and some organic solvents (Saeki et al., 1976; Silva and Loh, 1998; Spitzer et al., 2000, 2002a,b). Drohmann and Beckman (2002) report that PEG solubility in sc-$CO_2$ can be increased by decreasing its molecular weight or blocking the terminal hydroxyls by non-polar headgroups. The ether oxygens were found to enhance PEO solubility when compared to simple hydrocarbons, provided the oxygen was in a readily accessible position to the $CO_2$. As a general finding, carbonyl groups enhance the solubility of the polymer in sc-$CO_2$ by favourable cross-interactions, either by quadrupole ($CO_2$)–dipole (solute)interaction or Lewis acid/base, $CO_2$ being the Lewis acid (Kindfleisch et al., 1996; Kazarian et al., 1996; Meredith et al., 1996). End-group effects have also been examined extensively by Spitzer et al. (2000, 2002a,b). Despite its high water solubility, PEO can be extracted from water to organic solvent. This is due to the loss of polymer chain helicity when transferring from water to the apolar phase, resulting in an entropy increase (Bailey and Koleske, 1976). Spitzer et al. (2000, 2002a,b) showed that with increasing molecular weight, PEO favours an apolar phase. The molar mass at which PEO partitioning shifts its preference from the aqueous phase to the organic one occurred around 300–400 g mol$^{-1}$ for chloroform and dichloromethane. However, methylation of a sample of PEO 500 g mol$^{-1}$ led to a greater partitioning into apolar phase, showing that even above the 300–400 g mol$^{-1}$ range, the presence of glycol end-groups still contribute significantly to PEO partitioning into water. The hydrogen bond donating capability of the organic solvent was found to be crucial, so as to have strong enough interactions with the EO segments. The water displacement that resulted is associated to a high entropy increase that drives the transfer process by overcoming the loss in solvation energy.

The decrease in solubility upon heating, seen in the case of aqueous solutions of PEO, also occurs with systems of non-ionic surfactants in water, such as oligooxyethylene alkyl ethers bearing a hydrophobic alkyl tail and an EO headgroup. In such cases, the cloud point temperature occurs in the micellar phase, and depends not only on the strength of the interactions, but also on the shape and size of the micelles (Claesson et al., 1986).

Here, we report the phase behaviour of a range of common polymer and surfactant excipients in a model propellant (Rogueda, 2003), the partially fluorinated solvent 2H, 3H-perfluoropentane (HPFP), highlighting how the phase behaviour varies as a results of simple modification of the central EO moiety.

## 2. Materials and methods

### 2.1. Excipients

Poly(ethylene glycol), EO, $M_w$ = 200, 300, 400, 600 and 1000 g mol$^{-1}$, poly(propylene glycol), PO, $M_w$ = 1000 and 4000 g mol$^{-1}$, tetra(ethylene glycol) monododecyl ether, $C_{12}EO_4$ (Brij30™), deca(ethylene glycol) monododecyl ether, $C_{12}EO_{10}$, poly(ethylene oxide)-23-monododecyl ether, $C_{12}EO_{23}$ (Brij35™), poloxamers of molecular weight 1100 g mol$^{-1}$ ($EO_2PO_{16}EO_2$) and 5800 g mol$^{-1}$ ($EO_{20}PO_{70}EO_{20}$) and dodecane were purchased from normal sources (Sigma–Aldrich, Acros Chemicals, Apollo Scientific) and used without further purification. 2H, 3H-perfluoropentane (HPFP) (Apollo Scientific) was washed first with acidic and then basic alumina, filtered, dried and stored over molecular sieves.

### 2.2. Phase transition measurements

Samples were prepared by mass on a 3g scale in glass screw-top vials, sealed with polytetrafluoroethylene (PTFE) tape to prevent solvent evaporation, then wrapped into parafilm to protect against water penetration. After 48 h equilibration at room temperature, these samples were immersed in a temperature-controlled water bath and the temperature gradually raised from −20 °C at a rate of 1 °C every 30 min with constant agitation until the temperature reached 60 °C. Hysterisis effects were negated by invoking much slower and both heating and cooling temperature ramps once an approximate phase transition temperature had been estimated. Visual phase transition temperatures were recorded.

### 2.3. Phase composition assessment

Temperature-induced phase separation for samples spanning a wide range of polymer concentration led to two distinct layers. The composition of these layers was assessed by a direct dry-weight method in which the layers were separated into preweighted vials using a flat-ended-needle syringe and the solvent removed by drying in an oven at 60 °C until constant mass. Measurements were performed in triplicate and the average value presented.

### 2.4. Reproducibility

The phase transition measurements were performed in duplicate for each concentration. The composition of every sample was known accurately, spanning the concentration range 0.1–90 wt.% with a data frequency according to the phase transition profile. The temperature increment was typically 1 or 2 °C, again dependent on the phase behavior being recorded; close to the phase boundary, smaller increments were employed.

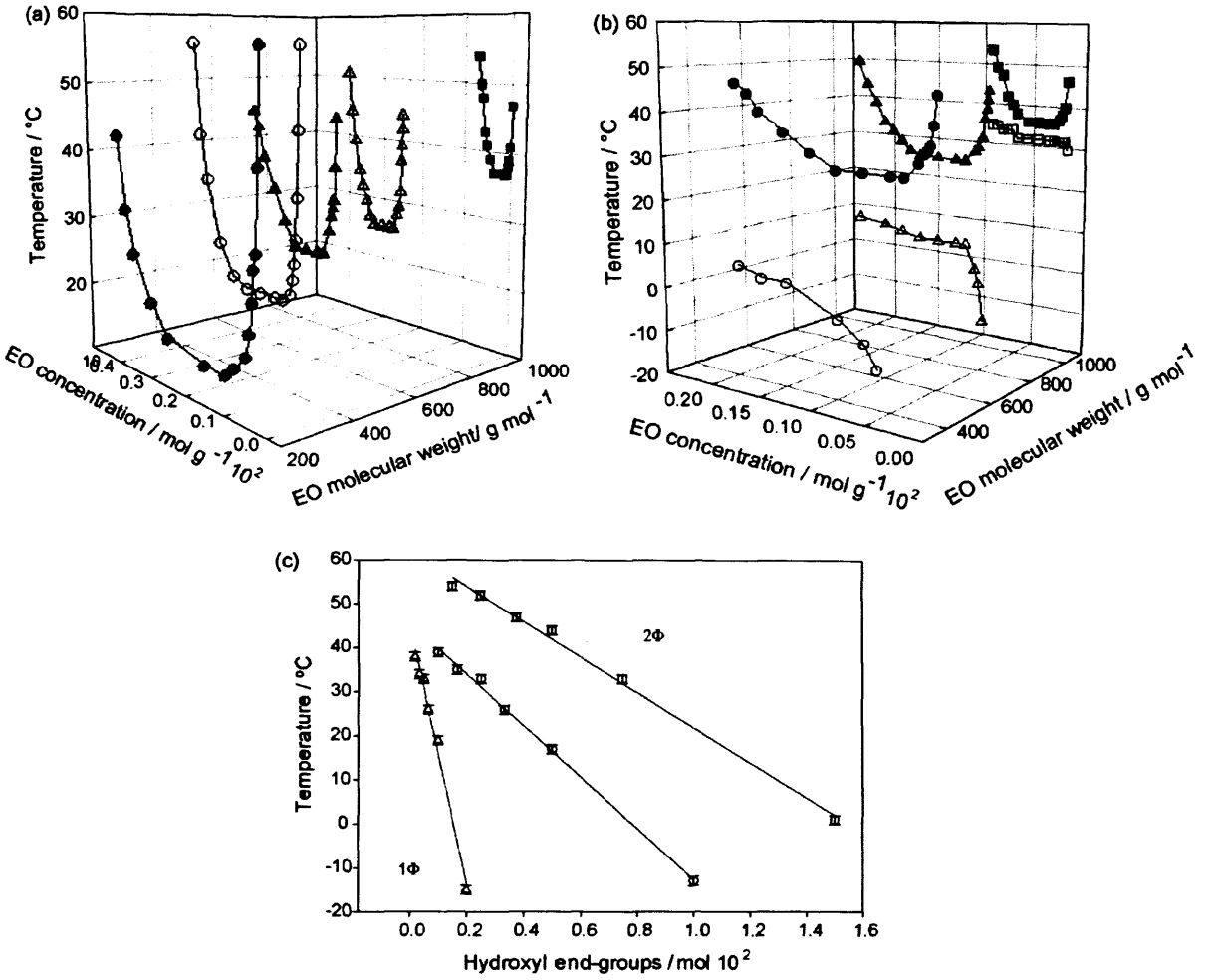


**Fig. 1.** (a) LCST for a series of PEG molecular weights in HPFP; EO 200 g mol$^{-1}$ (filled circles); EO 300 g mol$^{-1}$ (open circles); EO 400 g mol$^{-1}$ (filled triangles), EO 600 g mol$^{-1}$ (open triangles) and EO 1000 g mol$^{-1}$ (filled squares). (b) LCST (filled symbols) and melting point curves (open symbols) for a series of PEG molecular weights in HPFP; EO 400 g mol$^{-1}$ (circles); EO 600 g mol$^{-1}$ (triangles) and EO 1000 g mol$^{-1}$ (squares). (c) End-group analysis—cloud-point as a function of (di-)hydroxyl end-groups for a series of EO molecular weights 200, 300, 400, 600 and 1000 g mol$^{-1}$ at three representative concentrations, 10 wt.% (triangles); 50 wt.% (circles) and 75 wt.% (squares).

## 3. Results

### 3.1. Poly(ethylene oxide) homo-oligomers

On heating, originally clear monophasic solutions of hydroxyl end-capped EO in HPFP become opaque, and with time, separate into two clear layers. Onset of this phase separation defines the LCST. In the limited miscibility region (two phase region, 2Φ), *i.e.* $T$ > LCST, samples consist of a less dense polymer-enriched (upper) phase and a more dense polymer-depleted (lower) phase. These two phases may be separated and the polymer concentration quantified by mass after evaporation of the solvent. By projecting these concentrations onto the solute concentration axis, the solubility phase diagram may be constructed.

The LCST–concentration profile is presented in Fig. 1(a) as a function of EO molecular weight. The cloud point of EO in HPFP is strongly concentration-dependent for all molecular weights, displaying a sharp increase towards both very low and very high concentrations. In water, much higher molecular weights are required before LCST behavior is observed (Saeki et al., 1976), although similar behaviour at these low molecular weights are observed in non-aqueous solvents (Spitzer et al., 2000, 2002a,b).

The molecular weight 400, 600 and 1000 g mol$^{-1}$ EO samples were also found to exhibit limited solubility at lower temperatures, coinciding with their melting behavior, Fig. 1(b). At low temperatures, such systems are biphasic consisting of a coexisting liquid and waxy solid. As the temperature increases through the melting point of the polymer (5–8 °C for EO 400 g mol$^{-1}$, 17–22 °C for EO 600 g mol$^{-1}$ and 35–40 °C for EO 1,000 g mol$^{-1}$) samples first become monophasic, before reaching the higher LCST presented in Fig. 1(a).

An increase in molecular weight drives the LCST towards higher temperatures, implying a greater solubility window but the melting curve is also a strong function of molecular weight. Low molecular weight EO s are very soluble in HPFP but over a temperature range that is not easily accessible during manufacture of formulations or storage/use of the resultant products. Higher molecular weight hydroxyl terminated EO s are largely – and for most practical purposes – insoluble in HPFP. Indeed, for molecular weights greater than 1500 g mol$^{-1}$, the temperature required to melt the polymer is higher than the LCST and therefore samples are always biphasic, either solid/liquid or liquid/liquid.

In stark contrast, mono-methyl (and thus mono-hydroxy-) and di-methyl end-capped EOs are fully miscible with HPFP over the

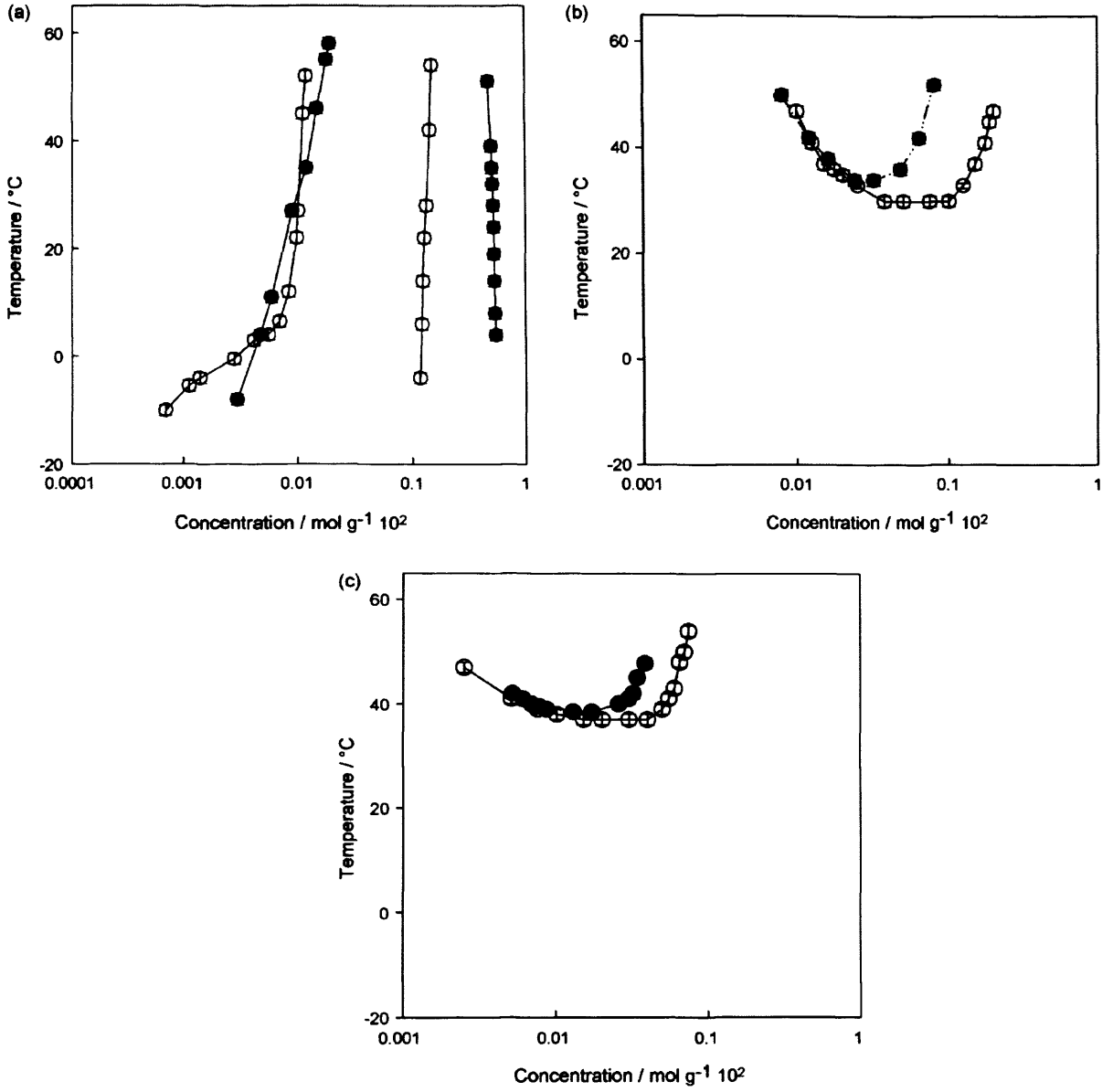


Fig. 2. (a) Phase behaviour of poly(ethylene glycol)-based surfactants in HPFP and representative comparitors in HPFP $C_{12}EO_3$ (filled symbols) and dodecane (open symbols). (b) Phase behaviour of poly(ethylene glycol)-based surfactants in HPFP and representative comparitors in HPFP $C_{12}EO_{10}$ (filled symbols) and EO 400 g mol$^{-1}$ (open symbols). (c) Phase behaviour of poly(ethylene glycol)-based surfactants in HPFP and representative comparitors in HPFP $C_{12}EO_{23}$ (filled symbols) and EO 1000 g mol$^{-1}$ (open symbols).

same temperature and concentration ranges, suggesting that the phase behavior is dominated by end-group/solvent interactions. By substituting HPFP for the fully fluorinated analogue perfluoropentane (PFP), the ability of these end-groups to interact with the solvent may be systemically varied and an LCST-type behavior can be induced in the previously fully miscible mono- and di-methyl end-capped EOs; concomitantly, the LCST of the di-hydroxyl end-capped EOs is driven to lower temperatures (Côte et al., 2008).

All the LCST data from the dihydroxyl ended polymers presented in Fig. 1(a) have been re-plotted in Fig. 1(c) in terms of the concentration of the end-groups. In this representation, samples at the same total polymer concentration will have an end-group concentration that is dependent on molecular weight. Accordingly, each plot on Fig. 1(c) arises due to a range of molecular weights at a fixed total concentration. However, the mono-hydroxyl data do not superimpose on the di-hydroxy data, implying that there must also be an underlying molecular weight effect. Most importantly, an increase in the number of hydroxy end-groups for a given polymer concentration, results in a decrease in the LCST and a contraction of the solubility window.

### 3.2. Poly(ethylene oxide)-based surfactants

The phase behaviour of Brij30 ($C_{12}EO_4$), $C_{12}EO_{10}$ and Brij35 ($C_{12}EO_{23}$) surfactants was also investigated in a likewise manner; results are shown in Fig. 2(a–c). For comparison, the phase behaviours of the molecular "fragments" of the excipient, *viz.* dodecane and ethylene glycol are also presented. $C_{12}EO_4$ – having the shortest EO headgroup – shows truncated hour-glass phase behaviour, a phase behaviour that is not that dissimilar to that observed for dodecane. $C_{12}EO_{10}$ and $C_{12}EO_{23}$ on the other hand, display LCST-type behaviour, with a melting curve (not shown),

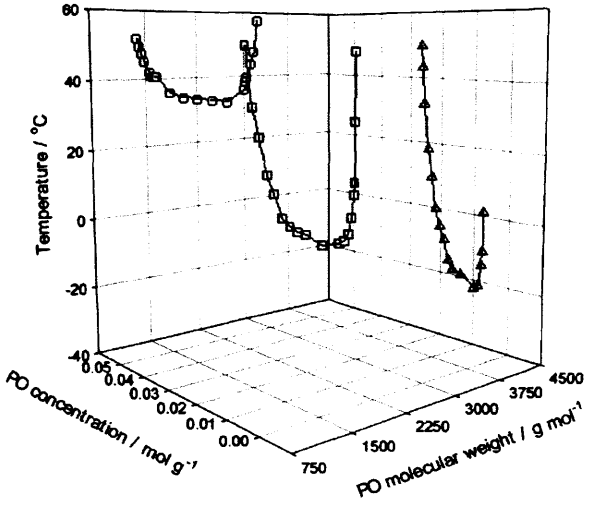


Fig. 3. Phase diagram of poly(propylene oxide) PO 1000 g mol$^{-1}$ (circles), 2000 g mol$^{-1}$ (squares) and 4000 g mol$^{-1}$ (triangles) in HPFP.

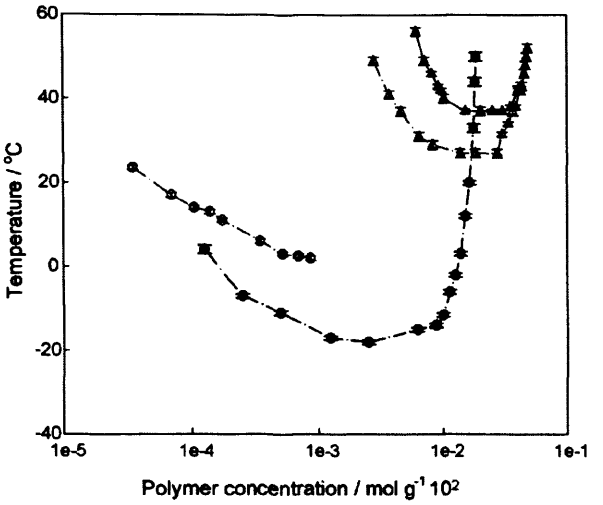


Fig. 4. Phase diagram of Pluronic copolymers $EO_2PO_{16}EO_2$ (open triangles), $EO_{20}PO_{70}EO_{20}$ (open circles), PO 1000 g mol$^{-1}$ (filled triangles) and PO 4000 g mol$^{-1}$ (filled circles) in HPFP.

again not that dissimilar to the observed behaviour of the appropriate EO fragment. Clearly, the dodecane fragment dominates the behaviour of the excipient bearing the short EO chain, especially at lower concentrations, whilst the ethylene glycol fragment dominates the behaviour of the excipients bearing the longer EO chain.

### 3.3. Poly(propylene oxide) homo-oligomers

Low molecular weight poly(propylene oxide) polymers however, exhibit much higher solubilities and over workable temperature windows, indeed samples with molecular weight of 400 and 750 g mol$^{-1}$ – even with hydroxyl end-groups – are entirely miscible with HPFP over the entire range of temperature and concentration. The phase behavior in HPFP of higher molecular weight PO – Fig. 3 – does however exhibit the pronounced concentration dependence at the extremes of concentration as in the EO case, Fig. 1(b), but with one striking difference; the LCST now *decreases* with *increasing* molecular weight, the opposite to that observed for EO.Poly(ethylene oxide)–poly(propylene oxide)–poly(ethylene oxide) copolymers

The phase behavior of two samples of poloxamer copolymers consisting of a low molecular weight copolymer $EO_2PO_{16}EO_2$ and a higher molecular weight copolymer $EO_{20}PO_{70}EO_{20}$ has also been recorded, Fig. 4. The molecular weights of the PO block in $EO_2PO_{16}EO_2$ and $EO_{20}PO_{70}EO_{20}$ are ~925 and 4050 g mol$^{-1}$ respectively; the striking effects of the EO blocks (and their -OH end-groups) may be observed by comparison with equivalent molecular weight homopolymer PO analogues, *viz.* 1000 and 4000 g mol$^{-1}$. For the lower molecular weight PO comparison, the effect of the EO block is a modest reduction (~15 °C) in the LCST over the majority of the concentration range, whereas for the larger copolymer the reduction is slightly greater (~20 °C). The phase diagram at higher concentrations of $EO_{20}PO_{70}EO_{20}$ has not been determined due to the solid nature of the sample.

## 4. Discussion

The presence of polar groups within the oligomeric or polymeric structure enhances the solubility of oxygen and nitrogen containing polymers in HPFP (Griffiths et al., 2005; James, 2005). The increase in solubility arises due to the presence of a specific, temperature-dependent interaction between the polar groups on the backbone of the polymer (*e.g.* the ether group of the EO moiety) and the –CH– group of the HPFP (Griffiths et al., 2005). The LCST behaviour may be rationalised by invoking an argument similar to that accounting for the aqueous behaviour, *viz.*, with increasing temperature, the EO coil adopts a less polar conformation reducing the (favourable) interactions that promotes solubility, thus leading to phase separation; a process that may be facilitated by the addition of a perfluorinated analogue (Côte et al., 2008). Accordingly, the phase behaviour is strongly dependent on the nature of the end-groups with both mono-methyl and di-methyl capped EOs exhibiting no LCST over the same wide ranges of temperature and composition over which LCST behaviour was exhibited by the di-hydroxyl EOs. Clearly, the hydroxyl groups exhibit a less favourable interaction with the solvent compared with the methyl groups, and this is manifested in terms of the molecular weight dependence of the di-hydroxyl phase behaviour—the LCST increases with increasing molecular weight as the number of unfavourable end-group/solvent contacts is reduced. The fact that there is a pronounced difference between the samples with "no" and "any" hydroxyl groups suggests that the phase separation is driven in part by a process of aggregation through the hydroxyl groups.

This model can then be simply extended to the interpretation of the phase behaviour of EO-based surfactants, tetra(ethylene glycol) monododecyl ether ($C_{12}EO_4$), deca(ethylene glycol) monododecyl ether ($C_{12}EO_{10}$) and poly(ethylene oxide)-23-monododecyl ether ($C_{12}EO_{23}$). For the two higher EO content materials – $C_{12}EO_{10}$ and $C_{12}EO_{23}$ – the phase behavior is only slightly different to that exhibited by the closest match EO analogues, EO 400 and EO 1000 g mol$^{-1}$, where in both cases the LCST–composition curve is largely unchanged in form, but merely shifted by a few degrees to slightly higher temperature values. If one considers the dodecyl group as a replacement for one of the hydroxyl groups compared to the di-hydroxyl comparator, the resultant increase in the solubility of the surfactant, is in agreement with observations of the EO homopolymers. However, these two surfactants still exhibit an LCST-type phase diagram implying that the dodecyl group does not interact as favorably with the solvent as the smaller methyl group (*i.e.* as a comparison with the mono-methyl and di-methyl EO

rivatives). Unlike the LCST-type behaviour shown by $C_{12}EO_{10}$ and $_2EO_{23}$, $C_{12}EO_4$ exhibits truncated hour-glass phase behaviour, *i.e.* e shape of its phase behaviour is dominated by the dodecane moiy, especially at the lower concentration range. However, the EO oups promote the solubility of the dodecane moiety at higher ncentrations, as evidenced by the wider solubility windows, iplying that the presence of EO groups modify the $\chi$-temperature haviour to a much greater degree at higher temperatures.Clearly, ethyl groups at the *terminus* of the polymer chain have a sigficant effect on the phase behaviour, as seem by comparisons the hydroxyl and dodecyl terminated analogues. The effects of ding methyl groups to the EO *backbone* may be probed by comring the phase behaviours of the EO and PO homopolymers, d ultimately, their copolymers.The most striking observations hen comparing the EO and PO homopolymers are the oppoe molecular weight dependencies of the LCST, and the much eater solubilities of the PO homopolymers. The decreasing LCST ith increasing molecular weight for PO implies the effects of e hydroxyl end-groups are significantly weaker than in the EO se, whereas the higher solubility reflects the presence of the ethyl groups. One might conclude therefore that the PO adopts conformation in solution that maximises the exposure of the ethyl groups to the HPFP whilst minimising that of the hydroxyl oups. Taking the EO and PO homopolymer behaviors together, e might hypothesize that the presence of ether oxygens promote e solubility of the polymer at lower temperatures but at higher mperatures there is a competing association process that ultiately induces the phase separation. Addition of methyl groups to e backbone weakens this tendency leading to higher the signifntly higher solubility of the PO. This hypothesis also accounts r the lowering of the LCST for $EO_2PO_{16}EO_2$ copolymer compared th EO 1000 g mol$^{-1}$, *viz.* "removal" of the $CH_3$– groups. The higher olecular weight copolymer data is however, most interesting; the ST for $EO_{20}PO_{70}EO_{20}$ is much higher than for both the simple mopolymer comparitors—in terms of the equivalent homopolyers, $EO_{110}$ (4800 g mol$^{-1}$) is insoluble in HPFP whereas $PO_{110}$ 300 g mol$^{-1}$) is also predicted to exhibit a low solubility (*Note*: 4000 g mol$^{-1}$ is presented in Fig. 4 but the LCST decreases with reasing molecular weight thus the solubility of PO 6000 g mol$^{-1}$ uld be even lower). Further work is on-going to establish the gin of this apparently peculiar behavior. The results reported re serve to illustrate the many interesting features of the solility of polymers and other common excipients in fluorinated uids.

## knowledgements

Financial support from Cardiff University and AstraZeneca is itefully acknowledged.

## ferences

baugh, H.S., Paulaitis, M.E., 2006. Monomer hydrophobicity as a mechanism for the LCST behavior of poly(ethylene oxide) in water. Ind. Eng. Chem. Res. 45, 5531–5537.
, Y.C., Lambert, S.M., Soane, D.S., Prausnitz, J.M., 1991. Cloud-point curves of polymer solutions from thermooptical measurements. Macromolecules 24, 4403–4407.
ley, F.E., Koleske, J.V., 1976. Poly ethylene oxide. Academic Press, New York.
on, P.R., 1990. Determinants of drug and polypeptide bioavailability from aerosols delivered to the lung. Adv. Drug Del. Rev. 5, 107–132.
sson, P.M., Kjellander, R., Stenius, P., Christenson, H.K., 1986. Direct measurement of temperature-dependent interactions between nonionic surfactant layers. J. Chem. Soc., Faraday Trans. 1 82, 2735–2746.
Chang, B.H., Bae, Y.C., 1998. Liquid–liquid equilibria of polymer solutions: a closed miscibility loop phase behavior. Macromol. Theory Simul. 7, 551–556.
Côte, M., Rogueda, P.G.A., Griffiths, P.C., 2008. The effect of molecular weight and end-group nature on the solubility of ethylene oxide oligomers in 2H. 3H-decafluoropentane and its fully fluorinated analogue perfluoropentane. J. Pharm. Pharmacol. 60, 593–599.
Courrier, H.M., 2002. Pulmonary drug delivery systems: recent developments and prospects. Crit. Rev. Ther. Drug Carrier Sys. 19, 425–498.
Craig, D.Q.M., Johnson, F.A., 1995. Pharmaceutical applications of dynamic mechanical thermal analysis. Thermochim. Acta 248, 97–115.
Drohmann, C., Beckman, E.J., 2002. Phase behaviour of polymers containing ether groups in carbon dioxide. J. Supercrit. Fluids 22, 103–110.
Goldstein, R.E., 1984. On the theory of lower critical solution points in hydrogen-bonded mixtures. J. Chem. Phys. 80, 5340–5341.
Griffiths, P.C., Paul, A., James, R., Rogueda, P.G.A., 2005. Explaining the phase behaviour of the pharmaceutically relevant polymers poly(ethylene glycol) and poly(vinyl pyrrolidone) in semi-fluorinated liquids. J. Pharm. Pharmacol. 57, 973–980.
Gupta, A., Stein, S.W., Myrdal, P.B., 2003. Balancing ethanol cosolvent concentration with product performance in 134a-based pressurized metered dose inhalers. J. Aerosol Med. 16, 167–174.
Hammouda, B., Ho, D.L., Kline, S., 2004. Insight into clustering in poly(ethylene oxide) solutions. Macromolecules 37, 6932–6937.
Hirschfelder, J., Stevenson, D., Eyring, H., 1937. A theory of liquid structure. J. Chem. Phys. 5, 896–912.
Israelachvili, J., 1997. The different faces of poly(ethylene glycol). Proc. Natl. Acad. Sci. 94, 8378–8379.
James, R., 2005. MSc Thesis, Cardiff University.
Karlström, G., Andersson, M., 1985. Conformational structure of 1,2-dimethoxyethane in water and other dipolar solvents, studied by quantum chemical, reaction field, and statistical mechanical techniques. J. Phys. Chem. 89, 4962.
Kazarian, S.G., Vincent, M.F., Bright, F.V., Liotta, C.L., Eckert, C.A., 1996. Specific intermolecular interaction of carbon dioxide with polymers. J. Am. Chem. Soc. 118, 1729–1736.
Keller, M., 1999. Innovations and perspectives of metered dose inhalers in pulmonary drug delivery. Int. J. Pharm. 186, 81–90.
Kjellander, R., Florin, E., 1981. Water structure and changes in thermal stability of the system polyethylene oxide– water. J. Chem. Soc., Faraday Trans. 1 77, 2053–2077.
Laube, B.L., Geller, D.E., Lin, T., Dalby, R.N., Diener-West, M., Zeitlin, P.L., 2005. Positive expiratory pressure changes aerosol distribution in patients with cystic fibrosis. Respir. Care 50, 1161–1176.
Meredith, J.C., Johnston, K.P., Seminario, J.M., Kazarian, S.G., Eckert, C.A., 1996. Quantitative equilibrium constants between $CO_2$ and Lewis bases from FTIR spectroscopy. J. Phys. Chem. 100, 10837–10848.
Peguin, R.P.S., Selvam, P, da Rocha, S.R.P., 2006. Microscopic and thermodynamic properties of the HFA134a–water interface: atomistic computer simulations and tensiometry under pressure. Langmuir 22, 8675–8683.
Pritchard, J., 2005. The future of metered-dose inhalers. Pharm. Technol. Eur. 17, 27–28.
Riess, J.G., 2002. Fluorous micro- and nanophases with a biomedical perspective. Tetrahedron 58, 4113–4131.
Rindfleisch, F., DiNoia, T.P., McHugh, M.A., 1996. Solubility of polymers and copolymers in supercritical $CO_2$. J. Phys. Chem. 100, 15581–15587.
Rogueda, P.G.A., 2003. HPFP, a model propellant for pMDIs. Drug Dev. Ind. Pharm. 29, 39–49.
Saeki, S., Kuwahara, N., Nakata, M., Kaneko, M., 1976. Upper and lower critical solution temperatures in poly(ethylene glycol) solutions. Polymer 17, 685–689.
Samii, A.A., Karlstrom, G., Lindman, B., 1991. Phase behavior of poly(ethylene oxide)–poly(propylene oxide) block copolymers in nonaqueous solution. Langmuir 7, 1067–1071.
Silva, L.H.M.D., Loh, W., 1998. Polymer induced multiphase generation in water/organic solvent mixtures: strategies towards the design of triphasic and tetraphasic liquid systems. Chem. Commun. 7, 787–788.
Siow, K.S., Delmas, G., Patterson, D., 1972. Cloud-point curves in polymer solutions with adjacent upper and lower critical solution temperatures. Macromolecules 5, 29–34.
Spitzer, M., Silva, L.H.M.D., Loh, W., 2000. Liquid biphase systems formed in ternary mixtures of two organic solvents and ethylene oxide oligomers or polymers. J. Braz. Chem. Soc. 11, 375–380.
Spitzer, M., Sabadini, E., Loh, W., 2002a. Entropically driven partitioning of ethylene oxide oligomers and polymers in aqueous/organic biphasic systems. J. Phys. Chem. B 106, 12448–12452.
Spitzer, M., Sabadini, E., Loh, W., 2002b. Poly(ethylene glycol) or poly(ethylene oxide)? Magnitude of end-group contribution to the partitioning of ethylene oxide oligomers and polymers between water and organic phases. J. Braz. Chem. Soc. 13, 7–9.
Wilby, M.J., 2005. Increasing performance consistency of pMDIs. Drug Del. Technol. 5, 56–58.

# Characterization of a Polymorphic System Exhibiting Substantial Variation of Solubility in a Fluorinated Solvent

**Marie Côte,[†] Colan E. Hughes,[†] Talbir K. Austin,[‡] Philippe G. A. Rogueda,[‡] Zhigang Pan,[†] Kenneth D. M. Harris,*[,†] and Peter C. Griffiths*[,†]**

*School of Chemistry, Cardiff University, Park Place, Cardiff, Wales, CF10 3AT, U.K., and AstraZeneca R&D Charnwood, Bakewell Road, Loughborough, LE11 5RH, U.K.*

*Received: January 29, 2008; Revised Manuscript Received: June 5, 2008*

We report several aspects of the characterization of a material (triacetylated-β-cyclodextrin) that exists in two crystalline polymorphic forms (denoted I and II). A striking feature of this polymorphic system is that polymorph I (MPt 194 °C) and polymorph II (MPt 219 °C) exhibit remarkably different solubility in the fluorinated solvent 2H,3H-decafluoropentane, with the solubility higher by a factor of ca. eight for polymorph I at ambient temperature. Structural information established from powder X-ray diffraction and high-resolution solid-state $^{13}C$ NMR spectroscopy for polymorphs I and II is reported, including crystal structure determination of polymorph II from the powder X-ray diffraction data. Differential scanning calorimetry and high-temperature powder X-ray diffraction demonstrate that the metastable polymorph I converts to the stable polymorph II over a range of elevated temperatures. The combined evidence of these and other techniques suggests that there is a monotropic relationship between polymorphs I and II.

## 1. Introduction

*In the molecular solid state, polymorphism arises when a given type of molecule is able to form different crystal structures.*[1–7] *Understanding the physical and chemical factors that underlie the formation of different polymorphs of a given molecule is a field of endeavor of considerable importance at the present time, both from the fundamental scientific viewpoint and from the perspective of optimizing industrial applications. Fundamentally, studies of polymorphic systems provide the opportunity to obtain a systematic understanding of structure–property relationships for crystalline materials, as in principle any solid-state property of interest (such as chemical and physical stability, color, melting point, dissolution rate, flow properties and solubility) should differ between different polymorphic forms of the same molecule. As an illustration, our own research in this field in recent years has encompassed aspects such as dynamic properties,*[8] *structural properties,*[9] *solid state reactions*[10] *and crystallization processes*[11,12] *of polymorphic systems. In the industrial context, if a solid material with industrial applications is found to exhibit polymorphism, there are important implications with regard to both scientific and legal issues, and recognition of this fact has led to intense investigations of polymorphism within the pharmaceuticals sector in recent years. Clearly, the ability to prepare a specific polymorph with a high degree of reproducibility and reliability is a key requirement in the manufacture of solid drugs.*[13] *Here we focus on physicochemical characterization of a polymorphic system that is of relevance in the pharmaceuticals industry and for which a striking difference in solubility of the different polymorphic forms in a fluorinated solvent is observed. The compound of interest is the hydrophobically modified triacetylated-β-cyclodextrin (TAβCD, Scheme 1), and we focus in particular on its solubility in liquid 2H,3H-decafluoropentane (HPFP).*

*SCHEME 1: Molecular Structure of TAβCD.*

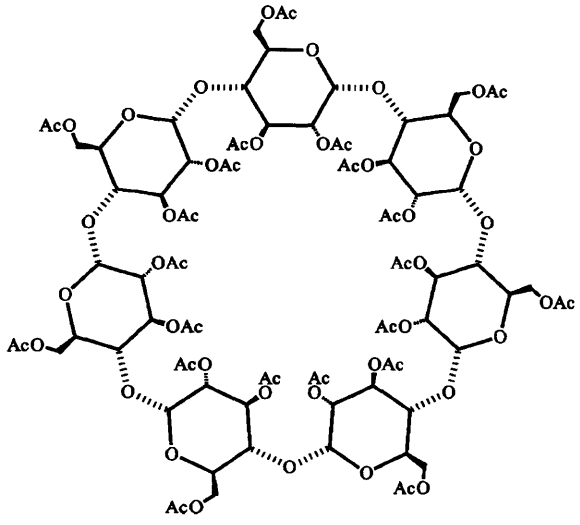


*In general, cyclodextrins and their derivatives offer the possibility of forming host–guest complexes by allowing guest molecules into their basket-shaped rings, thus enabling the controlled release of the guest (e.g., drug) molecule.*[14,15] *Indeed, previous studies have highlighted TAβCD as a sustained release carrier for various drugs such as azydothymidine (a potent anti-AIDS active)*[16] *or nicardipine hydrochloride (a calcium channel blocker).*[17,18] *In the pharmaceutical context, the necessity to adopt CFC-free propellants for applications such as pressurized metered-dose inhalers (pMDIs) often requires extensive product reformulation.*[19–23] *The combination of TAβCD as a drug carrier and HPFP as the propellant has considerable potential (e.g., in the formation of stable suspensions and solutions in pMDIs).*[24]

* To whom corresponse should be addressed. E-mail: HarrisKDM@cardiff.ac.uk (K.D.M.H.); GriffithsPC@cardiff.ac.uk (P.C.G.).
† Cardiff University..
‡ AstraZeneca R&D.

*10.1021/jp800848w CCC: $40.75* 
*Published on Web 08/21/2008*

However, given the discovery (vide infra) that TAβCD exhibits polymorphism, such potential applications rely on the ability to control the polymorphic forms of this material.

Polymorphism of TAβCD was first mentioned by Bettinetti et al. in 2006[25] and further studied by Corti et al.,[26] although there have been no previous studies to investigate structural properties of this polymorphic system nor to investigate its solubility in fluorinated solvents. In the present work, we focus on characterization of several aspects of polymorphism in the TAβCD system. For consistency of nomenclature, we denote the two polymorphs of TAβCD as polymorphs **I** and **II**, thus adopting the same nomenclature as previous literature.[25,26]

## 2. Experimental

In this work, four commercial samples of TAβCD were purchased from three different suppliers: Aldrich (Lot S05254-263 and Lot S35068), Cyclolab (batch number CYL-2116) and Molekula (batch number 21619). Samples were also prepared (i) by melting, followed by cooling and solidification, and (ii) by dissolving TAβCD in HPFP, then evaporating the solvent to dryness at ambient temperature. All samples of TAβCD were analyzed for chemical composition and no differences were identified among the different samples using solution-state NMR ($^1H$ and $^{13}C$) and mass spectrometry. All spectra obtained were as expected for pure TAβCD. The sample of HPFP (Fluorochem) used in this work was washed with acidic and then basic $Al_2O_3$ and stored over molecular sieves.

Routine powder X-ray diffraction data for all samples were recorded in transmission mode on a Bruker D8 diffractometer (Ge-monochromated Cu $KR_1$ radiation). For pure samples of polymorphs **I** and **II**, high-quality powder X-ray diffraction data were also recorded (at 293 K) on Station 9.1 at the SRS facility, Daresbury Laboratory ($\lambda$ ) 1.000237 Å), with the powder sample packed in a capillary tube (0.5 mm diameter) in each case. The powder X-ray diffraction patterns were indexed using the Crysfire[27a] and TOPAS[27b] programs to obtain initial lattice parameters, which were then refined by employing the Le Bail profile fitting technique[28] in the GSAS program.[29] The GSAS program was also used for Rietveld refinement for polymorph **II** (see Section 3.1).[30] High-temperature powder X-ray diffraction studies were carried out in reflection mode on a Bruker D8 diffractometer (Ge-monochromated Cu $KR_1$ radiation) fitted with an Anton Paar TCU 100 unit.

Solid-state $^{13}C$ NMR measurements were carried out at 75.48 MHz on a Chemagnetics Infinity Plus spectrometer. All experiments were performed using cross polarization from $^1H$ to $^{13}C$ at a MAS frequency of 12 kHz, with the powder sample contained in a rotor of 4 mm diameter. $^1H$ decoupling was applied during acquisition with a nutation frequency of 80 kHz. The duration of the measured FID was 51.2 ms, with a spectral width of 20 kHz.

Differential scanning calorimetry (DSC) measurements were carried out on a TA Instruments Q100 instrument. Unless otherwise stated, all experiments were carried out at a heating rate of 10 °C $min^{-1}$ and a cooling rate of 30 °C $min^{-1}$. Samples (with mass in the range 1-5 mg) were contained in sealed aluminum pans. In all data presented here, exothermic peaks are positive and transition temperatures are taken as the onset temperature of the peaks (estimated errors in transition temperatures were assessed to be ca. ( 1 °C, based on results from a large number of repeated measurements). Calibration was carried out using standard procedures based on the use of sapphire and indium standards.

Thermogravimetric analysis (TGA) was performed on a Mettler Toledo TGA/STD A851e instrument and on a TA Instruments SDT Q600 instrument, with sample masses in the range 4-6 mg. The temperature range investigated was 25-250 °C, with a heating rate of 10 °C $min^{-1}$. Calibration was carried out using a standard of known mass, and a sample of indium for temperature calibration.

Solution-state $^1H$ and $^{13}C$ NMR spectra were recorded on a Bruker 400 MHz spectrometer at 300 K in $CDCl_3$. $^1H$ NMR spectra were acquired with 16 scans and a spectral width of 6.4 kHz. $^{13}C$ NMR spectra were acquired with 256 scans and a spectral width of 17 kHz.

Scanning Electron Microscopy (SEM) measurements were made on a high-resolution v eeco FEI XL30 ESEM (Environmental Scanning Electron Microscope) FEG (Field Emission Gun) in high vacuum mode. Small amounts of each sample of TAβCD were deposited on double-sided carbon tabs stuck to aluminum stubs and were gently brushed with soft paper to remove excess material. Samples were then covered with a thin coating of gold/palladium (90:10). The maximum magnification investigated was 100 000.

Optical microscopy was carried out on an Olympus BX 50 microscope equipped with a high-temperature stage (Linkam THMSE 600, with Linkam TMS 93 temperature controller) and a color video camera (Jv C, model TK-C1380).

The solubility of TAβCD in HPFP was investigated at ambient temperature (ca. 20 °C), employing solution-state $^1H$ NMR to determine the concentration of TAβCD in HPFP (from the ratio of the measured intensities of peaks characteristic of TAβCD and HPFP). In these studies, known amounts of TAβCD and HPFP were mixed and, after equilibration, the samples were passed through a 0.2 μm Whatman disposable filter mounted at the tip of a plastic syringe. An aliquot of the filtered solution was added quickly to an NMR tube containing $CDCl_3$ and the $^1H$ NMR spectrum was recorded. Initially, a calibration was established from studies of solutions of known concentration (in the range 0.5-13 wt %), prepared using the highly soluble polymorph **I** of TAβCD in HPFP (for all solutions prepared for the calibration, complete dissolution was achieved, resulting in a clear solution). The ratio of the intensities of characteristic peaks due to TAβCD and HPFP was then determined and a linear correlation was obtained between the concentration in TAβCD in the solution and the ratio of intensities. This correlation was then used to determine the concentration of TAβCD in subsequent studies of solubility. In these studies, each solution was prepared in triplicate and two aliquots were taken from each solution, with all six aliquots then measured at the same time.

## 3. Results and Discussion

Two crystalline polymorphs of TAβCD, denoted polymorphs **I** and **II**, were identified among the four commercial samples investigated in this work. One sample from Aldrich (lot S05254-263) was found to be a pure sample of polymorph **II**, whereas a sample from Cyclolab (batch number CYL-2116) was found to be a pure sample of polymorph **I**. A second sample from Aldrich (lot S35068) and a sample from Molekula (batch number 21619) were found to be mixtures of polymorphs **I** and **II**. These assignments have been established on the basis of the results described below.

*3.1. Powder X-Ray Diffraction.* Powder X-ray diffraction patterns were recorded at ambient temperature for all samples of TAβCD and characteristic patterns for polymorphs **I** and **II** are shown in Figure 1. After indexing the powder X-ray diffraction pattern for each polymorph (see Section 2), profile refinement was carried out using the Le Bail profile fitting

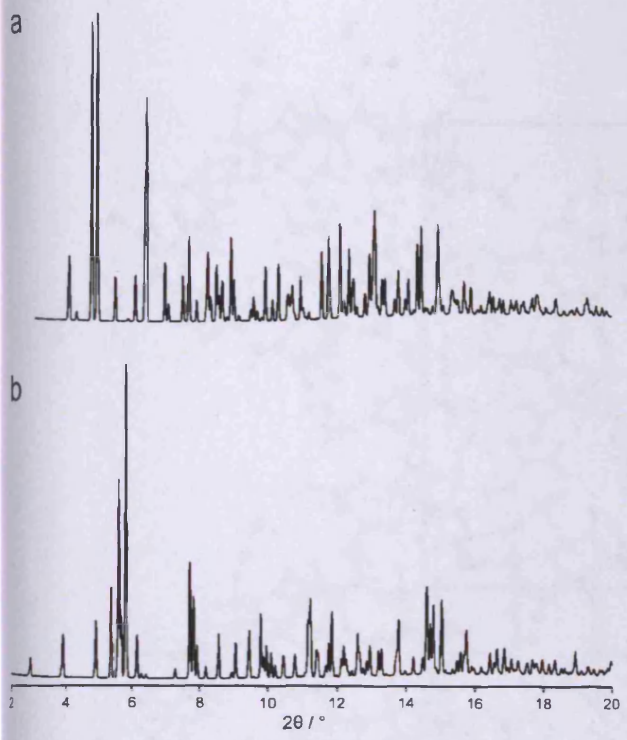


Figure 1. Powder X-ray diffraction patterns (synchrotron data) for (a) polymorph I and (b) polymorph II of TA$\beta$CD.

**TABLE 1: Unit Cell Parameters and Space Groups for Polymorphs I and II of TA$\beta$CD (at 20 °C), Established in the Present Work, and for the Methanol Solvate of TA$\beta$CD Reported by Añibarro et al.[31] (at −133 °C)**

| | polymorph I | polymorph II | methanol solvate |
|---|---|---|---|
| space group | $P2_1$ | $P2_1$ | $P2_1$ |
| a/Å | 14.2336(5) | 11.6881(4) | 11.576(8) |
| b/Å | 23.1570(6) | 21.3064(8) | 21.105(9) |
| c/Å | 16.4848(6) | 20.2225(10) | 20.300(15) |
| $\beta$/deg | 100.415(4) | 93.388(4) | 93.584(7) |
| volume/Å$^3$ | 5343.97(23) | 5027.25(22) | 4946(5) |

*technique (using the synchrotron X-ray powder diffraction data) and the resultant lattice parameters and space groups ($P2_1$ in each case) are given in Table 1, together with those reported by Añibarro et al.[31] for the crystal structure of a methanol solvate of TA$\beta$CD (at −133 °C). The unit cell volumes are 5344 and 5027 Å$^3$ for polymorphs* **I** *and* **II**, *respectively. Density considerations suggest that the structures of polymorphs* **I** *and* **II** *have one molecule of TA$\beta$CD in the asymmetric unit, with two molecules in the unit cell (corresponding to densities of 1.26 and 1.34 g cm$^{-3}$, respectively).*

*It is evident from Table 1 that the unit cells for polymorph* **II** *of TA$\beta$CD and the methanol solvate of TA$\beta$CD[31] are very similar. Consequently, a Rietveld refinement[30] was carried out on the powder X-ray diffraction data of polymorph* **II**, *using the atomic positions of the TA$\beta$CD molecule in the methanol solvate as the starting point for the refinement. The resulting fit ($R_{wp}$ ) 5.86%, $R_p$ ) 4.26%, $\chi^2$ ) 34.32, $R_F^2$ ) 0.0672, 2752 profile points, 776 reflections, 783 refined variables) is shown in Figure 2 and the final refined structure is shown in Figure 3. Clearly, the structure of polymorph* **II** *is very similar to the TA$\beta$CD component of the methanol solvate structure. The largest deviation in any given atom position between these two structures is ca. 0.55 Å and the root-mean-square difference for all corresponding atom positions is ca. 0.16 Å. Notwithstanding*

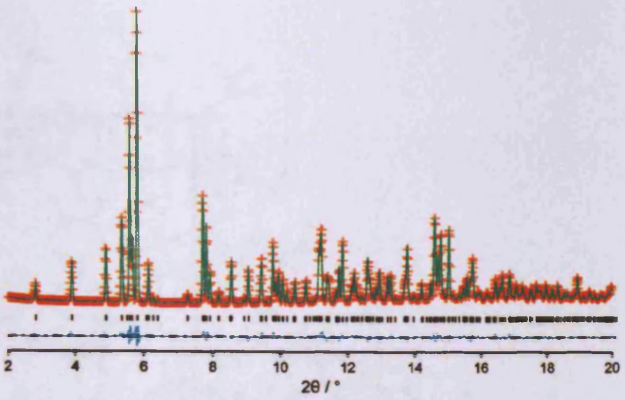


**Figure 2.** Comparison of experimental and calculated powder X-ray diffraction patterns in the final Rietveld refinement for polymorph II of TA$\beta$CD. Red crosses, experimental data; green line, calculated pattern; blue line, difference between experimental and calculated data. Tick marks indicate calculated peak positions.

*the fact that the two structures were determined at different temperatures, it is clear that the crystal structure of polymorph* **II** *is virtually identical to the TA$\beta$CD component of the methanol solvate structure. Thus, the absence of the methanol molecules (in the structure of polymorph* **II**) *is associated with only minor structural perturbations of the TA$\beta$CD molecules in comparison with the structure of the methanol solvate.*

*Both the sample obtained by solidification from the melt and the sample recovered by evaporation of solvent from HPFP solution gave powder X-ray diffraction patterns with no sharp Bragg peaks, suggesting that these samples are amorphous TA$\beta$CD. Powder X-ray diffraction also established that two of the commercial samples were a mixture of polymorphs* **I** *and* **II**, *as discussed in Section 2.*

*High-temperature powder X-ray diffraction studies were carried out on a sample of polymorph* **I** *of TA$\beta$CD, with the sample heated to 180 °C and held at this temperature while repeated powder X-ray diffraction patterns were measured. Representative powder X-ray diffraction patterns from this experiment are shown in Figure 4, and reveal clearly that the powder pattern characteristic of polymorph* **I** *disappears as a function of time and is replaced by that of polymorph* **II**. *This transformation from polymorph* **I** *to polymorph* **II** *at elevated temperature was examined further by DSC, as discussed in Section 3.3.*

*3.2. Solid-state NMR Spectroscopy. High-resolution solid-state $^{13}C$ NMR spectra recorded for polymorphs* **I** *and* **II** *are shown in Figure 5. Scheme 2 shows the TA$\beta$CD glucosidic unit with the carbon atoms numbered. Peaks around 20 ppm represent the methyl groups (C8, C10, C12), those around 60−80 ppm represent C2−C6, those around 90−105 ppm represent C1 and those around 170 ppm represent carbonyl groups (C7, C9, C11). In Figure 5b and d, the region between 85 and 110 ppm is expanded to show the C1 resonances more clearly. For each molecule in the asymmetric unit, we would expect to observe up to seven distinct C1 resonances, one for each of the seven sugars in the $\beta$-cyclodextrin ring. In this region, five resonances are observed for polymorph* **II** *and seven resonances are observed for polymorph* **I**. *The relative intensities of the peaks were determined by fitting to Lorentzian lineshapes. For polymorph* **II**, *the five peaks are in the approximate intensity ratio 2:1:2:1:1, suggesting that two of these peaks each represent a superposition of two C1 resonances, with the other peaks each representing a single resonance. For polymorph* **I**, *on the other hand, all seven expected C1 resonances have distinct chemical*

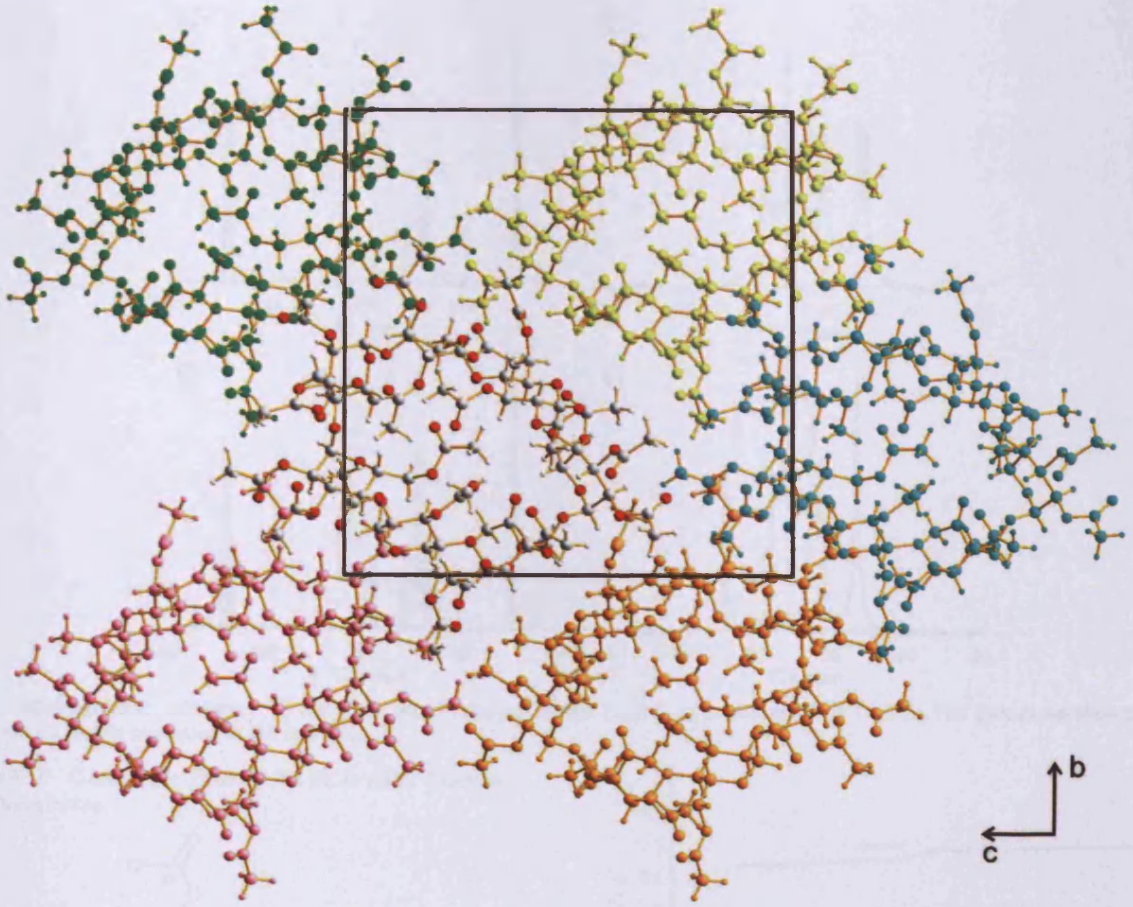


Figure 3. Crystal structure of polymorph II of TA$\beta$CD viewed along the a axis. For clarity, different colors are used for different molecules.

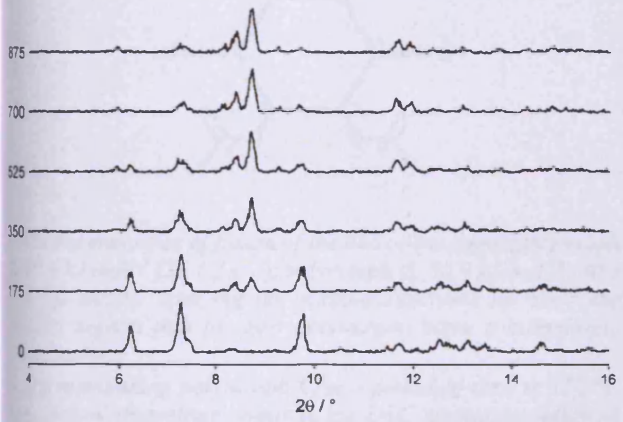


Figure 4. Powder X-ray diffraction data recorded as a function of time at 180 °C for polymorph I of TA$\beta$CD. The total time to record each powder X-ray diffraction pattern was 35 min. The time shown against each pattern is the time (in minutes) at which measurement of the pattern was started, relative to the time at which the sample temperature reached 180 °C. As shown, the initial sample was a monophasic sample of polymorph I, which transforms to polymorph II as a function of time.

*shifts. These observations are consistent with the proposal discussed above that, for each polymorph, there is one molecule of TA$\beta$CD in the asymmetric unit.*

*The $^{13}C$ NMR spectrum of the TA$\beta$CD sample prepared by solidification from the melt has broad signals in all four spectral regions discussed above, with no sharp peaks observed, consistent with the assignment of this sample as an amorphous phase of TA$\beta$CD.*

*3.3. Differential Scanning Calorimetry. DSC data for polymorphs* **I** *and* **II** *are shown in Figure 6. Polymorph* **II** *(Figure 6b) shows a single endotherm at 219 ( 1 °C, assigned as melting, whereas a sample starting as polymorph* **I** *(Figure 6a) shows two endotherms at 194 ( 1 and 219 ( 1 °C, the latter representing a much smaller peak than the former. This observation is consistent with the occurrence of a degree of conversion from polymorph* **I** *to polymorph* **II** *at elevated temperatures, as observed in the variable temperature powder X-ray diffraction study discussed above. On cooling from the melt, no recrystallization peak appears but an endothermic step is observed for all samples in the region 120 − 134 °C, which may be assigned as a glass transition. A two-cycle run was carried out on polymorph* **II** *to investigate the nature of the material after melting and cooling (Figure 7a). On the first heating ramp, a sharp melting peak is observed at 219 ( 1 °C. However, this peak is absent from the second heating ramp, for which only a shallow endothermic step at 123−137 °C is detected, consistent with the amorphous nature of the sample after the initial melting and cooling cycle.*

*When polymorph* **I** *is subjected to a higher heating rate (30 °C min$^{-1}$), only the melting transition at 194 ( 1 °C is observed (Figure 7b), suggesting that, under conditions of rapid heating, the polymorphic transformation does not occur to any significant extent within the much shorter time required to reach the melting point of polymorph* **I**. *The DSC data recorded with rapid heating allows the enthalpy of fusion of polymorph* **I** *to be measured.*

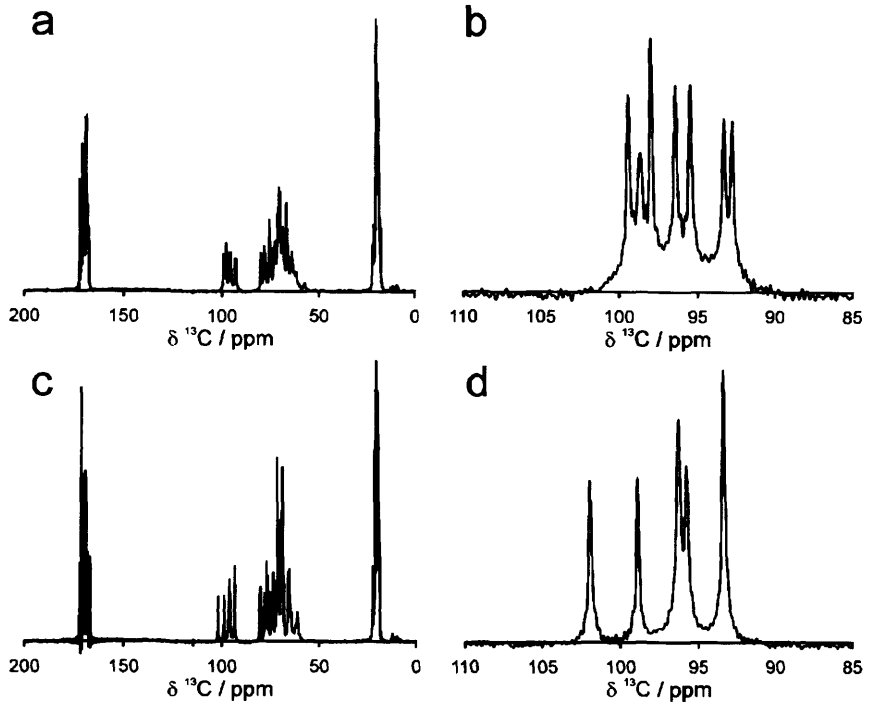


**Figure 5.** High-resolution solid-state $^{13}$C NMR spectra of (a,b) polymorph I and (c,d) polymorph II of TA$\beta$CD. Full spectra are shown in (a) and (c), with the C1 region expanded in (b) and (d).

*SCHEME 2: Glucosidic Unit of TA$\beta$CD with Carbon Atoms Numbered*

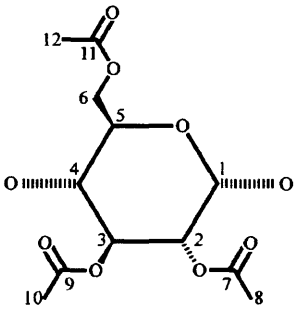


*From the enthalpies of fusion of the two polymorphs [polymorph I, 50.6 kJ mol$^{-1}$ (25.1 J g$^{-1}$); polymorph II, 80.9 kJ mol$^{-1}$ (40.1 J g$^{-1}$)] and by applying the method described by Yu,[32] the results suggest that the two polymorphs have a monotropic relationship.*

*By maintaining polymorph I for a period of time at 150 °C (i.e., below its melting point) in the DSC apparatus, followed by heating, the endotherm at 219 ( 1 °C is found to be enhanced whereas the endotherm at 194 ( 1 °C is diminished (Figure 7c). This observation suggests that conversion from polymorph I to polymorph II occurs during the period of time that polymorph I is maintained at 150 °C. In another DSC experiment in which the temperature was raised (at 10 °C min$^{-1}$) and maintained for a period of time at 210 °C (i.e., above the melting point of polymorph I but below the melting point of polymorph II), the endotherm at 219 ( 1 °C is again enhanced (Figure 7d). In this case, we may conclude that recrystallization from molten TA$\beta$CD occurs, seeded by polymorph II formed from polymorph I during the temperature ramp.*

*The two endotherms observed when starting from polymorph I correspond closely to those reported by Bettinetti et al.[25] These authors state that their observations were for samples that had desolvated during the DSC experiments and they carried out no further characterization of the materials with these melting points.*

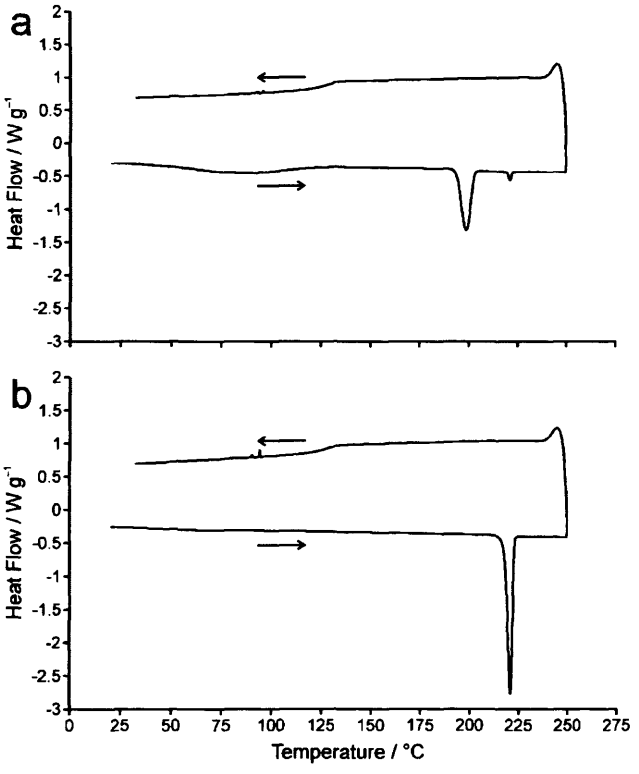


**Figure 6.** DSC data for (a) polymorph I and (b) polymorph II of TA$\beta$CD. Temperature ramps were 10 °C min$^{-1}$ for heating and 30 °C min$^{-1}$ for cooling.

*3.4. Thermogravimetric Analysis. All samples of TA$\beta$CD studied in this work were investigated by TGA to assess whether the transitions observed in the DSC studies are associated with*

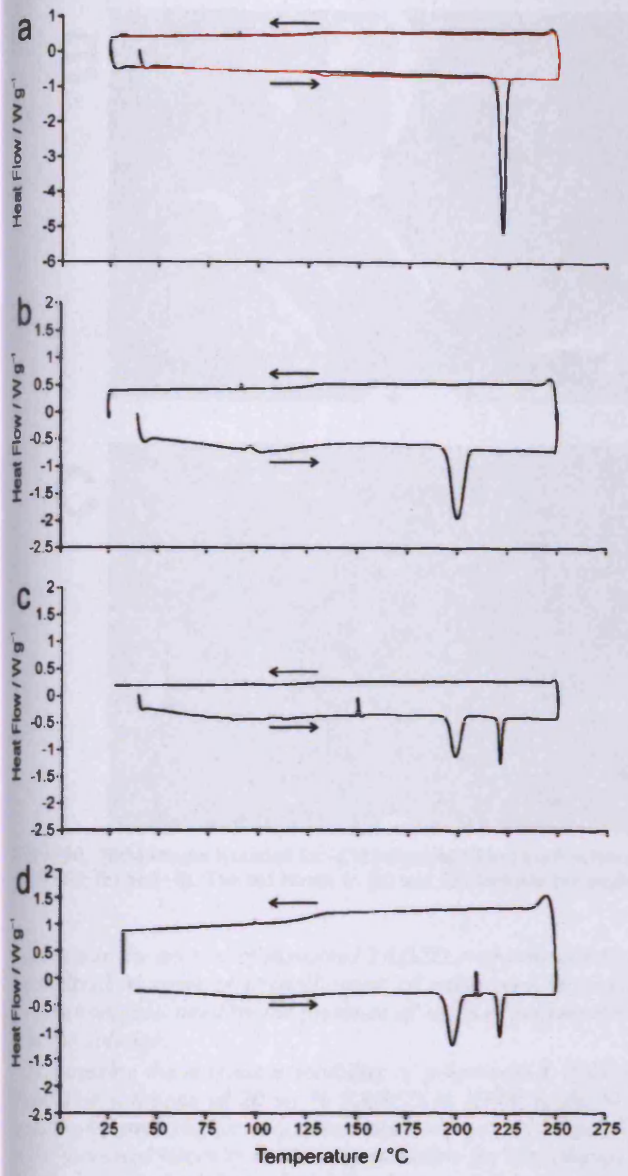


Figure 7. DSC data for (a) a two-cycle run on polymorph II (first cycle, black; second cycle, red), (b) polymorph I using a temperature ramp of 30 °C $min^{-1}$, (c) polymorph I with temperature held at 150 °C for 2 h and (d) polymorph I with temperature held at 210 °C for 1 h.

*any mass losses, which may provide evidence that the materials studied here are actually solvate structures.* No *mass losses were observed at any of these transitions, consistent with the assertion (established from other results presented here) that the solid phases of TAβCD investigated in the present work are not solvate structures.*

*3.5. Studies of Solubility in HPFP. All studies of solubility reported here were carried out at ambient temperature (ca. 20 °C). Figure 8 shows the physical appearance of separate solutions prepared by mixing HPFP with polymorphs* **I** *and* **II** *of TAβCD (10 wt %) at ambient temperature, after an equilibration time of 24 h and with the solutions either shaken or unshaken. For polymorph* **I**, *complete dissolution is observed, whereas for polymorph* **II**, *most of the solid remains suspended giving the sample an opaque white appearance.* Over *time (Figure 8b), the turbid sample eventually undergoes creaming, leading to a lower layer of HPFP (density 1.60 g* $cm^{-3}$*) and a*

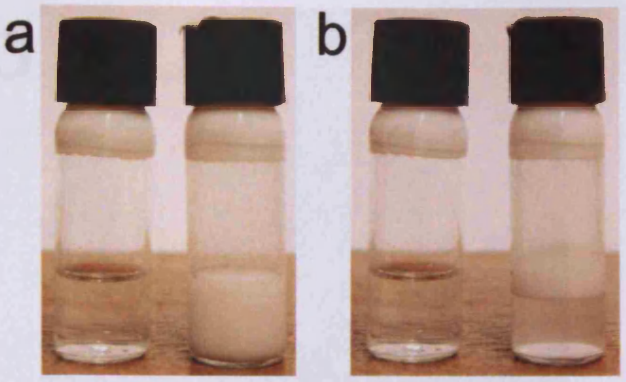


Figure 8. Physical appearance of solutions of polymorph I (left-hand vial) and polymorph II (right-hand vial) of TAβCD in HPFP at ambient temperature: (a) shaken, and (b) unshaken. All solutions were prepared by mixing HPFP with 10 wt % of TAβCD.

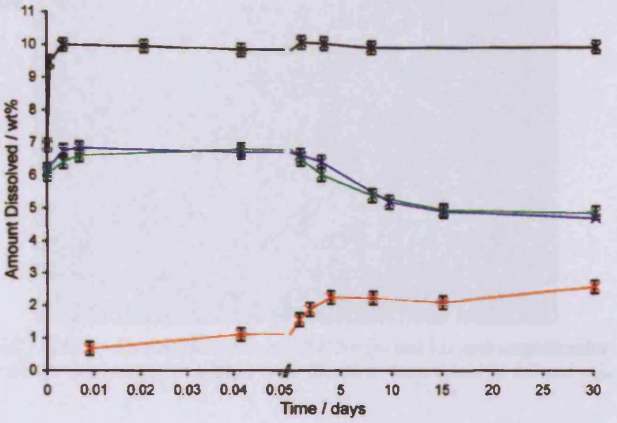


Figure 9. Amount of TAβCD dissolved in HPFP (measured via $^1H$ NMR) as a function of time for polymorph I (black), polymorph II (red) and two different mixtures of polymorphs I and II from commercial samples (green and blue). All solutions were prepared by mixing HPFP with 10 wt % of TAβCD. The estimated error bars are derived from the calibration.

*white upper layer of insoluble solid (i.e., polymorph* **II** *of TAβCD; density 1.34 g* $cm^{-3}$*). These samples were kept over periods of 5 months and did not undergo any changes in appearance during this time.*

*As shown in Figure 9, polymorphs* **I** *and* **II** *of TAβCD have dramatically different solubility in HPFP. Immediately after the addition of HPFP to polymorph* **I** *(10 wt %), the dissolved concentration of TAβCD is 6.9 ( 0.2 wt % and increases to 10.0 ( 0.2 wt % after 5 min, corresponding to complete dissolution. The concentration of this solution did not change over a period of 30 days. The solubility of polymorph* **II**, *on the other hand, is only 0.7 ( 0.2 wt % after 13 min and increases to reach 2.2 ( 0.2 wt % after 4 days, after which no significant changes are observed as a function of time. In addition to demonstrating the significant difference in solubility of polymorphs* **I** *and* **II** *in HPFP, these results also suggest that the two polymorphic forms have very different rates of dissolution in this solvent, with a substantially higher rate of dissolution for polymorph* **I**.

*Two different mixtures of polymorphs* **I** *and* **II** *(different commercial samples) showed very similar solubility profiles as a function of time. A maximum solubility of 6.8 ( 0.2 wt % was measured after 10 min, which then decreased to 4.7 ( 0.2 wt % after 30 days. The solutions in this case appeared as cloudy suspensions, similar to that observed for polymorph* **II**. *The*

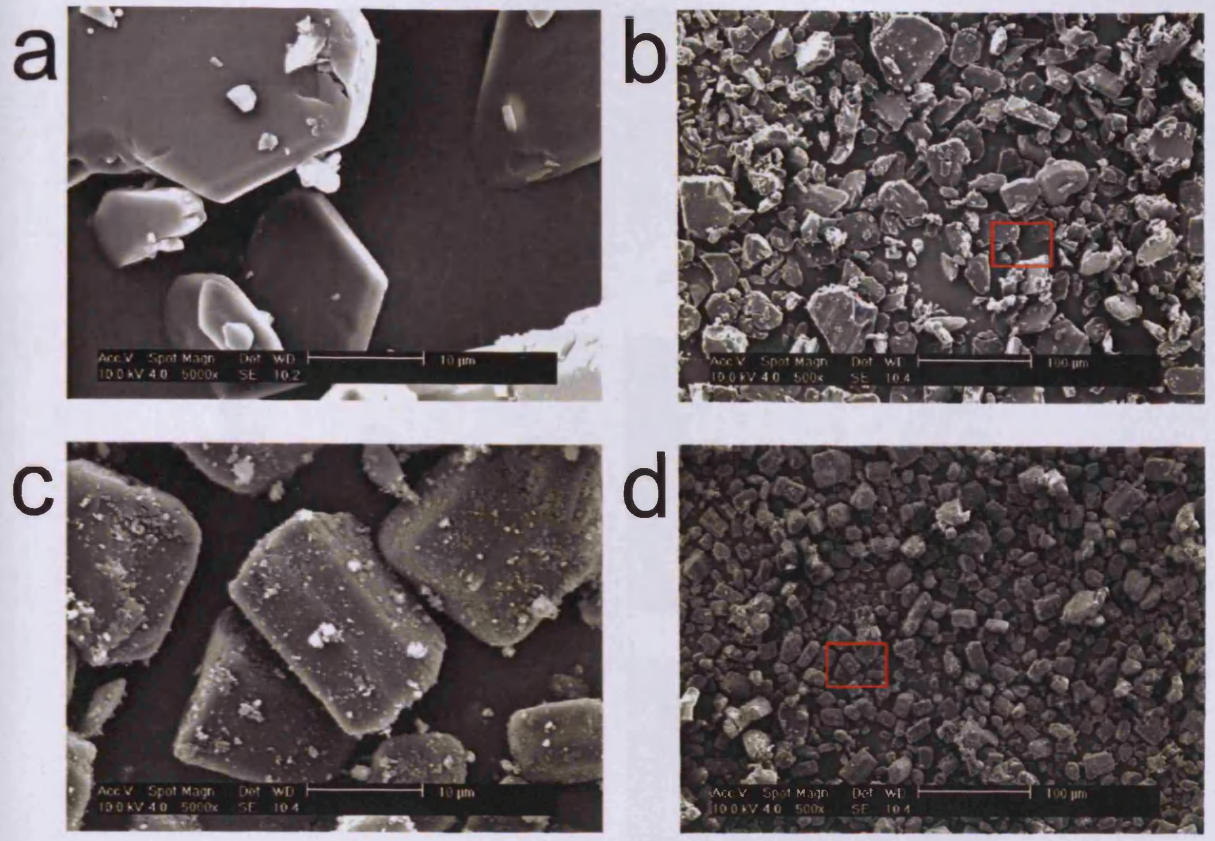


Figure 10. SEM images recorded for (a,b) polymorph I and (c,d) polymorph II of TAβCD with magnification of 5000 for (a) and (c), and magnification of 500 for (b) and (d). The red boxes in (b) and (d) indicate the regions for which the images of higher magnification were taken in (a) and (c).

*reduction in the amount of dissolved TAβCD over time can be rationalized in terms of crystallization of polymorph* **II** *from the solution, facilitated by the presence of seeds of polymorph* **II** *in the solution.*

*In assessing the maximum solubility of polymorph* **I**, *it was found that solutions of 20 wt % TAβCD in HPFP could be readily prepared. Higher concentrations were not investigated as the increased viscosity renders it impossible for the solution to pass through the 0.2 μm filter. However, solutions at these high concentrations were clear and homogeneous. Thus, the solubility of polymorph* **I** *at ambient temperature is greater than 20 wt %, representing a higher solubility than polymorph* **II** *(ca. 2.4 wt %) by a factor of at least 8. Although different polymorphic forms of a substance usually have different solubilities in a given solvent, we emphasize that such a large difference in solubility as that observed for polymorphs* **I** *and* **II** *of TAβCD in HPFP is very rare.*[33]

*Dissolution of amorphous TAβCD (obtained either from cooling a melted sample or by evaporation of solvent from HPFP solution) in HPFP led to similar concentrations to polymorph* **I**, *suggesting that, as for polymorph* **I**, *the solubility of amorphous TAβCD at ambient temperature is also greater than 20 wt %.*

*3.6. Scanning Electron Microscopy (SEM). It is well-known that dissolution can be influenced by the size and shape of the particles in a powder sample. For this reason, the particle size and morphology of polymorphs* **I** *and* **II** *of TAβCD were investigated using SEM. Images taken at a magnification of 5000 for powder samples of polymorphs* **I** *and* **II** *are shown in Figure 10, together with the corresponding images at a magnification of 500. We note that these samples of polymorphs* **I** *and* **II** *were those obtained directly from the supplier (i.e., the same samples used in the studies of solubility) and were not subjected to recrystallization. Polymorph* **II** *appears as regular parallelepipedic blocks, with a relatively narrow size distribution and typical dimensions 20 × 10 × 5 μm*$^3$. *In addition, some fine powder comprising particles of poorly defined shape is present on the blocks and confers an impression of roughness. Polymorph* **I** *appears as smooth-surfaced flat plates with sharp and regular angles, reminiscent of truncated hexagons but with a wider distribution in size, ranging from ca. 9 to 60 μm. Some smaller pieces that seem to come from broken plates are attached to the surface. Polymorph* **I** *also appears to be softer and is easily deformed and cracked by repeated exposure to the electron beam. Although particles from the highly soluble polymorph* **I** *appear flatter and have smoother surfaces, they are only slightly larger than those of the poorly soluble polymorph* **II**. *From these observations, we may be confident that the significant difference in dissolution behavior of polymorphs* **I** *and* **II** *in HPFP is unlikely to arise due to features of size and shape of the crystallite particles in the powder, but instead may be attributed solely to their different crystal structures.*

*3.7. Crystallization of TAβCD from the Melt. Finally, we report studies on the crystallization of TAβCD from the molten phase, probed using time-resolved optical microscopy. For this work, a sample of amorphous TAβCD was placed on the high-temperature stage of the optical microscope. The temperature was raised to 180 °C, and the sample was held at this temperature for 12 h. As the temperature was raised to 180 °C, the amorphous sample became a viscous, isotropic liquid (as investigated through crossed-polars on the optical microscope). Throughout the time that the sample was held at 180 °C, no*

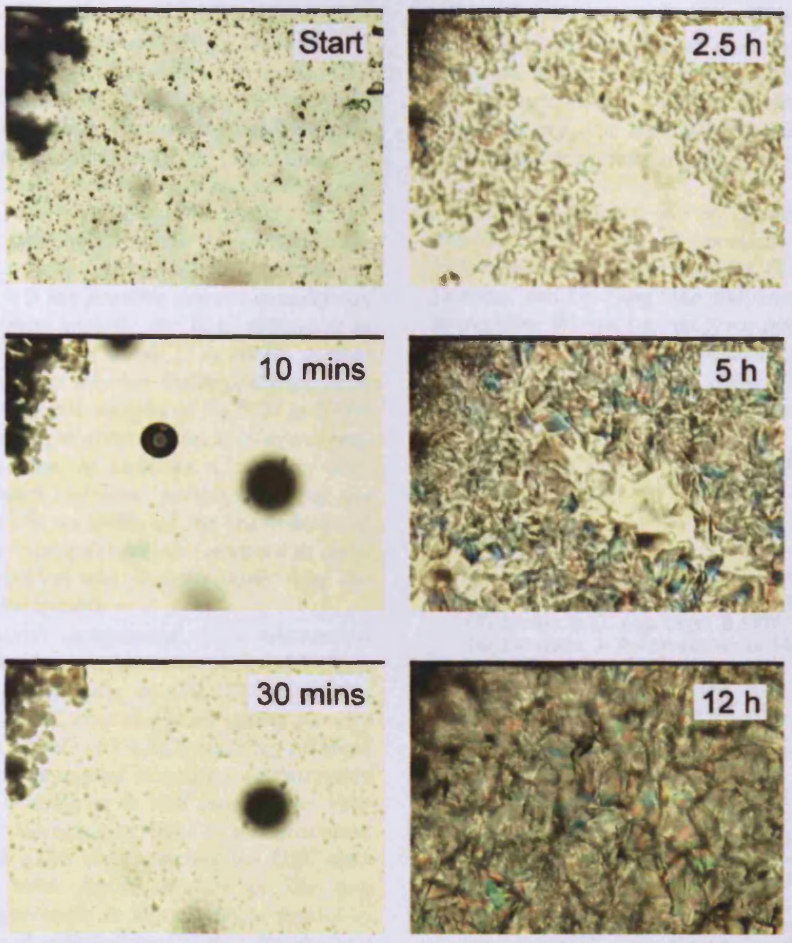


Figure 11. Selected optical micrographs recorded as a function of time at 180 °C during the crystallization of molten TAβCD (prepared by heating amorphous TAβCD) seeded by crystals of polymorph II. The seed crystals sprinkled on the molten TAβCD are clearly visible in the first micrograph shown. The circles observed in the micrographs at 10 and 30 min are bubbles within the molten TAβCD.

*crystallization was observed to occur (in spite of the fact that this temperature is below the melting temperature of polymorph* II).

*The experiment was then repeated with a small amount of a polycrystalline sample of polymorph* II *of TAβCD sprinkled onto the amorphous solid. The temperature was raised to 180 °C, held at this temperature for 12 h, and then raised to 250 at 10 °C min*$^{-1}$. *At 180 °C, the amorphous sample again became a viscous liquid, whereas the small amount of polymorph* II *remained as a crystalline solid. Over a period of time, the liquid TAβCD began to crystallize and after 5 h virtually the entire surface appeared crystalline. The sample was maintained for a further 7 h at 180 °C, before increasing the temperature in order to investigate the melting behavior of the solid phase obtained. The melting temperature of the solid phase was found to be 220 °C (i.e., very close to that of polymorph* II). *Figure 11 shows optical micrographs taken at different times during the crystallization process, and a 1000-fold time-compressed video version of the 12 h of recorded data is available as Supporting Information. These observations suggest that, in order for molten TAβCD to crystallize as polymorph* II *(when held below the melting point of the R polymorph), some amount of polymorph* II *is required to seed the crystallization process.*

## 4. Concluding Remarks

*This work has highlighted a case of polymorphism (for the cyclodextrin TAβCD) in which there is a substantial difference in solubility of the different polymorphic forms in the fluorinated solvent HPFP and has included detailed characterization of several properties of the different polymorphic forms using a range of experimental techniques. Thus, while at least 20 wt % of polymorph* I *of TAβCD could be readily dissolved in HPFP, the solubility of polymorph* II *is only ca. 2.4 wt %, representing a difference of solubility by a factor of at least 8 between the two polymorphic forms. Although different polymorphs generally exhibit different solubility in a given solvent, such a substantial difference as that observed for polymorphs* I *and* II *of TAβCD in HPFP is very rare.*[33] *In particular, from experimental solubility data for a set of 81 polymorphic systems reported in ref 33, only one polymorphic system has a solubility ratio higher than the value of (at least) 8 reported here, and none of the other 80 systems reported have a solubility ratio greater than 5. In addition, from calculated solubility data for a further set of 65 polymorphic systems reported in ref 33, again, only one polymorphic system has a solubility ratio higher than that reported here.*

*Furthermore, we have shown that the rates of dissolution of the two polymorphs of TAβCD in HPFP at ambient temperature are also substantially different. Structural studies using powder X-ray diffraction indicate that polymorph* I *has lower density (at ambient temperature) and converts to polymorph* II *across a range of elevated temperatures. The combined evidence from the investigations carried out indicates that there is a monotropic relationship between the stable polymorph* II *and the metastable polymorph* I. *Comparisons have also been established between*

properties of the two crystalline polymorphs of TAβCD and an amorphous phase of the same compound.

In more general terms, the unusually large difference in solubility observed for polymorphs I and II of TAβCD in HPFP suggests that this may represent a good system for carrying out systematic studies to explore fundamental aspects of the dependence of solubility on differing solid state properties (particularly structural properties) of polymorphs. However, while the crystal structure of polymorph II has been determined in the present work, we emphasize that the crystal structure of polymorph I has not yet been determined. As such, it is not possible even to speculate on the structural reasons that may underlie the huge difference in solubility of polymorphs I and II of TAβCD in HPFP. Further studies are also required to assess whether the large difference in solubility observed here for the polymorphs of TAβCD in HPFP is also observed for the same polymorphic system in other solvents, for which it would be relevant to consider a range of both fluorinated and nonfluorinated solvents. Investigations of the temperature dependence of the solubility of the polymorphs of TAβCD in HPFP (and other solvents) are also required in order to obtain more detailed fundamental insights concerning the solubility of this polymorphic system.

With regard to polymorph assignment, it is relevant to correlate the results obtained in the present work with those reported previously for polymorphs of TAβCD. In 2006, Bettinetti et al.[25] presented DSC data and poor-quality powder X-ray diffraction data for a sample of TAβCD that they believed to be a solvate structure (and, as quoted in their paper, "probably a hydrate"). A mass loss of 0.79 wt % was observed in their TGA studies (although the temperature range of this mass loss was not mentioned). Their DSC data matches the DSC data obtained in the present work for a mixture of the two polymorphs, with good agreement in the observed transition temperatures and the quoted enthalpies of fusion for the two polymorphs. A broad endothermic feature observed in the region 13–97 °C in their DSC data was interpreted as desolvation. A similar feature is also observed in our DSC data for polymorph I (Figure 6a), although our TGA results indicate that no mass loss occurs in this temperature range. Unfortunately, the quality of the powder X-ray diffraction data reported by Bettinetti et al.[25] was too poor to serve as a useful basis for polymorph identification. Desolvation of the methanol solvate of TAβCD was shown to produce a form with the same melting temperature as that of polymorph II in the present work. Bettinetti et al. also assigned the relationship between the polymorphs as monotropic (as discussed in Section 3.3, the results of the present work are in agreement with this conclusion).

Corti et al.[26] presented DSC and powder X-ray diffraction data on a sample of TAβCD that they believed to be the same as the sample of Bettinetti et al.[25] The results are again in good agreement with those that we obtained for a mixture of polymorphs I and II in the present work. In particular, the powder X-ray diffraction data reported by Corti et al. are significantly higher in quality than those of Bettinetti et al., and are consistent (also in comparison with the results of the present work) with the sample being a mixture of polymorphs I and II. A broad endothermic feature observed in the DSC data in the region of 90 °C was assigned (as in the study of Bettinetti et al.) as desolvation. values of enthalpies of fusion were not reported from the DSC data and no TGA data were presented. From detailed comparison of the results reported by Bettinetti et al. and Corti et al., we are confident that the assignment of polymorphs I and II in the present work is fully compatible with the nomenclature adopted in these previous studies.

In addition to the relevance of this work within the field of polymorphism research, we also emphasize the implications of this work in the context of pharmaceutical applications, given the well-established role of cyclodextrins, such as TAβCD, in drug delivery and the fact that HPFP is a CFC-free model propellant for pressurized metered-dose inhalers.

Acknowledgment. We are grateful to AstraZeneca for contributing to the cost of chemicals and for access to TGA instrumentation. We also thank Dr. Peter Fisher for the use of SEM facilities, and Dr. Fang Guo and Anabel Morte-Rodenas for help in recording the synchrotron X-ray powder diffraction data. C.E.H. is funded by the Basic Technology programme Control and Prediction of the Organic Solid State of the U.K. Research Councils. M.C. is funded by AstraZeneca and Cardiff University.

Supporting Information Available: This material is available free of charge via the Internet at http://pubs.acs.org.

## References and Notes

(1) Dunitz, J. D. Pure Appl. Chem. 1991, 63, 177.
(2) Bernstein, J. J. Phys. D - Appl. Phys. 1993, 26, B66.
(3) Dunitz, J. D. Acta Cryst. B 1995, 51, 619.
(4) Bernstein, J. Polymorphism in Molecular Crystals; Oxford University Press: Oxford, 2002.
(5) Davey, R. J. Chem. Comm. 2003, 1463.
(6) Bernstein, J. Chem. Comm. 2005, 5007.
(7) Harris, R. K. Analyst 2006, 131, 351.
(8) Kitchin, S. J.; Ahn, S. B.; Harris, K. D. M. J. Phys. Chem. A 2002, 106, 7228.
(9) Ahn, S. Y.; Guo, F.; Kariuki, B. M.; Harris, K. D. M. J. Am. Chem. Soc. 2006, 128, 8441.
(10) Xu, M. C.; Harris, K. D. M. J. Am. Chem. Soc. 2005, 127, 10832.
(11) Hughes, C. E.; Hamad, S.; Catlow, C. R. A.; Harris, K. D. M.; Griffiths, P. C. Faraday Discuss. 2007, 136, 71.
(12) Xu, M.; Harris, K. D. M. J. Phys. Chem. B 2007, 111, 8705.
(13) Mueller, M.; Meier, U.; Wieckhusen, D.; Beck, R.; Pfeffer-Hennig, S.; Schneeberger, R. Cryst. Growth Des. 2006, 6, 946.
(14) Challa, R.; Ahuja, A.; Ali, J.; Khar, R. K. AAPS PharmSciTech 2005, 6, 329.
(15) Uekama, K.; Hirayama, F.; Arima, H. J. Incl. Phenom. Macro. Chem. 2006, 56, 3.
(16) Seo, B.-Y.; Park, G.-B.; Lee, K.-P. Kor. Soc. Pharm. 1996, 26, 71.
(17) Bratu, I.; Veiga, F.; Fernandes, C.; Hernanz, A.; Gavira, J. M. Spectroscopy 2004, 18, 459.
(18) Fernandes, C. M.; Carvalho, R. A.; Costa, S. P. d.; Veiga, F. J. B. Eur. J. Pharm. Sci 2003, 18, 285.
(19) Rogueda, P. G. A. Drug DeV. Ind. Pharm. 2003, 29, 39.
(20) Ashayer, R.; Luckham, P. F.; Manimaaran, S.; Rogueda, P. Eur. J. Pharm. Sci 2004, 21, 533.
(21) Paul, A.; Griffiths, P. C.; James, R.; Willock, D. J.; Rogueda, P. G. J. Pharm. Pharmacol. 2005, 57, 973.
(22) Ridder, K. B.; Davies-Cutting, C. J.; Kellaway, I. W. Int. J. Pharm. 2005, 295, 57.
(23) Jones, S. A.; Martin, G. P.; Brown, M. B. Int. J. Pharm. 2005, 302, 154.
(24) Rogueda, P. NoVel Compounds, World Intellectual Property Organization, WO 2005/053637 A2, U. K., 2004.
(25) Bettinetti, G.; Sorrenti, M.; Catenacci, L.; Ferrari, F.; Rossi, S. J. Pharm. Biomed. Anal. 2006, 41, 1205.
(26) Corti, G.; Capasso, G.; F, M.; Cirri, M.; Mura, P. J. Pharm. Biomed. Anal 2007, 45, 480.
(27) (a) Shirley, R. The CRYSFIRE System for Automatic Powder Indexing. (b) Coelho, A. A. (2007) TOPAS Academic. http://members.optusnet.com.au/alancoelho.
(28) Le Bail, A.; Duroy, H.; Fourquet, J. L. Mater. Res. Bull. 1988, 23, 447.
(29) Larson, A. C.; Von Dreele, R. B. Los Alamos Natl. Lab. Rep. 2004, 86-748.
(30) Rietveld, H. M. J. Appl. Crystallogr. 1969, 2, 65.
(31) Añibarro, M.; Gessler, K.; Uson, I.; Sheldrick, G. M.; Harata, K.; Uekama, K.; Hirayama, F.; Abe, Y.; Saenger, W. J. Am. Chem. Soc. 2001, 123, 11854.
(32) Yu, L. J. Pharm. Sci. 1995, 84, 966.
(33) Pudipeddi, M.; Serajuddin, A. T. M. J. Pharm. Sci. 2005, 94, 929.

JP800848W

# Gelation of fluorinated liquids by non-fluorinated low-molecular-mass molecules†

P. C. Griffiths,*[a] M. Côte,[a] R. James,[a] Ph. G. Rogueda,[b] I. R. Morgan[a] and D. W. Knight[a]

*Received (in Cambridge, UK) 29th April 2005, Accepted 30th June 2005*
*First published as an Advance Article on the web 11th July 2005*
**DOI: 10.1039/b505938k**

**A family of tetrahydroxy diesters has been synthesised and observed to gel a range of fluorinated solvents and their mixtures; the phase behaviour and gel microstructure are reported for a homologous family of these diesters in blends of 1*H*,1*H*-heptafluorobutanol (HFB) and 2*H*,3*H*-perfluoropentane (HPFP).**

Low-molecular-mass organogelators are small molecules that spontaneously self-assemble to create a three-dimensional network capable of entrapping the solvent and creating gels.[1–4] Such systems exhibit great potential for use in the fields of food science, cosmetics and drug delivery.[5–8] Our interest focuses on gels where the entangled phase is a fluorinated solvent. Such solvents are already used as replacement media for blood, liquid ventilation and as contrast agents for ultrasound imaging.[9] However, they need to be formulated with polymers and surfactants in order to introduce the necessary additional physical characteristics. Gelation of fluorinated media has already been reported,[10] using partially fluorinated n-alkanes as the gelling agents. The incompatibility of the fluorocarbon and hydrocarbon segments drives the aggregation of the molecules. However, in this communication we report what we believe to be the first ever gelation of fluorinated solvents by non-fluorinated molecules.

A family of tetrahydroxy diesters was observed to form gels in mixtures of 1*H*,1*H* heptafluorobutanol (HFB) and 2*H*,3*H*-perfluoropentane (HPFP). Fig. 1 presents the structure of both the gelators and fluorinated solvents used in this work. These novel gelators are referred to as $G_n$, with $n$ = 3, 4, 5 or 8 according to their backbone length.

The synthesis of the gelator involves first a cross metathesis with isopropyl acrylate and the corresponding bis-alkene, using Grubb's second generation catalyst.[12,13] Then, these bis-α,β-unsaturated esters undergo asymmetric dihydroxylation affording the tetrahydroxy gelators in excellent yield and purity.[14] Enantiomeric purity (determined by gas chromatography on a Chiraldex GTA column) and yield obtained were respectively > 99% and > 90% (see ESI, Scheme 1† for details of the synthesis).

The tetrahydroxy diesters are soluble in HFB but not in HPFP. Gelation occurs either by first dissolving the gelator in HFB and subsequently adding HPFP, or by the addition of gelator directly to the solvent blend, in a known and controlled solvents ratio. However, gels prepared by adding the gelator directly to the solvent blend were found to be less reproducible. In this work, all gels were obtained by first dissolving the gelator in HFB then subsequently adding HPFP. Provided there is a significantly high gelator concentration, gelation of pure HFB can also be achieved, while this is not the case for pure HPFP. Often gelation requires a heating–cooling cycle,[15] but these present fluorinated gels form spontaneously at room temperature.

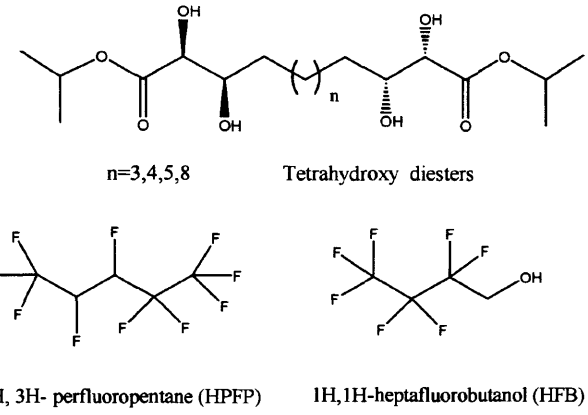


**Fig. 1** Structure of the tetrahydroxy diester gelators[11] and fluorinated solvents used in the gelling systems.

A simple measure of gelation has been used to quantify their phase behaviour. The sample must be stable to tube inversion: a gel shows no flow. The macroscopic phase behaviour was found to depend greatly on the solvent ratio, temperature, gelator alkyl chain length ($n$) and gelator concentration. The phase behaviour of the gelators in two solvent mixtures is presented in Fig. 2. All compositions are expressed as wt%.

Four different macroscopic states are observed which are indicated as $\Phi_\alpha$, $\Phi_\beta$, $\Phi_\chi$ and $\Phi_\delta$ in Figs. 2(a) and 2(b). At the lower concentration of gelator, a clear liquid is observed with a viscosity comparable to that of the pure solvents ($\Phi_\alpha$). With increasing gelator concentration, the sample becomes heterogeneous with agreggates of transparent gel forming within the fluorosolvent blend ($\Phi_\beta$). At higher concentration of gelator, a transparent macroscopically homogeneous gel forms ($\Phi_\chi$). Increasing the gelator concentration further introduces a "haze" to the gel, forming fibrils that may be collected by removal of the solvent, or simply gelator precipitation ($\Phi_\delta$). The kinetics of gel formation also correlates with the appearance of the gels. For highly concentrated gelator systems, the gels form instantaneously. At lower concentrations, gel formation appears to pass through a

[a]*School of Chemistry, Main Building, Cardiff University, Cardiff, Wales CF10 3AT. E-mail: griffithspc@cardiff.ac.uk; Fax: +44(0)29 2087 4030; Tel: +44(0)29 2087 5858*
[b]*AstraZeneca R&D Charnwood, Bakewell Road, Loughborough, Leics., UK LE11 5RH. E-mail: philippe.rogueda@astrazeneca.com; Fax: +44(0)15 0964 5555; Tel: +44(0)15 0964 4000*
† Electronic supplementary information (ESI) available: synthesis of the gelators. See http://dx.doi.org/10.1039/b505938k

 

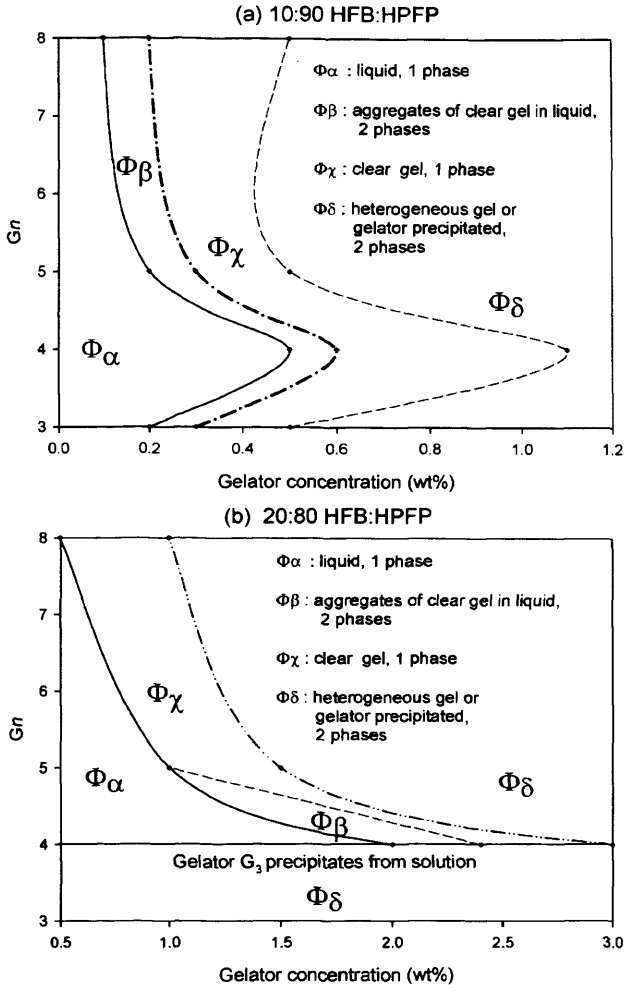


**Fig. 2** Macroscopic phase behaviour of $G_n$ for $n$ = 3, 4, 5, 8 in (a) 10 : 90 HFB : HPFP and (b) 20 : 80 HFB : HPFP. All gels were made by first dissolving the gelator in HFB then subsequently adding HPFP.

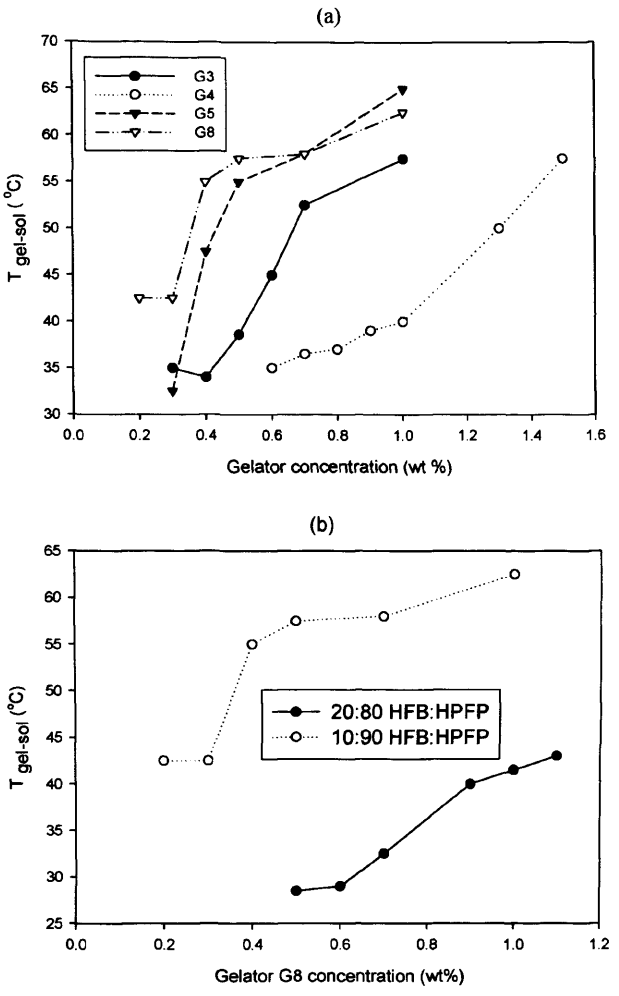


**Fig. 3** $T_{gel-sol}$ for (a) $G_3$, $G_4$, $G_5$, $G_8$ as a function of $G_n$ concentration in 10 : 90 HFB : HPFP and for (b) $G_8$ in the two different solvents ratios 10 : 90 and 20 : 80 HFB : HPFP.

growth stage – clear aggregates of gel coexisting with the remaining solvent appear within a few hours, and these coalesce to form a gel throughout the entire sample over a period of days.

For the solvents ratio 10 : 90 HFB : HPFP, from $G_{n\geq 4}$, the concentration above which gelation occurs is a decreasing function of increasing $n$: less gelator is required to achieve gelation. For a 10 : 90 HFB : HPFP ratio, transparent fluorinated gels are obtained with the $G_8$ gelator at a concentration as low as 0.2 wt%, thus $G_8$ may be considered a supergelator.[16] A deviation is observed for $G_3$, which requires less gelator than $G_4$ to obtain an apparently identical gelling behaviour. However, samples made with $G_3$ were not stable over 3 weeks: the gelator slowly precipitates within the gel.

In the solvent blend 20 : 80 HFB : HPFP, the same general trend is observed, but in this case no gels were formed with gelator $G_3$. This shows that there is a delicate balance as far as the chain length ($n$) is concerned: decreasing $n$ renders this family of gelators less susceptible to self-assembly. Moreover, in the 20 : 80 HFB : HPFP system, a higher concentration of gelator is required to achieve gelation (*i.e.* the phase behaviour is shifted to the right). The same trend is observed for both 30 : 70 and 50 : 50 HFB : HPFP as well as pure HFB. Indeed, HFB acts as the solubilising medium, whereas HPFP, unable to dissolve the gelator, destabilises the initially stable sol.

The gel-to-sol transition temperature ($T_{gel-sol}$) of the fully gelled samples was measured by immersing the glass vials containing the samples in a temperature controlled waterbath. The temperature at which a sample undergoes a gel to liquid phase transition was noted. $T_{gel-sol}$ for gelled samples in 10 : 90 HFB : HPFP is presented in Fig. 3(a). A comparison of $T_{gel-sol}$ obtained for gelator $G_8$ in 10 : 90 HFB : HPFP and 20 : 80 HFB : HPFP is presented in Fig. 3(b).

It is immediately apparent that, for a given gelator, $T_{gel-sol}$ increases with increasing gelator concentration and that for samples with the same solvent composition, $T_{gel-sol}$ increases with the chain length $n$, with the exception of $G_3$. Then, the same trend is observed in the 20 : 80 HFB : HPFP solvents ratio environment. However, as seen in Fig. 3(b), the $T_{gel-sol}$ measured are lower than in the 10 : 90 HFB : HPFP ratio, the gelled network requires more gelator to be formed and less energy to be disrupted.

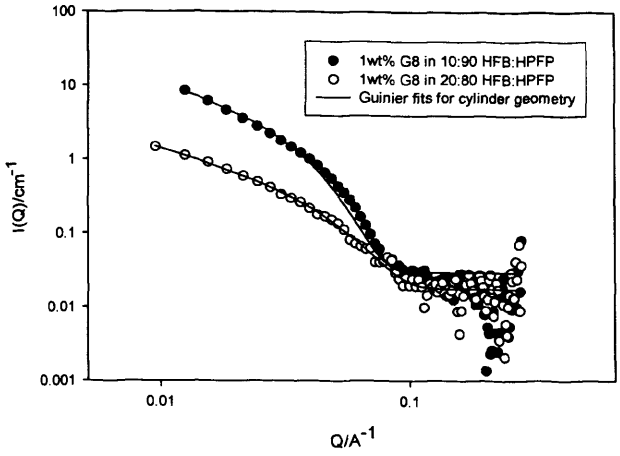


**Fig. 4** SANS data obtained for a constant concentration of $G_8$ in two different HFB : HPFP ratios, along with the Guinier analysis over the low $Q$ region for a cylinder geometry (data representative of all the gelled samples investigated with SANS).

To quantify the morphology of the aggregates formed, a preliminary small-angle neutron scattering (SANS) study has been carried out on the LOQ instrument at the ISIS facility, Rutherford Appleton Laboratories, Didcot, UK. Representative data are displayed in Fig. 4.

First, for a given solvent composition, the scattered intensity increases with concentration. For a fixed concentration of gelator, the solvent composition has a pronounced effect on the observed scattering, correlating well with the macroscopic phase behaviour observations. Stronger scattering is observed for gelator $G_8$ at 1 wt% in a 10 : 90 HFB : HPFP mix than in a 20 : 80 HFB : HPFP, indicating a different packing of the gelator. A Guinier analysis over the low $Q$ region of the data – $I(Q) \sim Q^{-1}\exp(-Q^2R^2/4)$ – clearly shows the characteristic signature of a cylinder geometry in the gelled samples, as presented in Fig. 4. The radius ($R$) of the cylinder extracted from the SANS analysis is found to vary both with gelator concentration and solvents ratio. First, for a given solvents ratio, the radius $R$ increases with gelator concentration. Let us consider the 50 : 50 HFB : HPFP ratio with gelator $G_8$. For $G_8$ = 3.75 wt%, $R$ = 25 (±1) Å, for $G_8$ = 5.0 wt%, $R$ = 32 (±1) Å and for $G_8$ = 6.0 wt%, $R$ = 42 (±1) Å. Then, $R$ varies according to the solvents ratio. Increasing the proportions of HPFP in the solvents mix results in an increase of $R$. In 100 : 0 HFB : HPFP (*i.e.* pure HFB), $R$ = 22 (±1) Å, in 50 : 50 HFB : HPFP $R$ = 30 (±7) Å, in 20 : 80 HFB : HPFP $R$ = 38 (±1) Å, and finally in 10 : 90 HFB : HPFP $R$ = 60 (±1) Å, although this behaviour is clearly modulated by the gelator concentration.

Thus the aggregated structures obtained in this gelling process appear to be entangled rod-like fibers that are built up through non-covalent interactions such as weak van der Waals attractions and strong hydrogen-bonding. Freeze-drying one gelled sample clearly shows a swollen structure. The volume of the freeze-dried sample, then constituted only by the entangled fibers of gelators arranged as they were in the original gelled system, is significantly larger than the volume obtained when the gel is left to dry in ambient air. In this last case, as the solvents evaporate, the gelator network collapses. It is not yet absolutely established what forces drive the gelation. These are however likely to be associated with hydrogen bonding in origin since (i) addition of small amounts of water disrupts the gelation[17] and (ii) there is a clear signature in the IR spectra for the presence of hydrogen bonding. This IR signal correlates well with the onset of gelation but not with the sol–gel transition. The band appears when sufficient gelator is present to achieve gelation but does not disappear as a heated gel passes through the gel to sol phase transition. Further work is concentrating on this issue.

We acknowledge financial support from AstraZeneca, the EPSRC and Cardiff University, whilst CCLRC is acknowledged for providing access to the neutron facilities.

## Notes and references

1 P. Terech and R. G. Weiss, *Chem. Rev.*, 1997, **97**, 3133.
2 D. J. Abdallah and R. G. Weiss, *J. Braz. Chem. Soc.*, 2000, **11**, 209.
3 O. Gronwald, E. Snip and S. Shinkai, *Curr. Opin. Colloid Interface Sci.*, 2002, **7**, 148.
4 P. Terech, I. Furman and R. G. Weiss, *J. Phys. Chem.*, 1995, **99**, 9558.
5 A. Juteau, N. Cayot, C. Chabanet, J. L. Doublier and E. Guichard, *Trends Food Sci. Technol.*, 2004, **15**, 394.
6 W. B. Davies, Patent Report, *General Pharmacology: the vascular system*, 1993, Vol. **24**, p. xiii.
7 C. Gallegos and J. M. Franco, *Curr. Opin. Colloid Interface Sci.*, 1999, **4**, 288.
8 D. Lichtenberg, P. L. Felgner and T. E. Thompson, *Biochim. Biophys. Acta*, 1982, **684**, 277.
9 J. G. Riess, *Fluorine Chem.*, 2002, **114**, 119; J. G. Riess, *Tetrahedron*, 2002, **58**, 4113; J. G. Riess and M. P. Krafft, *Biomaterials*, 1998, **19**, 1529; M. P. Krafft, A. Chittofrati and J. G. Riess, *Curr. Opin. Colloid Interface Sci.*, 2003, **8**, 251; M. P. Krafft, *Adv. Drug Delivery Rev.*, 2001, **47**, 209.
10 M. George, S. L. Snyder, P. Terech and R. G. Weiss, *Langmuir*, 2005, DOI: 10.1021/la050371z.
11 Work on the synthesis and on the application as catalysts of the tetrahydroxy diesters to be published.
12 A. K. Chatterjee and R. H. Grubbs, *Angew. Chem., Int. Ed.*, 2002, **41**, 3171.
13 S. Randl, S. J. Connon and S. Blechert, *Chem. Commun.*, 2001, 1791.
14 K. B. Sharpless, *J. Org. Chem.*, 1992, **27**, 2768.
15 C. Zhan, P. Gao and M. Liu, *Chem. Commun.*, 2005, 462; G. Clavier, M. Mistry, F. Fages and J. L. Posso, *Tetrahedron Lett.*, 1999, **40**, 9021; H. M. Willemen, T. Vermonden, A. T. M. Marcelis and E. J. R. Sudhölter, *Eur. J. Org. Chem.*, 2001, 2329.
16 A. Valkonen, M. Lahtinen, E. Virtanen, S. Kaikkonen and E. Kolehmainen, *Biosensors Bioelectronics*, 2004, **20**, 1233.
17 S. Tamaru, R. Luboradzki and S. Shinkai, *Chem. Lett.*, 2001, 336.

# Self-Assembling Chiral Gelators for Fluorinated Media

*Marie Côte[1], Tim Nicholls[1], David W. Knight[1], Ian R. Morgan[1], Philippe G.A. Rogueda[2], Steve M. King[3], Richard K. Heenan[3] and Peter C. Griffiths [1,*]*

*School of Chemistry, Cardiff University, Main Building, Park Place, Cardiff, CF10 3TB, U.K.*

CORRESPONDING AUTHOR

Peter C. Griffiths, School of Chemistry, Cardiff University, Main Building, Park Place, Cardiff, CF10 3TB, U.K. Email: Griffithspc@Cardiff.ac.uk Telephone +44 29 20875858 Fax +44 29 20874030

RECEIVED DATE

TITLE RUNNING HEAD Chiral gelators for fluorinated media

CORRESPONDING AUTHOR FOOTNOTE

(1) School of Chemistry, Cardiff University, Main Building, Park Place, Cardiff, CF10 3TB, U.K. (2) formerly AstraZeneca Research and Development, Charnwood, Bakewell Road, Loughborough, LH11 5RH, United Kingdom, (3) ISIS Facility, Rutherford Appleton Laboratory, Chilton, Didcot, OX11 0QX U.K.

**Abstract**

Formulation involving partially and fully fluorinated media represents a technological challenge given the lipophobic and hydrophobic nature of such liquids. The identification of self-associating materials with which to control the viscosity and solubilising characters of fluorinated solvents is a particularly interesting area of research. It is shown here that the presence of the stereogenic centres inherent in a family of α,β-dihydroxy diesters is an essential requirement for the thermoreversible gelation of mixtures of the partially fluorinated liquids 2H,3H-perfluoropentane (HPFP) and 1H,1H-heptafluorobutanol (HFB). Gelation is driven by hydrogen bonding which induces a non-preferred conformation around the *bis*-(α,β-dihydroxy ester) structural motif. An analysis of the melting temperature yields an enthalpy of melting that is consistent with 3-4 hydrogen bonds, commensurate with the end-group structure of the gelator. Small-angle neutron scattering demonstrated the existence of the common fibrillar structures whose dimensions showed no obvious correlation with the molecular structure of the gelator.

**Keywords** Gelators, fluorinated media, SAFINS, LMOGS, chiral non-racemic.

## Introduction

The spontaneous self-assembly and network formation of low molecular mass organogelators (LMOGS) has stimulated much research attempting to quantify the fundamental aspects of this fascinating phenomenon.[1-5] However, whilst a number of structurally diverse gelators have been identified, it is not yet possible to *a priori* design a gelator for a selected liquid. [3-11] A selection of gelator structures is presented in Scheme 1; except for often containing significant portions of hydrophobic substituents in the form of lengthy alkyl chains or polycyclic hydrocarbon residues, it is difficult to discern a common pattern to the disparate group of known organogelators. Lechithin **1**, with its rather soap-like structure, has been known as an effective LMOG for many years, as have a number of steroidal structures related to deoxycholic acid **2**. Both anthracenes and anthraquinones [e.g. **3**] having long hydrocarbon substituents can act as LMOGs, as can a combination of both the latter structural types in the form of esters derived from anthraquinonyl acids or other polyaromatic acids and sterols. Contrasting LMOG structures are represented by a series of *bis*-1,3-dione and tetracarboxylate complexes of copper, along with various calix[n]arenes, in all cases carrying a number of lengthy straight chain hydrocarbon substituents. Various peptide derivatives, represented by structures **4** and **5**, along with a few structures having two cholesterol units flanking a central heterocyclic or *bis*-acetylenic core, have also been found to act as gelators, along with aliphatic diamines grafted onto a dendritic L-lysine based peptide,[12-15] as have a series of benzylidene carbohydrate derivatives **6.** These latter structures are the most extensive series of LMOGs which do not contain large hydrophobic structural features, along with some sugar derivatives based on an azobenzene core.

Gelation by LMOGS is clearly not driven by a single molecular interaction, with a range of physical (non-covalent) interactions, principally hydrogen bonding but also solvophobic effects or $\pi$-$\pi$ interactions playing a role. Recently for example, Berkhardt *et al* [16] have studied the gelation

of a range of organic solvents by 12-hydroxy stearic acid (HAS) in the presence of added alcohol, known to disrupt hydrogen bonds. At sufficient high levels of added alcohol, gelation was precluded suggesting a hydrogen-bond based mechanism, underlining the predominance of this type of mechanism. Gelator solutions therefore, share many physical characteristics with surfactant solutions (*e.g.* thermoresponsiveness, thixotropy, micellisation, lyotropism and crystallization) as well as polymer solutions (*e.g.* swelling and microscopic mass motion).

Fluorinated liquids have also successfully been gelled, using molecules that were themselves also fluorinated to some extent.[17,18] George *et al* showed that N-alkyl perfluoroalkanamides ($F(CF_2)_mCONH(CH_2)_nH$ (denoted FmNHm) gelled a series of fluorinated liquids with varying degrees of success, the gelation driven predominantly by the incompatibility of the fluorocarbon and hydrocarbon segments coupled with intermolecular hydrogen bonding. Previously, we reported the phase behaviour of a homologous series of chiral, non-racemic *bis*-(α,β-dihydroxy ester)s found to gel mixtures of the partially fluorinated liquids, 2H,3H-perfluoropentane (HPFP) and 1H,1H-heptafluorobutanol (HFB).[19] Thermo-reversible gelation occurred and was shown to depend on both solvent composition and the molecular structure of the gelator. The effects of chirality within the molecular structure have been previously noted for a wide range of systems[11,20-33] , especially in relation to amino acid based molecules[34-39], where chiral molecules act as gelators but racemic analogues do not. Generally, the molecular chirality determines the chirality of the macroscopic structure. In the case of the partially fluorinated solvent case, the corresponding racemic dihydroxy esters did not form gels but rather precipitates[19], thus highlighting the importance of enantiomeric purity in such aggregation also pertains to fluorinated liquids. It is these observations that are elaborated here.

## Materials and Methods

*Materials*

2H,3H-Perfluoropentane (HPFP) (Apollo Scientific) was purified by filtration first through acidic and then basic alumina, then dried and stored over molecular sieves. 1H,1H-Heptafluorobutanol (HFB) (Apollo Scientific) was stored over molecular sieves, but otherwise used as received. The solvent mixtures are expressed in terms of the mass fraction of HPFP, $\alpha_{HPFP} = \frac{m_{HPFP}}{m_{HPFP} + m_{HFB}}$ where $m_{HPFP}$ *and* $m_{HFB}$ correspond to the masses of HPFP and HFB respectively.

*Synthesis of gelators*

The gelators were all synthesised in two high-yielding steps, either from a 1,ω-diene **7** or a cycloalkene **8**, depending upon commercial availability or the relative ease of preparation (Scheme 2). [19]

Cross metathesis with *iso*-propyl acrylate (many other alkyl acrylates were similarly employed) proceeded very smoothly and cleanly. Given that all components were scrupulously clean, this remarkable transformation could be completely catalysed with as little as 0.15 mol% of Grubb's Mark II catalyst and resulted in the isolation of the dienyl diesters **9** in 85~90% yields, solely as (*E,E*)-isomers to the limit of detection of both $^1$H NMR and GC analysis.

Subsequent double *bis*-hydroxylation using AD Mix-β then delivered excellent yields of the expected tetrahydroxy diesters **10**. Chiral GC analysis of the derived trifluoroacetates, against a racemic *dl*-mixture, showed the tetrahydroxy diesters **10** to be optically pure to the limits of the GC detection.

It should be noted that there is some potential for confusion amongst such structures depending upon the drawing style; this is illustrated in Scheme 3. Thus, a 'full' drawing of the (*2S,3R,12R,13S*) enantiomer of organogelator **10e** in a standard 'zig-zag' form has all hydroxyls positioned on wedges, whereas an abbreviated representation, the right hand structure, has the two pairs of hydroxyls on wedges and dashes; note also the alteration to the angle of the ester groups. A similar potential confusion arises with the corresponding *meso* form **11** and is also shown in Scheme 3.

*Nomenclature*

The space length, n, of the gelator - denoted $G_n$ - is defined as the number of carbons between the two stereogenic centres (headgroups) less 2, in turn defined by the structure of the 1,ω-diene or a cycloalkene precursor, **7** or **8**.

*Gel formation*

On a 1g scale, the gelator was first dissolved in HFB and the non-solvent HPFP added subsequently to give the desired composition. Gels prepared by adding the gelator directly to a predetermined solvent blend were found to be less reproducible. No heating-cooling cycle was necessary for these gels, which form spontaneously at room temperature. The time-scale for gel formation was found to differ according to the composition of the sample, ranging from a matter of seconds to a number of days. Here, only those gels that form over a period of an hour or less have been studied.

*Determination of gelation temperature $T_{gel\text{-}sol}$*

Glass vials containing the samples were equilibrated in a temperature-controlled water bath and the temperature increased from 15 °C initially in 2 °C steps with a 30 min equilibration time at each temperature. On approaching the gelation temperature, smaller increments (0.5 °C) were adopted. The simplest measure of gelation - that the gel be stable to inversion [3] - was used to quantify the gel-sol behaviour since the volatile nature of the solvents rendered a rheological characterisation unfeasible.

*IR spectroscopy*

Preformed gels were heated to 55°C and using a warm teat pipette, four drops of the liquid were transferred to a 0.1mm well Hellma cell, placing the matched quartz plate on top. This pathlength cell was found to be necessary to reduce the signal to an appropriate level. This quartz "sandwich" was sealed with Nescofilm. The plates were then secured in the sample holder and left to gel (minutes). FT-IR spectra were recorded on a JasCo 660Plus FT-IR spectrometer, scanning the region 400 – 4000 $cm^{-1}$ with 4 $cm^{-1}$ resolution and slits 2 nm. The gel was subsequently melted by *in situ* heating and the FT-IR spectrum of the liquid state recorded. This procedure was repeated in triplicate to ensure reproducibility. All the spectra presented here been background subtracted using the IR spectrum of the appropriate solvent mixture at an appropriate temperature.

*Small-Angle Neutron Scattering (SANS)*

Small-angle neutron scattering (SANS) measurements were performed on the fixed-geometry, time-of-flight LOQ diffractometer (ISIS Spallation Neutron Source, Oxfordshire, UK). By using neutron wavelengths spanning 2.2 to 10 Å, a $Q = 4\pi\sin(\theta/2)/\lambda$ range of approximately 0.008 to

0.25 $Å^{-1}$ (25Hz) is accessible, with a fixed sample-detector distance of 4.1 m. The samples were contained in 2 mm path length, UV-spectrophotometer grade, quartz cuvettes (Hellma) and mounted in aluminium holders on top of an enclosed, computer-controlled, sample chamber. Sample volumes were approximately 0.4 $cm^3$. Temperature control was achieved through the use of a thermostatted circulating bath pumping fluid through the base of the sample chamber. Under these conditions a temperature stability of better than ± 0.5 °C can be achieved. Experimental measuring times were approximately 40 minutes.

All scattering data were (a) normalized for the sample transmission, (b) background corrected using a quartz cell filled with the appropriate solvent (this also removes the inherent instrumental background arising from vacuum windows, *etc*) and (c) corrected for the linearity and efficiency of the detector response using the instrument-specific software package. The data were put onto an absolute scale by reference to the scattering from a partially deuterated polystyrene blend.

The Kholodenko-Dirac worm-like chain model[9] has been used to analyse the SANS data. This approach is derived from a Gaussian coil model, where long thin rods are made of a succession of $m$ cylindrical elements of statistical length $\ell$ and radius $R_{ax}$ The contour length of the chain, L, is equal to the product $m \cdot \ell$. The scattering intensity generated from Kholodenko-Dirac worm-like chains is proportional to two terms:

$$I(Q) \propto P_{Worm}(Q) * P_{Axial}(Q) \qquad (1)$$

The Kholodenko-Dirac model therefore smoothly interpolates between the Gaussian coil and rigid rod predictions and the number of segments ($m$) forming the chain and hence gives an indication regarding the flexibility of the chain. Smaller values of $m$ correspond to stiffer chains.

When $m$ tends towards infinity, the scatterer adopts a flexible Gaussian random coil whereas when tending towards unity, a rigid rod is obtained.

For long thin rods

$$P_{Worm}(Q) = \frac{2}{3n}\int_0^{3n}\left(1-\frac{y}{3n}\right)f(y)dy \qquad (2)$$

where for $Q \le \frac{3}{l}$, $f(y) = \frac{\sinh(Ey)}{E\sinh(y)}$ with $E = \left[1-\left(\frac{Ql}{3}\right)^2\right]^{1/2}$ whereas for $Q > \frac{3}{l}$,

$f(y) = \frac{\sin(Fy)}{F\sinh(y)}$ with $F = \left[\left(\frac{Ql}{3}\right)^2 - 1\right]^{1/2}$ given that $m$ is the number of chain elements, $l$ the statistical chain element length (giving the total chain length L = $ml$).

$P_{Axial}(Q)$ was adopted with a radial Guinier form, such as:

$$P_{Axial}(Q) = N(\rho_1 - \rho_3)^2(AL)^2\exp\left(-\frac{1}{2}Q^2R_{Ax}^2\right) \qquad (3)$$

with $\rho_1$ and $\rho_3$ the scattering length densities for the worm and solvent, $N$ worms per unit volume, A the cross sectional area and $R_{Ax}$ the cross sectional radius of the chain, assuming a Gaussian scattering density.

*CD Spectroscopy*

Preformed gels prepared as described previously were transferred to the CD cells and either equilibrated at each set temperature for 20 minutes prior to recording the CD spectra or melted *in*

*situ* and the gelation followed after a temperature jump. All spectra (180 – 400 nm) were recorded on a Chirascan (Applied Photophysics).

**Results**

*1. Non-gelling structures*

The inter-relationship between chirality and end-group structure play an important role in determining the ability of this family of tetrahydroxy diesters to gel mixtures of HPFP and HFB. Schemes 4 and 5 present the non-gelling structures – here "non-gelling" being defined as materials that are either insoluble or show no gelation up to a concentration of 1wt%. These very small changes in molecular structure reflect the surprisingly sensitive dependence on solubility – methyl; and ethyl tipped analogues (figure 4) showing minimal solubility, whilst iso-butyl, tert-butyl and iso-amyl being too soluble. Iso-propyl posseeses what seemingly seems to be the optimum structure for gelation.

*2. Thermodynamic analysis of the melting transition: $T_{gel\text{-}sol}$*

As described by Murata *et al.*[40] and Terech *et al.*[41], drawing on an analogy with the dissolution of crystals (Shröder-van Laar)[42], the enthalpy associated with the melting transition of the gelled networks can be evaluated *via*

$$\ln[G_n] = -\frac{\Delta H_m}{RT_m} + Cnst \qquad (4)$$

where $[G_n]$ represents the concentration of gelator of size n and $\Delta H_m$ represents the phase transition enthalpy. Figure 1(a) presents this analysis for gelators $G_3$, $G_4$, $G_5$, G6 and $G_8$ in a

$\alpha_{HPFP}=0.9$ *i.e.* 90/10 wt% HFPFP/HFB solvent ratio, whilst Figure 1(b) reports $T_{gel\text{-}sol}$ for G6 in a series of differing solvent ratios. Tables 1 and 2 respectively show the thus determined enthalpies ($\Delta H_m$) *viz* $G_3$, $G_4$, $G_5$, G6 and $G_8$ in $\alpha_{HPFP}=0.9$ (Table 1) and $G_6$ in $\alpha_{HPFP}=0.95$, $\alpha_{HPFP}=0.9$, $\alpha_{HPFP}=0.85$, $\alpha_{HPFP}=0.8$ and $\alpha_{HPFP}=0.7$ (Table 2). Firstly, all these $\Delta H_m$ values are positive, showing that the melting process is endothermic, leading to a system with higher entropy. Secondly, these $\Delta H_m$ values are largely unaffected by the solvent composition or by the gelator chain length suggesting the gelation is a feature dominated by the common structural motif, the end-group. These enthalpy values are in good agreement with those reported in the literature for *e.g.* cholesterol, [40] 2-anthraquinonyl steroid, [28] anthracene, [41] 1-*O*-methyl-4,6-*O*-benzylidene derivatives [11] and the dendritic aliphatic diamine [43] systems, much greater than that observed for HAS in ethylene glycol but smaller than that observed by van Gorp's $C_3$-symmetric molecules.[44]

*3. Driving force for self-assembly*

The importance of the chirality for the gelation, and the structure of the gelators, lend themselves to a gelation mechanism based on hydrogen bonding. Accordingly, IR spectroscopy has been used to probe the nature of the hydrogen bonding occurring in these systems, figure 2.

The hydrogen bonding region shows a number of features dependent on the gelator concentration: sharp peaks around 3680 and 3640 $cm^{-1}$ indicative of discrete H-bonds, whilst the broad region arises from a collection of ill-defined H-bonds. On gelation, there is a noticeable shift in the band towards lower wavenumbers and a broadening in this band, indicating a small but distinguishable difference in the hydrogen bonding framework in the solution and the gel. One may envisage hydrogen bonds between the hydrogen in the hydroxy group and the ester

oxygen. This bonding could be either inter- or intra-molecular, and it is theorised here that gelation induces a switch from intra- to inter-molecular interactions.

*4. Local structure of the aggregates*

Circular dichroism (CD) spectroscopy measures the differences in absorption of left-handed and right-handed polarized light arising due to structural asymmetry (chirality). Normally, the absence of regular structure results in no measurable CD intensity, whilst an ordered structure results in a spectrum, but one which may exhibit both positive and negative intensity. Our previous observation that gelators of specific stereochemistry are required to form gels implies that the gelation mechanism requires a specific molecular arrangement, but rather interestingly, $G_6$ in $\alpha_{HPFP} = 0.9$ in the gelled state showed only a weak, ill-defined CD spectrum but when the sample was melted, a strong CD spectrum was observed, contrary to the more common observation [e.g. 28,32,44,45] that the ordering introduced *via* gelation results in a strong CD spectrum.

The tetrahydroxy diesters studied here contain a CD-active chromophore – the α-hydroxy ester moiety - which may exist in two possible conformations; [46] the preferred conformation (the carbonyl and alcohol distal) gives rise to a strong positive signal at 210 nm whereas the less favoured conformation gives rise to a weaker negative signal at 230-240 nm. The shorter wavelength CD signature - the strong positive signal at 210-22nm - has also been associated with the formation of helical aggregates, when coincident with a negative signal at 201 nm.[32]

Accordingly, a solution of 1 wt% $G_6$ in $\alpha_{HPFP} = 0.9$ was melted and transferred into a 1 mm path length quartz cell, and allowed to gel by holding the cell at 5 °C for 30 min. The temperature was then increased and the sample equilibrated at each new temperature for 10 min before the CD spectrum was recorded, figure 3(a). An analogous experiment was also performed in which the

gelation process was followed by recording the CD spectrum from a sample initially at 60 °C (*i.e.* in the liquid state) that had been placed into the sample stage thermostatted at 20 °C, figure 3(b).

Both of the expected signals – 210 nm and 230-240 nm - are seen in figures 3(a and b), with the longer wavelength signal (230 nm) appearing upon gelation since this signal arises due to the less-preferred conformation of the α-hydroxy ester moiety; gelation imposes a conformational perturbation, rather than gelation being driven by such a conformational rearrangement.

*5. High resolution NMR*

A 'standard' $^1$H NMR spectrum of the tetrahydxoy diesters **10e** in dilute solution in deuteriochloroform at 32 °C (Fig 1; suppl. data) showed clear, essentially first order resonances for the protons around the key α,β-dihydroxy ester function – $\delta_H$ (400 MHz, $CDCl_3$) 4.08 (2H, dd, *J* 5.1 and 2.0 Hz, 2 x $H^{\alpha}$), 3.88 (2H, sl. broadened dtd, *J ca.* 9, 7 and 2 Hz, 2 x $H^{\beta}$), 3.05 (2H, d, *J* 5.1 Hz, 2 x α-OH) and 1.87 (2H, d, *J* 9.1 Hz, 2 x β-OH). The two resonances assigned to the hydroxyl groups, as expected disappeared after the sample was diluted with a drop of deuterium oxide. The rather small 2 Hz coupling constant between the vicinal C-H groups is consistent with a conformation (Scheme 6) in which a chair-form can be accommodated with the α-hydroxyl positioned axially and perhaps both hydroxyl hydrogens participating in hydrogen bonding to the ester carbonyl group.

Not surprisingly, similar spectra when run on gelled samples, derived both from organogelator **10e** and either deuteriochloroform or HPFP/HFB, showed very broad resonances and provided no useful information. However, when heated through the melting temperature, such gels melted to reveal the spectroscopic features described above.

*6. Morphology of gelled systems*

A series of samples made with gelator $G_6$ at concentrations 0.4 wt% < [G6] < 0.8 wt% in $\alpha_{HPFP} = 0.9$ were investigated by SANS at 25 °C and the scattering data interpreted in terms of the Kholodenko-Dirac worm-like chain, (Figure 4(a) and Table 3).

The initial scattering intensity increases with the gelator concentration, showing that even though the size and shape of the scatterers was not found to vary significantly with concentration, the number of scatterers does increase, leading to stiffer gels, and can be compared directly to the increase in $T_{gel\text{-}sol}$ observed for increasing gelator concentration. The morphology of the gelled structure seems insensitive to gelator concentration, *viz* the radius was not sensitive to the gelator concentration.

SANS was also used to explore the thermoreversibility of the gelation process. A sample of 0.7 wt% $G_6$ in $\alpha_{HPFP} = 0.9$ was examined as a function of temperature. Figure 4(b) presents the scattering data along with the Kholodenko-Dirac model fittings, and Table 7 the parameter values obtained.

Again, the geometry of the scatterers appears to remain constant throughout the temperature range. However, the initial intensity does vary with temperature and whilst the structure remains a gel at 50 °C ($T_{gel\text{-}sol}$ = 57 ± 2 °C), the decrease in initial intensity implies a loss of structural integrity. Furthermore, the re-building of the gelled structure was also investigated by heating a sample to ≈ 70 °C (*i.e.* fully liquid) and the scattering recorded once the sample is returned to 25°C (Figure 4(c)).

**Discussion**

The IR spectra do not reveal any significant changes in hydrogen bonding upon melting the gel, implying that if H-bonding is implicated in the gelation mechanism, and is either responsible for- or a reflection of the change in conformation around the ester, it is likely to be a switch from

*intra*-molecular to *inter*-molecular hydrogen bonding. A number of different molecular arrangements may be envisaged consistent with 4 hydrogen bonds per headgroup and the conformation implied in the NMR experiment, and one such is presented in Scheme 7. This conformation promotes the exposure of the *iso*-propyl groups to the fluorinated media, and parallels the increase in solubility observed of ethylene oxide polymers induced by methyl end-groups.[47,48] Increases in the inter-headgroup spacing, effectively n+2 (Scheme 3), introduces sufficient flexibility into the molecule that in these cases, the hydrogen bonding need not be predominantly inter-molecular, thereby resulting in a reduced propensity for association in turn leading to insolubility. Bulky headgroups (Scheme 5) introduce a steric barrier to efficient intermolecular hydrogen bonding, and therefore these molecules do not act as gelators. Similar conclusions were drawn by Samiyoshi *et al* [32] in their diamide system. From the enthalpy of melting values listed in Tables 1 and 2, each cross-link in the gel network consists of approximately 3-4 hydrogen bonds, consistent with the molecular structure.

The most common macroscopic structural arrangement formed by (chiral) gelators are fibrils formed from a stacking of the gelator molecules.[20,21,24,27,32,33,39,49-53] Compared to X-ray diffraction, there have been relatively few SANS studies of gelator systems, with most focussing on "signature" intensity *vs*. wave-vector (Q) relationships, *viz* $Q^{-1}$ (rod) at low Q becoming $Q^{-4}$ (solid objects) at higher Q, in conjunction with local maxima or oscillations at higher Q arising Bragg reflections or sharp interfaces[17,54,54-57,57,58,58-62]. We have applied a more elaborate model of the above, treating the gelator morphology as a flexible assembly of rod-like structures. The balance between the flexibility and rigidity of the system is defined by the parameter, *m*. Here, *m* = 4, indicating a rather rigid structure, with a Gaussian cross-section of 25 – 40 Å depending on gelator concentration and structure, consistent with that observed by van Gorp.[44] The length of the rod-like segment are typically 100s Å in size, indicating a stacked geometry. With an increase

in temperature, these structures "melt" rather than "dissolve" with the size of the structure largely invariant until the gel temperature is reached.

**Conclusions**

It is shown here that chiral tetrahydroxy diesters are able to gel partially fluorinated solvents, a process driven by hydrogen bonding. Racemic analogues did not act as gelators, exhibiting greatly reduced solubilities. The gelation ability was found to be sensitive to end-group structure and inter-headgroup spacer length. These facets point to an association driven by intermolecular hydrogen bonding between the headgroups. The ability of the headgroups to participate in this process depends on the mutual accessibility of the headgroups, bulky headgroups and larger inter-headgroup distance both preclude gelation. The macroscopic morphology was examined by SANS, interpreted in terms of aggregated rods, formed from a columnar packing of gelator molecules.

**Figure Captions**

Figure 1(a); Shröder-van Laar analysis of the gelation of a series of gelators with n = 3 (open circles), n = 4 (filled triangles), n = 5 (filled circles), n = 6 (open triangles) and n = 8 (open squares) in $\alpha_{HPFP} = 0.9$

Figure 1(b); Shröder-van Laar analysis of the gelation of gelator $G_6$ as a function of solvent composition, $\alpha_{HPFP}$; $\alpha_{HPFP} = 0.95$ (open squares), $\alpha_{HPFP} = 0.90$ (open circles), $\alpha_{HPFP} = 0.85$ (filled triangles), $\alpha_{HPFP} = 0.80$ (open triangles) and $\alpha_{HPFP} = 0.70$ (open squares).

Figure 2; IR spectra of the gelator 0.6 wt% $G_6$ in $\alpha_{HPFP} = 0.9$; upper trace (solution), lower trace (gel).

Figure 3(a); CD spectrum for a 1wt% solution of $G_6$ in $\alpha_{HPFP} = 0.9$ as function of temperature; 5 °C (diamonds), 25 °C (triangles), 45 °C (squares) and 55 °C (cirlces). Also shown is the absence of a CD spectra from the solvent (black line).

Figure 3(b); Loss of intensity of the CD spectrum for a 1wt% solution of $G_6$ in $\alpha_{HPFP} = 0.9$ induced by gelation following a drop in temperature from 55 °C to 20 °C. 60 CD spectra were recorded every 73 s following by an "infinite" spectrum recorded after a further delay of 12 hrs.

Figure 4(a); SANS from gelator G6 in $\alpha_{HPFP} = 0.9$ at concentrations of 0.4wt% (empty circles), 0.5 wt% (filled circles), 0.6 % (empty triangles), 0.7 wt% (filled triangles) and 0.8wt% (empty squares). The full lines are fits to the Kholodenko-Dirac model as described in the text.

Figure 4(b); SANS from 0.7wt% gelator $G_6$ in $\alpha_{HPFP} = 0.9$ as a function of temperature; 25°C (stars), 30°C (squares), 35°C (triangles, up), 40°C (diamonds), 45°C (triangles, down) and 50°C (circles). The full lines are fits to the Kholodenko-Dirac model as described in the text.

Figure 4(c); SANS from 0.7wt% gelator $G_6$ in $\alpha_{HPFP} = 0.9$ as a function of time after melting *in situ*; 50 min (open circles), 65 min (filled circles), 80 min (open triangles), 95 min (filled triangles), 110 min (open squares), end-point (filled circles).The full lines are fits to the Kholodenko-Dirac model as described in the text.

**Schemes**

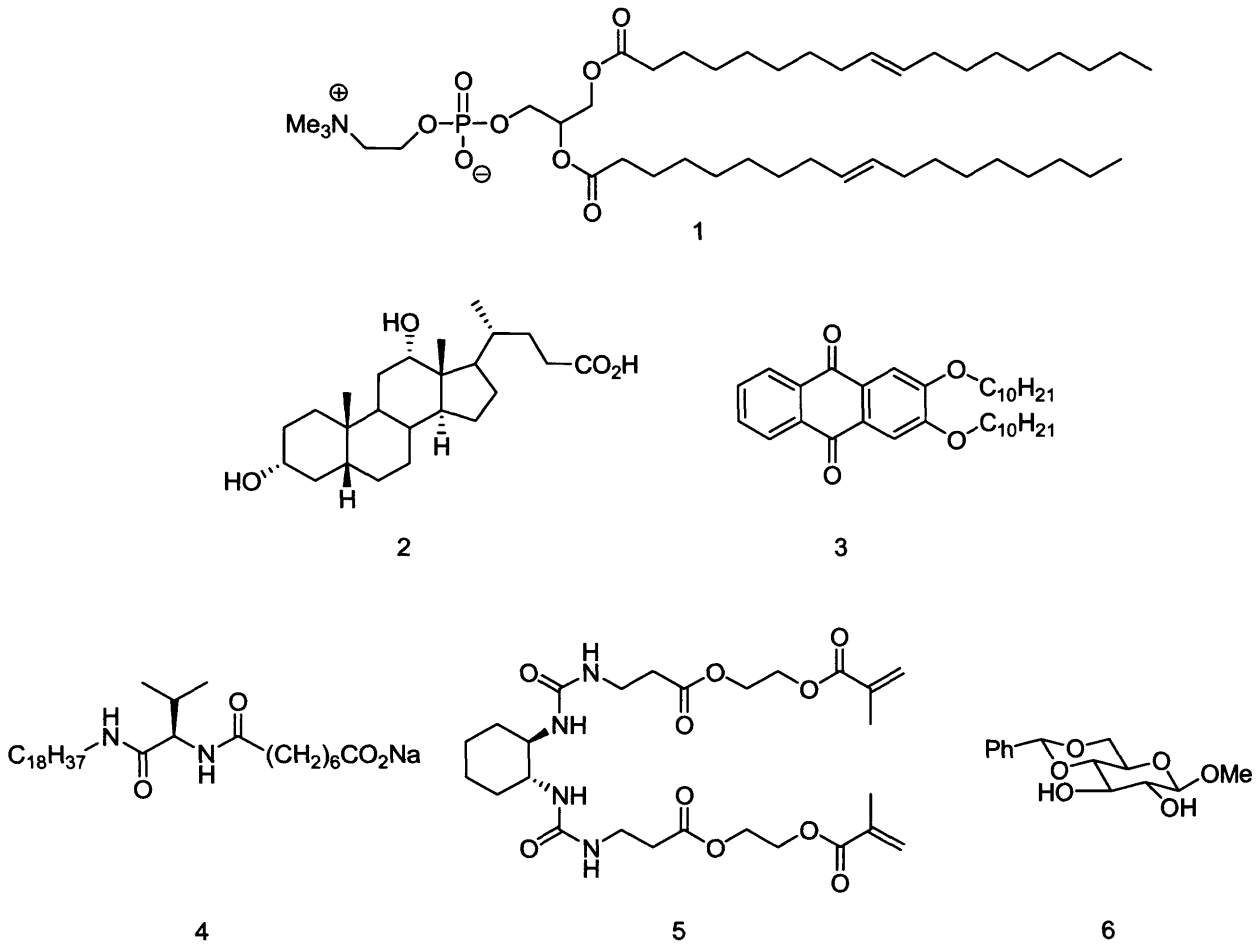


Scheme 1: Selection of structures known to form gelled systems

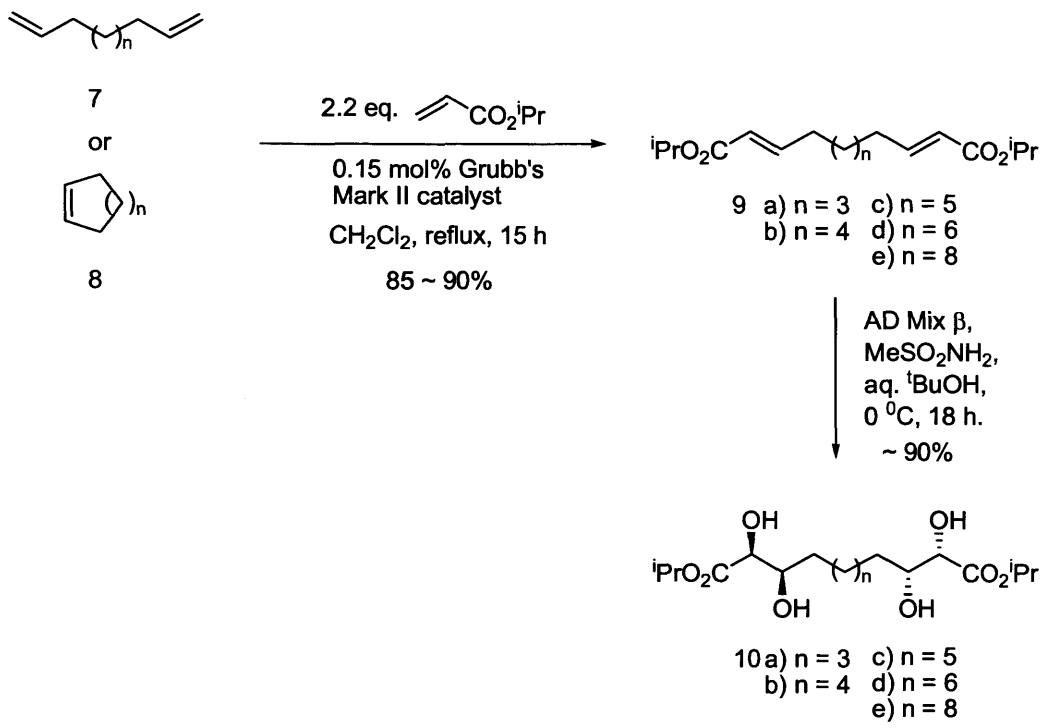


Scheme 2: Synthesis of chiral gelators.

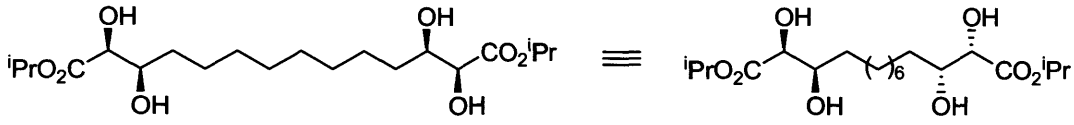

10e

A single (*S,R,R,S*) enantiomer, **10e**, of a *dl* pair.

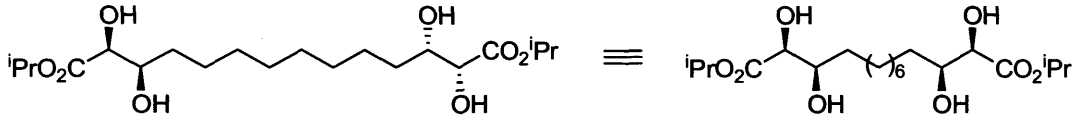

11

The related *meso* (*S,R,S,R*) form, **11**, in two contrasting stereodrawings.

Scheme 3: Stereochemical representations of chiral gelators.

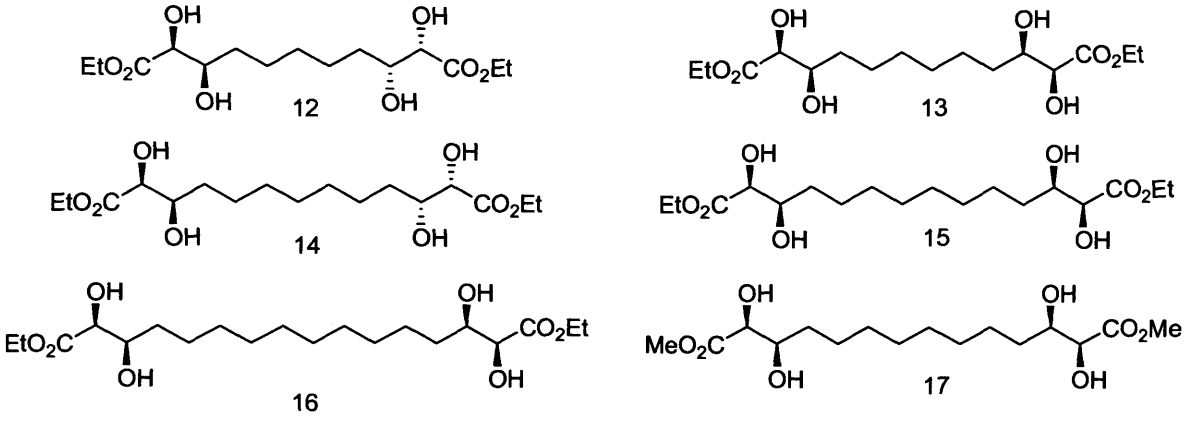


Scheme 4: Molecules identified in this work as being non-or pooly gelating

**Optimal gelating end-group** **Poorly gelating end-groups**

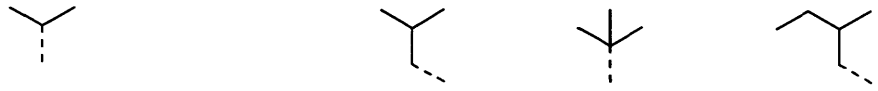

*iso*-propyl *iso*-butyl *tert*-butyl *iso*-amyl

n = 3-5, 8, 10. n = 4 and 8 n = 10 n = 4

Scheme 5: The dependence of end-group structure and gelation ability

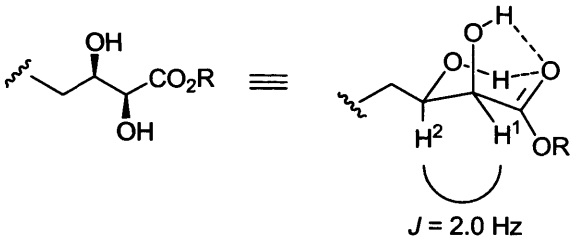


Scheme 6 : Chair conformation of the monomer structure.

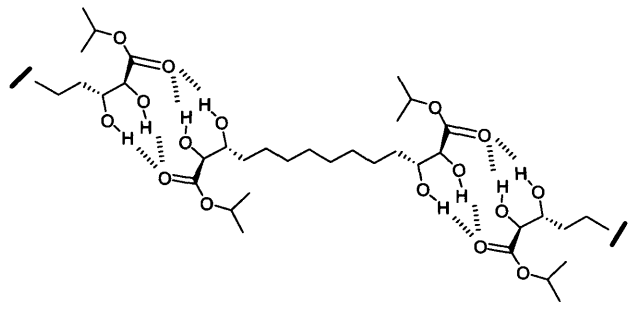

**A**

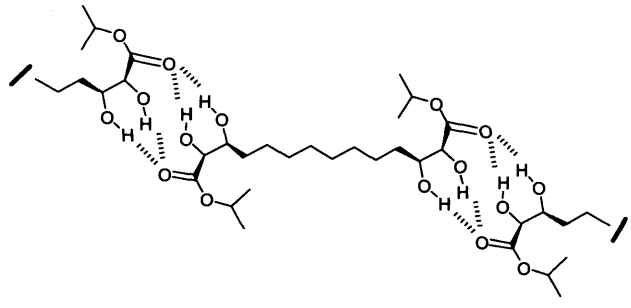

**B**

Scheme 7: Possible intermolecular hydrogen bonding structures that drive gelation. **A**: derived from the gelator **10e**; **B**: less favoured '*cis*' substituted structures derived from the *meso*-form, a much less active gelator.

## Tables

**Table 1**: Phase transition enthalpies for $G_3$, $G_4$, $G_5$, G6 and $G_8$ in a $\alpha_{HPFP} = 0.9$ solvent ratio

| $G_n$ | $G_3$ | $G_4$ | $G_5$ | G6 | $G_8$ |
|---|---|---|---|---|---|
| $\Delta H_m$ / kJ mol$^{-1}$ | 28 ± 2 | 38 ± 2 | 32 ± 2 | 32 ± 2 | 39 ± 2 |

**Table 2**: Phase transition enthalpies for $G_6$ in various HFB/HPFP solvents ratios

| $\alpha_{HPFP}$ | 0.95 | 0.9 | 0.85 | 0.8 | 0.7 |
|---|---|---|---|---|---|
| $\Delta H_m$ / kJ mol$^{-1}$ | 38 ± 2 | 32 ± 2 | 36 ± 2 | 34 ± 2 | 34 ± 2 |

**Table 3**: Kholodenko-Dirac model fit parameters for $G_6$ in $\alpha_{HPFP} = 0.9$, as a function of gelator concentration

| [gelator] / wt% | $R_{ax}$ (± 2) / Å | $m$ (± 0.2) | $l$ (± 10) / Å | $L = m*l$ / Å |
|---|---|---|---|---|
| 0.4 | 25 | 3.8 | 168 | 638 |
| 0.5 | 31 | 3.3 | 293 | 967 |
| 0.6 | 32 | 3.0 | 350 | 1050 |
| 0.7 | 31 | 3.2 | 306 | 979 |
| 0.8 | 30 | *4.3* | 256 | 1100 |

**Table 4**: Kholodenko-Dirac model fit parameters for 0.7 wt% $G_6$ in $\alpha_{HPFP} = 0.9$ as a function of temperature

| Temperature / °C | $R_{ax}$ (± 2) / Å | $m$ (± 0.2) | $l$ (± 10) / Å | $L = m*l$ / Å |
|---|---|---|---|---|
| 25 | 27 | 7.3 | 151 | 1102 |
| 30 | 28 | 6.7 | 155 | 1039 |
| 35 | 30 | 4.8 | 190 | 912 |
| 40 | 30 | 5.1 | 156 | 796 |
| 45 | 36 | 2.9 | 294 | 853 |
| 50 | 34 | 12.6 | 85 | 1071 |

References


1. Gronwald, O.; Snip, E.; Shinkai, S. *Current Opinion in Colloid & Interface Science* **2002,** *7* (1-2), 148-156.

2. Abdallah, D. J.; Weiss, R. G. *Journal of the Brazilian Chemical Society* **2000,** *11* (3), 209-218.

3. Terech, P.; Weiss, R. G. *Chemical Reviews* **1997,** *97* (8), 3133-3159.

4. Sangeetha, N. M.; Maitra, U. *Chemical Society Reviews* **2005,** *34* (10), 821-836.

5. Smith, D. K. *Tetrahedron* **2007,** *63* (31).

6. Escuder, B.; Miravet, J. F. *Langmuir* **2006,** *22* (18), 7793-7797.

7. Luboradzki, R.; Gronwald, O.; Ikeda, M.; Shinkai, S.; Reinhoudt, D. N. *Tetrahedron* **2000,** *56* (49), 9595-9599.

8. Mieden-Gundert, G.; Klein, L.; Fischer, M.; Vogtle, F.; Heuze, K.; Pozzo, J. L.; Vallier, M.; Fages, F. *Angewandte Chemie-International Edition* **2001,** *40* (17), 3164-3166.

9. Weiss, R.; Terech, P. *Moelcular Gels - Materials with Self-Assembled Fibrillar Networks;* Springer: Dordrecht, 2006.

10. Yoza, K.; Ono, Y.; Yoshihara, K.; Akao, T.; Shinmori, H.; Takeuchi, M.; Shinkai, S.; Reinhoudt, D. N. *Chemical Communications* **1998,** (8), 907-908.

11. Yoza, K.; Amanokura, N.; Ono, Y.; Akao, T.; Shinmori, H.; Takeuchi, M.; Shinkai, S.; Reinhoudt, D. N. *Chemistry-A European Journal* **1999,** *5* (9), 2722-2729.

12. Hirst, A. R.; Smith, D. K. *Organic & Biomolecular Chemistry* **2004,** *2* (20), 2965-2971.

13. Hirst, A. R.; Smith, D. K.; Feiters, M. C.; Geurts, H. P. M. *Chemistry-A European Journal* **2004,** *10* (23), 5901-5910.

14. Hirst, A. R.; Smith, D. K.; Harrington, J. P. *Chemistry-A European Journal* **2005,** *11* (22), 6552-6559.

15. Hirst, A. R.; Smith, D. K. *Chemistry-A European Journal* **2005,** *11* (19), 5496-5508.

16. Burkhardt, M.; Kinzel, S.; Gradzielski, M. *Journal of Colloid and Interface Science* **2008,** *submitted.*

17. George, M.; Snyder, S. L.; Terech, P.; Glinka, C. J.; Weiss, R. G. *Journal of the American Chemical Society* **2003,** *125* (34), 10275-10283.

18. George, M.; Snyder, S. L.; Terech, P.; Weiss, R. G. *Langmuir* **2005,** *21* (22), 9970-9977.

19. Griffiths, P. C.; Cote, M.; James, R.; Rogueda, P. G.; Morgan, I. R.; Knight, D. W. *Chemical Communications* **2005,** (31), 3998-4000.

20. Bao, C. Y.; Jin, M.; Lu, R.; Song, Z. G.; Yang, X. C.; Song, D. P.; Xu, T. H.; Liu, G. F.; Zhao, Y. Y. *Tetrahedron* **2007,** *63*, 7443-7448.

21. Bag, B. G.; Maity, G. C.; Pramanik, S. R. *Supramolecular Chemistry* **2005,** *17* (5), 383-385.

22. Brizard, A.; Oda, R.; Huc, I. *Low Molecular Mass Gelators: Design, Self-Assembly, Function* **2005,** *256*, 167-218.

23. Snijder, C. S.; deJong, J. C.; Meetsma, A.; vanBolhuis, F.; Feringa, B. L. *Chemistry-A European Journal* **1995,** *1* (9), 594-597.

24. Haino, T.; Tanaka, M.; Fukazawa, Y. *Chemical Communications* **2008,** 468-470.

25. Babu, P.; Sangeetha, N. M.; Maitra, U. *Macromolecular Symposia* **2006,** *241*, 60-67.

26. Jung, J. H.; John, G.; Masuda, M.; Yoshida, K.; Shinkai, S.; Shimizu, T. *Langmuir* **2001,** *17* (23), 7229-7232.

27. Hanabusa, K.; Maesaka, Y.; Kimura, M.; Shirai, H. *Tetrahedron Letters* **1999,** *40* (12), 2385-2388.

28. Mukkamala, R.; Weiss, R. G. *Langmuir* **1996,** *12* (6), 1474-1482.

29. Watanabe, Y.; Miyasou, T.; Hayashi, M. *Organic Letters* **2004,** *6* (10), 1547-1550.

30. Hafkamp, R. J. H.; Feiters, M. C.; Nolte, R. J. M. *Journal of Organic Chemistry* **1999,** *64* (2), 412-426.

31. Sagawa, T.; Chowdhury, S.; Takafuji, M.; Ihara, H. *Macromolecular Symposia* **2006,** *237*, 28-38.

32. Sumiyoshi, T.; Nishimura, K.; Nakano, M.; Handa, T.; Miwa, Y.; Tomioka, K. *Journal of the American Chemical Society* **2003,** *125* (40), 12137-12142.

33. Becerril, J.; Burguete, M. I.; Escuder, B.; Galindo, F.; Gavara, R.; Miravet, J. F.; Luis, S. V.; Peris, G. *Chemistry-A European Journal* **2004,** *10* (16), 3879-3890.

34. Doi, M.; Asano, A.; Yoshida, H.; Inouguchi, M.; Iwanaga, K.; Sasaki, M.; Katsuya, Y.; Taniguchi, T.; Yamamoto, D. *Journal of Peptide Research* **2005,** *66* (4), 181-189.

35. Caplar, V.; Zinic, M.; Pozzo, J. L.; Fages, F.; Mieden-Gundert, G.; Vogtle, F. *European Journal of Organic Chemistry* **2004,** (19), 4048-4059.

36. Makarevic, J.; Jokic, M.; Raza, Z.; Stefanic, Z.; Kojic-Prodic, B.; Zinic, M. *Chemistry-A European Journal* **2003,** *9* (22), 5567-5580.

37. Friggeri, A.; van der pol, C.; van Bommel, K. J. C.; Heeres, A.; Stuart, M. C. A.; Feringa, B. L.; van Esch, J. *Chemistry-A European Journal* **2005,** *11* (18), 5353-5361.

38. Ihara, H.; Sakurai, T.; Yamada, T.; Hashimoto, T.; Takafuji, M.; Sagawa, T.; Hachisako, H. *Langmuir* **2002,** *18* (19), 7120-7123.

39. Becerril, J.; Escuder, B.; Miravet, J. F.; Gavara, R.; Luis, S. V. *European Journal of Organic Chemistry* **2005,** (3), 481-485.

40. Murata, K.; Aoki, M.; Suzuki, T.; Harada, T.; Kawabata, H.; Komori, T.; Ohseto, F.; Ueda, K.; Shinkai, S. *Journal of the American Chemical Society* **1994,** *116* (15), 6664-6676.

41. Terech, P.; Meerschaut, D.; Desvergne, J. P.; Colomes, M.; Bouas-Laurent, H. *Journal of Colloid and Interface Science* **2003,** *261* (2), 441-450.

42. Abdallah, D. J.; Weiss, R. G. *Langmuir* **2000,** *16* (2), 352-355.

43. Lescanne, M.; Colin, A.; Mondain-Monval, O.; Fages, F.; Pozzo, J. L. *Langmuir* **2003,** *19* (6), 2013-2020.

44. van Gorp, J. J.; Vekemans, J. A. J. M.; Meijer, E. W. *Journal of the American Chemical Society* **2002,** *124* (49), 14759-14769.

45. Bao, C. Y.; Jin, M.; Lu, R.; Song, Z. G.; Yang, X. C.; Song, D. P.; Xu, T. H.; Liu, G. F.; Zhao, Y. Y. *Tetrahedron* **2007,** *63* (31), 7443-7448.

46. Craig, J. C.; Pereira, W. E.; Halpern, B.; Westley, J. W. *Tetrahedron* **1971,** *27* (6), 1173-1184.

47. Cote, M.; Rogueda, P. G. A.; Griffiths, P. C. *International Journal of Pharmaceutics* **2008,** *362* (1-2), 147-152.

48. Cote, M.; Rogueda, P. G. A.; Griffiths, P. C. *Journal of Pharmacy and Pharmacology* **2008,** *60* (5), 593-599.

49. Fu, X. J.; Yang, Y.; Wang, N. X.; Wang, H.; Yang, Y. J. *Journal of Molecular Recognition* **2007,** *20*, 238-244.

50. Das, D.; Dasgupta, A.; Roy, S.; Mitra, R. N.; Debnath, S.; Das, P. K. *Chemistry-A European Journal* **2006,** *12* (19), 5068-5074.

51. Smith, J. M.; Katsoulis, D. E. *Journal of Materials Chemistry* **1995,** *5* (11), 1899-1903.

52. Pantos, G. D.; Pengo, P.; Sanders, J. K. M. *Angewandte Chemie-International Edition* **2007,** *46*, 194-197.

53. Zhan, C. L.; Gao, P.; Liu, M. H. *Chemical Communications* **2005,** (4), 462-464.

54. George, M.; Funkhouser, G. P.; Terech, P.; Weiss, R. G. *Langmuir* **2006,** *22* (18), 7885-7893.

55. Okabe, S.; Ando, K.; Hanabusa, K.; Shibayama, M. *Journal of Polymer Science Part B-Polymer Physics* **2004,** *42* (10), 1841-1848.

56. Okabe, S.; Hanabusa, K.; Shibayama, M. *Journal of Polymer Science Part B-Polymer Physics* **2005,** *43* (24), 3567-3574.

57. Terech, P.; Bouaslaurent, H.; Desvergne, J. P. *Journal of Colloid and Interface Science* **1995,** *174* (1), 258-263.

58. Terech, P.; Clavier, G.; Bouas-Laurent, H.; Desvergne, J. P.; Deme, B.; Pozzo, J. L. *Journal of Colloid and Interface Science* **2006,** *302* (2), 633-642.

59. Dastidar, P.; Okabe, S.; Nakano, K.; Iida, K.; Miyata, M.; Tohnai, N.; Shibayama, M. *Chemistry of Materials* **2005,** *17* (4), 741-748.

60. Terech, P.; Furman, I.; Weiss, R. G. *Journal of Physical Chemistry* **1995,** *99* (23), 9558-9566.

61. Terech, P.; Allegraud, J. J.; Garner, C. M. *Langmuir* **1998,** *14* (15), 3991-3998.

62. Willemen, H. M.; Marcelis, A. T. M.; Sudholter, E. J. R.; Bouwman, W. G.; Deme, B.; Terech, P. *Langmuir* **2004,** *20* (6), 2075-2080.

ACKNOWLEDGMENT.

EPSRC, Cardiff University and AstraZeneca are gratefully thanked for the provision of studentships (MC, IRM)), whilst STFC are acknowledged for access to neutron facilities.

SYNOPSIS TOC

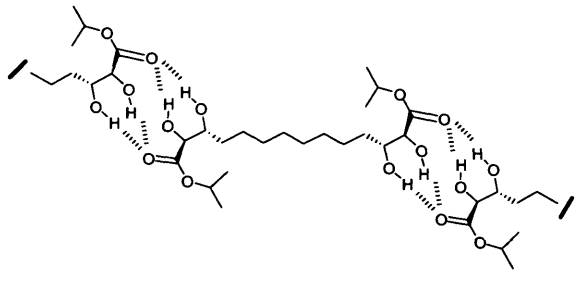

Gelation of fluorinated media is driven by the intermolecular hydrogen bonding between gelator molecules.

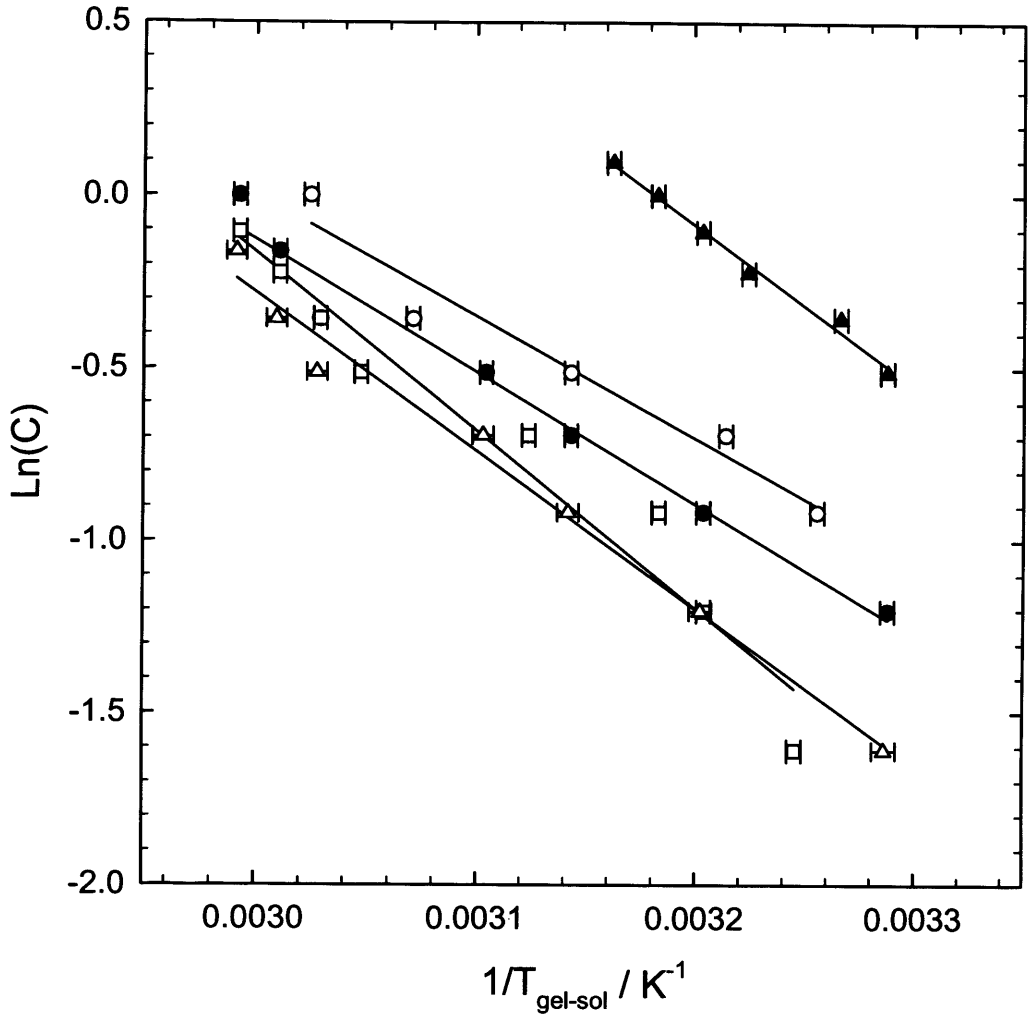


1a

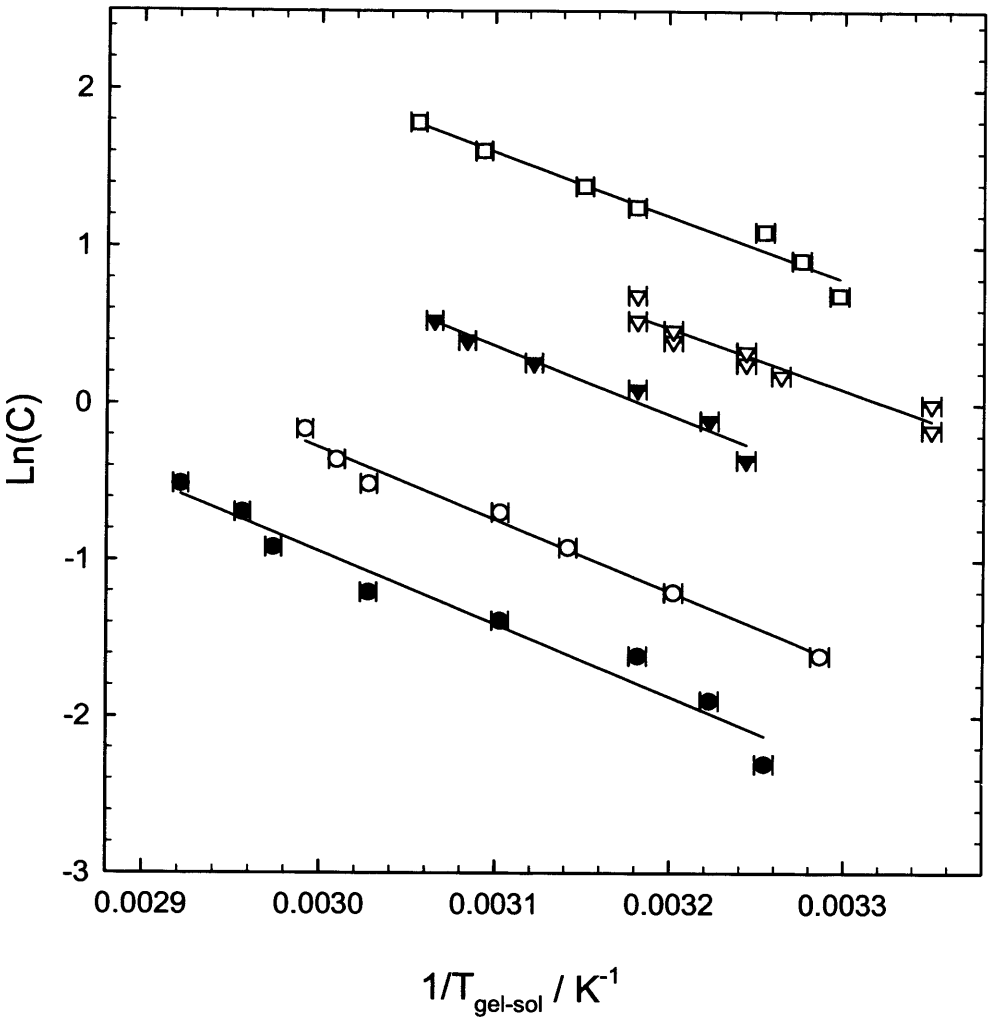


1b

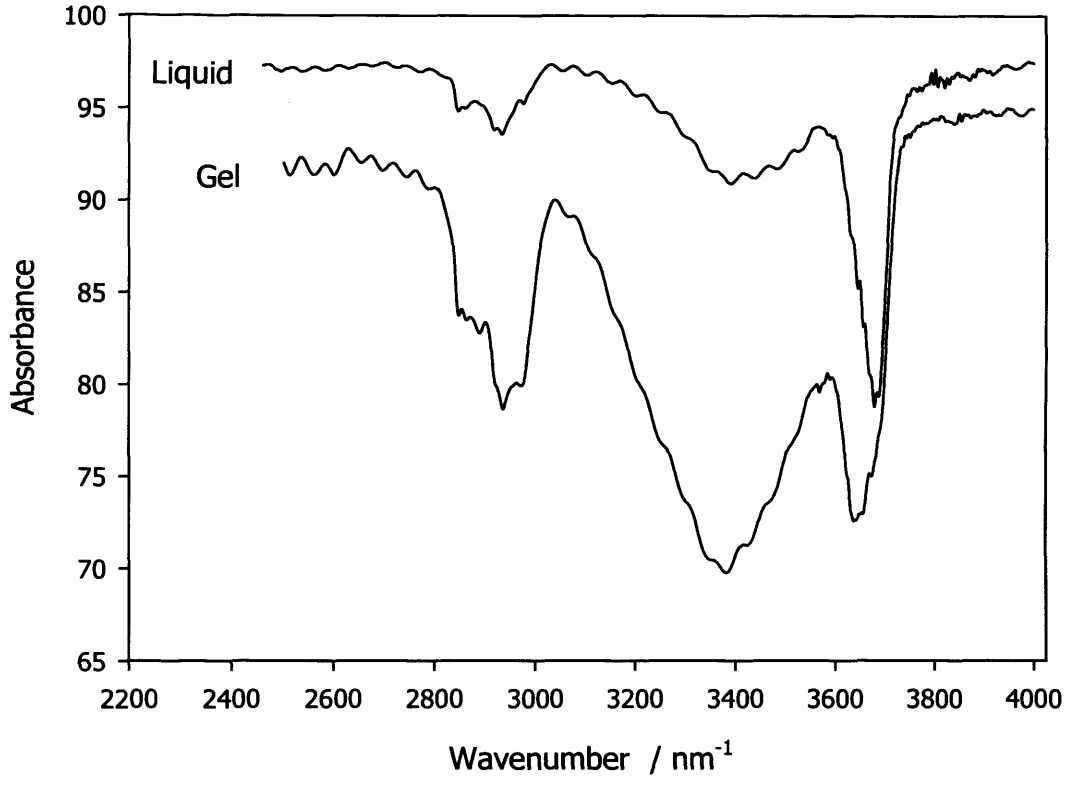
Liquid
Gel
Absorbance
100
95
90
85
80
75
70
65
2200
2400
2600
2800
3000
3200
3400
3600
3800
4000
Wavenumber / nm-1

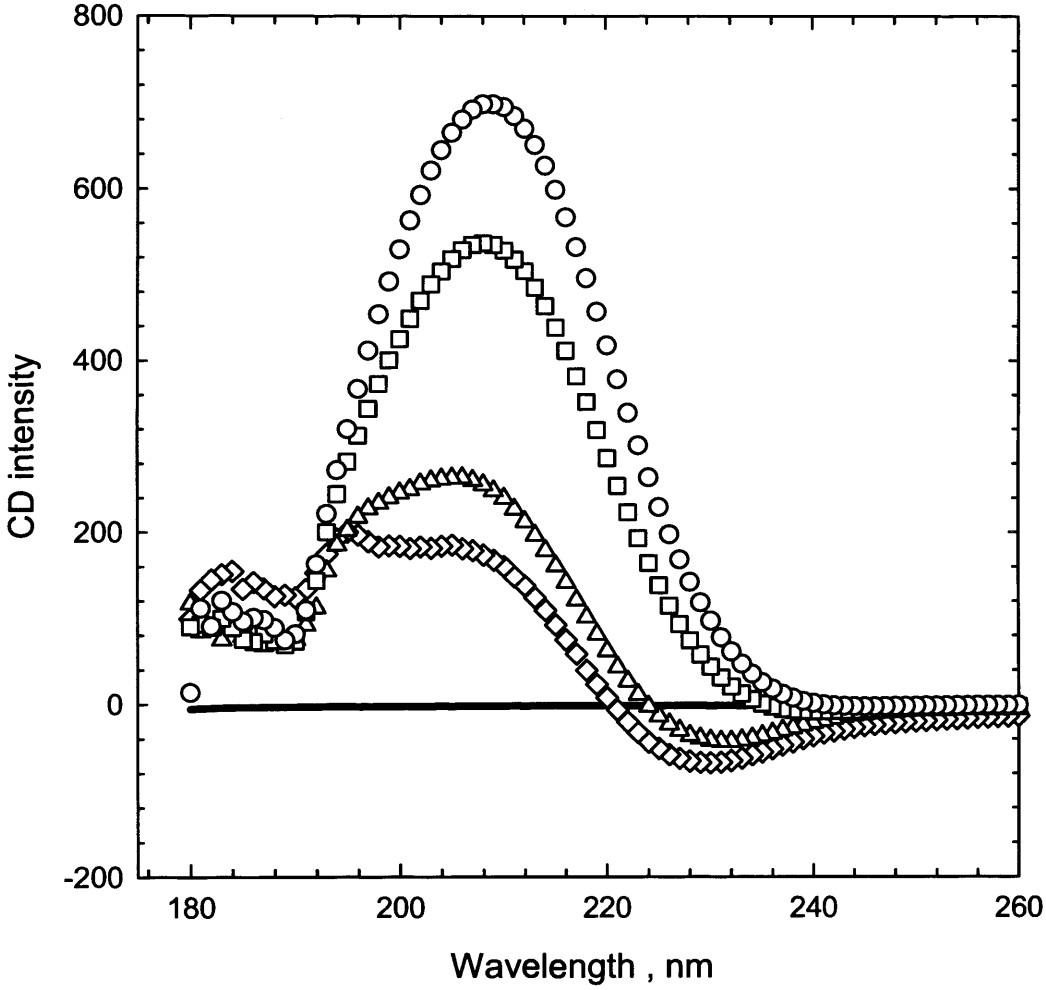
800
600
400
200
0
-200
CD intensity
180
200
220
240
260
Wavelength , nm

3a

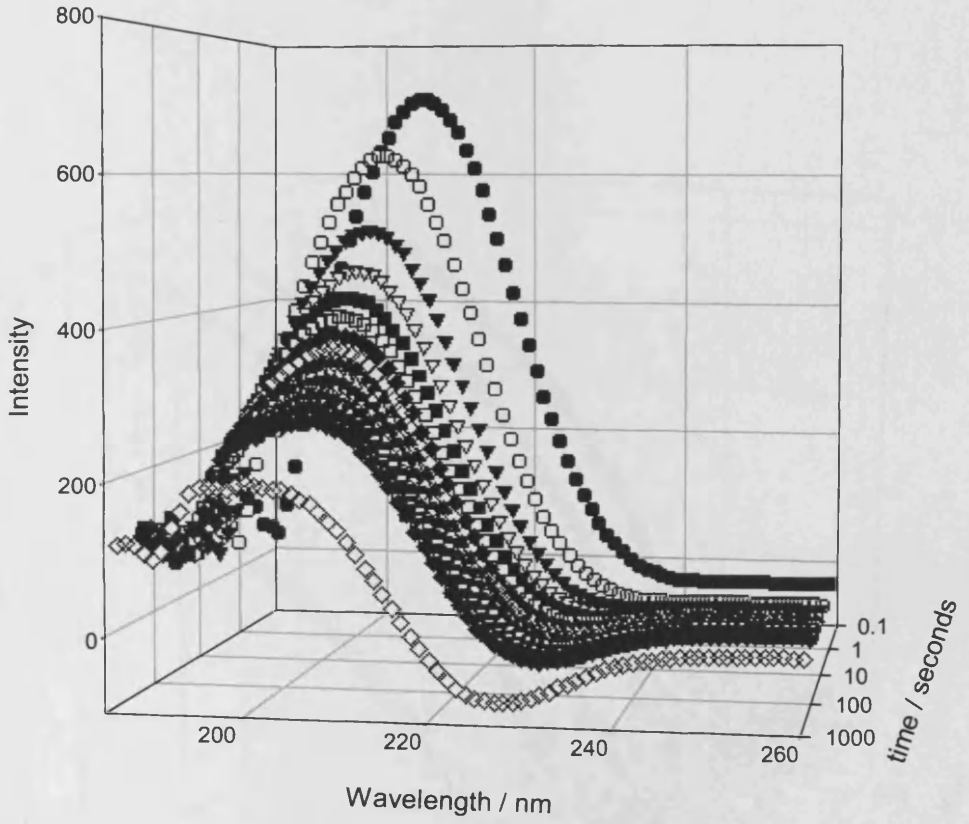
800
600
400
200
0
Intensity
200
220
240
260
Wavelength / nm
0.1
1
10
100
1000
time / seconds

3b

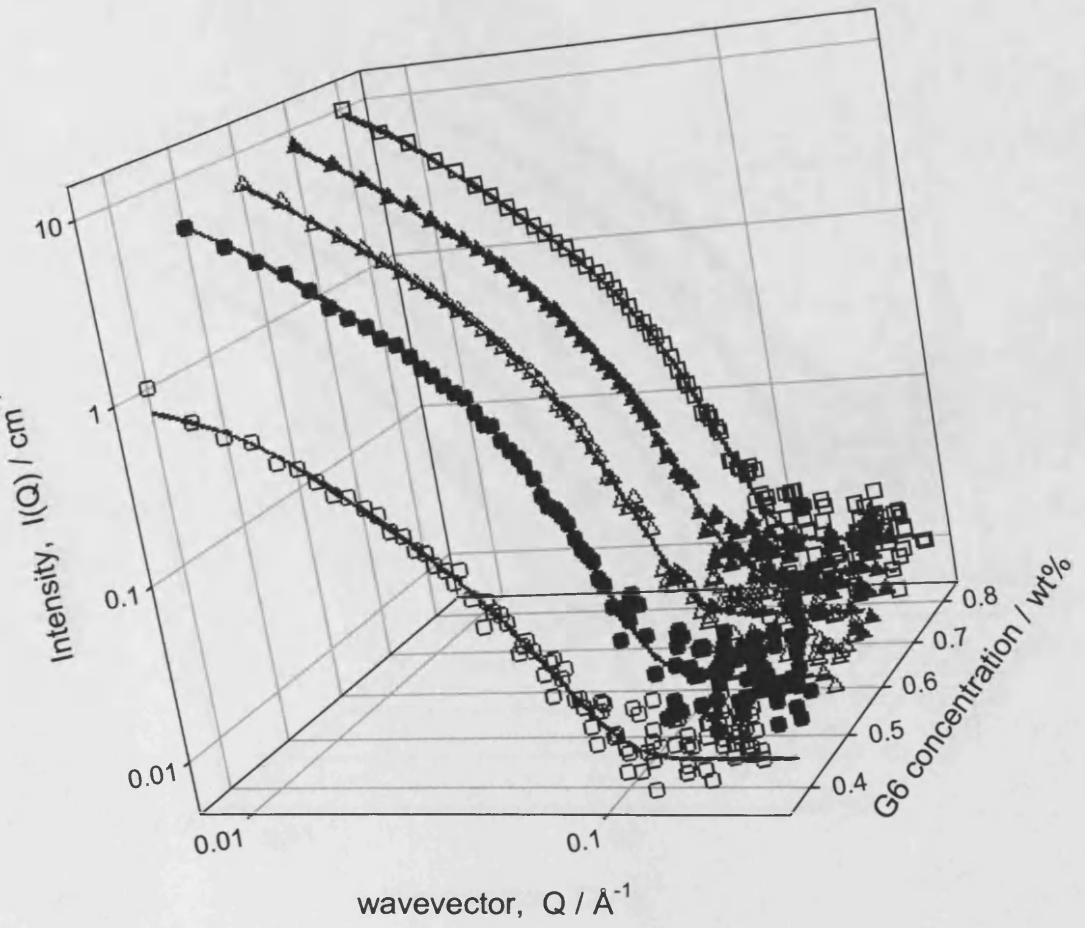
10
1
0.1
0.01
Intensity, I(Q) / cm$^{-1}$
0.01
0.1
wavevector, Q / Å$^{-1}$
0.4
0.5
0.6
0.7
0.8
G6 concentration / wt%

4a

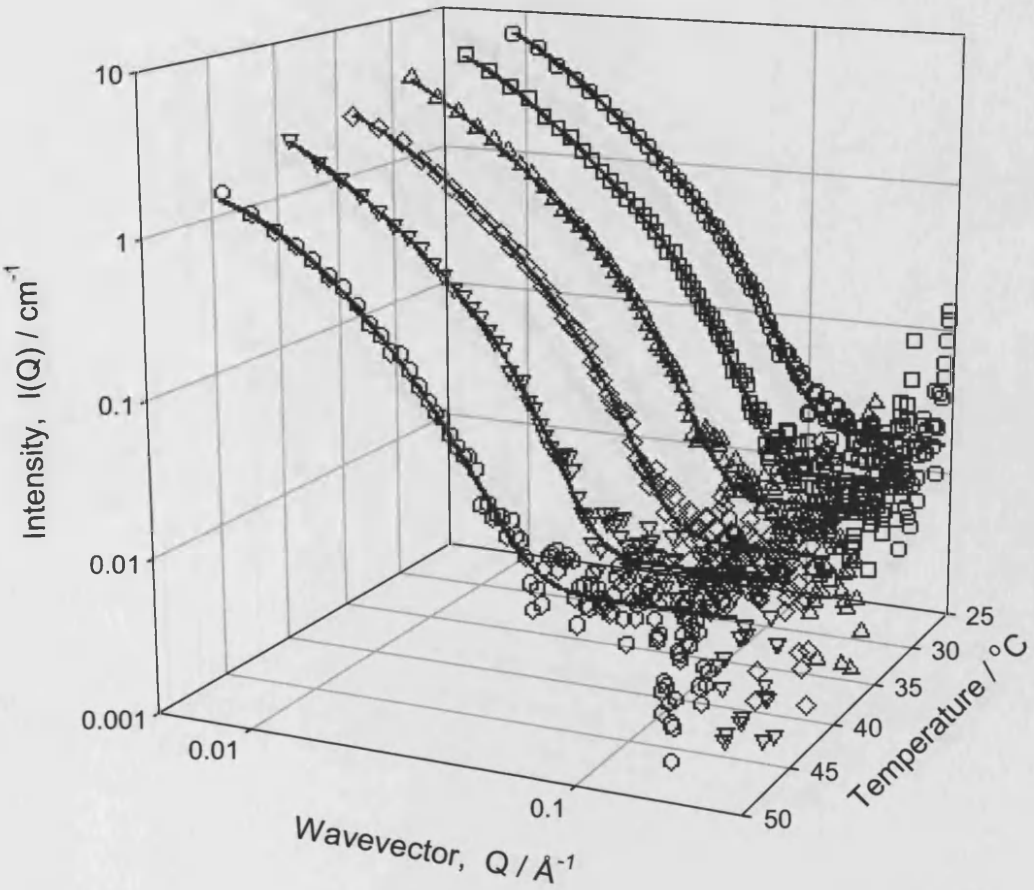
10
1
0.1
0.01
0.001
Intensity, I(Q) / cm-1
0.01
0.1
Wavevector, Q / Å-1
25
30
35
40
45
50
Temperature / °C

4b

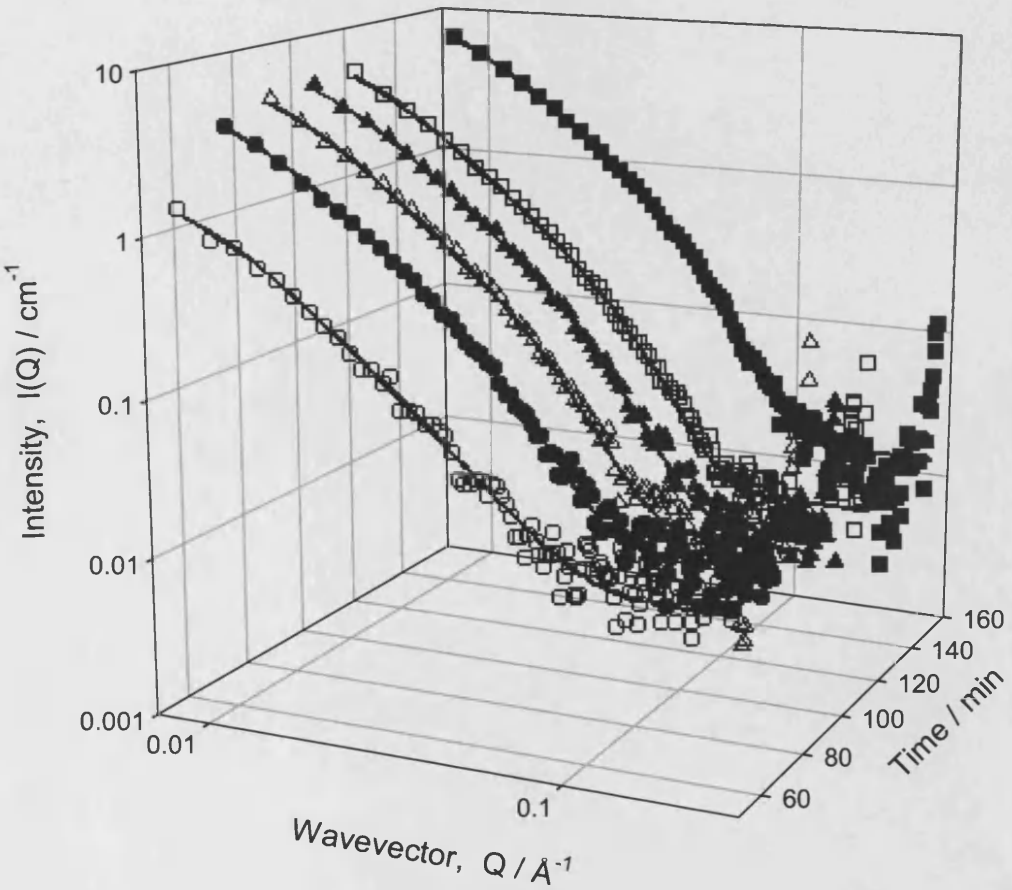


4c